Permafrost Degradation within Continuous Permafrost Zones due to Mining Disturbances in Canadian Northern Regions

(Contract 870055-11-0480: R493.1)

FINAL REPORT

Richard Wan, PhD, PEng
Ahmad Booshehrian, MSc.

Department of Civil Engineering
University of Calgary
Calgary, Alberta, T2N 1N4
CANADA

April 2015

EXECUTIVE SUMMARY

The work presented in this report is concerned with the numerical analysis of permafrost degradation within the continuous permafrost zone due to mining activities in Canadian Northern Regions. The study targeted the Kiggavik Uranium Mine project proposed in Nunavut where four open pits and one underground mine would be excavated into permafrost. The stability of the underlying permafrost is examined in both the short term corresponding to the mine operation period which is around 20 years, and the long term which encompasses both mine decommissioning and the climate change effect over a period of 2000 years and beyond.

The numerical computational work follows a series of incrementally complex hydro-thermal models whereby various physical processes such as phase change and unsaturated flow are considered to address the proper response of permafrost and tailings materials in a scientifically sound framework. Consolidation of tailings in the pits was assessed with large strain consolidation theory in conjunction with hydro-thermal analysis. All numerical computations, being time dependent, non-linear and hence iterative in nature, were successfully completed with the COMSOL commercial software in both two-dimensional and three-dimensional settings.

Part 1 of this report begins with an overview of the objectives and potential issues inherent in the Kiggavik project, and hence sets the scope of this study. This is then followed by a literature review on permafrost degradation and climate change modelling based on observational, theoretical, and numerical methods. This part sets the scene for the numerical modelling framework that will be used throughout this study for both the short-term and the long-term stability of permafrost.

Part 2 is concerned with the numerical modelling of the issues related to mining operation of the proposed four open pit mines (East Zone, Centre Zone, Main Zone and Andrew Lake). In particular, we investigated salient geotechnical aspects resulting from mining operations such as permafrost degradation, pit bottom heave due to pit excavation and underneath artesian porewater pressure, and groundwater inflow into the pits through a fault zone that cut through the pits. One important component of this part of the

report also relates to the calibration of the thermal models with available field and lab experimental data in view of determining the most plausible values of the various material parameters within a calculated level of confidence. These same data are also used for the long-term numerical modelling presented in Part 3. Main findings of the study conducted in Part 2 indicate that permafrost degradation around the pits or the tailings management facilities (TMFs) is not significant during mine operation and limited talik or no talik formation will occur as a result of depositing warm tailings into the pits. Under the assumed geotechnical conditions, the pit bottom floor heave is in the range of 30 to 50 mm, while the deformation of pit walls is in the range of 70 to 100 mm with some tensile stress zones developing along slope walls and crest of the pit. In addition, potentially non-negligible groundwater flow through faults at the bottom of the pit has also been calculated with sensitivity analyses.

Part 3 of the report addresses the long-term evolution of the permafrost starting from mine decommissioning. It begins with a brief review of the climate change issues and forecasts as reported in the recent Intergovernmental Panel on Climate Change (IPCC) reports. As such three climate change scenarios are selected for this study: (1) the *status quo* in temperature (i.e. no climate change), (2) a mean annual ground surface temperature increasing from -6°C to -1°C over 100 years, and (3) an extreme scenario where mean annual ground surface temperature would rise from -6°C to +1°C over 100 years. In the latter scenario, it is expected that all permafrost will thaw and the groundwater flow regime is specifically investigated. In Scenario 1, the permafrost thickness will reduce to about 120m and does not regain its original thickness (200m) even after 2000 years for both the Main and Centre Zone pits except for the East Zone pit where the permafrost could regain its original thickness. In Scenario 2 where a warming of +5°C is considered, it is shown that tailings will not freeze back under the Central Zone and the Main Zone where there is potential for contaminants migrating outward or downgradient to reach underground water aquifers and surface water bodies depending on the hydraulic conditions of the rock that is thawed. At the same time, a thickness of 35m permafrost layer would be maintained or produced on top. In Scenario 3, which considers the worst case with a temperature increase of +7°C, it is found that the whole permafrost layer (i.e. around 200m) would be thawed completely in about 600 years. However, the water level would remain at about 30m below the ground surface. The contaminants in the tailings pore

water will not likely to reach the ground surface at the location of the TMFs to pose significant adverse impacts to the surface environment immediately surrounding the decommissioned TMFs.

Part 1

A Review of Observational, Theoretical, Numerical Modelling

TABLE OF CONTENTS

LIST OF TABLES

LIST OF FIGURES

INTRODUCTION

The presence of permafrost and its susceptibility to naturally freeze and thaw under changes in the environment, whether natural (climate change) or anthropogenic (engineering activities), is a major problem in cold regions. Cold regions encompass most of Northern Canada where the mean annual ground temperature is below zero with extensive areas of ground remaining frozen throughout the year. Such frozen ground underlies nearly 50% of Canada's land surface (Heginbottom, 1995), which greatly complicates engineering activities and design in cold regions.

The definition of permafrost (Muller, 1943) as the thermal condition in the ground having a temperature below $0°C$ persisting over two consecutive winters and the intervening summer is somewhat vague and misleading since no distinction is normally made between the ground types. Permafrost is generally envisaged as frozen sediments and ice, but it also may consist of bedrock and organic material. Thus, a variety of materials is included in the permafrost. In some instances, the matrix may largely consist of ice, but in other cases permafrost may be a mixture of frozen mineral materials and ice. Ice may fill voids between the mineral particles and the quantity of ice in permafrost may be substantial. Moreover, the quantity of ice can show great variation. In some other situations the ice content may be so low that the condition is referred to as dry permafrost. Ice wedges are widespread throughout the permafrost zone. Permafrost can also contain unfrozen water at sub-zero temperatures due to surface tension and capillarity acting at the pore level to modify the thermodynamics and thereby cause a freezing point depression due to the so-called Kelvin's effect (Thomson, 1871). Thus, understanding the transitions between the solid and liquid phases of water is fundamental in evaluating the consequences of thermal disturbances on the properties and behaviour of permafrost.

Over periods of years, or decades, the frozen ground may slowly thaw or slowly increase in extent, either because of changes at the ground surface that modify the exchange of heat energy through it, or because of slow changes in the atmospheric climate (climate change). Therefore, a surface layer thaws and refreezes every year. Additionally, engineering activities often disturb the frozen ground through changes of the properties (e.g. mechanical strength, thermal and hydraulic conductivities) at temperatures near $0°C$. These are particularly problematic to the design of gas pipelines, highways and mines.

Major engineering problems in permafrost are caused by frost heave in finely porous materials such as soils, wherein water moves from warmer underlying regions into the freezing material followed by continuous expansion of water upon freezing. The development of large heaving pressures produces uneven ground displacements as illustrated in a naturally occurring land form structure such as a Pingo (Mackay, 1972). The latter structure forms a mound above ground due to the growth of a massive core of ice under the action of massive heaving pressures over the years. On somewhat a smaller scale, the same process may be at work in a slow creeping slope movement, causing

distress to engineering structures such as roads, railways or pipelines. Thawing of ice rich permafrost is another problem whereby cavities in the soil pores are formed leading to ground surface subsidence (settlements) due to gravity effects. From an engineering viewpoint, there is a loss in mechanical strength of the permafrost upon thawing due to attendant liberation of water and pore pressure created, thus compromising the stability of any structures built on or founded into the ground. This phenomenon can be fairly well described within the theory of thaw consolidation (Morgenstern and Nixon, 1971).

On the other hand, naturally-occurring features resulting from the differential thawing of ground ice fall under the term thermokarst with lake growth (Hopkins, 1949, Burn and Smith, 1993). More precisely, events that cause permafrost to melt such as climate variations or human activities may destroy the ground cover and thereby create thermokarst topography. In the same context, a talik is a layer of year-round unfrozen ground that lies in permafrost areas (Lachenbruch et al. 1962; Mackay, 1997; Burn, 2002). In regions of continuous permafrost, taliks often occur underneath shallow thermokarst lakes and rivers, where the deep water does not freeze in winter and thus the ground underneath will not freeze either. Sometimes closed, open and through talik are distinguished. These terms refer to different situations as to whether the talik is completely surrounded by permafrost, is open to the top, or open to both top and unfrozen layers beneath the permafrost, respectively.

Talik development has a significant influence on the physical, chemical, biological, and geomorphological processes occurring in the ground under and around thaw lakes. Taliks cause thaw settlement and permafrost degradation, decreasing the ability of the permafrost to support a load and seriously affecting the performance of structures constructed in permafrost regions (Johnston and Brown, 1964).

Mining development in permafrost regions mostly concerns permafrost degradation issues. For instance, the construction of open pit mines in permafrost with subsequent filling with tailings materials and water presents a scenario similar to a thermokarst lake that causes a local drift from ground temperatures, thus resulting in talik formation in the underlying permafrost. Such a mechanism is central to permafrost degradation which greatly complicates mining activities under such ground conditions. The thawing of the permafrost underneath the open pit increases the mobility (diffusion) of fluids such as acids and radionuclides (Moore and Shackelford, 2011) through pores or fractures in the ground which was previously a barrier to any fluid flow in the frozen state. Although the mechanisms by which taliks are formed are somewhat well-known, its proper numerical analysis depends on the accuracy of the initial temperature profile in the underlying ground, thermal boundary conditions, surface temperature changes characterizing the ground disturbance, water depth and configuration (including physical, thermal and hydraulic characteristics) of the permafrost beneath the lake. The most current numerical modelling of talik formation under thaw lakes is attributed to the work of Ling and Zhang (2003). Even then, the mathematical model is classic and based on a two-dimensional heat transfer formulation with phase change in axi-symmetric conditions. Approximate analytical solutions for determining the depth of a talik formed below a lake as a function of size and geometry are given in Burn (2002).

In this report we review general theoretical/analytical/numerical methods that are currently used to model permafrost freezing and thawing in relation to the Kiggavik Project. Most of the work discussed revolves around the central topic of heat flow in porous media with phase change. More complexities can be further embedded in the modelling by coupling other pieces of physics involving various transport mechanisms. For instance, heat flow, fluid flow and mechanical aspects of the porous material can be all coupled together with added features of unsaturated flow, thermal/hydraulic depend material properties and mechanical discontinuities in the form of fractures and shear zones, among others. The modelling of climate change related disturbances will also be touched upon.

The review materials we have chosen are not exhaustive, but the links to the Kiggavik Project are clear.

THE KIGGAVIK PROJECT

The project outline was given in the contract documents, while more details can be found in the NIRB (Nunavut Impact Review Board) documents. Here, we just recall succinctly the major issues in this project as a prelude to this brief literature review.

Essentially, the project relates to the numerical evaluation of both short term and long term stability of deep permafrost into which four open pit uranium mines will be excavated. The mine plan will be such that the problematic waste rock will be stored in one of the pits subsequently flooded with water whereas other three will be converted to in-pit tailings management facilities (TMFs). Hence, the main questions at stake are as follows:

- How deep can the open pit mines be before the underlying permafrost is disturbed, and hence degrades? The thickness of the permafrost below the pits is expected to vary between 0 and 120m at the Kiggavik site, and the Andrew Lake pit at the Sissons site will penetrate permafrost.

- What is the potential for talik formation (open or bulb type) into the permafrost, given that the pits will be filled up with water, special waste rock, or tailings materials? Once an open talik is formed or the excavation penetrates permafrost, this will cause a drainage path for uranium leachates and radionuclides to seep into the deeper layers into the aquifer, or artesian groundwater beneath permafrost to recharge back into the pits with potential floor heave, which eventually could overflow the pits if no mitigation measures are taken. The existence of a fault zone could facilitate the groundwater flow if it acts as a preferential flow channel. Hence, these could cause potential environmental problems; see Figure 1.

- What are the extents of permafrost evolution during the mine operation/decommissioning period (which is around 20 years) and in the long

term, considering the effects of climate change and global warming? This includes degradation and restoration of permafrost in both short and long terms following different plausible scenarios.

The Kiggavik site project area is located within the continuous permafrost zone of Canada. The general surficial geology consists mainly of glacial till (silty sand, gravel and clay), a metre to several metres thick, underlain by frozen bedrock which is exposed along the fault controlled escarpments. The thickness of the active layer is variable from 1 to 2m. The shallow part of the bedrock, approximately 9m thick, shows signs of some fracturing by frost action and is composed of sandstone conglomerate, orthoquartize, granite, metasediments and intrusive units. Deeper into the ground at 200m typically, fractured unfrozen basement rock is present in which ground water flow occurs with some indication of artesian pressure.

The geothermal gradient is $32\text{m}/^{\circ}\text{C}$ while the mean annual ground temperature of the undisturbed permafrost is between -6° and -7°C.

Figure 2 shows schematically the problem at hand and its mathematical representation with several processes occurring. The tailings, made up of about 60% water at relatively warm temperature (10-20 $^{\circ}\text{C}$) in the mine pit, act as a heat source that induces heat flow into the surrounding permafrost in the form of conduction with phase change. This heat source translates into a convective type of boundary condition from the mathematical modelling view point. Thawing of the permafrost increases hydraulic conductivity that could facilitate ground water flow and mine contaminants through the fault up to the ground surface. The problem at hand is surely multiphysics in nature, involving several coupled processes.

MODELLING APPROACHES

There exists a whole palette of models including various physics with increasing complexity to mathematically and computationally evaluate processes occurring in permafrost. On the other hand, the amount of data needed to obtain reasonable results increases with model sophistication as more processes are added. As such, the question at hand is about choosing the most appropriate model in relation to the availability of data for the problem under investigation as pointed out by Riseborough et al. (2008). For instance, in the Kiggavik project, details of lateral variations of surface and subsurface conditions are very important aspects that must be included into the modelling and one-dimensional conditions would not be appropriate. Also, thermal boundary conditions have to be well defined in relation to the ground/air temperature and the characteristics of the tailings materials in the pit, including sequence of dumping.

In general, so-called process based permafrost models determine the thermal state of the ground both temporally and spatially based on principles of heat transfer. Turning to the temporal aspect, either equilibrium (steady state) permafrost conditions for a given annual thermal regime, or the transient evolution of permafrost conditions from some

initial state to a modeled current or future state are sought. As for the thermal aspect, simple models may define the permafrost, active layer depth, or mean annual ground temperature based on empirical and statistical relations or transfer functions between the atmosphere and the ground. As such, numerical models based on finite elements or finite differences are used to compute the annual and longer term evolution of the subsurface temperature field both spatially and temporally. The surface energy exchange enters through boundary conditions defined by simplified parameters such as freezing/thawing indices and n-factors, or air temperature and snow cover (Lunardini, 1978). Even better, fully explicit energy balance equations requiring data from atmospheric conditions may be used.

To motivate the following treatment, we note that the theoretical approach is based on the heat flow through simple materials as a provisional assumption. Then, the porous media and multiphasic character of the permafrost with inherent heterogeneities will be considered.

Basic heat flow

The basic heat flow theory is covered in celebrated works such as those of Carslaw and Jaeger (1959). Before going into frozen ground physics, we start off with the basic 1-D heat flow under transient conditions with conduction as main heat transfer mechanism, i.e.

$$C\frac{\partial T}{\partial t} = k\frac{\partial^2 T}{\partial z^2} \tag{1}$$

where $T =$ temperature (°C), $z =$ depth (m), $t =$ time (s), $C =$ volumetric heat capacity ($\mathrm{Jm^{-3}}$) and $k =$ thermal conductivity ($\mathrm{Wm^{-1}K^{-1}}$).

Analytical solutions of Eq. (1) for a semi-infinite and isotropic half-space define the ground temperature at any time t and depth z with the ground surface experiencing either a sinusoidal temperature variation or a step temperature change (ΔT_s) solution exist. These are given as:

$$\text{sinusoidal case: } T(z,t) = \overline{T} + A_s e^{-z\sqrt{\frac{\pi}{\alpha P}}} \sin\left(\frac{2\pi t}{P} - z\sqrt{\frac{\pi}{\alpha P}}\right) \tag{2a}$$

$$\text{step change case: } \Delta T(z,t) = \Delta T_s \, erfc\left(\frac{z}{2\sqrt{\alpha t}}\right) \tag{2b}$$

where $A_s =$ annual temperature amplitude at ground surface (°C), $T_s =$ surface temperature, $\overline{T} =$ mean annual temperature, $\alpha = k/C$, thermal diffusitivity and $P =$ period of temperature wave in seconds.

The solutions given in Eqs. (2a, b) obviously do not include phase change due to freezing or thawing of permafrost. Latent heat of fusion release or absorption which dominates heat flow in ground freezing or thawing must be considered. Also, the temperature dependence of the thermal conductivity of water and ice need to be introduced. Another level of complexity arises from the fact that we are faced with a porous multiphasic medium so that volume fractions of the water and ice and grain mineral phases must enter the heat flux balance equation. As such, exact analytical solutions as in Eqs. (2a, b) with phase change are limited to only a few idealized conditions. For instance, the Stefan-Neumann solution is very often used to finding the moving freezing (or thaw) front with the assumption that the diffusive effects are small relative to the rate of frost front motion and the initial temperature of the ground is close to 0°C (Lunardini, 1981).

Numerical techniques are thus used to solve the complex governing equations that now involve temperature dependent thermal properties, variation of volume fractions of the various phases and the position of a propagating freezing or thawing front. This refers to the so-called free boundary value problems in mathematical physics involving an internal moving front as part of the solution to the problem, which are not easy to solve due to inherent non-linearities (Ockendon et al., 1999).

According to the literature, most numerical analyses of permafrost degradation due to both natural and engineering disturbances are based on solving the classical heat transfer (conduction and advection) with phase change problem in a porous medium. The most popular solution methods include the so-called heat enthalpy method, first proposed by Eyres et al. (1946), in which the problem is reformulated in such a way that the Stefan condition (jump in heat flux due to phase change) is implicitly bound into a new form of the heat equations that are now applied over the whole fixed domain. Variations of the heat enthalpy method with a focus to track down the sharp discontinuous ice/water front can be found in Wan et al. (2003) using a freezing index method that modifies the variational principles of the original governing equations of heat flow with phase change.

In the next sections, the enthalpy method will be outlined with just enough detail for the reader to appreciate the versatility in dealing numerically with the phase change aspect, even under non-isothermal conditions.

Heat enthalpy method

The heat enthalpy conservation equation has been the basis of describing heat transport in a three-phase porous medium comprising rock matrix, ice and water such as permafrost, see Bense et al. 2009; Delisle, 1998 and Hartikainen, 2006, among others. Other phases and transport mechanisms can be readily added (e.g. Mallants, 2006).

Thus, considering heat transport only occurring by conduction,

$$C_{eq}\frac{\partial T}{\partial t}+\nabla.(-K_{eq}\nabla T)-Q=0 \qquad (3)$$

where C_{eq} = volumetric heat capacity (J/K.m^3), K_{eq} = effective thermal conductivity (W/m.K) and Q = heat source (W/m^3).

Both an equivalent volumetric heat capacity and an effective thermal conductivity are herein introduced to account for the thermal effects of freezing and thawing in the presence of the three phases, i.e. rock matrix, ice and water, through the definition of volume fractions θ_i $(i = m, w, i)$ referring to matrix, water and ice, respectively:

$$\theta_m = 1 - \phi;\ \theta_w = \phi\Theta;\ \theta_i = \phi - \theta_f \qquad \theta_m + \theta_w + \theta_i = 1 \tag{4}$$

As such, the three-phase medium is basically characterized by ϕ, the porosity of the rock and Θ, the fraction of the pore space occupied by water.

Equivalent heat capacity

To account for the phase change whereby latent heat of freezing/fusion, L, of water is liberated (absorbed) during freezing (thawing), its effect is incorporated into the so-called equivalent heat capacity worked out as a volume average, i.e.

$$C_{eq} = \theta_m \rho_m c_m + \theta_f \rho_f \left(c_f + \frac{\partial \Theta}{\partial T} L \right) + \theta_i \rho_i \left(c_i + \frac{\partial \Theta}{\partial T} L \right) \tag{5}$$

where ρ_i = the density (kg/m^3) of the various phases, and c_i = specific heat capacity of the various phases (J/K.Kg).

A discontinuity in heat flux is to be expected at the interface between ice and water where complicated processes occur in the porous medium in the presence of a so-called mushy zone (mixture of solid and liquid phases between the solidus and liquidus temperatures). As such, this is idealized through the addition of energy sources (sinks) due to freezing (thawing) involving a normalized pulse ($\partial\Theta / \partial T$) around the temperature transition. The integral of $\partial\Theta / \partial T$ must be equal to unity to satisfy the condition that the 'pulse' width denotes the range between the liquidus and solidus temperatures (see Mottaghy and Rath, 2006, or Noetzli and Gruber, 2009). Figure 3 illustrates the functional shape of the equivalent heat capacity with the 'pulse' to accommodate for latent heat during phase change.

The equivalent heat capacity is also able to describe non-isothermal phase change with variable solidification/melting temperatures. This aspect is particularly relevant to permafrost implicating very fine porous materials like rock with microfractures where supercooling due to capillarity may exist, i.e. Kelvin's effect (Thomson, 1871). It is to be noted that the current project involves permafrost in mainly metasedimentary rock

containing fractures caused by episodes of post glaciations frost action and traversed by a major fault or shear zone.

Heat conductivity

Normally during freezing/thawing, thermal conductivity of water and ice are normally introduced depending on the phase change progression in space. However, Mottaghy and Rath, 2006) consider the use of an equivalent thermal conductivity calculated as a weighted square-root mean of the individual properties of the various phases has greater physical significance than considering thermal conductivity to be discontinuous with temperature. Also, it provides easier implementation in numerical models. Thus, introducing matrix, water and ice content dependencies,

$$K_{eq} = \left(\theta_m \sqrt{K_m} + \theta_i \sqrt{K_i} + \theta_w \sqrt{K_w} \right)^2 \tag{6}$$

where K_i $(i = m, i, w)$ refer to thermal conductivities of rock matrix, ice and water phases, respectively.

Water flow in permafrost – fractured rocks

Permafrost is considered to be virtually impervious, except in the active zone where water flow is relevant. We note further the important question of discontinuous and continuous permafrost as this will allow ground water flow. The dumping of tailing materials into the pit may lead to the formation of taliks that would act as conduits for ground water flow. At the Kiggavik site, the hydraulic conductivity of permafrost in metasedimentary rock containing fractures caused by episodes of post glaciations frost action and traversed by a major fault can be as low as 10^{-10} m/s . However, upon thawing due to the dumping of tailings into the pit, taliks may form and act as conduits for ground water flow. The increase in permeability of permafrost is essentially due to the thawing of ice within the fractures/microfractures. The problem is then reduced to the analysis of flow through a network of fractures. Classical treatment of this type of problem can be found in ground water flow modelling and contaminant transport in fractured rocks or in petroleum engineering problems (Freeze and Cherry, 1979; Evans and Nicholson, 1987; Preuss and Narasimhan, 1985). As an improvement on existing models, a mechanistic approach would be to develop pertinent mathematical equations in such a way that a fracture network undergoing freeze/thaw can be encapsulated into a continuum formulation with equivalent physical and thermal properties derived by means of a homogenization technique (Wan et al. 1990). Knowing the fracture spacing and orientation, the equivalent permeability tensor can be derived, which then enters into a classic fluid flow model. Figure 4 shows a fracture network which can be extracted from geological mapping (fracture frequency, spacing and orientation) and its mathematical representation through a second-order fracture tensor that can be used to derive a

permeability tensor and other thermal parameters through homogenization and as discussed in the above.

Climate change issues

Several approaches have been used in the literature to predict the effects of climate change ranging from surface energy balance models to empirical permafrost index models. For instance, surface energy balance models attempt to account for energy exchanges involved in the surface heat balance in which ground surface (or snow) temperature and a large number of radiative, thermal and aerodynamic parameters are required as input in the model (Outcalt, 1972; Anisinov, 1989). Essentially, we require substantial amount of data to enter a heat transport model, i.e., the original thermal state of the permafrost, thermal properties of each soil layer, geothermal heat flow and the magnitude as well as timing of the warming.

It is important to explicitly account for the various transfer processes that dictate the surface temperature regime in terms of soil, vegetation, topographic and snow cover conditions. However, fully explicit energy balance approaches are not suitable for regional impact assessment due to limited data base characterizing the microclimate of a broad range of vegetation and terrain conditions. Hence, for regional permafrost model, a simplification of surface energy balance computations is needed to reduce the number of local variables by correlating microclimatic variables with ground temperatures in a variety of microclimatic environments (Jorgensen and Kreig, 1988).

Semi-empirical models involve the determination of the soil temperature from air temperature through the use of empirical n-factors (Lunardini, 1978). Then, rather than using heat-transport equations to determine the ground-thermal regime response, a frost number or index is calculated based on the ratio of the depth of freezing and thawing (Nelson and Outcalt, 1983). As such, the method uses minimal climatic, soil and snow cover information to delineate the broad equilibrium features of permafrost distribution.

In the absence of any climatic data, Kane et al. (1991) steadily increased surface temperature boundaries in a heat conduction model by $4^{\circ}C$ over 50 years to simulate climatic change. The active layer doubled from 0.5 to 1.0m. The model does not accommodate for any seasonal changes, nor examine changes in snow cover, even though those are important as pointed out in the works of Goodrich (1982) and Stuart et al. (1991).

In summary, the dynamics of freezing and thawing due to climatic change is complex and relatively little research has been focused on explicitly understanding the climatic relations of processes in permafrost environments. It seems that the degradation or aggradation of permafrost close to the ground surface may well be modelled with input stemming from climate models, but extrapolation into the ground underneath must be done with caution. For an objective study, we may have to include (a) relations between permafrost temperatures and past climates, (b) relations between near-surface ground

thermal conditions and climatological parameters; and (3) the effects of climate changes on processes and features in permafrost terrain.

In this project, we may consider various plausible scenarios for the post decommissioning phase of the mines based on a more profound study of climate change issues in the Northern Regions as a number of challenges in developing long term prediction models remain. For instance, we may explore three cases: (1) no climate change whereby the mean annual ground temperature remains between -6° and $-7^{\circ}\mathrm{C}$, (2) a steady increase of ground surface temperature of $3^{\circ}\mathrm{C}$ during 30 years after closure, followed by another $5^{\circ}\mathrm{C}$ increase in the next 100 years or so, and (3) using air temperature data predictions by Environment Canada that include the anticipated seasonal changes for the next 150 years or more, converted into ground surface temperatures using n-factors to account for snow cover and vegetation, among others.

Some preliminary numerical modelling

As a preliminary exercise, some numerical modelling of permafrost warming has been carried using the multiphysics software COMSOL Multiphysics (2011). At this stage no new model implementation has been carried out and only the heat transfer module with phase change was used. Also, the porous medium aspect of the problem is not considered so that respective volume fractions of water, ice and solid matrix do not enter the computations. It is noted that some numerical modelling work on the Kiggavik project, also based on the COMSOL software, has been previously carried out for preliminary assessment by CNSC (Canadian Nuclear Safety Commission), see Dagher et al., 2012.

Figure 5 shows a 2-D cross-section in axi-symmetry of a pit with dimensions comparable to those in the Kiggavik project. The boundary conditions are such that the bottom of the permafrost layer is subjected to a heat flux corresponding to the geothermal gradient. The tailings in the pit represent a heat source that can be mathematically replaced by a convective thermal boundary condition (Robin type) as opposed to imposing a fixed temperature (Dirichlet type) on the pit bottom and sides. The ground surface is fixed to $-9^{\circ}\mathrm{C}$ while the far lateral boundary and the centre line of the pit are fixed to zero thermal flux conditions. The temperature of the pit is set to $25^{\circ}\mathrm{C}$. Table 1 gives the various thermal parameters used in the modelling for ice and water.

The simulation was run until steady state is reached after 350 years or more when an open talik is finally formed under the bottom of the pit. Figure 6 shows the progression of warm temperatures in the permafrost, whereas Figure 7 depicts the evolution of temperature profiles with depth along the centre line of the pit. After 450 years, the thawed depth below the bottom of the pit has reached approximately 100m.

The numerical simulations reported in this section, although somewhat crude, serve as a basis upon which more complicated models will be developed with various boundary

conditions that mimic the different aspects of operations in the mine pit, and several scenarios of climate change will be ultimately considered.

SUMMARY

This literature review has been conducted on the mathematical modelling of permafrost degradation under natural processes and due to engineering disturbances in northern climates. One of the findings is that the problem of open pit mining disturbance to an underlying deep continuous permafrost layer can be examined in a similar manner to the study of thermokarst lake and talik formation in permafrost terrain due to disturbances caused by climate warming. According to the literature, most numerical analyses of permafrost degradation due to both natural and engineering disturbances are based on solving the classical heat transfer (conduction and advection) with phase change problem in a porous medium. The most popular solution methods include the so-called heat enthalpy technique in which the problem is reformulated in such a way that the Stefan condition (jump in heat flux due to phase change) is implicitly bound into a new form of the heat equations that are applied over the whole fixed domain. Another method reviewed is the effective heat capacity method whereby the heat capacity of the geomaterial is made directly proportional to the stored and release energy during phase change and specific heat. As such it is possible to describe non-isothermal phase change with variable solidification/melting temperatures. This aspect is particularly relevant to permafrost implicating very fine porous materials like rock with microfractures where supercooling due to Kelvin's effect may exist. It is to be noted that the current project involves permafrost in mainly metasedimentary rock containing fractures caused by episodes of post glaciations frost action and traversed by a major fault. Concerning the modelling of freeze/thaw in permafrost, it is important to incorporate thermal and hydraulic properties as a function of ice content. These include the effects of ice on the thermal conductivity, hydraulic conductivity and heat capacity change as a function of ice content based on volume weighted averages. In particular reference to the project, the problem of freezing and thawing in a fractured rock has been researched in the literature. The literature on the thermo-hydro-mechanical behaviour of permafrost in fractured rock is scarce. However, concepts can be borrowed from other areas of geomechanics. One idea is to develop pertinent mathematical equations in such a way that a fracture network undergoing freeze/thaw can be encapsulated into a continuum formulation with equivalent physical and thermal properties derived by means of a homogenization technique.

The permafrost and climatic change issue has been briefly touched upon in this preliminary literature review. The dynamics of freezing and thawing due to climatic change is complex and relatively little research has been focused on explicitly understanding the climatic relations of processes in permafrost environments. It is important to include transient aspects of the problem and there must be some coupling between the atmospheric climate and the ground. The latter can be simply accomplished by using generalized methods based on n-factors (Lunardini, 1978; Nixon, 1990), while seasonal fluctuations of precipitation and temperature should be incorporated as well.

Table 1. Thermal parameters used for water and ice

	Water	Ice
Density [kg/m^3]	997	918
Specific heat [J/kg K]	4180	2090
Thermal conductivity [W/mK]	0.6	2.2

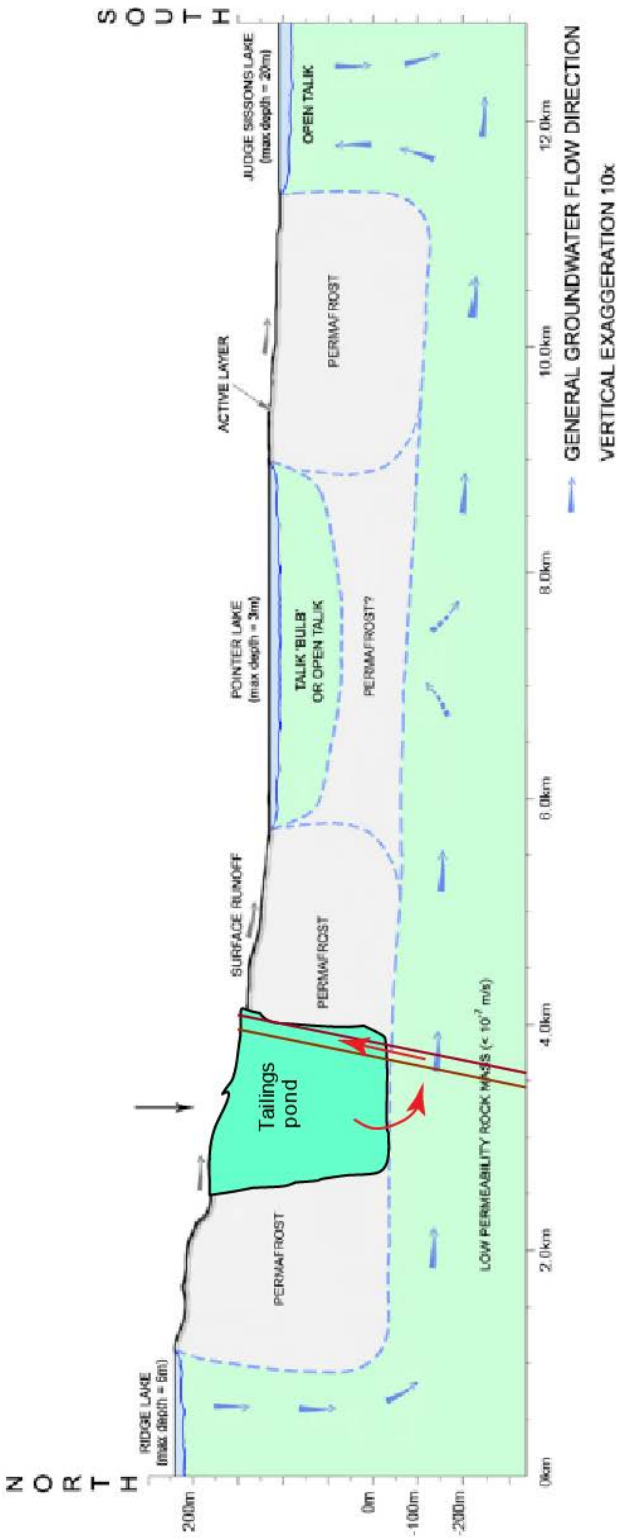

Figure 1. Potential ground water flow due to permafrost degradation

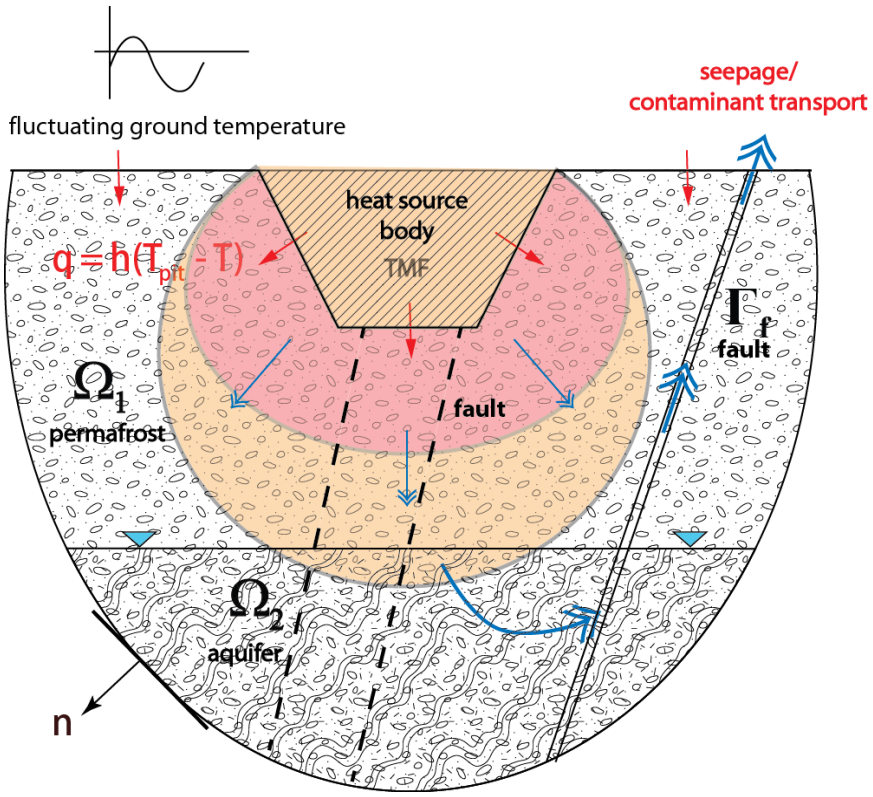

Figure 2. Idealization of the physical problem - mathematical representation

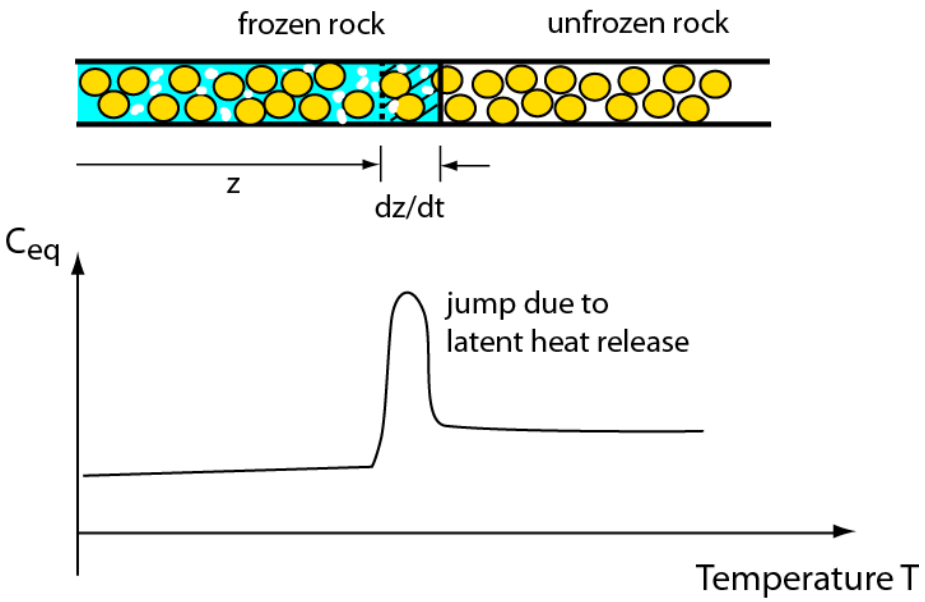

Figure 3. Incorporation of latent heat through an equivalent heat capacity with a pulse

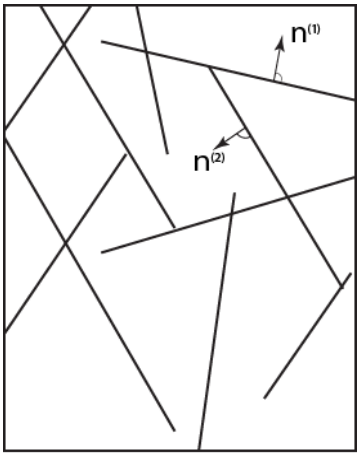

fracture tensor:

$$K_{ij} = \frac{1}{4\pi}\int_{\Omega} n_i n_j \; f(\mathbf{n})\, d\Omega$$

Figure 4. Mathematical representation of fracture network through a fracture tensor

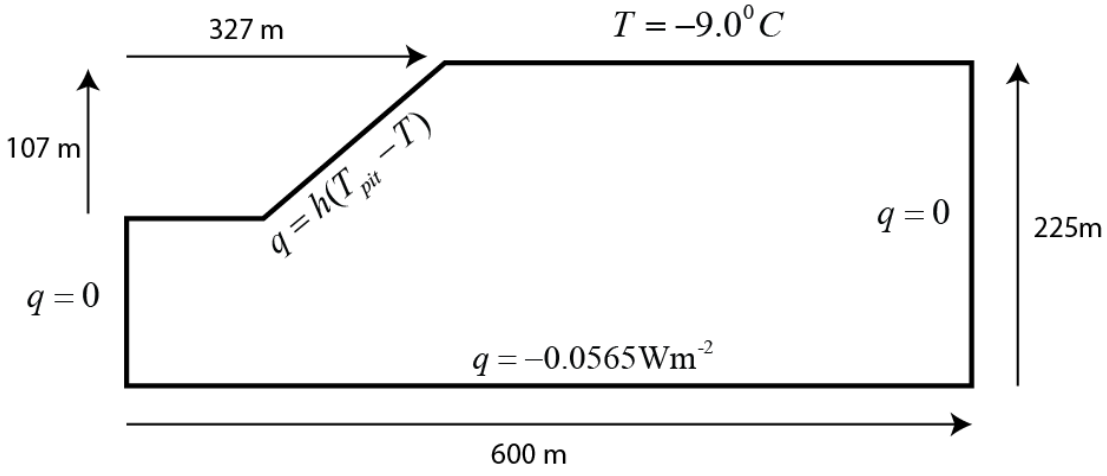

Figure 5. Finite element mesh representing a 2D section of pit (in axi-symmetry)

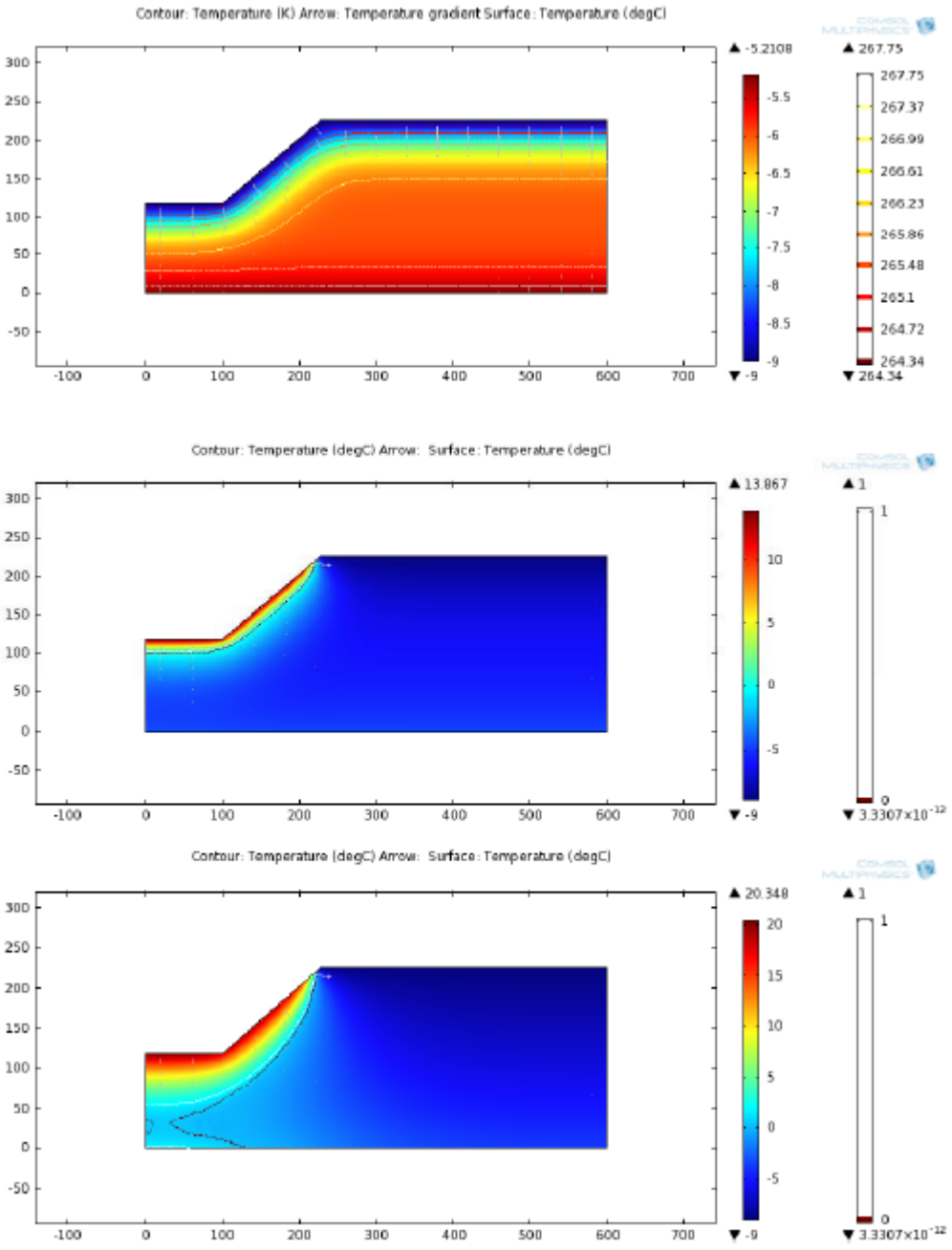

Figure 6. Evolution of temperatures underneath pit and open talik formation: (a) initially, (b) after 60 years, (c) after 350 years – dark line refers to zero degree isothermal

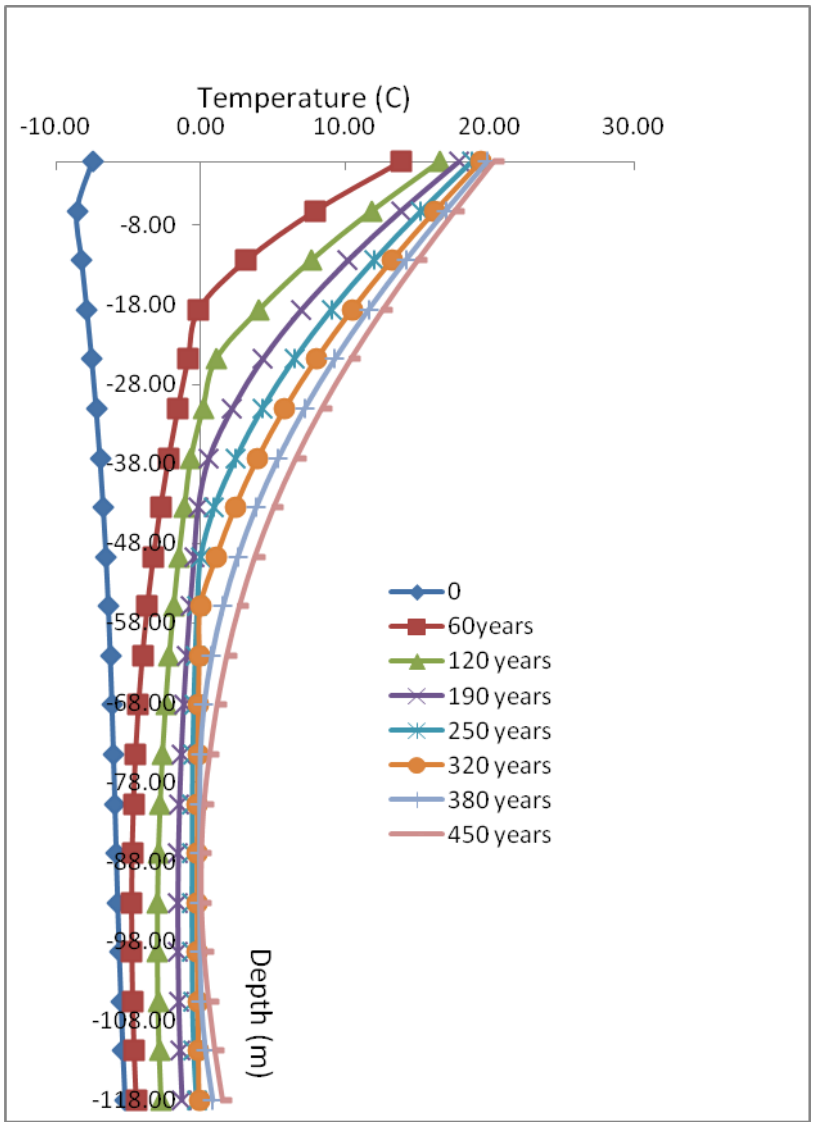

Figure 7. Temperature profiles with time along centre of the pit

REFERENCES

1. Anisimov, O. A. 1989. Changing climate and permafrost distribution in the Soviet Arctic. Physical Geography, 10, 285-293.
2. Bense, V.F., Ferguson, G., Kooi, H. 2009. Evolution of shallow groundwater flow systems in areas of degrading permafrost. Geophysical Research Letters, 36.
3. Burn, C. R. 2002. Tundra lakes and permafrost, Richards Island, Western Arctic Coast, Canada, Can. J. Earth Sci., 39, 1281– 1298.
4. Burn, C.R. and Smith, M.W. 1993. Issues in Canadian Permafrost Research. Progress in Physical Geography June 1993, 17(2), 156-172.
5. Carslaw H.S., Jaeger J.C. 1959. Conduction of Heat in Solids, 2nd Ed. Oxford University Press: Oxford.
6. Dagher, E.E., Nguyen, T.S., Su, J.G. 2012. Numerical Modelling of Coupled Heat Transfer and Groundwater Flow: Applications to Tailings Management Facility in Permafrost Environments in Northern Canada, Proceedings of the 65th Canadian Geotechnical Conference, September 30-October 3, 2012, Winnipeg, Manitoba, 10p.
7. COMSOL, 2011, COMSOL Multiphysics 4.2a, Earth Science Module, COMSOL Inc. Los Angeles, CA 90024, USA.
8. Delisle, G. 1998. Numerical simulation of permafrost growth and decay. Journal of Quaternary Science 13, 325-333.
9. Eyres, N.R., Hartree, D.R., Ingham, J., Jackson, R., Sarjant, R.J. and Wagstaff, J.B. 1946. The calculation of variable heat flow in solids, Phil. Trans. R. Soc. London, A 240, 1-57.
10. Evans, D., and T. Nicholson (eds.). 1987. Flow and Transport Through Unsaturated Fractured Rock, Geophys. Monograph 42, American Geophysical Union, Washington, D.C.
11. Freeze, R.A., and J.A. Cherry. 1979. Groundwater, Prentice-Hall, Inc., Englewood Cliffs, N.J.
12. Goodrich, L. E. 1982. The influence of snow cover on the ground thermal regime. Canadian Geotechnical Journal, 19, 421-432.
13. Hartikainen, J. 2006. Numerical Simulation of Permafrost Depth at Olkiluoto. Posiva 2006-52.
14. Heginbottom, J.A., Dubreuil, M.A., and Harker, P.A. 1995. Canada – Permafrost; National Atlas of Canada, Natural Resources of Canada, Ottawa (MCR 4177), scale 1:7 500 000.
15. Hopkins, D. M. 1949. Thaw lakes and thaw sinks in the Imuruk lake area, Seward Peninsula, J. Geol., 57, 119–131.
16. Johnston, G. H., and Brown, R.J.E. 1964. Some observations on permafrost distribution at a lake in the Mackenzie delta, N.W.T., Canada, Arctic, 17, 162–175.
17. Jorgenson, M. T. and Kreig, R. A. 1988. A model for mapping permafrost distribution based on landscape component maps and climatic variables.

Permafrost, 5th International Conference Proceedings, 1, Trondheim, Norway, Tapir, 176-182.
18. Kane, D.L., Hinzman, L.D. and Zarling, J.P. 1991. Thermal response of the active layer to climatic warming in a permafrost environment. Cold Regions Science and Technology 19, 111-22.
19. Lachenbruch, A. H., M. C. Brewer, G. W. Greene, and Marshall B.V. 1962. Temperatures in permafrost, in Temperature—Its Measurement and Control in Science and Industry, vol. 3, part 1, pp. 791– 803, Reinhold, New York.
20. Lunardini V.J. 1981. Heat transfer in cold climates. Van Nostrand Reinhold: New York.
21. Lunardini, V.J. 1978: Theory of n-factors and correlation of data. In Permafrost, Third International Conference, Proceedings, Volume 1, Ottawa, Ontario: National Research Council of Canada, 40-46.
22. Mackay, J. R. 1997. A full-scale field experiment (1978 –1995) on the growth of permafrost by means of lake drainage, western Arctic coast: A discussion of the method and some results, Can. J. Earth Sci., 34, 17–33.
23. Mackay, J.R. 1972. The world of underground ice. Annals of the Association of American Geographers, 62(1), 1-22, March 1972.
24. Mallants, D., 2006. Basic concepts of water flow, solute transport, and heat flow in soils and sediments, second edition. SCK•CEN-BLG-991, 169-183.
25. Moore, S.M., Shackelford, C.D, 2011. Uranium diffusion in soils and rocks, Proceedings Tailings and Mine Waste 2011, Vancouver, BC, November 6-9, 2011, 13p.
26. Morgenstern, N.R and Nixon, J.F. 1971. One dimensional consolidation of thawing soils. Can. Geotech. J. 8, 558-565.
27. Mottaghy, D., Rath, V. 2006. Latent heat effects in subsurface heat transport modelling and their impact on palaeo-temperature reconstructions. International Journal of Geophysics 164, 236–245.
28. Muller, S.W. 1943. Permafrost or permanently frozen ground and related engineering problems. U.S. Army, Office Chief of Engineers, Military Intelligence Div. Strategic Eng. Study 62, 231 p.
29. Nelson, F.E. and Outcalt, S.I. 1983. A frost index number for spacial prediction of ground-frost zones. Proceedings of the 4th International Permafrost Conference, National Academy Press, Washington DC, 1, 907-911.
30. Nixon, J.F. 1990. Seasonal and climatic warming effects on pile creep in permafrost. In Permaftost - Canada, Proceedings of the Fifth Canadian Permafrost Conference, Quebec City, Quebec: Centre d'études nordiques, 335-40.
31. Noetzli, J., Gruber, S. 2009. Transient thermal effects in Alpine permafrost. The Cryosphere 3, 85–99.
32. Ockendon, J., Howison, S., Lacey, A., and Movchan, A. 1999. Applied Partial Differential Equations. Oxford, New York, 1999.
33. Outcalt, S. I. 1972. The development and application of a simple digital surface climate simulator. Journal of applied meteorology, 11, 629-636.
34. Preuss, K., and T.N. Narasimhan. 1985. A Practical Method for Modeling Fluid and Heat Flow in Fractured Porous Media. Soc. of Pet. Engr. J., 25:14-26.

35. Riseborough, D., Shiklomanov, N, Etzelmuller, B., Gruber, S., and Marchenko, S. 2008. Recent Advances in Permafrost Modelling. Permafrost and Periglacial Processes, 19, 137-156.
36. Stuart, R.A., Etkin, D.A. and Judge, A.S. 1991. Recent observations of air temperature and snow depth in the Mackenzie Valley area and their implications on the stability of permafrost layers, Canadian Climate Centre Report 91-2, Downsview, Ontario: Environment Canada, Atmospheric Environment Service.
37. Thomsom, W. 1871. On equilibrium of vapour at a curved surface of a liquid. Philo. Mag. 42, 448-452.
38. Wan, R., Lui, Z, Muldrew, K., and Rewcastle, J. 2003. A Finite Element Model for Ice Ball Evolution in a Multi-probe Cryosurgery. Computer Methods in Biomechanics and Biomedical Engineering, 6(3), June 2003, 197–208.
39. Wan, R., Chan, D.H. and Morgenstern, N.R. 1990. A Finite Element Method for the Analysis of Shear Bands in Geomaterials, Finite Elements in Analysis and Design, 7(2), 129-143.

PART 2

Numerical Modelling of Mining Operational Sequences and Related Issues

Table of Contents

List of Figures

List of Tables

EXECUTIVE SUMMARY

The work presented in this report describes the numerical modelling of various scenarios pertaining to the proposed uranium ore mining into continuous permafrost at the Kiggavik project site in the region of Nunavut. Four open pit mines are studied, namely: East Zone, Centre Zone, Main Zone and Andrew Lake, with the Main Zone pit being the largest of the four with a diameter of about 850 m and a depth of 235 m approximately into and through the continuous permafrost layer. The numerical modelling focuses on three main aspects resulting from mining operations: (1) permafrost degradation under operation time, (2) bottom pit heave due to both excavation and high artesian pressure, and (3) fluid flow through regional faults that traverse the proposed locations of the open pits. The analysis is carried out using the multiphysics software COMSOL (2012), in which heat transfer, phase change, fluid flow and solid (rock) matrix stresses and deformations are all coupled together. While the porous rock contains water and ice that can freeze and thaw under thermal disturbances, it can also deform under external loading such as during excavation.

Main findings of this study for each of the abovementioned three aspects are briefly reported as follows. Numerical results indicate that an open talik would not form below the excavated area as a result of depositing warm tailings in both East Zone and Centre Zone pits during operation time. In the Main Zone where excavation breaks through the permafrost boundary, a small thawed zone would form around the open pit with limited talik formation. With regards to floor heave concerns, bottom pit vertical displacements ranging from 30 to 50 mm were calculated when the excavation level reaches 5 m above the permafrost layer, which is deemed to be the most critical stage. Wall deformations were between 70 and 100 mm with some tensile stress zones developing along the slope's surface and the top surface of the pit. Finally, the parametric study conducted on underground fluid flow through faults into the pits revealed potentially non-negligible inflow rates that very much depend on fault width and hydraulic properties of concerned geological materials.

Permafrost Degradation

1.1 Preamble

In this chapter, the computational model that will be used to analyze permafrost degradation will be first calibrated and verified based on available experimental and field data. This step is very important in order to ensure that any subsequent computations or predictions are made with a level of confidence and credibility high enough for making a sensible engineering judgement. The expected result of the model verification and calibration is the quantified level of agreement between experimental or field data and model predictions. The second part of this chapter essentially describes the numerical modelling of permafrost degradation under the open pit over both time and space while following as accurately as possible the sequencing of mining events.

1.2 Model Calibration

1.2.1 Introduction

The starting point of this exercise is a systematic verification of the validity of our numerical model results. In other words, the numerical model should be calibrated against any available thermal field data, including history. In this study, the most important parameters that should be calibrated are the thermal and hydraulic properties (such as thermal conductivity, heat capacity, and permeability) of concerned geological materials, and the empirical n-factors that are to be used to define ground surface temperature as a function of climate conditions.

In this section, first, climate-permafrost interaction, ground surface n-factors, and the factors affecting them will be briefly defined. Then, the work conducted by other researchers on the interaction between climate and ground surface temperature in Northern Canada will be discussed. Thereafter, data submitted by Areva on the geology and climate of the various sites reported in the Areva technical appendixes will be reviewed. Finally, the assumptions and results of numerical modelling will be presented.

1.2.2 Ground Surface and Air Interaction

Ground surface temperature is one of the most important boundary conditions needed in permafrost modelling. In order to find the ground surface temperature, the interaction between air and ground surface should be considered in addition to the interaction between ground surface and the permafrost. The relation between mean annual air and mean annual permafrost surface temperature is normally separated into: (1) the difference between the annual mean temperature at the ground surface and at the top of permafrost (T_{TOP}; Smith and Riseborough, 2002) or the so-called thermal offset; and (2) the difference between the annual mean temperature at the ground surface and the annual mean air temperature, or the so-called surface offset (Lachenbruch et al., 1986).

The thermal offset is a function of the frozen and thawed ground thermal conductivities (Romanovsky and Osterkamp, 1995; Smith and Risebrough, 2002). On the other hand, the surface offset is function of the surface energy balance and is controlled by surface characteristics such as snow cover, vegetation, and moisture content (Oke, 1978; Eaton et al., 2001; Beltrami and Kellman, 2003).

As mentioned previously, the ground surface temperature links the surface and thermal offsets and is dependent on the surface energy balance:

$$Q^* = Q_E + Q_H + Q_G \qquad 1\text{-}1$$

where Q^* is the net radiation, and Q_E, Q_H, and Q_G are the latent, sensible, and ground heat fluxes respectively (Oke, 1978). For any surface, a specific combination of these fluxes leads to a unique surface temperature (Outcalt, 1972). At the site scale, canopy cover controls Q^* at the ground surface (Smith 1975), moisture content controls Q_E and Q_H (Betts et al., 2001), and the ground thermal conductivity controls Q_G (Williams and Smith, 1989).

The n-factor was originally developed to summarize the surface energy balance for engineering purposes (Carlson, 1952; Lunardini, 1978). The n-factors are calculated using freezing and thawing indices determined through the integration of temperature variations over both the freezing and thawing seasons. Then, the n-factor (Lunardini, 1978) emerges as:

$$n = \frac{\int_0^{\theta_s} \left(T_f - T_s\right) dt}{\int_0^{\theta_a} \left(T_f - T_a\right) dt} \qquad 1\text{-}2$$

where θ_s and θ_a are the lengths (duration in time) of the surface and air freezing or thawing seasons, T_s and T_a are the ground surface and air temperatures, and T_f is the freezing point. Integration of the temperature over the freezing and thawing seasons is usually accomplished and expressed in degree-days. Thus,

$$n_f = \frac{FDD_s}{FDD_a} \quad \text{1-3}$$

$$n_t = \frac{TDD_s}{TDD_a} \quad \text{1-4}$$

where FDD_s, TDD_s and FDD_a, TDD_a are the freezing and thawing degree-days for the surface and air respectively (Klene et al., 2001). Thawing degree-days (TDD) are defined as the summation of daily mean temperatures above freezing point (0°C) during the thawing season, and freezing degree-days (FDD) are the summation of daily mean temperatures below freezing point (0°C) during the freezing season.

The closer values of n_f and n_t are to 1.0, the more similar air temperature indices are to ground surface indices. Values of n_t tend to be higher in open areas, and lower in areas with greater shading (Taylor, 1995). Important factors that affect the value of n_t are: the near surface thermal diffusivity, vegetation, and subsurface conditions. Values of n_f are mainly controlled by the snow cover and the thermal conditions of the subsurface material (Karunaratne and Burn, 2004). The buffering effects of snow cover on air to ground surface temperatures are reflected in values of n_f less than 1.0 for most natural areas (Taylor, 1995).

1.2.3 Ground Surface and Permafrost Interaction

The thermal offset is defined as the difference between the MAGST (Mean Annual Ground Surface Temperature) and T_{TOP} (ground temperature at the top of permafrost and beneath the active layer) (Smith and Riseborough, 2002), and is calculated using:

$$Thermal\ Offset = T_{TOP} - MAGST \quad \text{1-5}$$

As mentioned previously, the thermal offset is a function of the frozen and thawed ground thermal conductivities. Since the thermal conductivity of ice is higher (about four times) than thermal conductivity of water, the ground thermal conductivity is higher for frozen ground than that for active layer where moisture is present in the ground material. This change in the thermal

conductivity of active layer leads to the thermal offset. Larger thermal offsets occur in grounds with higher moisture content due to significant seasonal changes in thermal properties (Burn, 2004; Throop, 2010).

1.2.4 Factors Affecting Permafrost Temperature

Snow

Snow is a very good insulator with a very low thermal conductivity, and therefore, has a strong influence on the thermal regime of the ground (Williams and Smith, 1989). Snow primarily affects winter ground temperatures. The most important factors which influence ground thermal regime are the first accumulation of snow on the surface, the duration of snow cover, and the maximum thickness reached during the winter (Goodrich, 1982). An effective method which is used to consider both the depth and duration of snow is Snow Depth Days (SDD) usually reported in cm.days (Throop, 2010).

Vegetation

Vegetation is an effective buffer that could make the ground temperature cooler than the surrounding climate by making shadows in the summer, and can aid the accumulation of snow in the winter causing warmer ground temperatures than in the air (Smith, 1975; French and Slaymaker, 1993), and overall leading to smaller amplitudes of ground temperature waves. Depending on the type, vegetation can also intercept snow leading to a thinner snow cover on the ground.

Unfrozen Moisture and Latent Heat

According to the effect of capillary forces or presence of various mineral in the pore water, unfrozen moisture could be present in ground materials at temperatures below 0°C. This causes the release or absorption of latent heat over a range of temperatures during phase change (Riseborough, 1990). Non-conductive heat flow has been observed beneath the active layer, in the near-surface permafrost, indicating that unfrozen moisture is present at sub-zero temperatures (Outcalt and Hinkel, 1996).

1.2.5 Related Study in the vicinity of Project

In this section, a study done on the interaction of air and permafrost temperatures in the vicinity of the proposed project will be reviewed.

Spatial and Temporal Variability of Permafrost Condition in Northern Canada

In this study, the data (Jennifer Throop 2010) from nine permafrost thermal monitoring sites at widely separated locations across Northern Canada were examined individually, spatially, and temporally. Three sites are located in Nunavut (Alert, Iqaluit, and Baker Lake). Due to proximity to the Kiggavik project area, the examined site at Baker Lake could be a good representation of permafrost conditions for our area of study.

At each site, the local characteristics were assessed using various methods including mean annual temperatures, surface and thermal offsets, n-factors, and the apparent thermal diffusivity. Regional mean annual air temperatures were defined as the primary determinant of permafrost temperatures at the study sites, but this relationship is modulated by snow (depth, duration, and timing) and vegetation characteristics, the substrate material, and the moisture content, both frozen and unfrozen, within the active layer and the permafrost.

The permafrost thermal monitoring site at Baker Lake, Nunavut, lies within the zone of continuous permafrost. The area has permafrost thicknesses of up to 200 m (Smith et al., 2005), and is an arctic tundra site with moderate vegetation. There are four (BH1-BH4) boreholes at this site that were drilled to a depth of 3 m in 1997, forming a transect perpendicular to a snow fence that was installed in 1981. The boreholes are located in till composed of coarse gravels and sands with a peat layer at the surface that is less than 15 cm thick, and the materials have low ice contents.

As a reference point, BH1 is located 135 m downwind from the snow fence; BH2 is 45 m downwind from the snow fence (Figure 1-1), and is beneath the large snow drift that forms each winter; BH3 is 180 m upwind of the snow fence; and BH4 is 400 m upwind of the snow fence and is the least affected.

Figure 1-1 BH2 downwind of snow fence (Throop, 2010)

Temperatures at BH2 are significantly affected by the snow drift, resulting in higher winter ground temperatures than at the other three boreholes (Figure 1-2). BH1, further downwind from the snow fence, has been affected by the snow fence in a different way. BH1 receives less snow as a result of the fence, making ground temperatures colder than those at BH3 and BH4 (Figure 1-2). BH3 appears most similar to BH4, showing only limited effects from its proximity to the snow fence. The inter-annual variability in temperatures at 3 m depth appears to be somewhat dependent upon winter average temperatures, but must also be somewhat attributed to snow characteristics.

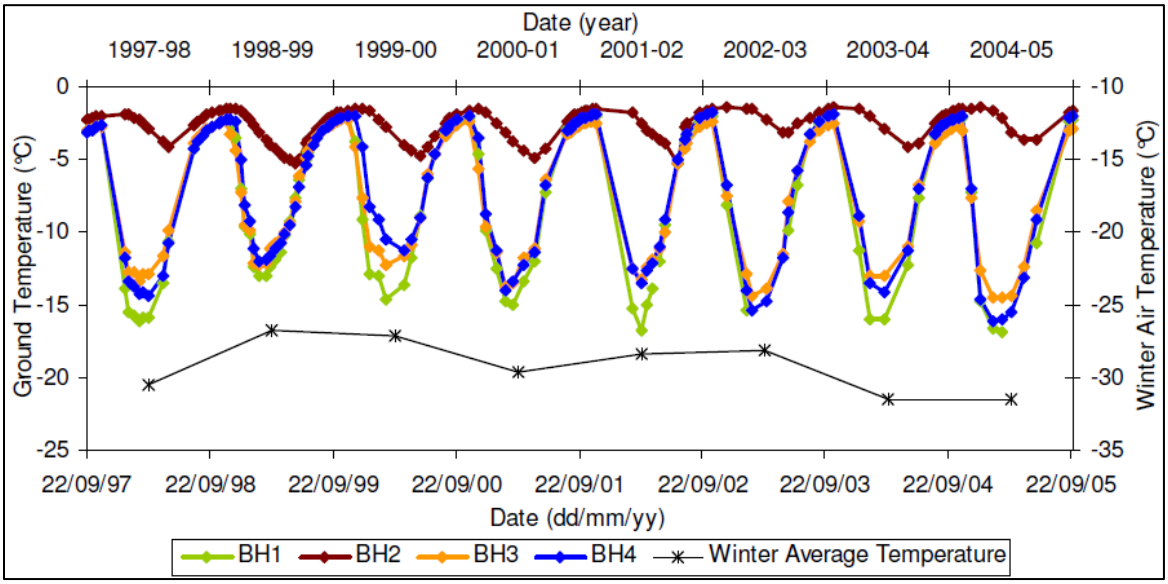

Figure 1-2 Ground surface temperature vs time for four boreholes and average winter air temperature, Baker Lake, Nunavut (Throop, 2010)

Snow cover at BH4 varied significantly inter- and intra-annually. This site has low tundra vegetation, and is prone to drifting snow. Between 2002 and 2006, the average snow depth ranged between 13 cm and 28 cm. A summary of on-site data at Baker Lake BH4, including FDD_s, TDD_s, FDD_a, TDD_a, SDD, n_f and n_t are presented in Table 1-1. Parameters such as FDD (Freezing Degree Days) and SDD (Snow Depth Days) are explained in Sections 1.2.2 and 1.2.4. Moreover, the Coefficient of Variation (CV) is presented by the author (Throop, 2010) to show the relative variability over the monitoring period.

Table 1-1 Data for BH4 (Throop, 2010)

Year	FDD_a	FDD_s	n_f	SDD	Year	TDD_a	TDD_s	n_t
2002-03	4777	3793	0.79	4339	2003	1018	904	0.89
2003-04	5311	3491	0.66	3478	2004	827	703	0.85
2004-05	5107	3939	0.77	3003	2005	925	831	0.90
2005-06	4131	2709	0.66	7282	2006	1001	871	0.87
2006-07	4471	2818	0.63	*M*	2007	862	778	0.90
2007-08	*M*	4019	*M*	*M*	2008	*M*	*M*	*M*
CV	0.10	0.16	0.10	0.42	CV	0.09	0.10	0.02

(Note: "*M*" indicates missing data)

Table 1-1 shows the difference between MAAT, MAGST, and surface offset at BH4, while Table 1-2 indicates on-site data at Baker Lake BH2. A comparison between Baker Lake BH2, beneath the large snow drift, and BH4, representing natural conditions for the local area, illustrates the significant microclimatic effect that snow may have on air-to-ground temperature relations. The MAGSTs have warmed by 4°C to 8°C at BH2 since the snow-fence was installed in 1981, as indicated by the difference between MAGSTs at BH2 and BH4. The surface offset has increased at BH2 from 7.7°C to 10.5°C, compared to that at BH4 which is from 2.4°C to 4.7°C. In terms of n-factors, n_f is strongly affected with an average of 0.19 at BH2 and 0.70 at BH4. Values of n_t are similar despite the shortened thaw season at BH2.

Table 1-2 Data for BH2 (Throop, 2010)

Year	FDD_a	FDD_s	n_f	Year	TDD_a	TDD_s	n_t
2002-03	4794	713	0.15	2003	701	730	1.04
2003-04	5326	1070	0.20	2004	470	389	0.83
2004-05	5122	723	0.14	2005	515	434	0.84
2005-06	4140	781	0.19	2006	643	581	0.90
2006-07	4490	1280	0.29	2007	809	618	0.76
2007-08	*M*	924	*M*	2008	*M*	*M*	*M*
CV	0.10	0.25	0.30	CV	0.22	0.25	0.12

1.2.6 Site Geology

The surficial deposits in the Kiggavik Project area comprise mainly glacial till overlying Precambrian intrusive igneous and metamorphic bedrock that are typically quartzite, schist or granite. The glacial till varies in texture and composition from well-graded silty sand with some gravel and a trace of clay to well-graded gravelly sand with some silt and a trace of clay. The

glacial till samples exhibited little to no plasticity. The water content of the glacial till ranged from 8 to 15 percent, approximately (Technical Appendix 5B).

A typical soil profile in the Kiggavik Project area consists of a thin organic layer underlain by glacial till varying in thickness from less than a meter on ridges to several meters in depressions, overlying bedrock. Post-glacial frost action has shattered much of the exposed and near-surface bedrock. Large areas of boulders (boulder-fields) exist on the ground surface where the finer fraction of the glacial till has been removed by erosion or the boulders have been frost-jacked to surface by the repetitive freeze-thaw action of the active layer (Technical Appendix 5B).

Landforms in the Project area are dominated by hummocky, bouldery glacial till and scattered boulder till moraines with frequent outcrops and shattered bedrock features in isolated exposures, elevated plateaus and elongated ridges. The localized north-northwest-trending glacial drumlins preserve evidence or regional ice flow (Technical Appendix 5B).

The Kiggavik project area is located within the continuous permafrost zone. The permafrost thickness depends on various factors such as proximity to lakes and ground slope, among others. However, the permafrost thickness in the vicinity of Kiggavik site is between 210 m and 230 m from ground surface, and the permafrost thickness in the Sissons area is between 240 m and 250 m.

The thickness of the active layer (the top layer of soil that thaws during the summer and freezes again during the winter) is variable. In general, the active layer thickness at the Project area is in the order of 1 m to 2 m, except where bedrock is found close to surface or is outcropping. Where bedrock outcrops, the active layer could be as thick as 5 m. The thickness of the active layer is dependent on many factors, including the type and thickness of the organic cover and the underlying mineral soils and bedrock. Where frost fracturing has occurred below the depth of the active layer, the fractures are typically ice filled, and high ice contents govern geotechnical design (Technical Appendix 5B).

The ground ice content of permafrost soil and rock in the Project area is expected to be between 0% and 10% (dry permafrost) based on regional scale compilation data. Excess ground ice is expected to be greater in areas such as lowlands that are characterized by poorly drained conditions commonly expressed as patterned ground and other periglacial process features.

According to local geological data, basement host rocks are composed of metasediments, and to a lesser extent altered granite and intrusive rocks. Metasediments are sedimentary rocks that have been metamorphosed. Intrusive rocks are igneous rocks that intruded into pre-existing rocks. Uranium mineralization in the Kiggavik area is hosted mostly in altered metasedimentary rocks, and to a much lesser extent in altered granite and intrusive rocks. In the vicinity of the project, most parts of both metasedimentary and igneous rocks are composed of quartz and feldspar minerals, which could lead to moderate to high thermal conductivity. The Andrew Lake

deposit is located in metasediments overlying granitic gneiss and granodiorite (an igneous rock). These formations have been strongly metamorphosed and altered, tectonized, and intruded. The rocks have gently dipping foliation, small scale recumbent folding, and low angle thrusting.

1.2.7 Ground Temperature Condition

Historical data were collected at the project site from 1988 to 1991, while more recent data were gathered from 2007 to 2011. During the 2009 field season, thermistors were installed in four boreholes (END-09-01, ANDW-09-03, MZ-09-02, and MZ-09-04) to depths of up to 300 m below ground surface. These data have been used to calibrate the numerical model used in this study. Most of these data are available in Technical Appendix 5B.

Figures 1-3 and 1-4 show the historical and recent temperature profiles recorded in the Kiggavik area. Multi-level-thermistor data collected from 2007 to 2011 indicate that permafrost extends to a depth of about 210 m to 230 m below ground surface in the area of the Main Zone. This is somewhat shallower, but generally consistent with data from historical thermistor installations, which suggests permafrost depths at the site ranging from 220 m to 240 m below ground surface. Moreover, at odds with Figures 1-3 and 1-4, other sources of information (Technical Appendix 5B and 5J) suggest that the zero annual amplitude is about 20 m below ground surface

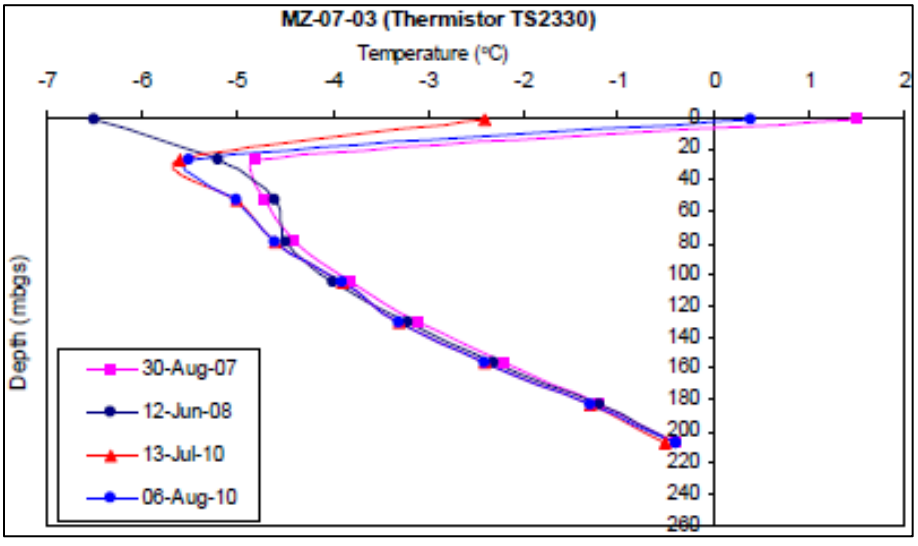

Figure 1-3 Permafrost temperature profile from 2007 to 2010 (Borehole MZ-07-03) (Ref. Technical Appendix 5B)

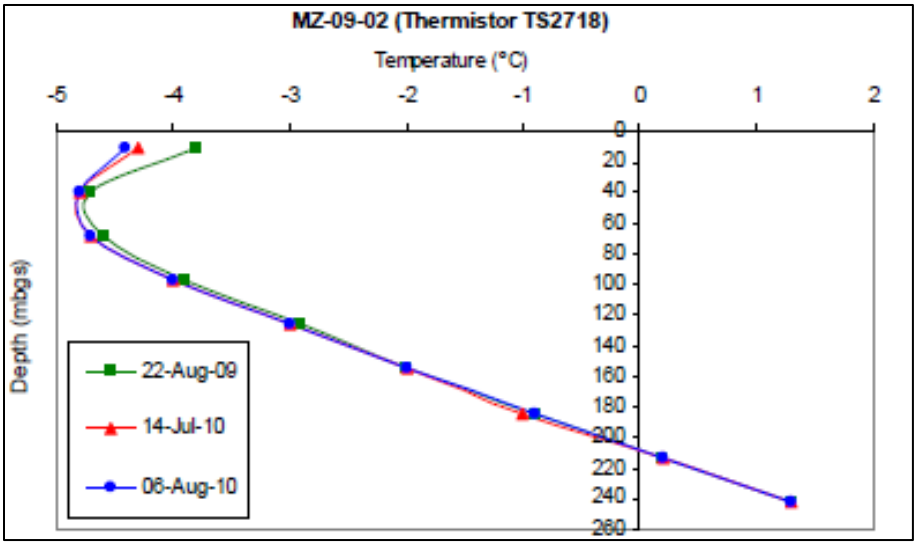

Figure 1-4 Recent permafrost temperature profile from 2009 to 2010 (Borehole MZ-09-02) (Ref. Technical Appendix 5B)

1.2.8 Climate Data

As mentioned in the Technical Appendixes submitted by Areva, climate data have been collected since early 1980's at different time intervals. Most of these data were collected in regional climate stations which are located within 300 km of the project. The nearest climate station is located at Baker Lake which is about 80 km away from the proposed site location. However, since 2009, a local climate station has been installed at the Kiggavik site location. This local station parameters include air temperature, rainfall, atmospheric pressure, wind speed and direction, humidity, solar radiation and ultra-violate radiation. Some of these data have been presented by Areva in Technical Appendix 4A. For instance, the monthly air temperatures between 2009 and 2010 for the climate station which has been installed at the Kiggavik site location are herein presented in Table 1-3 and Table 1-4 (Technical Appendix 4A).

Table 1-3 Air temperature statistics for Kiggavik, May to December 2009 (Technical Appendix 4A)

Month	Warmest and Coldest Day in the Month				Mean Monthly ˚C
	Extremes		Means		
	Maximum ˚C	Minimum ˚C	Maximum ˚C	Minimum ˚C	
May	-0.9	-18.9	-7.4	-12.0	-9.6
June	20.8	-6.6	8.4	0.2	4.6
July	22.4	1.3	16.3	6.6	11.7
August	22.3	0.3	14.2	5.5	9.8
September	11.5	3.7	-	-	-
October	2.3	-23.9	-6.0	-9.7	-7.8
November	-5.2	-24.2	-12.9	-18.8	-15.8
December	-8.1	-34.6	-20.7	-25.8	-23.4

Table 1-4 Air temperature statistics for Kiggavik, January to August 2010 (Technical Appendix 4A)

Month	Warmest and Coldest Day in the Month				Mean Monthly ˚C
	Extremes		Means		
	Maximum ˚C	Minimum ˚C	Maximum ˚C	Minimum ˚C	
January	-8.3	-33.9	-22.0	-28.1	-25.2
February	-11.8	-39.1	-22.7	-27.6	-25.1
March	-5.8	-31.9	-15.4	-21.1	-18.2
April	0.6	-19.4	-5.5	-10.6	-7.9
May	-1.2	-17.1	-5.7	-10.1	-7.7
June	18.7	-5.4	7.5	0.8	4.4
July	23.8	2.7	17.2	8.2	12.9
August	21.8	1.6	14.6	6.3	10.4

In Technical Appendix 5G, according to the collected data from various climate stations, a sine function is proposed for reproducing the air temperature during one year, i.e.

$$Air\,Temperature = MAAT + A\sin\left(\frac{2\pi * time}{365}\right) \qquad 1\text{-}6$$

in order to match this function to the measured data in the climate stations, the Mean Annual Air Temperature (MAAT) is set to $-12^{\circ}C$ and the air temperature amplitude (A) is considered as $+25°C$, which will result in air temperature variation between $+13\,°C$ and $-37°C$. This function is shown in Figure 1-5.

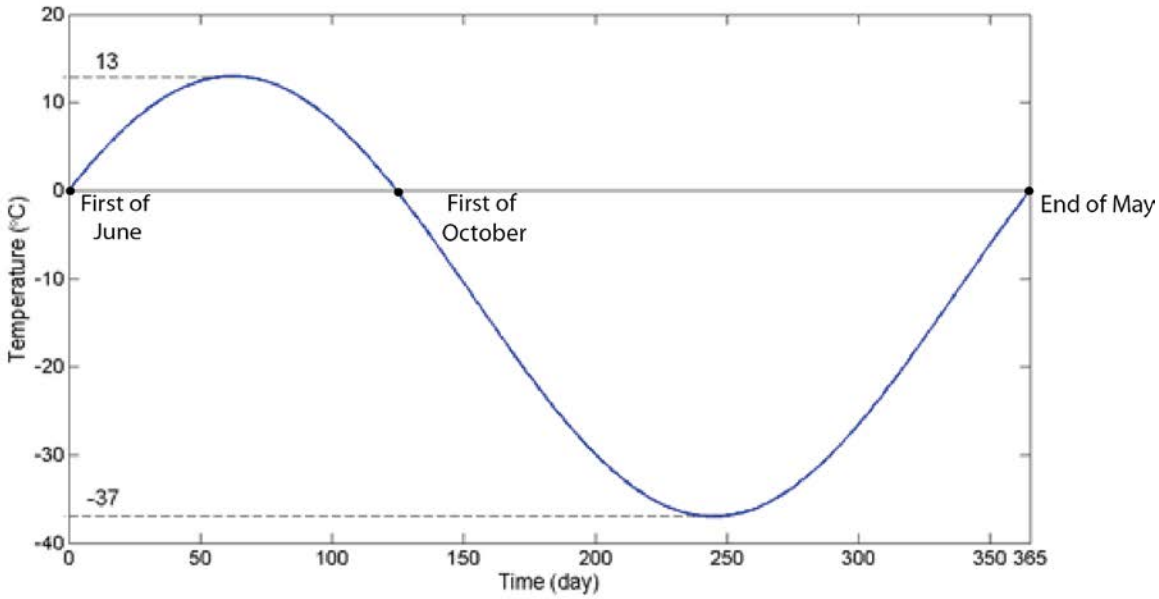

Figure 1-5 Air temperature defined as sine function

1.2.9 Heat Transfer in Porous Media with Phase Change

Pore spaces in the frozen rocks in permafrost are filled with a mixture of frozen and unfrozen water according to the ground temperature. Therefore, the governing equation of heat transfer should consider different material properties in addition to the possibility of phase change during the heat transfer process. Moreover, due to the complex geometry of porous media, it is not possible to formulate the problem in terms of actual fluid flow through pore spaces. As in most studies of flow through porous media, the heterogeneous solid-fluid system is treated as a continuum, which allows an average governing equation to be applied (Rubin and Scheitzer, 1972).

In order to derive the governing equation for heat transfer in a porous media, various physics including fluid flow through pore spaces, mass balance, and energy balance should be considered.

The equation of flow in the homogenized (equivalent) medium is classically given by Darcy's law, i.e.

$$\mathbf{u} = -\frac{K}{\mu}\nabla p \qquad 1\text{-}7$$

where $\mathbf{u}$ is the Darcy velocity, K, the hydraulic conductivity of the fluid, μ the viscosity and p the fluid pressure. Darcy's law is restricted to flow in which viscous forces dominate over inertia forces, i.e. Reynolds number should be small.

The mass conservation equation may be written in the form of:

$$\phi \frac{\partial \rho_f}{\partial t} + \nabla . \left(\rho_f \mathbf{u} \right) = 0 \qquad \text{1-8}$$

where ϕ is the porosity, and ρ_f is the fluid density.

The average energy equation is written for the equivalent medium in the form of:

$$\left(\rho C_p \right)_{eq} \frac{\partial T}{\partial t} + \rho_f C_{pf} \mathbf{u} \nabla T = \nabla . (K_{eq} \nabla T) + Q \qquad \text{1-9}$$

in terms of the equivalent heat capacity of the whole matrix $(\rho C_p)_{eq}$ and C_{pf}, the heat capacity of the fluid, and in the presence of a heat source Q. When there is phase change, latent heat has to be included in Eq. (1-9) though heat enthalpy. This was discussed in the first literature report (Wan, 2012) where it was mentioned that the heat enthalpy conservation equation is the basis of describing heat transport in a three-phase porous medium comprising rock matrix, ice and water such as permafrost, see Bense et al., 2009; Delisle, 1998 and Hartikainen, 2006, among others. Other phases and transport mechanisms can be readily added (e.g. Mallants, 2006), if necessary.

To simplify the problem, and to be consistent with the case of a small Reynolds number, it is usually assumed that the flow velocity $\mathbf{u}$ is slow enough so the temperature of the solid and the adjacent fluid are equal. Thus, considering heat transport only occurring by conduction, we get:

$$(\rho C)_{eq} \frac{\partial T}{\partial t} + \nabla . (-K_{eq} \nabla T) - Q = 0 \qquad \text{1-10}$$

where C_{eq} = volumetric heat capacity (J/K.m^3), K_{eq} = effective thermal conductivity (W/m.K) and Q = heat source (W/m^3).

Both an equivalent volumetric heat capacity and an effective thermal conductivity are herein introduced to account for the thermal effects of freezing and thawing in the presence of the three phases, i.e. rock matrix, ice and water, through the definition of volume fractions θ_i $(i = m, w, i)$ referring to matrix, water and ice, respectively:

$$\theta_m = 1 - \phi; \ \theta_w = \phi \Theta \ ; \ \theta_i = \phi - \theta_w \qquad \theta_m + \theta_w + \theta_i = 1 \qquad \text{1-11}$$

As such, the three-phase medium is basically characterized by ϕ, the porosity of the rock and Θ, the fraction by volume of the pore space occupied by water.

1.2.10 Equivalent Heat Capacity

To account for the phase change whereby latent heat of freezing/fusion, L, of water is liberated (absorbed) during freezing (thawing), its effect is incorporated into the so-called equivalent heat capacity worked out as a volume average, i.e.

$$(\rho C)_{eq} = \theta_m \rho_m c_m + \theta_w \rho_w \left(c_w + \frac{\partial \Theta}{\partial T} L \right) + \theta_i \rho_i \left(c_i + \frac{\partial \Theta}{\partial T} L \right) \qquad 1\text{-}12$$

where $\rho_i =$ the density (kg/m^3) of the various phases, and $c_i =$ specific heat capacity of the various phases (J/K.Kg).

A discontinuity in heat flux is to be expected at the interface between ice and water where complicated processes occur within the porous medium in the presence of a so-called mushy zone (mixture of solid and liquid phases between the solidus and liquidus temperatures). As such, this is idealized through the addition of energy sources (sinks) due to freezing (thawing) involving a normalized pulse ($\partial\Theta / \partial T$) around the transition temperature. The integral of $\partial\Theta / \partial T$ must be equal to unity to satisfy the condition that the 'pulse' width denotes the range between the liquidus and solidus temperatures (see Mottaghy and Rath, 2006, or Noetzli and Gruber, 2009). Figure 1-5 illustrates the functional shape of the equivalent heat capacity with the 'pulse' to accommodate for latent heat during phase change.

The equivalent heat capacity is also able to describe non-isothermal phase change with variable solidification/melting temperatures. This aspect is particularly relevant to permafrost implicating very fine porous materials like rock with microfractures where supercooling due to capillarity may exist, i.e. Kelvin's effect (Thomson, 1871). It is to be noted that the current project involves permafrost in mainly metasedimentary rock containing fractures caused by tectonics and/or episodes of post glaciations and traversed by a major fault or shear zone.

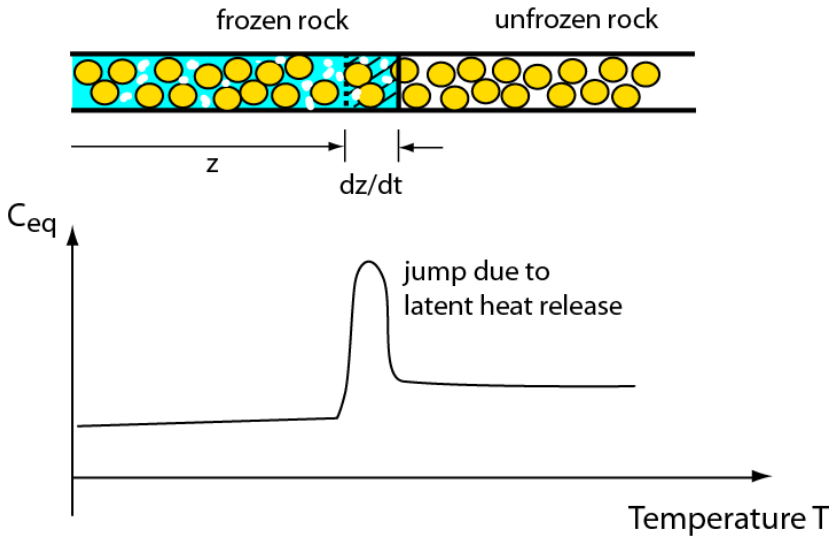

Figure 1-6 Incorporation of latent heat through an equivalent heat capacity with a pulse

1.2.11 Modeling Assumptions for Calibration

1.2.11.1 Calibration Plan

As mentioned in the beginning of this section, the numerical model should be calibrated against any thermal field data, including history. Based on the Technical Appendixes presented by Areva, the ground thermal profile of only four boreholes are available at Kiggavik and Sissons to calibrate the numerical model. However, climate data is only available for the Kiggavik site so that calibration of the numerical model was only conducted on two boreholes, see Figures 1-3 and 1-4. The latter figure presents ground temperature profiles during the years 2009 and 2010 only. Because there is lack of ground thermal data prior to 2009, the numerical calibration will start at year 2009 with the corresponding ground temperature profile as initial conditions. Then, the objective is to find a combination of freezing and thawing n-factors to match the measured ground thermal profile in 2010. Similar calibration procedure will be applied to the other borehole (Figure 1-3) with the ground temperature profile in year 2007 as initial condition.

In order to carry out this plan, some reasonable assumptions have been made on the ground profile, material properties, and boundary conditions. In the following sections, these assumptions will be discussed.

1.2.11.2 Ground Profile

Figures 1-3 and 1-4 (Ref. Technical Appendix 5B) are ground thermal profiles corresponding to boreholes MZ-07-03 and MZ-09-02 whose positions are circled (in green) in Figure 1-7 and also the location of bore hole MZ-09-02 can be seen in Figure 1-8. Based on the position of boreholes and the ground cross-section in Figure 1-9, a simplified ground profile is proposed for numerical modelling as shown in Figure 1-10. This ground profile comprises 10 m of overburden, 150 m of metasediment rock, and 50 m of granite for the permafrost zone.

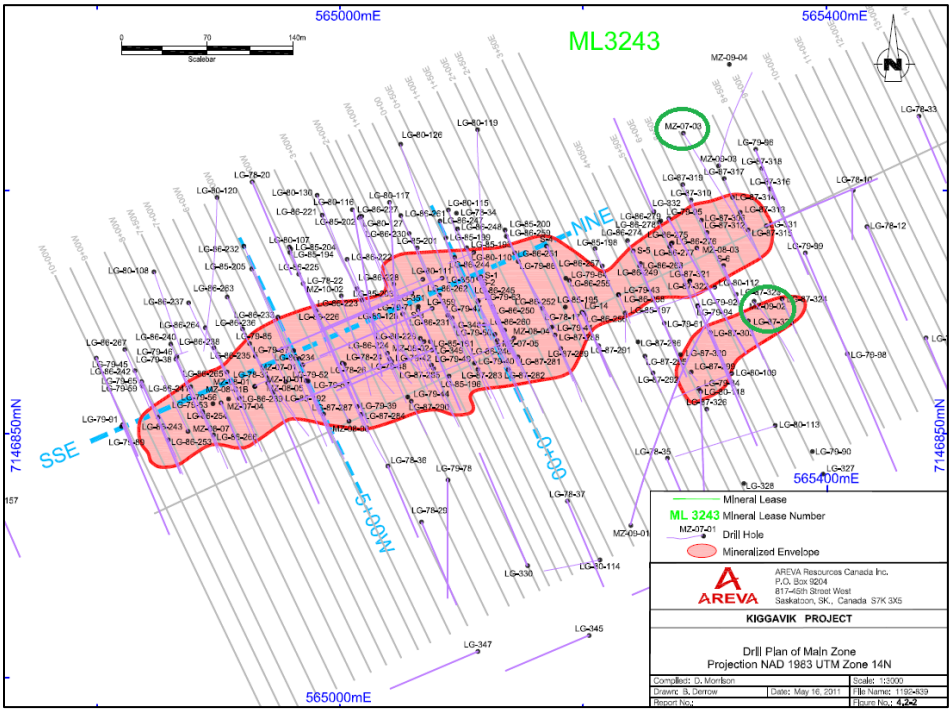

Figure 1-7 Locations of MZ-07-03 and MZ-09-02 on the plan

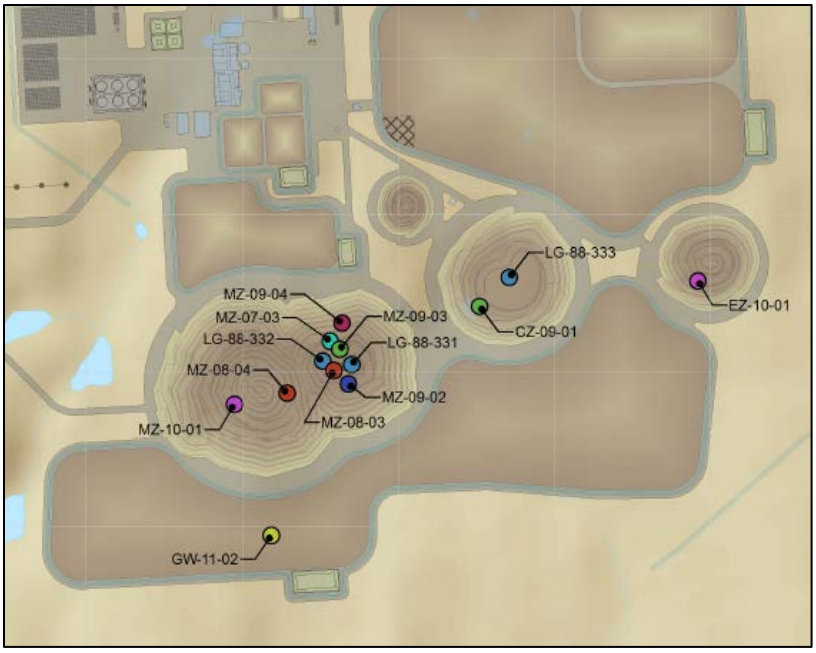

Figure 1-8 Position of MZ-09-02 in the Kiggavik site

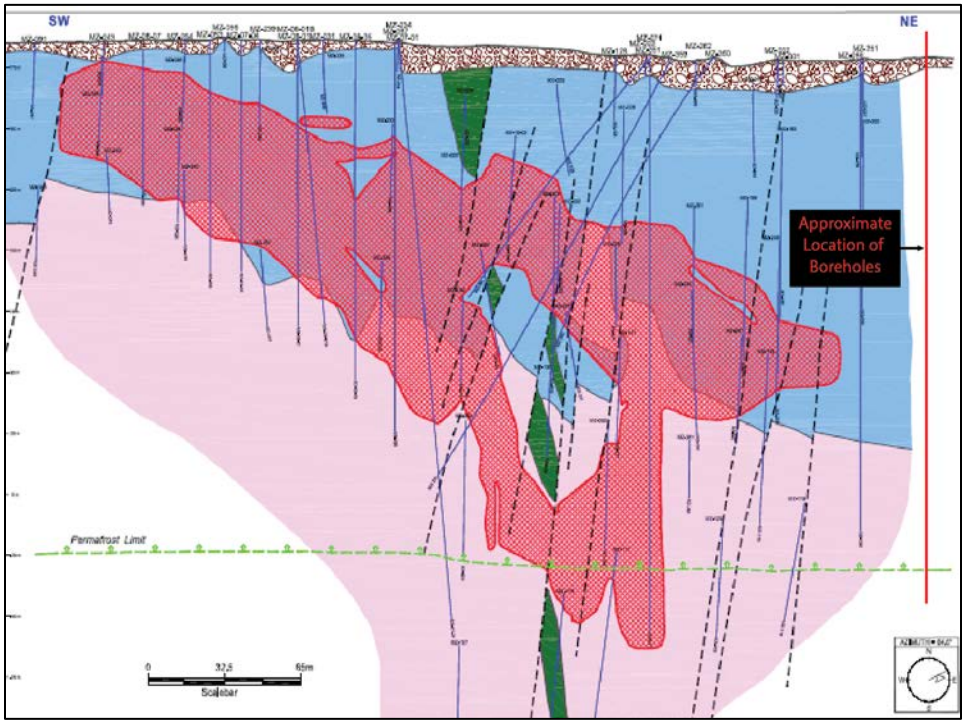

Figure 1-9 Approximate position of boreholes MZ-07-03 and MZ-09-02

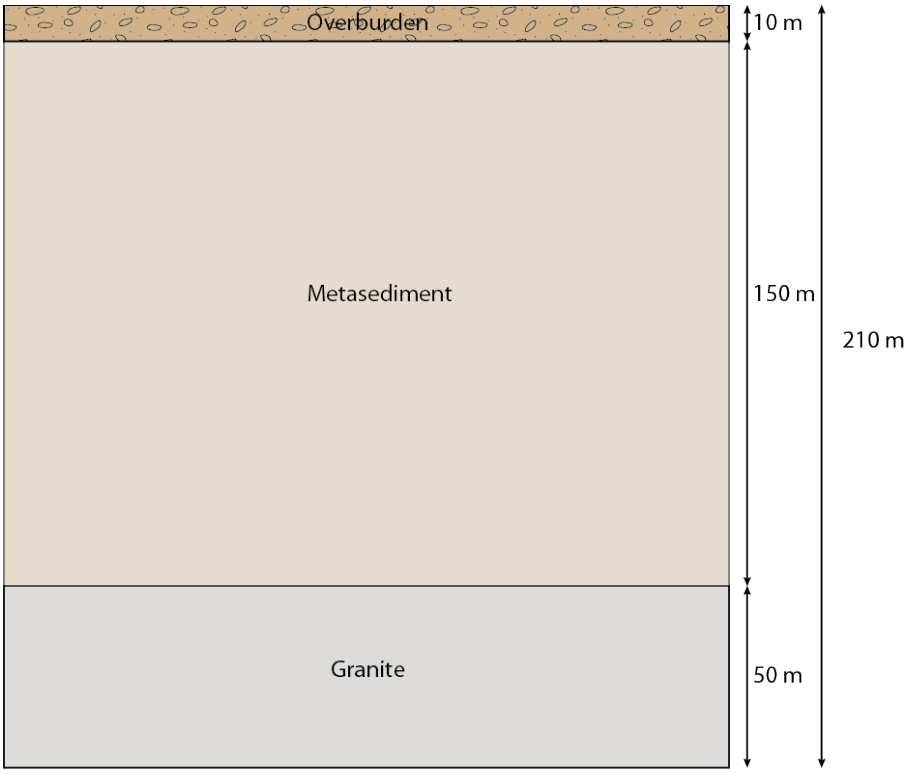

Figure 1-10 Proposed ground profile for numerical modelling

1.2.11.3 Zero Annual Amplitude Depth

In the Technical Appendix 5B, it is estimated that the Zero Annual Amplitude (ZAA) depth is about 20 m (Technical Appendix 5B and 5J) in the vicinity of the project. This information can be used to find a first approximation for the thermal diffusivity, $\alpha = k / C$, of the metasediment rock that will be used in the calibration of the model through an iterative process. Recall the analytical solution that gives the temperature change at a given depth z and time t for a step temperature change ΔT_s at the surface, i.e.

$$\Delta T(z,t) = \Delta T_s \, erfc\left(\frac{z}{2\sqrt{\alpha t}}\right) \qquad 1\text{-}13$$

According to the definition of the ZAA, the Zero Annual Amplitude is the depth at which the change in temperature (ΔT) is less than $0.1^{\circ}\mathrm{C}$ during a time period of one year. By assuming approximately $\Delta T_s \approx 16^{\circ}\mathrm{C}$ (based on a mean ground surface temperature between -6 and $-7^{\circ}\mathrm{C}$ and a maximum ground surface temperature of about $+2^{\circ}\mathrm{C}$ according to Figures 1-3 and 1-4), and inserting $t = 1\,\text{year}\left(3.15 * 10^{7}\,\text{s}\right)$ and $z = 20$ m (Technical Appendix 5B) in Eq.(1-13), we find $\alpha = 1.6\times10^{-6}\,\mathrm{m^2/s}$. This value will serve as an initial guide to determine the

actual thermal properties of the metasediment based on the history matching of the thermal curves in Figures 1-3 and 1-4.

1.2.11.4 Boundary Conditions

Thermal boundary conditions are very important in this numerical modelling exercise for the purpose of calibration and permafrost degradation analysis. The main thermal boundary conditions are shown schematically in Figure 1-10 where the ground surface temperature needs to be defined according to air temperature and the ground surface n-factors. For the bottom boundary, the geothermal heat flux q must be applied. A value of $q = 0.08\,\mathrm{W/m^2}$ (Technical Appendix 5J) was found to be a suitable value compatible with the geothermal gradient and the rock thermal properties.

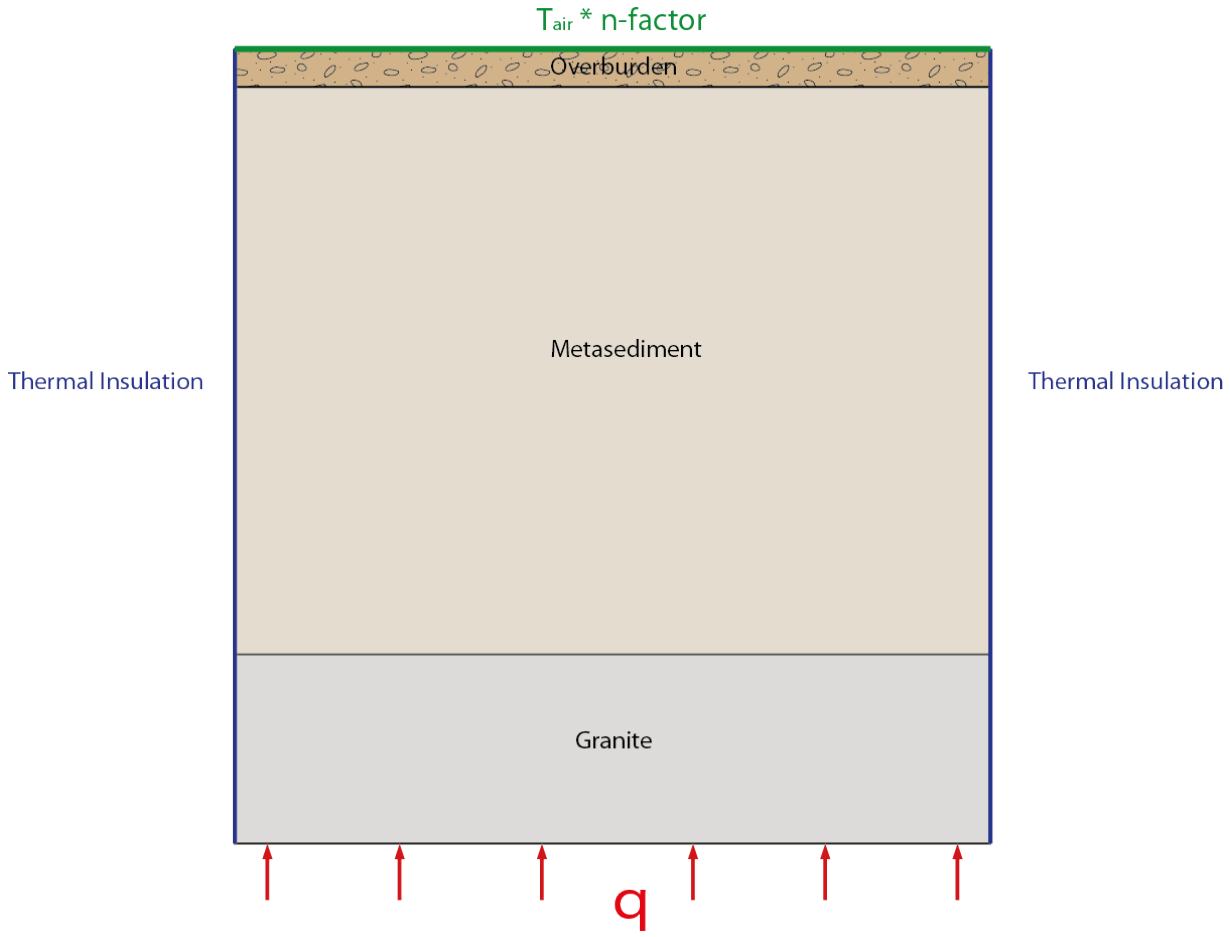

Figure 1-11 Thermal Boundary Condition in numerical modeling

1.2.12 Material Properties

Material properties for the various geological units together with respective ice content values are available in Areva Technical Appendixes 5B and 5J based on both lab and field geotechnical investigations. This information will serve as a guide for the model calibration study in conjunction with other data such as ground thermal profiles, among others.

It should be mentioned here that due to the lack of pertinent measured data in Areva's Technical Appendixes, the only available ground thermal profiles which could be used in this model calibration are those presented in Figures 1-3 and 1-4. Therefore, the prime purpose of the calibration in this study is to adjust the ground material properties in addition to ground surface n-factors to capture the ground thermal profiles presented in the above-mentioned figures.

The most appropriate material properties used in the model calibration are summarized in Table 1-5. These are still consistent with values reported in Areva Technical Appendixes 5B and 5J.

Table 1-5 Material properties used in calibration model

Material	Thermal Conductivity $\frac{W}{m.K}$	Heat Capacity $\frac{J}{kg.K}$	Ice content %
Overburden	2.8	700	5
Metasediment	3.0	670	3
Granite	3.0	670	1

1.2.13 Ground Surface Temperature Boundary Condition

In order to find suitable freezing and thawing n-factors, various combination of n_f and n_t were used. Then, according to the chosen n_f and n_t, and knowing the air temperature, the resulting ground surface temperature was applied at the top of the domain. Air temperature as described with a sine curve is shown in Figure 1-5. As an illustrative example, if we were to choose $n_f = 0.4$ and $n_t = 0.7$, the ground surface temperature that would enter as top boundary condition in the numerical simulations is illustrated in Figure 1-12.

Referring back to Figures 1-3 and 1-4, the initial ground temperature profiles for both boreholes start at the end of August of the respective years. Hence, in the model calibration the applied ground surface temperature curve as boundary condition will also start at the end of August as shown in Figure 1-12.

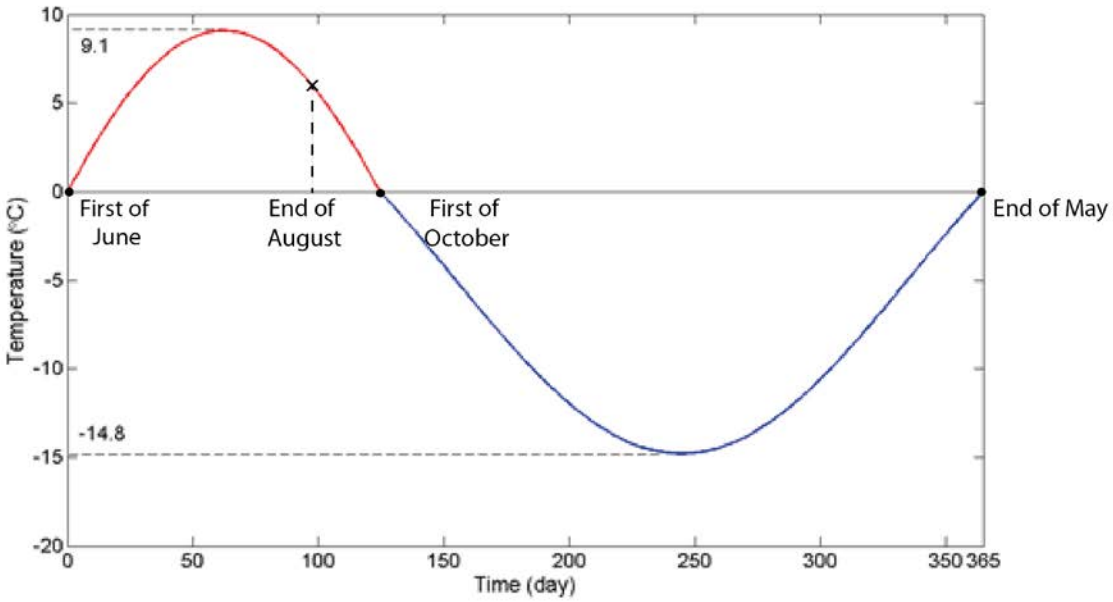

Figure 1-12 Ground Surface Temperature with n_f = 0.4 and n_t = 0.7

1.2.14 Results

The freezing and thawing ground surface n-factors were found by trial and error using various combinations of these parameters and thereafter comparing the results with the measured data as given in Figures 1-3 and 1-4 for boreholes MZ-07-03 and MZ-09-02 respectively. The best fits of n-factors for both boreholes are found when $n_f = 0.65$ and $n_t = 0.9$. For completeness, Figures 1-13 and 1-14 show the goodness of the fit for boreholes MZ-09-02 and MZ-07-03 respectively.

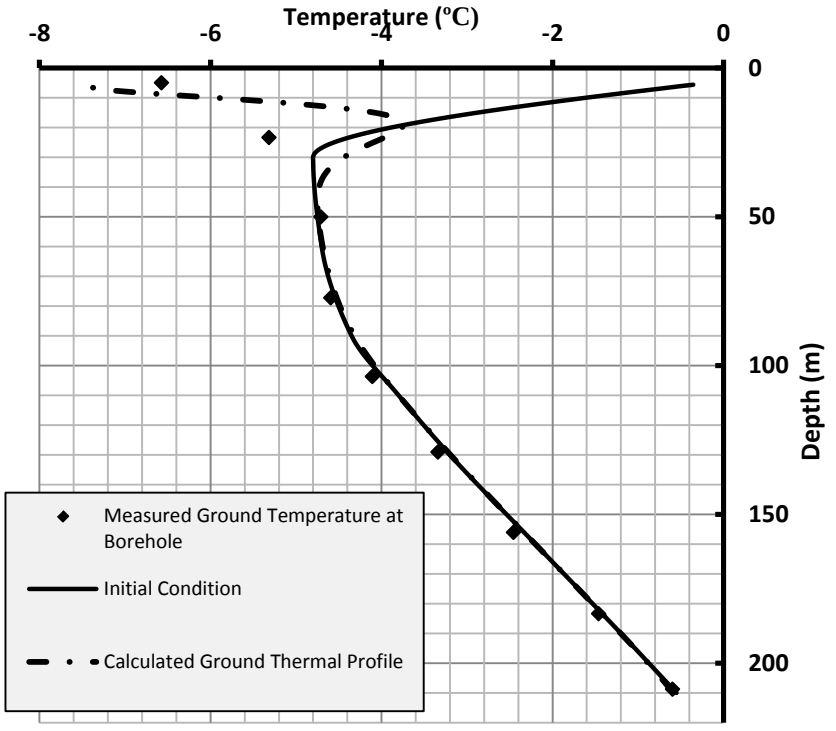

Figure 1-13 Numerical and Measured results for borehole MZ-09-02 with n_f = 0.65 and n_t = 0.9

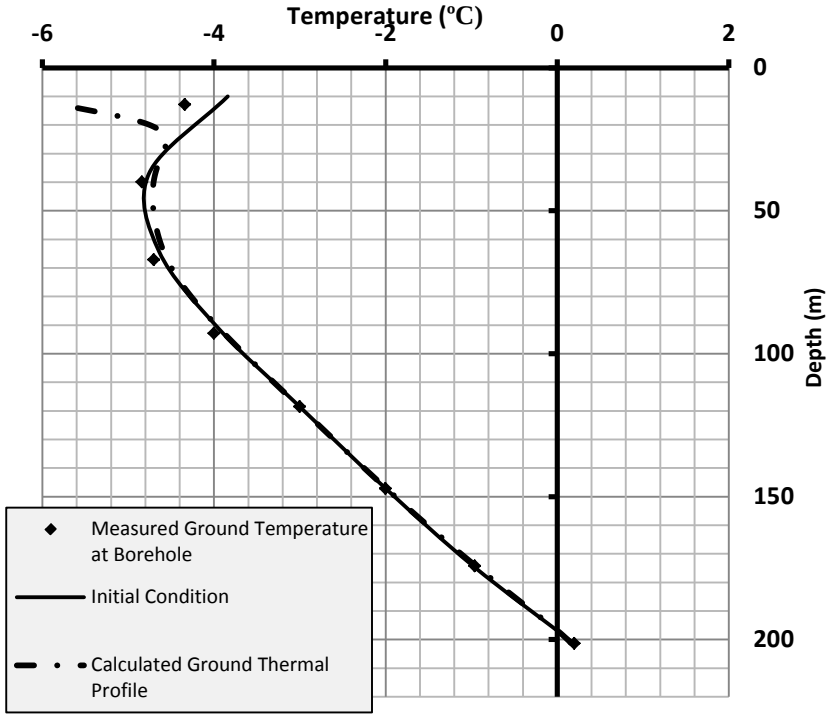

Figure 1-14 Numerical and Measured results for borehole MZ-07-03 with n_f = 0.65 and n_t = 0.9

Values of $n_f = 0.65$ and $n_t = 0.9$ will be used in subsequent permafrost degradation computations. Furthermore, it is worth mentioning that these n-factors are consistent with those determined by Throop (2010) from borehole measurements near Baker Lake which is about 80 km away from boreholes MZ-09-02 and MZ-07-03; refer to Tables 1-1 and 1-2. This suggests that the field conditions such as snow cover and vegetation which would eventually affect the ground surface n-factors might have been similar in Throop's study and at the Kiggavik project site.

1.3 Permafrost Degradation Modelling

1.3.1 Introduction

Over periods of years, or decades, the frozen ground may slowly thaw or slowly increase in extent, either because of changes at the ground surface that modify the exchange of heat energy through it, or because of slow changes in the atmospheric climate (climate change). Therefore, a surface layer thaws and refreezes every year. Additionally, engineering activities often disturb the frozen ground through changes in the material properties (e.g. mechanical strength, thermal and hydraulic conductivities) at temperatures near 0°C. These are particularly problematic to the design of gas pipelines, highways and mines.

From an engineering viewpoint, there is a loss in mechanical strength of the permafrost upon thawing due to attendant liberation of water and pore pressure created, thus compromising the stability of any structures built on or founded into the ground. This phenomenon can be fairly well described within the theory of thaw consolidation (Morgenstern and Nixon, 1971).

On the other hand, naturally-occurring features resulting from the differential thawing of ground ice fall under the term thermokarst with lake growth (Hopkins, 1949, Burn and Smith, 1993). More precisely, events that cause permafrost to melt such as climate variations or human activities may destroy the ground cover and thereby create thermokarst topography. In the same context, a talik is a layer of year-round unfrozen ground that lies in permafrost areas (Lachenbruch et al., 1962; Mackay, 1997; Burn, 2002). In regions of continuous permafrost, taliks often occur underneath shallow thermokarst lakes and rivers, where the deep water does not freeze in winter and thus the ground underneath will not freeze either. Sometimes closed, open and through talik are distinguished. These terms refer to different situations as to whether the talik is completely surrounded by permafrost, is open to the top, or open to both top and unfrozen layers beneath the permafrost, respectively.

Talik development has a significant influence on the physical, chemical, biological, and geomorphological processes occurring in the ground under and around thaw lakes. Taliks cause thaw settlement and permafrost degradation, decreasing the ability of the permafrost to support a load and seriously affecting the performance of structures constructed in permafrost regions (Johnston and Brown, 1964).

Mining development in permafrost regions mostly concerns permafrost degradation issues. For instance, the construction of open pit mines in permafrost with subsequent filling with tailings materials and water presents a scenario similar to a thermokarst lake that causes a local drift from ground temperatures, thus resulting in talik formation in the underlying permafrost. Such a mechanism is central to permafrost degradation which greatly complicates mining activities under such ground conditions. The thawing of the permafrost underneath the open pit increases the mobility (diffusion) of fluids such as acids and radionuclides (Moore and Shackelford, 2011) through pores or fractures in the ground which was previously a barrier to any fluid flow in the frozen state. Although the mechanisms by which taliks are formed are somewhat well-known, its proper numerical analysis depends on the accuracy of the initial temperature profile in the underlying ground, thermal boundary conditions, surface temperature changes characterizing the ground disturbance, water depth and configuration (including physical, thermal and hydraulic characteristics) of the permafrost beneath the lake. The most current numerical modelling of talik formation under thaw lakes is attributed to the work of Ling and Zhang (2003). Even then, the mathematical model is classic and based on a two-dimensional heat transfer formulation with phase change in axi-symmetric conditions. Approximate analytical solutions for determining the depth of a talik formed below a lake as a function of size and geometry are given in Burn (2002).

In this section of the study, talik formation and thermal behavior of permafrost will be assessed as a result of open pit mining excavation in addition to filling of open pits with warm tailings. In the following sections, first, the sequences of modelling together with assumptions and boundary conditions used will be explained. Finally, numerical modelling results will be discussed.

1.3.2 Modelling Mining Sequences

As defined in the Kiggavik project description (Tier 2, Volume 2), the three pits in the Kiggavik project site (East, Centre, and Main zones) will be used as a pond for mill processing tailings by the end of excavation. Therefore, it is very important to follow the mining and tailing production schedule (proposed by Areva) in the numerical modelling. Based on the proposed plan, the mining activity will start with the East Zone followed by the Centre Zone. Finally, the Main Zone will be excavated.

Based on the information in the project description and technical appendixes, the depth of permafrost is between 210 m and 220 m in the vicinity of Kiggavik site. The depth of open pits varies from 100 m in the East Zone to about 235 m in the Main Zone. Hence, each of the open pits individually could be a cause for talik formation due to the high temperature of tailings and proximity of bottom of pits to permafrost boundary. As a preliminary step, the effect of each open pit on the thermal regime of permafrost has been analyzed individually using two dimensional axisymmetric models.

The proposed excavation and backfilling plan which was presented in the summary of scenarios in Progress Report 1 (Wan and Booshehrian, 2012) is recalled in Table 1-6. In addition, the schedule of excavating and backfilling of the open pits according to the proposed mining plan is presented in Table 1-7.

For the purpose of considering the worst scenario, various temperatures have been considered in the permafrost degradation modelling exercise. For each of the open pits two initial tailing temperatures were considered, i.e. 10°C and 5°C.

Table 1-6 Proposed excavation and backfilling steps

Open Pit	Excavation Duration (Year)	Proposed Number of Excavation Steps	Proposed Number of Backfilling Steps	Total Open Pit Depth (m)	Thickness of Excavation Layers (m)	Thickness of Backfilling Layers (m)
Kiggavik East Zone	1	2	2	100	50	50
Kiggavik Centre Zone	1	2	2	110	55	55
Kiggavik Main Zone	5	10	6	235	23.5	23.5

Table 1-7 schedule of excavating and filling

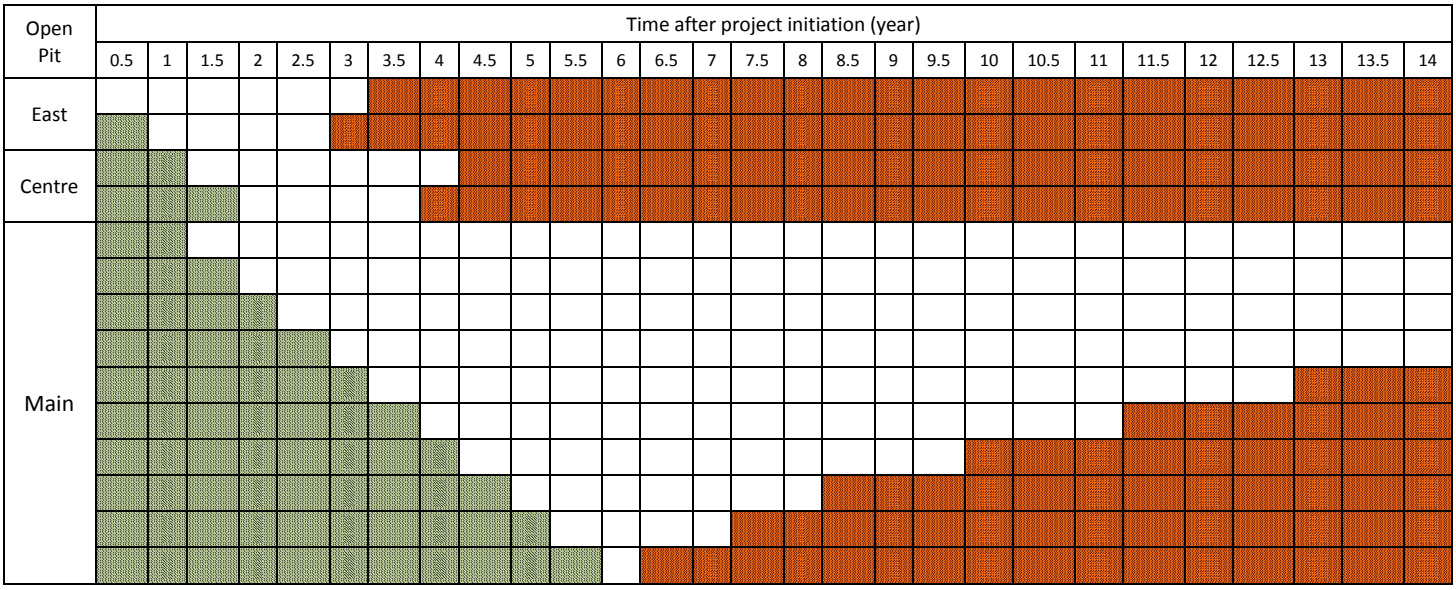

- Not Excavated
- Excavated
- Backfilled with Tailings

1.3.3 Material Properties

Thermal properties of all materials, except the mill processing tailing, were explained and presented in Table 1-5 in Section 1.2.12. In the numerical simulations of permafrost degradation the same material properties are used. Here, the thermal properties of tailing material will be explained.

Figures 1-15 and 1-16 show the thermal properties of frozen and unfrozen tailings as a function of saturated porosity of the tailing material which is presented in Technical Appendix 5J.

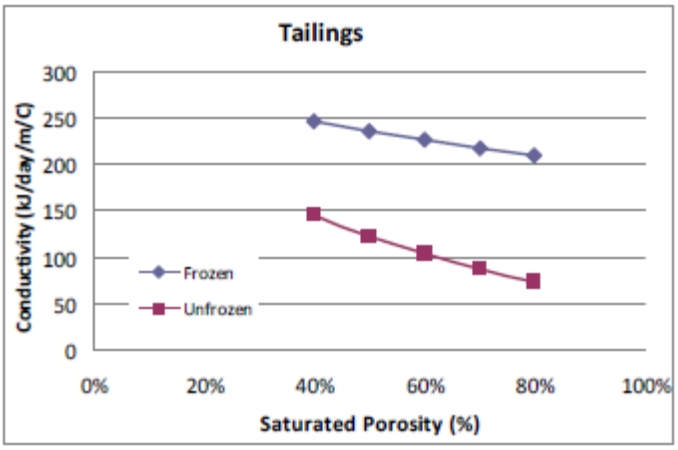

Figure 1-15 Thermal conductivity of tailing material (Ref. Technical Appendix 5J)

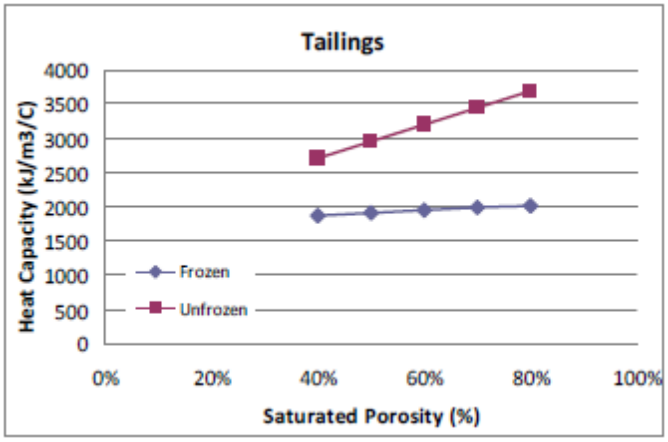

Figure 1-16 Volumetric heat capacity of the tailing material (Ref. Technical Appendix 5J)

As presented in Figure 1-15, the thermal conductivity of tailing mixture (particles and water) changes with water content. An averaging technique can be used to calculate the thermal conductivity of the mixture of tailing particles and water such as:

$$K_{eq} = \theta_s * K_s + \theta_w K_w \qquad 1\text{-}14$$

where θ_s and K_s are the solid particle fraction and thermal conductivity of solid particles, while θ_w and K_w are the (frozen or unfrozen) water fraction and water thermal conductivity respectively. Thermal conductivity values of solid particles contained in the tailing material can be back-calculated based on Eq. 1-14 and are summarized in Table 1-8. It is noted that thermal conductivity of frozen and unfrozen water were taken as $2.18\,\text{W/m.C}$ and $0.58\,\text{W/m.C}$ respectively in the calculations.

Table 1-8 Thermal conductivity of tailing solid particles with water content

Water content	Thermal Conductivity of Tailing Mixture as from Fig. 1.15 (KJ/day.m.C)	Thermal Conductivity of Tailing Solid Particles (W/m.C)
Unfrozen Tailing		
0.4	150	2.51
0.5	125	2.31
0.6	100	2.02
0.7	85	1.93
0.8	70	1.73
Frozen Tailing		
0.4	240	3.18
0.5	230	3.14
0.6	220	3.10
0.7	210	3.02
0.8	200	2.85
Average Value		**2.50**

Moreover, the volumetric heat capacity of the tailing mixture can be determined from Eq. 1-12 given in Section 1.2.10 which defines the equivalent volumetric heat capacity. Without considering any phase change and assuming that the solid part of the tailing material has the same density as the host rock which is about $2500\,kg/m^3$, the value of heat capacity for tailing solid particles could thus be found. These values are summarized in Table 1-9.

In the numerical simulations, a thermal conductivity value of $2.5\,W/m.C$ and a specific heat capacity of $680\,J/kg.C$ were used when characterizing the solid part of the tailing material. These are average values, given that the moisture content does not vary and remains at 30% in the calculations. Also, these numbers are in good agreement with those used by Nixon and Holl (1998) in a study on the thermal behaviour of tailings of two Uranium mines, Key Lake and Rabbit Lake mines, in Northern Saskatchewan.

Table 1-9 Heat capacity of tailing solid material with water content

Water content	Volumetric Heat Capacity as from Fig. 1.16 (kJ/m^3.C)	Specific Heat Capacity of Tailing Solid Particles (J/kg.C)
Unfrozen Tailing		
0.4	2700	680
0.5	3000	720
0.6	3200	680
0.7	3450	680
0.8	3700	680
Frozen Tailing		
0.4	1800	653
0.5	1850	660
0.6	1900	670
0.7	1950	687
0.8	2000	720
Average		**680**

1.3.4 Modelling Scenarios

Material properties and boundary conditions in the previous model calibration are herein used in the permafrost degradation analysis. Calibrated material properties and ice content were given in Table 1-3. The freezing and thawing n-factors were found to be 0.4 and 0.7 respectively. With regard to the open pit boundaries, it will be assumed that there is no snow or vegetation cover during the operational time due to mining activities and the presence of construction equipment. Therefore, both freezing and thawing n-factors for the ground surface inside the open pit are considered to be 1.0. These n-factors are applied to Eq. 1-6 which is considered to represent the air temperature during one year.

In all simulations, the initial ground temperature field is defined based on the mean ground temperature profile which starts at $-7°C$ at ground surface and increases linearly to $0°C$ at the permafrost boundary located at a depth of 210 m for the East and Centre Zone pits. For the Main Zone pit, the bottom of the excavated pit penetrates warm ground beneath permafrost.

For the purpose of permafrost degradation analysis, two scenarios are considered:

Scenario I

In this scenario, it is assumed that a water cover with an average thickness of 5 m will be placed on top of deposited tailings during the operational time. As explained in Technical Appendix 5B, if the thickness of the water cover is equal or greater than 1.5 m, the water will not freeze completely during the winter season. As a result, the water temperature at the bottom of the cover will remain at $+3\,°C$ all the time.

In this scenario, to model the effect of water cover, the thermal boundary condition at the top of tailings is considered as $+3\,°C$ for the whole operational period. For this scenario, two initial temperatures of $+10\,°C$ and $+5\,°C$ are considered for the warm tailings.

Scenario II

In this scenario, it is assumed that the water cover is used just for deposition of warm tailings and after putting the last layer in each pond, the water cover will be removed, and the warm tailing in the ponds will be exposed to air temperature up to the end of operational time. Like in the calibration phase and ground surface temperature, air temperature is considered to vary following the sine curve presented in Eq. 1-6. Also, for this scenario, two initial temperature of $+10\,°C$ and $+5\,°C$ are considered for the warm tailings.

1.3.5 Results and Discussions

In this section, permafrost degradation numerical results as a function of mining activities according to Tables Table 1-4 and 1-5 are discussed. A parametric study was conducted by varying the temperature of warm tailings ($+10\,°C$ and $+5\,°C$) as the open pits were backfilled. In this section, only the results of initial temperature of $+10\,°C$ for both scenarios are presented with the other cases relegated to the Appendix for reference purposes.

1.3.5.1 East Zone

Figure 1-17 shows the temperature field after the excavation is completed over a period of 2.5 years. Since the open pit boundaries are exposed directly to the air without any snow or vegetation cover, there are some noticeable thermal changes occurring over a thin layer. Subsequently, backfilling of the pit proceeds in two stages over a period of 1 year as shown in Figures 1-18, 1-19, and 1-21. It is reminded that two scenarios are considered in the simulations.

In the first scenario, the result of which is shown in Figure 1-19, a 5m thick layer of water has been included on the top of the tailings surface. As a result of water cover, the temperature of tailing at the top remains constant during the winter. In this modelling scenario, this constant $+3°C$ temperature is kept on top of the tailing for the whole year. In the second scenario, after depositing the last layer, tailings are simply exposed to air temperatures following a sine curve following Eq. 1-6.

The backfilling with warm tailings causes some thawing of the permafrost near the pit/tailings interface over a thin zone of approximately 3 m. Over the next 10 years which correspond to the end of operational time (Figures 1-19 and 1-21), the above thawed zone increases up to approximately 7 m for both scenarios. At the same time, the ground temperature below the thawed zone increases, but still remains frozen. The tailings temperature distribution eventually homogenizes with cooling occurring along all exposed boundaries. However, the tailing temperature decreases a little more especially at the top in the second scenario in which the tailing is exposed to air temperature.

For completeness, the evolutions of the temperature profiles for vertical sections under the bottom of the pit after the end of backfilling for both scenarios are shown in Figures 1-20 and 1-22. A warming trend is observed during the post backfilling period which spans over 10 years. However, this warming trend does not result in the complete thawing of the frozen ground beneath the open pit. It is interesting to point out that even for this case which corresponds to the worst condition (very warm tailings) an open talik could not be formed during the 14 years of operational time. Results of other initial tailings temperatures can be found in Appendix A.

1.3.5.2 Centre Zone

The Centre Zone pit is slightly larger in size than the East Zone pit and the ground thermal regime is very similar for the two pits. Figures 1-23 to 1-28 show the temperature field and thermal profile for the various excavation and backfilling stages according to Table 1-5 and assuming an initial tailings temperature of $10°C$. Similar trends as those observed in the East Zone pit are foundd. Here the thawed zone around the pit's boundaries is slightly larger, extending from an initial thickness of 5 m to 10 m at the end of operational time.

1.3.5.3 Main Zone

The Main Zone pit is the largest of the three pits in the Kiggavik area with the bottom of the excavation penetrating 25 m beyond the permafrost boundary into the warm unfrozen ground. The ground thermal condition 6 months after completion of excavation is shown in Figure 1-29.

The temperature disturbance is limited to the vicinity of the exposed pit surface due to extreme cold temperatures during the excavation period.

The backfilling of the pit occurs in 6 stages taking over 7 years approximately. According to mining management plans (Technical Appendix 5J), the Main Zone pit will only be backfilled to a height of 140 m approximately, i.e. half filled. The gradual thermal disturbance caused by the warm tailings to the surrounding permafrost is not shown in this section, and the results are presented in Appendix. Talik formation and growth along the lateral sides of the pit can be observed. At the end of 15 years, the talik has extended over a distance of 15 m approximately along the lateral sides of the pit; see Figures 1-30 and 1-31. Also, by that time the vertical extension of the talik along the sides of the pit has progressed over a distance of 160 m above the bottom of the pit.

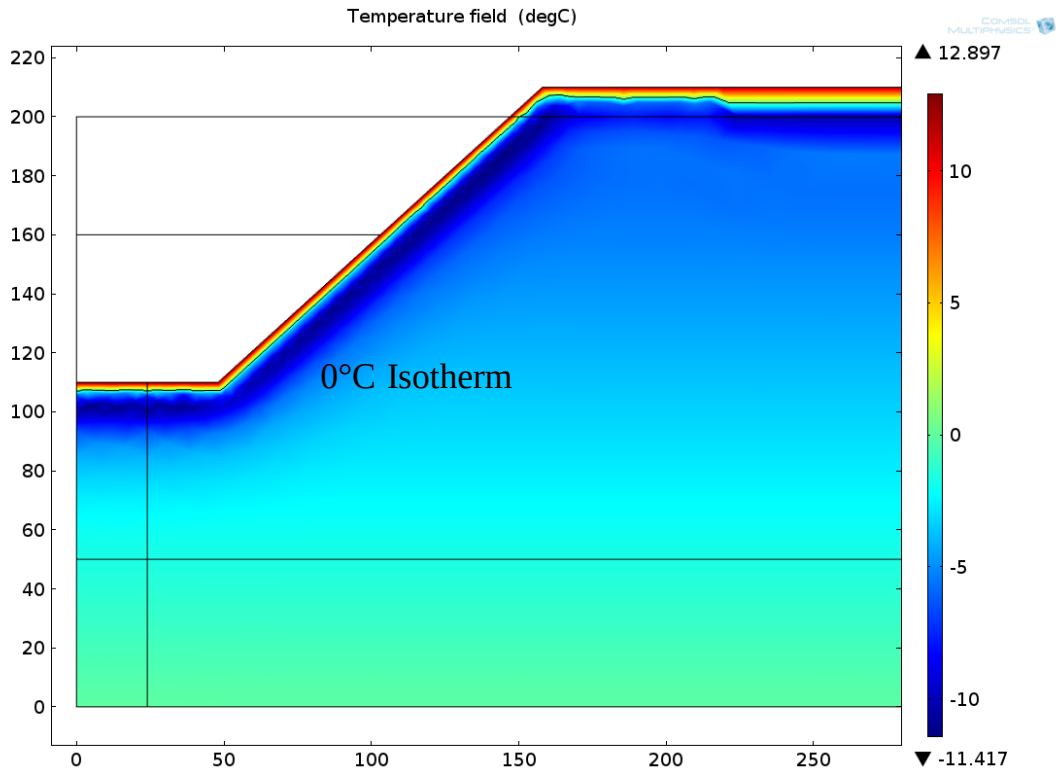

Figure 1-17 East Zone, Thermal Condition, 2.5 years after start of excavation (before filling starts)

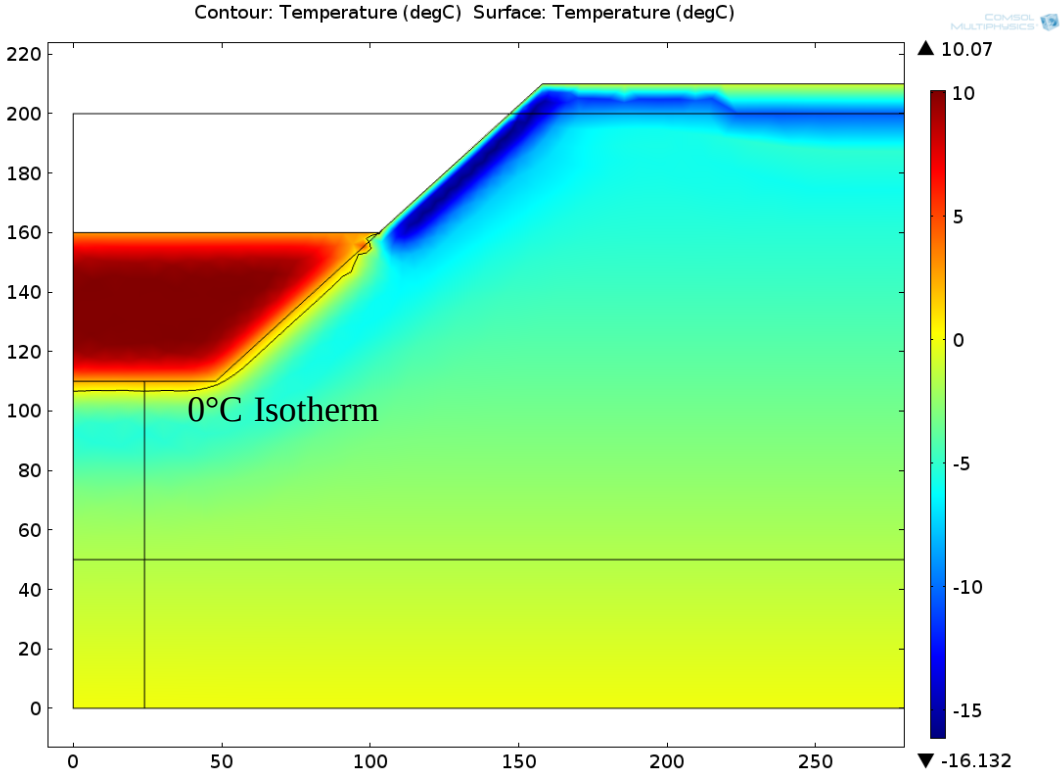

Figure 1-18 East Zone, Thermal Condition, 6 months after putting first layer of tailings

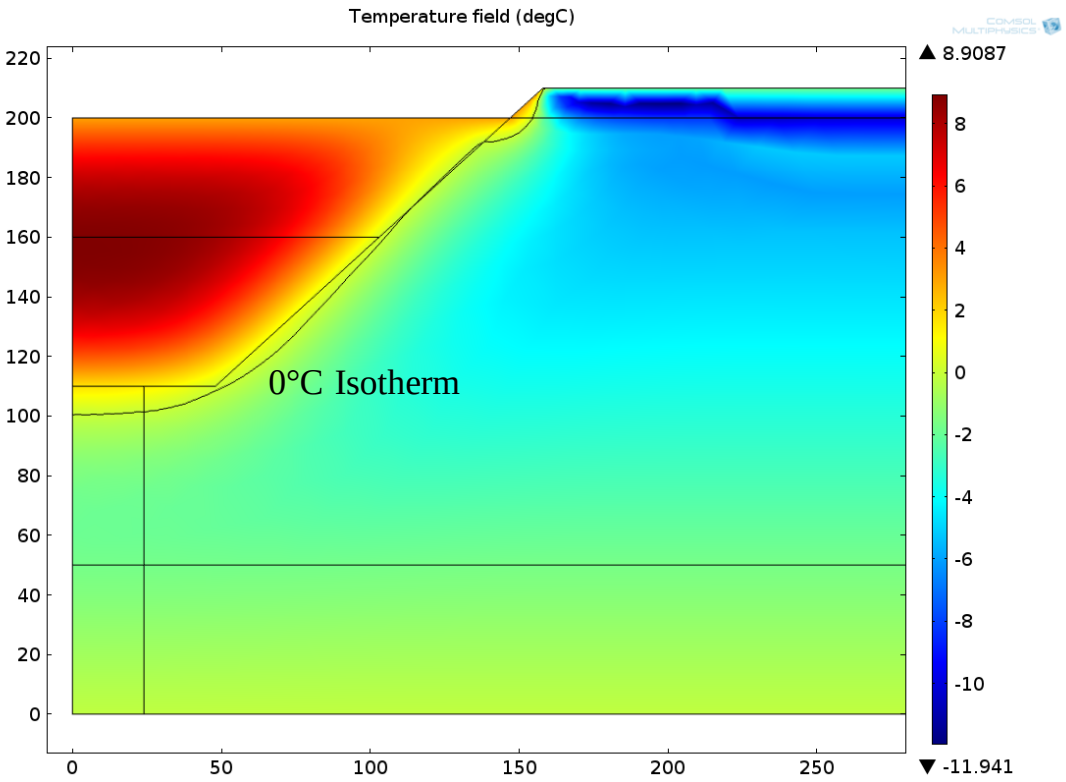

Figure 1-19 East Zone, Thermal Condition, scenario I, at the end of operational time

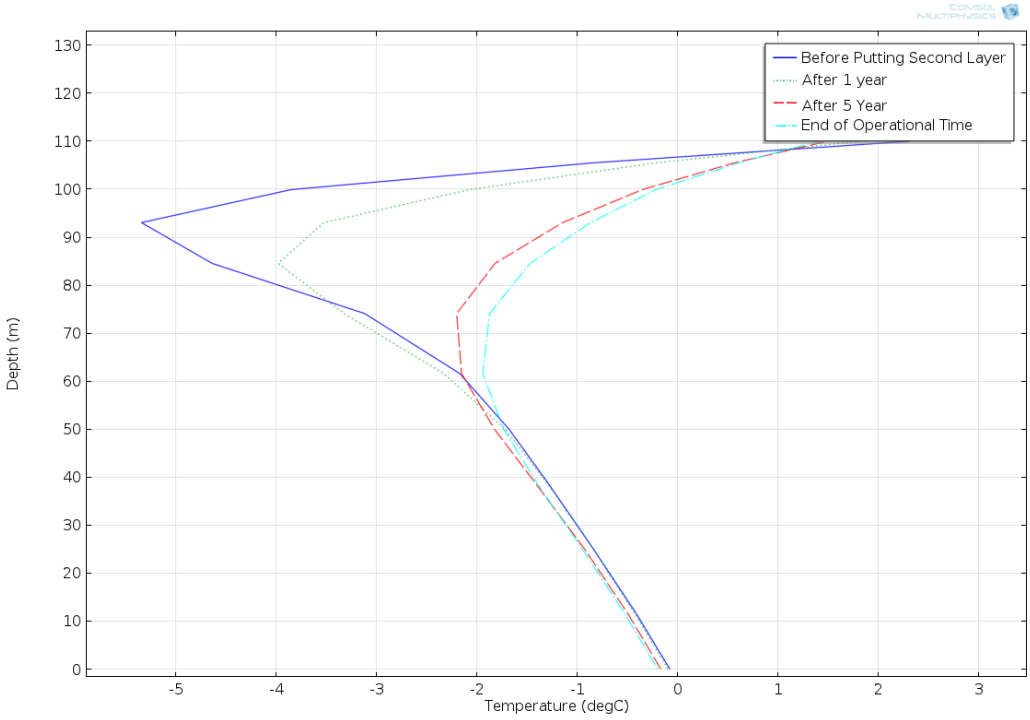

Figure 1-20 East Zone, Thermal Profile beneath tailing pond with tailing at $+10^{\circ}C$, scenario I, different times after putting second layer of tailings

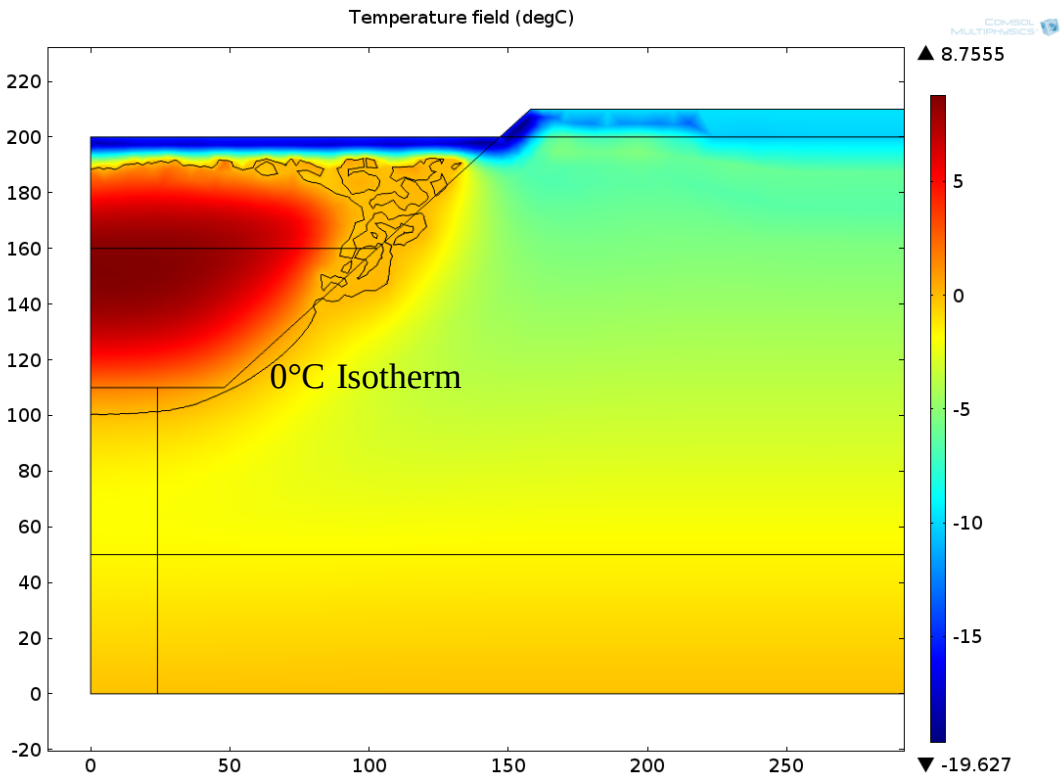

Figure 1-21 East Zone, Thermal Condition, scenario II, at the end of operational time, tailing exposed to air temperature

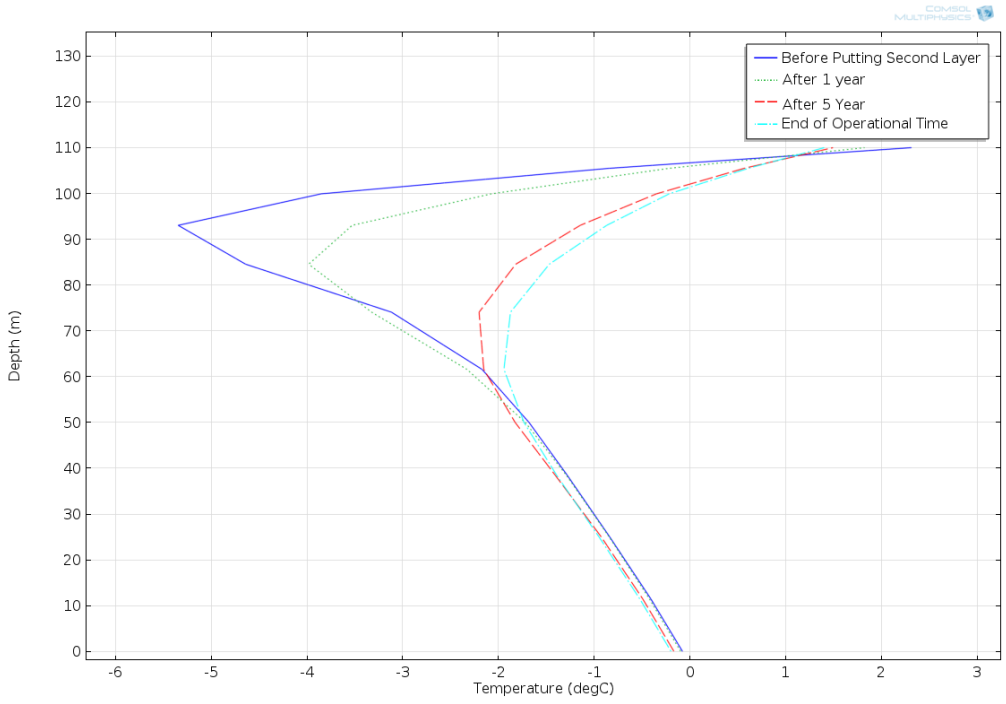

Figure 1-22 East Zone, Thermal Profile beneath tailing pond with tailing at $+10^{\circ}C$, scenario II, different times after putting second layer of tailings and tailing exposed to air temperature

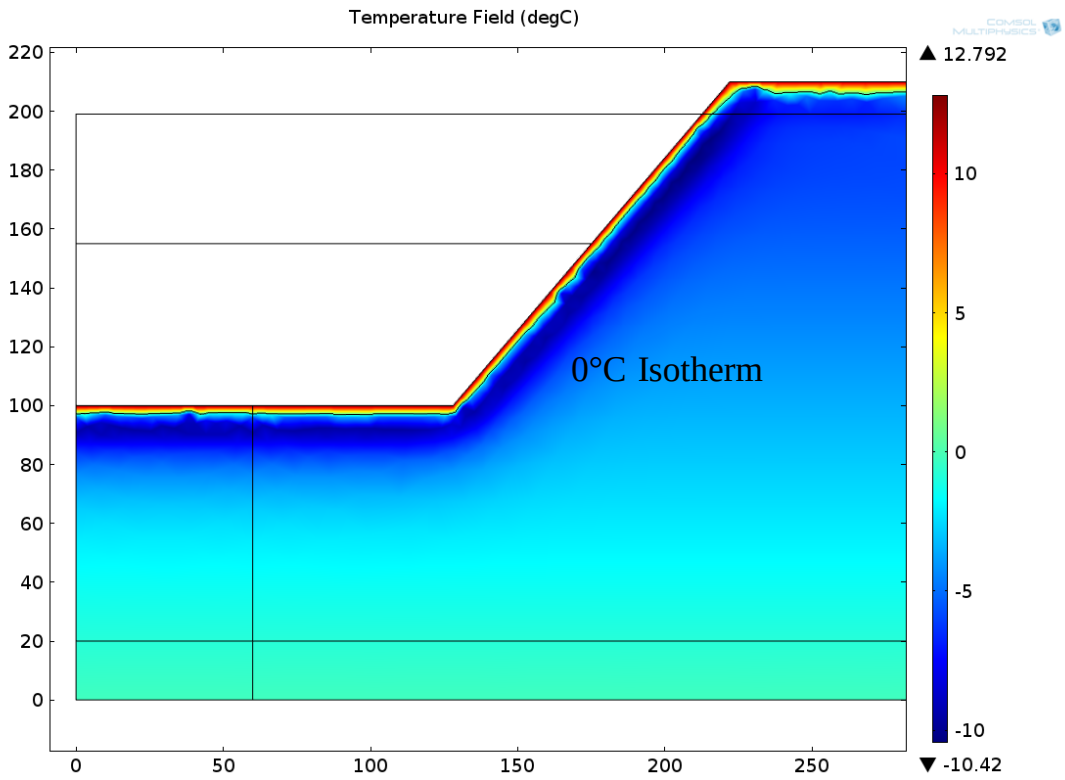

Figure 1-23 Centre Zone, Thermal Condition, 2.5 years after start of excavation (before filling start)

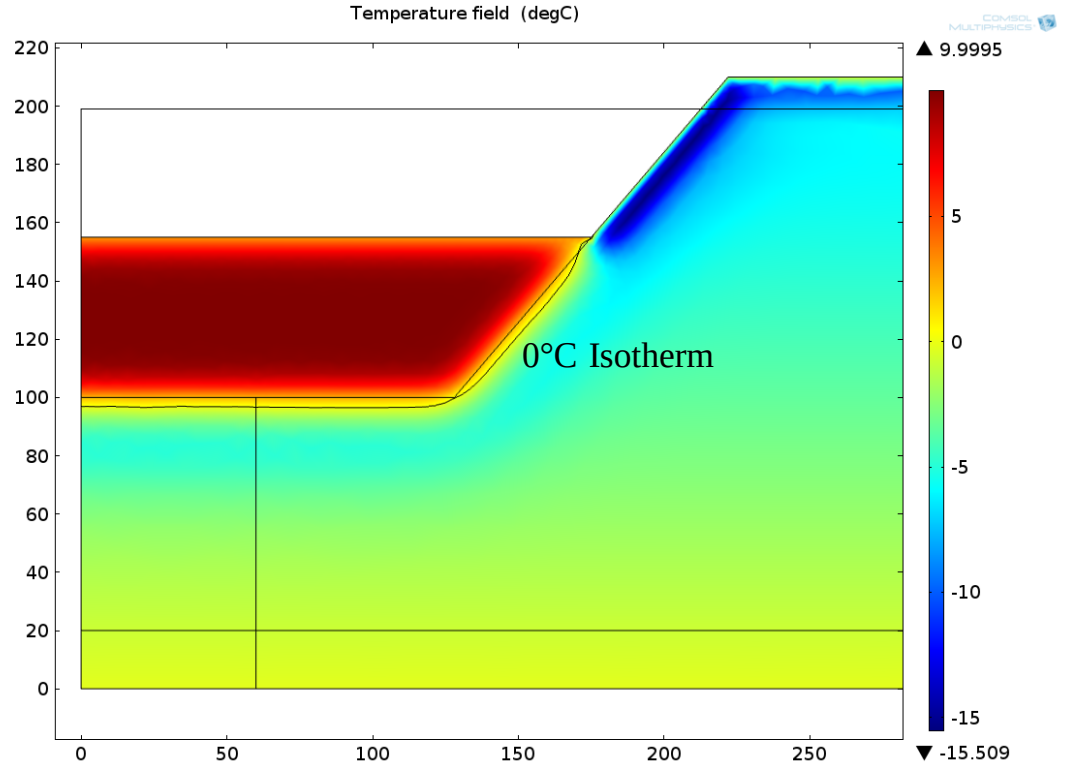

Figure 1-24 Centre Zone, Thermal Condition, 6 months after putting first layer of tailings

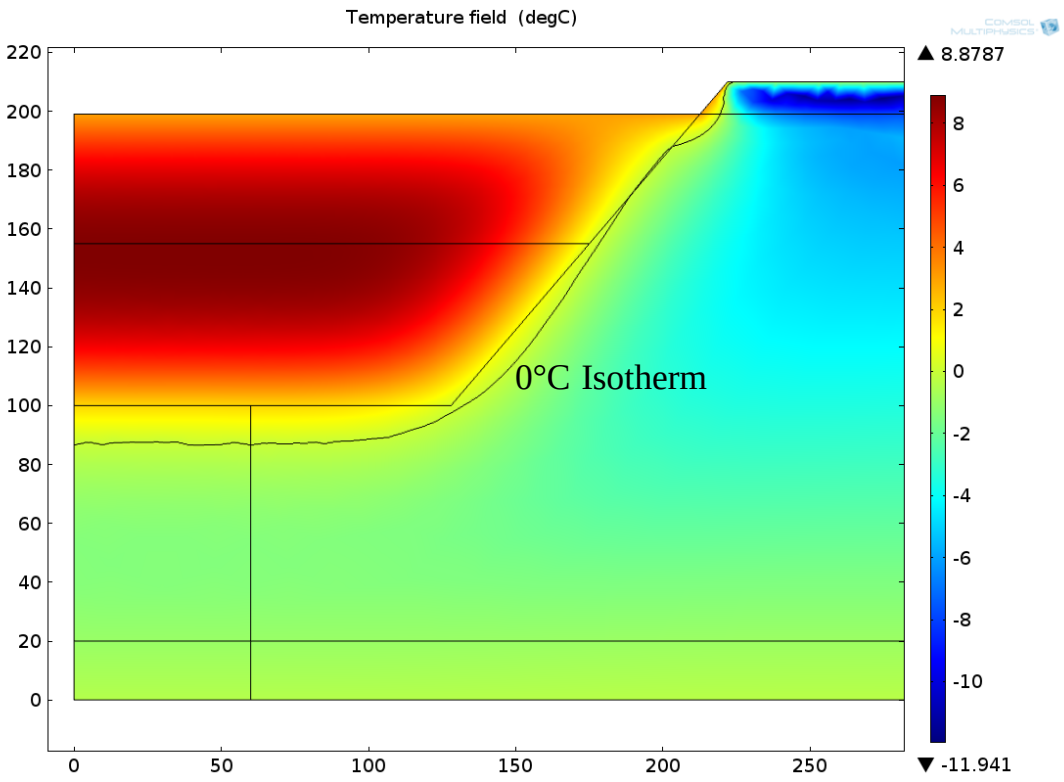

Figure 1-25 Centre Zone, Thermal Condition, scenario I, at the end of operational time

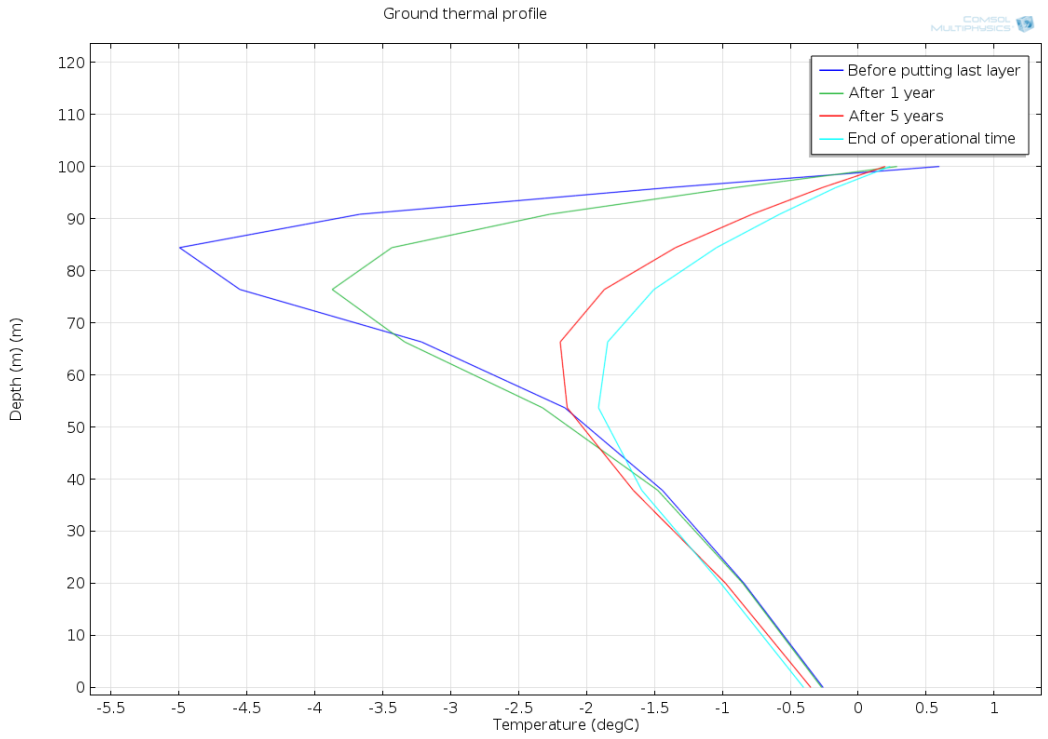

Figure 1-26 Centre Zone, Thermal Profile beneath tailing pond with tailing at $+10^{\circ}C$, scenario I, different times after putting second layer of tailings

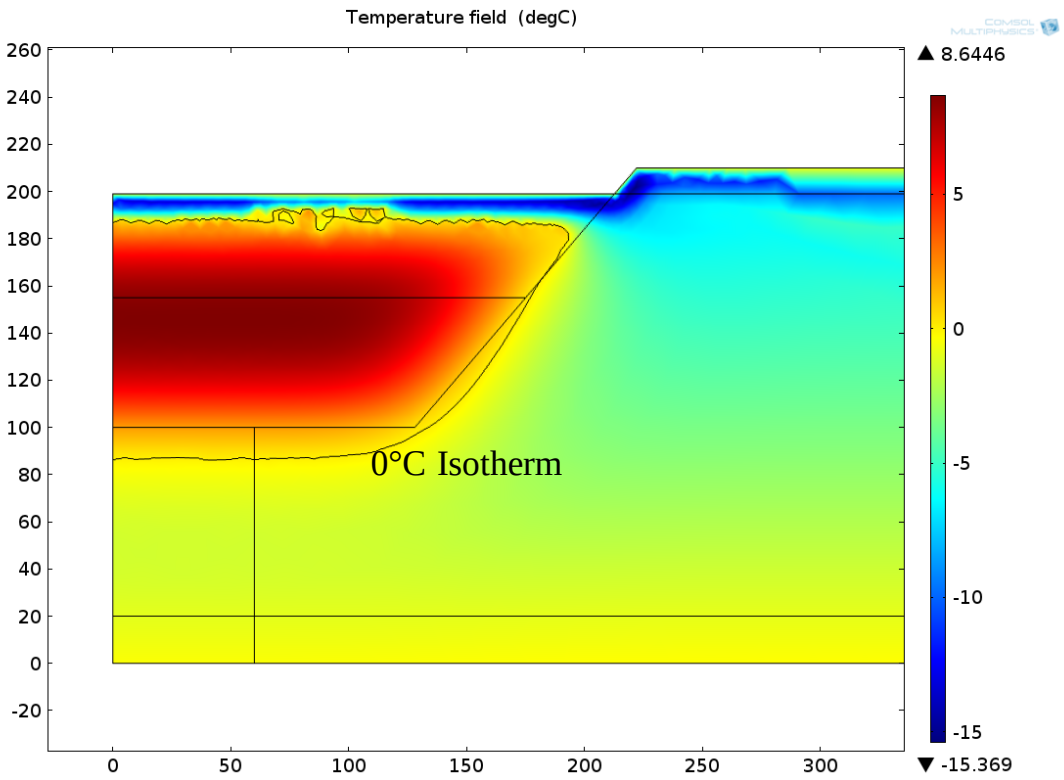

Figure 1-27 Centre Zone, Thermal Condition, scenario II, at the end of operational time, tailing exposed to air temperature

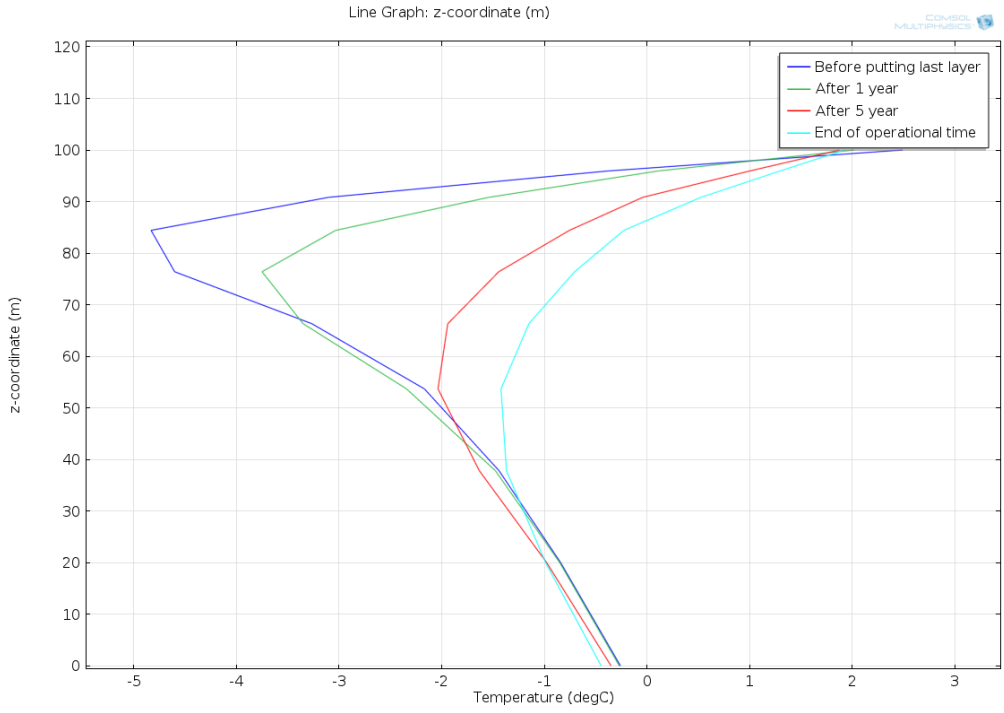

Figure 1-28 Centre Zone, Thermal Profile beneath tailing pond with tailing at $+10^{\circ}C$, scenario II ,different times after putting second layer of tailings, tailing exposed to air temperature

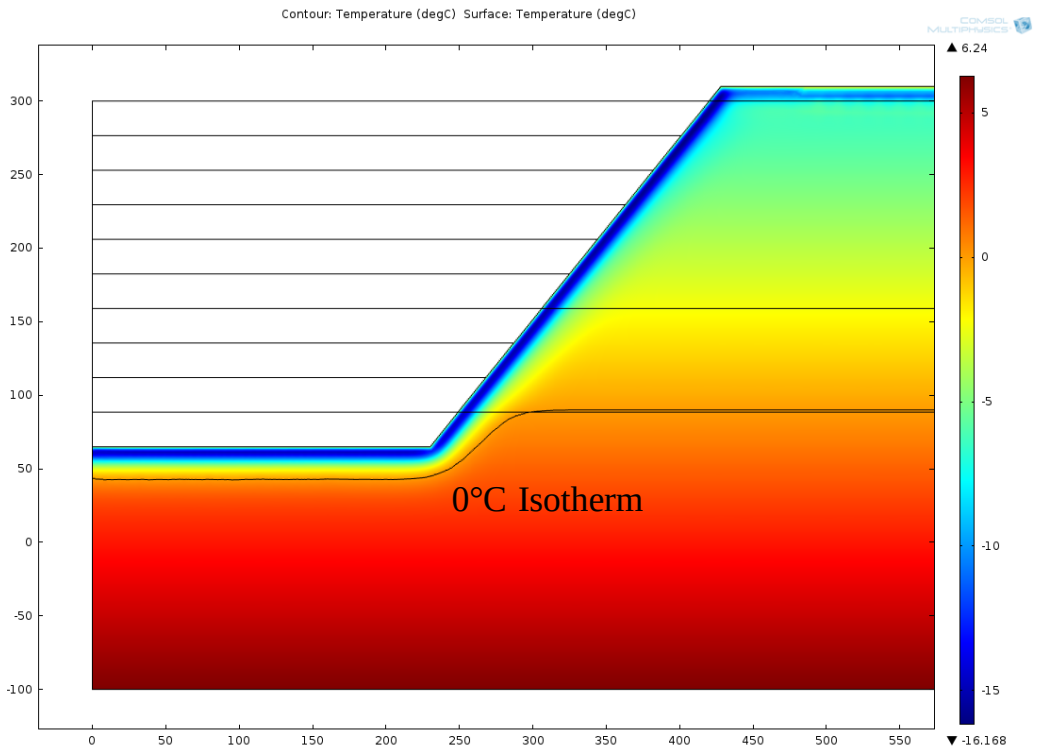

Figure 1-29 Thermal Ground Condition, after end of excavation (6 years after starting of excavation)

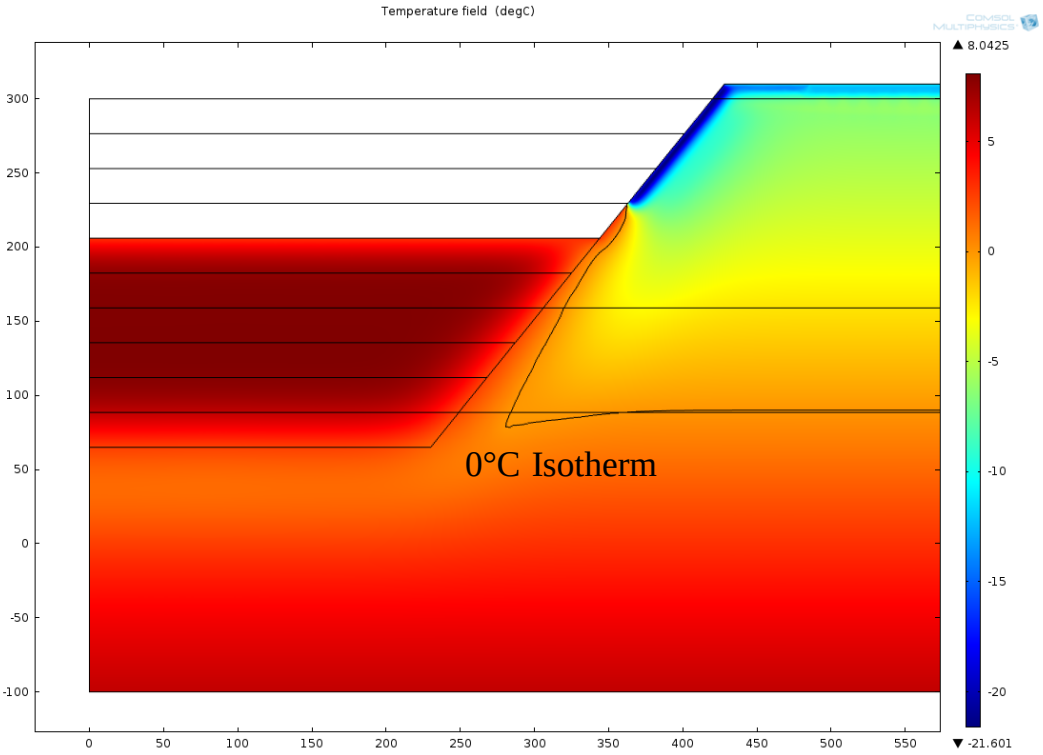

Figure 1-30 Main Zone, thermal condition, scenario I, end of operational time, with water cover on top of warm tailing

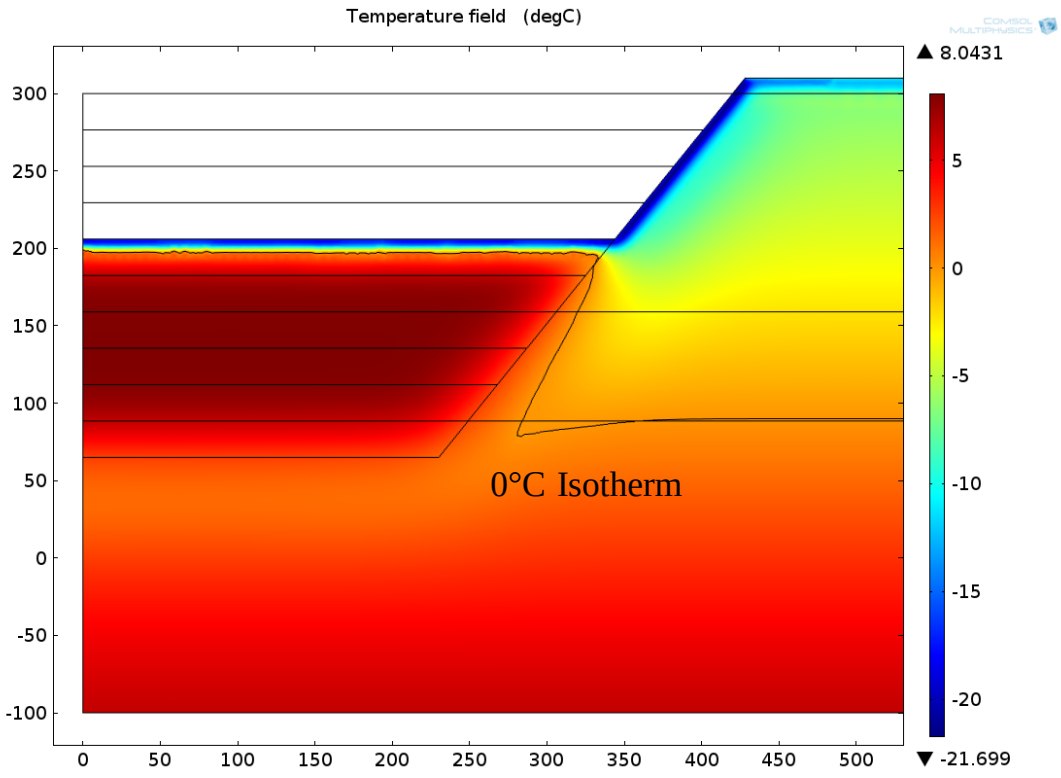

Figure 1-31 Main Zone, thermal condition, scenario I, end of operational time, warm tailing exposed to air temperature

Floor Heave

2.1 Introduction

According to the studies conducted by Areva, groundwater is present at high pressure under the zone of the permafrost. In the permafrost layer, since the pore spaces are filled mostly with frozen water, the hydraulic conductivity of the frozen rock is very low indeed. As a result, when the pit is excavated, this groundwater pressure will remain relatively undisturbed, while the vertical stress above the permafrost boundary is reduced. This could result into floor heave in the Kiggavik Main Zone and the Andrew Lake open pits. Therefore, detailed analysis should be carried out to anticipate whether floor heave is probable or not.

In order to study the possibility of floor heave through numerical modelling, the condition of in-situ horizontal and vertical stresses should be well understood first. In addition, the rock mass ratio (RMR) should be taken into account to consider how fractured the rock is, and hence account for its plastic deformational behaviour. In the following sections, first, the in-situ stress condition in the Northern Canada will be reviewed according to the available literature. Then, the rock conditions according to Areva studies will be studied. Finally, the Hoek and Brown (1980) failure criterion which can be expressed in terms of RMR and other rock condition parameters will be described. A correspondence will be made with the well-known Mohr-Coulomb failure criterion, and results of numerical modelling will be finally discussed.

2.2 In-situ Stress Condition in Northern Canada

Usually, both stress magnitude and direction are needed in any underground stress and deformation analysis. For the purpose of open pit design in mining activities, both vertical and horizontal in-situ stresses are required to investigate the deformation in the wall and floor of the pits especially when high underground water pressure is present. In this section, studies conducted by Maloney and Kaiser (2006), Arjang and Hergert (1997), and Martin et al. (2003) have been reviewed to choose a suitable stress condition for the floor heave analysis.

In the study done by Maloney and Kaiser (2006), the authors tried to re-assess the stress condition in the Canadian Shield. Most of the data used in this study have been obtained from mining locations in Ontario, Manitoba, and Quebec. The data cover depths from 9 m to more than 2000 m with the majority of measurements made above 1500 m. These stress domains typically exist in the upper crust and are a result of various loading and unloading processes. Therefore, the stress state in the upper 1500 m does not exhibit a simple relationship to depth. In

fact, near the surface (depths above 300 m), stresses are disturbed and the original stress conditions are modified by some features such as structural weaknesses and rock mass stiffness variation, which lead to stresses that are typically lower than that acting at the boundary. In-situ stresses in rock masses are rarely uniform, and their distribution depends rock mass complexity and loading history. Figure 2-1 shows the stress magnitude data for the Canadian Shield.

a

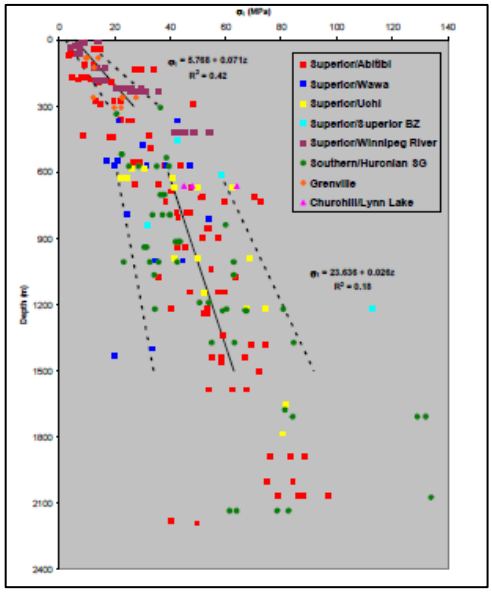

b

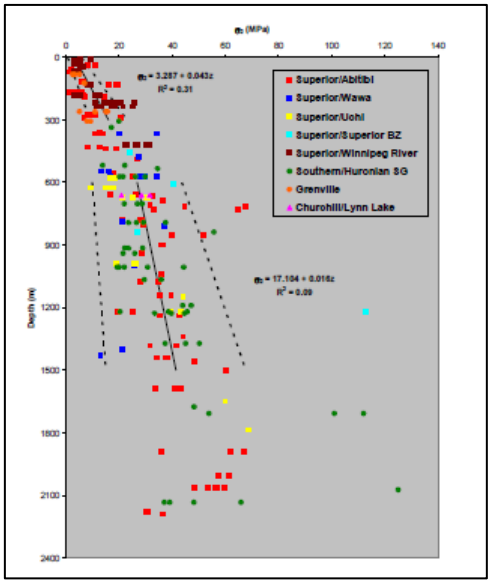

c

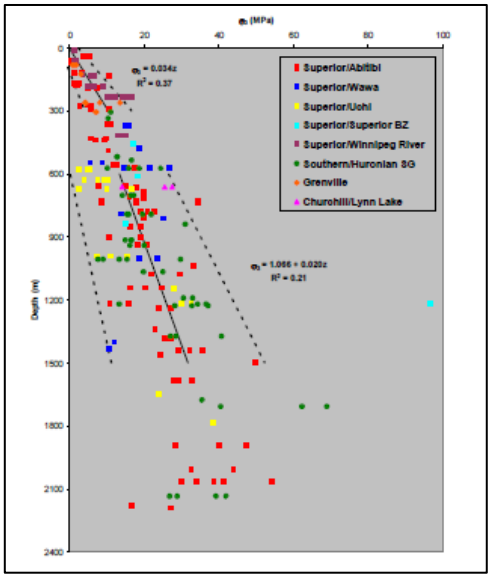

Figure 2-1 Measured magnitude of a) Major, b) Intermediate, and c) Minor principal stresses in Canadian Shield (Maloney and Kaiser 2006)

The authors have considered three zones for the domain: 0 to 300 m, 300 to 600 m, and 600 to 1500 m. Regarding this figure, it is concluded that the gradient of the stress is not constant, but changes with depth.

According to available Canadian Shield database, Maloney and Kaiser (2006) suggested some stress fitting expressions based on magnitude. For instance, the best fits from ground surface to a depth of 300 m with linear regression analysis are:

$$\sigma_1(\text{MPa}) = 5.768\left[\pm 3.358\right] + 0.071\left[\pm 0.019\right] z \qquad 2\text{-}1$$

$$\sigma_2(\text{MPa}) = 3.287\left[\pm 2.600\right] + 0.043\left[\pm 0.015\right] z \qquad 2\text{-}2$$

$$\sigma_3(\text{MPa}) = 0.034\left[\pm 0.005\right] z \qquad 2\text{-}3$$

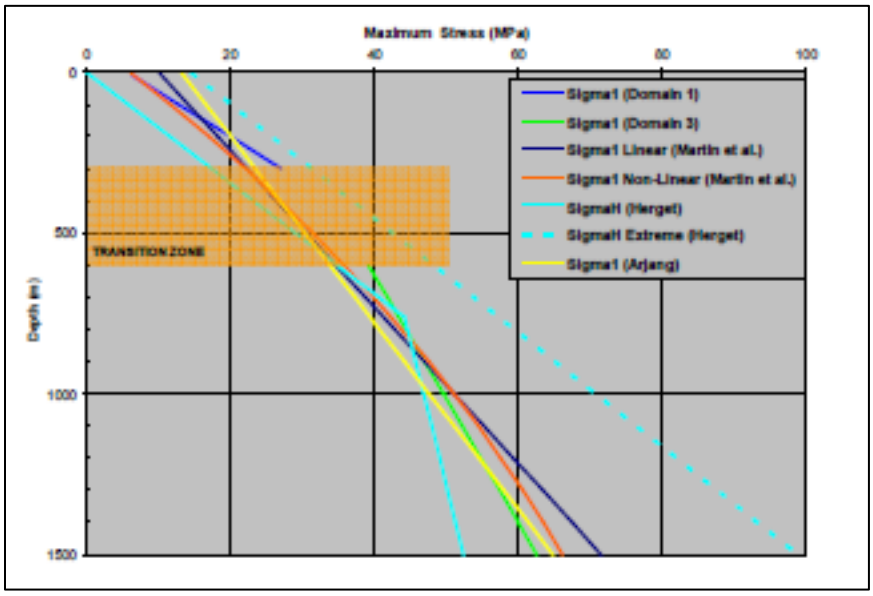

Figure 2-2 Comparisons of stress relationships proposed by Herget, Martin et al, and Arjang, see ref Maloney and Kaiser (2006)

Also, in Figure 2-2, Maloney and Kaiser (2006) have compared their expressions with the work of Arjang (2004), Martin et al (2003), and Herget (1988). From Figure 2-2, it can be seen that the "Herget" expressions underestimate the maximum stress since they are most likely associated with faults or shear zones.

In addition to previous results, Figures 2-3 and 2-4 present the stress ratios (σ_1 / σ_3 and σ_2 / σ_3). In the Canadian Shield, σ_1 corresponds to the maximum horizontal stress, σ_2 refers to minimum horizontal stress, and σ_3 is the vertical stress which as a good first approximation could be considered as the weight of the overburden rock or soil.

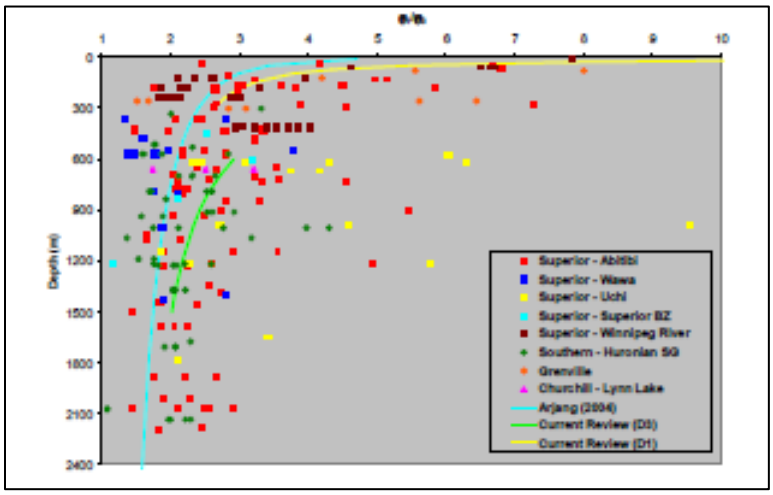

Figure 2-3 Ratio of Major to Minor principal stresses (Maloney and Kaiser, 2006)

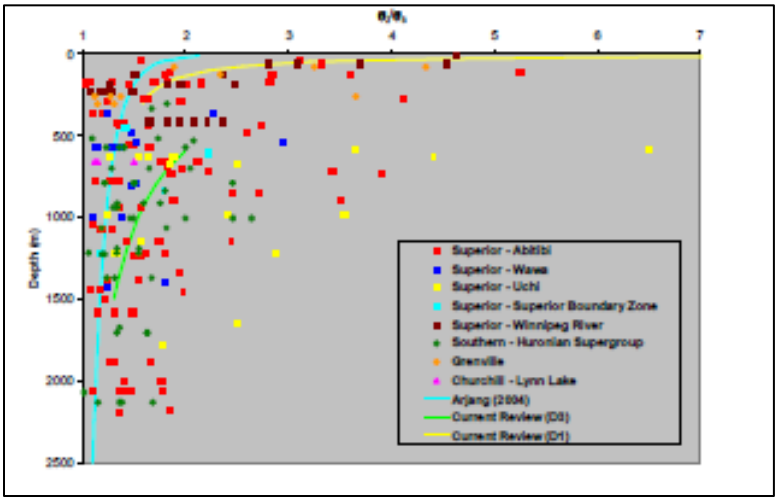

Figure 2-4 Ration of Intermediate to Minor principal stresses (Maloney and Kaiser, 2006)

Most recent expressions for the stress state in the Canadian Shield are summarized in Table 2-1.

Table 2-1 Suggested expressions for principal stresses in the Canadian Shield

	Arjang	Martin et al.	Maloney and Kaiser
σ_1(MPa)	$13.16+0.0345z$	$117.1-111e^{-0.00052z}$	$23.636+0.026z$
σ_2(MPa)	$7.82+0.0232z$	$61.8-59.9e^{-0.00077z}$	$17.104+0.016z$
σ_3(MPa)	$3.01+0.0180z$	$0.025z$ *to* $0.030z$	$1.066+0.020z$

As presented in Table 2-1, Arjang provided a linear expression, while the expression presented by Martin et al is exponential and provides a better fit for the measured data. However, Maloney and Kaiser mentioned that their suggested expressions should be employed for the full depth range, i.e. from surface to 1500 m. Therefore, the suggested relationship by Maloney and Kaiser could not be used in our studies since it does not cover the full depth. Therefore, in this study, the expressions suggested by Martin et al (2003) are used to find the in-situ stress conditions for numerical simulations (Figure 2-5).

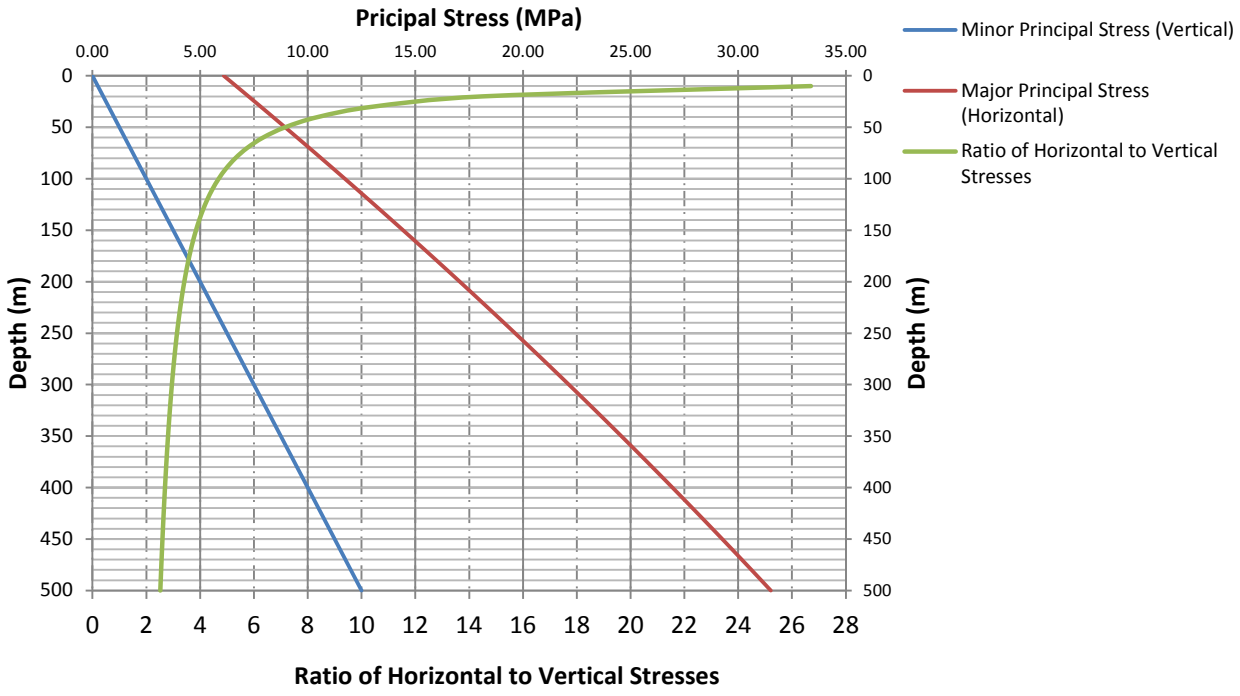

Figure 2-5 In-situ stress conditions, and horizontal to vertical stress ratios according to Martin et al (2003) expression

2.3 Bedrock Geotechnical Conditions

Representative samples for the Kiggavik Main and Centre Zone pits were collected as part of the 2009 geotechnical investigation, and strength tested in the laboratory. Based on the result of assessments, the wall rocks for the Kiggavik Main and Centre pits are generally competent to very competent rocks and exhibit brittle rock characteristics. The unaltered granites and metasediment rock units showed similar strengths, ranging from strong to very strong. The metasediments were shown to be slightly weaker than the granites, but are still very competent with respect to providing a stable wall for an open pit. Results from the laboratory strength testing program are summarized in Table 2-3.

Table 2-2 Main and Centre zone, summary of UCS tests by rock type (Appendix E2)

Rock Type	Alteration	Uniaxial Compression Strength UCS (MPa)	Young Modulus (GPa)	Density (g/cm^3)	Poisson's Ratio
Metasediments	Highly altered	21.8	6.6	2.37	0.01
	Fresh	98.4 ± 26.1	44.6 ± 6.3	2.69 ± 0.10	0.17 ± 0.02
Granite	Slightly to Moderately altered	55.9 ± 27.0	23.9 ± 18.2	2.42 ± 0.22	0.10 ± 0.03
	Fresh	112.3 ± 28.5	45.1 ± 3.4	2.64 ± 0.05	0.15 ± 0.01

All rock strength testing was conducted on thawed cores. The strength characteristics of rock types tested are unlikely to differ significantly in a frozen state due to very low moisture content/void ratios. Recommendations for Rock Mass Ratios (RMR) and strengths for the rock units at Kiggavik Main and Centre are given in Table 2-3. Rock mass qualities for the majority of the pit walls are generally fair to good, with strong to very strong intact rock strength.

Table 2-3 Main and Centre Zone recommended RMR and strengths parameters (Appendix E2)

Rock Unit	RMR	Strength
Upper Metasedimets	46 to 66 (fair to good)	R4/R5 Strong to very strong
Lower Metasediments	62 to 71 (good)	R4/R5 Strong to very strong
Granite	62 to 76 (good)	R4/R5 Strong to very strong
Fault or Mineralization Altered Zones	46 to 62	R3 Moderately strong

For the Andrew Lake area, the granite and metasediments at depths away from zones of alteration are shown to be moderately strong to strong. Results from the laboratory strength testing program are summarized in Table 2-4.

Table 2-4 Andrew Lake, summary of UCS testing by rock type (Appendix E1)

Rock Type	Alteration	UCS (MPa)	Young's Modulus (GPa)	Density (g/cm^3)	Poisson's Ratio
Metasediments	Low to moderately altered	29.9 ± 13.2	11.3 ± 6.5	2.46 ± 0.17	0.08 ± 0.04
	Moderately to High altered	15.9 ± 1.7	2.8 ± 1.5	2.39 ± 0.17	0.09 ± 0.05
Granite	Low to moderately altered	66.5 ± 20.4	22.4 ± 2.5	2.53 ± 0.10	0.15 ± 0.02
	Moderately to High altered	24.7	6.1	2.45	0.24

At Andrew Lake, considerable variability in RMR was observed in the boreholes due to improved ground conditions with depth, as well as due to the inferred proximity to faulting and mineralization zones. The recommended RMR and strengths based on statistically significant intervals of quality and strength for the upper metasediments, lower metasediments, and granite are summarized in Table 2-5.

Table 2-5 Andrew Lake recommended RMR and strengths parameters (Technical Appendix 5B)

Rock Unit	RMR	Strength
Upper Metasedimets	42 to 62 (fair)	R2/R3 Weak to Moderately strong
Lower Metasediments	52 to 74 (fair to good)	R4 Strong
Granite	52 to 65 (fair to good)	R3/R4 Moderately strong to strong
Fault or Mineralization Altered Zones	42 to 52	R2 Weak

2.4 Material Properties used in Designed Open Pits

Limit equilibrium analysis were performed and results presented in AREVA Appendixes E1 and E2. In these assessments, rock mass properties are considered according to the results of strength tests and by considering the ratio of compressive to tensile strength of the rocks. Summary of these properties for Kiggavik Main Zone and Andrew Lake open pits are shown in Tables 2-6 and 2-7. These basic material properties pertaining to intact rock mass strength are taken from Appendix E1 (Appendix D) and Appendix E2 (Appendix D). These will be used as basis in the numerical study presented in this report.

Table 2-6 Kiggavik Main Zone material properties used for limit equilibrium analysis

Rock Mass Unit	GSI=RMR	UCS (MPa)	Intact rock mass constant m_i	Disturbance factor D	γ (kN/m^3)
Upper Metasediment	55	100	12	0.5 or 1	26
Lower Metasediment	65	100	12	0.5 or 1	26
Granite	65	110	12	0.5 or 1	26

Table 2-7 Andrew Lake material properties used for limit equilibrium analysis

Rock Mass Unit	GSI=RMR	UCS (MPa)	Intact rock mass constant m_i	Disturbance factor D	γ (kN/m^3)
Upper Metasediment	55	30	10	0.5 or 1	24
Lower Metasediment	55	50	12	0.5 or 1	25
Granite	65	65	12	0.5 or 1	25

2.5 Hoek and Brown Failure Criterion

Hoek and Brown (1980) introduced their empirical failure criterion for designing of underground excavations in hard rock. Their criterion started with the properties of the intact rock. Then, they added some factors to take into account the characteristics of joints in a rock mass. They also tried to link the empirical criterion to geological observations by means of one of the available rock mass classification schemes. For this purpose, they used the Rock Mass Ratio (RMR). Latter, they replaced RMR with the Geological Strength Index (GSI).

Hoek et al. (2002) defined the original relationship in terms of principal stresses as:

$$\sigma_1^{'} = \sigma_3^{'} + \sigma_{ci}\sqrt{m\frac{\sigma_3^{'}}{\sigma_{ci}} + s} \qquad 2\text{-}4$$

where $\sigma_1^{'}$ and $\sigma_3^{'}$ are the major and minor effective principal stresses, σ_{ci} is the uniaxial compressive strength of the intact rock, m and s are material constants ($s = 1$ is for intact rock).

Later on, Hoek and Brown introduced their Generalized Failure Criterion in which the rock failure parameters are related to the rock mass quality.

$$\sigma_1' = \sigma_3' + \sigma_{ci}\left(m_b\frac{\sigma_3'}{\sigma_{ci}} + s\right)^a \qquad 2\text{-}5$$

where m_b is the reduced value of the intact rock constant m_i and is given by:

$$m_b = m_i \exp\left(\frac{GSI - 100}{28 - 14D}\right) \qquad 2\text{-}6$$

For finding parameters s and a, the following equations are used:

$$s = \exp\left(\frac{GSI - 100}{9 - 3D}\right) \qquad 2\text{-}7$$

$$a = \frac{1}{2} + \frac{1}{6}\left(e^{-GSI/15} - e^{-20/3}\right) \qquad 2\text{-}8$$

In the above expressions, D is a factor which shows the degree of disturbance to which the rock mass has been subjected (Hoek et al. 2002). Figure 2-6 shows Hoek-Brown failure criterion for various GSI numbers by considering for D = 0 and UCS = 100 MPa as an illustrative example.

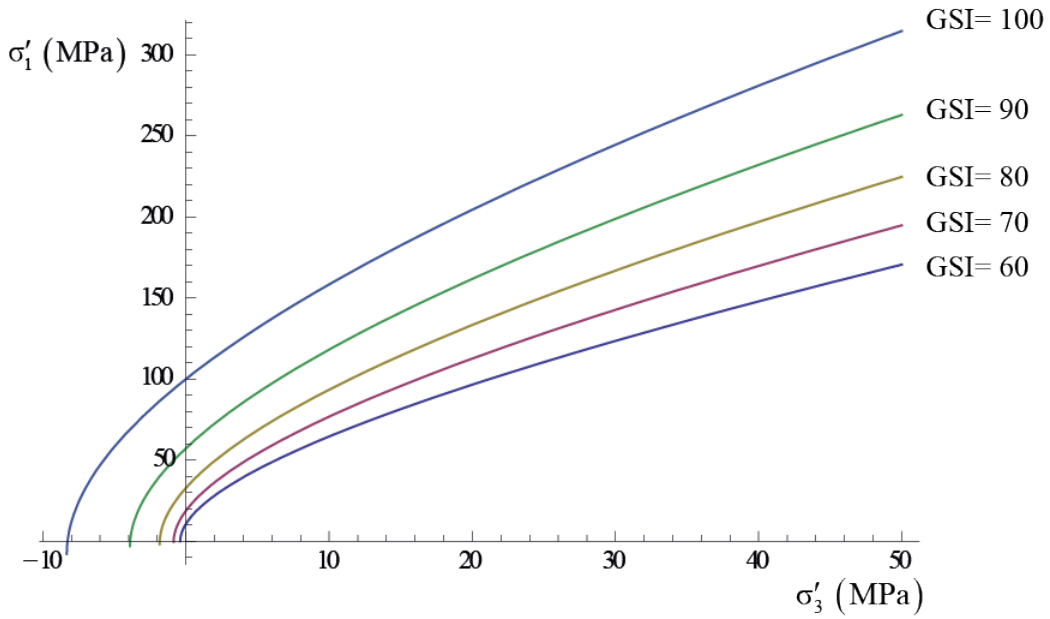

Figure 2-6 Hoek-Brown failure criterion with various GSI values for UCS = 100 MPa and D = 0

2.6 Mohr-Coulomb and Hoek-Brown Failure Criteria Compared

In Figure 2-6, the Hoek-Brown failure criterion is plotted for various GSI numbers. It is found that, by decreasing GSI while both the Uniaxial Compressive Strength (UCS) and disturbance factor (D) are kept constant, both tensile and compressive zones below the failure curve become small. However, it seems that the tensile zone is more affected by variation in Geological Strength Index (GSI). For instance, in the case for which GSI equal to 60, the failure criterion can barely admit any tensile stresses.

Bedrock material properties in the vicinity of the Kiggavik and Sissons projects are presented in Section 2.5. It is found that most of the materials concerned in the project area are fair to good with Rock Mass Ratings (RMR) varying between 50 and 65. As a result, the tensile zone in the Hoek-Brown failure criterion would be very small for these materials, which is not reasonable. Therefore, using an equivalent failure criterion such as Mohr-Coulomb with more range in the tensile stress zone is found to be more appropriate for the purpose of numerical simulations where tension can become quite pronounced during excavation.

In this study, to investigate the effect of open pit mining on the ground deformation, Mohr-Coulomb failure criterion with appropriate cohesive strength (c') and friction angle (φ') values which are compatible with rock mass ratios presented in Tables 2-6 and 2-7 are used.

Equivalent friction angles and cohesive strengths for the various rock masses can be found by fitting an average linear relationship to Eq. 2-5, the original Hoek-Brown failure criterion. The following analytical expressions are thus obtained based on best fit calculations whereby the areas below and above the Mohr-Coulomb plot are balanced over a range of principal stress values between the tensile stress σ_t and a maximum compressive stress $\sigma'_{3\max}$. Thus,

$$\varphi' = \sin^{-1}\left(\frac{6am_b\left(s+m_b\sigma'_{3n}\right)^{a-1}}{2(1+a)(2+a)+6am_b\left(s+m_b\sigma'_{3n}\right)^{a-1}}\right) \qquad 2\text{-}9$$

$$c' = \frac{\sigma_{ci}\left((1+2a)s+(1-a)m_b\sigma'_{3n}\right)\left(s+m_b\sigma'_{3n}\right)^{a-1}}{(1+a)(2+a)\sqrt{1+\dfrac{6am_b\left(s+m_b\sigma'_{3n}\right)^{a-1}}{(1+a)(2+a)}}} \qquad 2\text{-}10$$

with

$$\sigma'_{3n} = \sigma'_{3\max} / \sigma_{ci} \qquad 2\text{-}11$$

2.7 Parameters used in this Numerical Study

The mechanical properties of materials used in the numerical modelling for the purpose of floor heave analysis have been summarized in Tables 2-8 and 2-9. Rock mass units and material properties are taken from Appendixes E1 (Appendix D) and E2 (Appendix D).

According to the rock mass conditions of the different materials presented in Tables 2-2 and 2-4, a wide range of Young's Modulus values could be selected for each material. For instance,

Young's modulus for Granite rock ranges between 6 and 45 GPa based on whether the rock is fresh or altered. Besides, according to the rock mass quality presented in Tables 2-3 and 2-5, Granite rock quality can be considered moderately to highly strong. This would mean that the upper end of the range of 6 to 45 GPa could be selected as Young's modulus. However, the rock quality could be degraded as a result of mining activities such as excavation or blasting. Therefore, Young's modulus for Granite rock has been chosen as 35 GPa for the Kiggavik Main Zone. For Lower Metasediment and Upper Metasediment rocks, a Young's modulus of 25 and 20 GPa has been chosen respectively based on the same above argument.

Table 2-8 Kiggavik Main Zone Material properties used in numerical modelling

Rock Mass Unit	GSI= RMR	UCS (MPa)	m_i	D	m_b	s	Young's Modulus (GPa)	γ (KN/m^3)	c (MPa) Equivalent Cohesion	φ (deg) Equivalent Friction Angle
Upper Metasediment	55	100	15	0.5	1.76	0.0025	20	26	5.03	29
Lower Metasediment	65	100	15	0.5	2.83	0.0094	25	26	6.08	35
Granites	65	110	20	0.5	3.78	0.0094	35	26	7.24	37

Table 2-9 Andrew Lake Material properties used in numerical modelling

Rock Mass Unit	GSI= RMR	UCS (MPa)	m_i	D	m_b	s	Young's Modulus (GPa)	γ (KN/m^3)	c (MPa) Equivalent Cohesion	φ (deg) Equivalent Friction Angle
Upper Metasediment	55	30	12	0.5	1.41	0.0025	15	25	1.41	29
Lower Metasediment	55	50	12	0.5	1.76	0.0025	20	25	2.51	31
Granites	65	65	15	0.5	2.27	0.0094	25	25	3.72	33

Referring to the strength testing results presented in Appendixes E1 and E2, the bedrock in the vicinity of the Sissons project is made up of weaker materials in comparison to the materials in the area of Kiggavik project. Therefore, lower values of Young's Modulus for rock materials are considered for the purpose of numerical modelling. For the case of Andrew Lake open pit, Young's Modulus values of 25, 20, and 15 GPa for Lower Metasediments, Granitodis, and Upper Metasediments have been chosen respectively.

Permeability values of rocks have been selected according to the data presented in Technical Appendixes 5B and 5D. In these documents the hydraulic conductivity of permafrost material is considered as 10^{-12} m/s which is equivalent to a permeability value of about 10^{-20} m^2. For Granite rock which forms most part of the unfrozen domain in the vicinity of the project, a value of 10^{-15} m^2 was selected which refers to a hydraulic conductivity of 10^{-8} m/s that is reported in Technical Appendix 5D.

2.8 Mohr-Coulomb Equivalent Failure Criteria

As discussed in Section 2.6, and based on material properties presented in Tables 2-8 and 2-9, in this numerical study, Mohr-Coulomb failure criterion is used for the computation of plastic behaviour of the ground materials. In Figures 2-7 and 2-8, various generalized Hoek-Brown failure criteria with their equivalent Mohr-Coulomb envelopes are shown for the different materials involved in this numerical simulation. A value of $\sigma'_{3n} = \sigma'_{3\max} / \sigma_{ci} = 0.25$ was used in the fit.

a

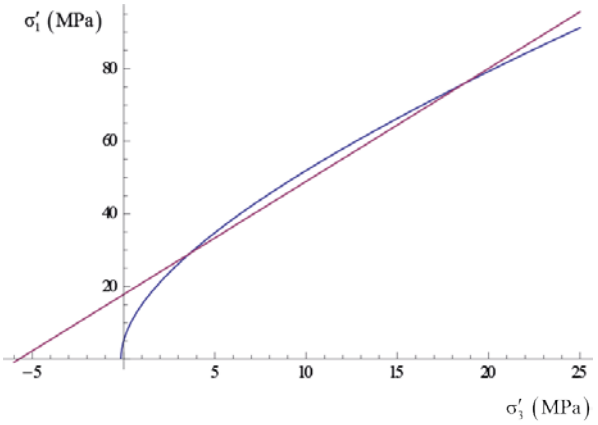

b

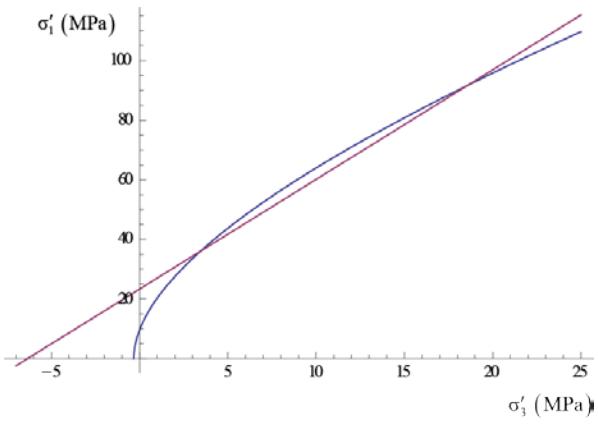

c

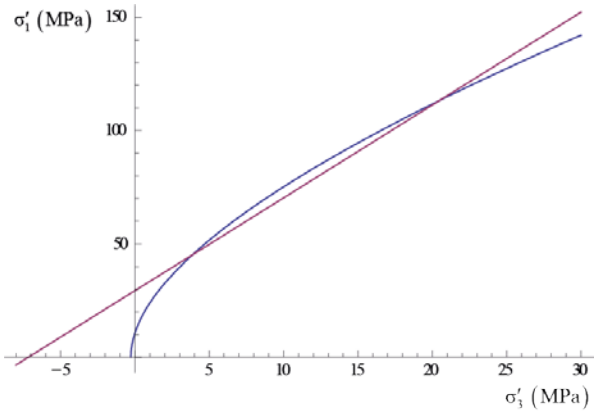

Figure 2-7 Kiggavik Main Zone, Equivalent Mohr-Coulomb failure criterion for a) Upper Metasediment b) Lower Metasediment, and c) Granite

a

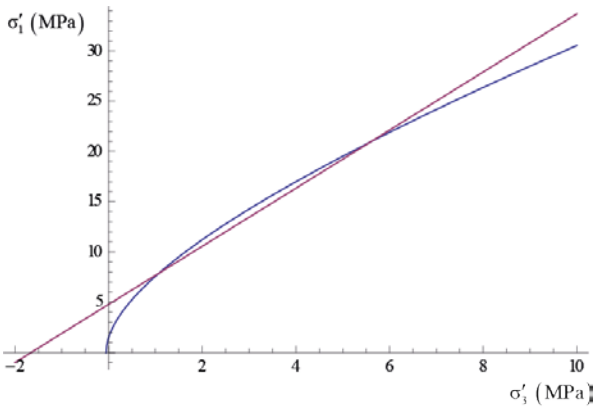

b

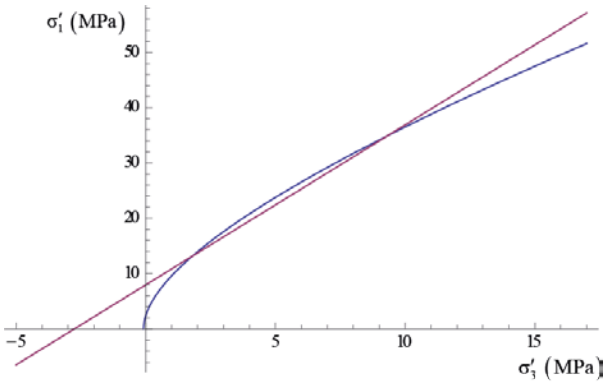

c

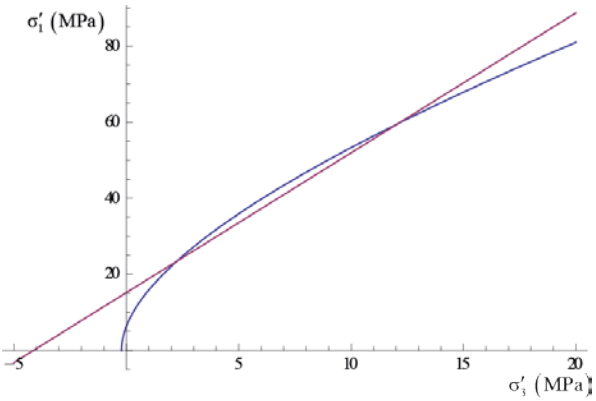

Figure 2-8 Andrew Lake, Equivalent Mohr-Coulomb failure criterion for a) Upper Metasediment b) Lower Metasediment, and c) Granite

2.9 Water Pressure Condition

There are many lakes located near the proposed location of both Kiggavik and Sissons pits. Some of these lakes are large and deep enough to support open taliks in the continuous permafrost in the vicinity of the project. Since the permafrost layer has a very low permeability, most of the water will flow within the warm unfrozen ground beneath the permafrost layer. Water flows from lakes with higher hydraulic head to the ones with lower hydraulic head.

As a result of this flow, the pressure head below the impermeable permafrost rises above ground surface level. According to Tier 3 Technical Appendix 5B, in 2009 thermistors have been installed in four boreholes: END-09-01, ANDW-09-03, MZ-09-02, and MZ-09-04. Moreover, during the 2011 field investigations, multilevel thermistor strings were installed in two boreholes GW-11-01 and GW-11-02. The hydraulic head measured in the piezometer located beneath the permafrost in the area of the End Grid deposit, END-09-01, was about 9 m above ground surface, while in the area of the Andrew Lake deposit the hydraulic head measured in a piezometer, ANDW-09-03, was about 3 m above the ground surface. The hydraulic head measured in the one piezometer located in the area of the Main Zone deposit, MZ-09-04, was about 25 m above ground.

For this numerical study, in order to consider the worst case scenarios, the pressure head below the permafrost layer at Kiggavik Main Zone is considered to be 25 m above ground surface level. For the Andrew Lake open pit the pressure head is considered as 9 m above ground surface level. Water pressure conditions are shown in Figures 2-9 and 2-10.

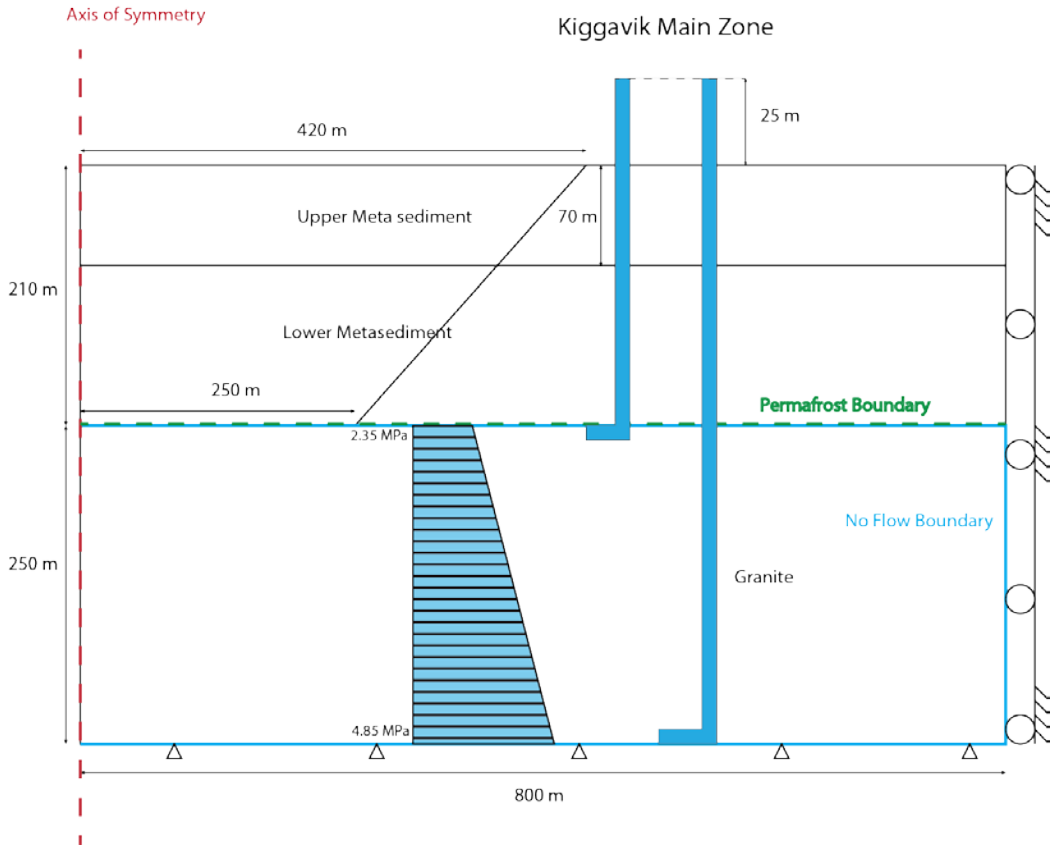

Figure 2-9 Kiggavik Main Zone water pressure condition beneath permafrost layer

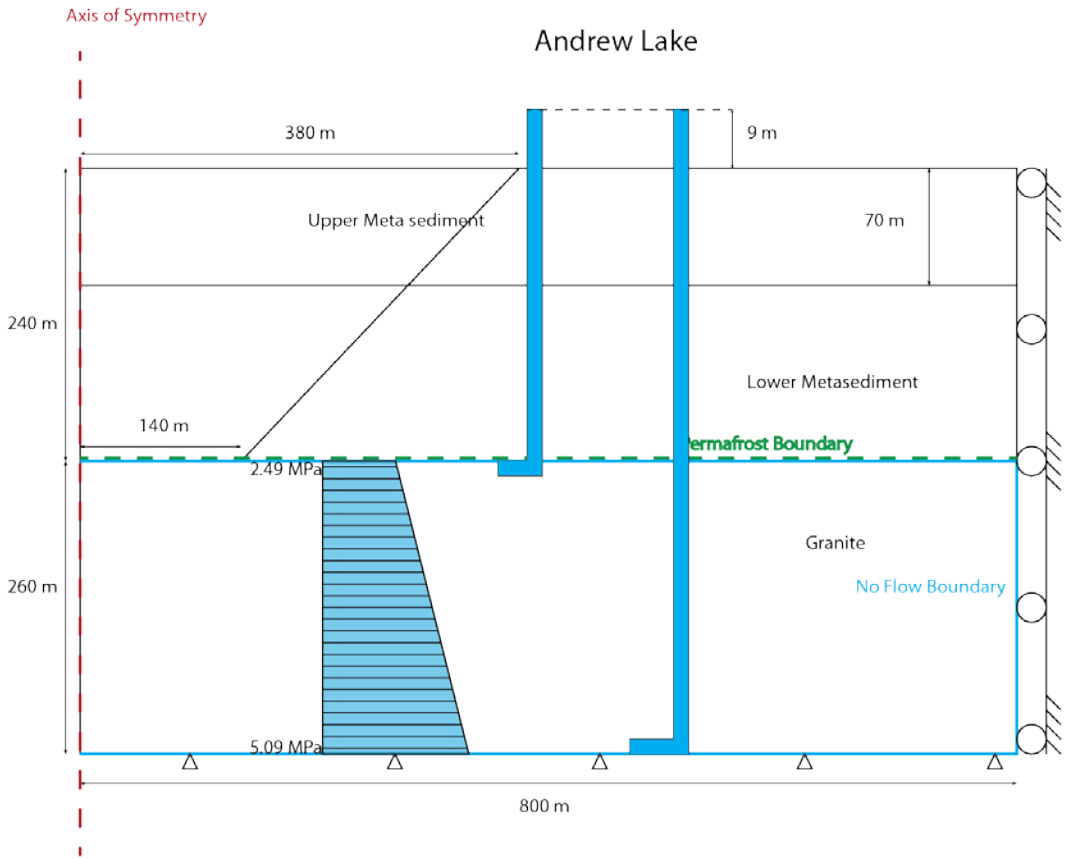

Figure 2-10 Andrew Lake water pressure condition beneath permafrost layer

2.10 Initial Stress and Boundary Conditions

The boundary conditions, domain materials, and initial in-situ stress conditions used in the numerical modelling are shown schematically in Figures 2-11 and 2-12. They are self-explanatory and follow the expressions of in-situ stresses proposed by Martin et al. (2003).

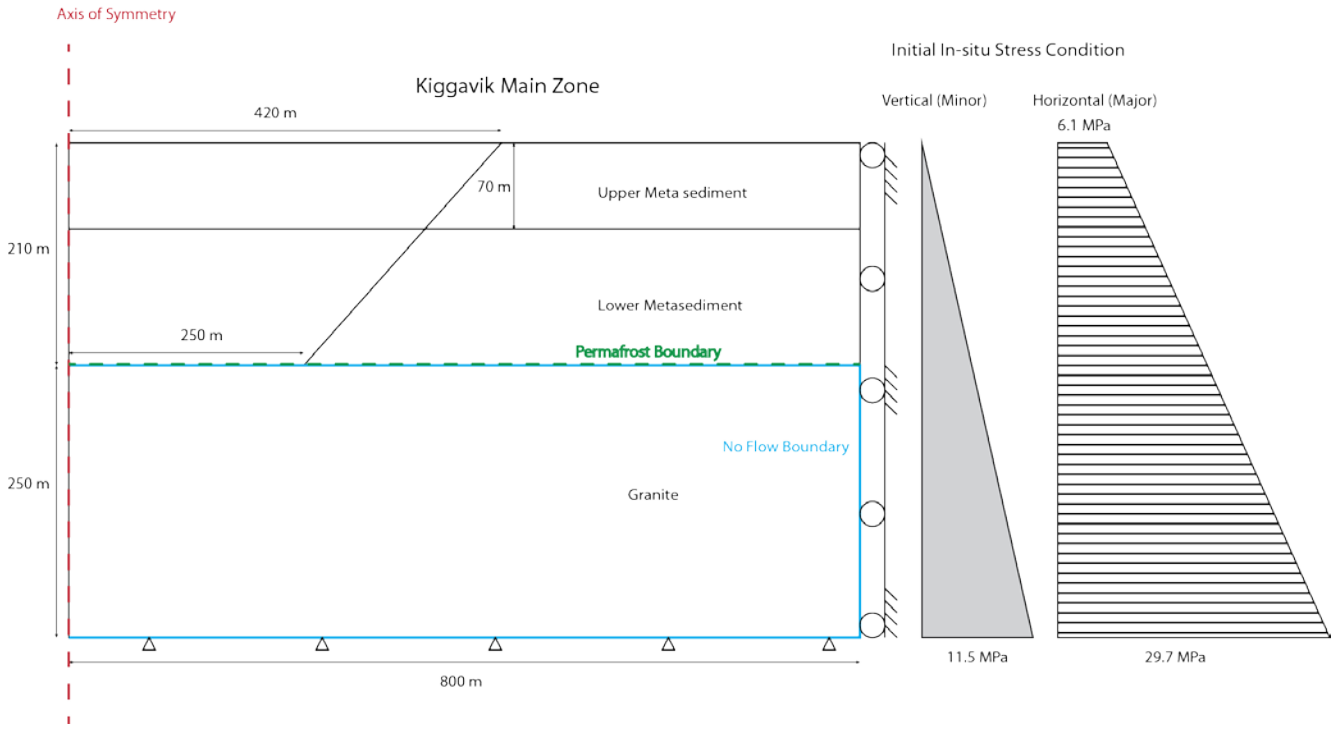

Figure 2-11 Kiggavik Main Zone Boundary conditions for numerical modelling

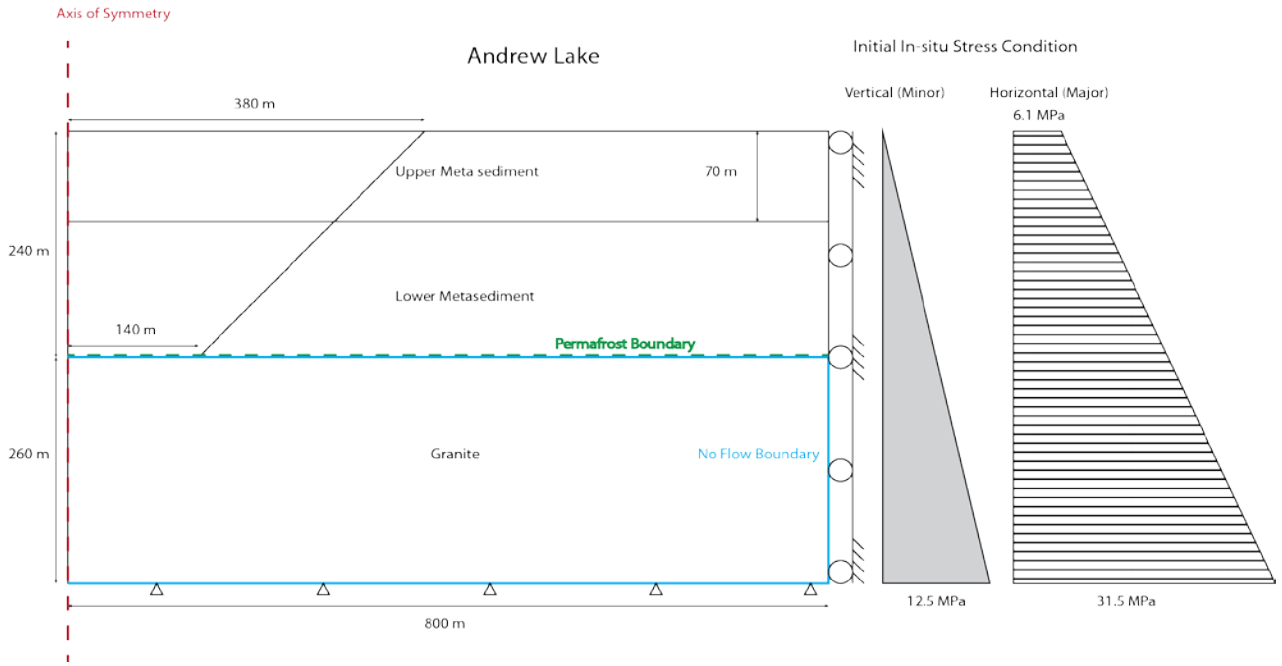

Figure 2-12 Andrew Lake Boundary conditions for numerical modelling

2.11 Results

In this section, results of numerical studies on the floor heave analysis on Kiggavik Main Zone pit (slope angle of 51 deg) and Andrew Lake pit (slope angle of 45 deg) are presented. It is recalled that the initial in-situ stresses are based on Martin et al. (2003) relationship as discussed previously. Accordingly, in all simulations the major (σ_1) and intermediate (σ_2) principal stresses are horizontal, while the minor (σ_3) principal stress is in the vertical direction. Note that in COMSOL, negative in stress means compression, while positive means tension.

In order to assess the ground deformation as a result of mining activity, two scenarios are considered in the numerical studies presented. In the first scenario, both the floor and wall deformations are computed down to an excavation level at 5 m above the permafrost boundary. In this model, it is assumed that the water is present at high pressure beneath permafrost at all stages of excavation. In the second scenario, in the last excavation stage it is assumed that mining process breaks through the permafrost so that the water under high pressure can drain out from the bottom of the pit so that the underlying water pressures redistribute in both space and time.

In this section for both Kiggavik Main Zone and Andrew Lake open pits projects, the results of last stage are presented. Due to the large number of figures, the results of other steps are presented in Appendix B.

2.11.1 Main Zone

Artesian pressure conditions with the piezometric level located at 25 m above ground surface exist in the layer underneath the permafrost. In the numerical simulations, these conditions have to be reflected into the initial pore water pressure distribution. Hence, at the bottom of the pit which is 210 m below ground surface, a water pressure head of 235 m (= 210 + 25 m) was imposed as explained previously in Section 2.9.

Scenario I (Excavation reaches 5 m above permafrost)

Figures 2-13 and 2-14 show the vertical and horizontal displacements respectively after excavating down to 5 m above the permafrost boundary in several stages. The maximum vertical displacement at the bottom of the pit is found to be 30 mm, while the maximum horizontal displacement is 68 mm.

Figures 2-15 and 2-16 give the mean and deviatoric effective principle stresses respectively. Some stress concentration at the bottom corner of the pit is observed as a result of high displacement being localized and due to the kinematics of the deformations.

Finally, Figure 2-17 shows areas within which the minor principal stress (σ_3') are in tension after excavation to this level. Figure 2-18 displays the pore pressure condition below the frozen impermeable layer as the excavation reaches 5 m above permafrost layer.

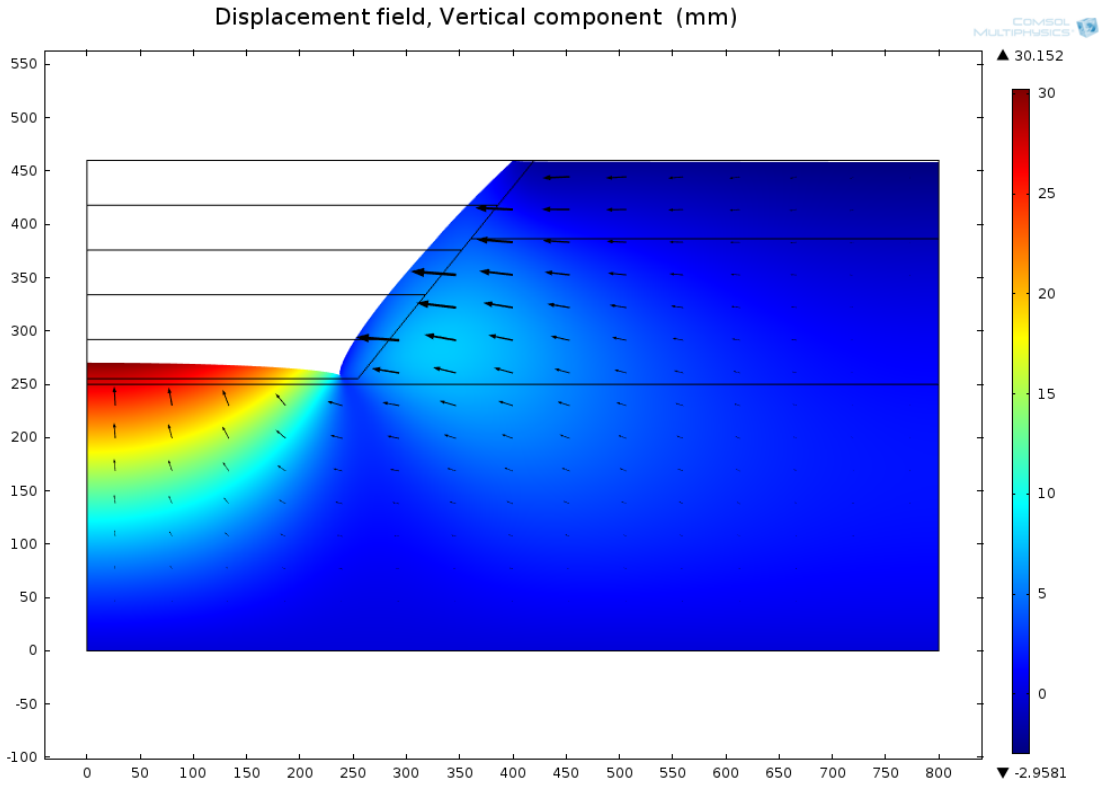

Figure 2-13 Vertical displacement field (mm), excavation up to 5 m above permafrost boundary

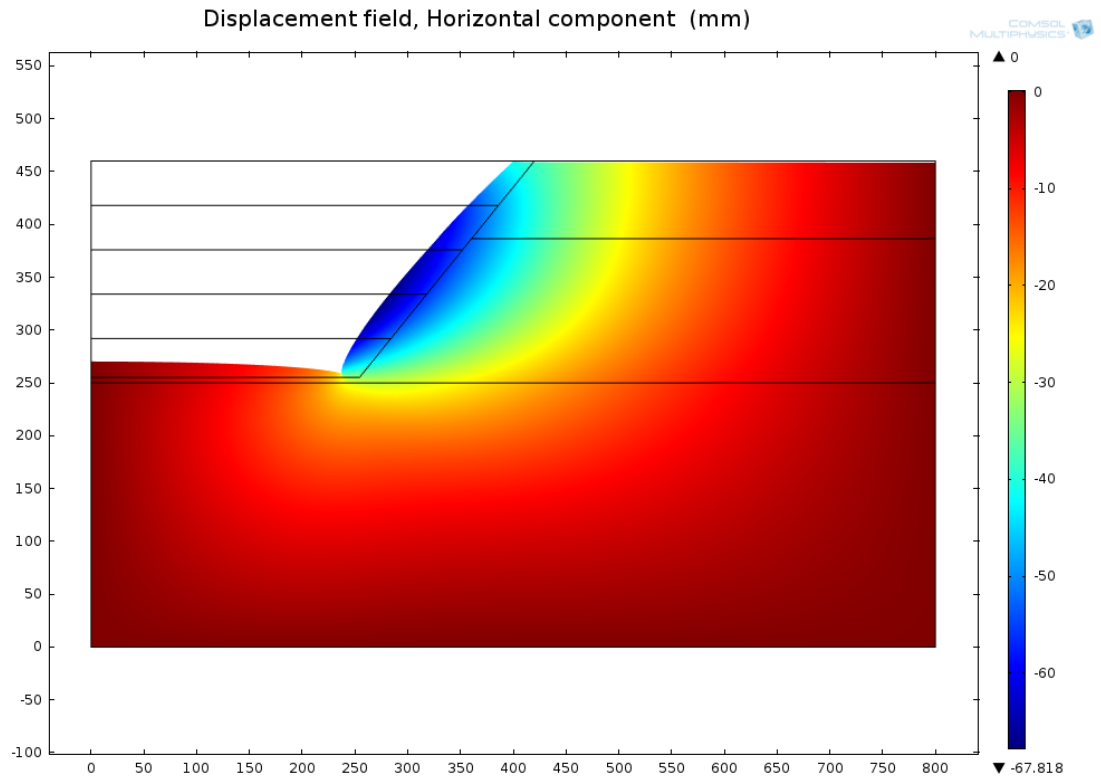

Figure 2-14 Horizontal displacement field (mm), excavation up to 5 m above permafrost boundary

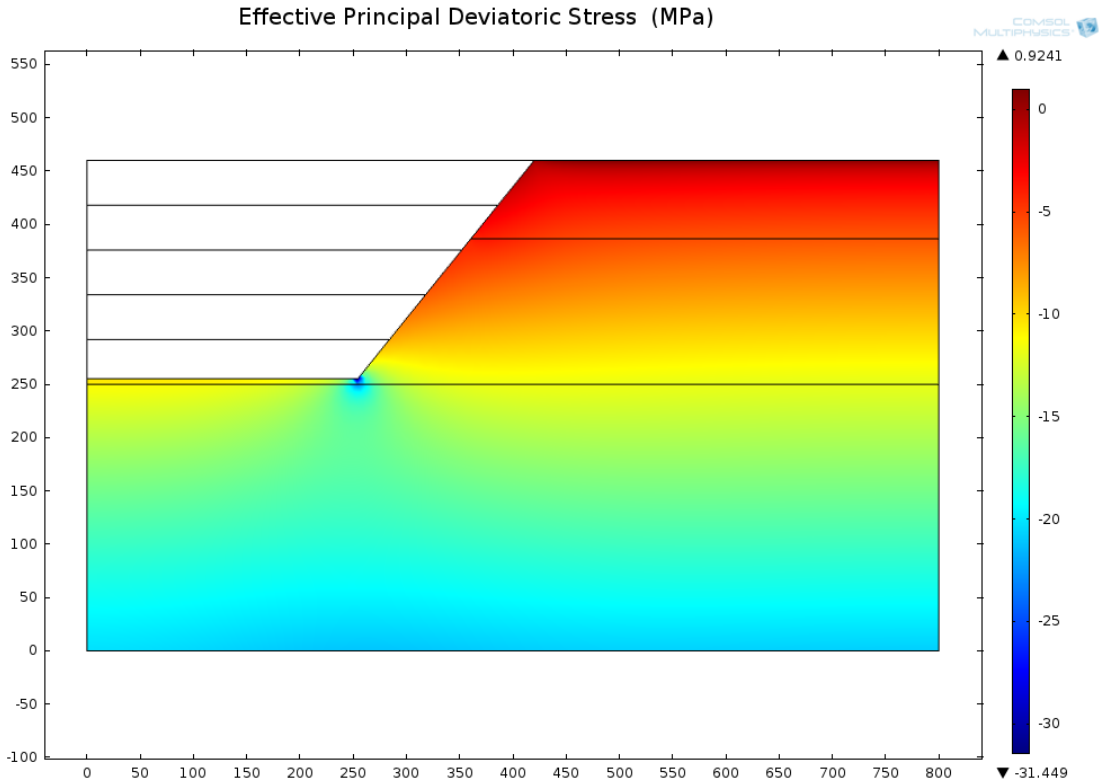

Figure 2-15 Mean effective principal stress (MPa), excavation up to 5 m above permafrost boundary

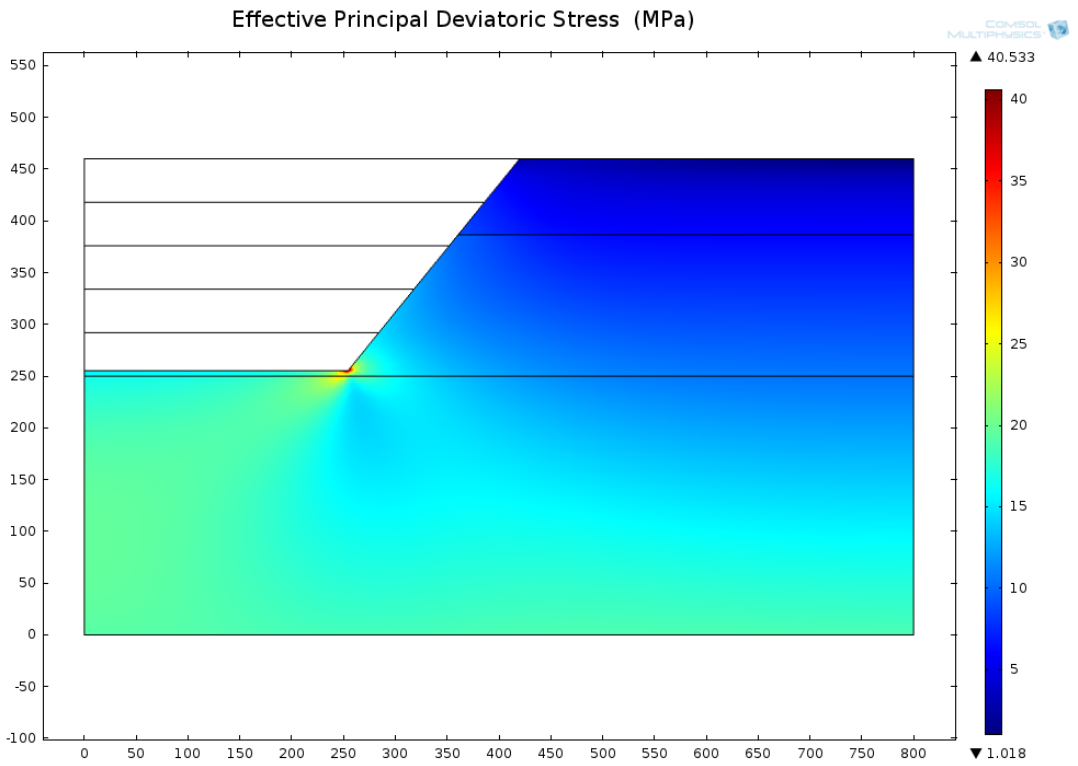

Figure 2-16 Effective deviatoric stress (MPa), excavation up to 5 m above permafrost boundary

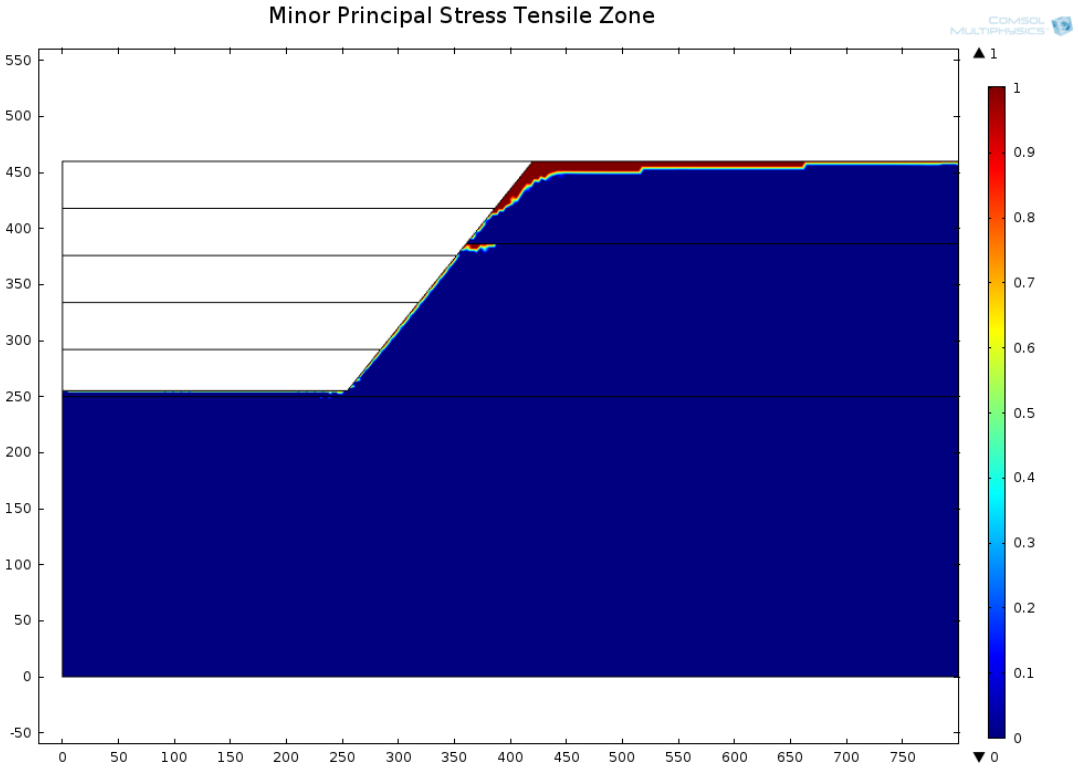

Figure 2-17 Minor principal stress tensile zone ($\sigma_3' > 0$)

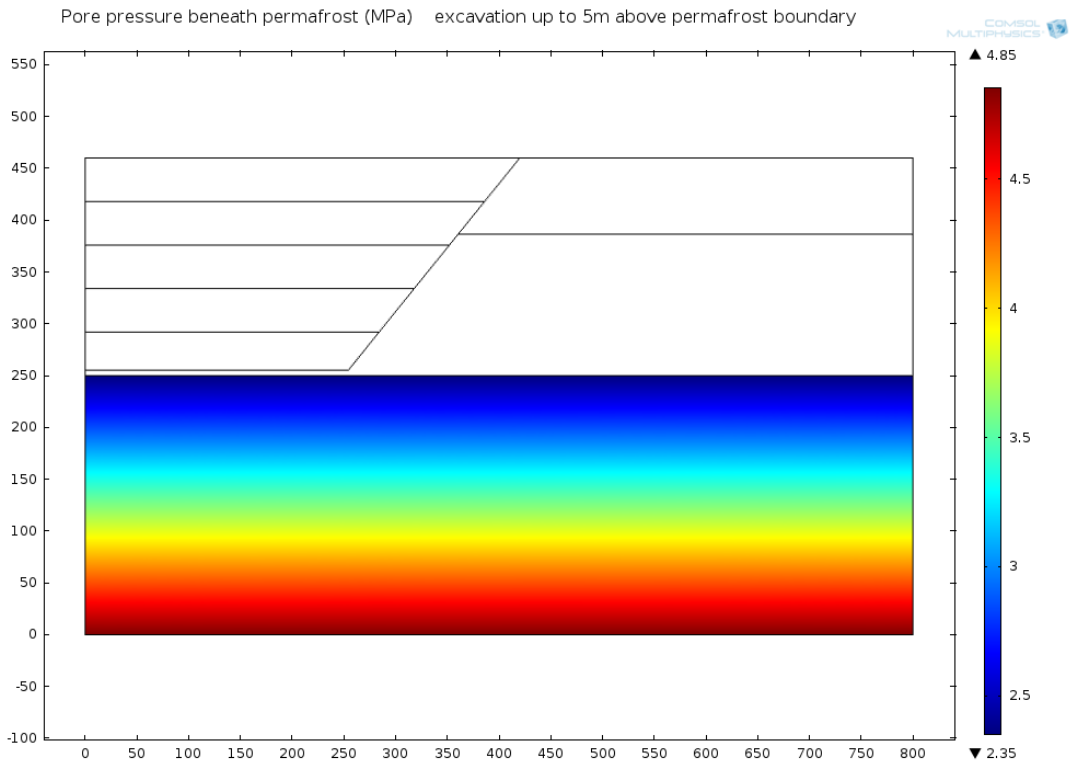

Figure 2-18 Pore pressure beneath permafrost, excavation up to 5m above permafrost boundary

Scenario II (Excavation reaches permafrost boundary)

Figures 2-19 and 2-20 show the vertical displacements just after the excavation breaks through the permafrost boundary and after one year. The maximum vertical displacement at the beginning is 41 mm, while after one year some consolidation/settlement occurs and the maximum vertical deformation ultimately becomes 31 mm. Figures 2-21 and 2-22 indicate the horizontal displacements after breaking through the permafrost boundary, as well as one year later. In the beginning, the maximum horizontal displacement is 69 mm, while after one year it increases further and reaches 70 mm.

Figures 2-23 and 2-24 give the mean effective stress and deviatoric stress respectively one year after breaking through the permafrost boundary. Some stress concentration at the bottom corner of the pit is observed as a result of high displacements being localized and due to the kinematics of the deformations.

Figure 2-25 shows areas within which the minor principal stress (σ'_3) become tensile one year after excavation to this level. Most of the tensile zones are located at the crest of the slope consistent with the analyses carried out in Areva Appendix E2, whereas tensile stresses also appear at the bottom of the pit, but to a minor extent. Figures 2-26 and 2-27 display the pore

pressure distribution below the frozen impermeable layer as the excavation reaches the permafrost layer and one year later, respectively. It is noted that when the excavation breaks through the permafrost layer, water flows through the bottom of the pit, which changes the pore pressure distribution in the warm underlying layer with the effect of lowering moderately the initial piezometric line.

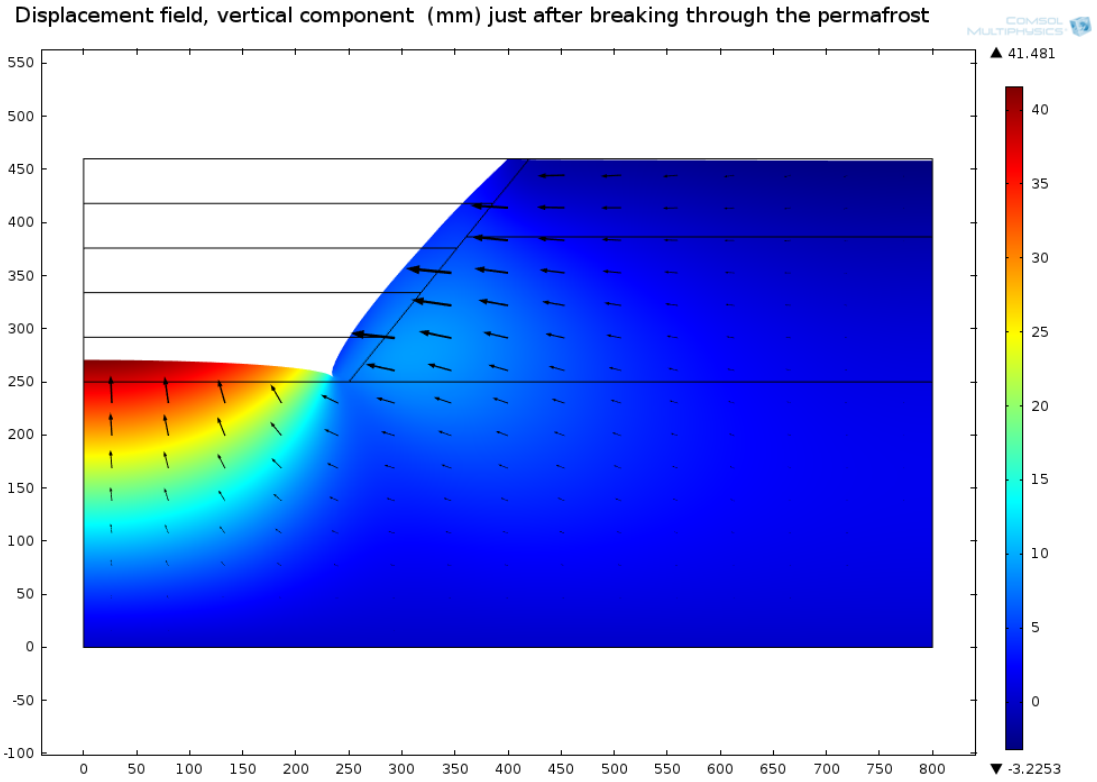

Figure 2-19 Vertical displacement field (mm), just after excavation break through permafrost boundary

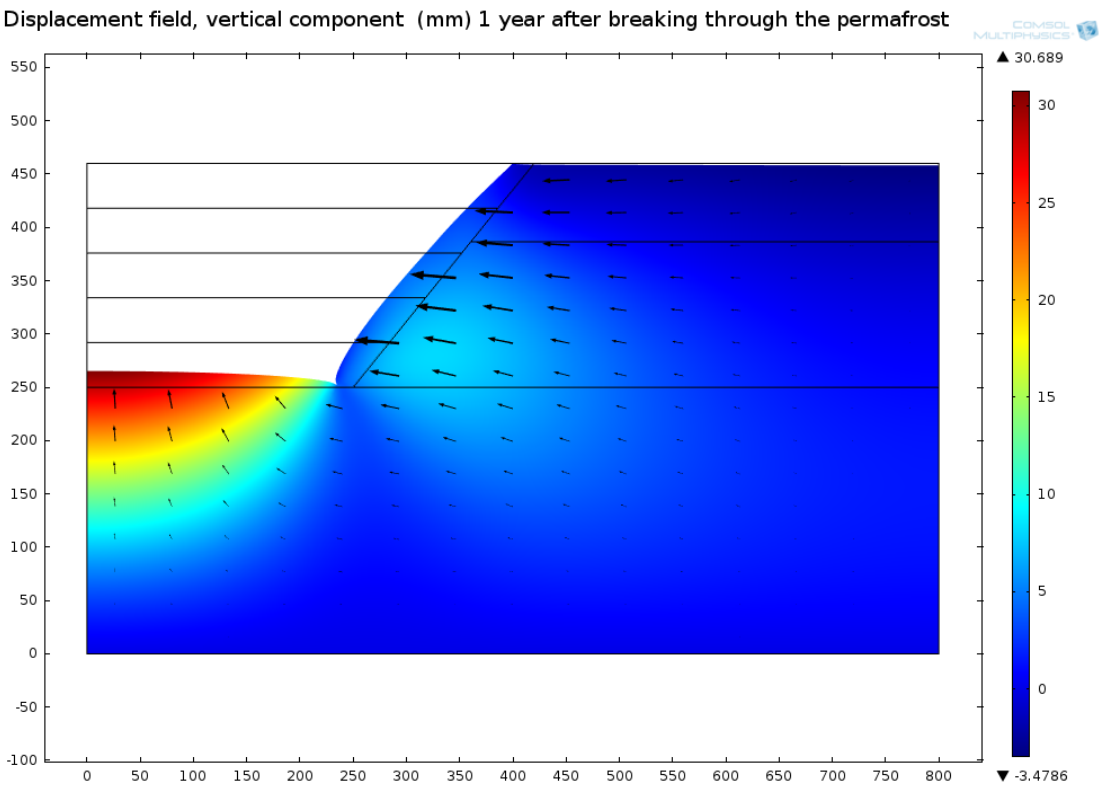

Figure 2-20Vertical displacement field (mm), 1 year after excavation break through permafrost boundary

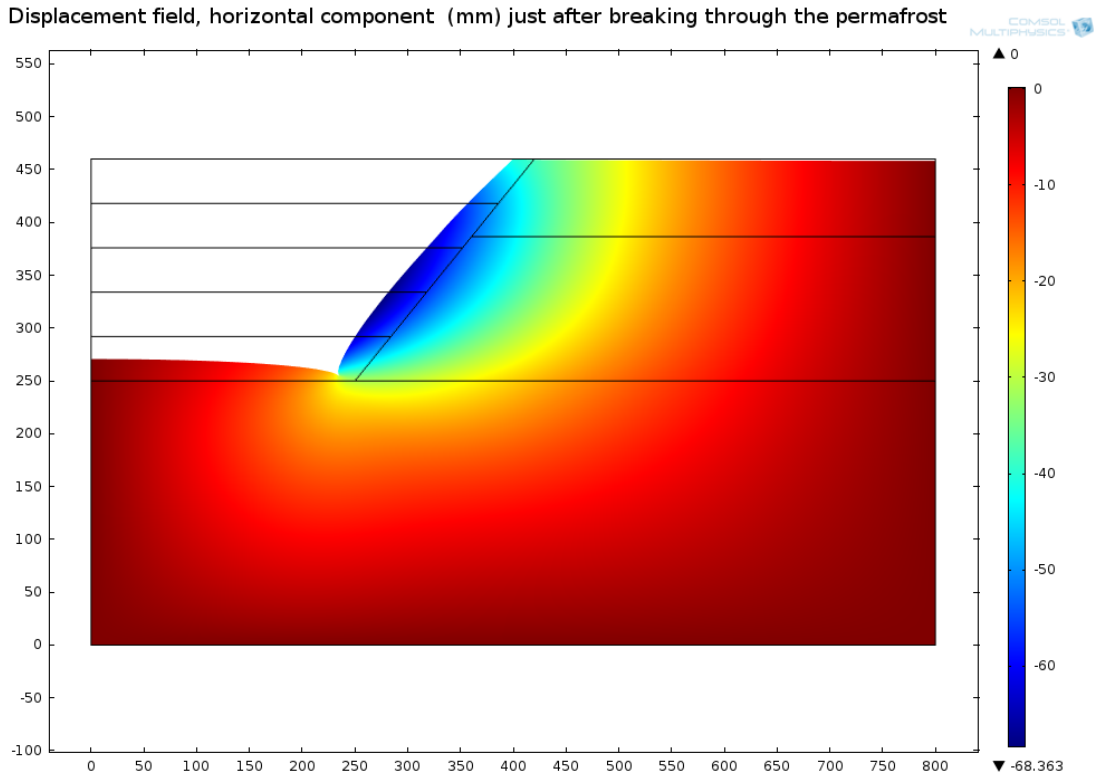

Figure 2-21Horizontal displacement field (mm), just after excavation break through permafrost boundary

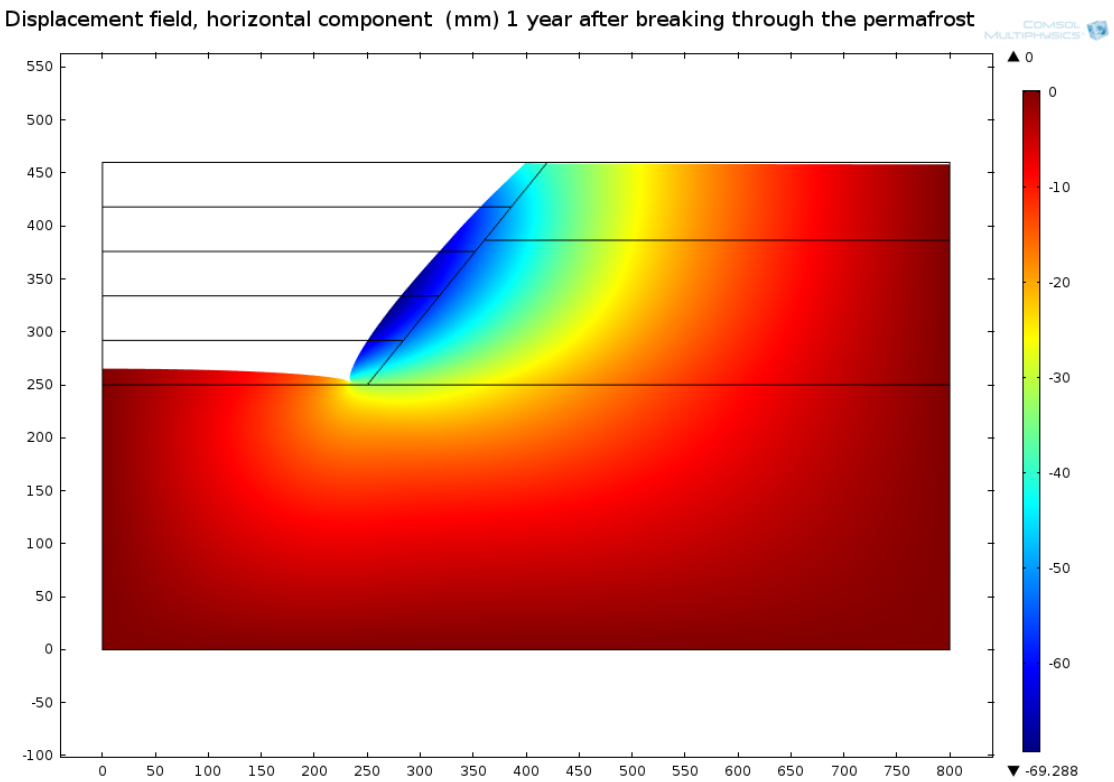

Figure 2-22Horizontal displacement field (mm), 1 year after excavation break through permafrost boundary

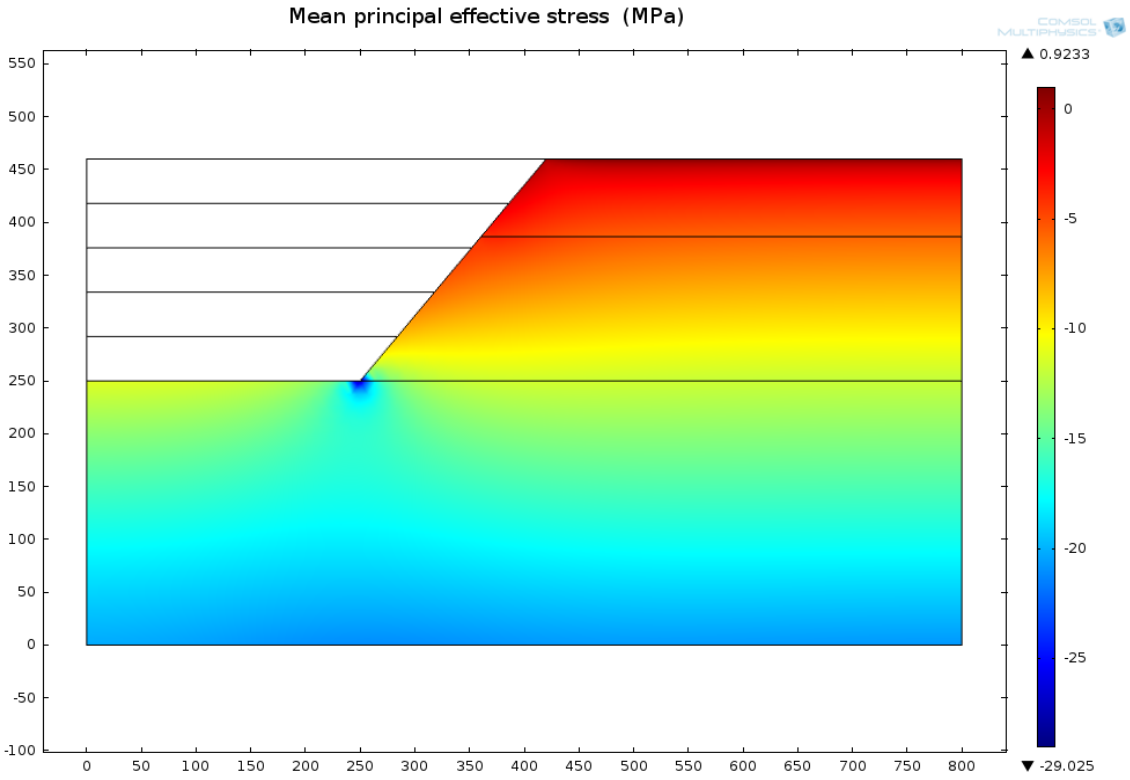

Figure 2-23 Mean effective principal stress (MPa), excavation break through permafrost boundary

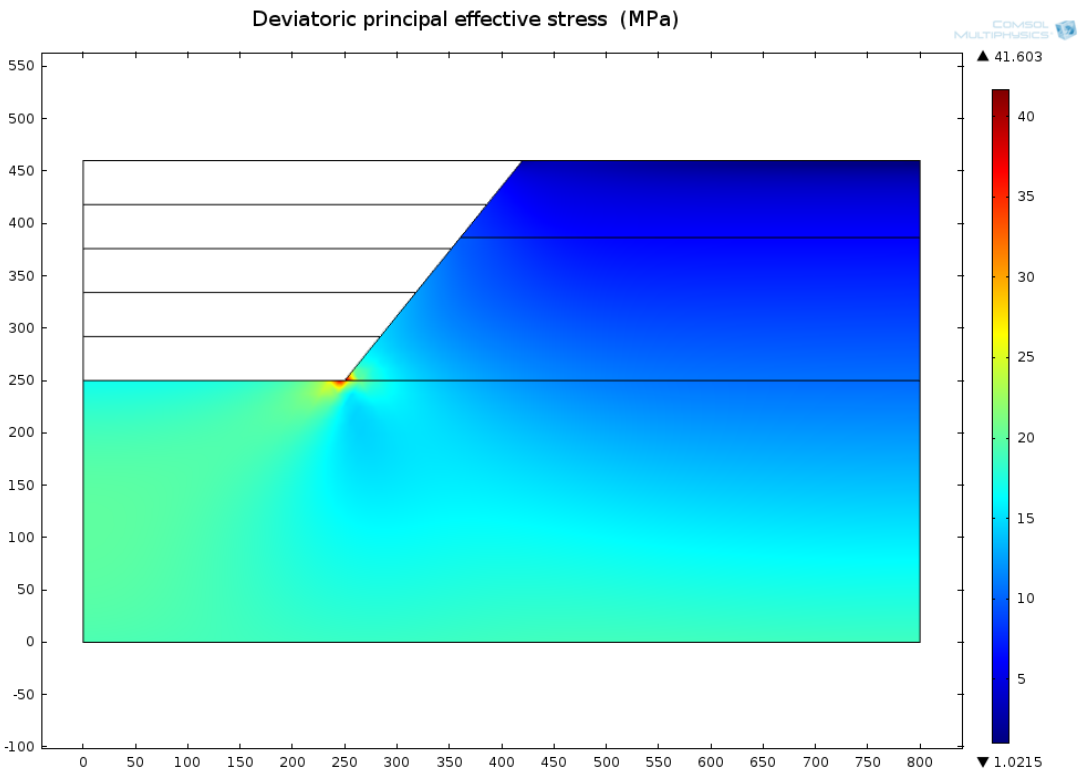

Figure 2-24 Effective deviatoric stress (MPa), excavation break through permafrost boundary

Figure 2-25 Minor principal stress tensile zone ($\sigma_3' > 0$)

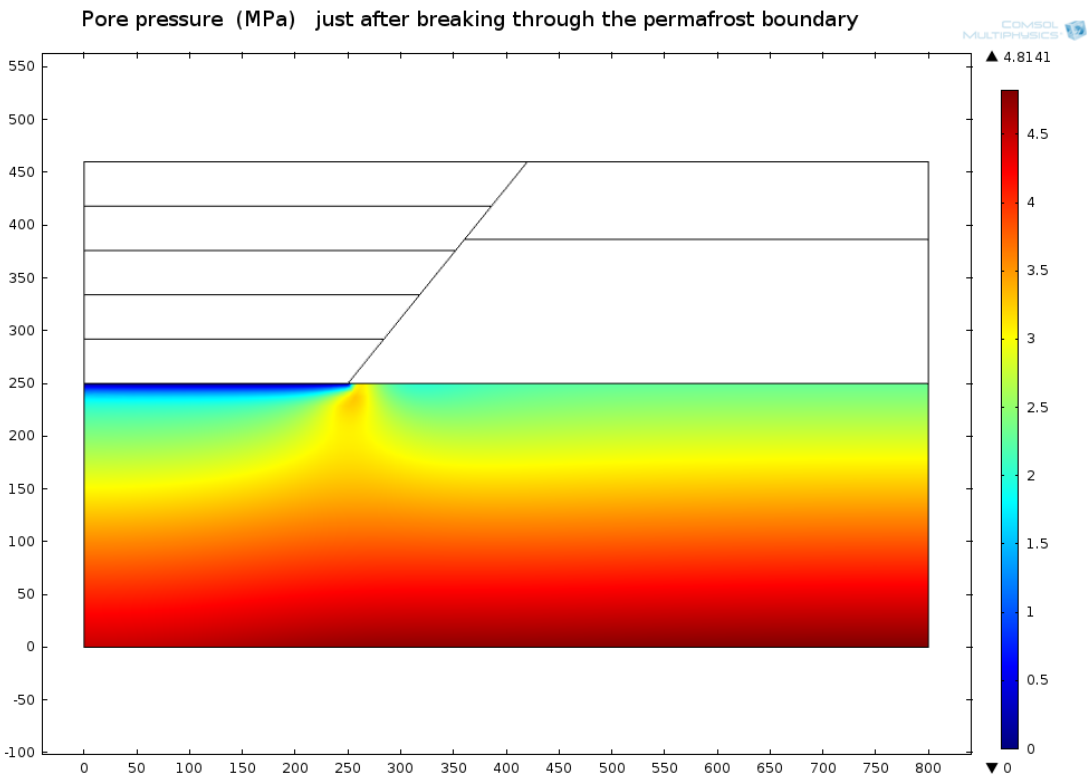

Figure 2-26 Pore pressure beneath permafrost, just after excavation break through permafrost boundary

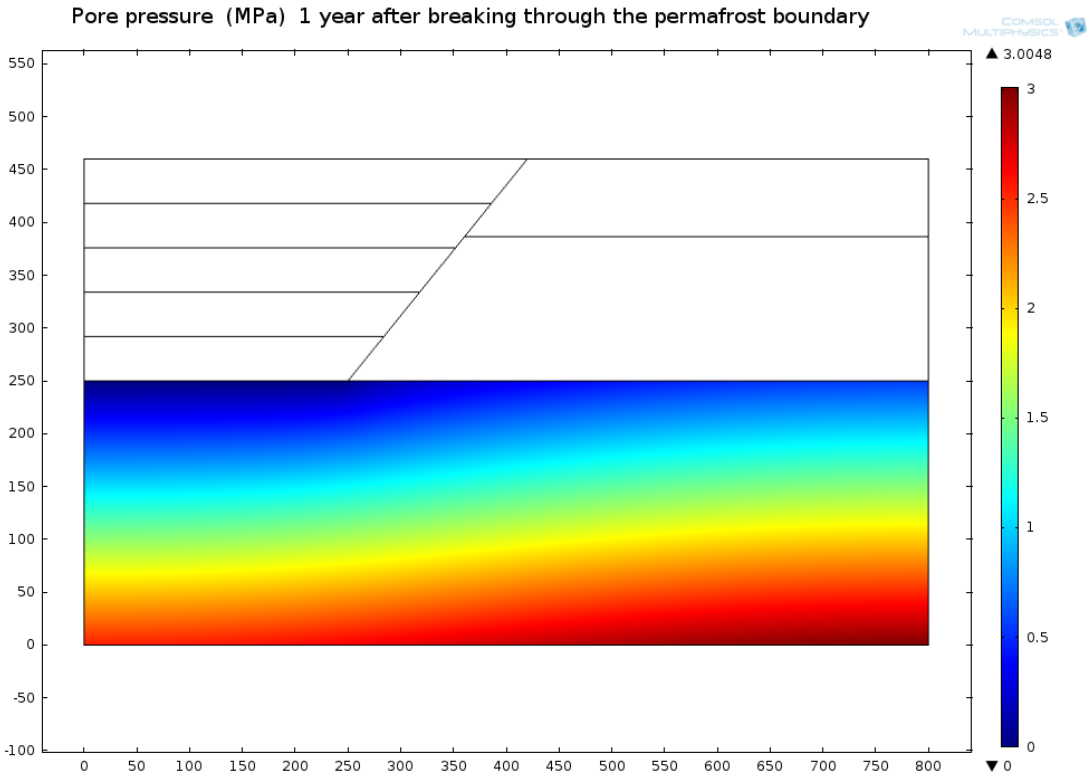

Figure 2-27 Pore pressure beneath permafrost, 1 year after excavation break through permafrost boundary

2.11.2 Andrew Lake

Numerical results obtained for the Andrew Lake pit are given in Figures 2-28 to 2-42. The same trends as observed in the Main Zone pit were obtained. Here, artesian pressure conditions were slightly different from the previous case. At the bottom of the pit which is 250 m below ground surface, an artesian pressure equivalent to 259 m of water pressure head was imposed based on the data provided in Technical Appendix 5B which was explained in Section 2.9.

Scenario I (Excavation reaches 5m above permafrost)

Figures 2-28 and 2-29 show the vertical and horizontal displacements respectively after excavating down to 5 m above the permafrost boundary in several stages. The maximum vertical displacement at the bottom of the pit is found to be 37 mm, while the maximum horizontal displacement is 93 mm.

Figures 2-30 and 2-31 give the mean effective stress and deviatoric stress respectively. As to be expected, some stress concentration at the bottom corner of the pit is observed as a result of high displacement being localized and due to the kinematics of the deformations.

Figure 2-32 shows areas within which the minor principal stress (σ'_3) become tensile after excavation to this level. Finally, Figure 2-33 displays the pore pressure distribution below the frozen impermeable layer as the excavation reaches 5 m above permafrost layer.

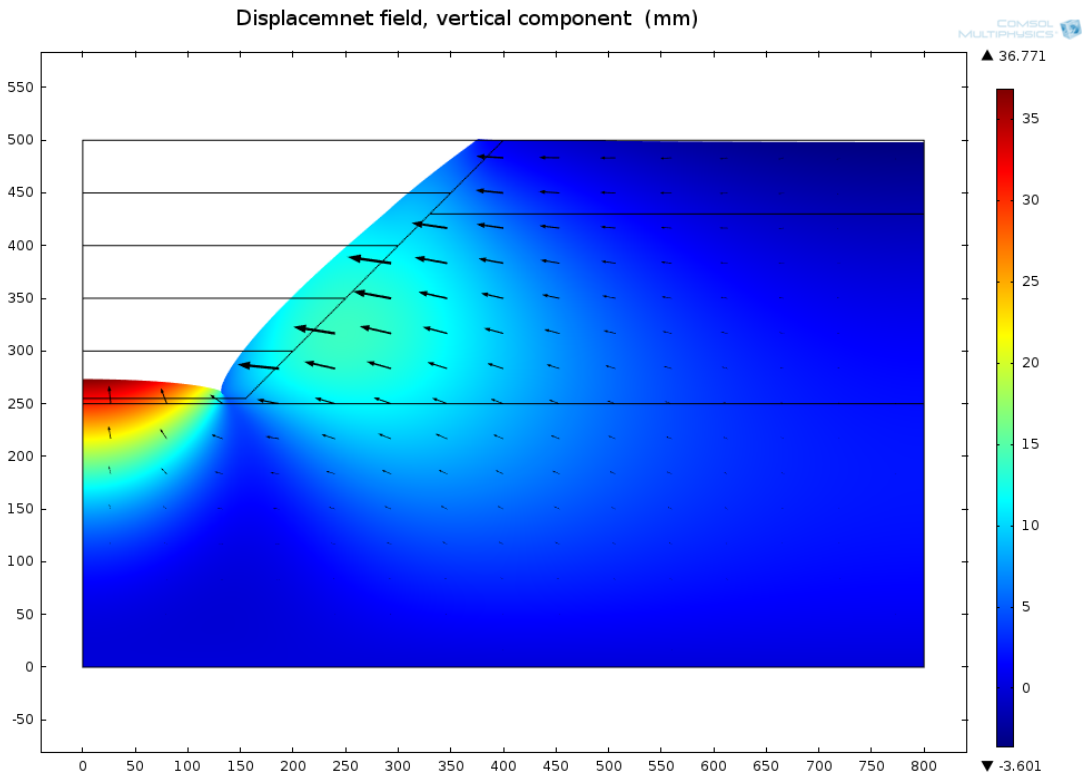

Figure 2-28 Vertical displacement field (mm), excavation up to 5m above permafrost boundary

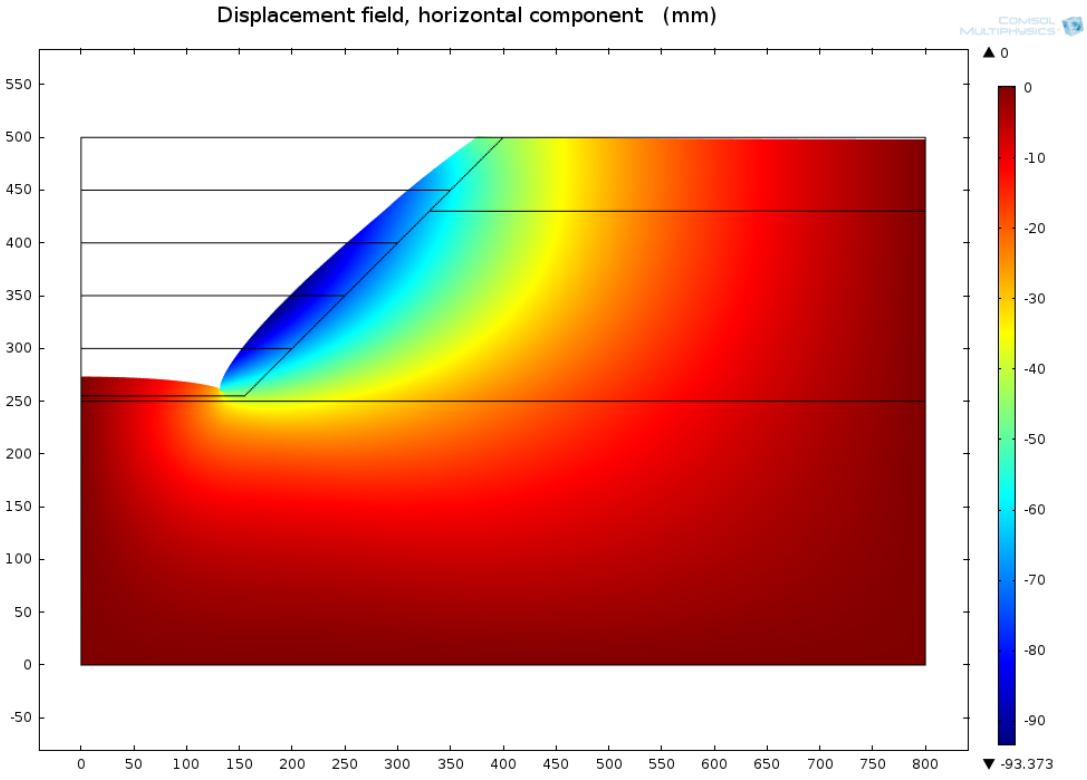

Figure 2-29 Horizontal displacement field (mm), excavation up to 5m above permafrost boundary

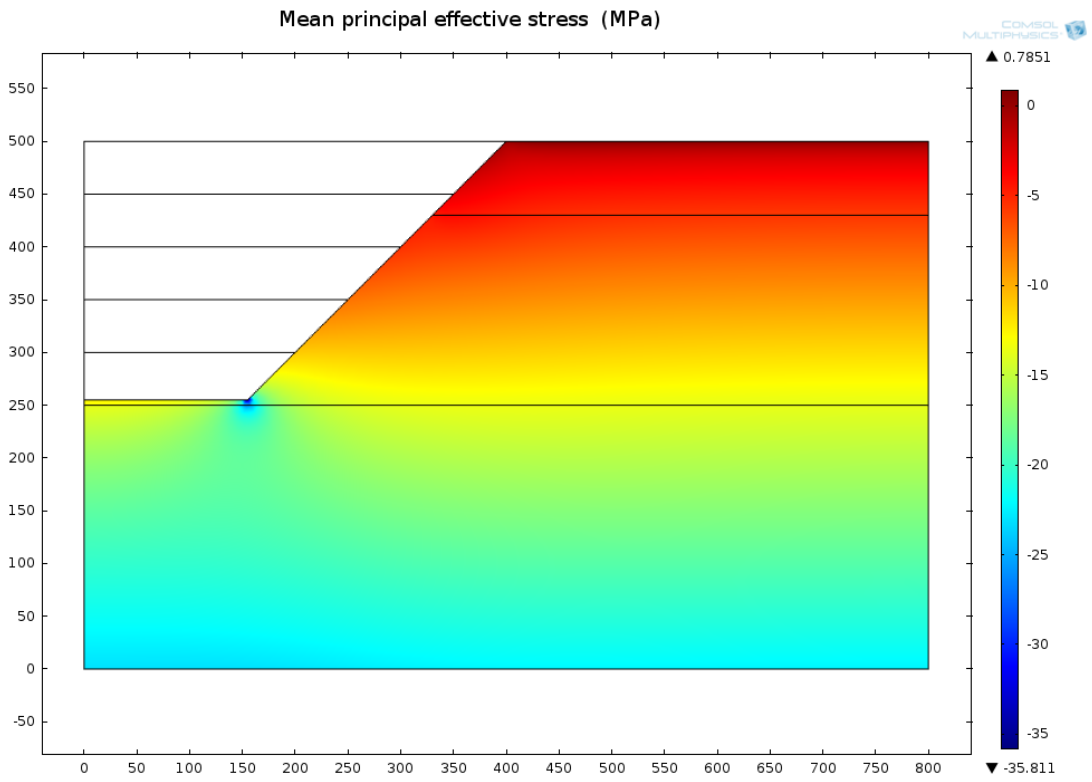

Figure 2-30 Mean effective principal stress (MPa), excavation up to 5m above permafrost boundary

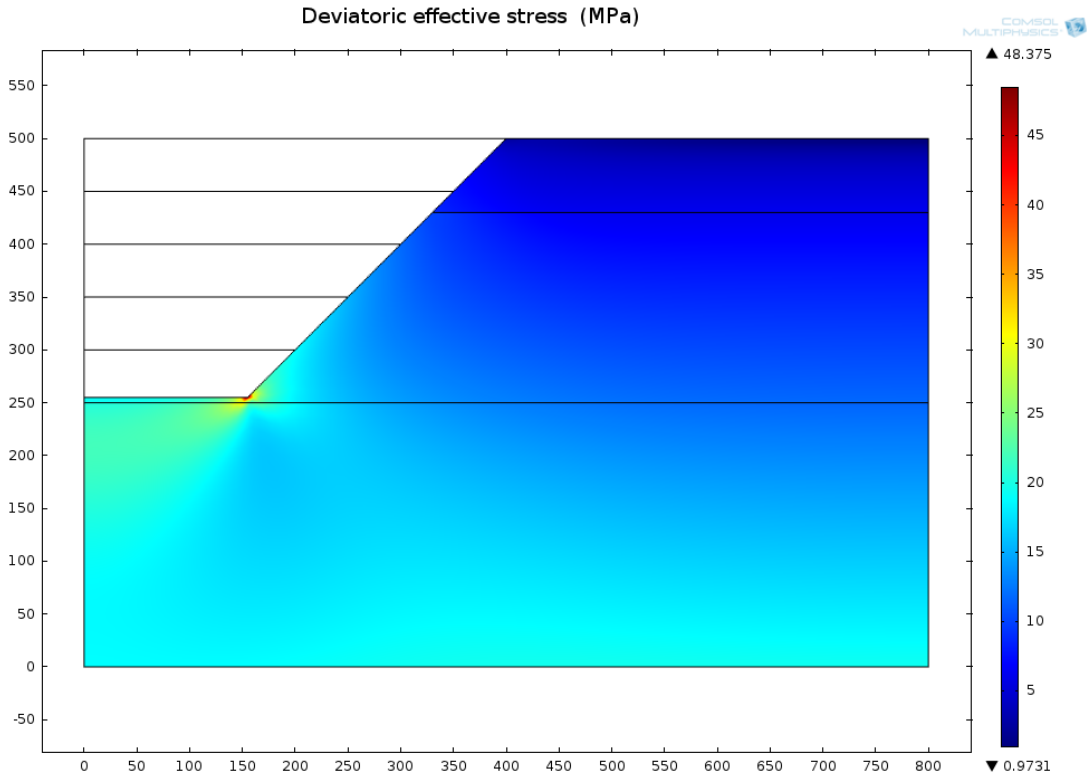

Figure 2-31 Effective deviatoric stress (MPa), excavation up to 5m above permafrost boundary

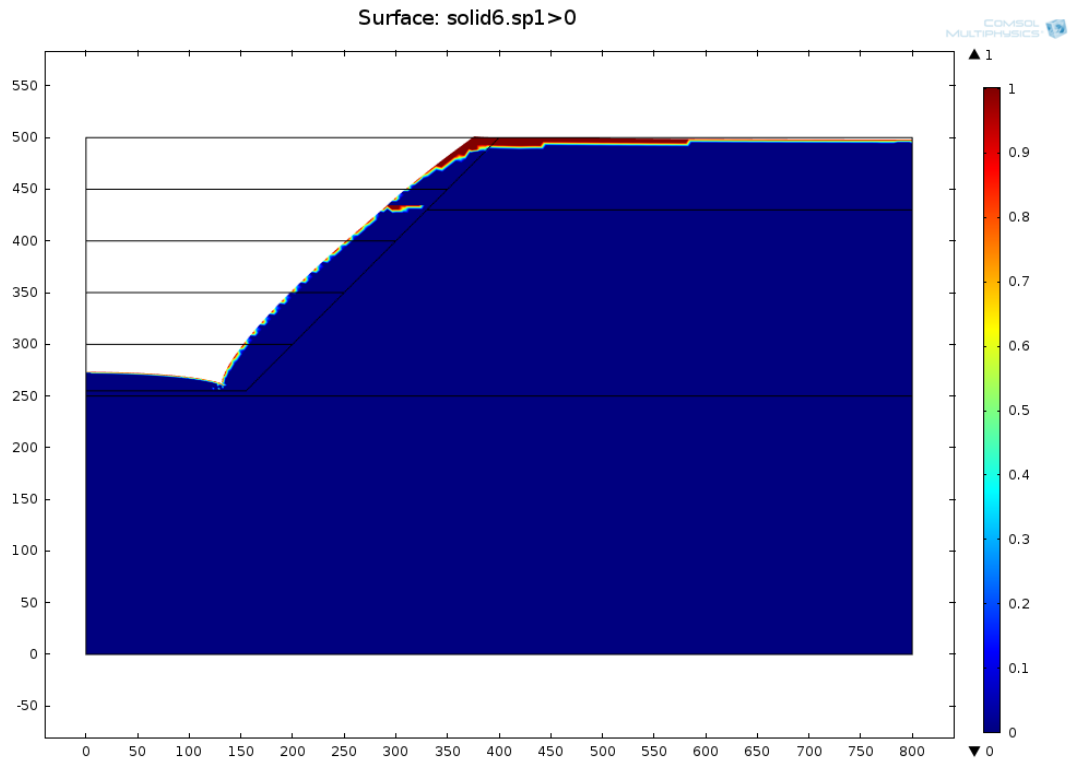

Figure 2-32 Minor principal stress tensile zone ($\sigma_3' > 0$)

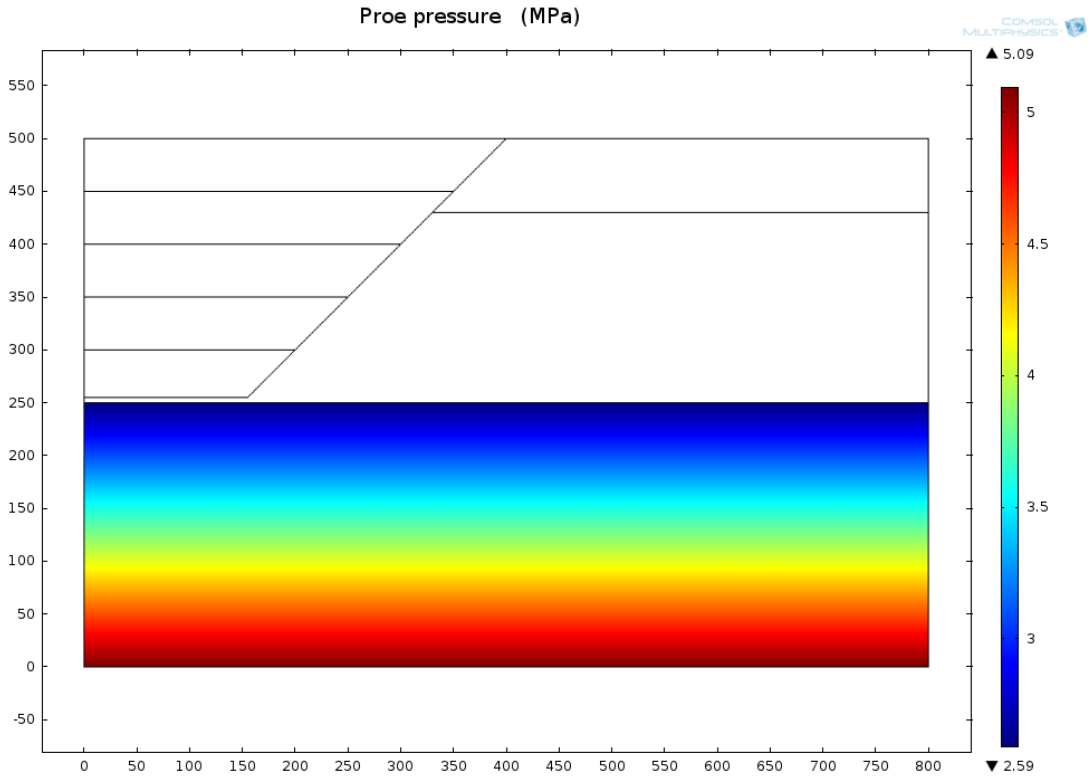

Figure 2-33 Pore pressure beneath permafrost, excavation up to 5m above permafrost boundary

Scenario II (Excavation reaches permafrost boundary)

Figures 2-34 and 2-35 show the vertical displacements just after excavating break through the permafrost boundary and after one year. The maximum vertical displacement at the beginning is 51mm while after one year, some consolidation occurs after which the maximum vertical deformation becomes 38 mm. Figures 2-36 and 2-37 indicate the horizontal displacements after breaking through the permafrost boundary and one year later. In the beginning, the maximum horizontal displacement is 93 mm, while after one year it increases a little and reaches 95 mm.

Figures 2-38 and 2-39 give the mean effective stress and deviatoric stress respectively one year after breaking through the permafrost boundary. Some stress concentration at the bottom corner of the pit is observed as a result of high displacement being localized and due to the kinematics of the deformations.

Figure 2-40 shows areas within which the minor principal stress (σ_3') become tensile one year after excavation to this level. Figures 2-41 and 2-42 display the pore pressure distribution below the frozen impermeable layer as the excavation reaches the permafrost layer and one year later.

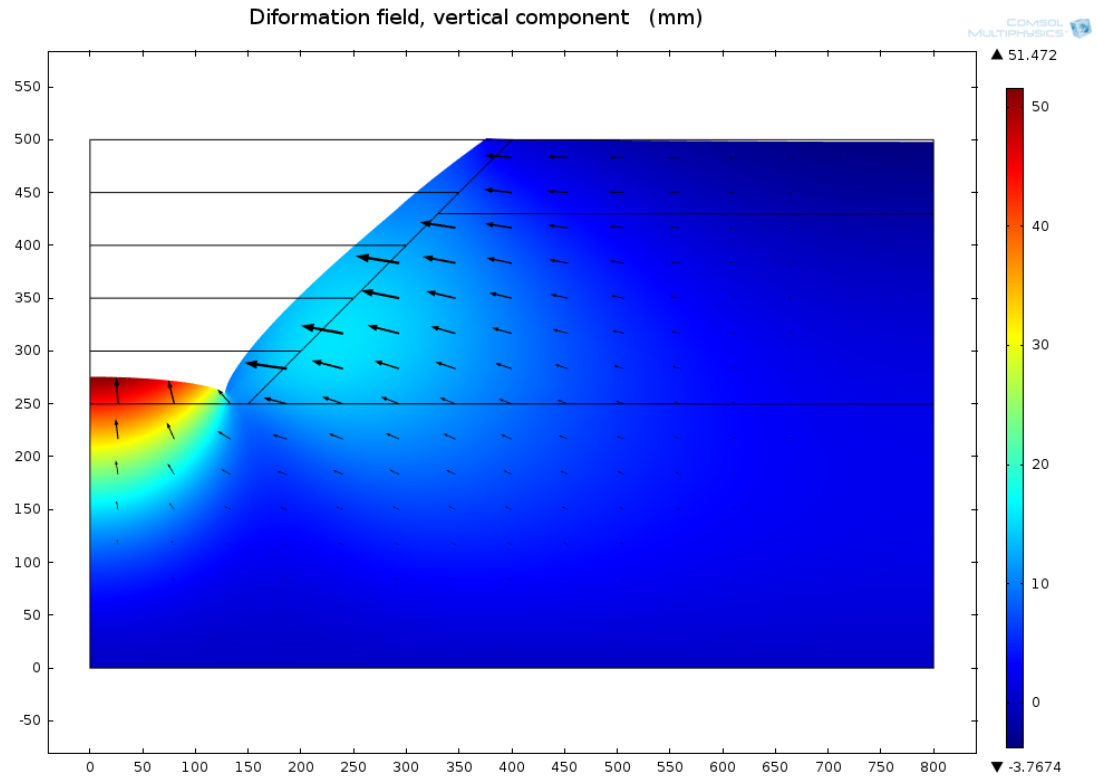

Figure 2-34 Vertical displacement field (mm), just after excavation break through permafrost boundary

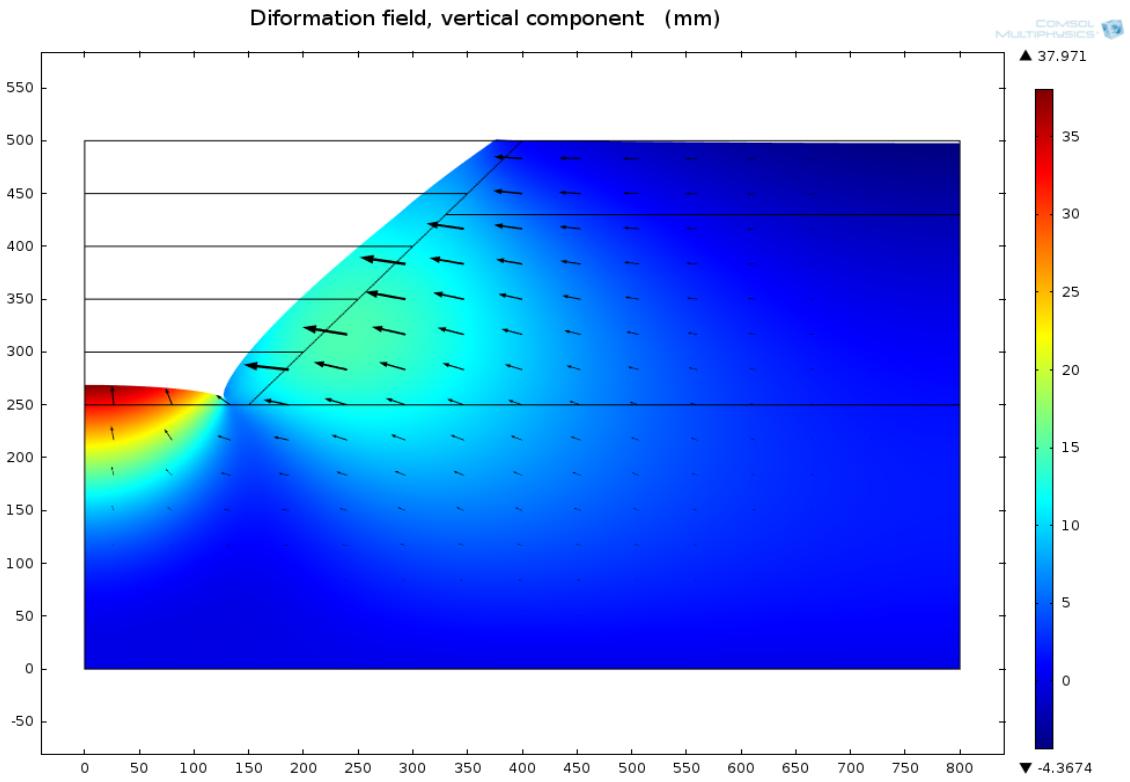

Figure 2-35 Vertical displacement field (mm), 1 year after excavation break through permafrost boundary

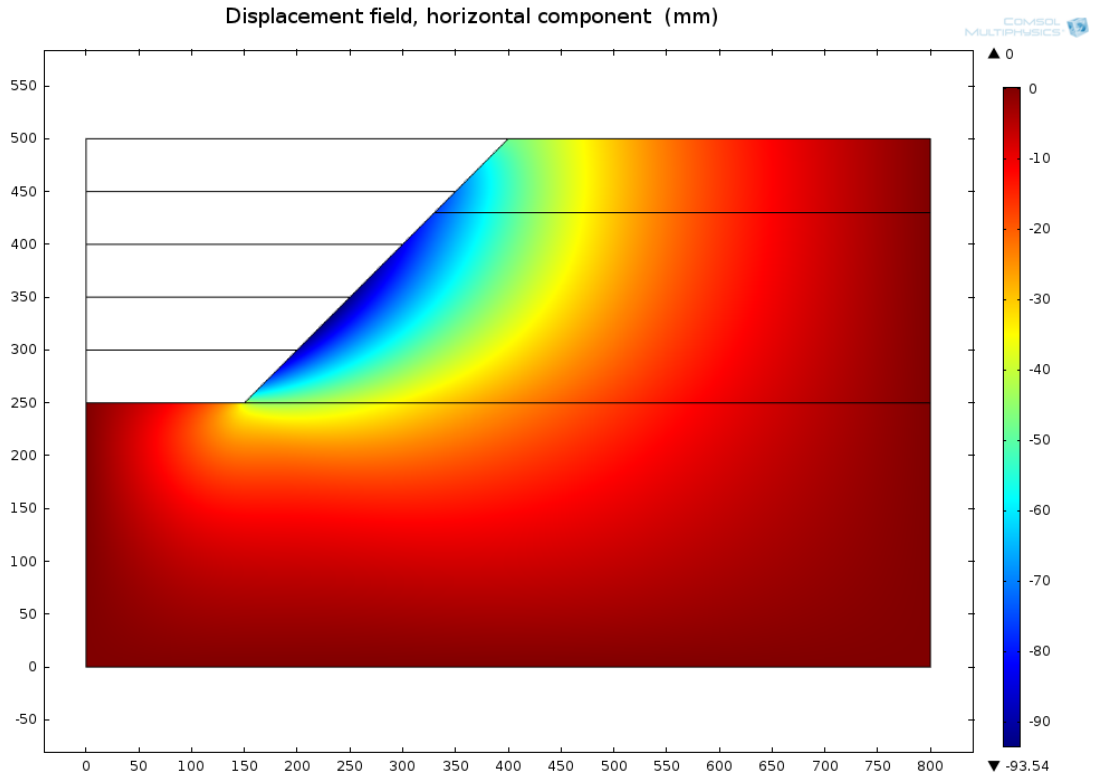

Figure 2-36 Horizontal displacement field (mm), just after excavation break through permafrost boundary

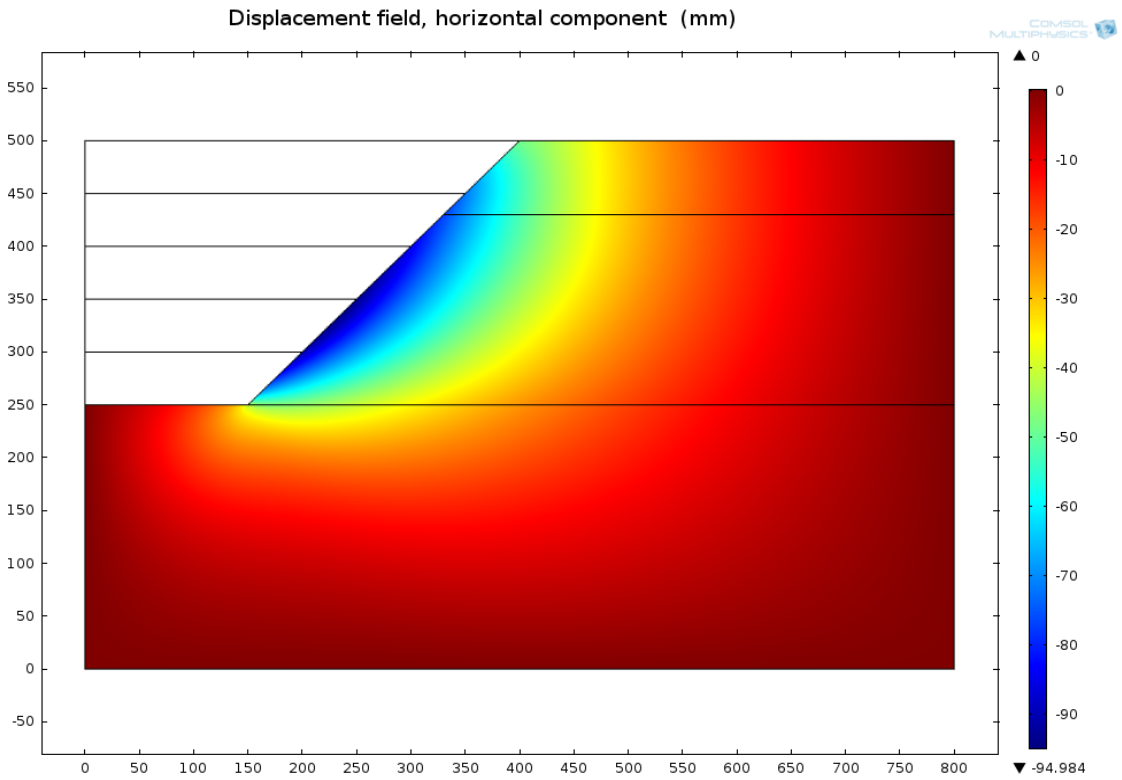

Figure 2-37 Horizontal displacement field (mm), 1 year after excavation break through permafrost boundary

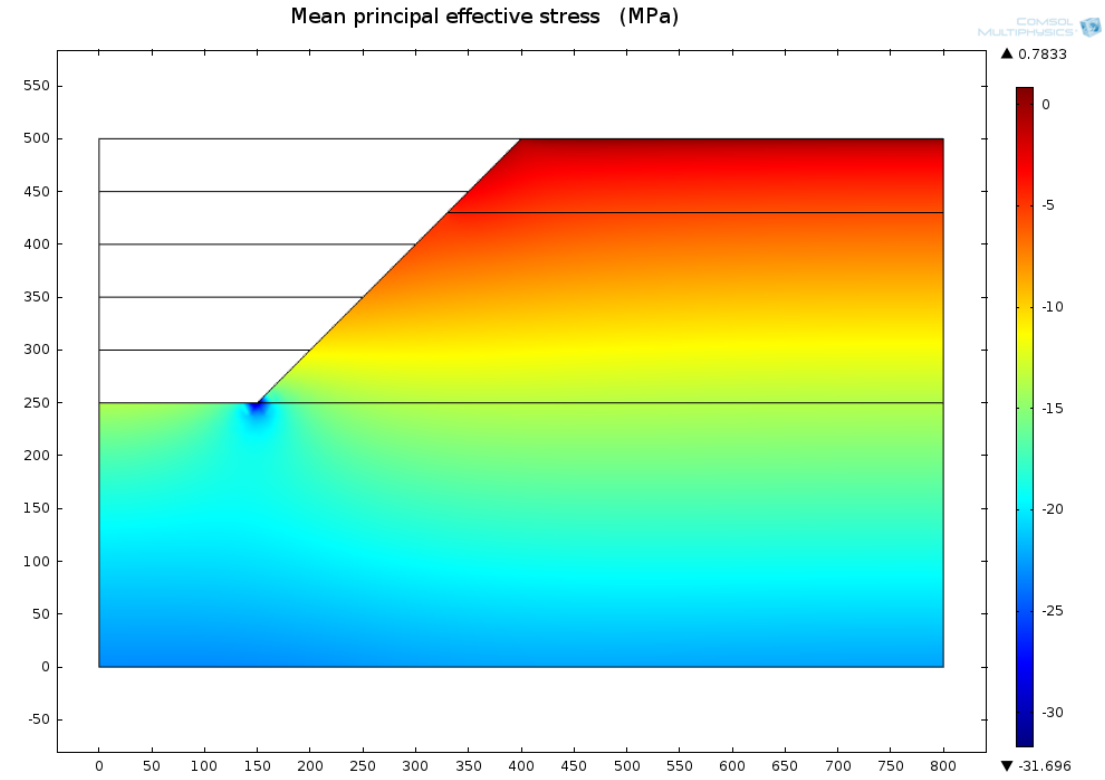

Figure 2-38 Mean effective principal stress (MPa), excavation break through permafrost boundary

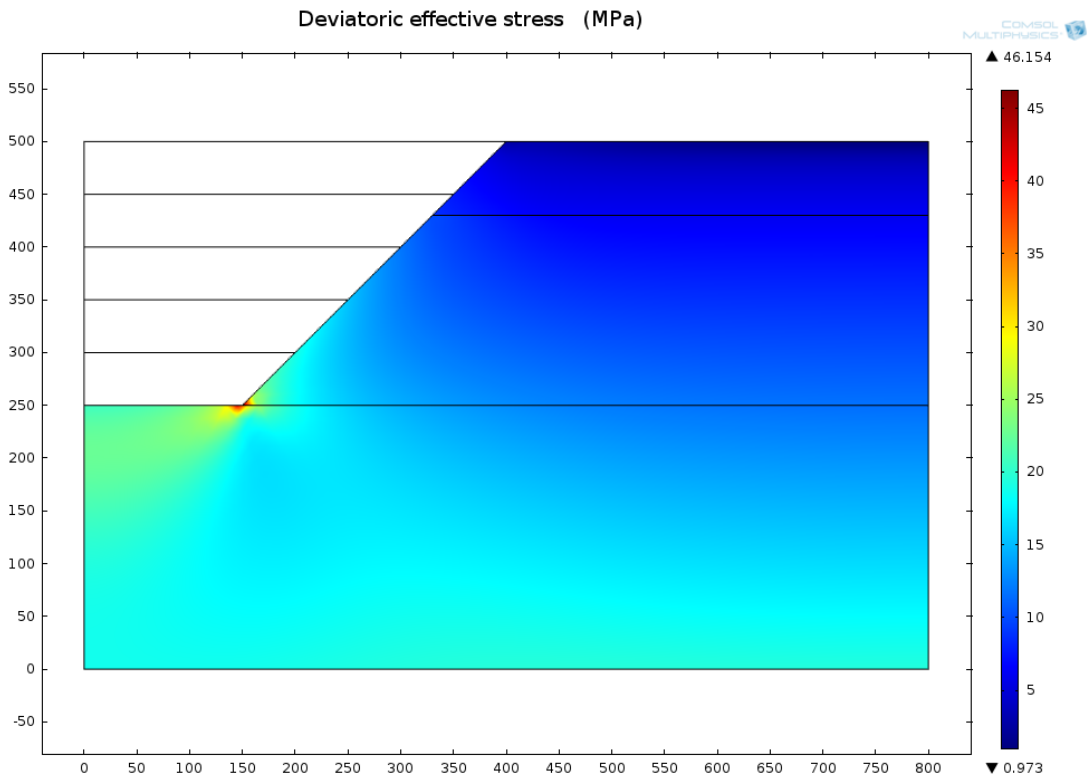

Figure 2-39 Effective deviatoric stress (MPa), excavation break through permafrost boundary

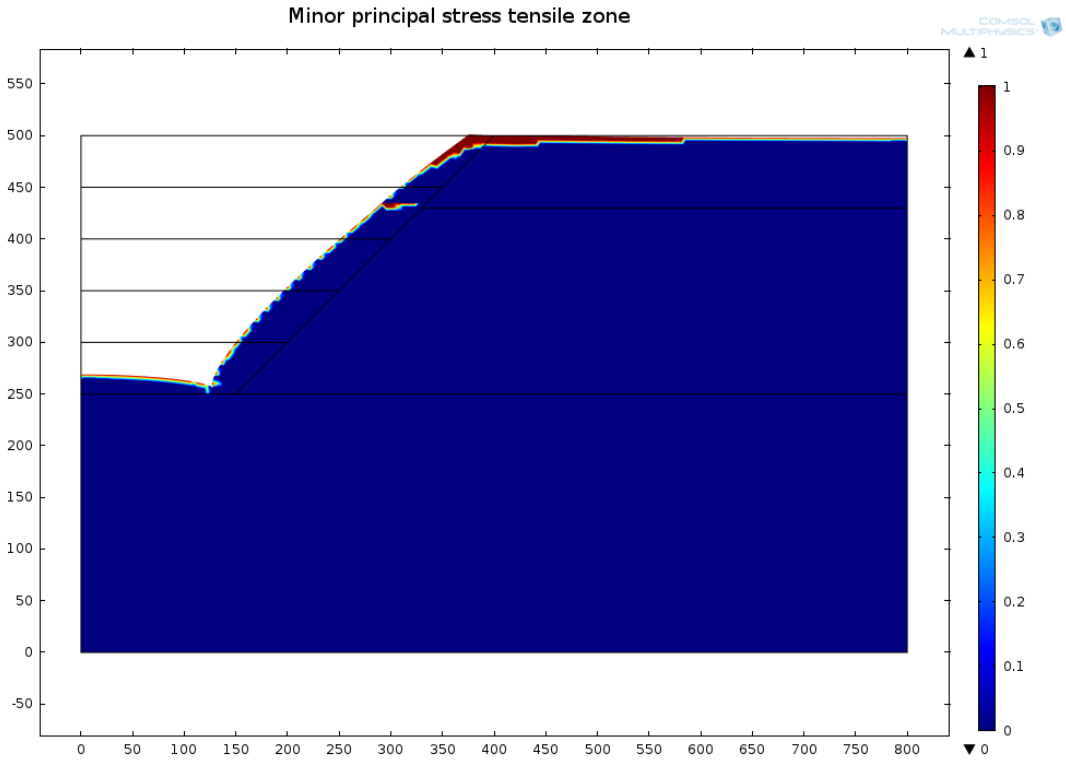

Figure 2-40 Minor principal stress tensile zone ($\sigma_3' > 0$)

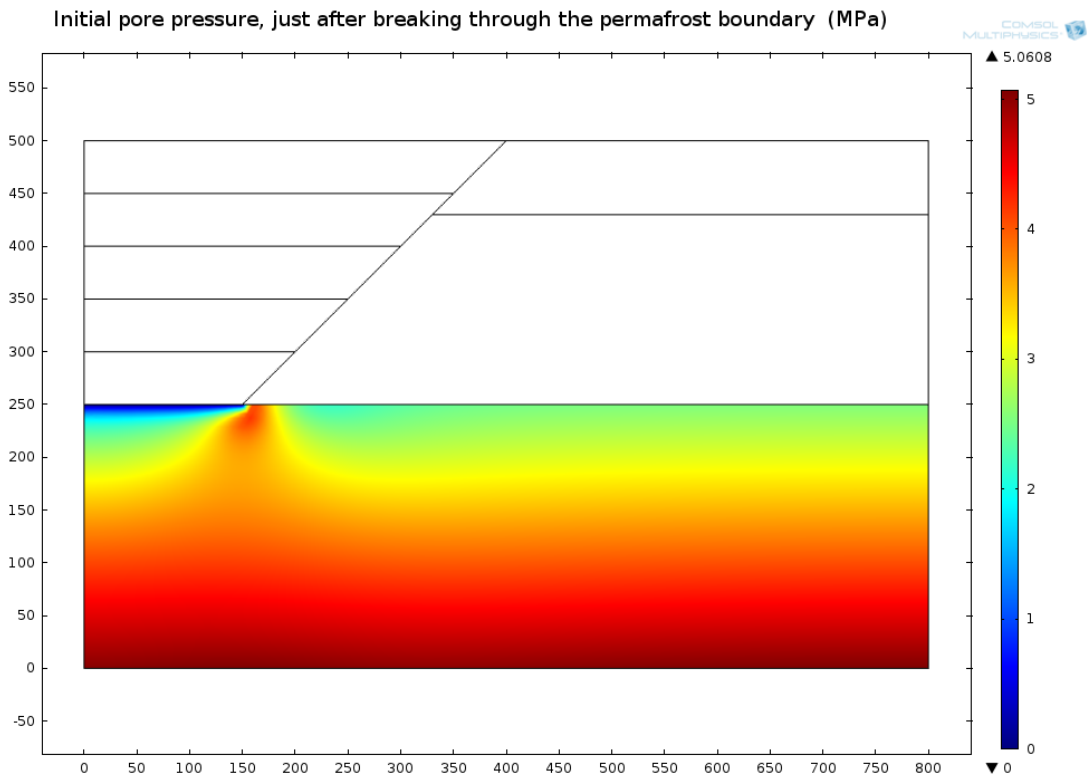

Figure 2-41 Pore pressure beneath permafrost, just after excavation break through permafrost boundary

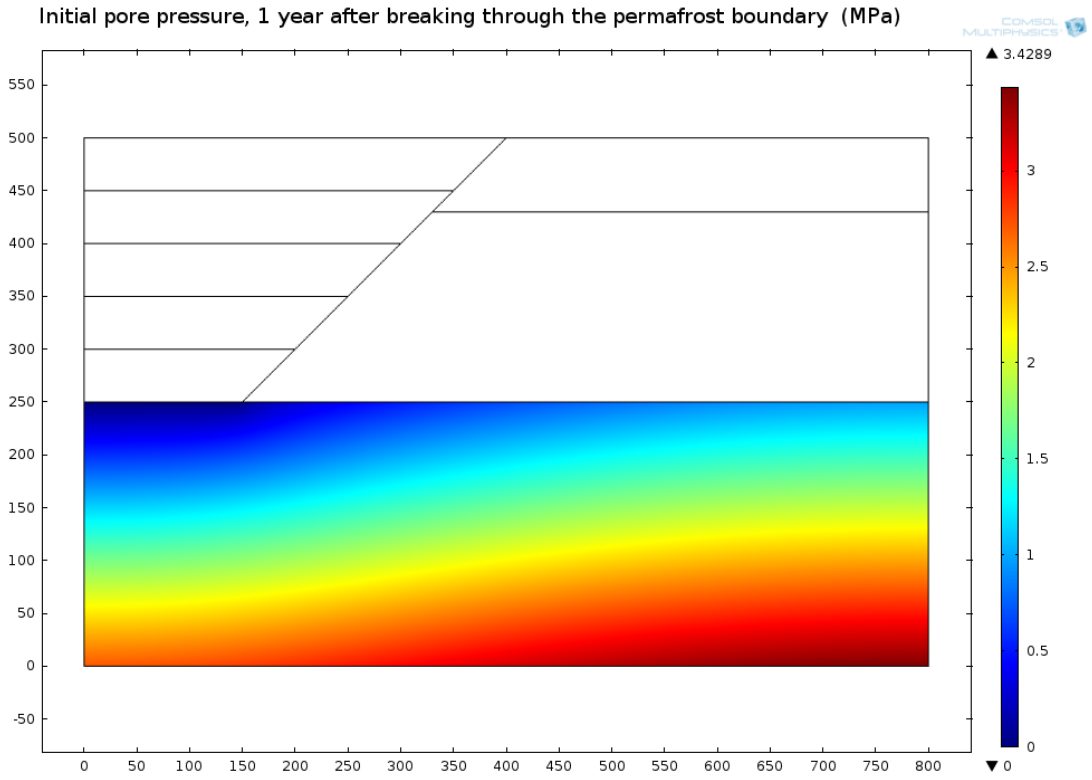

Figure 2-42 Pore pressure beneath permafrost, 1 year after excavation break through permafrost boundary

2.12 Discussions

Regarding the results presented in Section 2.11 and in Appendix, it is clear that during the excavation of each lift, both the vertical and horizontal ground displacements increase for both open pits. This deformation takes place as a result of a decrease in vertical stress with sustained high horizontal in-situ stresses.

Since all the domains in the numerical model are considered as porous materials, the removal of each lift during excavation induces unloading so that it is expected that the pore pressures beneath the open pit should decrease initially with a subsequent increase to a new equilibrium value with sufficient time. However, this anticipated pore pressure does not occur because the groundwater under the permafrost layer is being recharged from the flow between the lakes subjected to different hydraulic heads. This is true as long as the bottom of the excavation does not reach the permafrost boundary which would otherwise cause drainage from the underlying groundwater.

The rate at which vertical deformations at the bottom of the pit decrease for each lift as the excavation proceeds down to the boundary of the permafrost. This is to be anticipated since the Young's modulus for each of the underlying domains increases with depth, see Section 2.7.

When the excavation breaks through the permafrost boundary, initially a large vertical deformation occurs as a result of decrease in the effective stresses in both vertical and horizontal directions. However, with time, the water pressure within the unfrozen underlying rock layer decreases due to drainage conditions through the bottom of the pit. Therefore, both horizontal and vertical effective stresses increase, which causes some consolidation displacements in the vicinity of the open pit.

As shown in Figures 2-17, 2-25, 2-32, and 2-40 after excavation, the minor principal stress becomes tensile. These tensile stresses could cause fractures in the rock in the areas indicated, i.e. at the crest and the walls of the pit. As such, these tensile stresses could potentially cause damages, especially in the Andrew Lake project since the rocks in this area are weaker than those in the Kiggavik area.

Fluid Flow through Faults

3.1 Introduction

Taliks beneath larger lakes can extend down to the deep groundwater regime with the elevations of these lakes providing the driving force for deep groundwater flow. However, the presence of thick permafrost beneath land masses results in negligible recharge to the deep groundwater flow regime from these areas. Consequently, recharge to the deep groundwater flow regime is predominantly limited to areas of taliks beneath large surface water bodies. Generally, groundwater will flow from higher-elevation lakes to lower-elevation lakes. The host rock lithology is expected to exhibit a very low primary (matrix supported) hydraulic conductivity, with the main flow related to secondary conductivity such as open faults or fractures. In the permafrost area, the assumption is that the pore spaces, fractures, and faults are filled with ice. However, when the frozen ground thaws, the fractures and faults, which are now filled with unfrozen water, could increase the mobility of water and hence hydraulic conductivity.

There exist some regional and local faults present in the vicinity of Kiggavik and Sissons project sites. When the open pits are excavated and/or filled with tailings, the ground hydraulic conditions will generally be modified. In particular, the combination of high artesian pressure at the site and fault zones which cut through the bottom of the pits with potentially higher hydraulic conductivities than the host rock could result in high fluid flow into the open pits. In this section, fluid flow through faults will be analyzed as a result of open pit excavation.

3.2 Methodology

In order to investigate fluid flow through faults into the open pits, the underground water flow regime should be determined. For this purpose, different factors such as the location of water sources, ground surface topography, and underground material hydraulic properties should be taken into account in the analysis.

There are many lakes in the vicinity of Kiggavik and Sissons project locations. Therefore, lakes which could potentially support open taliks should be identified. The elevation of the bottom of each of these lakes in combination with their depths will define the hydraulic boundary conditions for the fluid flow simulations.

After identifying the lakes and associated open taliks, the ground surface elevation should be defined in such a way to resemble as closely as possible the actual topography of the project site.

Since the depths of excavations are measured from ground surface level, ground surface topography could play an important role in defining the hydraulic boundary condition.

Finally, ground hydraulic properties should be defined correctly to find the 'real' underground fluid flow regime. To define these hydraulic properties, both the ground material (rock or soil) and geological formations (e.g. regional or local faults) should be considered.

In the following sections, the above-mentioned three important issues will be discussed.

3.3 Lakes Potentially Supporting Open Taliks

Most lakes in the Kiggavik Project area are relatively shallow and many freeze to the bottom in winter. However, several lakes near the project site satisfy both the minimum dimensional and depth requirements to support an open talik extending to the deep groundwater flow system. Figure 3-1 indicates the lakes that satisfy these requirements (Technical Appendix 5B), Table 3-1 presents the data on the depth and elevation of the lakes in the vicinity of the project sites.

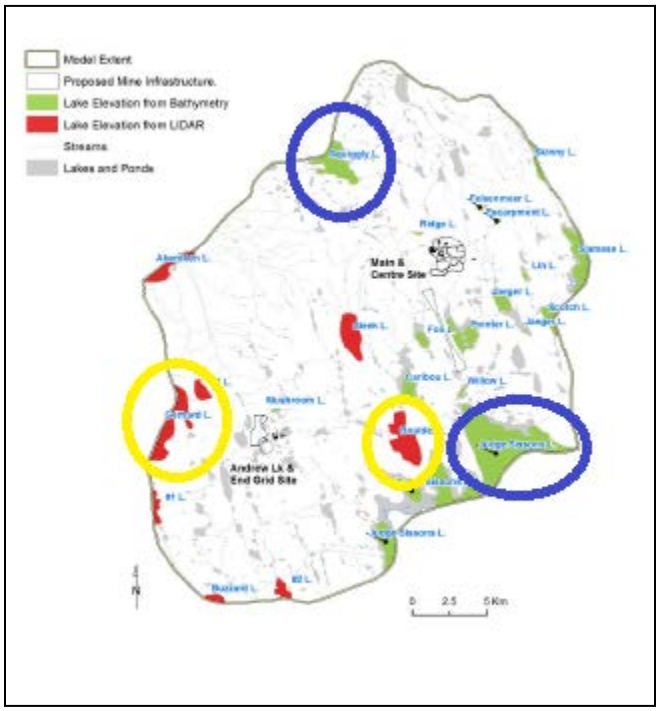

Figure 3-1 Location of lakes with potential open taliks (ref: Technical Appendix 5B)

Table 3-1 Elevation and depth of lakes with potential open taliks (Ref. Technical Appendix 5B)

Lake ID	Surface (km^2)	Mean Depth (m)	Max Depth (m)	Average Lake Elevation (masl)
Aberdeen	11.20	NA	NA	79.0
Boulder	4.78	NA	NA	135.0
Buzzard	3.19	NA	NA	160.0
Caribou	3.41	1.40	2.70	136.9
Cirque	0.06	2.60	4.00	211.3
Escarpment	0.13	2.20	8.00	182.4
Felsenmeer	0.21	2.00	6.00	222.8
Fox	1.28	1.70	2.60	142.8
Gerhard	10.73	NA	NA	185.1
Jaeger	2.81	1.60	4.00	150.6
Judge Sissons	95.50	4.60	20.00	132.4
Lin	0.48	1.30	NA	164.5
Mushroom	0.32	1.89	8.90	173.2
Pointer	3.93	1.39	2.90	141.9
Ridge	0.17	2.30	7.10	230.7
Rock	0.32	0.71	1.45	134.3
Scotch	0.20	3.60	6.00	155.8
Siamese	27.92	4.10	11.60	160.5
Skinny	1.97	3.10	12.00	167.7
Sleek	3.76	NA	NA	149.7
Squiggly	6.38	6.00	14.00	213.0
Willow	0.55	1.40	NA	133.0

3.4 Ground Surface Elevation

As mentioned previously, the ground surface elevation could play an important role in defining hydraulic boundary conditions after excavating the open pits. Ground surface elevation changes with probable groundwater flow regime are shown schematically in Figures 3-2 and 3-3 which are not drawn to scale with the vertical dimensions exaggerated.

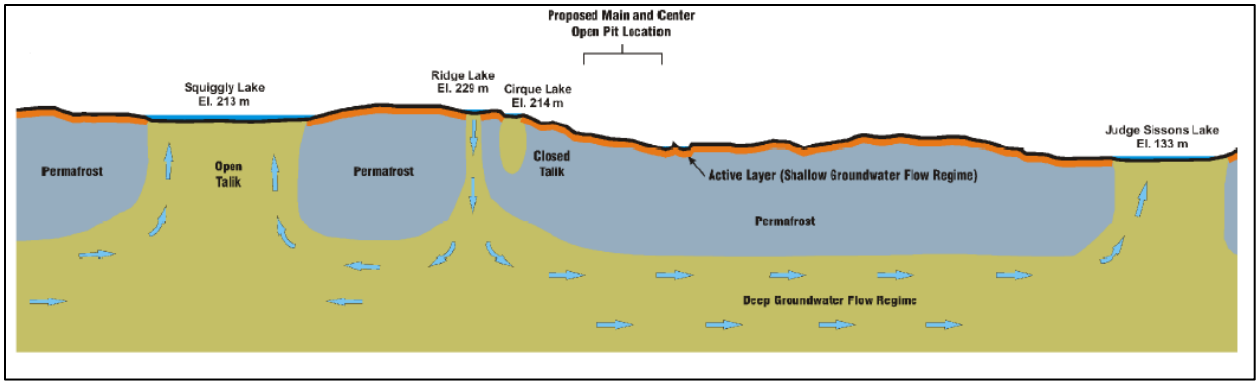

Figure 3-2 Conceptual model of groundwater flow for Kiggavik Main Zone (not to scale – Technical App. 5B)

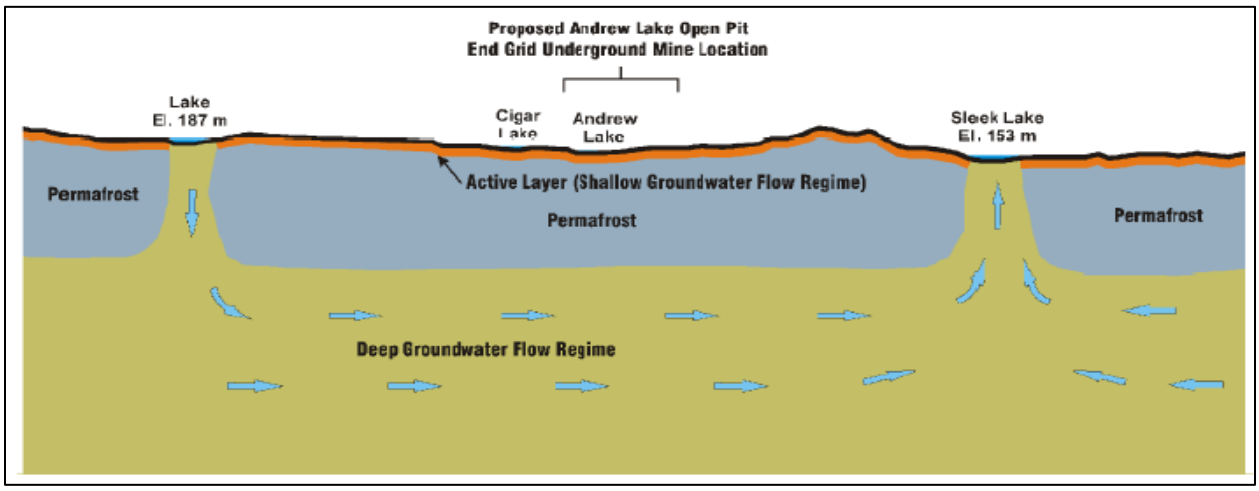

Figure 3-3 Conceptual model of groundwater flow for Andrew Lake (not to scale - Technical App. 5B)

In order to reconstruct the ground surface topography as accurately as possible when defining the geometry of the numerical models, Canadian Digital Elevation Data (CDED) were used as obtained at the GeoBase portal (www.geobase.ca).

Figure 3-4 indicates the Digital Elevation Data of the vicinity of the Kiggavik and Sissons project locations. Proposed locations of open pits for both projects are shown in this figure in addition to the location of important lakes near the project sites.

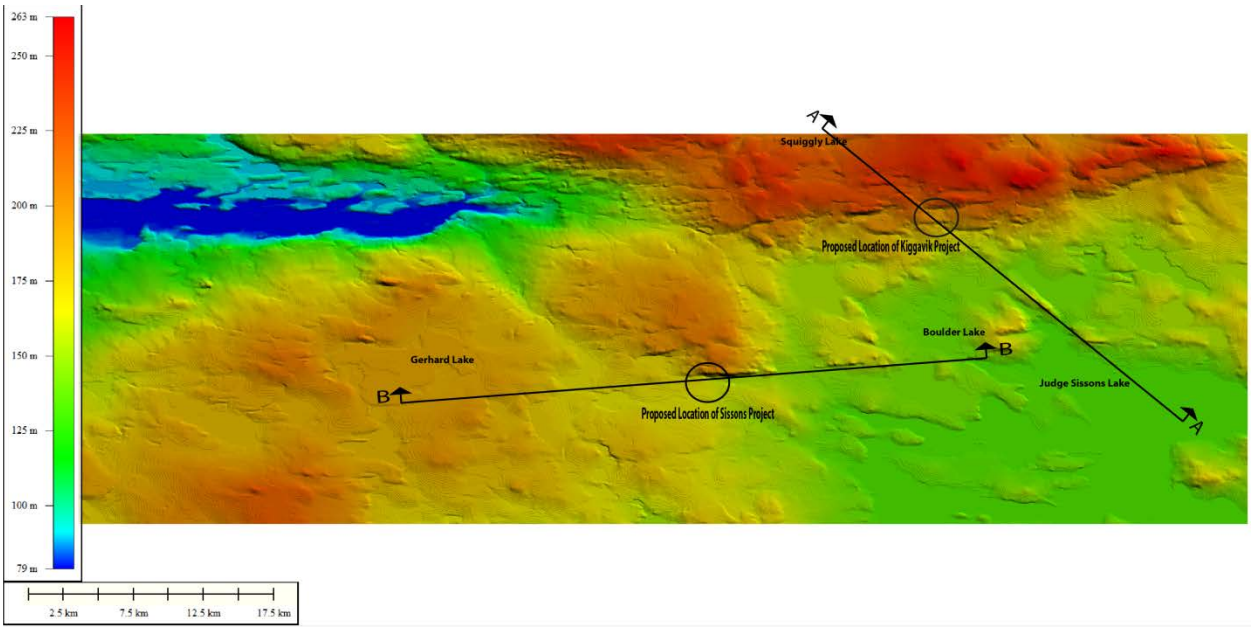

Figure 3-4 Digital Elevation Data from GeoBase Portal in the vicinity of Kiggavik and Sissons projects (ref: geobase portal)

Figures 3-5 and 3-6 give the ground surface elevation profiles corresponding to cross-sections shown in Figure 3-4 as determined from Digital Elevation Data. These will be used for numerical simulations for both Kiggavik Main Zone and Andrew Lake open pits.

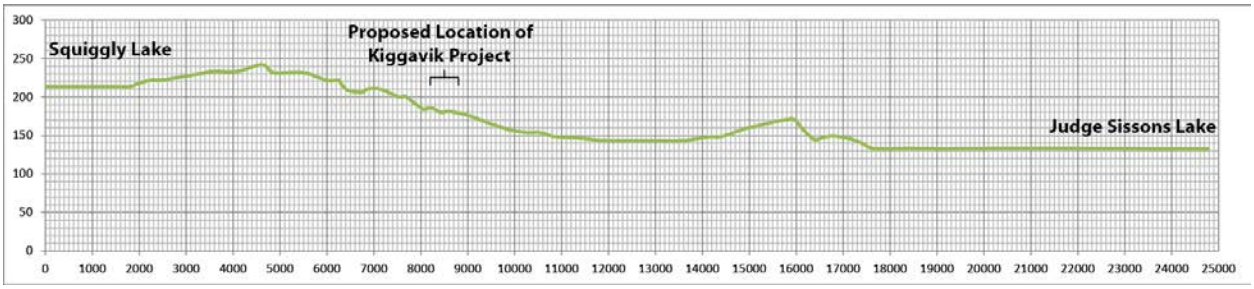

Figure 3-5 Ground surface cross section for Kiggavik project site, section A-A (not to scale)

Figure 3-6 Ground surface cross section for Sissons project site, section B-B (not to scale)

3.5 Material Properties

The values of rock hydraulic conductivity for pre-mining conditions have been selected based on data presented in Technical Appendixes 5B, 5D, and 5E. In these documents the hydraulic conductivity of permafrost is considered as 10^{-12} m/s. Based on the ground cross sections presented in Technical Appendix 5B, it could be concluded that in the vicinity of the project, most of the rock type above the permafrost boundary is composed of Metasediment rocks, while the major ground material below this boundary is Granite rock. Based on this assumption, the material hydraulic properties used in numerical simulations are summarized in Table 3-2.

Table 3-2 Material hydraulic properties (Technical Appendix 5E and 5D)

Depth (m)	Hydraulic Conductivity (m/s)		
	Permafrost	Metasediment	Granite
0-5	1×10^{-12}	5×10^{-5}	-
5-100	1×10^{-12}	5×10^{-8}	-
100-215	1×10^{-12}	-	5×10^{-8}
215-450	-	-	1×10^{-8}
450-900	-	-	1×10^{-9}

Since faults are considered as geological features with potentially higher hydraulic conductivity than that of the surrounding materials, the hydraulic conductivity of fault zones should be higher than that of the 'unfrozen' rock in which the fault lies. Additionally, because of the fact that there is no information about the faults in the documents submitted by Areva, various scenarios were considered to assess the effect of higher hydraulic conductivity of fault zone on the water flow at the bottom of the open pit. These scenarios selected consider faults with hydraulic conductivities 1, 3, and 5 orders of magnitude higher than the surrounding rock.

In modelling fluid flow in porous materials, a question arises as to whether hydraulic material properties such as hydraulic conductivity and compressibility of the matrix changes with the degree of saturation. To account for this a so-called storage parameter was used for the unfrozen material below the permafrost layer, see Technical Appendix 5E. Such unsaturated conditions can be addressed using Richard's equation (Freeze, 1971; Brooks et al. 1966; and Van Genuchten, 1980), a nonlinear form of Darcy's flow equation, with a storage parameter. In saturated conditions, Richard's flow equation reduces to Darcy's law. In this study, it is assumed that the unfrozen material is fully saturated so that all hydraulic properties remain constant as a result of uncoupling with deformations.

3.6 Selected Lakes and Geometry of Models

For the Kiggavik Main Zone, Squggly and Judge Sissons lakes located at the north and south of the Kiggavik site location respectively have been chosen to investigate the effect of ground flow regime. The locations and elevations of the lakes relative to the Main Zone open pit are shown schematically in Figure 3-7.

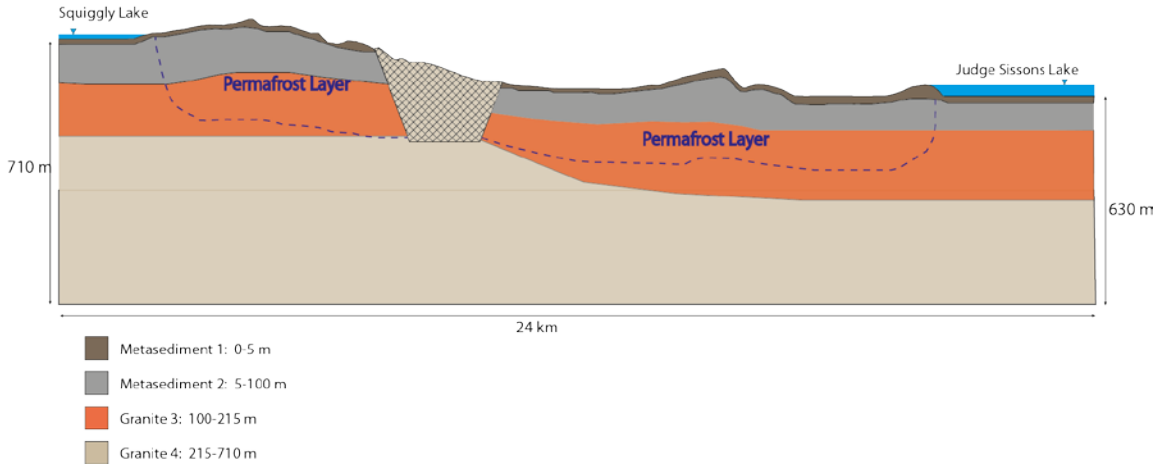

Figure 3-7 Main Zone open pit and Lakes near the open pit which potentially support open talik (not to scale - vertical scale exaggerated ×10)

For Andrew Lake open pit, Gerhard and Boulder lakes are chosen which are on the west and east sides of the open pit, respectively, see Figures 3-1 and 3-4. The location of these two lakes relative to the Andrew Lake open pit and the elevation of lakes are shown in Figure 3-8.

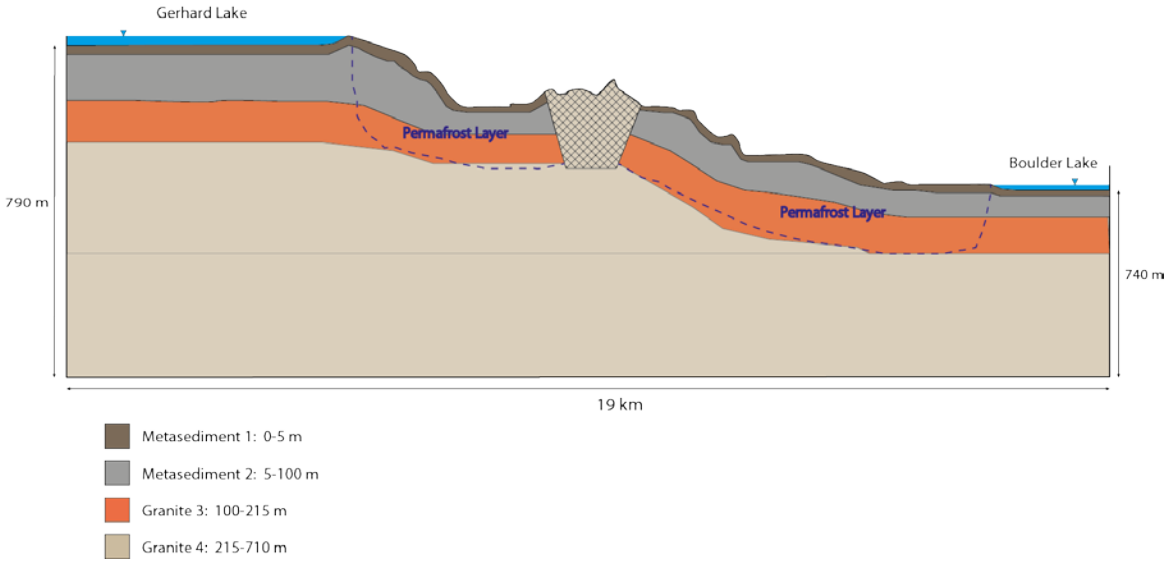

Figure 3-8 Andrew Lake open pit and Lakes near the open pit which potentially support open talik (Not to scaled-vertical scale exaggerated ×7)

3.7 Faults in the Project Area

There are many local faults cutting the ground profile in the vicinity of project sites both at Kiggavik and Sissons. However, there is no information available about these faults. More importantly, there are some major local or regional faults passing through Kiggavik Main Zone and Andrew Lake. Although there is not enough information available for these faults, some reasonable assumptions will be made to investigate the influence of these faults on the groundwater flow into the open pits.

In the absence of pertinent information in the studies done by Areva on the width of the major local faults, widths of 1, 5, 10, and 20 meters in both Kiggavik Main Zone and Andrew Lake pits will be considered in this preliminary study.

3.8 Hydraulic Boundary Conditions

In order to define the hydraulic boundary conditions, it is reminded that the main hydraulic driving force which induces underground fluid flow is the difference in total hydraulic head (summation of elevation and pressure heads) between the bottom of each lake that support the open taliks. Therefore, at the lake locations, the pressure head would be defined as the depth of water according to the data in Table 3-1. In this table, for some lakes both maximum and mean depths are reported while for some others such as Gerhard Lake none of these have been presented. Also, average elevations are reported for these lakes which are the ground elevation at bottom of each lake (Not including water level in the lakes).

Additionally, according to Tier 3 Technical Appendix 5B, in 2009 thermistors have been installed in four boreholes: END-09-01, ANDW-09-03, MZ-09-02, and MZ-09-04. Moreover, during the 2011 field investigations, multilevel thermistor strings were installed in two boreholes GW-11-01 and GW-11-02. In general, hydraulic heads measured beneath permafrost at the site were near to or above ground surface in all three deposits. The hydraulic head measured in the piezometer located beneath the permafrost in the area of the End Grid deposit, END-09-01, was about 9 m above ground surface, while in the area of the Andrew Lake deposit the hydraulic head measured in a piezometer, ANDW-09-03, was about 3 m above the ground surface. The hydraulic head measured in the one piezometer located in the area of the Main Zone deposit, MZ-09-04, was about 25 m above ground.

Hence, the pressure heads at lakes are defined in such a way to match these hydraulic heads in pre-mining conditions in the unfrozen ground at the boundary of permafrost in both Kiggavik

Main Zone and Andrew Lake. Since the End Grid deposit is close to the Andrew Lake open pit, the hydraulic head was chosen as 9 m above ground surface.

Other boundaries in the numerical model are considered as 'No-Flow' boundaries except at the bottom of pits. For the bottom of pits, when the excavation reaches the boundary of permafrost, the pressure head is considered as zero. This boundary condition indicates the situation in which the water can easily enter the excavated area of the open pits. Boundary condition for both Kiggavik Main Zone and Andrew Lake projects are shown in Figures 3-9 and 3-10.

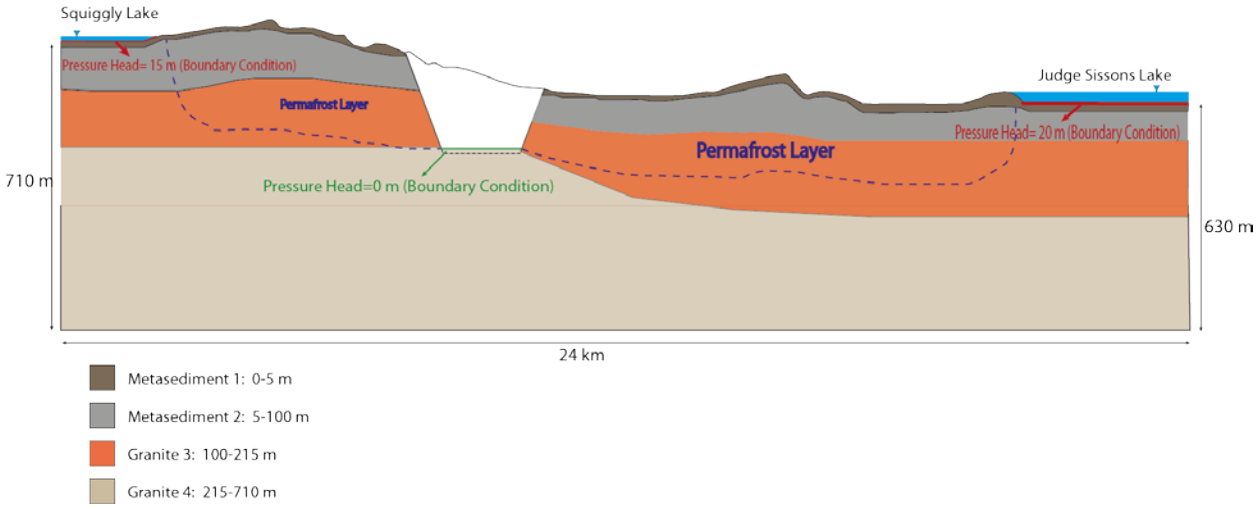

Figure 3-9 Boundary conditions at Kiggavik Main Zone

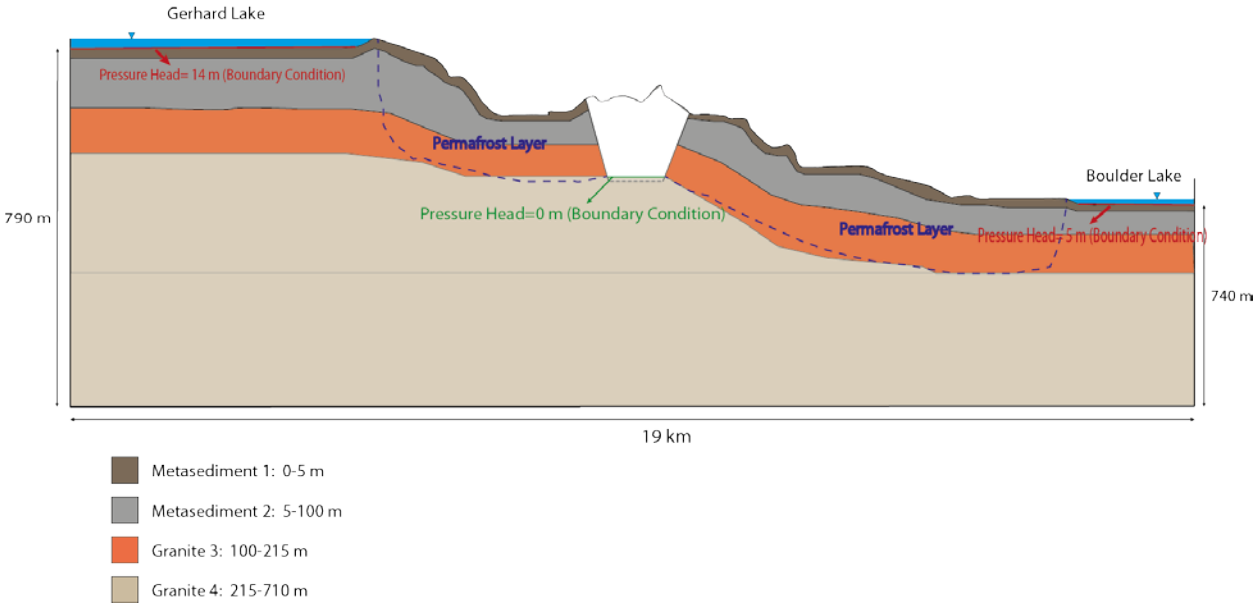

Figure 3-10 Boundary Conditions at Andrew Lake

3.9 Results

3.9.1 Different scenarios

As described in section 3.5 (Material Properties), different hydraulic conductivities are reported for various materials at respective depths that are considered in the numerical simulations. Since there are not any useful information available in the Technical Appendixes submitted by Areva on fracture properties (e.g. fracture orientation) in the rock domains, some assumption are to be made prior starting the numerical modelling. For the current study, two hydraulic conductivity scenarios have been considered:

1) All the materials behave like an isotropic material (hydraulic conductivity is the same in all directions). This is referred as the baseline case for comparison purposes.

2) Granite rock and material within the fault zone have different hydraulic conductivities in horizontal and vertical directions. For this scenario, hydraulic conductivity of Granite in the horizontal direction is considered two times the one in the vertical direction. By contrast, the horizontal hydraulic conductivity of the fault zone material is assumed to be half of the horizontal one.

3.9.2 Numerical Results

Due to the large number of numerical simulations conducted, in this section only figures of the model with a fault width of 20 m and hydraulic conductivity of 3 orders of magnitude higher than the surrounding rock under isotropic condition for the Kiggavik Main Zone pit are presented. The results of other numerical simulations are similar in trends, but different in quantity of water flow.

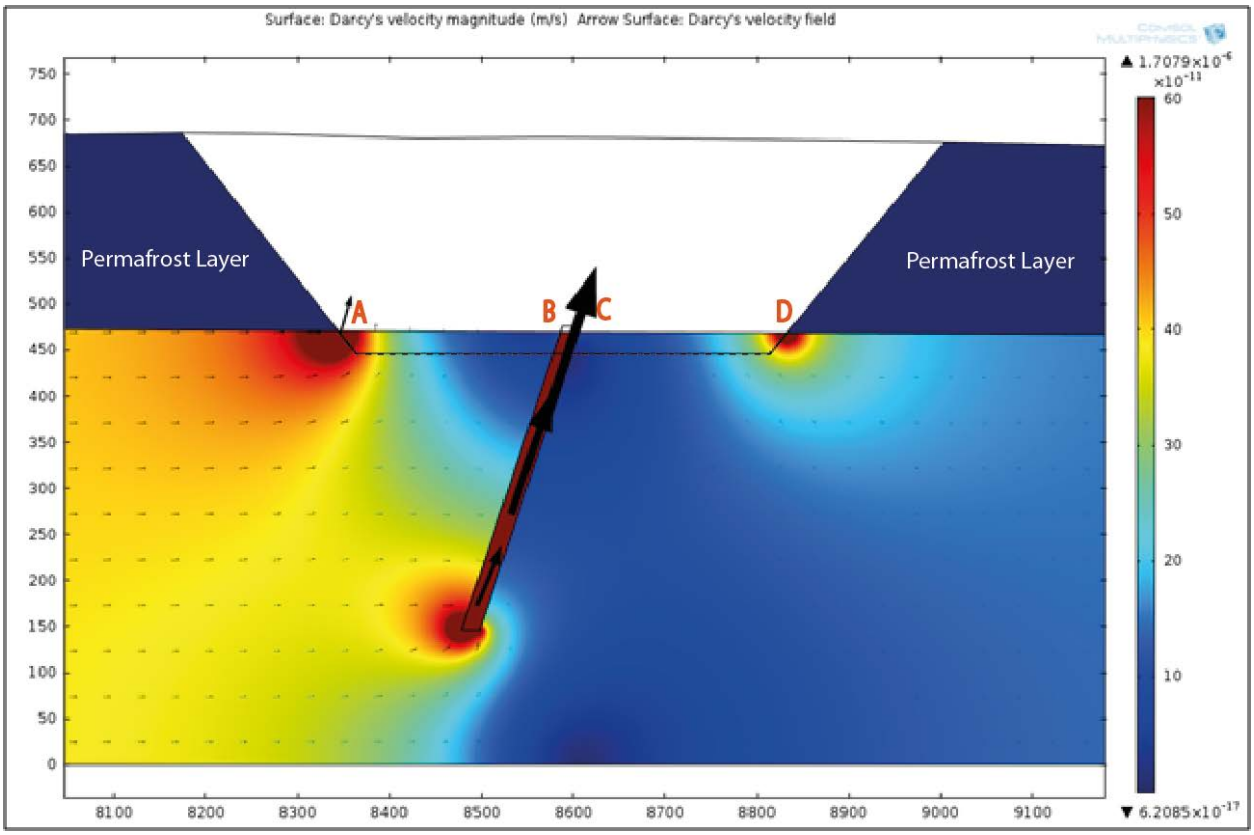

Figure 3-11 Darcy's Velocity field with contours representing magnitude (m/s) underneath Kiggavik Main Zone Pit

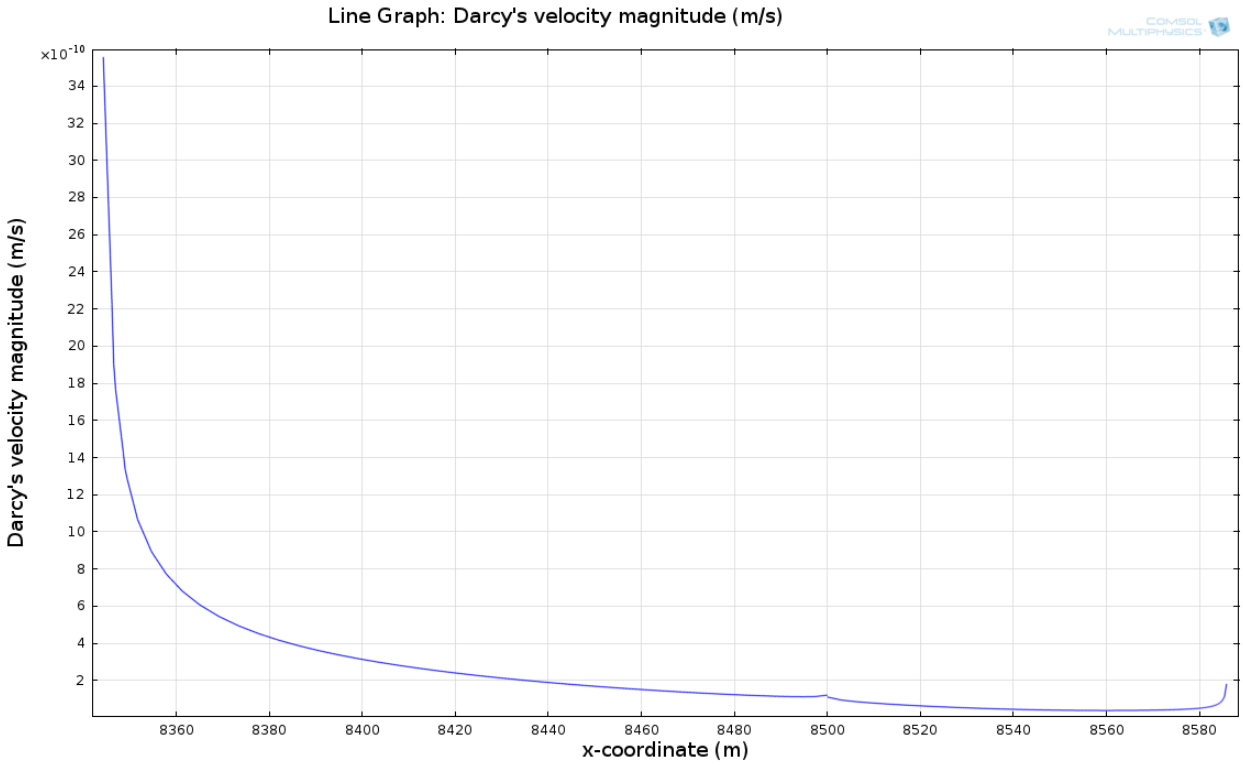

Figure 3-12 Darcy's velocity distribution along AB on the left side of the fault

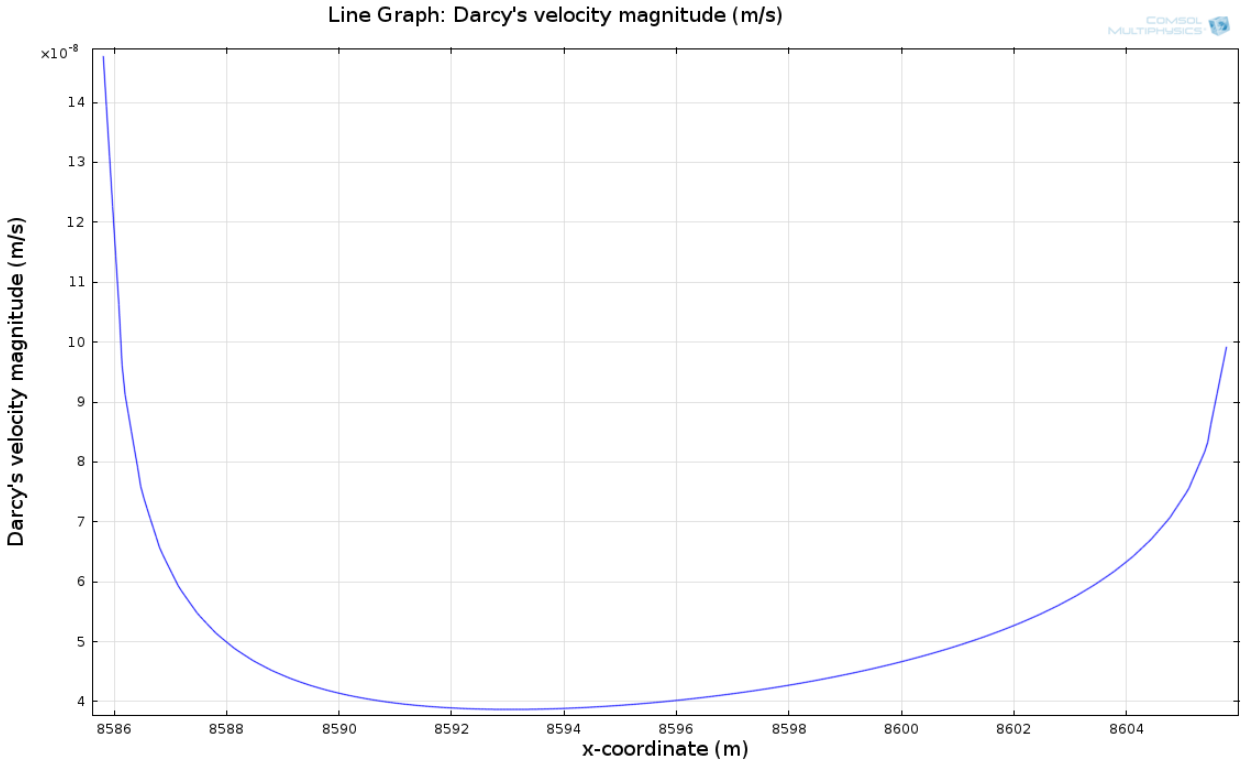

Figure 3-13 Darcy's velocity distribution along BC inside the fault

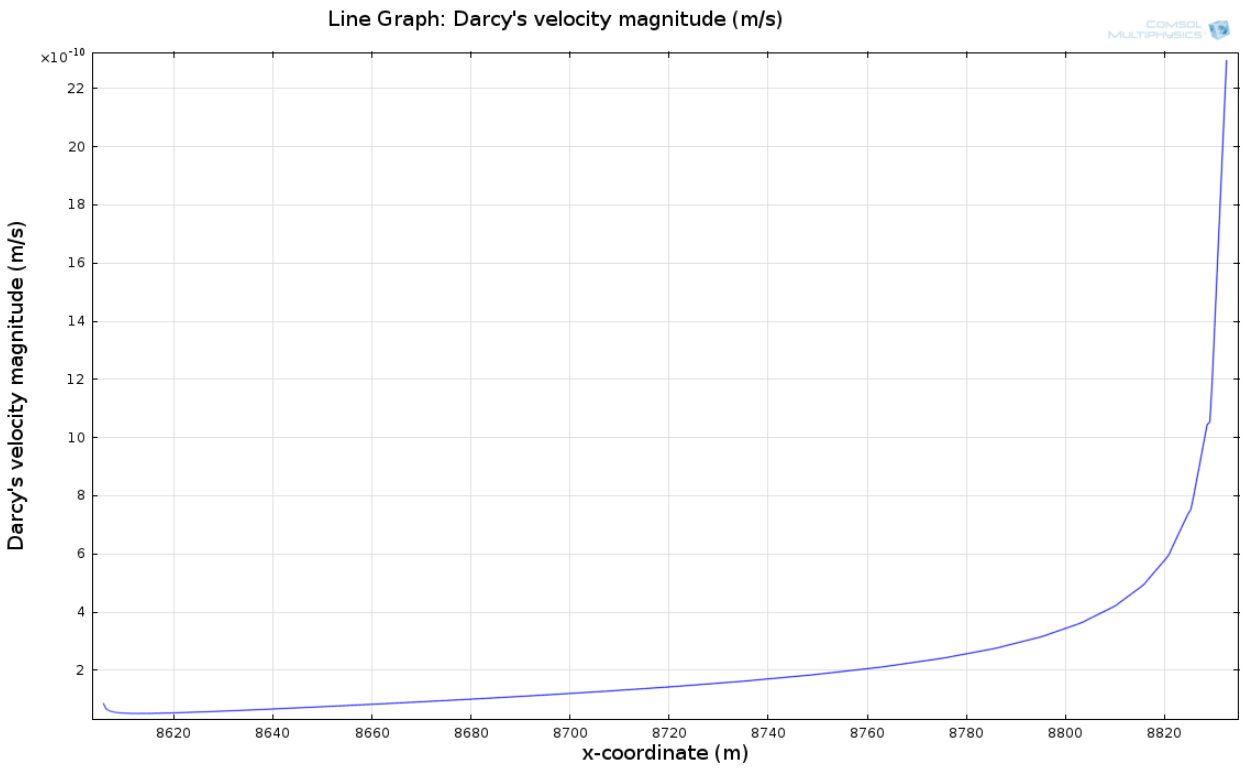

Figure 3-14 Darcy's velocity distribution along CD on the right side of the fault

3.9.3 Flux Calculation

In this section, the method used for calculation of fluxes is explained. As shown in Figure 3-15a, the bottom of the pit can be separated into 3 distinct areas (Areas 1, 2 and 3). These areas are further shown in the plan view of the excavated open pit in Figure 3-15b. Areas 1 and 3 are half circles residing on the right and left sides of the fault zone respectively. The fault zone (Area 2) is considered as a rectangular zone.

In Section 3.9.2, the results of numerical study are illustrated in Figures 3-11 to 3-14 which give the Darcy's velocity distribution are presented along lines AB, BC, and CD. These distributions pertain to Areas 1, 2, and 3 of Figure 3-15.

For finding the inward flux in each area, the respective Darcy's velocity distribution is simply integrated over the concerned domain. Figures 3-15 and 3-16 show elemental areas A_1 and A_3 involved in the flux calculation through an annulus defined by radii r_1 and r_2. The elemental flux for the annulus is simply the average velocity between r_1 and r_2 multiplied by the elemental area of the annulus. Finally, the total flux through the bottom of the pit is the summation of all elemental fluxes that were calculated as explained in the above.

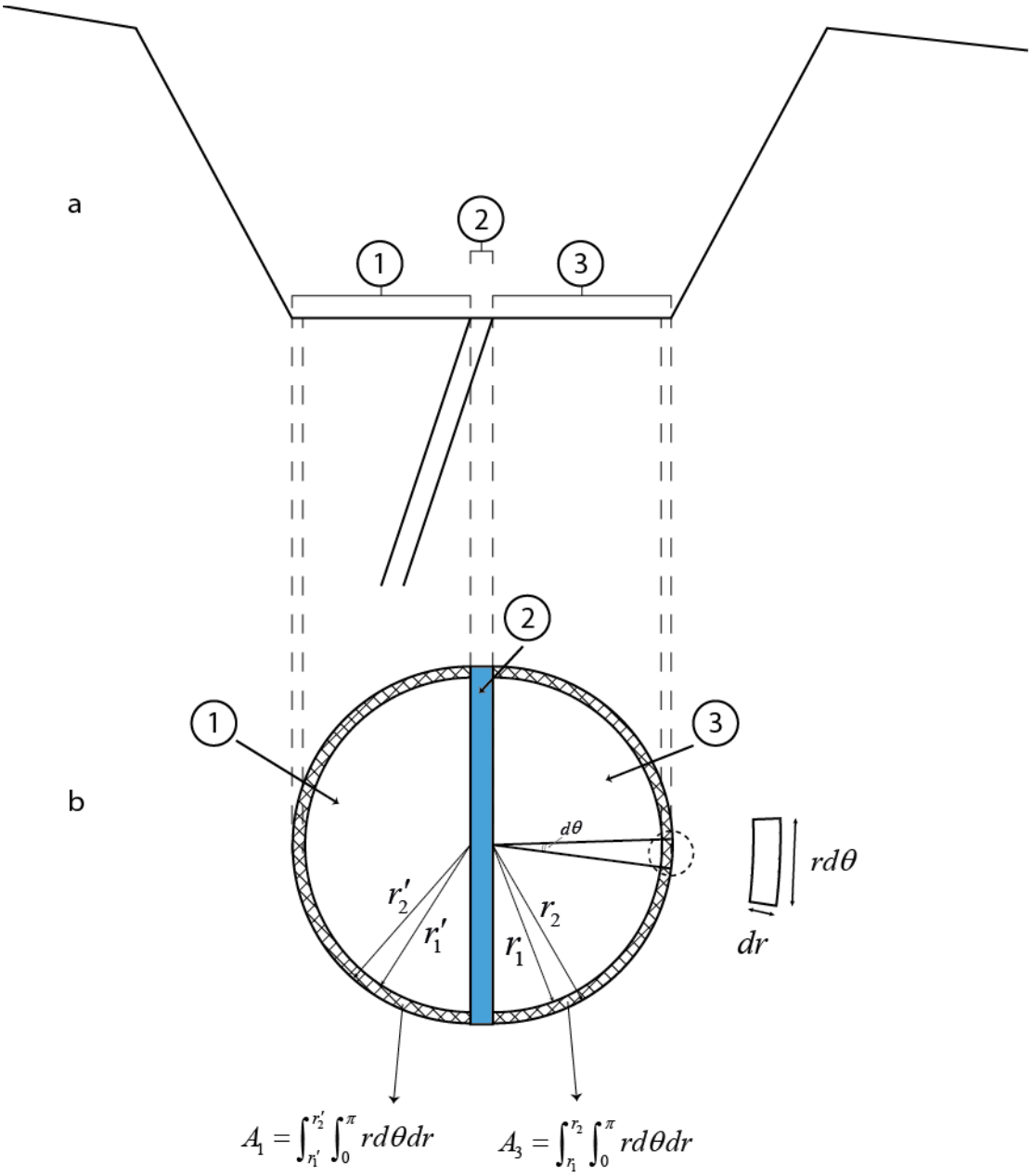

Figure 3-15 Distinct areas in a) cross section of open pit and b) in the plan of the open pit

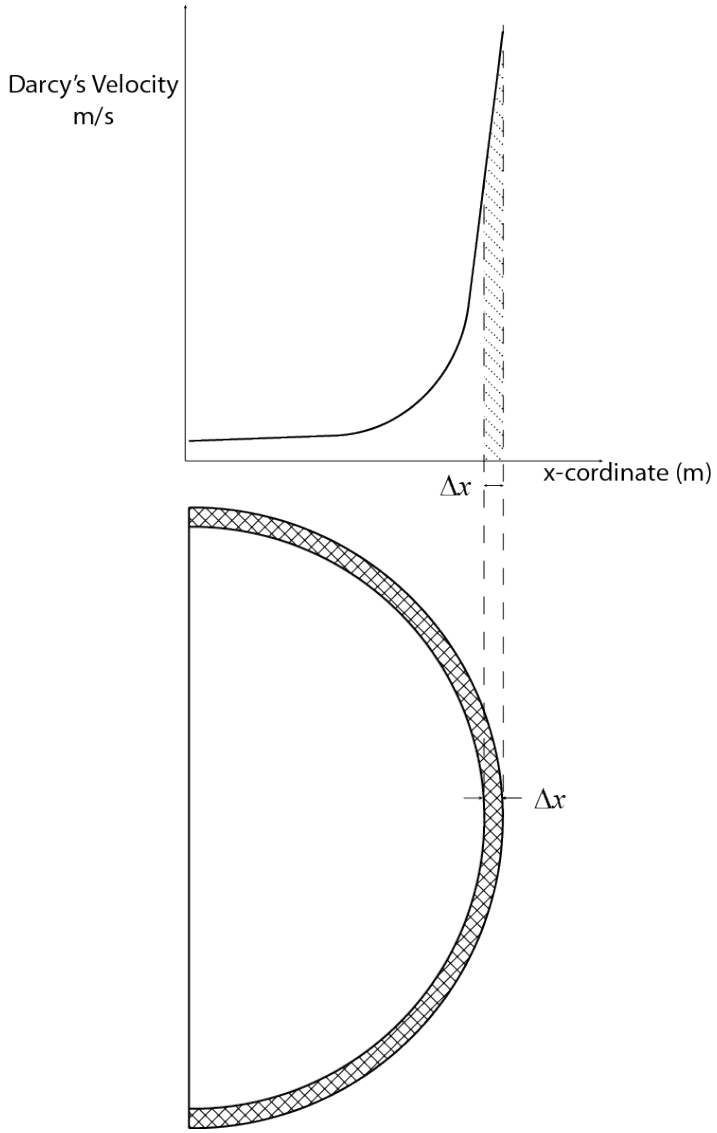

Figure 3-16 Darcy's velocity distribution and selected area

3.9.4 Isotropic Scenario

In Tables 3-3 and 3-4, results of underground water flow into the open excavations for Kiggavik Main Zone and Andrew Lake are summarized. In these tables, three different values for the fault zone hydraulic conductivity and four different widths for the fault zone are considered. Additionally, as a baseline, one other numerical model is developed in which the hydraulic conductivity of the fault zone is the same as the surrounding rock material.

Table 3-3 Kiggavik Main Zone: Summary of calculated underground water flux through the bottom of the open pit - isotropic hydraulic conductivity

Hydraulic Conductivity of Fault the same as the Surrounding Rock			
Fault Width (m)	Flux Through Fault (m^3/day)	Flux Through Bottom of Pit (m^3/day)	Total Flux (m^3/day)
-	-	10.45	10.45
Hydraulic Conductivity of Fault 1 order higher than Surrounding Rock			
Fault Width (m)	Flux Through Fault (m^3/day)	Flux Through Bottom of Pit (m^3/day)	Total Flux (m^3/day)
20	1.82	9.16	10.98
10	1.03	9.54	10.57
5	0.55	10.06	10.61
1	0.12	10.53	10.65
Hydraulic Conductivity of Fault 3 orders higher than Surrounding Rock			
Fault Width (m)	Flux Through Fault (m^3/day)	Flux Through Bottom of Pit (m^3/day)	Total Flux (m^3/day)
20	41.74	5.32	47.06
10	20.47	5.73	26.20
5	11.05	6.09	17.14
1	4.30	7.36	11.66
Hydraulic Conductivity of Fault 5 orders higher than Surrounding Rock			
Fault Width (m)	Flux Through Fault (m^3/day)	Flux Through Bottom of Pit (m^3/day)	Total Flux (m^3/day)
20	4218.16	5.21	4223.37
10	2105.42	5.52	2110.94
5	1052.72	5.68	1058.40
1	209.95	5.83	215.78

Table 3-4 Andrew Lake: Summary of calculated underground water flux through the bottom of the open pit - isotropic hydraulic conductivity

Hydraulic Conductivity of Fault the same as Surrounding Rock			
Fault Width (m)	Flux Through Fault (m^3/day)	Flux Through Bottom of Pit (m^3/day)	Total Flux (m^3/day)
-	-	9.00	9.00
Hydraulic Conductivity of Fault 1 order higher than Surrounding Rock			
Faul Width (m)	Flux Through Fault (m^3/day)	Flux Through Bottom of Pit (m^3/day)	Total Flux (m^3/day)
20	2.67	6.38	9.05
10	1.57	7.57	9.14
5	0.87	8.32	9.19
1	0.19	9.08	9.27
Hydraulic Conductivity of Fault 3 orders higher than Surrounding Rock			
Fault Width (m)	Flux Through Fault (m^3/day)	Flux Through Bottom of Pit (m^3/day)	Total Flux (m^3/day)
20	26.31	2.62	28.93
10	13.95	2.99	16.94
5	8.74	3.34	12.08
1	5.41	4.81	10.22
Hydraulic Conductivity of Fault 5 orders higher than Surrounding Rock			
Fault Width (m)	Flux Through Fault (m^3/day)	Flux Through Bottom of Pit (m^3/day)	Total Flux (m^3/day)
20	2639.57	2.51	2642.08
10	1316.97	2.76	1319.73
5	655.59	2.90	658.49
1	126.52	3.06	129.58

3.9.5 Anisotropic Scenario

The result of anisotropic condition is summarized in Tables 3-5 and 3-6. For these anisotropic simulations, for the fault zone material, the vertical hydraulic conductivity is 2 times the horizontal one. For the Granite rock, the horizontal hydraulic conductivity is 2 times the vertical one.

Table 3-5 Kiggavik Main Zone: Summary of calculated underground water flux through the bottom of the open pit - anisotropic hydraulic conductivity

Hydraulic Conductivity of Fault the same as the Surrounding Rock			
Fault Width (m)	Flux Through Fault (m^3/day)	Flux Through Bottom of Pit (m^3/day)	Total Flux (m^3/day)
-	-	19.82	19.82
Hydraulic Conductivity of Fault 1 order higher than Surrounding Rock			
Fault Width (m)	Flux Through Fault (m^3/day)	Flux Through Bottom of Pit (m^3/day)	Total Flux (m^3/day)
20	5.41	15.74	21.15
10	3.28	16.99	20.27
5	1.84	18.38	20.22
1	0.41	19.75	20.16
Hydraulic Conductivity of Fault 3 orders higher than Surrounding Rock			
Fault Width (m)	Flux Through Fault (m^3/day)	Flux Through Bottom of Pit (m^3/day)	Total Flux (m^3/day)
20	47.52	8.12	55.64
10	24.85	8.76	33.61
5	15.64	9.32	24.96
1	10.30	11.60	21.90
Hydraulic Conductivity of Fault 5 orders higher than Surrounding Rock			
Fault Width (m)	Flux Through Fault (m^3/day)	Flux Through Bottom of Pit (m^3/day)	Total Flux (m^3/day)
20	4859.99	7.95	4867.94
10	2423.03	8.41	2431.44
5	1211.79	8.65	1220.44
1	240.28	8.88	249.16

Table 3-6 Andrew Lake: Summary of calculated underground water flux through the bottom of the open pit - anisotropic hydraulic conductivity

Hydraulic Conductivity of Fault the same as Surrounding Rock			
Fault Width (m)	Flux Through Fault (m^3/day)	Flux Through Bottom of Pit (m^3/day)	Total Flux (m^3/day)
-	-	16.74	16.74
Hydraulic Conductivity of Fault 1 order higher than Surrounding Rock			
Fault Width (m)	Flux Through Fault (m^3/day)	Flux Through Bottom of Pit (m^3/day)	Total Flux (m^3/day)
20	7.28	10.25	17.53
10	4.65	12.80	17.45
5	2.73	14.61	17.34
1	0.64	16.62	17.26
Hydraulic Conductivity of Fault 3 order higher than Surrounding Rock			
Fault Width (m)	Flux Through Fault (m^3/day)	Flux Through Bottom of Pit (m^3/day)	Total Flux (m^3/day)
20	30.87	3.84	34.71
10	19.05	4.37	23.42
5	15.82	4.87	20.69
1	12.44	7.10	19.54
Hydraulic Conductivity of Fault 5 order higher than Surrounding Rock			
Fault Width (m)	Flux Through Fault (m^3/day)	Flux Through Bottom of Pit (m^3/day)	Total Flux (m^3/day)
20	3041.98	3.69	3045.67
10	1515.70	4.06	1519.76
5	752.55	4.25	756.80
1	143.60	4.48	148.08

3.10 Discussions

In this section, results of numerical simulations which are presented in Section 3.9 will be discussed. Since there are various scenarios, the results for isotropic hydraulic conductivity conditions will be first analyzed. Then, they will be compared with the results obtained in the case of anisotropic hydraulic conductivity.

3.10.1 Isotropic Scenario

Results of all isotropic scenarios vs fault width are plotted in a semi-logarithmic diagram in Figure 3-17. Moreover, the results for all isotropic scenarios vs hydraulic conductivity of fault zone are plotted in a logarithmic diagram in Figure 3-18. In both figures, the calculated water fluxes into the open pit bottom are plotted for both Kiggavik Main Zone (solid line) and Andrew Lake (dashed line) open pits.

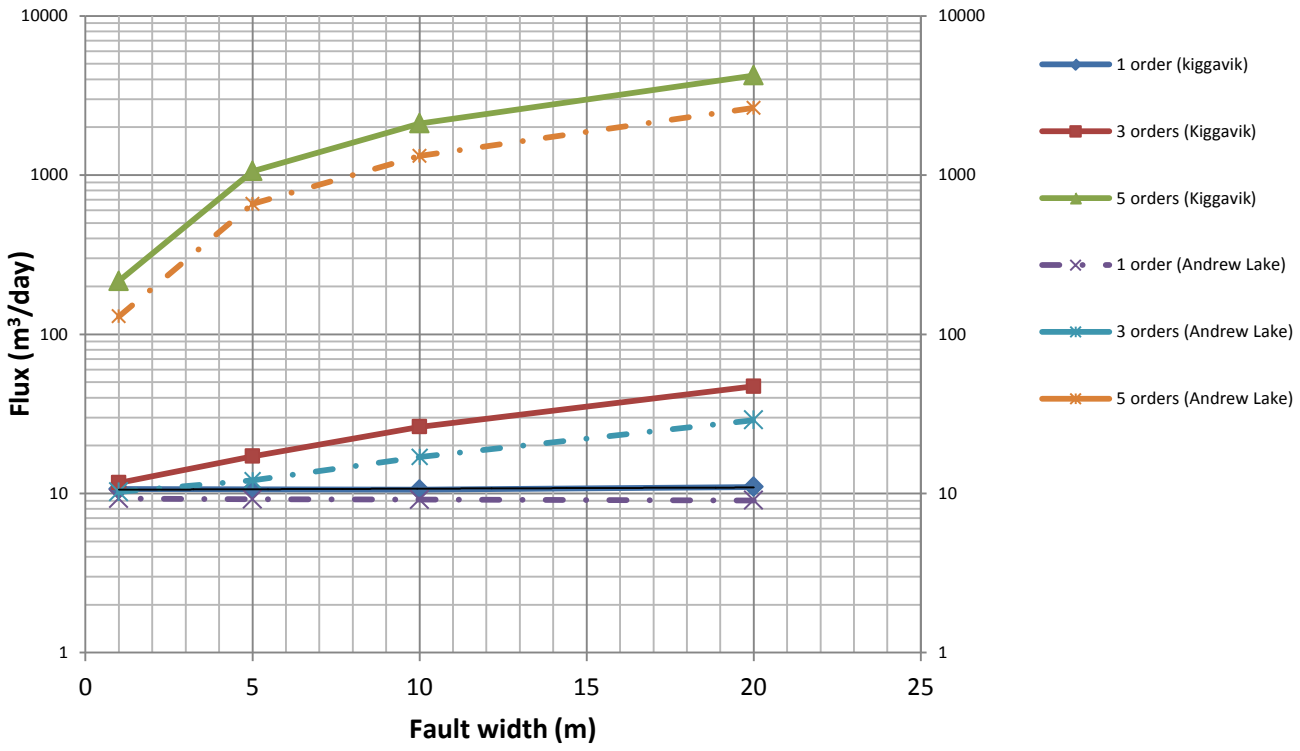

Figure 3-17 Inward Flux vs Fault Width into the open pit for isotropic condition for both Kiggavik Main Zone and Andrew Lake

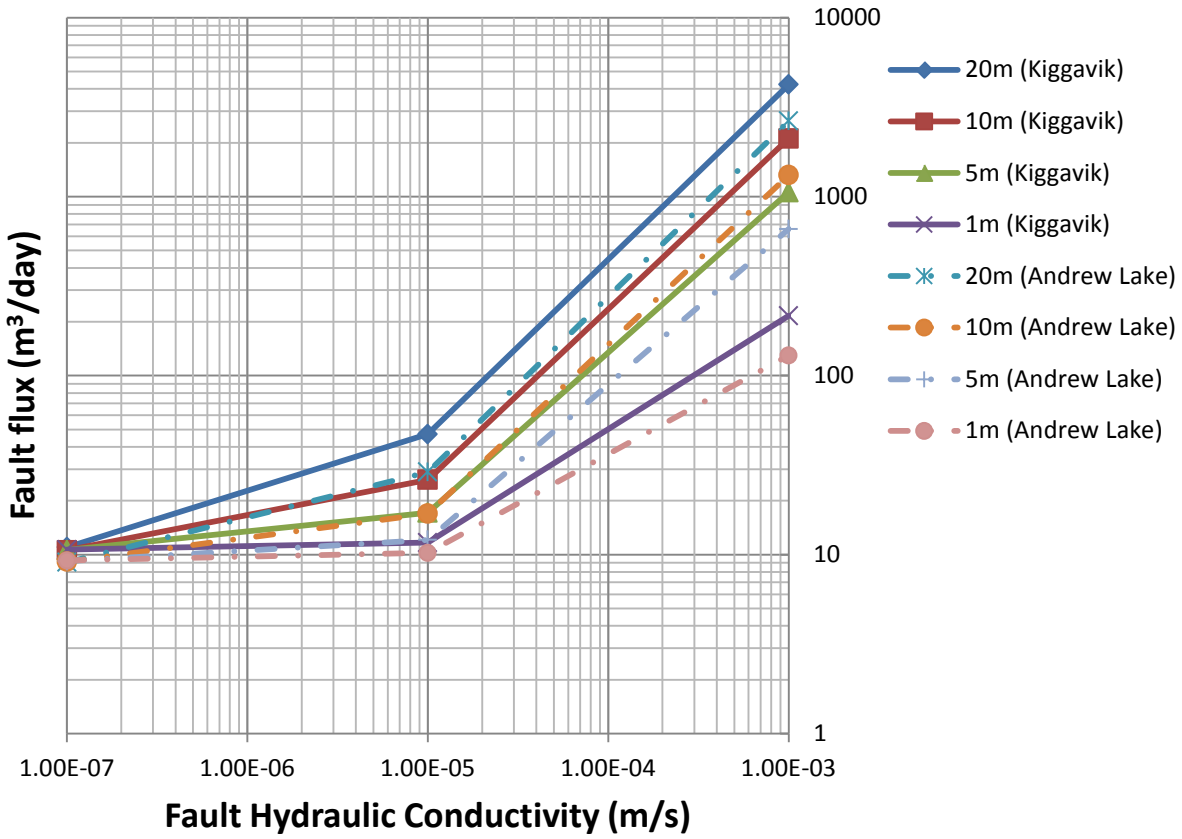

Figure 3-18 Inward Flux vs Fault Hydraulic Conductivity into the open pit for isotropic condition for both Kiggavik Main Zone and Andrew Lake

From the results presented in Tables 3-3 and 3-4 which are also plotted in Figure 3-17, for the isotropic hydraulic conductivity case, the following points can be made:

- When the hydraulic conductivity of the fault zone is the same as that of the surrounding rock, the inward water flux into the pits are 10.45 and 9.00 m^3/day for Kiggavik Main Zone and Andrew Lake, respectively. When the hydraulic conductivity of the fault zone is increased in the numerical simulation by one order of magnitude, it is found that the amount of inward water flux increases by less than 2% in both models.

- By comparing the result of simulations for various fault widths, it is found that in both Kiggavik Main Zone and Andrew Lake models the fault width also does not affect significantly the total flux migrating into the open pit when the hydraulic conductivity of the fault is one order of magnitude higher than the surrounding rock. It should be mentioned that although the total flux escaping through the whole bottom of the pit does

not change, the water flux through the fault zone increases with fault width. Meanwhile, the flux entering the open pit from the whole bottom of excavation decreases.

- When increasing the hydraulic conductivity of the fault zone by 3 orders of magnitude higher than the surrounding rock, the water passing through the fault increases considerably in both open pits. This is to be expected since at that hydraulic conductivity contrast, the fault zone produces a clear pathway for underground water to move more easily toward boundaries with lower total hydraulic heads.

- When decreasing the fault width, in the simulations in which the hydraulic conductivity of the fault zone is 3 orders higher than the surrounding rock, the amount of the water flowing through the fault zone decreases while the amount of the water entering the pit from the bottom of excavation increases at the same time. However the total flux decreases in both conditions.

- When the hydraulic conductivity of the fault zone becomes 5 orders of magnitude higher than the surrounding rock, this is if the fault zone was filled with totally crushed rock or coarse boulder sized rocks. With such a high hydraulic conductivity (10^{-3} m/s) for the fault zone in, a large amount of water will enter the open pit. In the case of Kiggavik Main Zone which is the largest open pit in the Kiggavik project with the bottom area of about $180{,}000\,m^2$, a water flux of $4223\,m^3/day$ will increase the water level by about 2 cm/day inside the open pit if the water was not pumped out, which is not a plausible event.

- Even in the case of faults with hydraulic conductivity 5 order higher than the surrounding rock, the total inward flux into the open pits increases by increasing the fault width. However, the gradient of the flux change is much higher than the case of fault with hydraulic conductivity 3 orders higher.

3.10.2 Anisotropic Scenario

Results of all anisotropic scenarios vs fault width are plotted in a semi-logarithmic diagram in Figure 3-19. Also, the results for all anisotropic scenarios vs vertical hydraulic conductivity of fault zone (which is two times the horizontal one) are plotted in a logarithmic diagram in Figure 3-20. In both figures, the calculated water fluxes into the open pit bottom are plotted for both Kiggavik Main Zone (solid line) and Andrew Lake (dashed line) open pits.

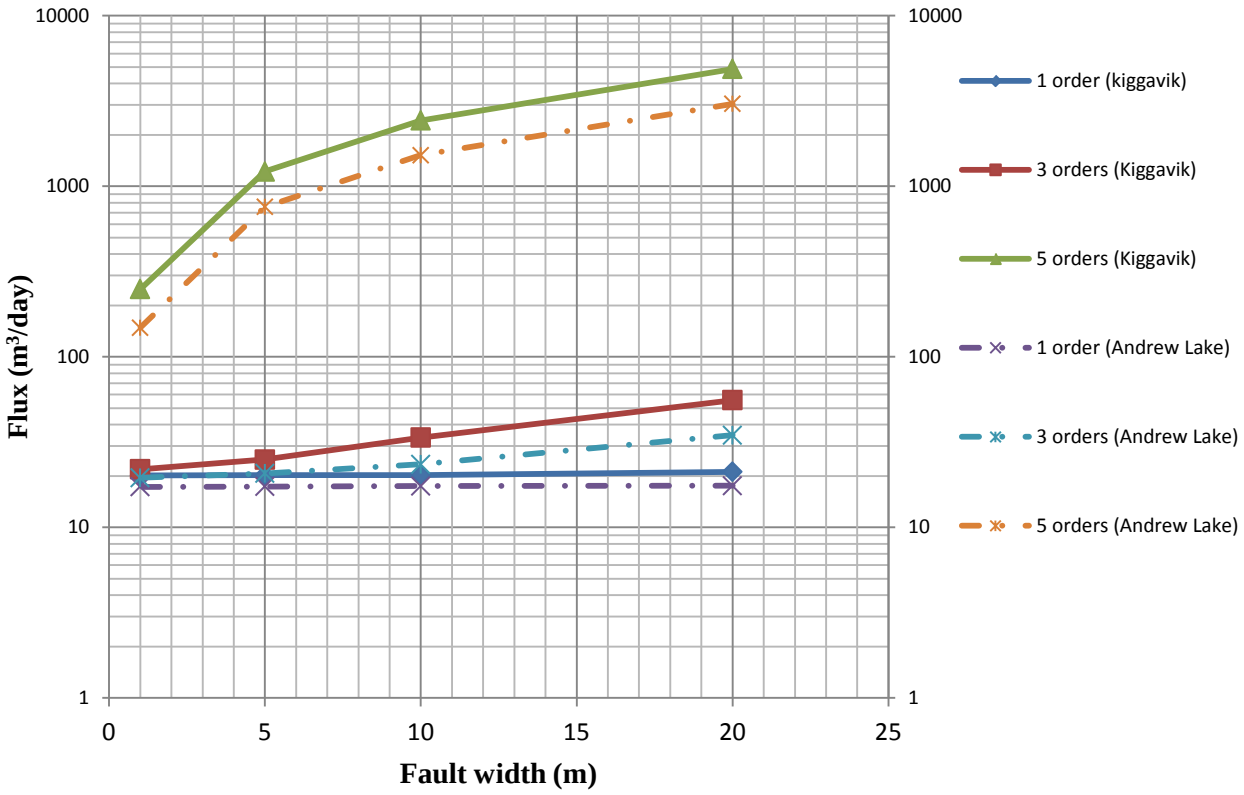

Figure 3-19 Water flux vs fault width for both Kiggavik Main Zone and Andrew Lake – anisotropic hydraulic conductivity

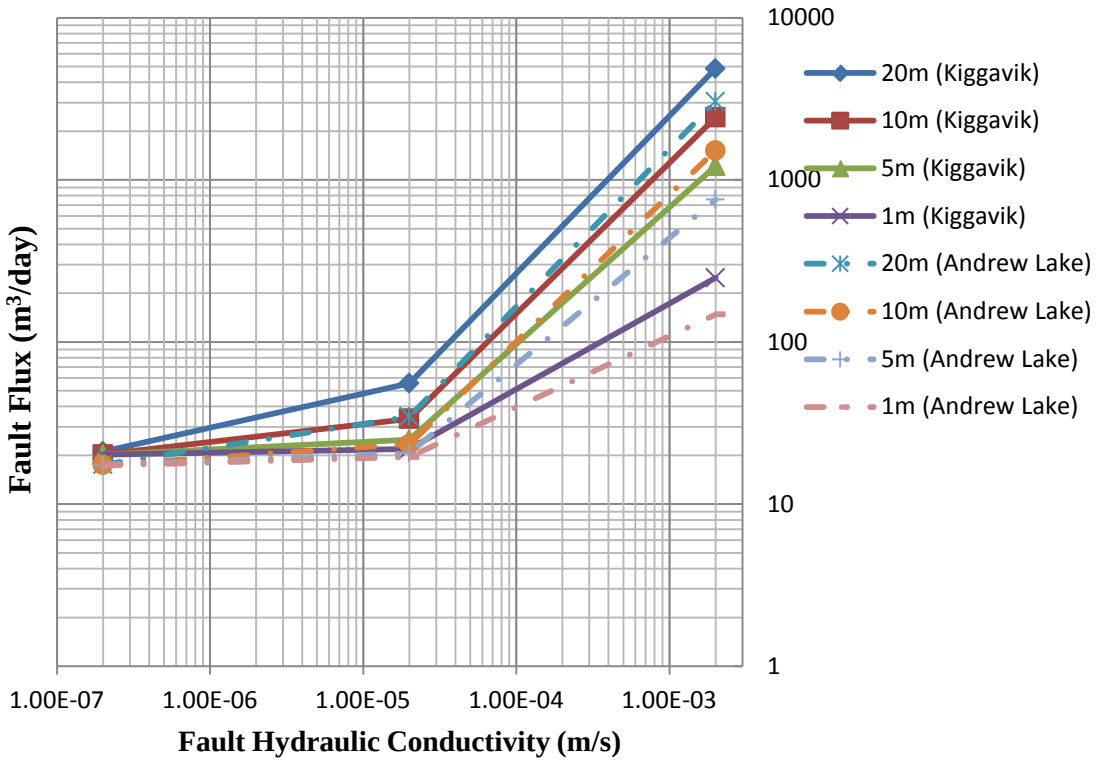

Figure 3-20 Inward Flux vs Fault Hydraulic Conductivity into the open pit for anisotropic condition for both Kiggavik Main Zone and Andrew Lake

The same trends in water fluxes as in the isotropic hydraulic conductivity case are obtained with the following observations.

- An increase in the horizontal hydraulic conductivity of Granite rock which is the predominant material in the domain beneath the permafrost layer leads to more water fluxes entering the bottom of the open pits.

- Although the increase in the horizontal hydraulic conductivity of Granite rock has increased the inward flux through both fault zone and bottom of the pits, the increase in the amount of flux through the bottom of pit is more sensitive when the hydraulic conductivity of fault is just one order higher.

- Even in cases with hydraulic conductivities 3 and 5 orders higher, the relative increase in flux entering the pits through the bottom of excavation is higher. In these cases, the flux entering the pits from bottom shows 50 to 60% increase while the flux passing through the fault has increased only between 10 and 20%. For this reason, under conditions where flux through the bottom plays a more important role, the increase in flux is more sensitive.

References

1. Anisimov, O. A. 1989. Changing climate and permafrost distribution in the Soviet Arctic. Physical Geography, 10, 285-293.
2. Arjang, B. 2004. Database on Canadian in situ ground stresses. CANMET Division Report MMSL 01-029 (TR).
3. Arjang, B., and Herget, G. 1997. In situ ground stresses in the Canadian hardrock mines : An update. International Journal of Rock Mechanics and Mining Sciences, Volume 34, Issues 3-4, pp. 15.e1-15.e16.
4. Beltrami, H., and Kellman, L. 2003. An examination of short-and long-term air-ground temperature coupling. Global and Planetray Changes, 38 : 291-303.
5. Betts, A.K., Ball, J.H., and McCaughey, J.H. 2001. Near-surface climate in the breal forest. Journal of Geophysical Research, 106(D24) : 33529-33541.
6. Bense, V.F., Ferguson, G., Kooi, H. 2009. Evolution of shallow groundwater flow systems in areas of degrading permafrost. Geophysical Research Letters, 36.
7. Brooks, R.H., and Corey, A.T. 1966. Properties of Porous Media Affecting Fluid Flow. J. Irrig Drainage Div., ASCE Proc., vol. 72 (IR2).
8. Burn, C.R. (2004). The Thermal Regime of Cryosols, in Cryosols: Permafrost-Affected Soils, Edited by J.M. Kimble. Springer, Germany: 391-413.
9. Burn, C. R. 2002. Tundra lakes and permafrost, Richards Island, Western Arctic Coast, Canada, Can. J. Earth Sci., 39, 1281– 1298.
10. Burn, C.R. and Smith, M.W. 1993. Issues in Canadian Permafrost Research. Progress in Physical Geography June 1993, 17(2), 156-172.
11. Carlson, H. 1952. Calculation of Depth of Thaw in Frozen Ground. Frost Action in Soils: A Symposium, In Highway Research Board Special Report2. National Research Council, Washington, D.C., pp. 192-223.
12. Carslaw H.S., Jaeger J.C. 1959. Conduction of Heat in Solids, 2nd Ed. Oxford University Press: Oxford.
13. COMSOL, 2012, COMSOL Multiphysics 4.3a, COMSOL Inc. Los Angeles, CA 90024, USA.
14. Dagher, E.E., Nguyen, T.S., Su, J.G. 2012. Numerical Modelling of Coupled Heat Transfer and Groundwater Flow: Applications to Tailings Management Facility in Permafrost Environments in Northern Canada, Proceedings of the 65th Canadian Geotechnical Conference, September 30-October 3, 2012, Winnipeg, Manitoba, 10p.
15. Delisle, G. 1998. Numerical simulation of permafrost growth and decay. Journal of Quaternary Science 13, 325-333.
16. Eaton, A.K., Rouse, W.R., Lafleur, P.M.,Marsh, P., and Blanken, P.D. 2001. Surface energy balance of the Western and Central Canadian Subarctric: Variations in Energency Balance among Five Major Terrain Types. Journal of Climate, 14: 3692-3703.
17. Eyres, N.R., Hartree, D.R., Ingham, J., Jackson, R., Sarjant, R.J. and Wagstaff, J.B. 1946. The calculation of variable heat flow in solids, Phil. Trans. R. Soc. London, A 240, 1-57.
18. Evans, D., and T. Nicholson (eds.). 1987. Flow and Transport Through Unsaturated Fractured Rock, Geophys. Monograph 42, American Geophysical Union, Washington, D.C.

19. Freeze, R.A., and J.A. Cherry. 1979. Groundwater, Prentice-Hall, Inc., Englewood Cliffs, N.J.
20. Freeze, R.A. 1971. Three-dimensional, Transient, Saturated-unsaturated Flow in a Groundwater Basin. Water Resour.Res., vol. 7, no. 2, 1971.
21. French, H.M. and O. Slaymaker (1993). Canada's Cold Land Mass. Canada's Cold Environments, Edited by H.M. French and O. Slaymaker. McGill-Queen's University Press, Montreal and Kingston: 3-27.
22. Goodrich, L. E. 1982. The influence of snow cover on the ground thermal regime. Canadian Geotechnical Journal, 19, 421-432.
23. Goodrich, L. E. (1978). Some results of a numerical study of ground thermal regimes, in Proceedings, Third International Conference on Permafrost, July, Edmonton, Canada. National Research Council of Canada, Ottawa, 1: 29-34.
24. Gruber, S., L. King, T. Kohl, T. Herz, W. Haeberli, and M. Hoelzle (2004). Interpretation of Geothermal Profiles Perturbed by Topography: the Alpine Permafrost Boreholes at Stockhorn Plateau, Switzerland. Permafrost and Periglacial Processes, 15: 349-357.
25. Hartikainen, J. 2006. Numerical Simulation of Permafrost Depth at Olkiluoto. Posiva 2006-52.
26. Heginbottom, J.A., Dubreuil, M.A., and Harker, P.A. 1995. Canada – Permafrost; National Atlas of Canada, Natural Resources of Canada, Ottawa (MCR 4177), scale 1:7 500 000.
27. Herget, G. 1988. Stresses in Rock. Rotterdam: Balkema.
28. Hoek E., Brown E. T., (1980b). Empirical strength criterion for rockmasses. Journal of Geotechnical Engineering (ASCE), V 10 (GT9), pp 1013-1036.
29. Hoek, E., Carranza Torres, C., and Corkum, B. 2002. HOEK-BROWN FAILURE CRITERION-2002 EDITION. Proc. NARMS-TAC Confrence, Toronto, 2002, 1, 267-273.
30. Hopkins, D. M. 1949. Thaw lakes and thaw sinks in the Imuruk lake area, Seward Peninsula, J. Geol., 57, 119–131.
31. Ishikawa, M. (2002). Thermal regimes and the snow-ground interface and their implications for permafrost investigation. Geomorphology, 52: 105-120.
32. Johnston, G. H., and Brown, R.J.E. 1964. Some observations on permafrost distribution at a lake in the Mackenzie delta, N.W.T., Canada, Arctic, 17, 162–175.
33. Jorgenson, M. T. and Kreig, R. A. 1988. A model for mapping permafrost distribution based on landscape component maps and climatic variables. Permafrost, 5th International Conference Proceedings, 1, Trondheim, Norway, Tapir, 176-182.
34. Kane, D.L., Hinzman, L.D. and Zarling, J.P. 1991. Thermal response of the active layer to climatic warming in a permafrost environment. Cold Regions Science and Technology 19, 111-22.
35. Karunaratne, K.C. and C.R. Burn (2004). Relations between air and surface temperature in discontinuous permafrost terrain near Mayo, Yukon Territory. Canadian Journal of Earth Sciences, 41: 1437-1451.
36. Klene, A.E., F.E. Nelson, N.I. Shiklomanov, and K.M. Hinkel (2001). The N-Factor in Natural Landscapes: Variability of Air and Soil-Surface Temperatures, Kuparuk River Basin, Alaska, USA. Arctic, Antarctic, and Alpine Research, 33, 2: 140-148.

37. Lachenbruch, A. H., M. C. Brewer, G. W. Greene, and Marshall B.V. 1962. Temperatures in permafrost, in Temperature—Its Measurement and Control in Science and Industry, vol. 3, part 1, pp. 791– 803, Reinhold, New York.
38. Lachenbruch, A.H. and B.V. Marshall (1986). Changing Climate: Geothermal Evidence from Permafrost in the Alaskan Arctic. Science, 234: 689-696.
39. Lunardini V.J. 1981. Heat transfer in cold climates. Van Nostrand Reinhold: New York.
40. Lunardini, V.J. 1978: Theory of n-factors and correlation of data. In Permafrost, Third International Conference, Proceedings, Volume 1, Ottawa, Ontario: National Research Council of Canada, 40-46.
41. Mackay, J. R. 1997. A full-scale field experiment (1978 –1995) on the growth of permafrost by means of lake drainage, western Arctic coast: A discussion of the method and some results, Can. J. Earth Sci., 34, 17–33.
42. Mackay, J.R. 1972. The world of underground ice. Annals of the Association of American Geographers, 62(1), 1-22, March 1972.
43. Mallants, D., 2006. Basic concepts of water flow, solute transport, and heat flow in soils and sediments, second edition. SCK•CEN-BLG-991, 169-183.
44. Maloney, S. M., Kaiser P. K. 2006. A Re-assessment of In Situ Stresses in Canadian Shield. ARMA/USRMS 06-1096.
45. Martin, C.D., P.K. Kaiser and R. Christiansson. 2003. Stress, instability and design of underground excavations. Int. J. Rock Mech. & Min. Sci. 40: 1027-1047.
46. Moore, S.M., Shackelford, C.D, 2011. Uranium diffusion in soils and rocks, Proceedings Tailings and Mine Waste 2011, Vancouver, BC, November 6-9, 2011, 13p.
47. Morgenstern, N.R and Nixon, J.F. 1971. One dimensional consolidation of thawing soils. Can. Geotech. J. 8, 558-565.
48. Mottaghy, D., Rath, V. 2006. Latent heat effects in subsurface heat transport modelling and their impact on palaeo-temperature reconstructions. International Journal of Geophysics 164, 236–245.
49. Muller, S.W. 1943. Permafrost or permanently frozen ground and related engineering problems. U.S. Army, Office Chief of Engineers, Military Intelligence Div. Strategic Eng. Study 62, 231 p.
50. Nelson, F.E. and Outcalt, S.I. 1983. A frost index number for spacial prediction of ground-frost zones. Proceedings of the 4th International Permafrost Conference, National Academy Press, Washington DC, 1, 907-911.
51. Nixon, J.F. 1990. Seasonal and climatic warming effects on pile creep in permafrost. In Permaftost - Canada, Proceedings of the Fifth Canadian Permafrost Conference, Quebec City, Quebec: Centre d'études nordiques, 335-40.
52. Nixon, J.F., and Holl, N. 1998. Geothermal modeling of soil or mine tailings with concurrent freezing and deposition. Can. Geotech. J. 35, pp 234-250.
53. Noetzli, J., Gruber, S. 2009. Transient thermal effects in Alpine permafrost. The Cryosphere 3, 85–99.
54. Ockendon, J., Howison, S., Lacey, A., and Movchan, A. 1999. Applied Partial Differential Equations. Oxford, New York, 1999.
55. Oke, T.R. 1978. Boundary Layer Climates. Routledge, New York.
56. Outcalt, S.I. and K.M. Hinkel (1996). The Response of Near-Surface Permafrost to Seasonal Regime Transitions in Tundra Terrain. Arctic and Alpine Research, 28, 3: 274-283.

57. Outcalt, S. I. 1972. The development and application of a simple digital surface climate simulator. Journal of applied meteorology, 11, 629-636.
58. Preuss, K., and T.N. Narasimhan. 1985. A Practical Method for Modeling Fluid and Heat Flow in Fractured Porous Media. Soc. of Pet. Engr. J., 25:14-26.
59. Riseborough, D., Shiklomanov, N, Etzelmuller, B., Gruber, S., and Marchenko, S. 2008. Recent Advances in Permafrost Modelling. Permafrost and Periglacial Processes, 19, 137-156.
60. Riseborough, D.W. (1990). Soil latent heat as a filter of the climate signal in permafrost, in Proceedings, 5th Canadian Permafrost Conference, Université Laval, Quebec City, Quebec, Nordicana 54: 199-205.
61. Romanovsky, V.E. and T.E. Osterkamp (1995). Interannual Variations of the Thermal Regime of the Active Layer and Near-Surface Permafrost in Northern Alaska. Permafrost and Periglacial Processes, 6: 313-335.
62. Rubin, A. M., Scheitzer (1972). Heat transfer in porous media with phase change. Int. J. Heat Transfer. Vol 15, pp 43-60.
63. Smith, M.W. and D.W. Riseborough (2002). Climate and the Limits of Permafrost: A Zonal Analysis. Permafrost and Periglacial Processes, 13, 1-15.
64. Smith, M.W. (1975). Microclimatic Influences on Ground Temperatures and Permafrost Distribution, Mackenzie Delta, Northwest Territories. Canadian Journal of Earth Sciences, 12: 1421-1438.
65. Smith, S.L., M.M. Burgess, D.W. Riseborough, and F.M. Nixon (2005). Recent Trends from Canadian Permafrost Thermal Monitoring Network Sites. Permafrost and Periglacial Processes, 16: 19-30.
66. Stuart, R.A., Etkin, D.A. and Judge, A.S. 1991. Recent observations of air temperature and snow depth in the Mackenzie Valley area and their implications on the stability of permafrost layers, Canadian Climate Centre Report 91-2, Downsview, Ontario: Environment Canada, Atmospheric Environment Service.
67. Taylor, A.E. (1995). Field measurements of n-factors for natural forest areas, Mackenzie Valley, Northwest Territories, in Current Research 1995-B, Geological Survey of Canada: 89-98.
68. Taylor, A.E., K. Wang, S.L. Smith, M.M. Burgess, and A.S. Judge (2006). Canadian Arctic Permafrost Observatories: Detecting contemporary climate change through inversion of subsurface temperature time series. Journal of Geophysical Research, 111.
69. Thomsom, W. 1871. On equilibrium of vapour at a curved surface of a liquid. Philo. Mag. 42, 448-452.
70. Throop, J. (2010). Spatial and Temporal Variability in Permafrost Conditions, Northern Canada. Ottawa: University of Ottawa, Department of Geography.
71. Van Genuchten, M.Th. 1980. A Closed-form Equation for Predicting the Hydraulic Conductivity of Unsaturated Soils. Soil Sci. Soc. Am. J., vol. 44.
72. Wan, R., Lui, Z, Muldrew, K., and Rewcastle, J. 2003. A Finite Element Model for Ice Ball Evolution in a Multi-probe Cryosurgery. Computer Methods in Biomechanics and Biomedical Engineering, 6(3), June 2003, 197–208.
73. Wan, R., Chan, D.H. and Morgenstern, N.R. 1990. A Finite Element Method for the Analysis of Shear Bands in Geomaterials, Finite Elements in Analysis and Design, 7(2), 129-143.

74. Wan, R 2012. Permafrost Degradation in Northern Climates: A Review of Observational, Theoretical, Numerical Modelling, Progress Report 1, Submitted to CNSC, University of Calgary.
75. Wan, R., Booshehrian, A. 2012. Summary of scenarios for numerical analysis of open pit mines in Kiggavik and Sissons projects, Submitted to CNSC, University of Calgary.
76. Williams, P.J. and M.W. Smith (1989). The Frozen Earth: Fundamentals of Geocryology. New York: Cambridge University Press.

Appendix A

In this appendix, the results of permafrost degradation analysis are presented which are not shown in chapter 1.

East Zone, Warm Tailing with $+5^{\circ}C$

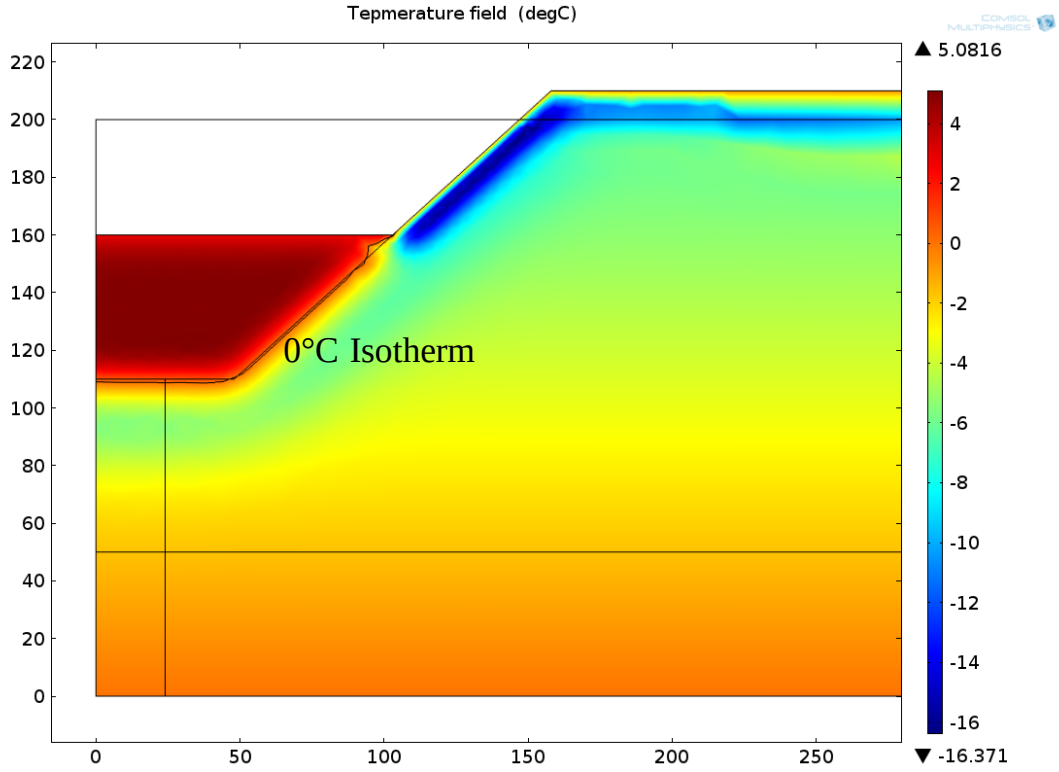

Figure A-1 East Zone, Thermal Condition, 6 months after putting first layer of tailings

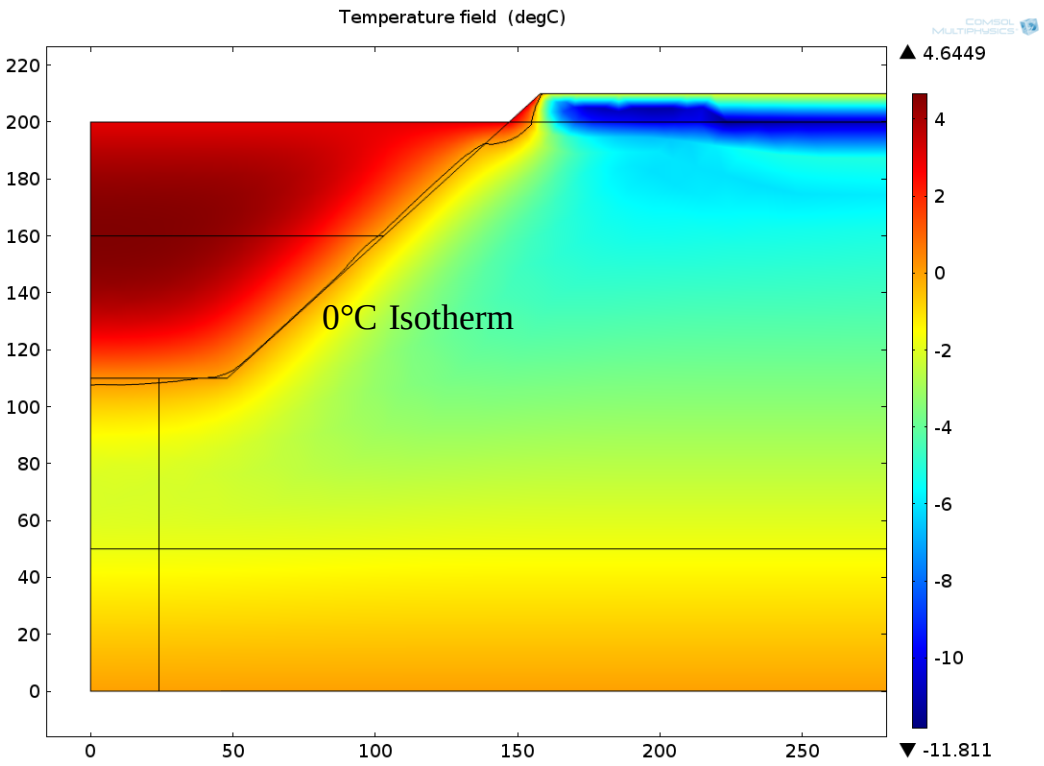

Figure A-2 East Zone, Thermal Condition, end of operational time, with water cover on top of tailings

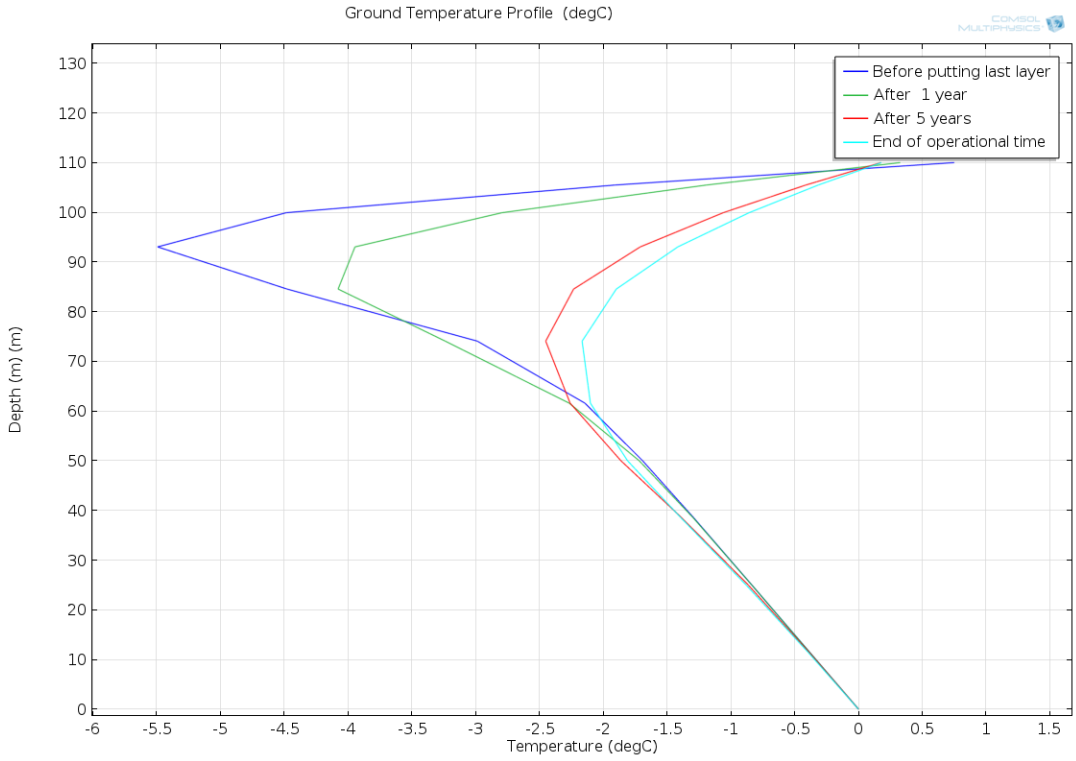

Figure A-3 East Zone, Thermal Profile beneath tailing pond with tailing at $+5^{\circ}C$,different times after putting second layer of tailings with water cover

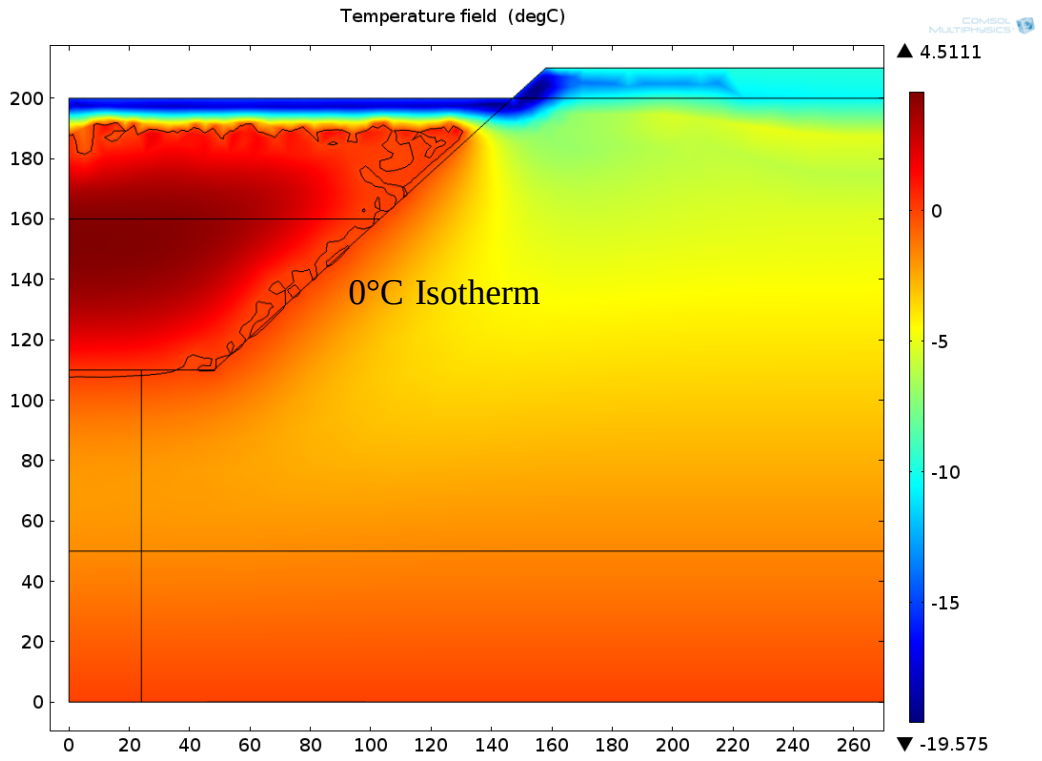

Figure A-4 East Zone, Thermal Condition, end of operational time, tailings exposed to air temperature

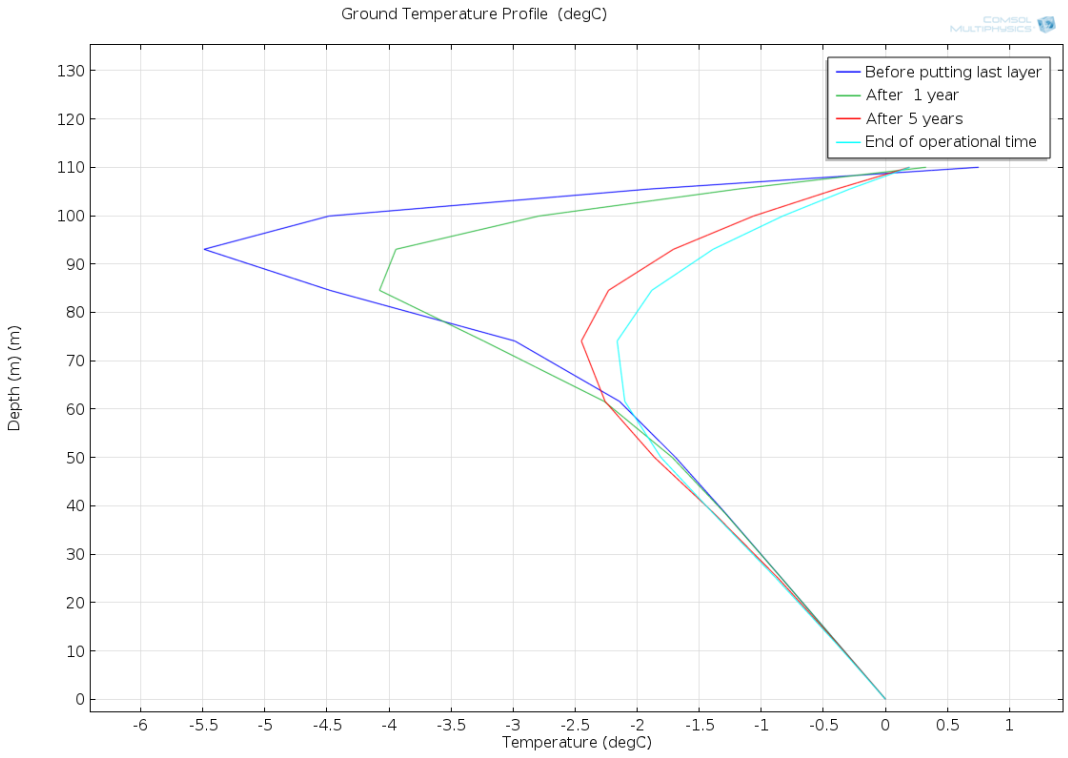

Figure A-5 East Zone, Thermal Profile beneath tailing pond with tailing at $+5^{\circ}C$,different times after putting second layer of tailings, tailings exposed to air temperature

Centre Zone, Warm Tailing with $+5^{\circ}C$

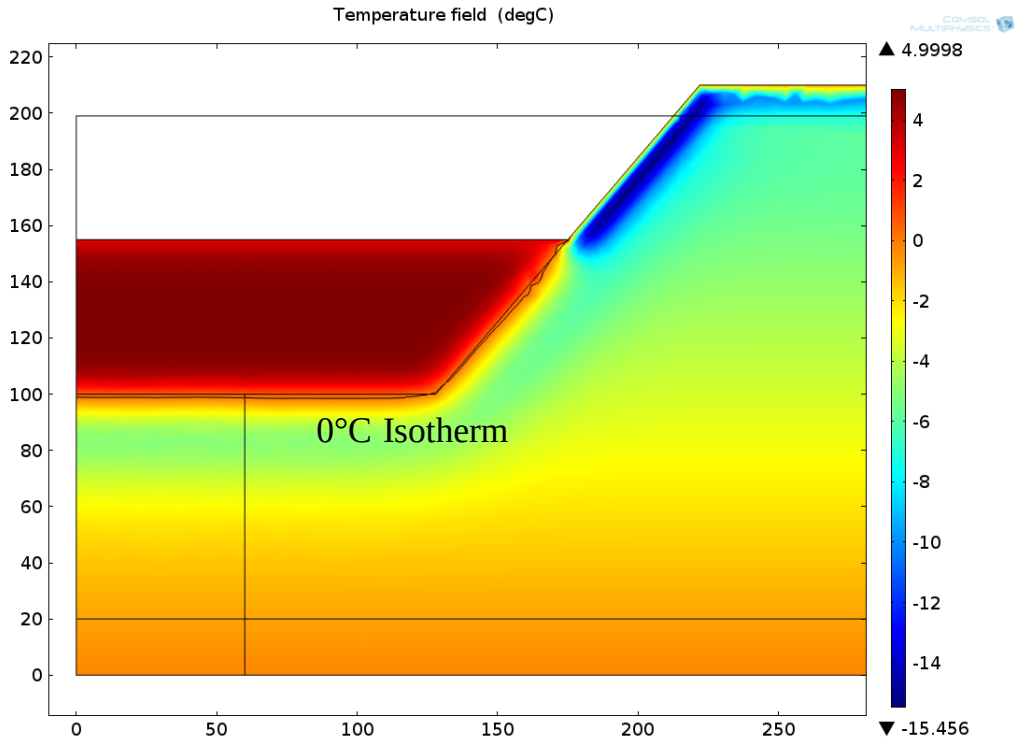

Figure A-6 Centre Zone, Thermal Condition, 6 months after putting first layer of tailings

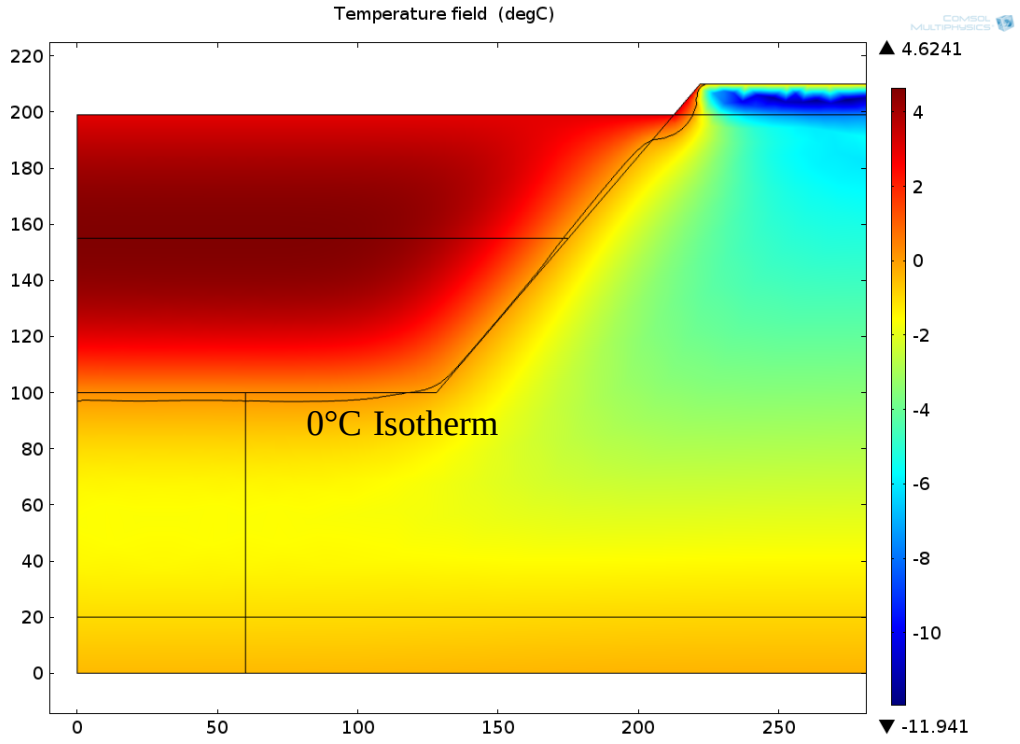

Figure A-7 Centre Zone, Thermal Condition, end of operational time, with water cover on top of tailings

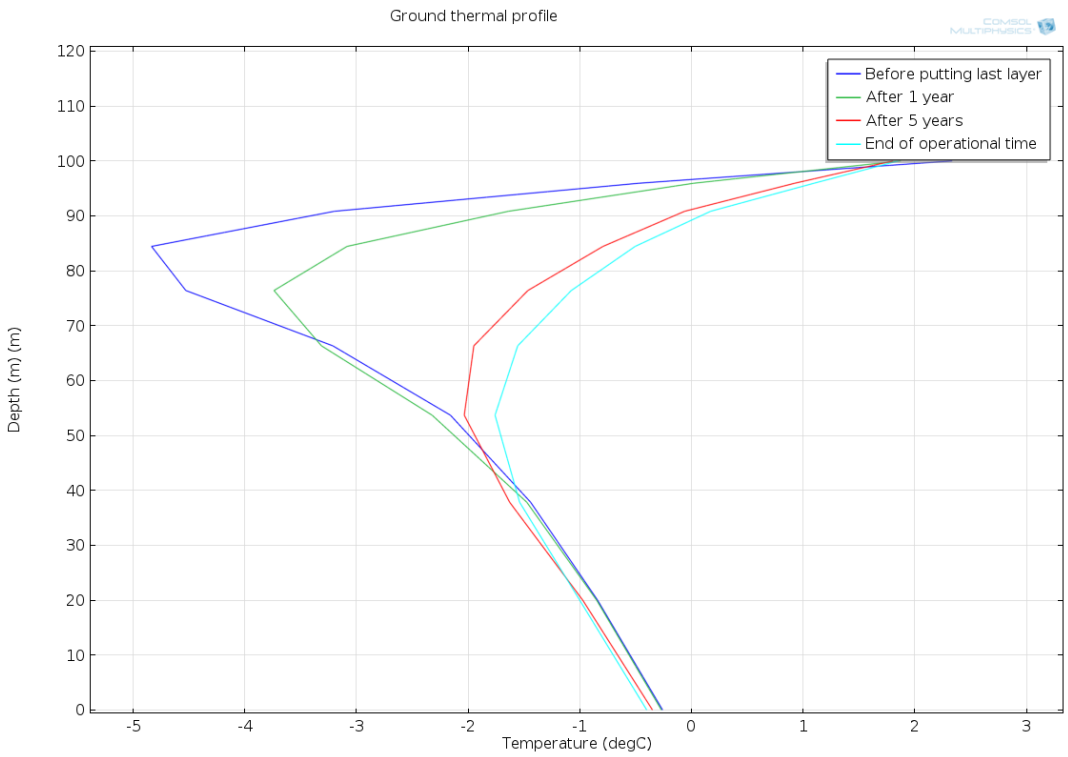

Figure A-8 Centre Zone, Thermal Profile beneath tailing pond with tailing at $+5^{\circ}C$,different times after putting second layer of tailings with water cover

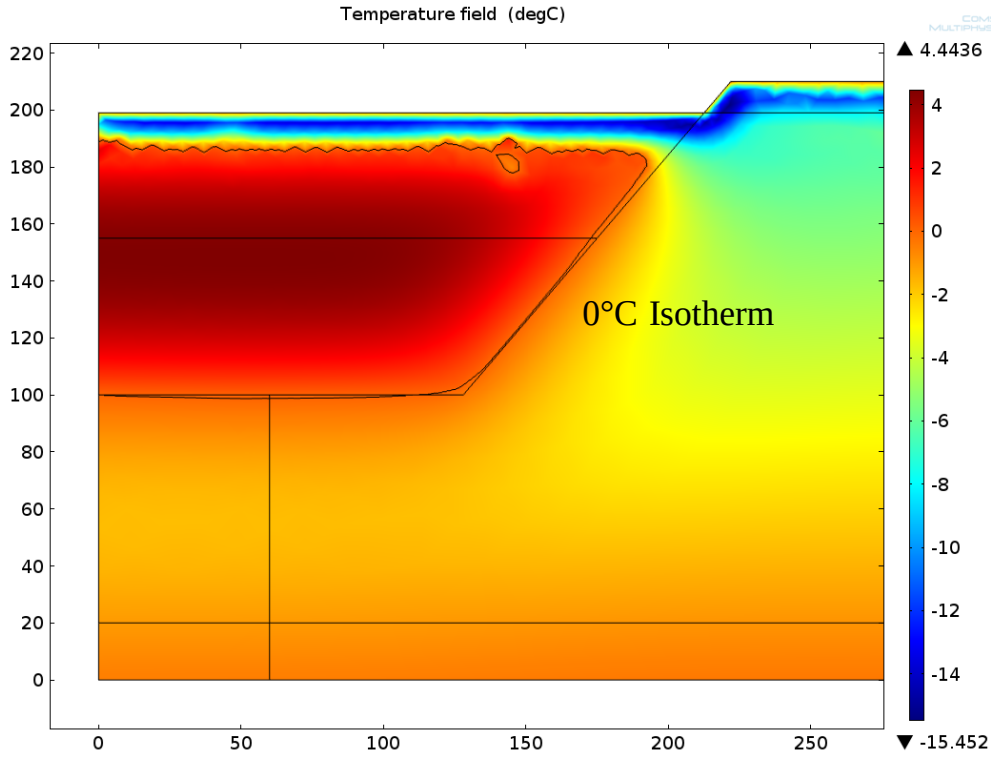

Figure A-9 Centre Zone, Thermal Condition, end of operational time, tailings exposed to air temperature

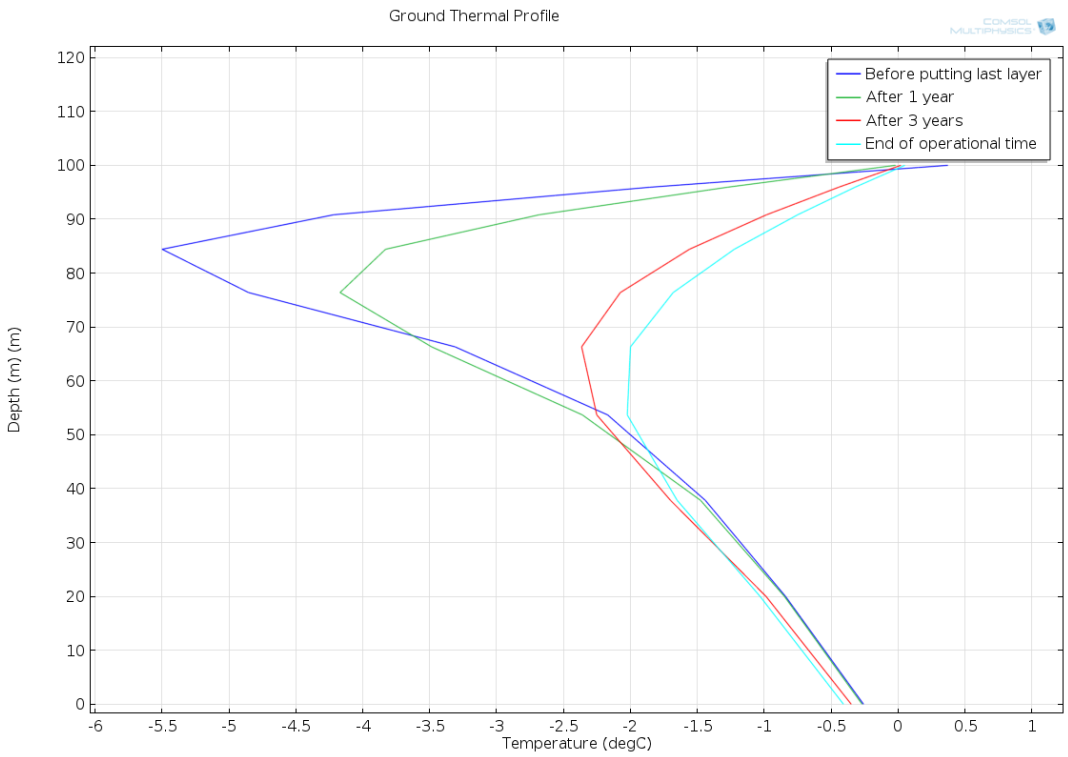

Figure A-10 Centre Zone, Thermal Profile beneath tailing pond with tailing at $+5^{\circ}C$,different times after putting second layer of tailings, tailings exposed to air temperature

Main Zone, Warm Tailing with $+10^{\circ} C$

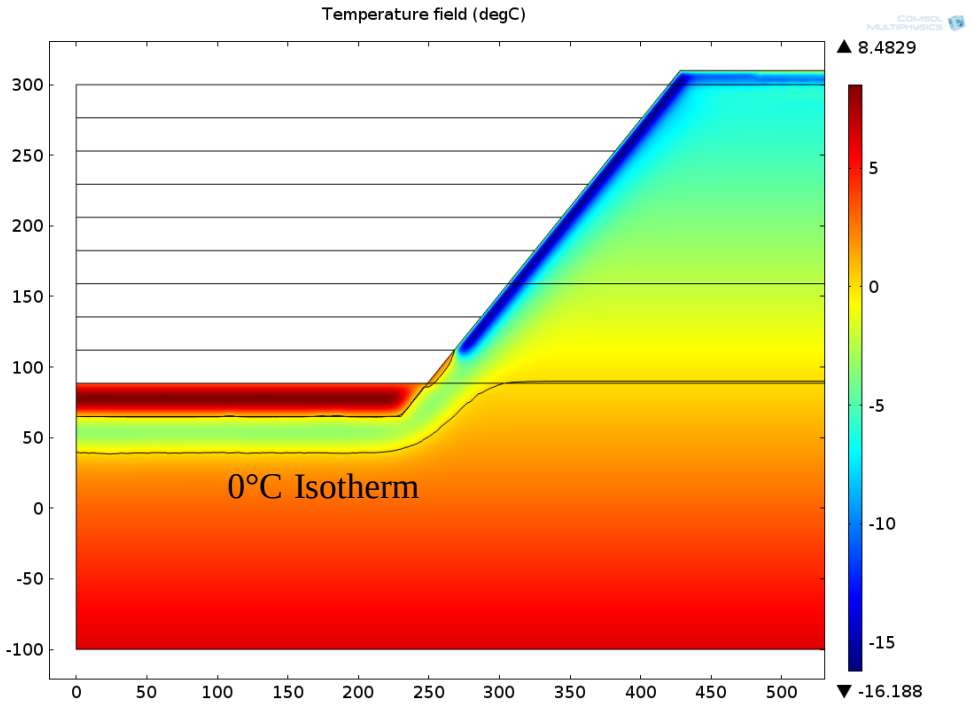

Figure A-11 Main Zone, thermal condition 1 year after putting first layer of tailing, water cover on top of tailings

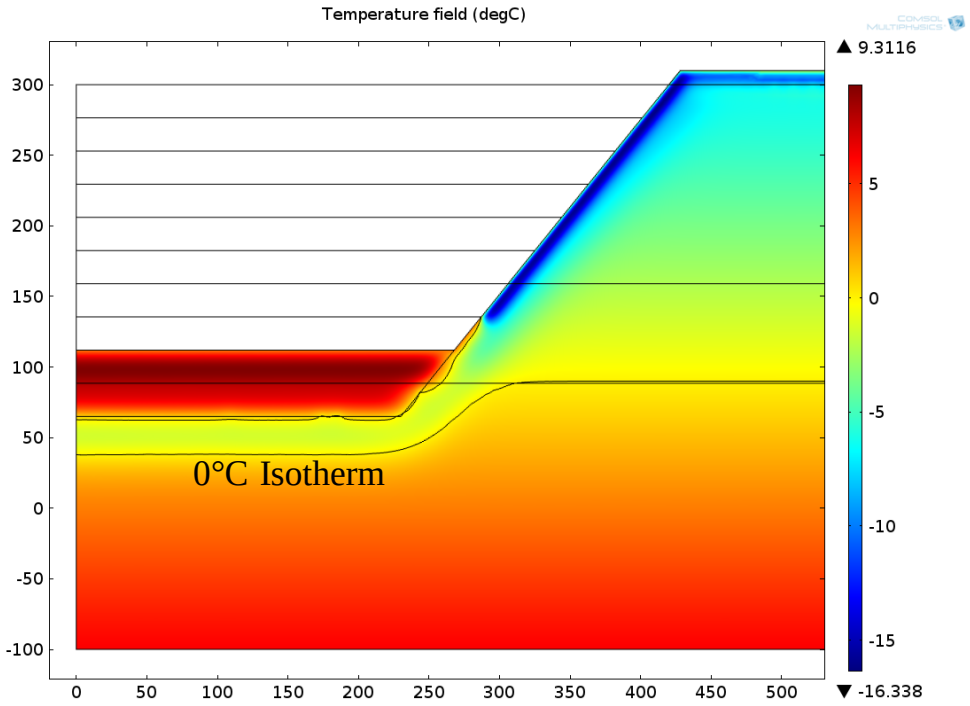

Figure A-12 Main Zone, thermal condition 1 year after putting second layer of tailing, water cover on top of tailings

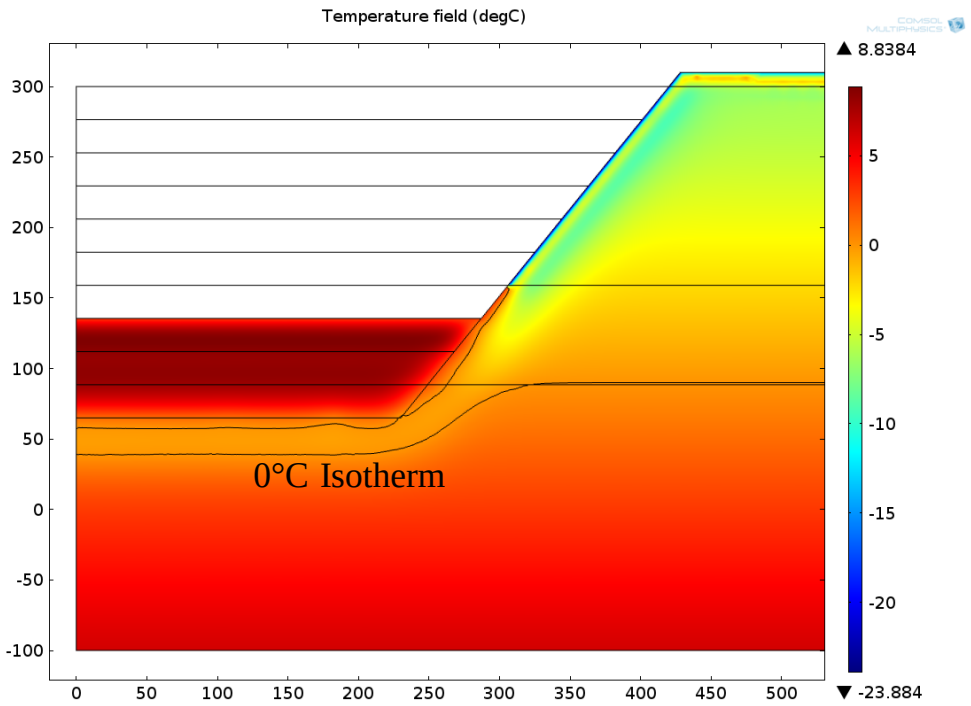

Figure A-13 Main Zone, thermal condition 1.5 year after putting third layer of tailing, water cover on top of tailings

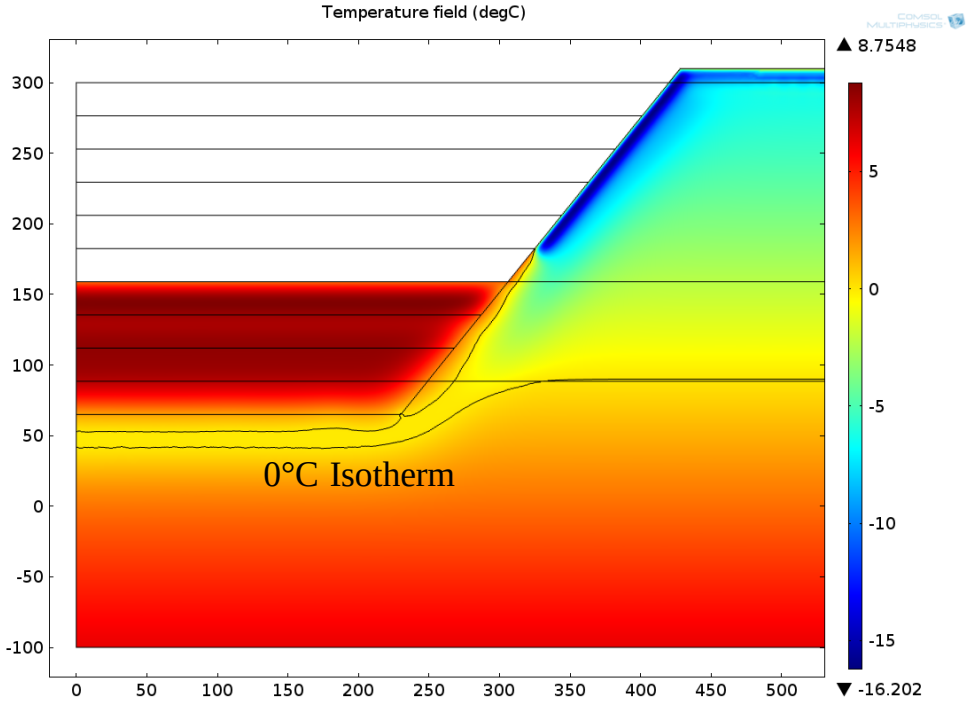

Figure A-14 Main Zone, thermal condition 1.5 year after putting fourth layer of tailing, water cover on top of tailings

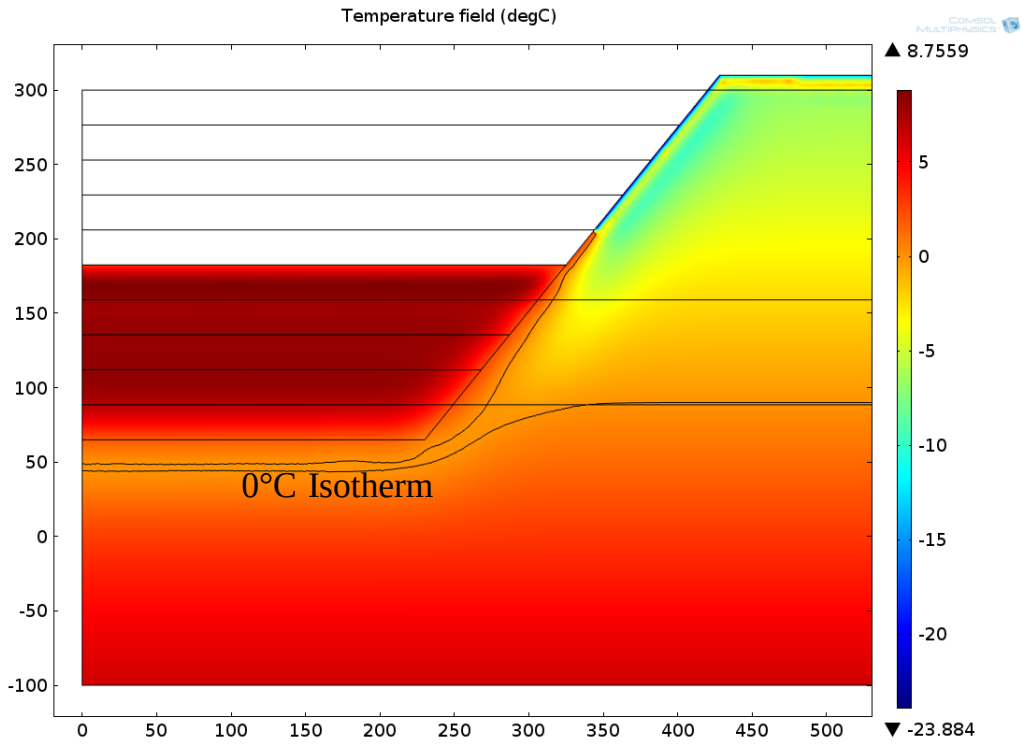

Figure A-15 Main Zone, thermal condition 1.5 year after putting fifth layer of tailing, water cover on top of tailings

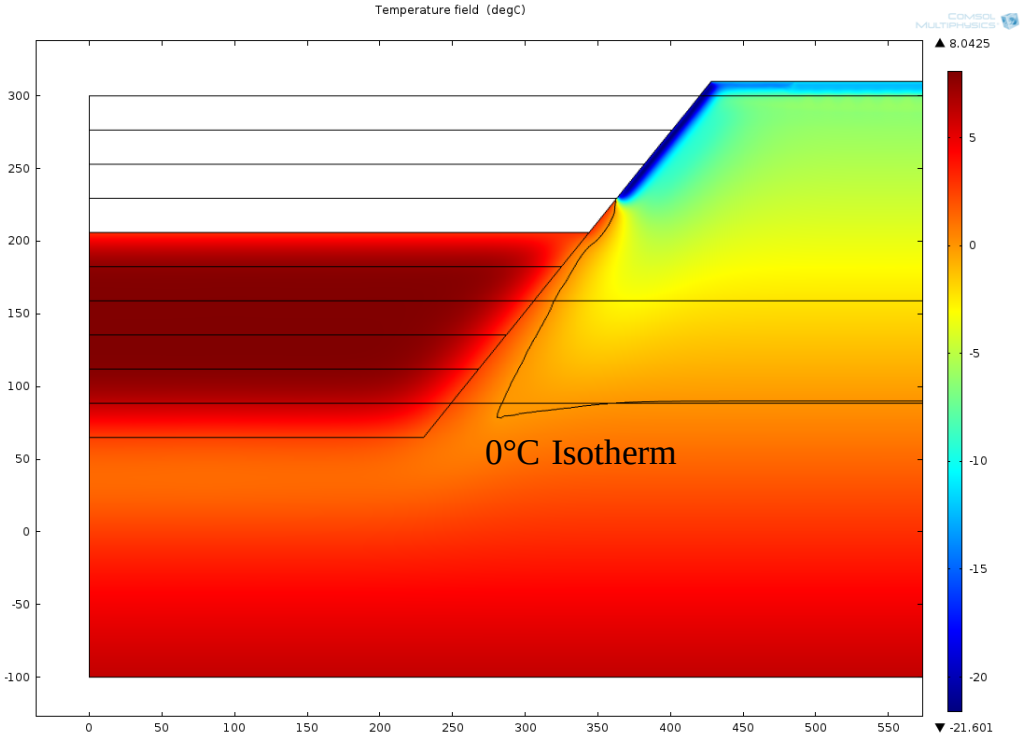

Figure A-16 Main Zone, thermal condition, end of operational time, water cover on top of tailings

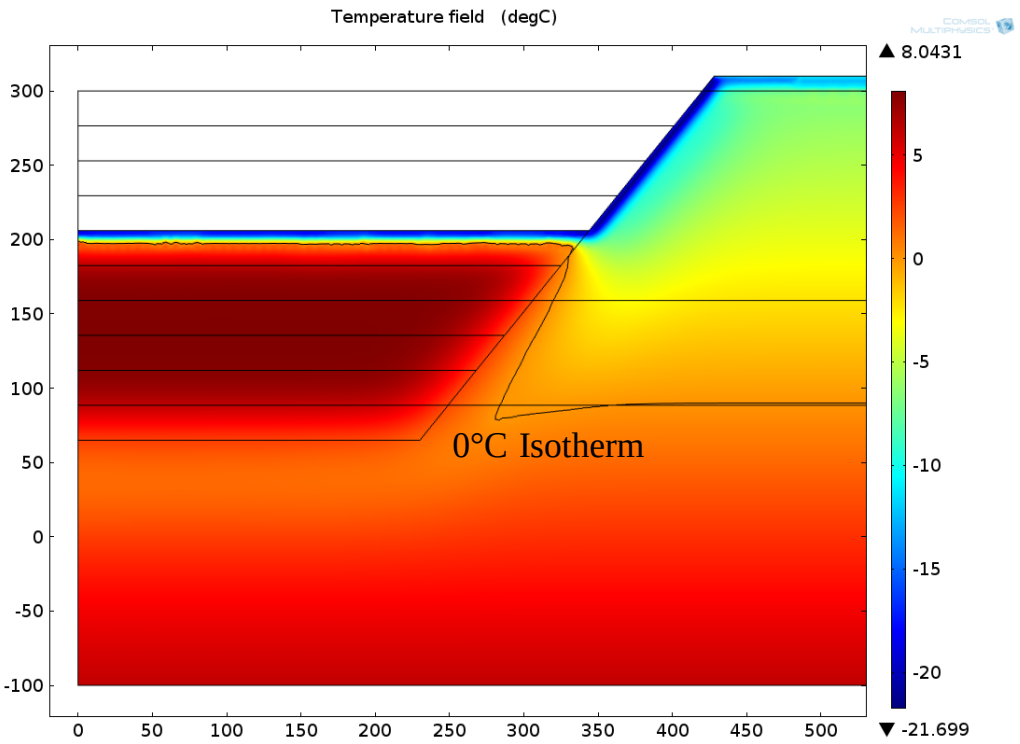

Figure A-17 Main Zone, Thermal Condition, end of operational time, tailings exposed to air temperature

Main Zone, Warm Tailing with $+5^{\circ} C$

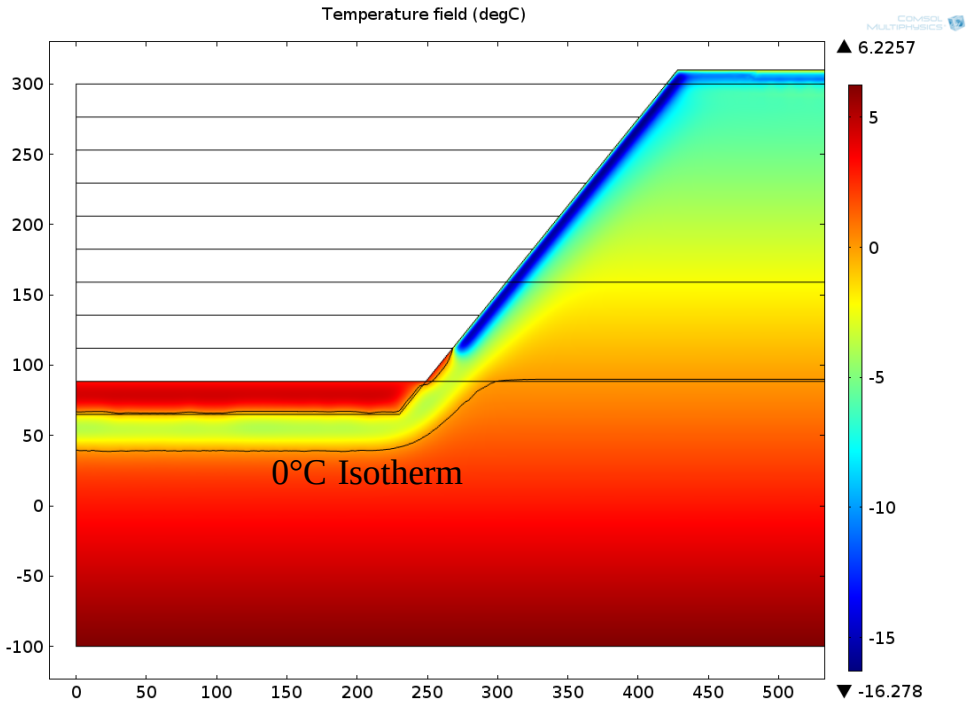

Figure A-18 Main Zone, thermal condition 1 year after putting first layer of tailing, water cover on top of tailings

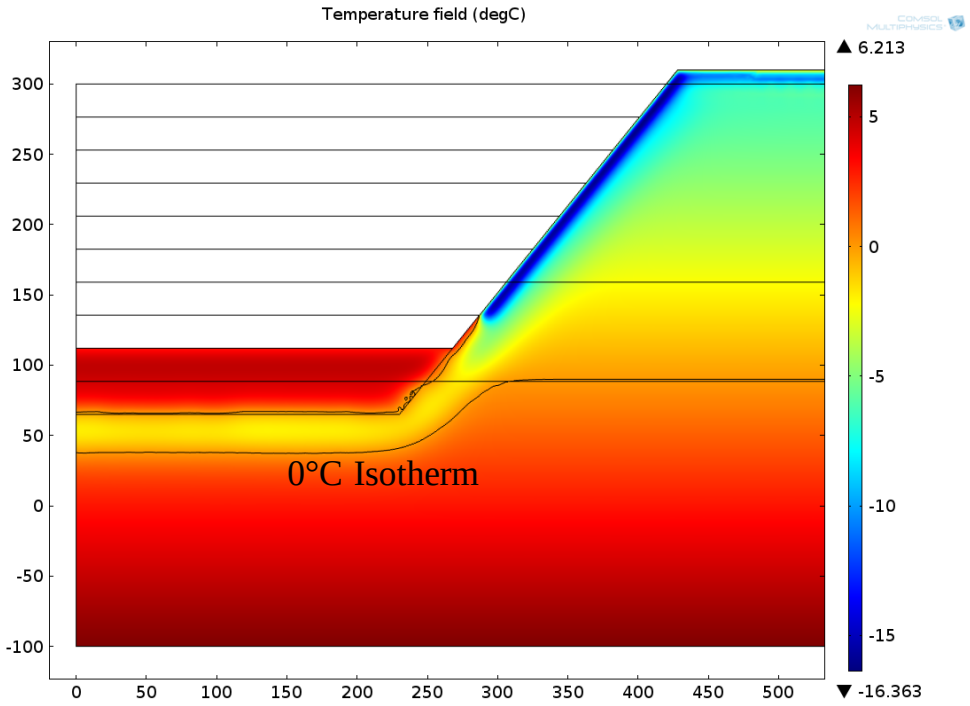

Figure A-19 Main Zone, thermal condition 1 year after putting second layer of tailing, water cover on top of tailings

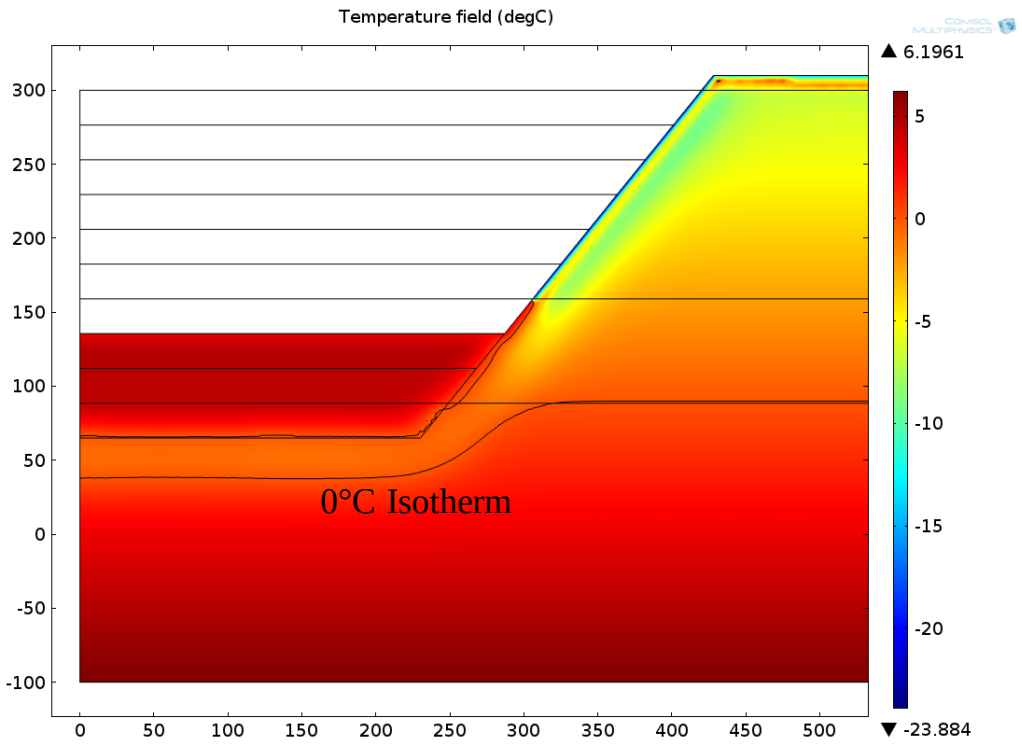

Figure A-20 Main Zone, thermal condition 1.5 year after putting third layer of tailing, water cover on top of tailings

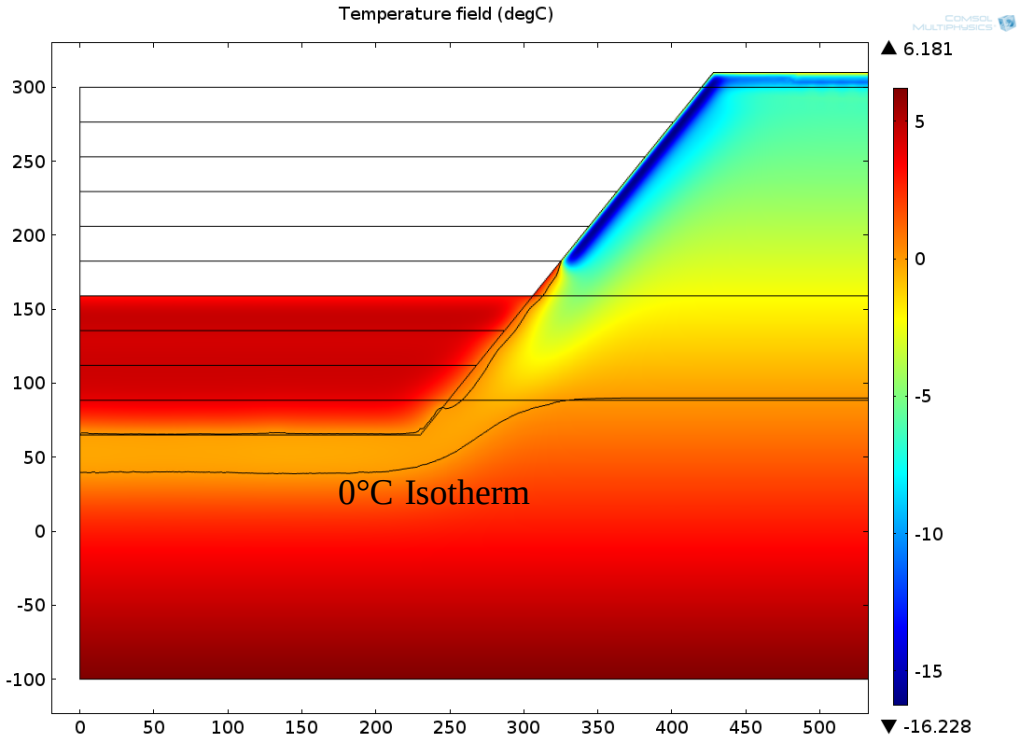

Figure A-21 Main Zone, thermal condition 1.5 year after putting fourth layer of tailing, water cover on top of tailings

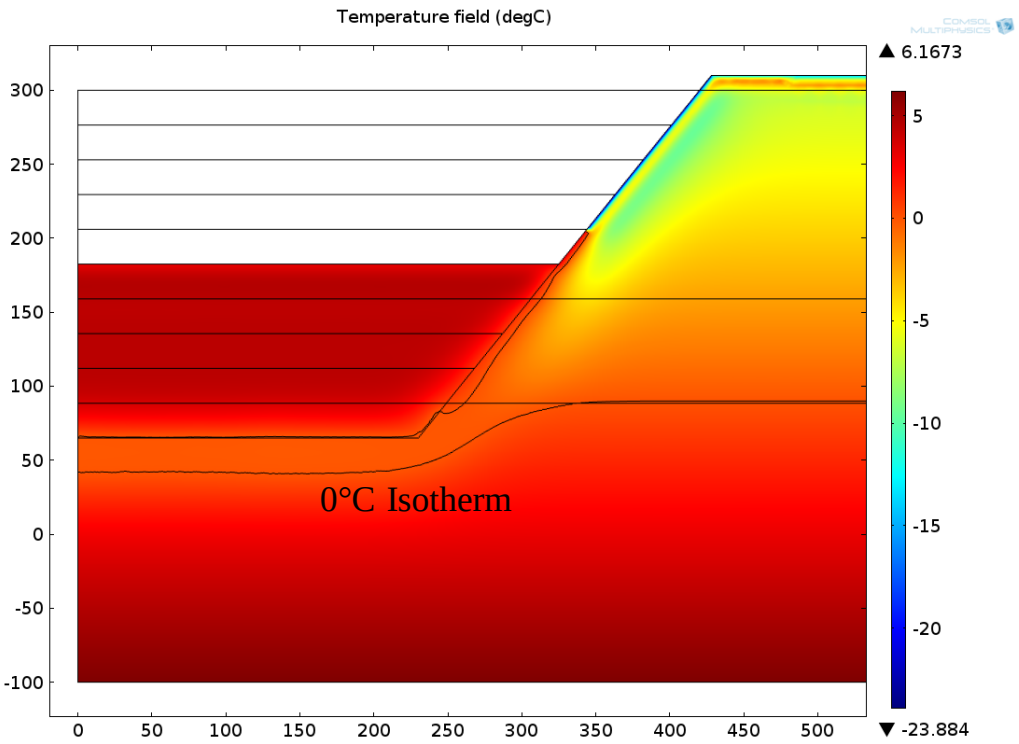

Figure A-22 Main Zone, thermal condition 1.5 year after putting fifth layer of tailing, water cover on top of tailings

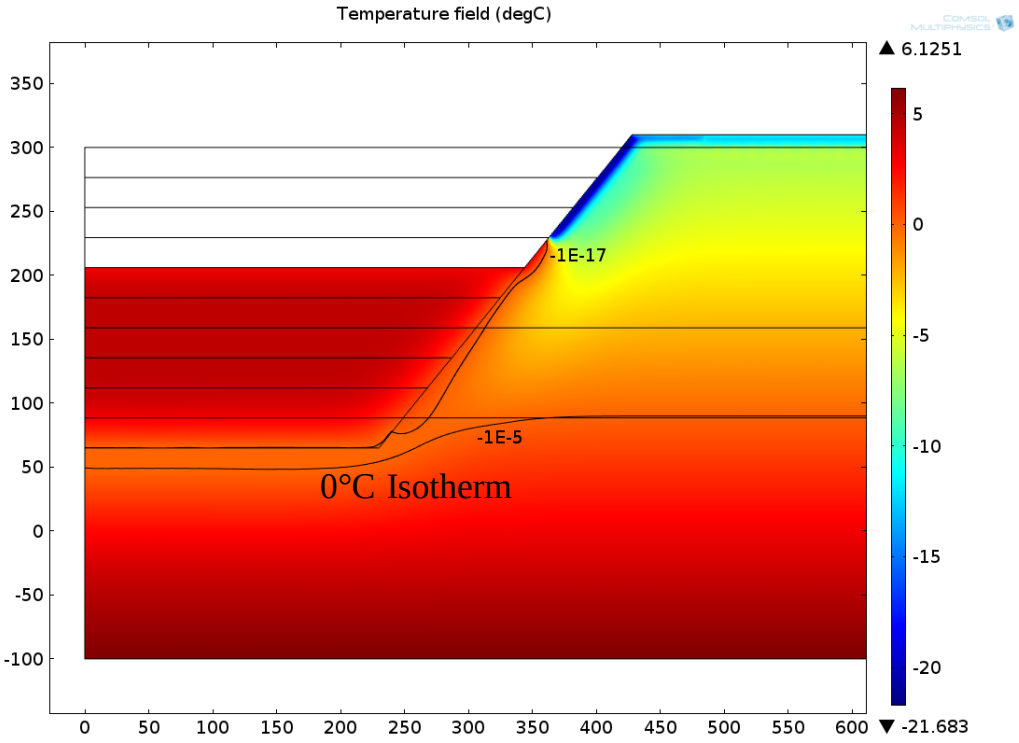

Figure A-23 Main Zone, thermal condition, end of operational time, water cover on top of tailings

Scenario II (Tailing exposed to air temperature after depositing the last layer)

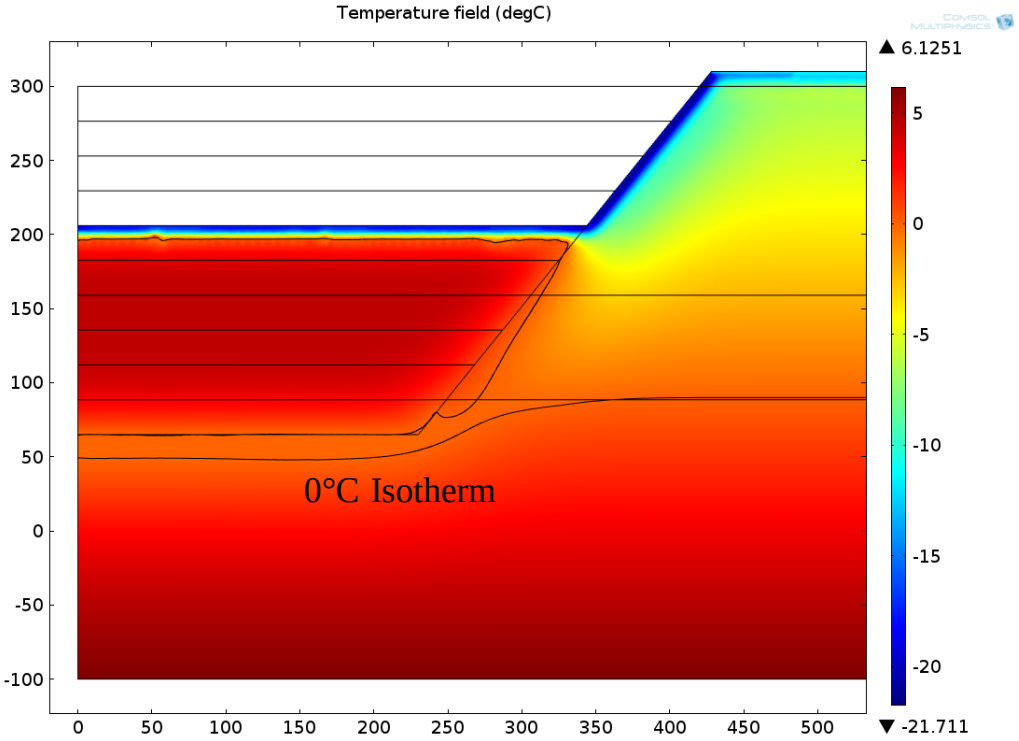

Figure A-24 Main Zone, Thermal Condition, end of operational time, tailings exposed to air temperature

Appendix B

In chapter 2, floor heave as a result of ground excavation was analyzed. In that section, results of numerical studies for both Kiggavik Main Zone and Andrew Lake open pits presented just for the last stage of excavation. Here, in this appendix, the results of other stages are shown as a record.

Kiggavik Main zone

First Layer of Excavation

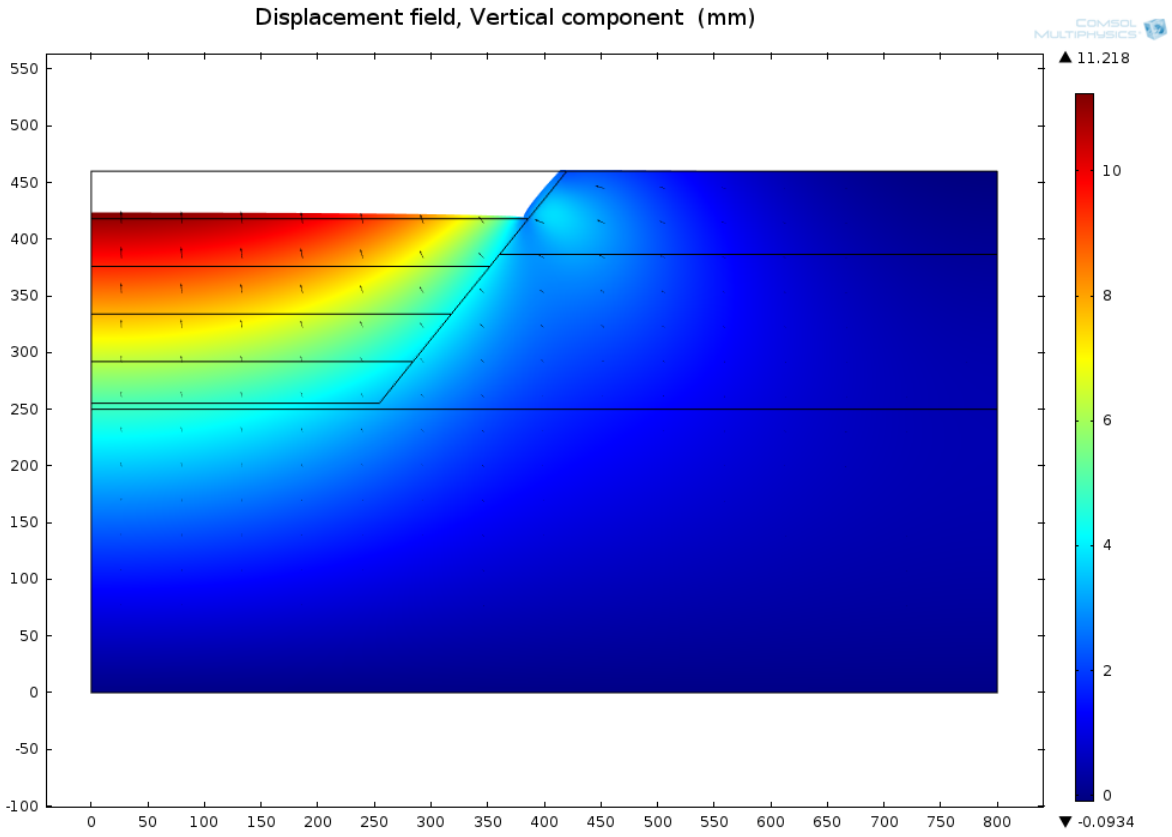

Figure B-1 Vertical displacement field (mm), excavation up to depth of about 42m

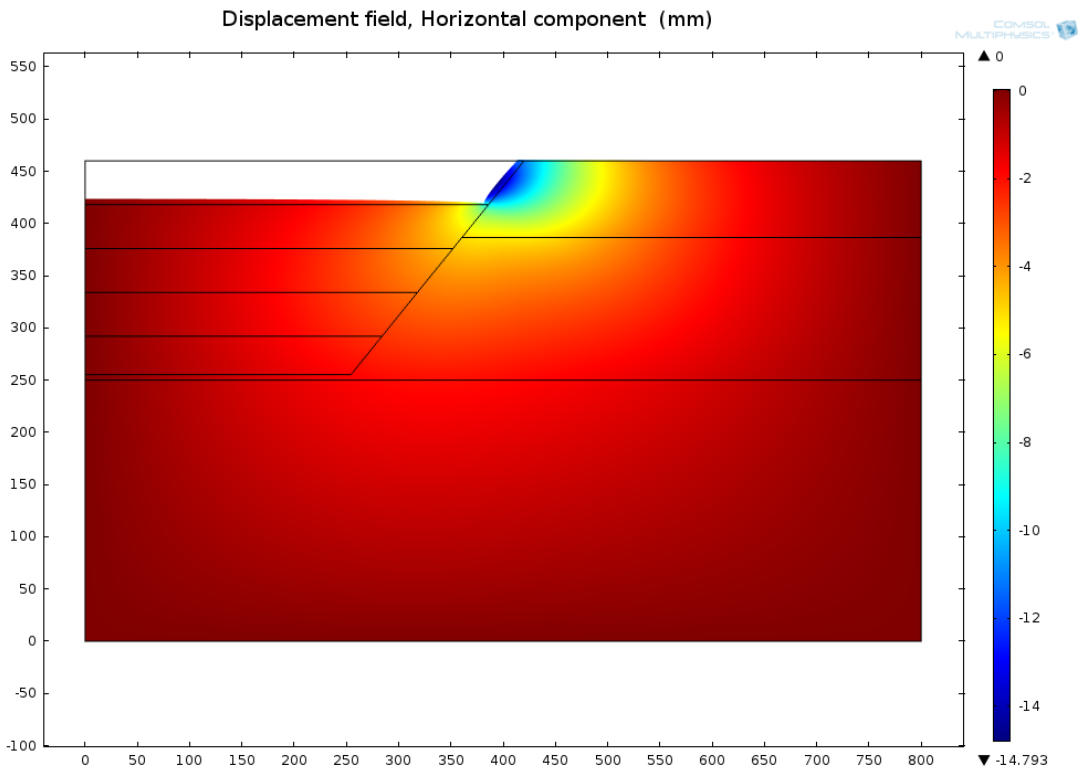

Figure B-2 Horizontal displacement field (mm), excavation up to depth of about 42m

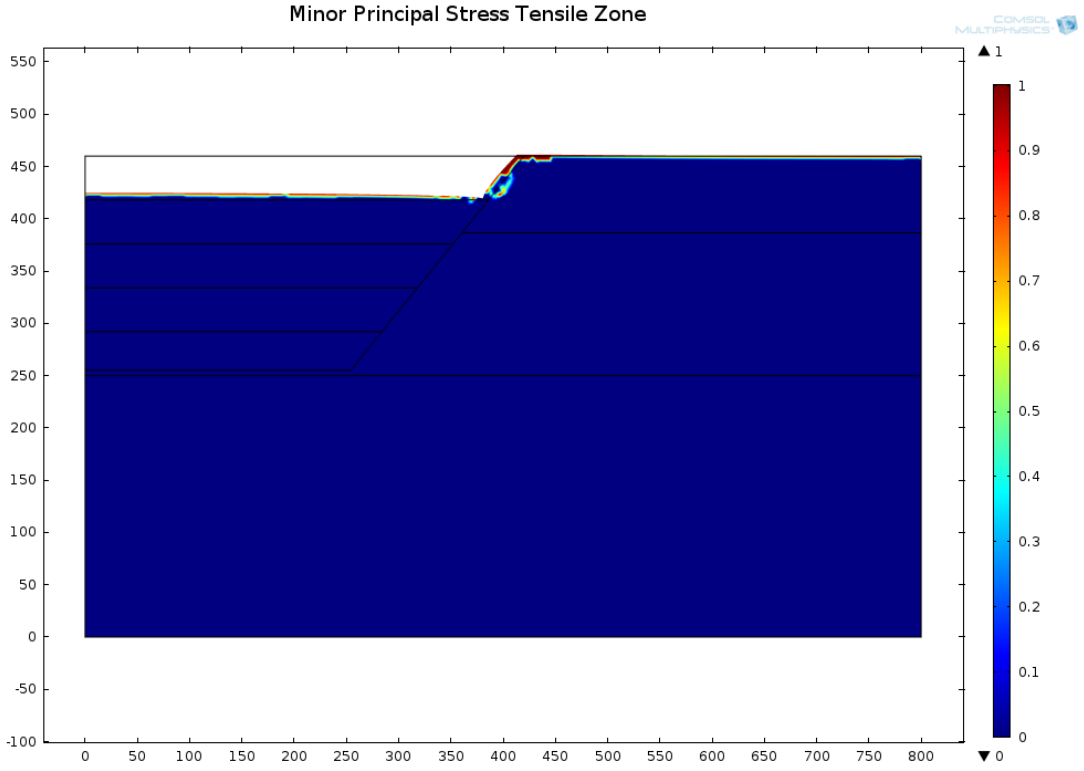

Figure B-3 Minor principal stress tensile zone ($\sigma_3' > 0$), Excavation up to depth of about 42m

Second Layer of Excavation

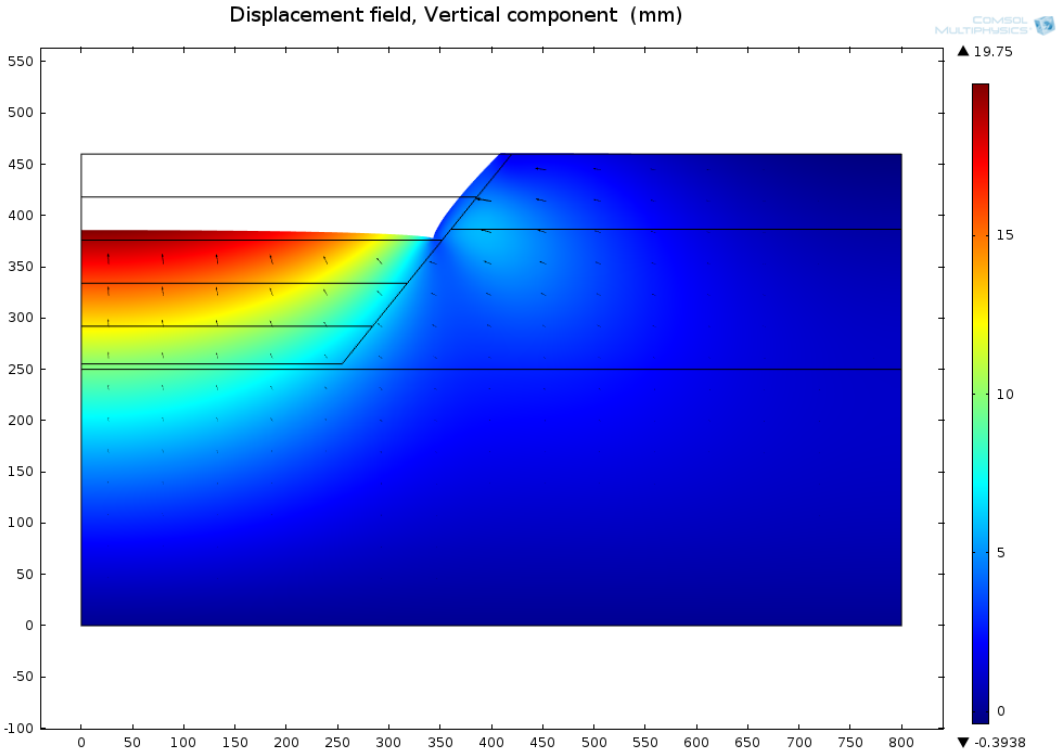

Figure B-4 Vertical displacement field (mm), excavation up to depth of about 85m

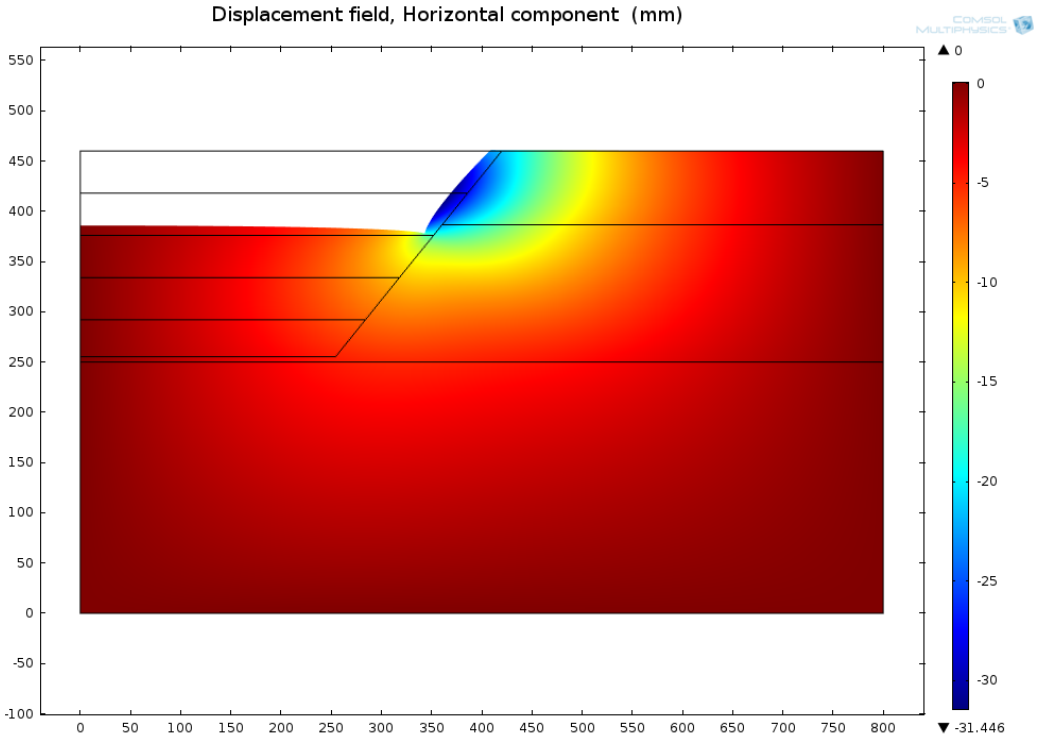

Figure B-5 Horizontal displacement field (mm), excavation up to depth of about 85m

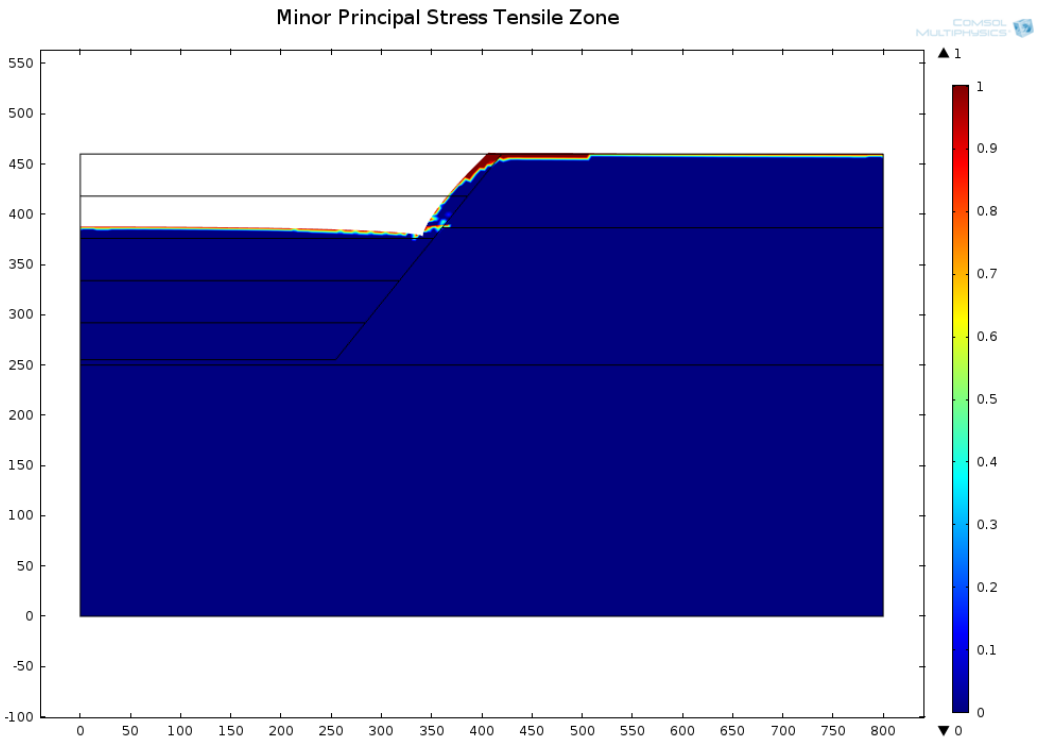

Figure B-6 Minor principal stress tensile zone ($\sigma_3' > 0$), Excavation up to depth of about 85m

Third Layer of Excavation

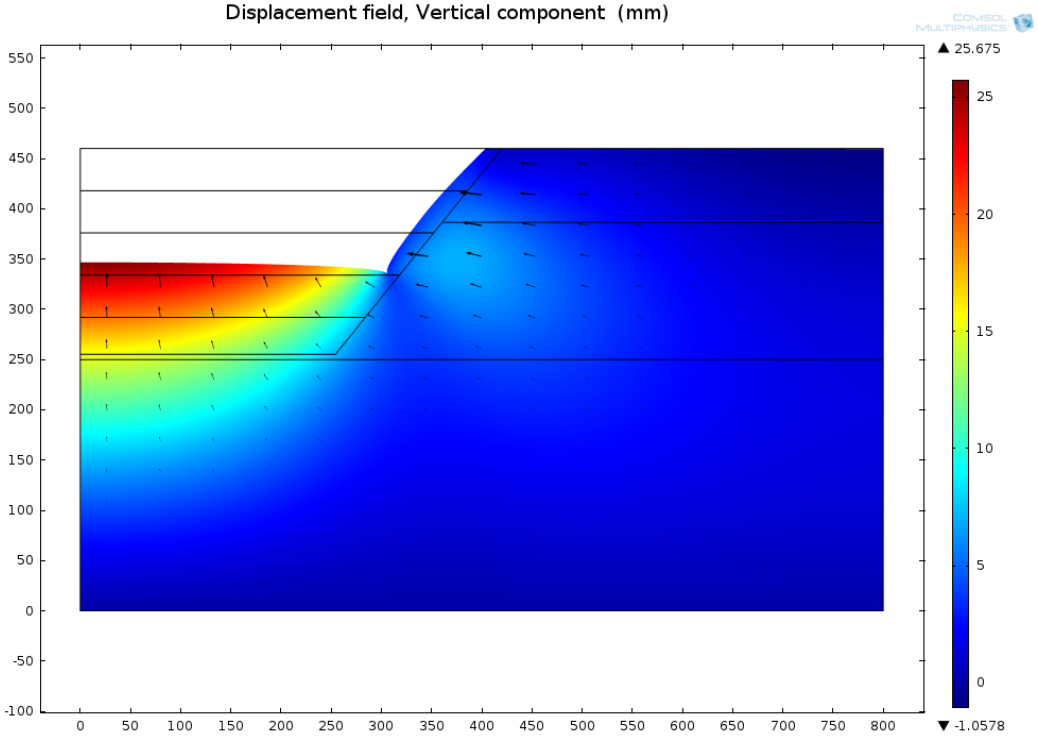

Figure B-7 Vertical displacement field (mm), excavation up to depth of about 125m

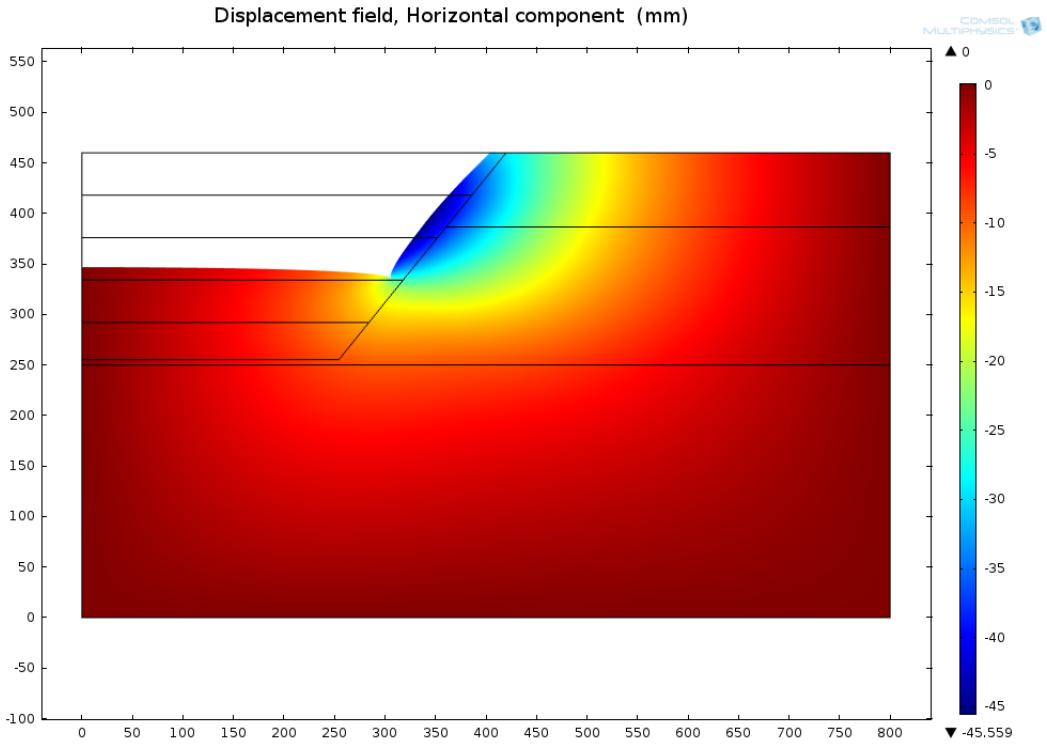

Figure B-8 Horizontal displacement field (mm), excavation up to depth of about 125m

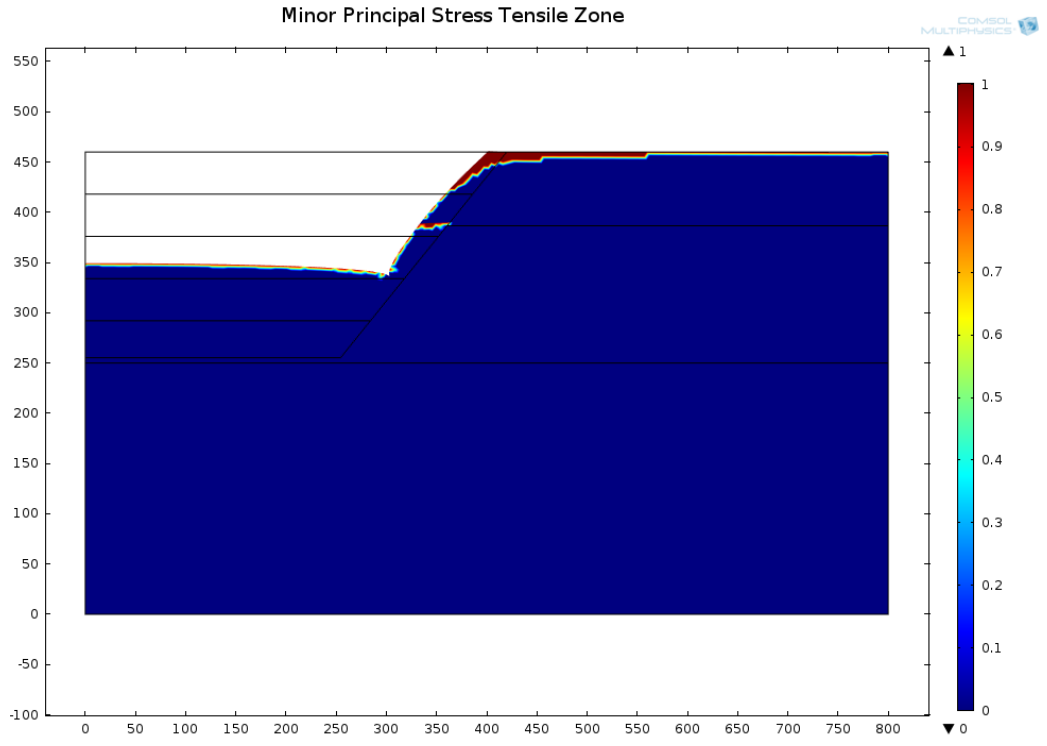

Figure B-9 Minor principal stress tensile zone ($\sigma_3' > 0$), Excavation up to depth of about 125m

Fourth Layer of Excavation

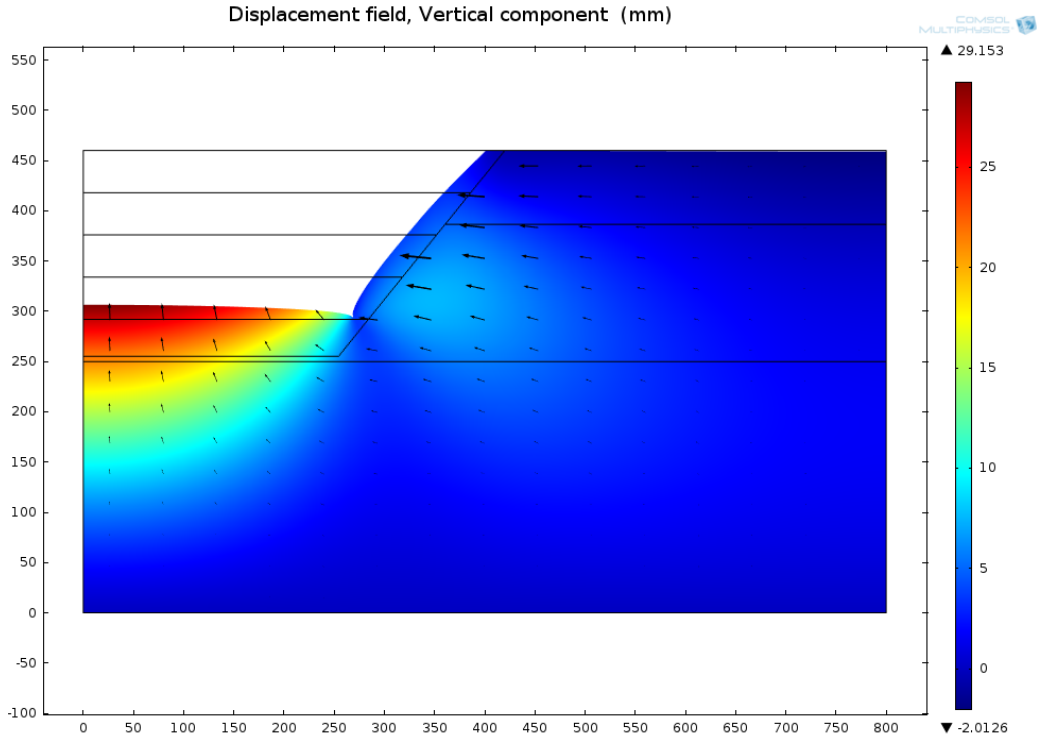

Figure B-10 Vertical displacement field (mm), excavation up to depth of about 170m

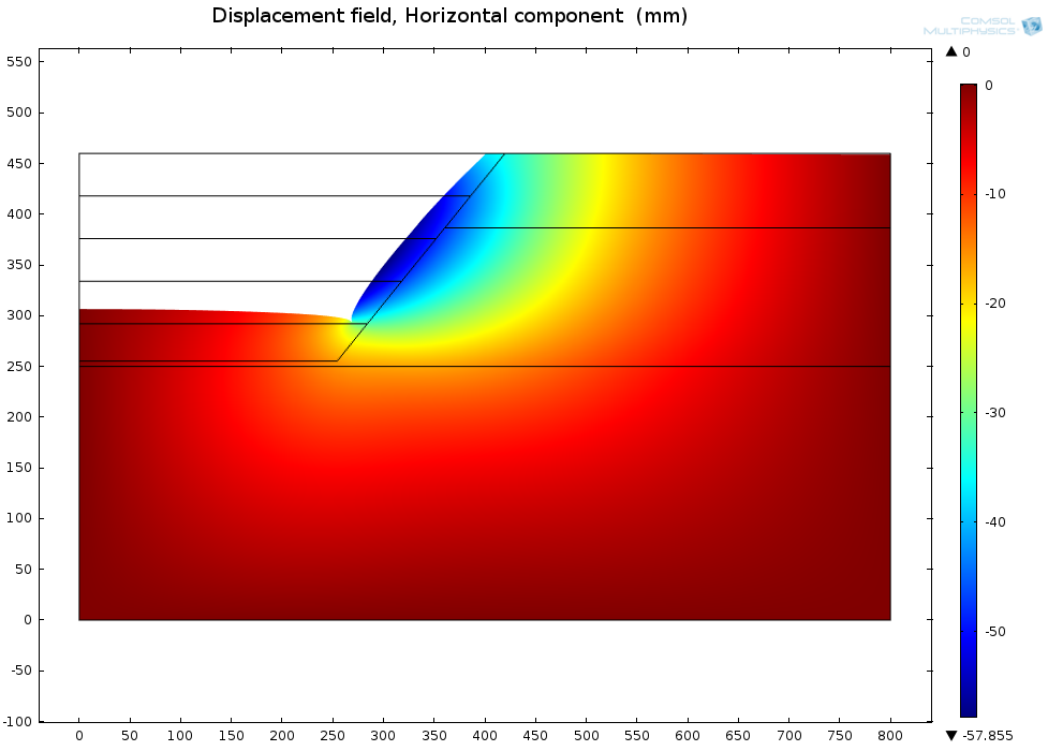

Figure B-11 Horizontal displacement field (mm), excavation up to depth of about 170m

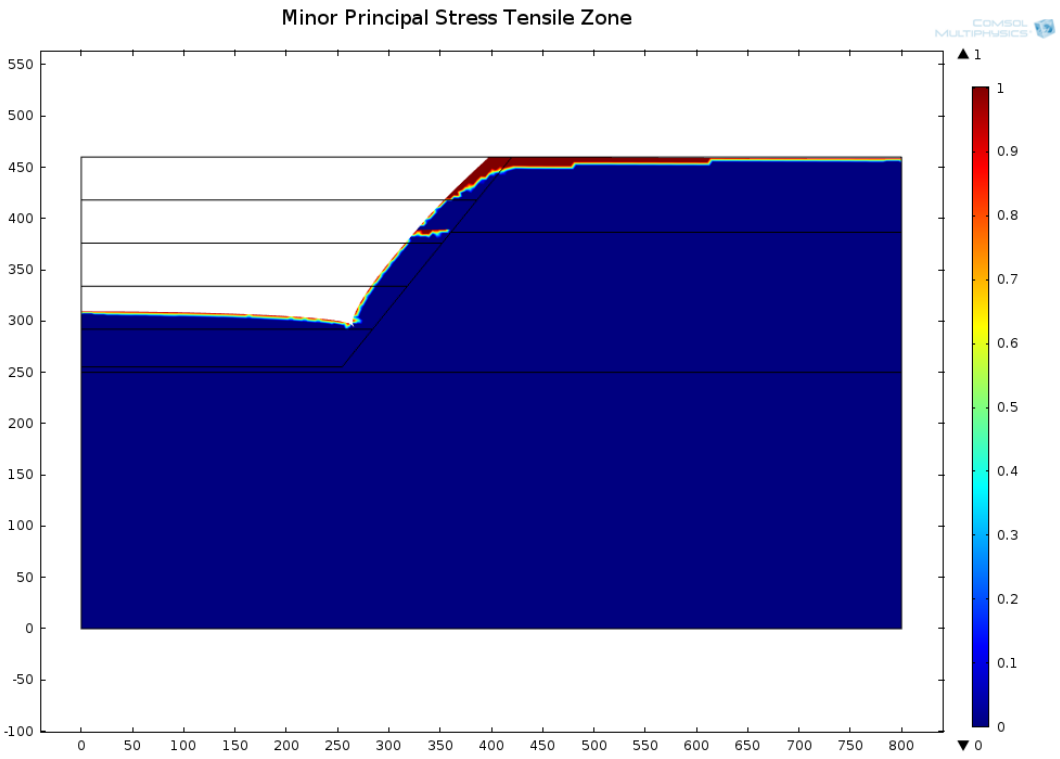

Figure B-12 Minor principal stress tensile zone ($\sigma_3' > 0$), Excavation up to depth of about 170m

Andrew Lake

First Layer of Excavation

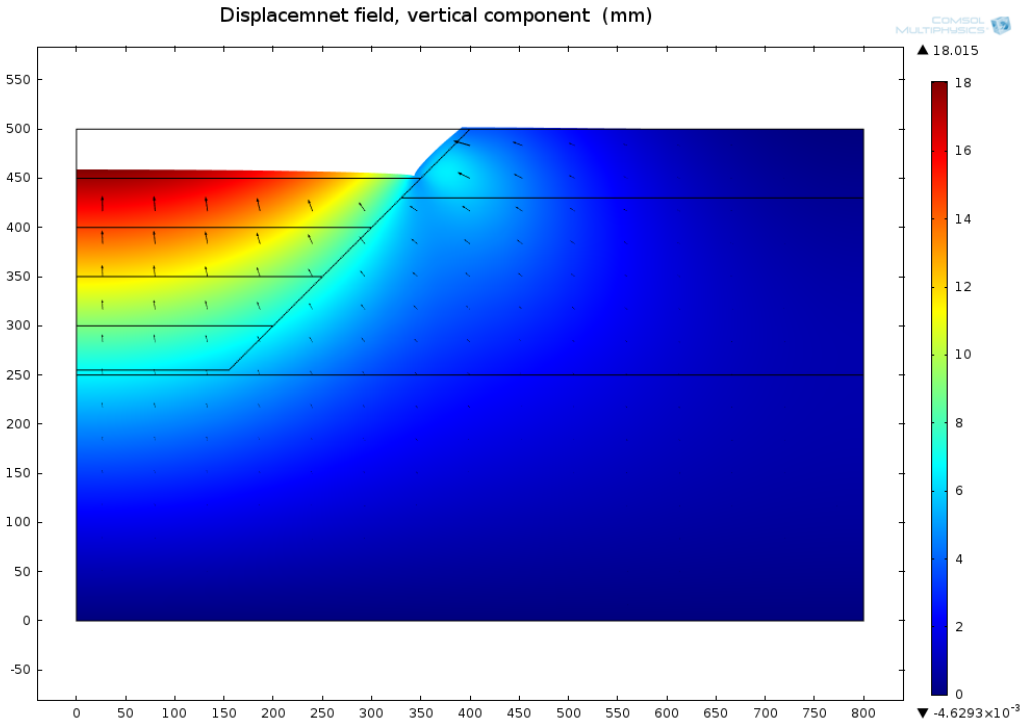

Figure B-13 Vertical displacement field (mm), excavation up to depth of about 50m

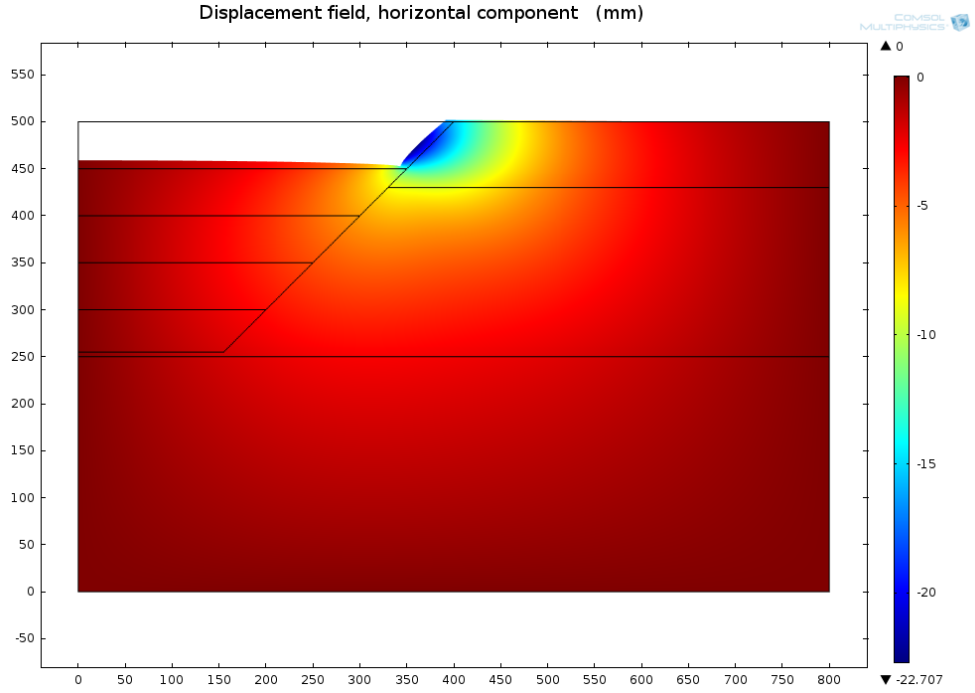

Figure B-14 Horizontal displacement field (mm), excavation up to depth of about 50m

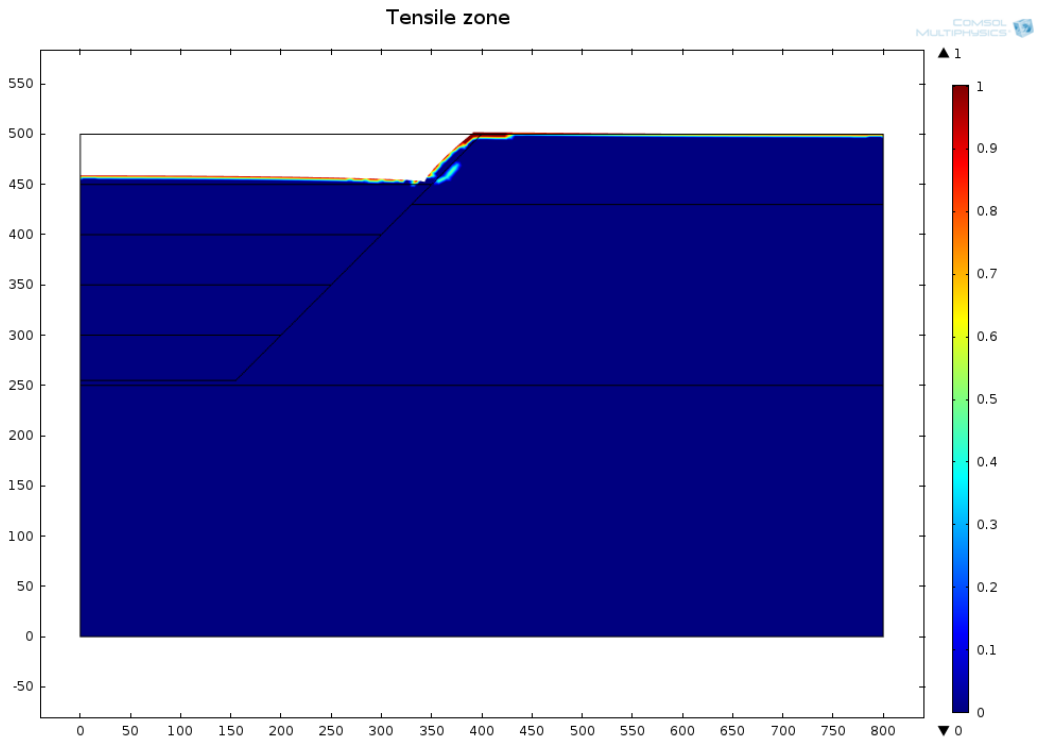

Figure B-15 Minor principal stress tensile zone ($\sigma_3' > 0$), Excavation up to depth of about 50m

Second Layer of Excavation

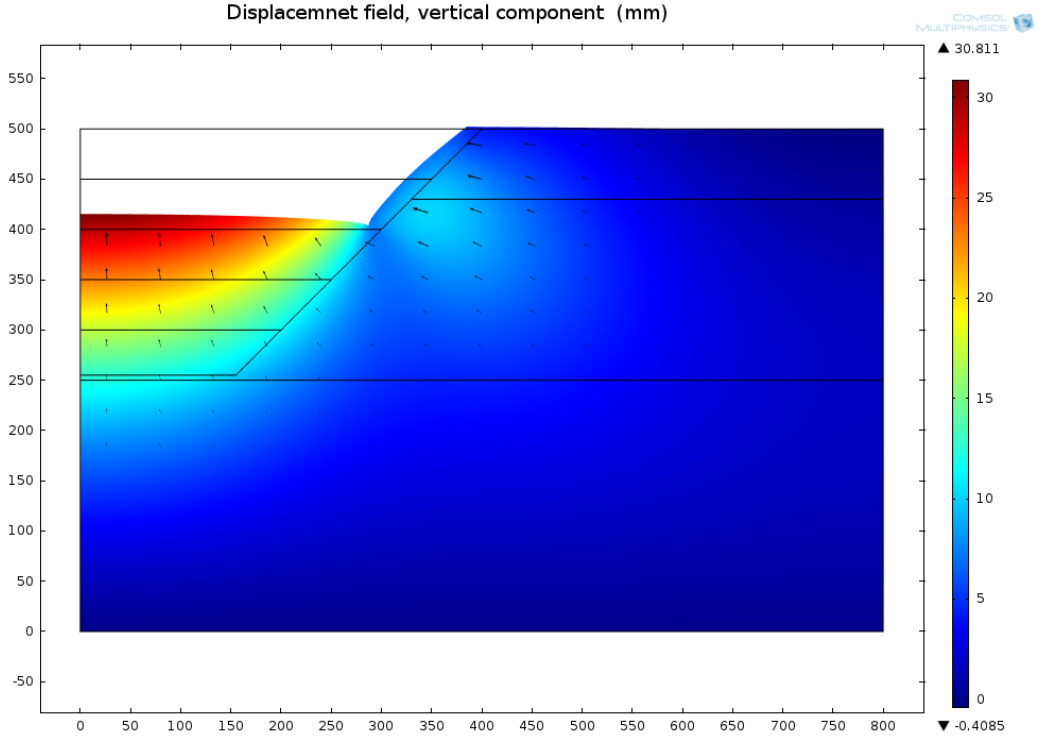

Figure B-16 Vertical displacement field (mm), excavation up to depth of about 100m

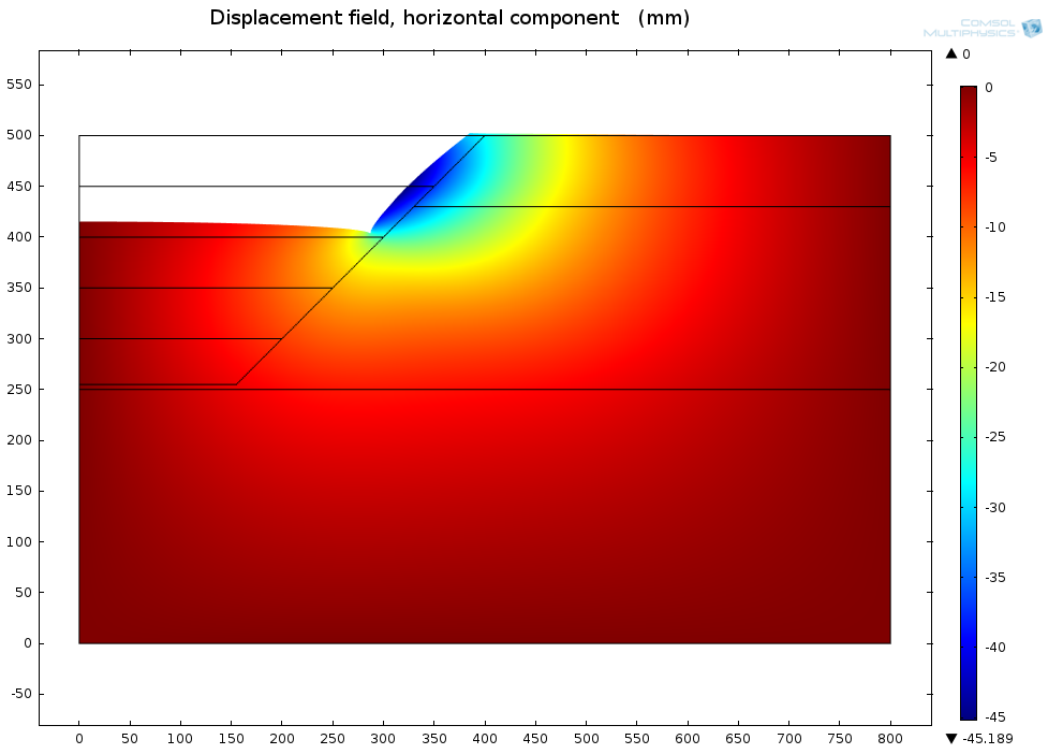

Figure B-17 Horizontal displacement field (mm), excavation up to depth of about 100m

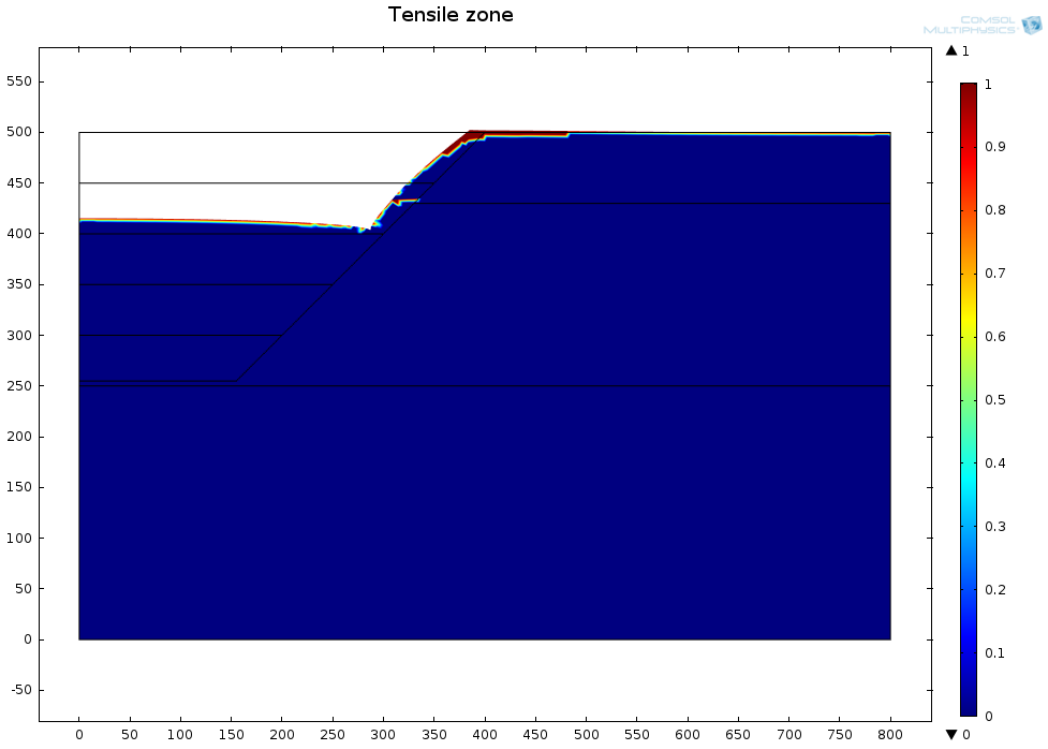

Figure B-18 Minor principal stress tensile zone ($\sigma_3' > 0$), Excavation up to depth of about 100m

Third Layer of Excavation

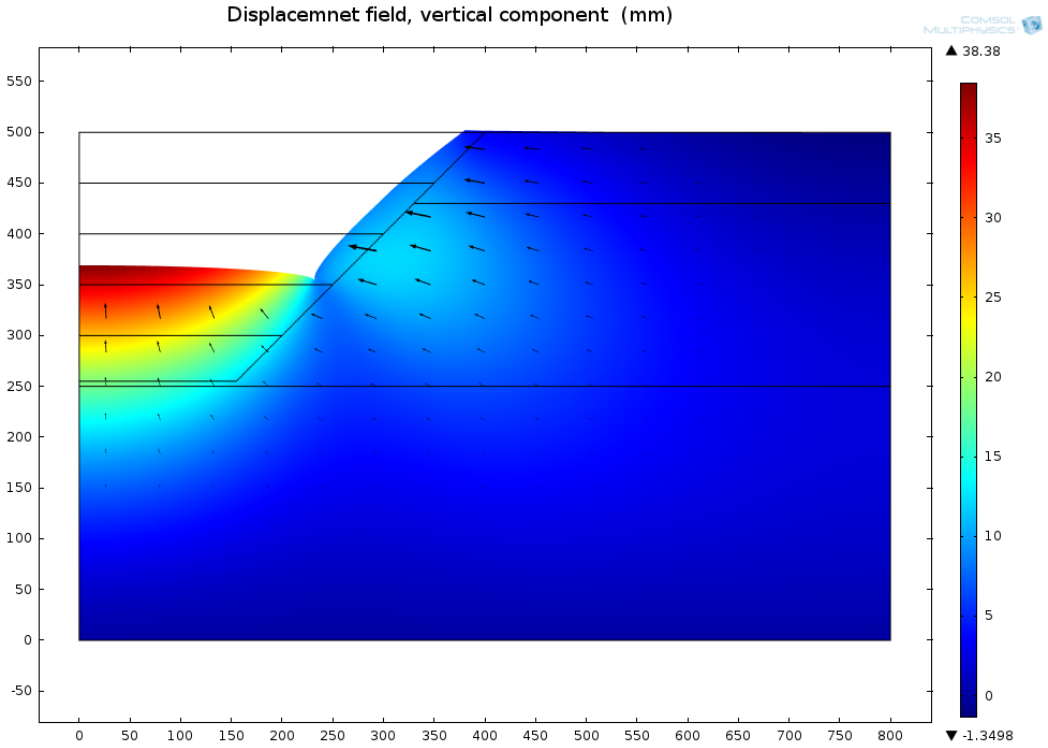

Figure B-19 Vertical displacement field (mm), excavation up to depth of about 150m

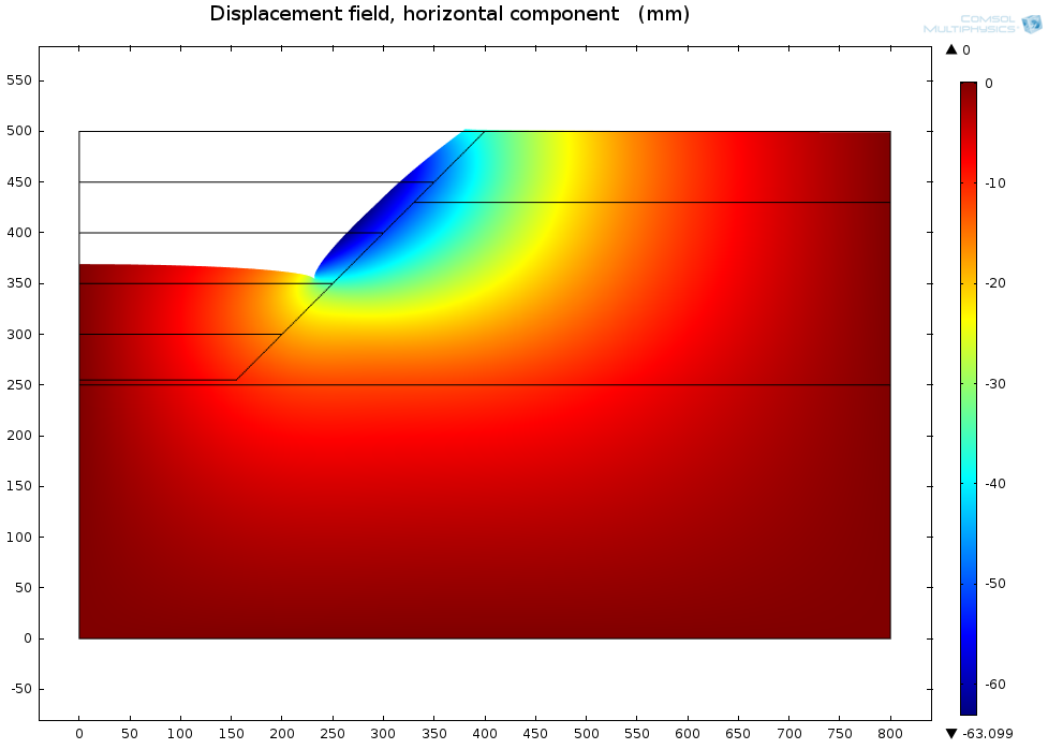

Figure B-20 Horizontal displacement field (mm), excavation up to depth of about 150m

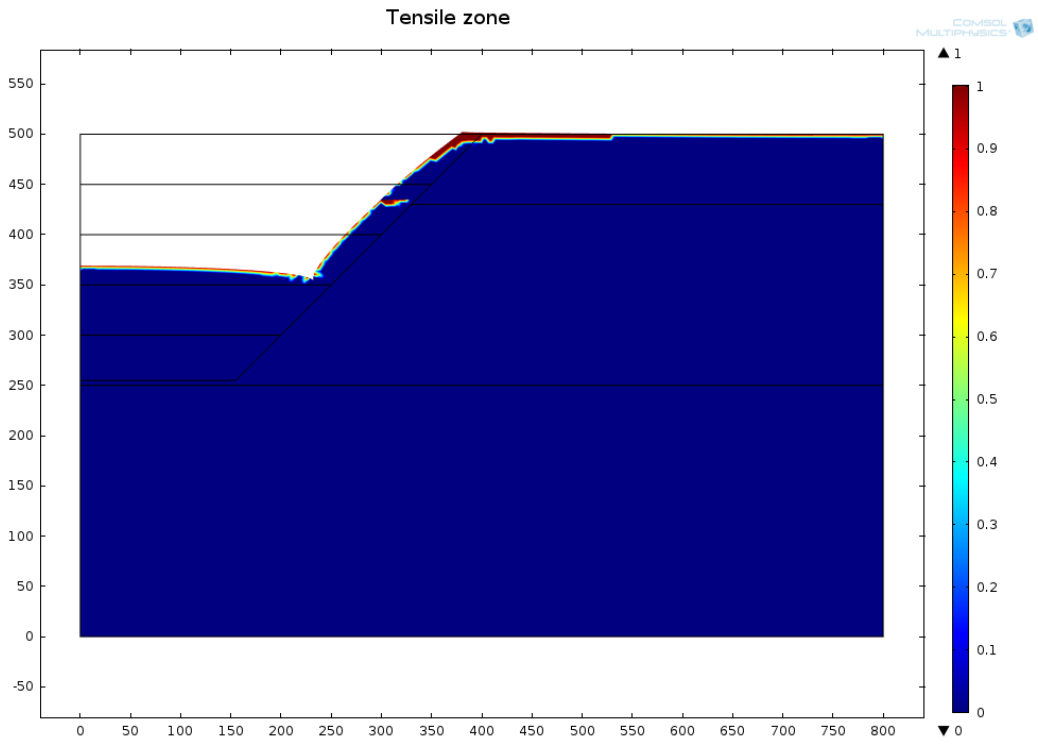

Figure B-21 Minor principal stress tensile zone ($\sigma_3' > 0$), Excavation up to depth of about 150m

Fourth Layer of Excavation

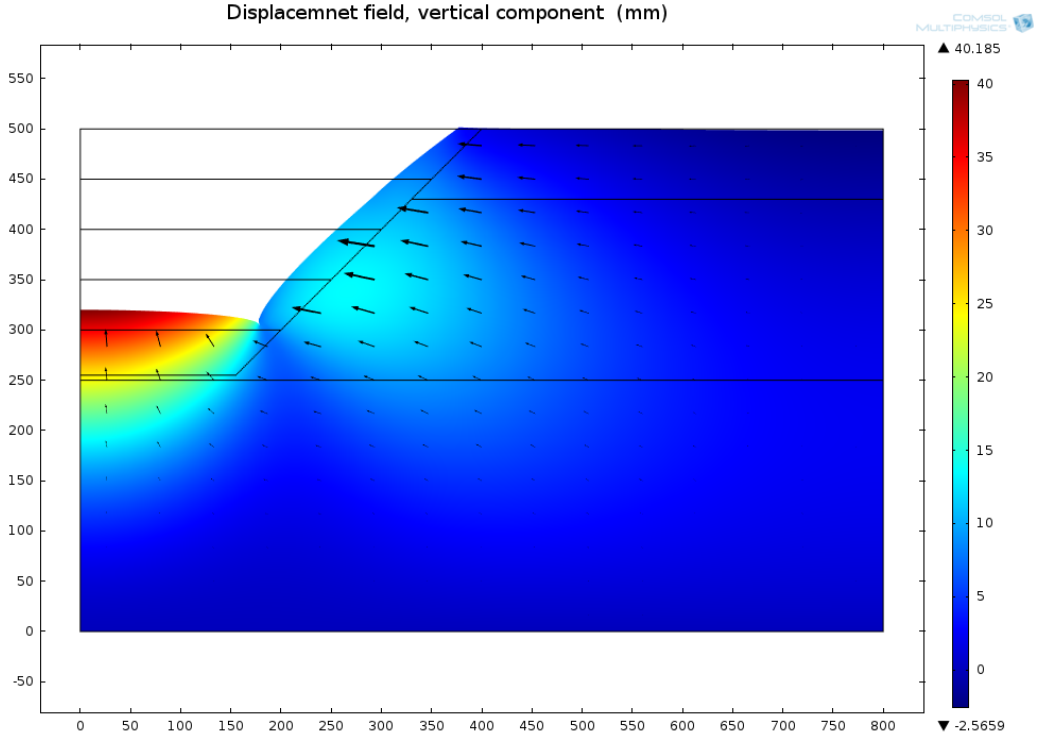

Figure B-22 Vertical displacement field (mm), excavation up to depth of about 200m

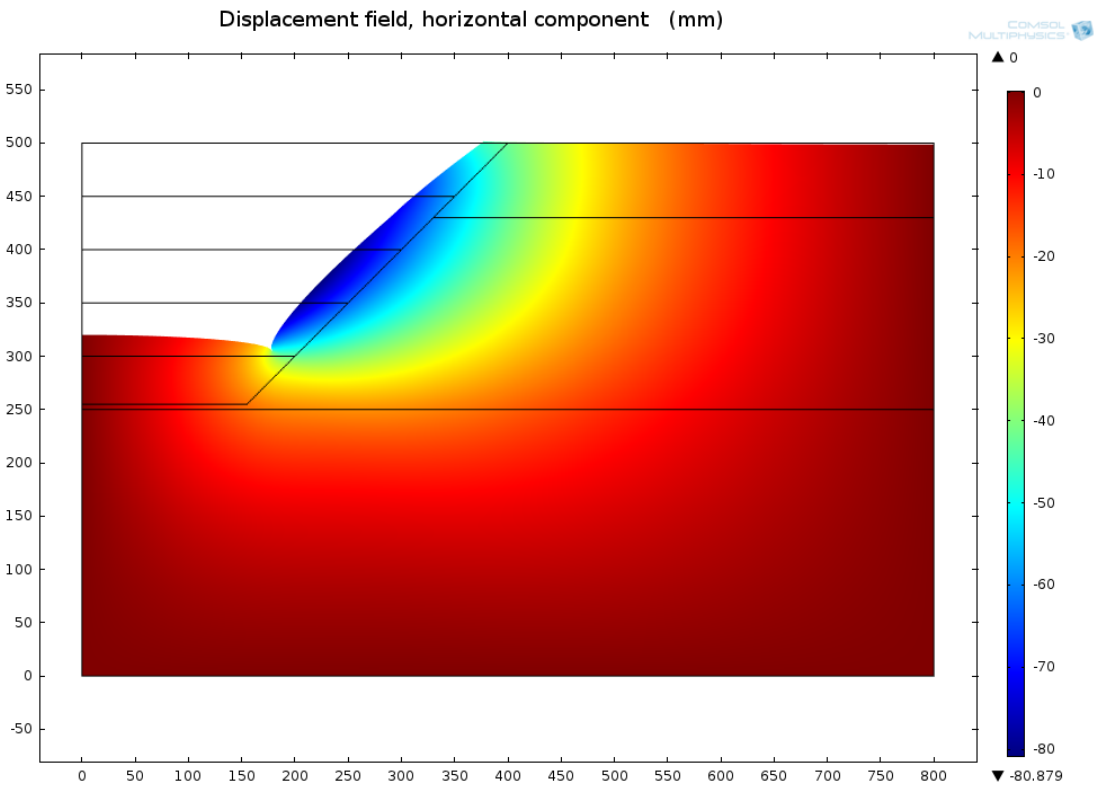

Figure B-23 Horizontal displacement field (mm), excavation up to depth of about 200m

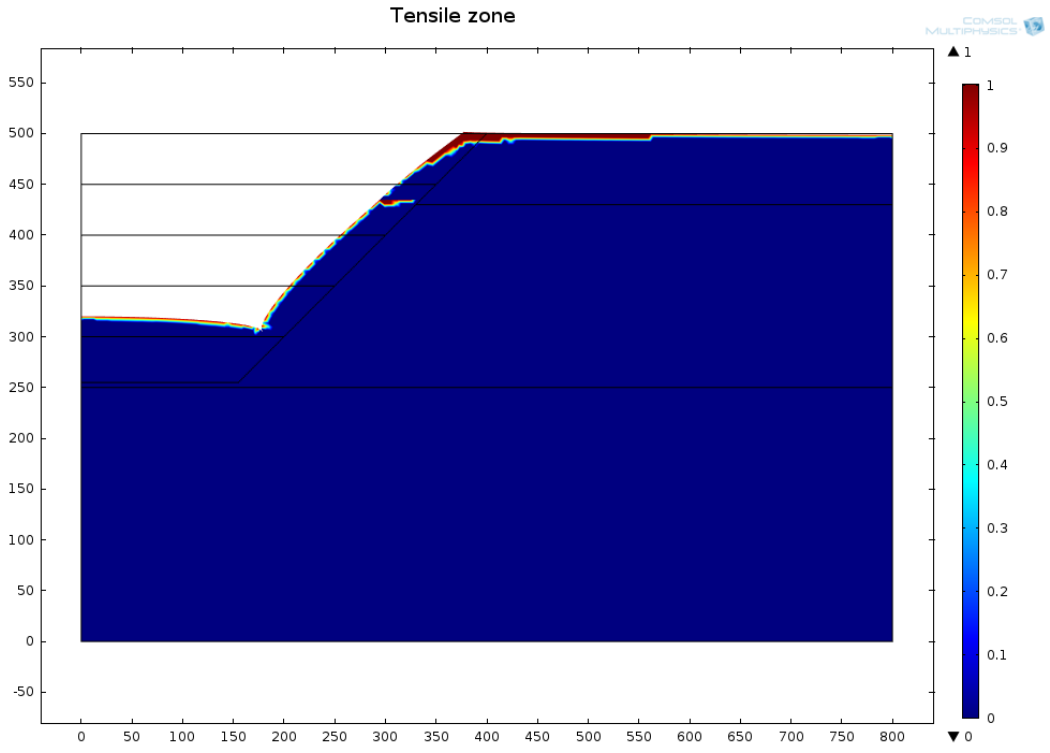

Figure B-24 Minor principal stress tensile zone ($\sigma_3' > 0$), Excavation up to depth of about 200m

PART 3

Long-Term Modelling of Permafrost Disturbances due to Decommissioning and Climate Change

Contents

List of Figures

List of Tables

1 Introduction

In the Phase 1 studies of the Kiggavik project, effects of mining activities on the surrounding frozen ground were analyzed in the continuous permafrost for the operational time period of 15 years as indicated in the mining schedule (Wan and Booshehrian, 2013). Our numerical studies on the thermal behaviour of frozen ground indicated that open taliks would not form near both the East Zone and Centre Zone during the operational time, whereas, for the Main Zone where the mine excavation breaks through the permafrost boundary, there would be an open talik forming. The above-mentioned numerical predictions are, however, within the limits of assumptions made on material properties, thermal boundary conditions, time, and geometries in the computations.

In this new phase of the study, the long-term behaviour of permafrost under the presence of disposed tailings will be assessed adequately through numerical simulation. For this purpose, some important issues will be addressed in relation to various aspects such as the decommissioning plan, material thermal and hydraulic properties, and long term climatic conditions following a number of plausible climate change scenarios.

Climate change and its impact on permafrost is inarguably a subject of intense debate and controversy nowadays. Evidences from site measurements surely exist to support climate-induced changes to permafrost that have occurred during the last decades (e.g. see Lachenbruch and Marshall, 1986; Burn, 1992, 1998; Halsey et al., 1995). As a result of a warming trend, permafrost degradation with attendant physical and hydraulic responses of the ground material is to be expected. Additionally, climate warming could also alter the hydrology of permafrost areas, which could modify the active layer thickness, and thereby result in changes in water table, infiltration, and ground water movements.

Of equal interest and consideration is the nature of the tailings from the mill processing of uranium ores which contain radioactive and other hazardous materials that could affect the environment, especially surficial and underground water streams. Since some radioactive materials have very long half-lives, it is very important to investigate the effects of climate change on the thermal and hydraulic behaviours of permafrost over extended periods of time, exceeding 1000 years or more.

To analyze objectively the long-term impacts of climate change and mining activities on the underlying permafrost, numerical simulation key points such as the choice of material thermal and hydraulic properties, climate conditions, and probable climate change scenarios should be defined with care. In the following sections, first, assumptions made in the simulations are clearly defined followed by discussions of important issues. Then, the long-term numerical modelling results with the relevant analyses and conclusions are presented.

2 Climate Change

Climate change refers to the change in climatic conditions that can be identified by changes in the mean and/or the variability of its properties persisting for an extended period such as a decade (IPCC AR5, 2014). The most important mechanism that impacts the climate condition is the amount of energy received by the earth's surface from the sun. Various processes, whether natural such as modulations of the solar cycles and volcanic eruptions or anthropogenic such as persistent changes in the composition of the atmosphere due to human activities, could ultimately affect the amount of energy received.

2.1 Impacts of Climate Change

The shifts in the climate condition could impose drastic changes to the high latitude areas where large amounts of frozen water have accumulated on the ground surface or within the pore spaces of frozen ground materials for many years. Evidences from site measurements exist for climate-induced changes in permafrost during the last decades. For instance, Lachenbruch and Marshall (1986) indicated a warming trend in Alaska by analyzing borehole temperatures. During the last 100 years, air temperature in the Western Arctic region has warmed by 1.5ºC (Maxwell, 1997). This warming trend has affected the discontinuous permafrost and increased the permafrost temperature in both the Yukon Territory and Western North-West Territories (Burn, 1992, 1998a; Halsey et al., 1995). There are also some indications of permafrost degradation in Manitoba (French and Egorov, 1998) and in the subarctic and boreal peatlands of Quebec, especially between 1957 and 1973 (Laberge and Payette, 1995).

The most recent report of the Intergovernmental Panel on Climate Change (IPCC AR5, 2014) gives a broad view of observed impacts attributed to climate change reported in the scientific literature. Shrinkage of glaciers across western and northern North America, increased coastal erosion in Alaska and Canada, widespread permafrost degradation, especially in the southern Arctic, and decreasing snow cover extent across the Arctic are just some of the recent observed impacts of climate change in North America and Polar Regions.

2.2 Most Recent Climate Change Predictions

Several approaches have been used in the literature to predict the effects of climate change ranging from surface energy balance models (Outcalt, 1972; Anisinov, 1989) to empirical permafrost index models (Nelson and Outcalt, 1983). In the absence of sufficient climate data, steadily increased surface temperature boundaries are sometimes used in heat transfer numerical models (Kane et al., 1991).

In the recent decades, general circulation models, based on the physical sciences, are usually used in theoretical analyses to match past climate data, predict future conditions, and link causes and effects in climate change. The Intergovernmental Panel on Climate Change (IPCC) has published five reports since 1990 which cover the scientific and technical information relevant to understand the basic risk of human-induced climate change. The main scientific focus in the IPCC reports is the anthropogenic persistent changes in the atmosphere that could result in climate changes.

In the last two recent IPCC reports (AR4, 2007 and AR5, 2014), various scenarios are considered for different population growth or industry developments. In each scenario, the emission and concentration of greenhouse gases are different--so the long-term response of the climate would be different. Based on various scenarios considered in the fourth Assessment Report of IPCC (2007), a range of 1.1ºC to 6.4ºC is forecasted as the likely increase in Global temperature over the next century (Figure 2-1).

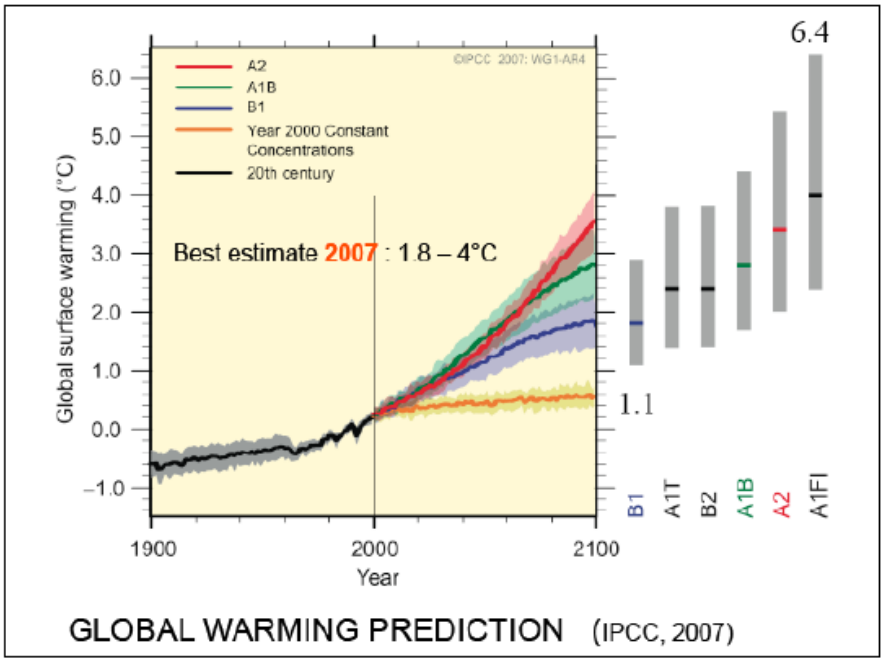

Figure 2-1 Climate change predictions based on various emission scenarios (IPCC AR4, 2007)

As indicated in Figure 2-1, the best estimate for global temperature increase is between 1.8º C and 4.0º C. For the case of high population growth and low technology improvement (Scenario A2) the average global temperature increase is predicted to be 0.35º C per decade. However, based on the regional and local studies for Northern Canada, the average temperature increase would be approximately 0.5ºC per decade which is about 40% higher than the predicted global temperature increase.

However, climate change models have been improved since the previous IPCC assessment report (IPCC AR4, 2007) in many aspects, and now the models can predict changes in climate conditions with higher confidence (IPCC AR5, 2014). In the IPCC fifth assessment report (IPCC AR5, 2014), based on recent studies and modified emission scenarios, new global and regional temperature increases are predicted. In Figure 2-2, both the observed and predicted global temperature increases are presented. As indicated in Figure 2-2-B, the best estimate for global mean temperature increase is approximately between 1º C and 4º C. Also, considering the area on the east side of the Hudson Bay in Northern Canada in Figure 2-2-C, the temperature increase for our region of interest is between 2ºC and 3ºC according to the low emission scenario, and

between 5ºC to 6ºC for the high emission scenario up to the end of the 21st century as calculated by the global climate models.

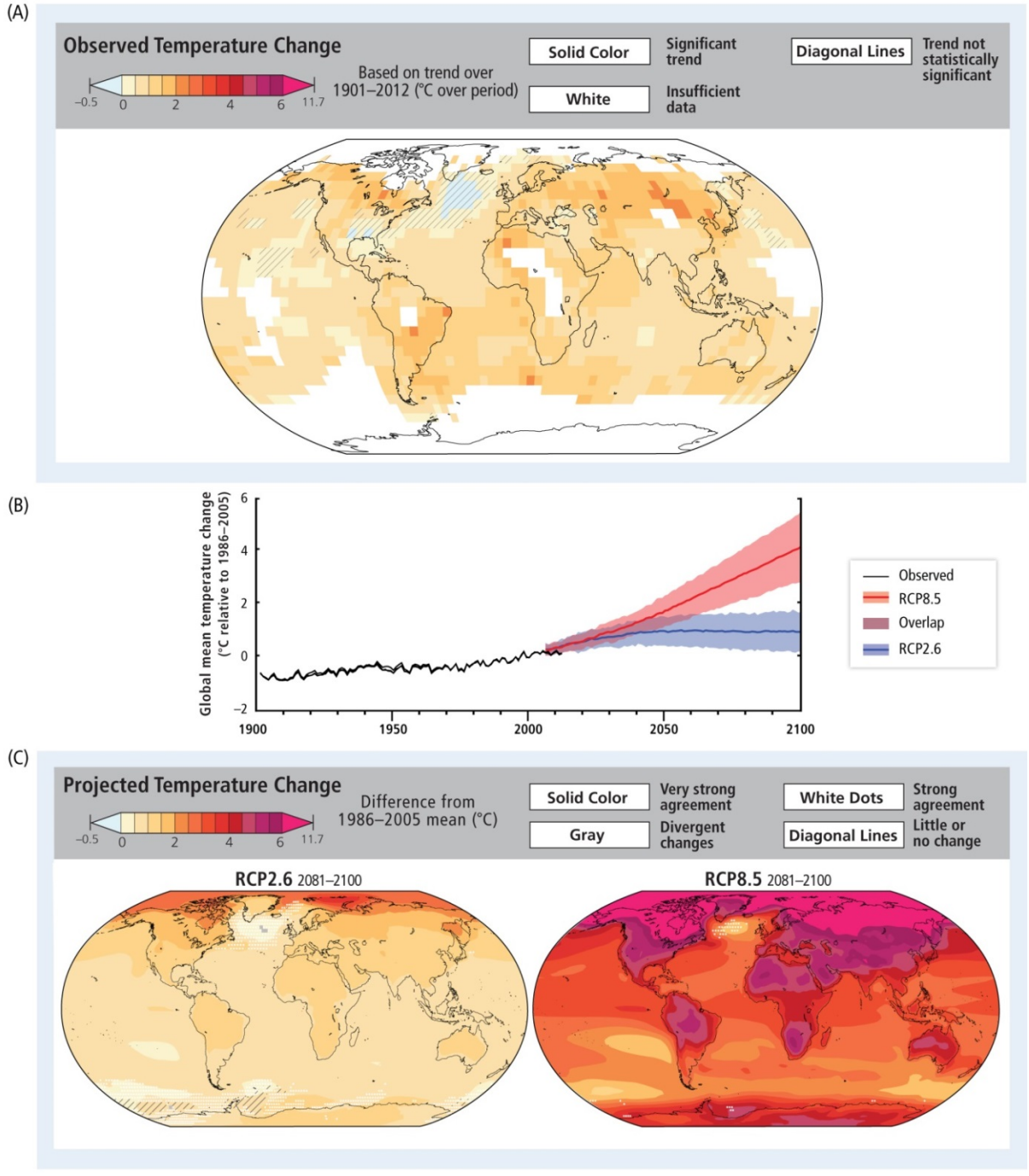

Figure 2-2 Observed and projected changes in annual average surface temperature. This figure illustrates temperature change observed to date and projected warming under continued high emissions (IPCC AR5, 2014)

Besides the global models, results of many local and regional studies are also presented in the IPCC assessment report (IPCC AR5, 2014). In Figures 2-3 and 2-4, the possible climate change predictions for the high latitude regions are presented for the future summers and winters, respectively.

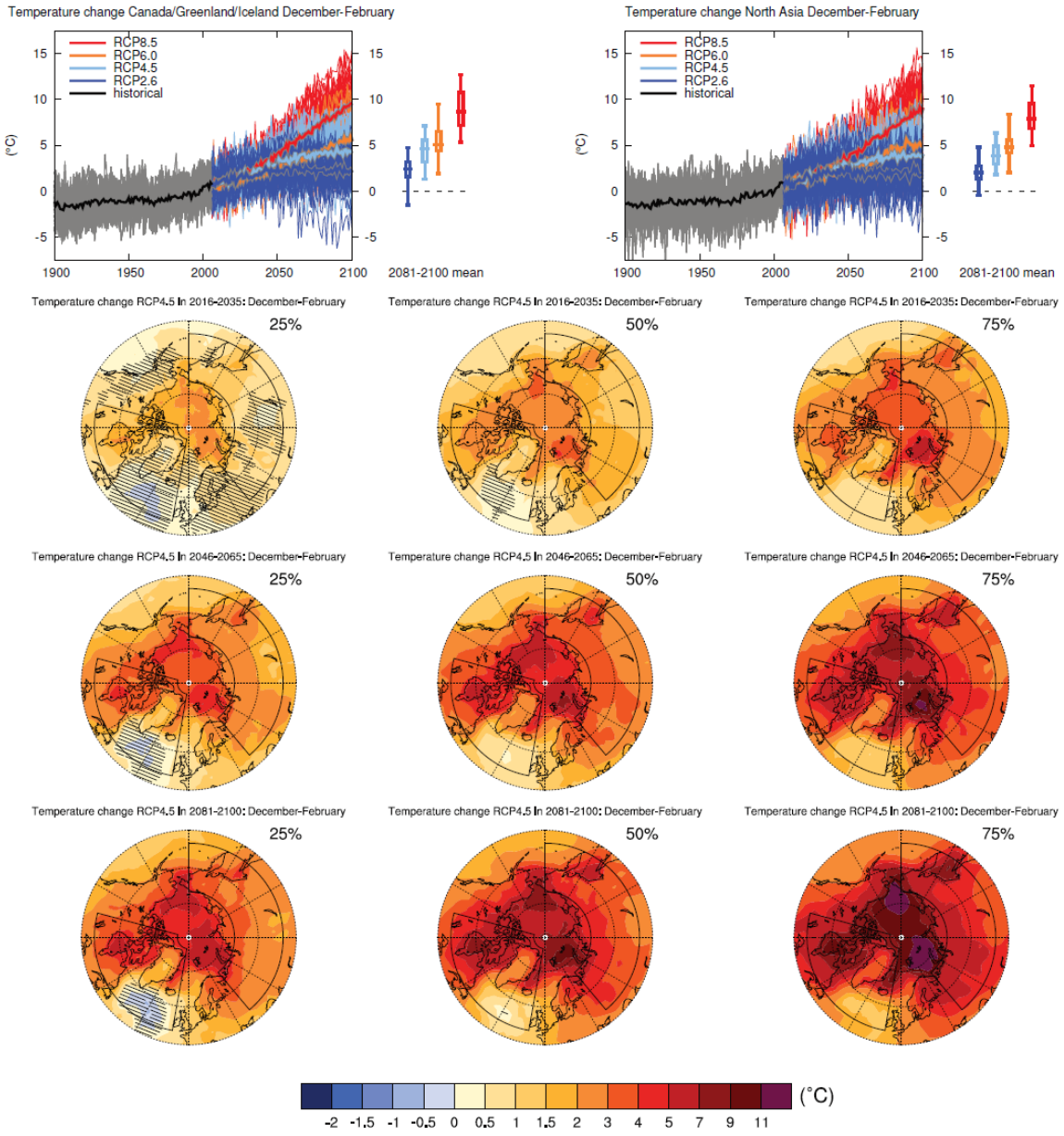

Figure 2-3 Time series of temperature change relative to 1986–2005 averaged over land grid points in Canada, Greenland, Iceland, and North Asia in December to February (IPCC AR5, 2014)

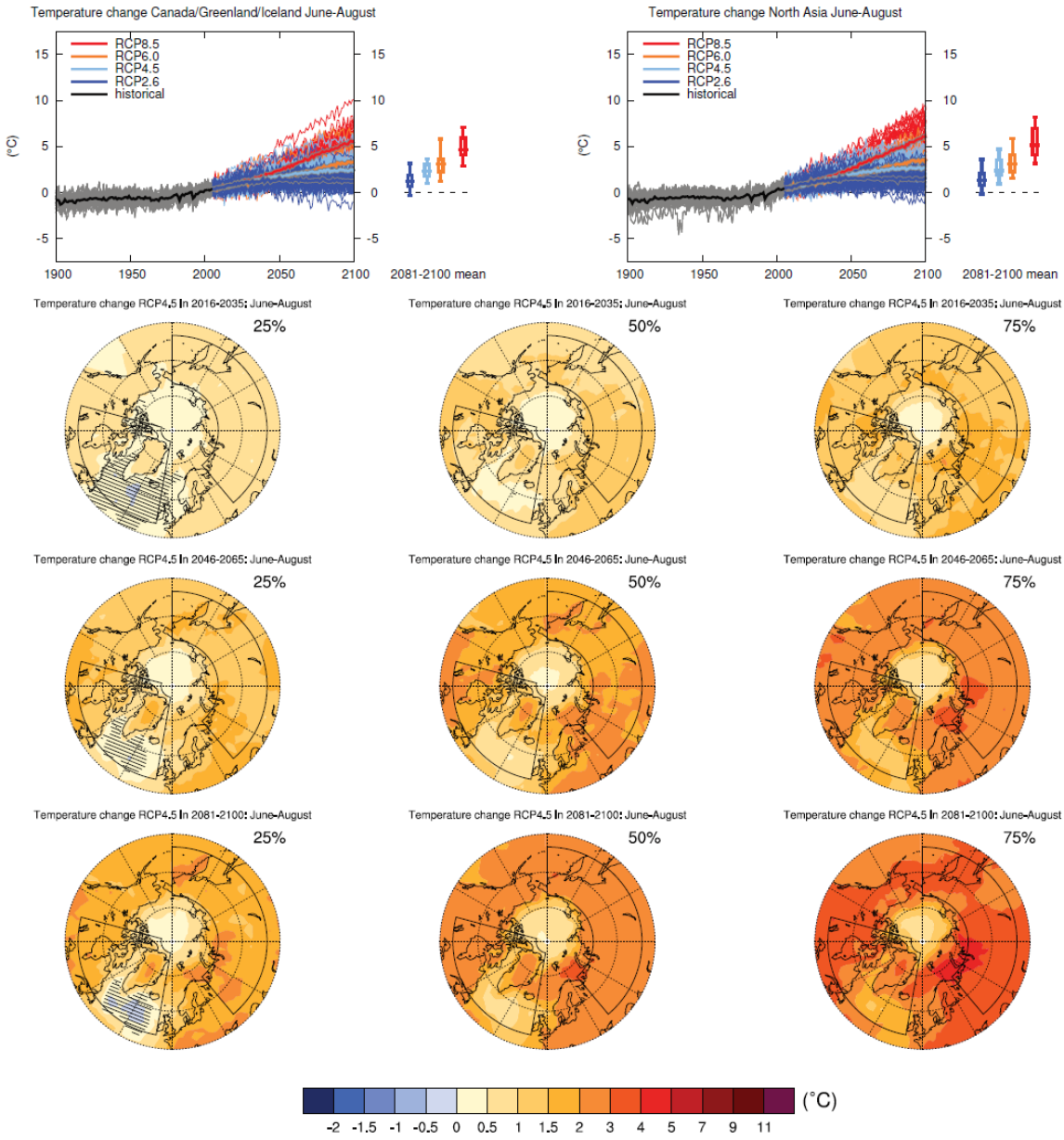

Figure 2-4 Time series of temperature change relative to 1986–2005 averaged over land grid points in Canada, Greenland, Iceland, and North Asia in June to August (IPCC AR5, 2014)

In Figure 2-3, the time series of temperature change for different emission scenarios are presented for Northern Canada, Greenland, and Iceland for the winter periods. Based on the result of these climate models, the mean average winter temperature would possibly increase between 3ºC and 8ºC up to the end of this century. In addition, the change in the mean summer temperature for the same emission scenarios would range between 2ºC and 6ºC.

Based on the above review of the IPCC information, a mean temperature increase of between 2.5ºC and 7ºC could be considered for the purpose of numerical modelling of the Kiggavik project for up to the end of 21st century. Moreover, since the emission of greenhouse gases, population growth, and technology improvements are vague for longer periods of time, climate scientists could not predict the climate conditions beyond the 21st century with confidence. Therefore, hopefully the technology improvements in the future can control the high emission of greenhouse gases, so that climate conditions can become stable afterwards.

For the purpose of our numerical modelling exercise, we assume that the temperature increase will occur exclusively in this century, and thereafter remain constant for longer periods of time.

3 Mine Decommissioning Plan

Closure of the tailings facilities will be conducted mainly to control the release of contaminants and radioactive materials and also to reproduce the landform comparable with the local topography. Based on the plan proposed by AREVA Resources Canada Inc., closure of the tailings facilities will progress in a multi stage operation including the tailings consolidation, removing tailing water cover, backfilling the TMFs above the tailings mass with mine rocks, and constructing the surface cover. For East and Centre Zone TMFs, these operations will likely be completed during operation; while the Main Zone TMF will likely be closed upon termination of the mill operation.

The conceptual decommissioning plan for the East Zone and Centre Zone is summarized in Figure 3-1 and 3-2. In this plan, the TMFs will be fully backfilled with mine rocks and a till cover will be placed on top of the mine rocks. However, for the Main Zone TMF, based on the current evaluations, the TMF will be filled partially with the tailings. It is possible that additional resources will be found over the life of the project. Therefore, the Main Zone TMF could be completely filled with tailings by the end of mill operation. Finally, mine rocks will be placed on the top of tailings mass to fully backfill the TMF (Figure 3-2).

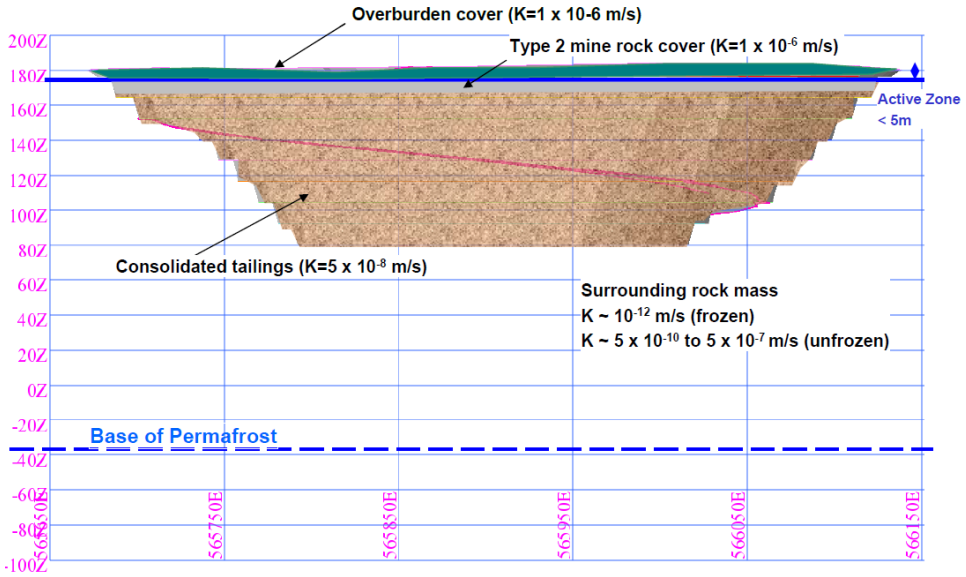

Figure 3-1 East Zone and Centre Zone decommissioning plan

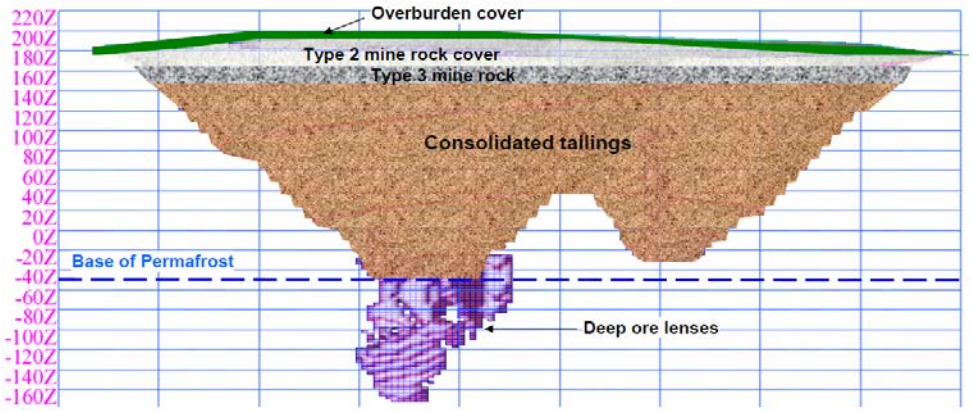

Figure 3-2 Main Zone decommissioning plan

One of the important stages in the decommissioning of all the TMFs is the tailings consolidation process. Based on the information presented in Technical Appendix 5J (AREVA, 2013), the excavated open pit mines will be converted to tailings facilities. These pits will be backfilled with mill processed tailings up to approximately 80% of the pits' height. Then, the tailings material will be allowed to consolidate under its own weight. After completion of the consolidation, to use the TMFs space more efficiently, more tailings will be placed on top of the consolidated tailings. This process will continue until about 70 to 80 percent of the pits' height is filled with consolidated tailings. At this stage, mine waste rocks will be placed on top of the

tailings to facilitate the tailings consolidation and close the pit. These processes are depicted schematically in Figure 3-3 for the East Zone TMF in the Kiggavik project.

Tailings consolidation processes should be considered in the numerical simulations since the time dependent tailings consolidation changes the material properties within the TMFs.

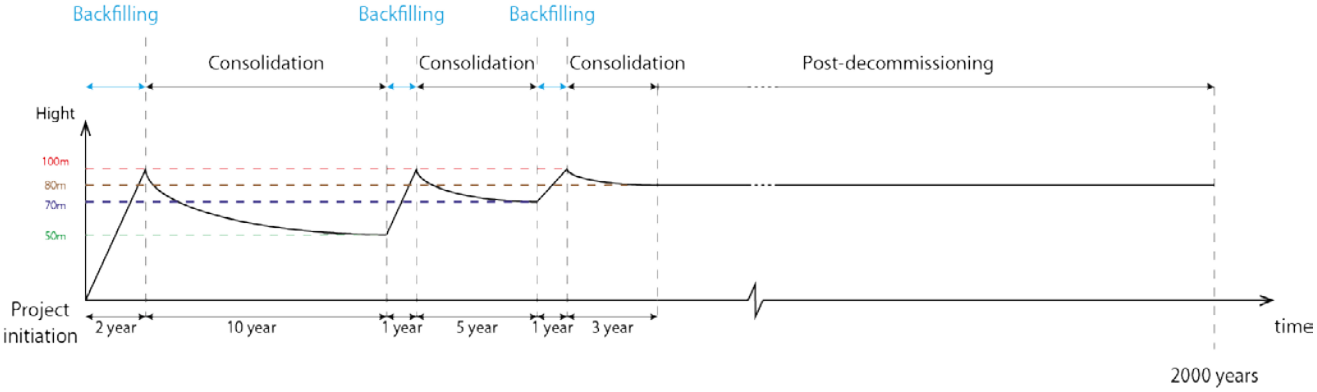

Figure 3-3 Schematic tailings consolidation and backfilling process for the East Zone TMF

4 Proposed Climate Change Scenarios in this Study

Since radioactive materials have very long half-lives, it is very important to investigate the effect of climate change on the thermal and hydraulic behaviours of permafrost over extended periods of time, exceeding 1000 years or more. Improvements in the climate change science have enabled us during the recent years to predict the future climate conditions with more confidence and accuracy. However, all these predicting models are based on simulations and numerical studies with assumptions and theories that could be modified with further improvements in the future studies.

The last decade has experienced a surge in green house emission gases, i.e. CO_2, and yet the temperature increase for the past 15 years has only been 0.06°C. By contrast, under such circumstances, most climate change models would predict an increase of 0.25°C approximately for the past 10 years. Moreover, some recent researches on the sea-level indicate some doubts on the results of climate change models. For instance, in a research by Austermann et al. (2013), based on the dating of fossil corals, the sea level during the Last Glacial Maximum (20,000 to

26,500 years ago) should be about 10m deeper than what current climate models predict. This 10m difference could result in a large amount of ice that has not been taken into account in the models. Therefore, there could possibly be a warmer climate change trend.

Since the issue of global warming is under a cloud of doubt, we should be prepared for various scenarios including either optimistic or worst cases. In the climate change section, based on the recent findings from the climate change studies, the possible warming trend for Northern Canada over the next 100 years would possibly range between 2.5ºC and 7ºC with an average of 5ºC.

For the purpose of this study, three climate change scenarios as illustrated in Figure 4-1 are considered to evaluate the long-term changes in permafrost. These are outlined in the following subsections.

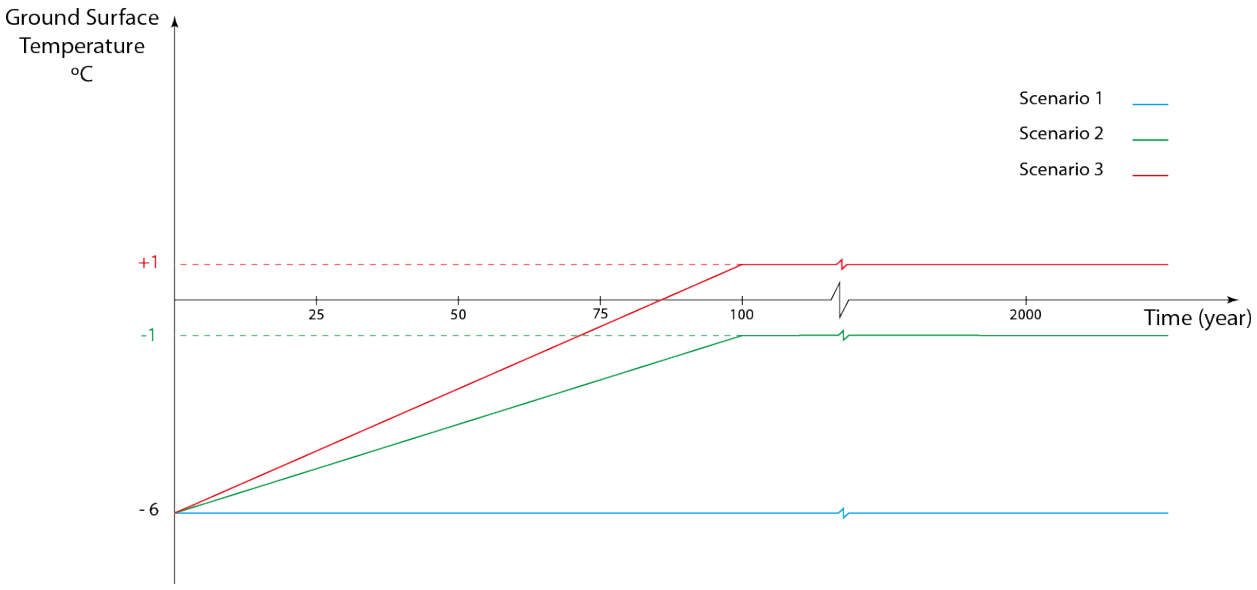

Figure 4-1 Climate Change scenarios considered for the numerical simulation

4.1 Scenario 1: No Climate Change

This could be the most optimistic climate change scenario which assumes that the climate conditions would remain unchanged at the current condition. Therefore, the mean annual ground

surface temperature remains at -6ºC for thousands of years (Figure 4-1). The main goal in this scenario is to verify whether the permafrost around the TMFs could be restored in the future, despite the thermal changes induced by the mining activities. A thermal analysis with phase change is adopted in this study.

4.2 Scenario 2: Ground Surface Temperature Increase from -6ºC to -1ºC

The mean annual ground surface temperature at the Kiggavik project location is about -6ºC as measured in the boreholes at the Kiggavik Project location (AREVA, Technical Appendix 5J, 2013). Considering the average temperature increase over the next 100 years for Northern Canada, the mean annual ground surface temperature could possibly increase from -6ºC to -1ºC (Figure 4-1). The main purpose in this scenario is to investigate the change in the thickness of permafrost in both the presence and the absence of the open pit mining activity. Herein, the numerical simulation also requires a thermal analysis with phase change.

4.3 Scenario 3: Ground Surface Temperature Increase from -6ºC to +1ºC:

The highest predicted warming trend for Northern Canada by the end of 21st century is an increase of about 7ºC in the air temperature (Figure 4-1). When the ground surface temperature increases over the freezing point of pore spaces, the permafrost will disappear eventually. The complete thawing of permafrost could possibly exceed 1000 years depending on the thickness of the frozen layer and the ground material properties.

In this scenario of extreme conditions, it is obvious that after some time the permafrost will vanish. One of the important issues in this case will be the change in the underground water flow regime which could impact the transport of contaminants within the TMFs. For this reason, the numerical simulations will encompass coupled hydro-thermal processes in frozen/partially frozen ground. As such, the impact of climate change and mining activities on the ground water flow system will be evaluated.

4.4 3D Fluid Flow Analysis

All the above mentioned scenarios are conducted within the framework of 2D numerical simulations. In the case of Scenario 3 where the underground fluid flow is coupled with the heat

transfer, the most dominant lakes surrounding the Kiggavik project site are considered. However, there are some other major lakes close to the open pits that also support the underground water flow, especially when the permafrost is completely thawed. Therefore, an additional numerical modelling exercise is conducted in which a steady state 3D seepage computation is contemplated so as to determine the water level in the long-term when the ground material becomes completely unfrozen.

5 Heat Transfer with Phase Change in Porous Media

The heat transfer with phase change was explained previously in Report No.2 (Wan and Booshehrian, 2013, Section 1-2). Here, a brief review of the physics is presented. Pore spaces in the frozen rocks in permafrost are filled with a mixture of frozen and unfrozen water according to the ground temperature. Therefore, the governing equation of heat transfer should consider different material properties in addition to the possibility of phase change during the heat transfer process.

In order to derive the governing equation for heat transfer in a porous media, various physics including fluid flow through pore spaces, mass balance, and energy balance should be considered. The average energy equation is written for the equivalent medium in the form of:

$$\left(\rho C_p\right)_{eq}\frac{\partial T}{\partial t}+\rho_f C_{pf}\mathbf{u}\nabla T=\nabla.(K_{eq}\nabla T)+Q \qquad 5\text{-}1$$

in terms of the equivalent heat capacity of the whole matrix $(\rho C_p)_{eq}$ and C_{pf}, the heat capacity of the fluid, and in the presence of a heat source Q. When there is phase change, latent heat has to be included in Eq. (5-1) through heat enthalpy. This was discussed in Report No.2 (Wan and Booshehrian, 2013, Section 1-2) where it was mentioned that the heat enthalpy conservation equation is the basis of describing heat transport in a three-phase porous medium comprising rock matrix, ice and water such as permafrost.

To simplify the problem, and to be consistent with the case of a small Reynolds number, it is usually assumed that the flow velocity **u** is slow enough so the temperature of the solid and the adjacent fluid are equal. Thus, considering heat transport only occurring by conduction, we get:

$$(\rho C)_{eq}\frac{\partial T}{\partial t}+\nabla.(-K_{eq}\nabla T)-Q=0 \qquad 5\text{-}2$$

where $C_{eq}=$ volumetric heat capacity (J/K.m^3), $K_{eq}=$ effective thermal conductivity (W/m.K) and $Q=$ heat source (W/m^3).

Both an equivalent volumetric heat capacity and an effective thermal conductivity are herein introduced to account for the thermal effects of freezing and thawing in the presence of the three phases, i.e. rock matrix, ice and water, through the definition of volume fractions $\theta_i \quad (i=m,w,i)$ referring to matrix, water and ice, respectively:

$$\theta_m=1-\phi;\ \theta_w=\phi\Theta\ ;\ \theta_i=\phi-\theta_w \qquad \theta_m+\theta_w+\theta_i=1 \qquad 5\text{-}3$$

As such, the three-phase medium is basically characterized by ϕ, the porosity of the rock and Θ, the fraction by volume of the pore space occupied by water.

5.1 Equivalent Heat Capacity

To account for the phase change whereby latent heat of freezing/fusion, L, of water is liberated (absorbed) during freezing (thawing), its effect is incorporated into the so-called equivalent heat capacity worked out as a volume average, i.e.

$$(\rho C)_{eq}=\theta_m\rho_m c_m+\theta_w\rho_w\left(c_w+\frac{\partial\Theta}{\partial T}L\right)+\theta_i\rho_i\left(c_i+\frac{\partial\Theta}{\partial T}L\right) \qquad 5\text{-}4$$

where $\rho_i=$ the density (kg/m^3) of the various phases, and $c_i=$ specific heat capacity of the various phases (J/K.Kg).

A discontinuity in heat flux is to be expected at the interface between ice and water where complicated processes occur within the porous medium in the presence of a so-called mushy

zone (mixture of solid and liquid phases between the solidus and liquidus temperatures). As such, this is idealized through the addition of energy sources (sinks) due to freezing (thawing) involving a normalized pulse ($\partial\Theta / \partial T$) around the transition temperature. The integral of $\partial\Theta / \partial T$ must be equal to unity to satisfy the condition that the 'pulse' width denotes the range between the liquidus and solidus temperatures (Mottaghy and Rath, 2006, Noetzli and Gruber, 2009). Figure 5-1 illustrates the functional shape of the equivalent heat capacity with the 'pulse' to accommodate for latent heat during phase change.

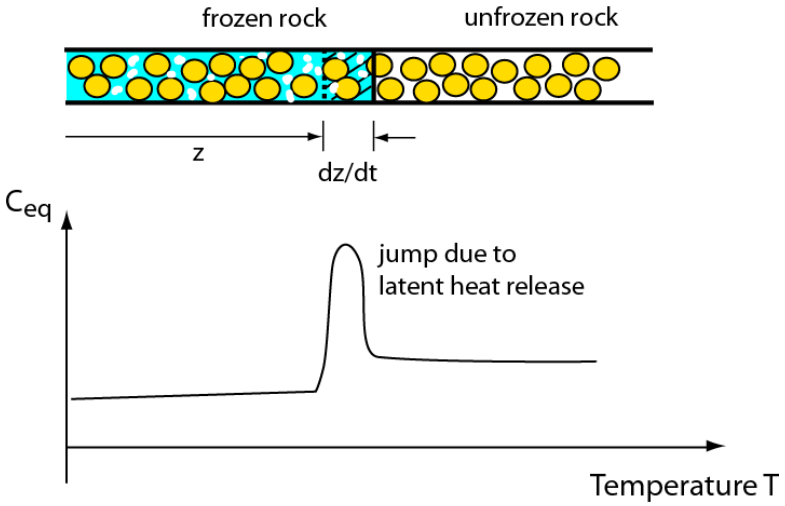

Figure 5-1 Incorporation of latent heat through an equivalent heat capacity with a pulse

6 Material Properties

6.1 Existing Ground Material Properties

In Report No.2 (Wan and Booshehrian, 2013, Section 1), the thermal behaviour of permafrost due to mining activity and tailing impoundment were assessed. Most of the material properties have been presented in Technical Appendix 5B and 5J (Areva, 2013) from lab experiments or site investigations. In order to verify the material properties, some calibration modelling analyses were conducted against available borehole and lab data. The final material properties and the

ice/water content of material from the calibration studies which were used in the permafrost degradation analysis are presented in Table 6-1.

Table 6-1 Material thermal properties used in the first phase of studies

Material	Thermal Conductivity $\frac{W}{m.K}$	Heat Capacity $\frac{J}{kg.K}$	Ice content %
Overburden	2.8	700	5
Metasediment	3.0	670	3
Granite	3.0	670	1
Tailings	2.5	680	30

As it was explained in Report No.2 (Wan and Booshehrian, 2013, Section 1), properties presented in Table 1 are restricted to the solid/particle part of the materials. To find the bulk thermal properties of the materials including the frozen/unfrozen material in the pore spaces or fractures, these solid properties should be combined with the properties of the pore material.

In addition to the thermal properties, material hydraulic properties are also required to analyze the effect of long-term effects on the ground hydraulic conditions. In the analysis conducted on the water flow into the Main Zone, the hydraulic properties presented in Table 6-2 were used for different layers of ground.

Table 6-2 Hydraulic properties of different ground materials

Depth (m)	Hydraulic Conductivity (m/s)		
	Permafrost	Metasediment	Granite
0-5	1×10^{-12}	5×10^{-5}	-
5-100	1×10^{-12}	5×10^{-8}	-
100-215	1×10^{-12}	-	5×10^{-8}
215-450	-	-	1×10^{-8}
450-900	-	-	1×10^{-9}

In addition to the ground materials used in the first phase of study, properties of waste rocks Type 2 and Type 3 are also needed to conduct numerical simulations on long-term behavior of permafrost. Properties presented in Table 6-3 and 6-4 are reported as the properties for these two types of materials in Technical Appendixes 5J and 5G (Areva, 2013).

Table 6-3 Hydraulic Properties of TMF materials

Material	Thickness (m)	Hydraulic Conductivity (m/s)
Overburden cover – All TMFs	1	1×10^{-6}
Mine rock Type 2 – All TMFs	5-10	1×10^{-6}
Mine rock Type 3 – Main Zone TMF only	12	1×10^{-6}
Tailings	>80	5×10^{-8}

Table 6-4 Thermal properties of waste rock and bedrock materials

Material	Thermal Conductivity $\frac{W}{m.K}$		Volumetric Heat Capacity $\frac{KJ}{m^3.K}$		Porosity	Volumetric Water Content
	Unfrozen	Frozen	Unfrozen	Frozen		
Waste rock traffic	1.56	1.86	2099	1722	0.30	0.18
Waste rock	0.82	0.86	1597	1471	0.30	0.06
Bedrock	3.15	3.19	2314	2293	0.01	0.01

6.2 Tailings Properties

According to the proposed mining plan for the Kiggavik project, the Uranium ores will be processed in a mill at the project site location (Technical Appendix 5J, Areva 2013), and the produced tailings will be disposed of into the excavated open pits. The produced tailings is a slurry material with an approximate 70% water content by volume, and the solid part mainly consists of silt or fine sand size material. Therefore, the time for consolidation of this material spans over a long period of time that could take more than 10 years in some cases. Tailings

consolidation will reduce the material porosity and therefore change the material water content. In the numerical simulations, when the heat transfer with phase change in a porous media is analyzed, the amount of water within the pore spaces defines the energy required for the phase change to occur.

During the consolidation, tailings will undergo large deformations due to the high initial water content. Therefore, the tailing consolidation should be analyzed within large strain consolidation theory. The first theory enabling the prediction of one-dimensional consolidation in soils was published by Terzaghi (1924). Some simplifying assumptions made for this theory limited its application to the relatively stiff thin layers at large depths. For instance, in this theory, it is assumed that the strains are small, and relationship between volume change and effective stress is linear.

While many authors offered alternatives to Terzaghi's 1D equation (Shiffman and Gibson, 1964); Davis and Raymond, 1965)), the first general theory of 1D consolidation in soils was published by Gibson, England, and Hussey (1967). In their theory, Finite Strain Consolidation (Gibson et. al., 1967) considered unique dependence of permeability and effective stress on the void ratio. They did not assume small strains, so the theory could calculate the large strain consolidation of soft soils.

In this section, only consolidation results of tailings for the East Zone, Centre Zone, and Main Zone TMFs are presented. The Finite Strain Consolidation governing equation (Gibson et. al, 1967) and its mathematical basis are explained in details in Appendix 1 of this report. Since in the Finite Strain Theory, both the effective stress and permeability are only functions of void ratio, the necessary relations that enter numerical simulations must be measured through lab experiments.

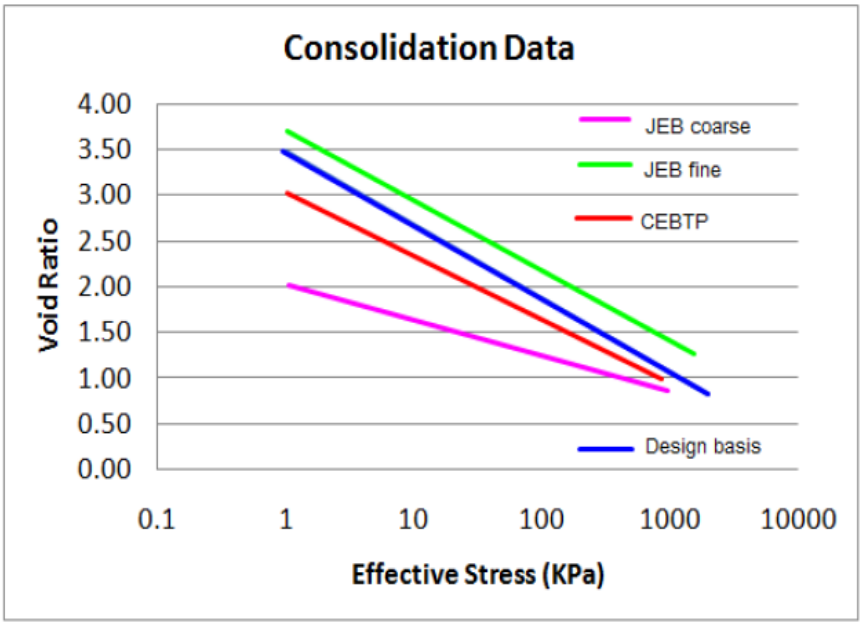

Figure 6-1 Tailings void ratio as a function of effective stress (Technical App. 5J, Areva 2013)

As indicated in Figure 6-1, the relation between tailings void ratio and effective stress for some other Uranium mines in Canada are presented, and the design basis is considered as an average among other graphs. The same relation is considered between void ratio e and effective stress σ' in this study, i.e.

$$e = -0.357 \ln(\sigma') + 3.529 \qquad 6\text{-}1$$

Moreover, Figure 6-2 shows the dependency of tailings hydraulic conductivity on void ratio for the same Uranium mines. Since it is not clearly stated in the Technical Appendix 5J (AREVA, 2013) which graph is used for the design purposes, an average relation among two graphs labeled as "$\mathrm{Ksat}\,4.0e-7$" and "$\mathrm{Ksat}\,2.5e-7$" is considered in this study to simulate the tailings consolidation process (Figure 6-3). Therefore, the following relation is considered between tailings hydraulic conductivity K and void ratio e:

$$K = 2 \times 10^{-7}(e - 1.0) \qquad 6\text{-}2$$

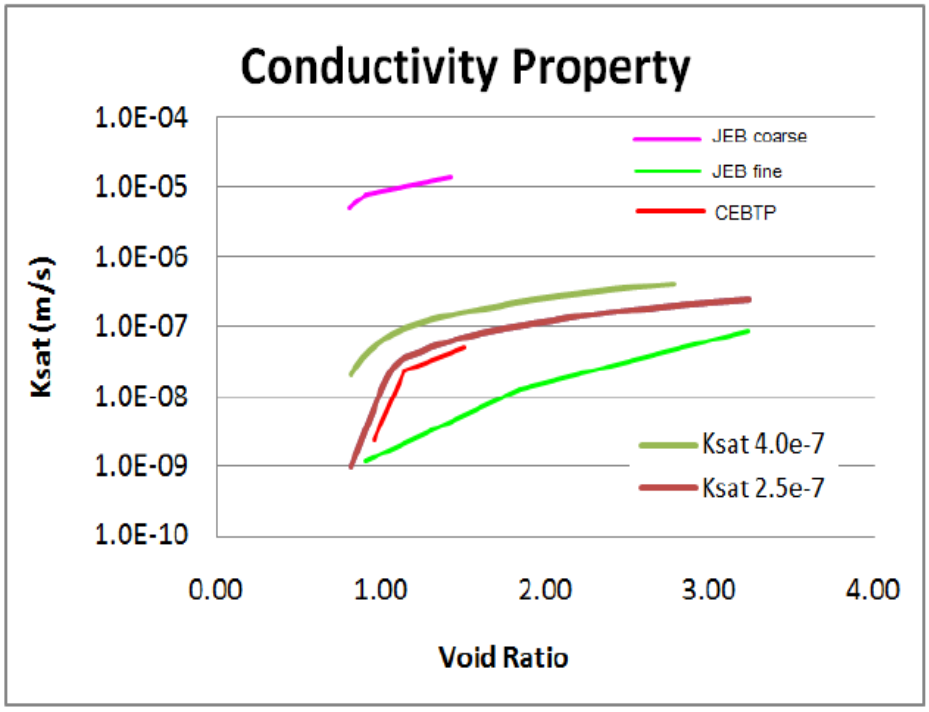

Figure 6-2 Tailings hydraulic conductivity as a function of void ratio (Technical App. 5J, Areva 2013)

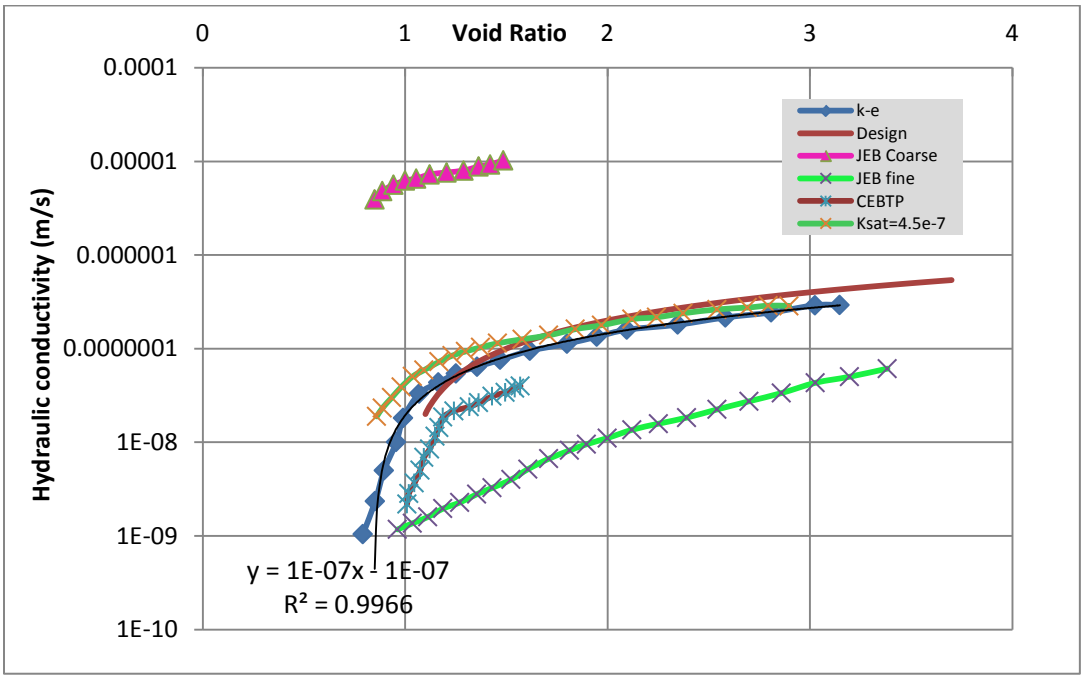

Figure 6-3 Tailings hydraulic conductivity as a function of void ratio

6.2.1 East Zone TMF Consolidation

The maximum excavation depth for the East Zone pit is about 100 m below the ground surface according to the mining plan (Appendix 5J, Areva 2013). Therefore, it could be assumed that the produced tailings will be disposed of into the East Zone TMF up to an approximate height of 85 m to 90 m from the bottom of the pit. The tailings height change as a function of time is shown in Figure 6-4.

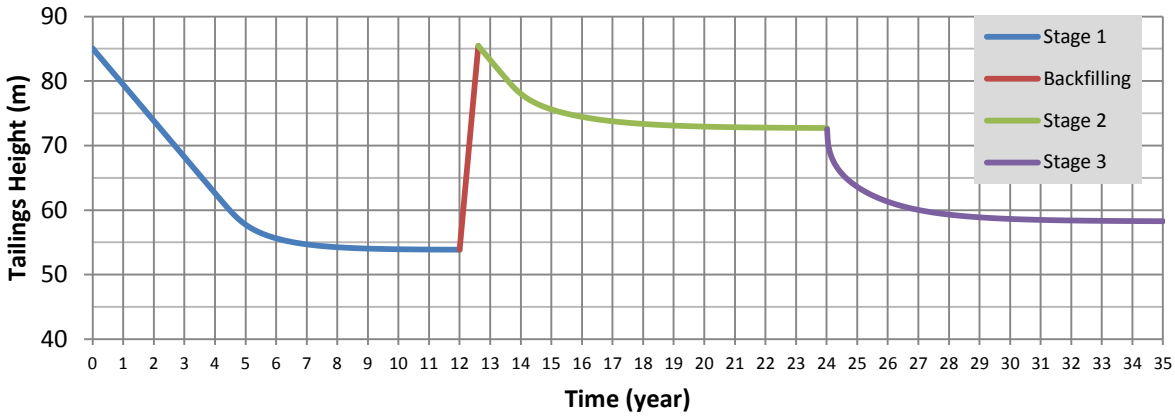

Figure 6-4 East Zone TMF tailings consolidation process and final tailings height

As indicated in Figure 6-4, three consolidation stages and one backfilling are considered for the tailings in this TMF. After the completion of the first stage of consolidation, to optimize the space use, it is assumed that newly produced tailings are placed on the top of the consolidated tailings after about 12 years. Mixture of newly produced and previously consolidated tailings will consolidate after another 12 years. At this stage, the mine waste rocks will be placed on top of the consolidated tailings in order to further facilitate the tailings consolidation and decommission the TMF. The third stage of consolidation occurs after the waste rocks are placed on top of the tailings. The average calculated tailings void ratio (e) over time is shown in Figure 6-5.

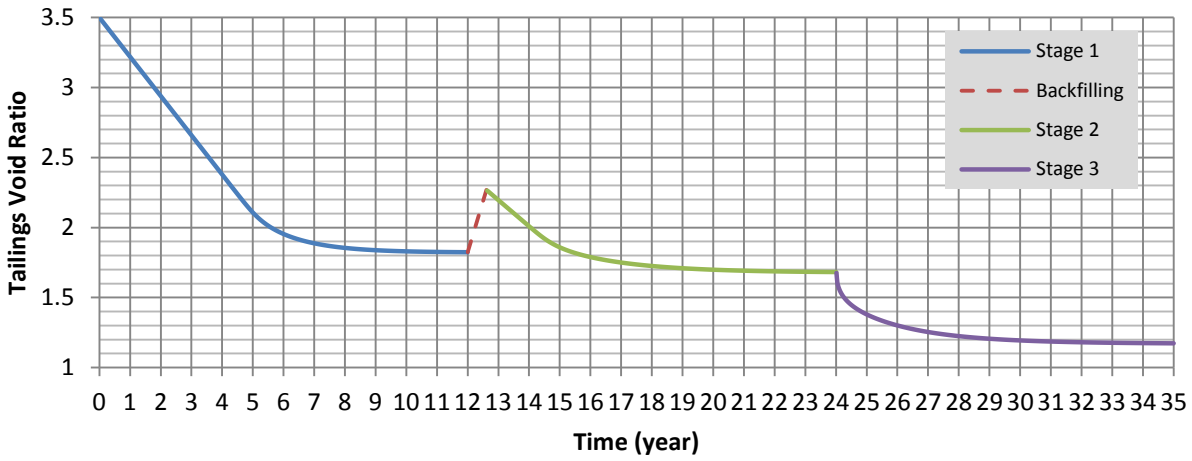

Figure 6-5 East Zone TMF tailings void ratio change during consolidation stages

As reported in the Technical Appendix 5J (AREVA 2013), the solid content of the newly produced tailings is about 40% by weight, so the initial void ratio is about 3.5 as indicated in Figure 6-5. Based on the calculations from the numerical simulations, the final average tailings void ratio is about 1.17 corresponding to an average porosity of 53%. Therefore, by considering the density of solid parts and the water within the pore spaces, the final average solid content of the consolidated tailings inside the East Zone TMF is about 70% by weight.

6.2.2 Centre Zone TMF Consolidation

Since Gibson consolidation theory (Gibson et. al, 1967) is restricted to 1D consolidation of soils, only the depth of the pit is important. So, in the case of the East Zone and Centre Zone, the process of tailings deposition and consolidation is almost the same. Based on the mining plan, the maximum depth of Centre Zone TMF is about 110 m which is about 10 m deeper that the East Zone TMF. It is reasonable to assume that the maximum height of deposited tailings within the Centre Zone TMF is between 90 m and 100 m. The stages of consolidation and backfilling are the same as those for the East Zone TMF as explained in previous section. The tailings height change computed during the consolidation process is shown in Figure 6-6. The final height of consolidated tailings within the Centre Zone TMF is about 65 m above the bottom of the pit.

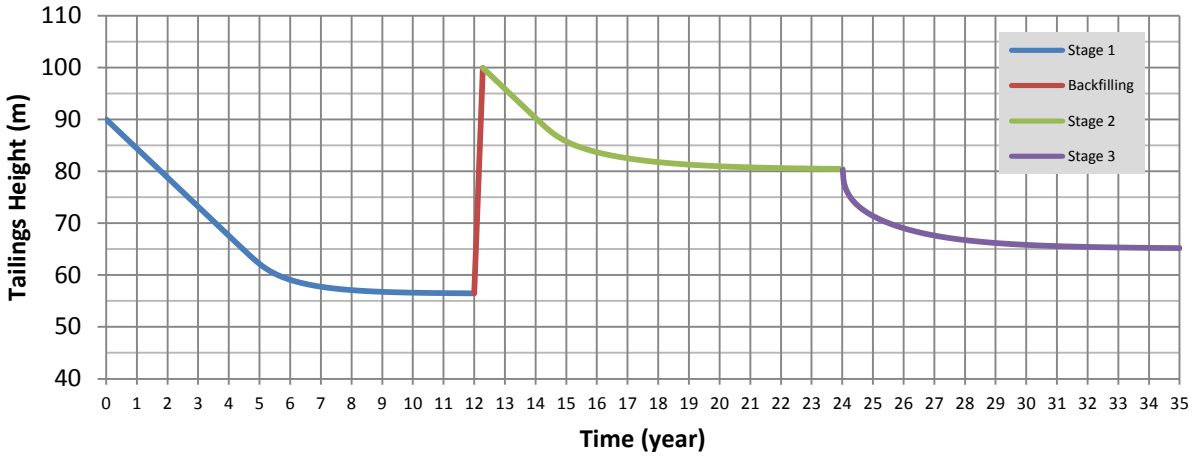

Figure 6-6 Centre Zone TMF tailings consolidation process and final tailings height

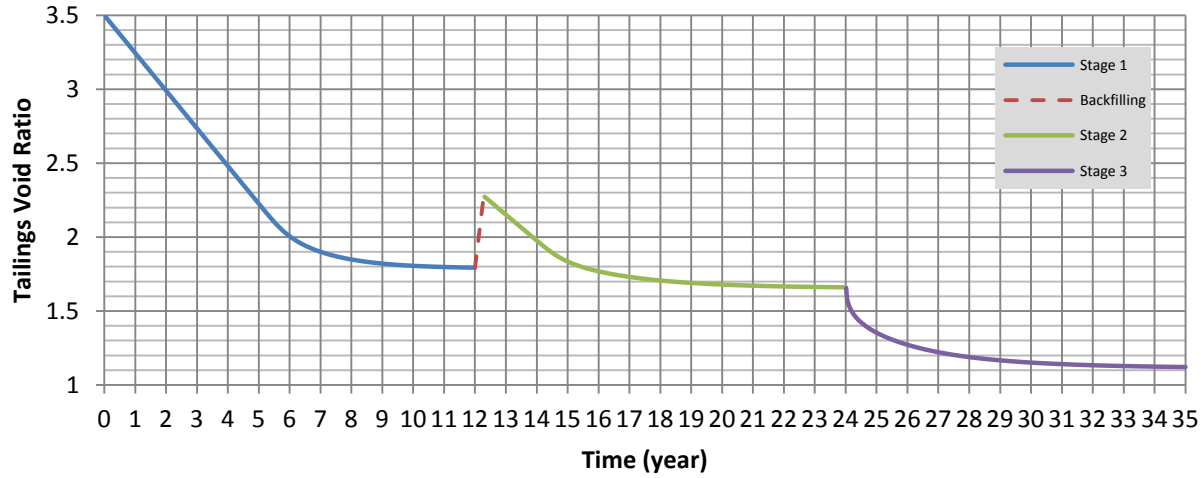

Figure 6-7 Centre Zone TMF tailings void ratio change during consolidation stages

The initial tailings void ratio is 3.5, the same as the East Zone TMF. The final average tailings void ratio is about 1.12 as shown in Figure 6-7 corresponding to the porosity of 52%. The initial and final solid content by weight is 40% and 70%, respectively.

6.2.3 Main Zone TMF Consolidation

The Main Zone TMF is the largest one in the Kiggavik Project. According to the proposed mining plan, the East Zone and Centre Zone pits will be first excavated and converted to a Tailing Management Facility. Then, the Main Zone pit will be used to deposit the mill processing tailings. Based on the current estimation, only half of the Main Zone TMF will be filled with tailings. However, there is a possibility of finding new resources during the mining operation. In such a case, more tailings will be produced which should be deposited in the Main Zone TMF to efficiently use the available space within the pit.

It is assumed that at the first step, the current estimated tailings will fill about 180 m of the Main Zone TMF. Afterwards, if there is any fresh tailings available, it will be deposited on top of the previously consolidated tailings in a multi-stage procedure as indicated in Figure 6-8. Finally, 27 to 28 years after the conversion of the Main Zone pit to a tailing facility which is almost at the end of the operational time, the mine waste rocks will be placed on top of the consolidated tailings layers, and the final stage of consolidation, stage 7 in Figure 6-8, will take place.

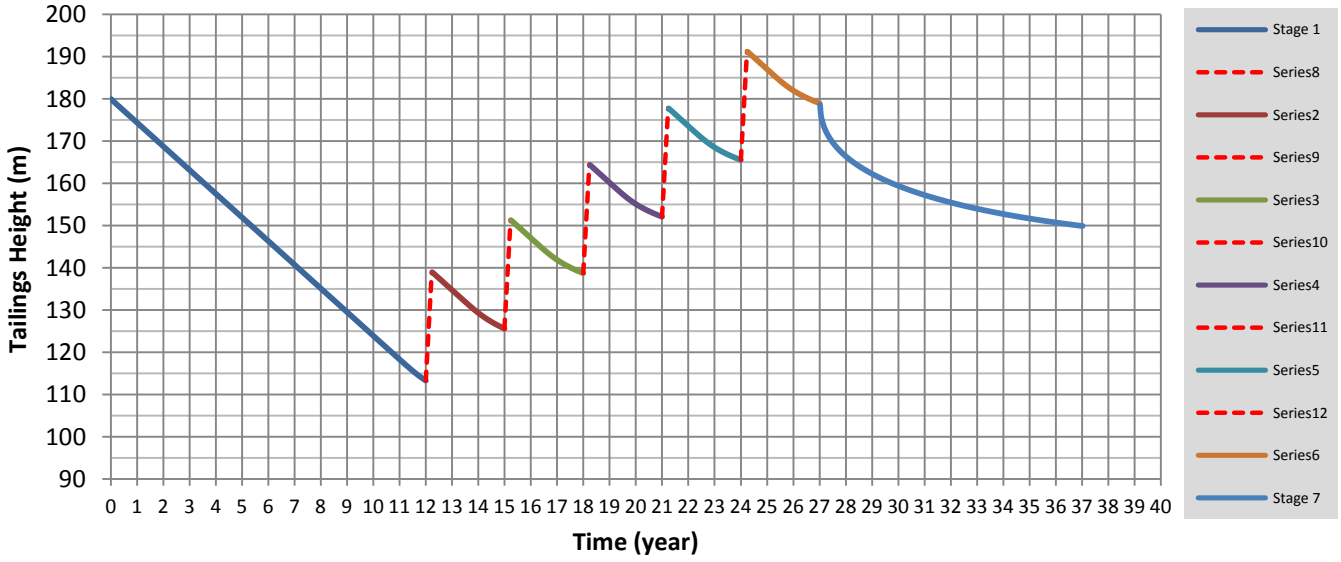

Figure 6-8 Main Zone TMF tailings consolidation process and final tailings height

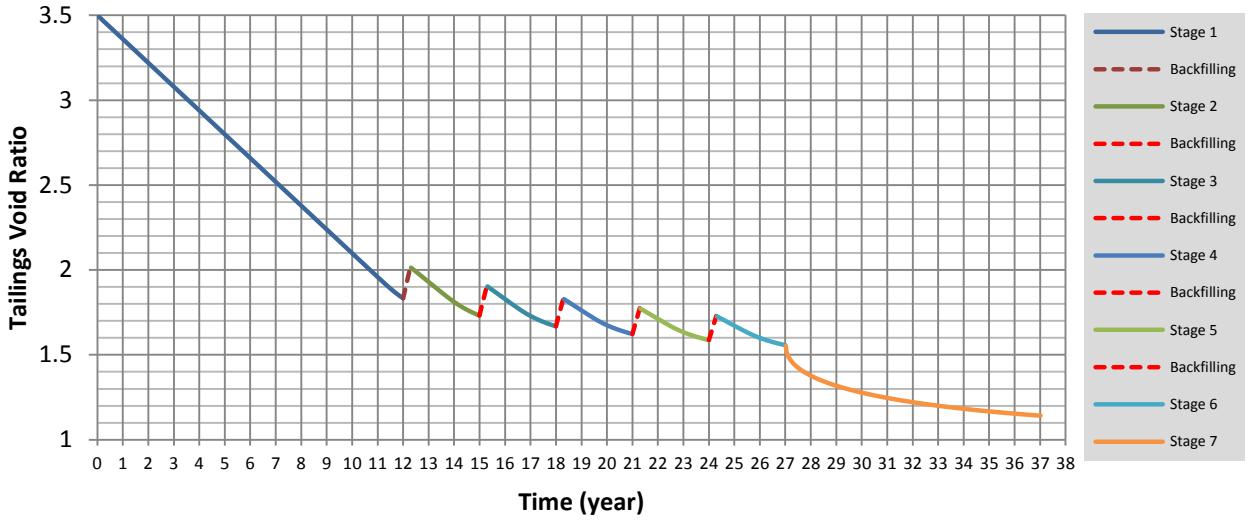

Figure 6-9 Main Zone TMF tailings void ratio change during consolidation stages

The final average tailings void ratio is about 1.14 as shown in Figure 6-9 corresponding to the porosity of about 52%. Therefore, the final solid content by weight is about 70% for the Main Zone TMF.

The various parameters computed during the consolidation phases will enter the numerical modelling of the various climate change scenarios.

7 Scenario 1: No Climate Change

We recall the first climate change scenario where it is assumed that the mean annual ground surface temperature remains at the current temperature of -6ºC for the next 2000 years. Numerical simulation results under this scenario will give us an estimation of required time for the disturbed permafrost to be reproduced under this climate condition. Two tailings initial temperatures of +5ºC and +10ºC are considered in this numerical analysis.

In the following sections, only numerical simulation results pertaining to the case of initial tailings temperature of +5ºC for all the TMFs are presented. These are then compared with simulation results from AREVA. The results for the initial temperature of +10ºC are presented in Appendix 2 of this report.

In all simulations, tailings consolidation processes are included into the thermal analysis by updating the tailings height at each pertinent stage. It should be noted that the new tailings height at each step is calculated as an average between the initial and final depths as computed from the 1D large strain consolidation model as described in Section 6.2.

7.1 Summary of Numerical Simulation Results

Numerical simulations results mainly indicate that the thermal disturbances which were made to the frozen ground because of mining would persist for long periods of time, exceeding 1000 or 2000 years, even if the climate condition is stable as intended to be in Scenario 1.

The main issues and findings can be summarized as follows.

The permafrost could be reproduced after about 2000 years only in the case of East Zone TMF. The thermal profiles shown in Figures 7-8 and 7-9 indicate that after 2000 years, the permafrost boundary reaches a depth of 210m to 215m below ground surface, while the initial depth of permafrost in the vicinity of the project is about 220m based on borehole measurements.

Within the Centre Zone and Main Zone TMF's, the permafrost depth reaches a value of about 120m and 110m, respectively. Therefore, the permafrost regains almost half of its original thickness even when the climate is not changing. Although the depths of the Centre Zone and East Zone TMFs are almost the same, i.e. about 100m, the tailings capacity of the Centre Zone is much higher than that of the East Zone. As such, more thermal energy would be needed from the Centre Zone to reproduce the permafrost. The numerical simulation results in Figure 7-7 and 7-17 confirm this.

As a comparison, in the long-term thermal assessments presented in Technical Appendix 5J (Areva 2013), it is herein predicted that the permafrost will be reproduced after 2000 years within the Centre Zone TMF. It is also seen that the permafrost boundary will reach a depth of about 200m for both Centre Zone and East Zone. It should be noted that the long-term results presented in Technical Appendix 5J (Areva 2013) are conducted with the aid of 1D numerical modelling. While in the 1D numerical simulation the only important parameter is the thickness of unfrozen tailings, the volume of tailings with high water content defines the amount of energy required for the phase change to happen.

As shown in Figures 7-9, 7-19, and 7-29, the final depth of permafrost after 2000 years is not affected by the initial temperature of the warm tailings. In fact, the tailings lose energy until they reach the freezing point where the latent heat of fusion should be exchanged. Therefore, for tailings with higher initial temperature (+10ºC), the time to get to the freezing point is longer. In other words, the ground thermal profiles with time are different for the two cases of initial tailings temperature, but the final result is almost the same.

Figures 7-10 and 7-20 indicate the permafrost time evolution within the East Zone and Centre Zone TMFs. At the end of operational procedure in the East Zone and Centre Zone, the ground material is still frozen in the area beneath the TMF (Figures 7-3 and 7-13). However, warm tailings within the TMF in combination with the geothermal heat flux will eventually thaw the frozen area. Meanwhile, the tailings material eventually freezes back from the top due to the operative cold climate above ground surface. Therefore, ground material and tailings are simultaneously freezing back from top and thawing from the bottom. After about 1000 years for the East Zone and 300 years for Centre Zone, two freezing boundaries merge together, and afterwards only one freezing front is visible in the simulation results.

In the case of Centre Zone and Main Zone where the tailings will not fully freeze back even with no climate change conditions, the contaminants in the tailings could reach the underground water aquifers or surface water bodies eventually in this case.

Although the No Climate Change scenario is a very optimistic condition which will not happen with the current rate of greenhouse gases emission, it gives us the vision that the thermal disturbances in the permafrost could hardly be recovered in the future. To investigate the time necessary for the Centre Zone TMF to regain its original freezing condition, an additional numerical simulation for a longer period of time is conducted. The results indicate that the material inside and around the Centre Zone TMF will freeze back after about 3000 years (Figures 7-30 and 7-31).

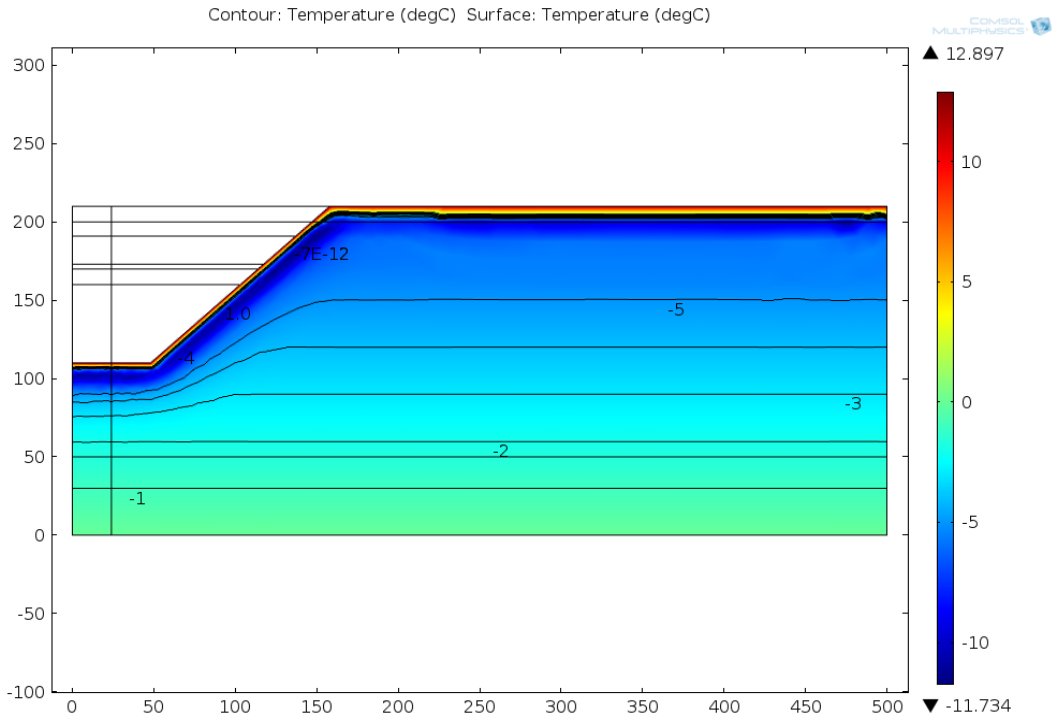

Figure 7-1 East Zone, end of excavation and before filling with tailings

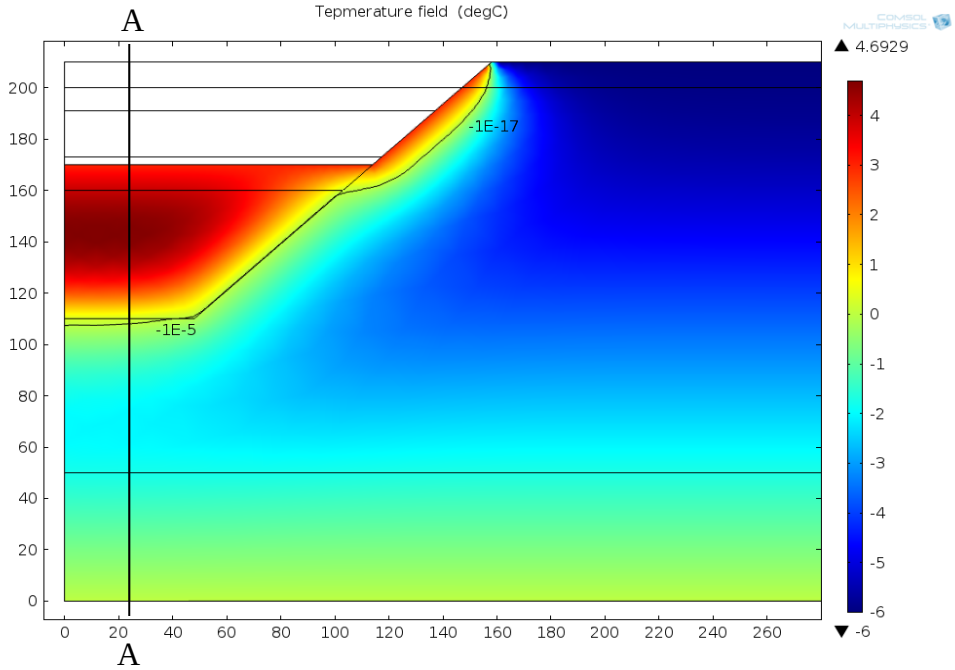

Figure 7-2 East Zone TMF, thermal changes during stage 1 of consolidation, Initial tailings temperature +5ºC

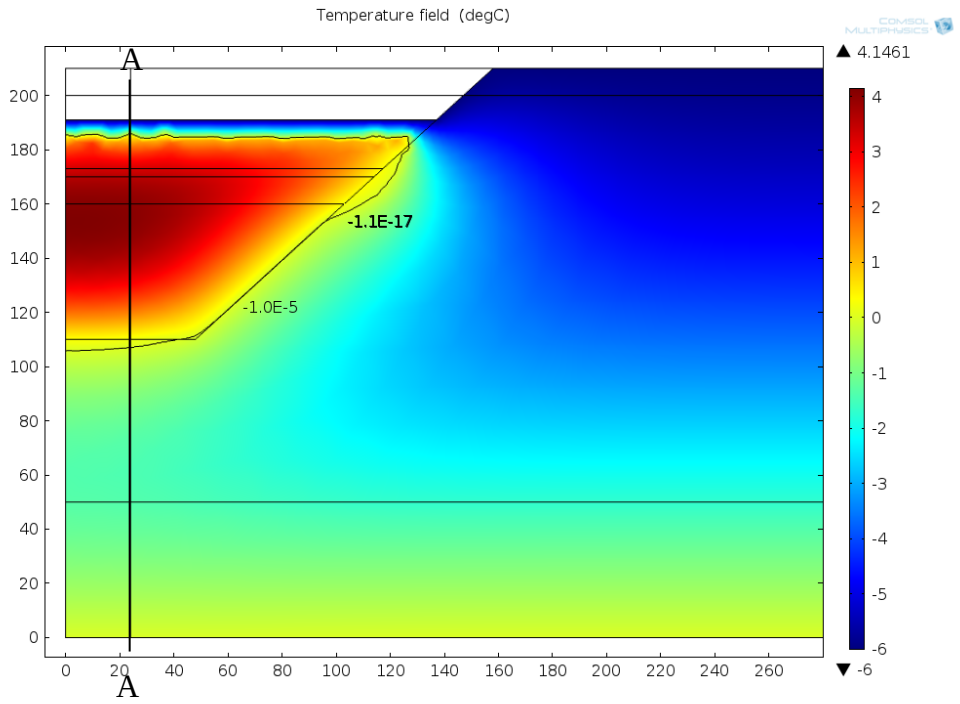

Figure 7-3 East Zone TMF, thermal changes during stage 2 of consolidation, Initial tailings temperature +5ºC

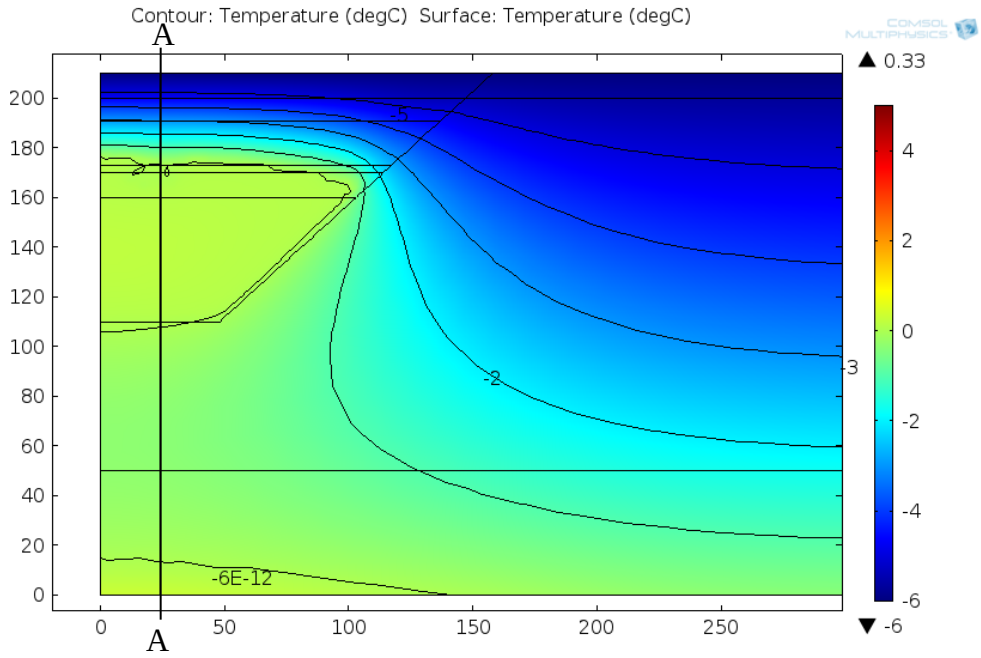

Figure 7-4 East Zone TMF, thermal changes after 100 years, mine rocks are places on top of tailings, Initial tailings temperature +5ºC

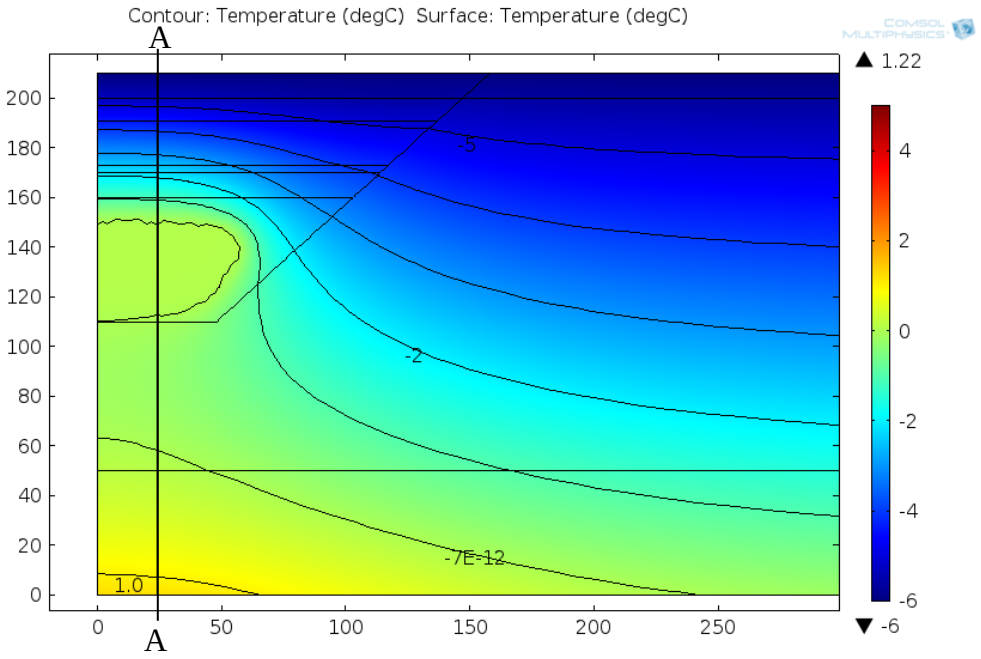

Figure 7-5 East Zone TMF, thermal changes after 500 years, mine rocks are places on top of tailings, Initial tailings temperature +5ºC

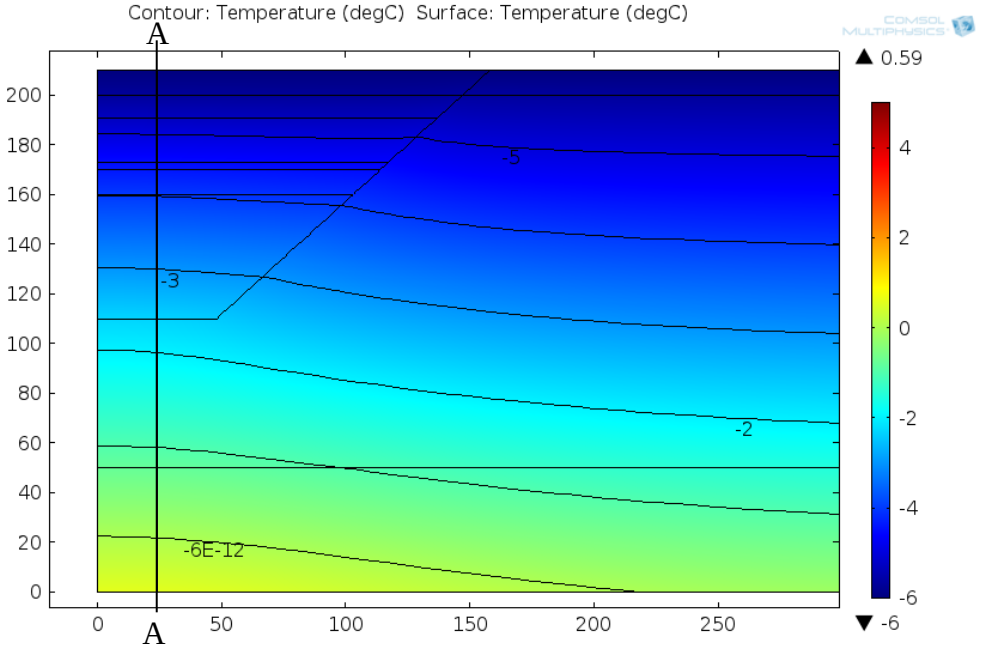

Figure 7-6 East Zone TMF, thermal changes after 1000 years, mine rocks are places on top of tailings, Initial tailings temperature +5ºC

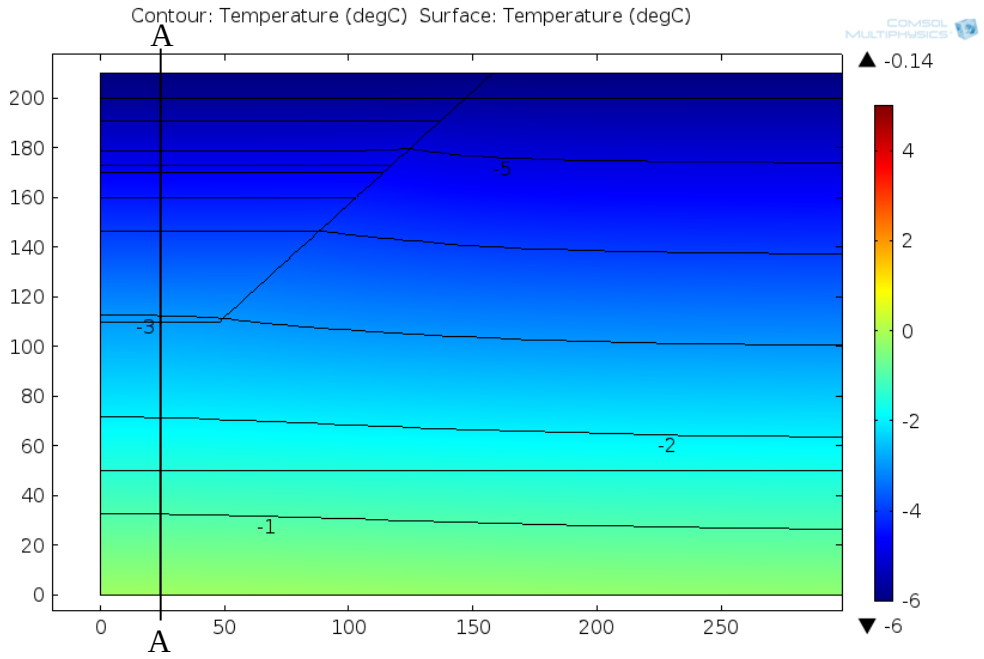

Figure 7-7 East Zone TMF, Thermal changes after 2000 years, mine rocks are places on top of tailings, Initial tailings temperature +5ºC

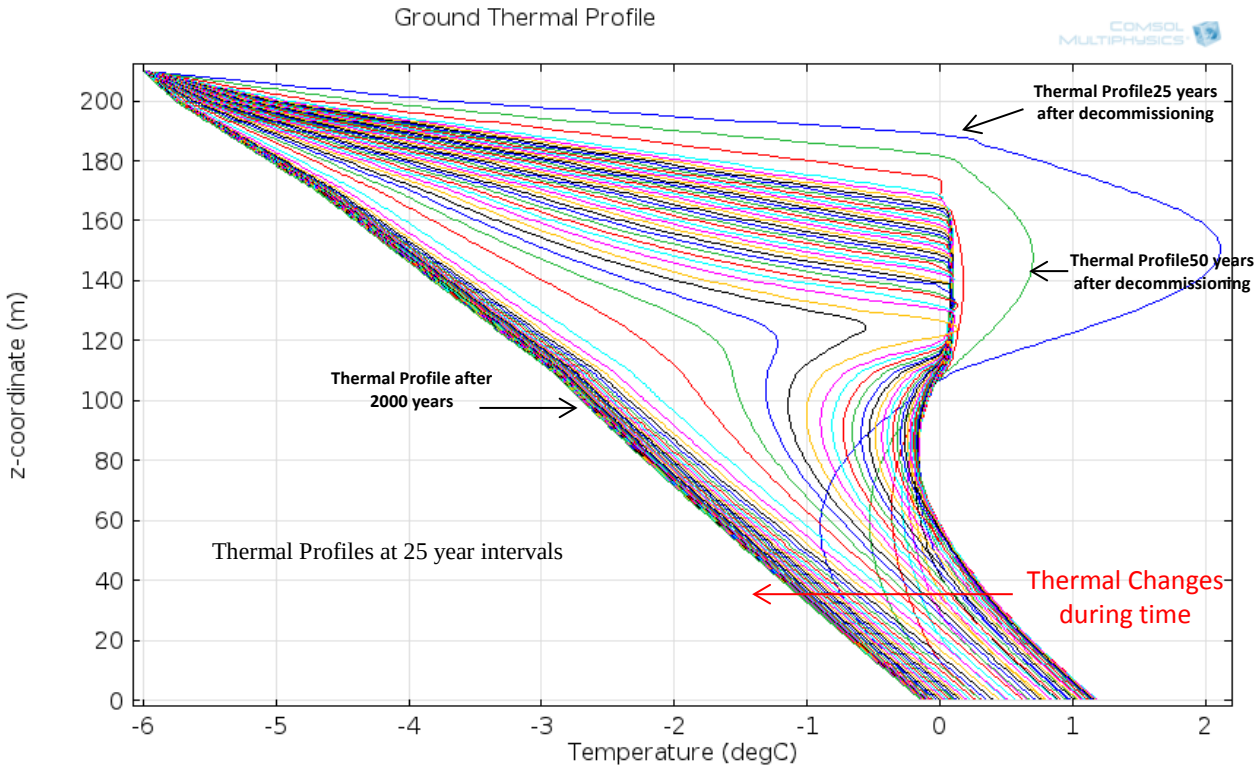

Figure 7-8 Thermal profile changes along line A-A within the East Zone TMF up to 2000 years after decommissioning at 25 year intervals, Initial tailings temperature +5ºC

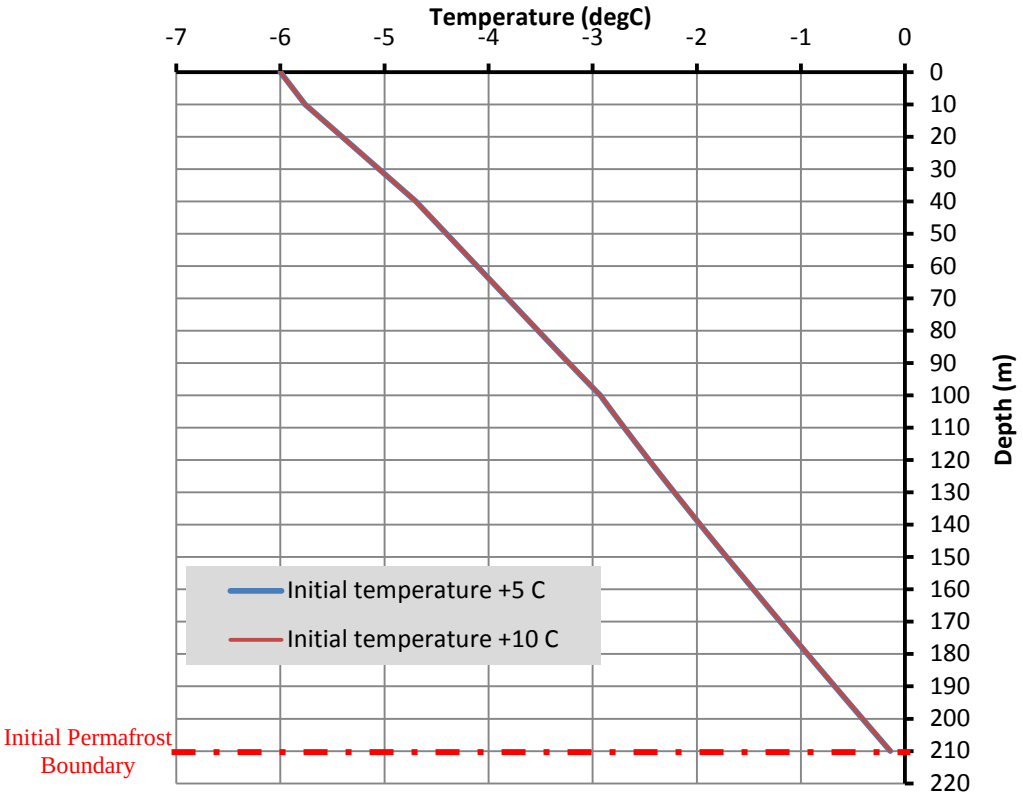

Figure 7-9 Thermal profile along line A-A within the East Zone TMF after 2000 years for two different initial tailing temperature

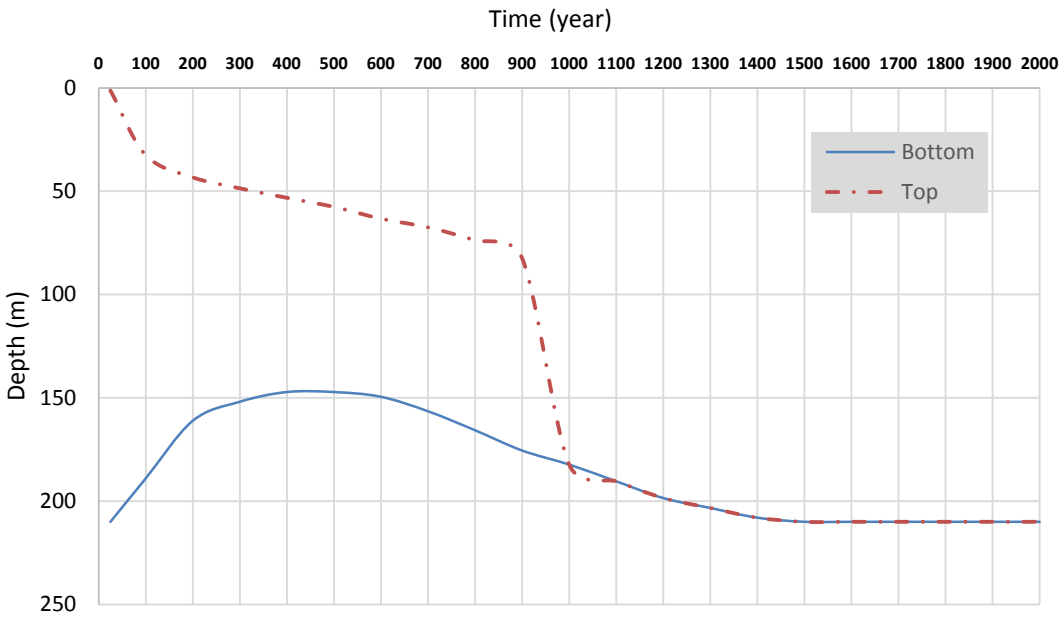

Figure 7-10 Permafrost evolution within the East Zone TMF up to 2000 year

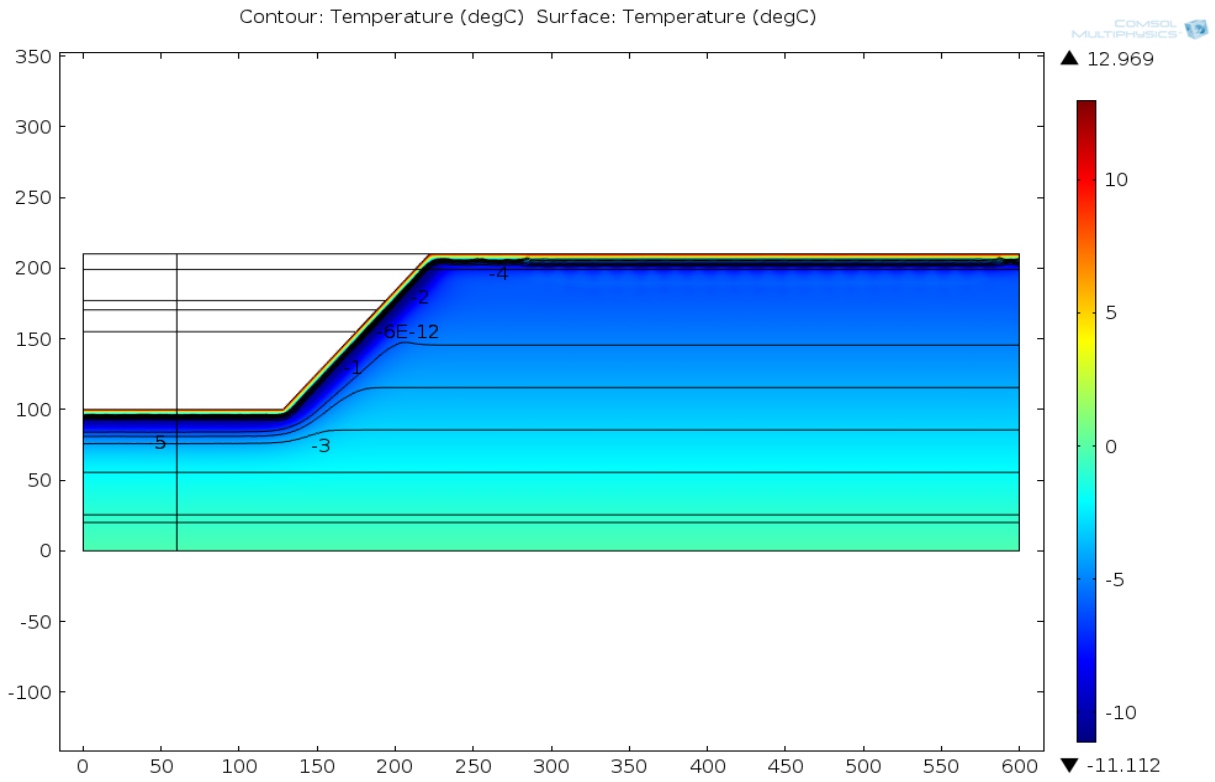

Figure 7-11 Centre Zone, End of excavation process and before filling with tailings

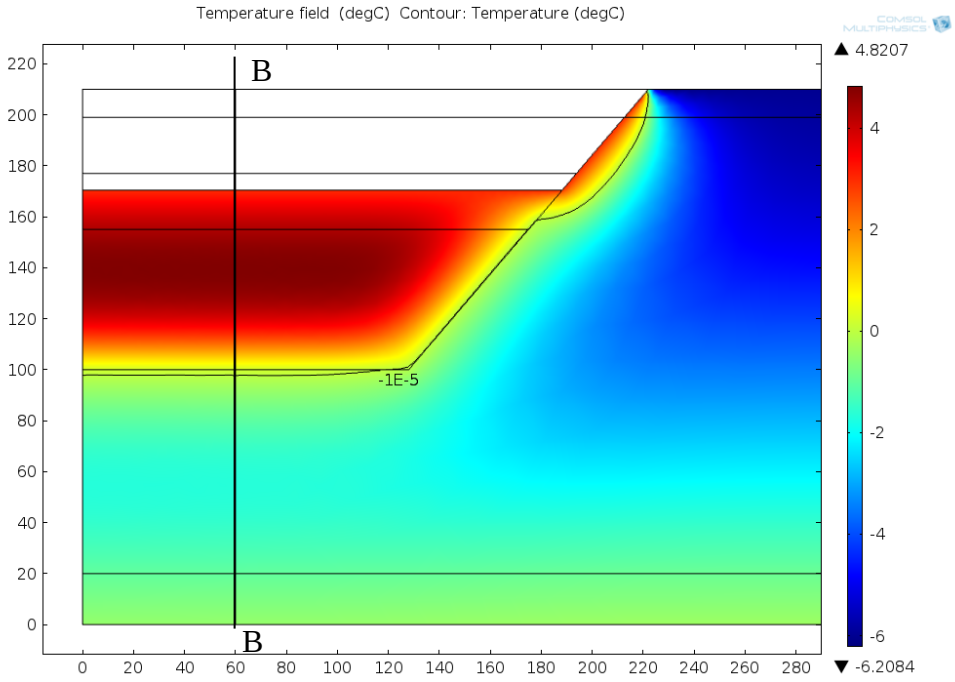

Figure 7-12 East Zone TMF, Thermal changes during stage 1 of consolidation, Initial tailings temperature +5ºC

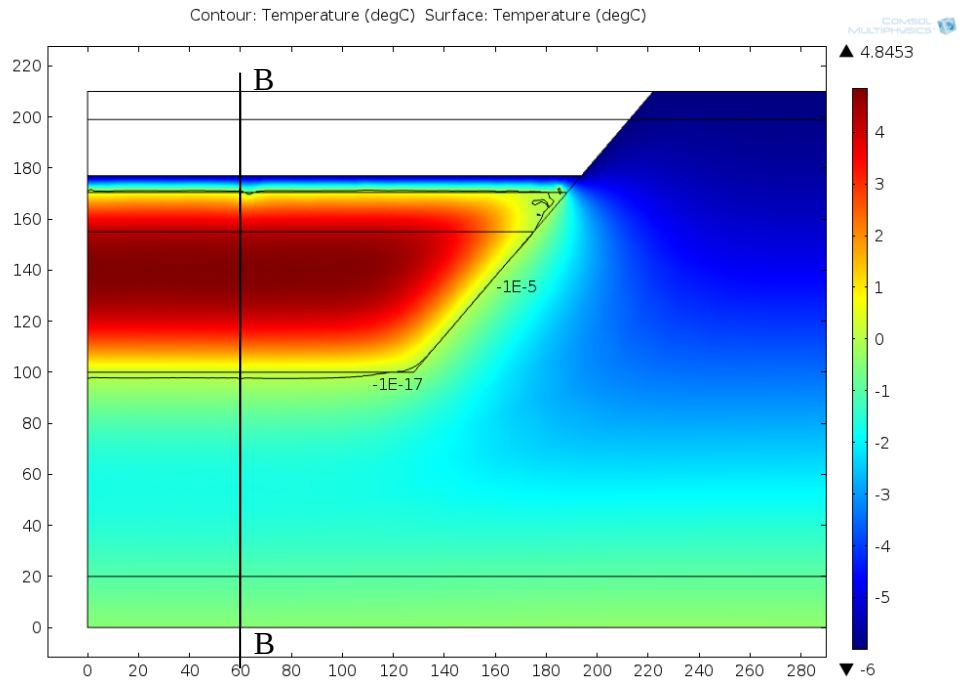

Figure 7-13 Centre Zone TMF, Thermal changes at the end of stage 2 of consolidation, Initial tailings temperature +5ºC

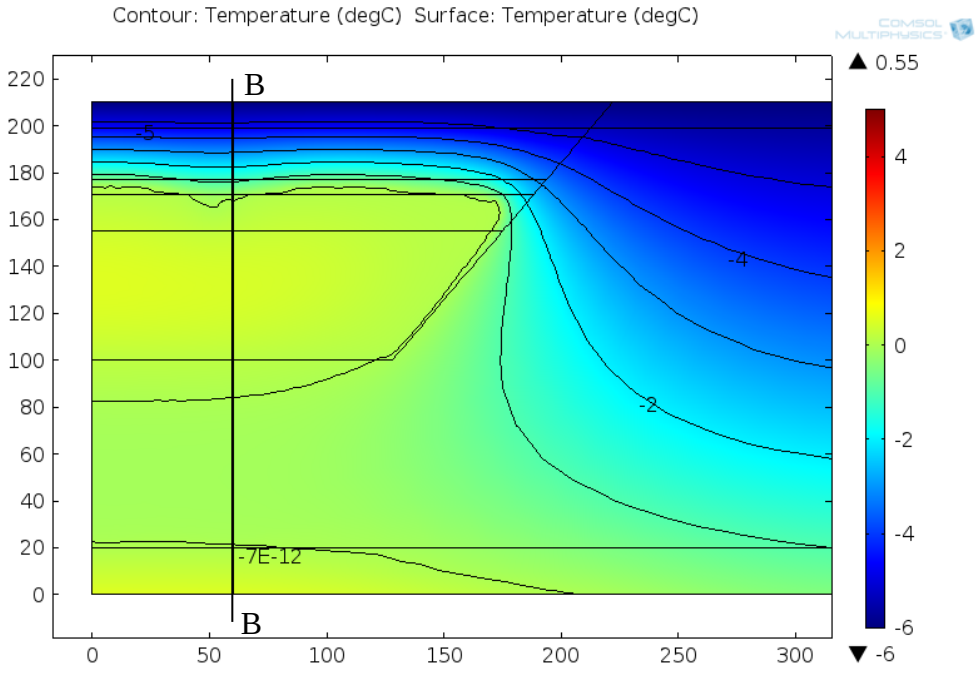

Figure 7-14 Centre Zone TMF, Thermal changes after 100 years, mine rocks are places on top of tailings, Initial tailings temperature +5ºC

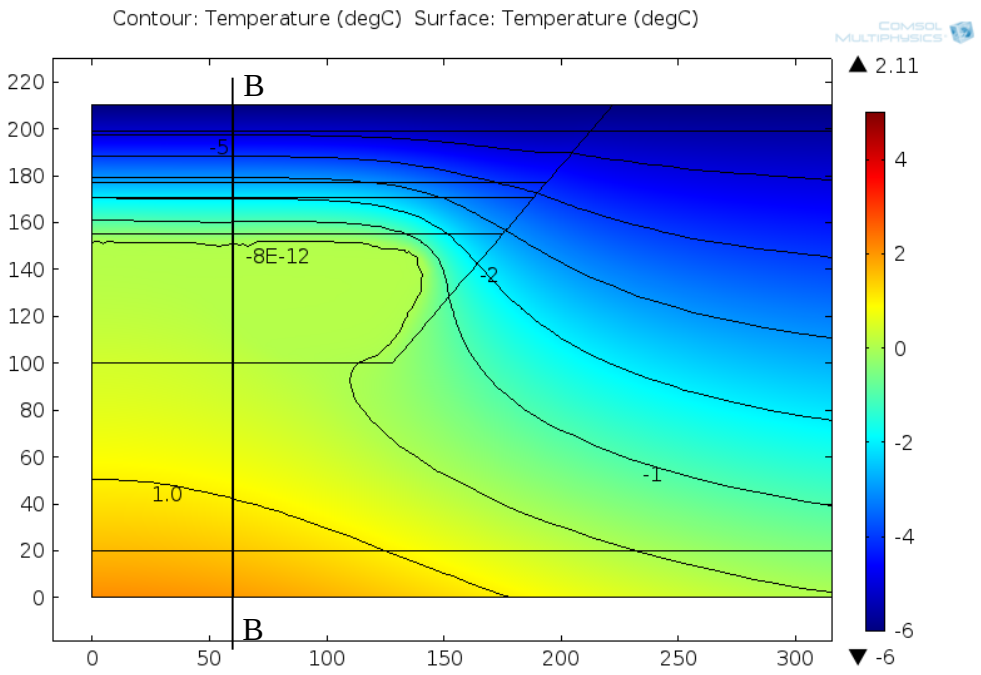

Figure 7-15 Centre Zone TMF, Thermal changes after 500 years, mine rocks are places on top of tailings, Initial tailings temperature +5ºC

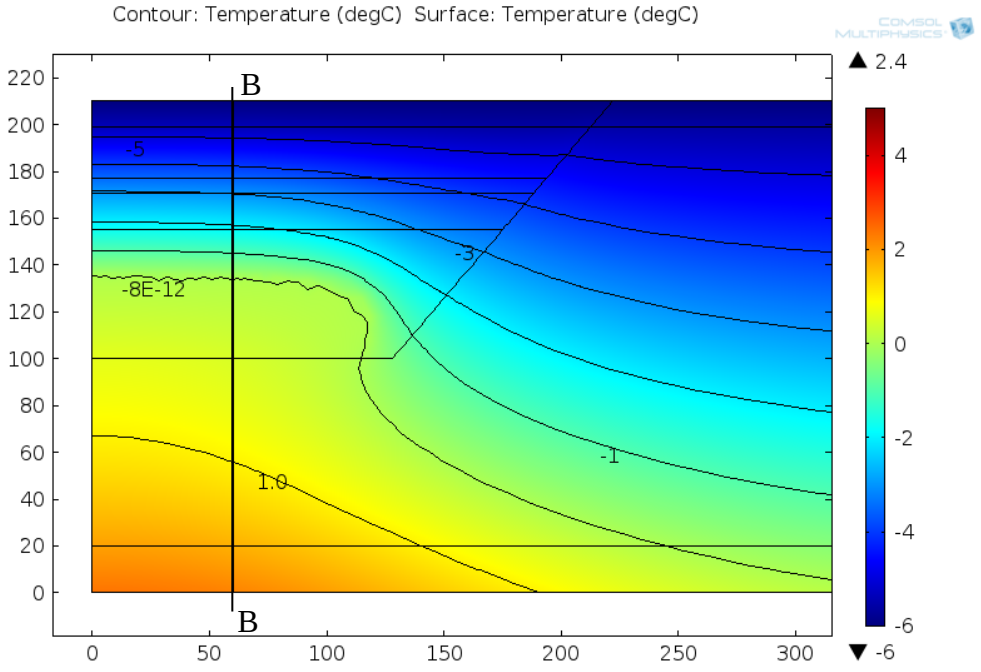

Figure 7-16 Centre Zone TMF, Thermal changes after 1000 years, mine rocks are places on top of tailings, Initial tailings temperature +5ºC

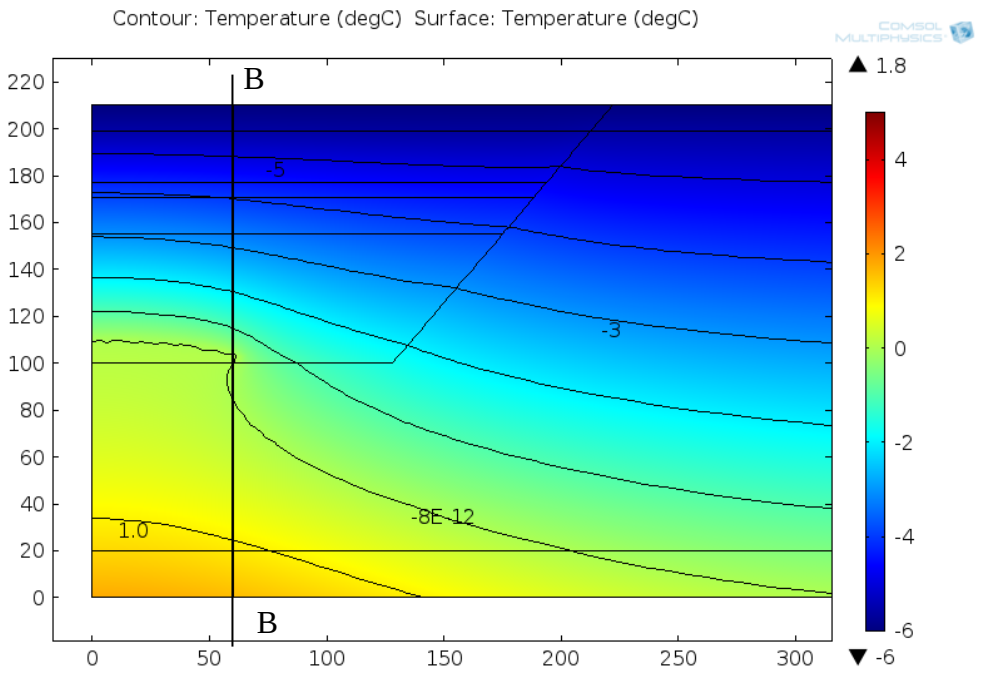

Figure 7-17 Centre Zone TMF, Thermal changes after 2000 years, mine rocks are places on top of tailings, Initial tailings temperature +5ºC

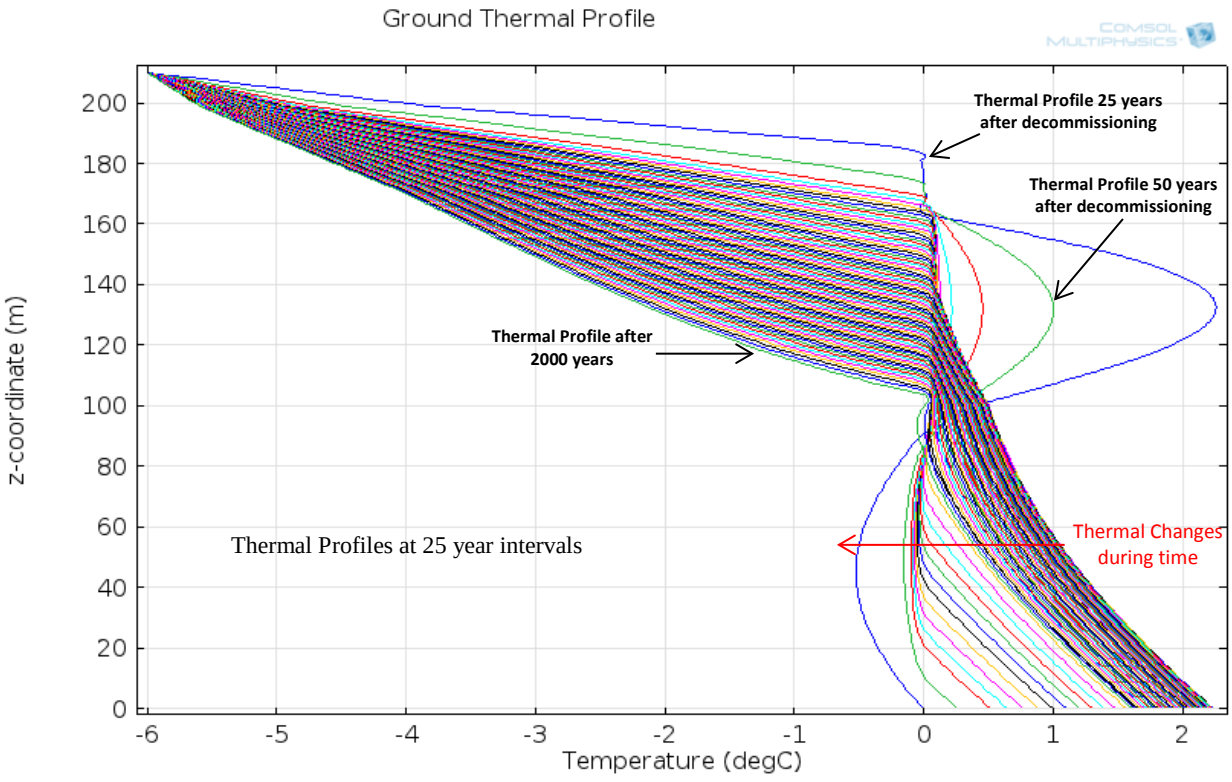

Figure 7-18 Thermal profile changes along line B-B within the Centre Zone TMF up to 2000 years after decommissioning at 25 year intervals: Initial tailings temperature +5ºC

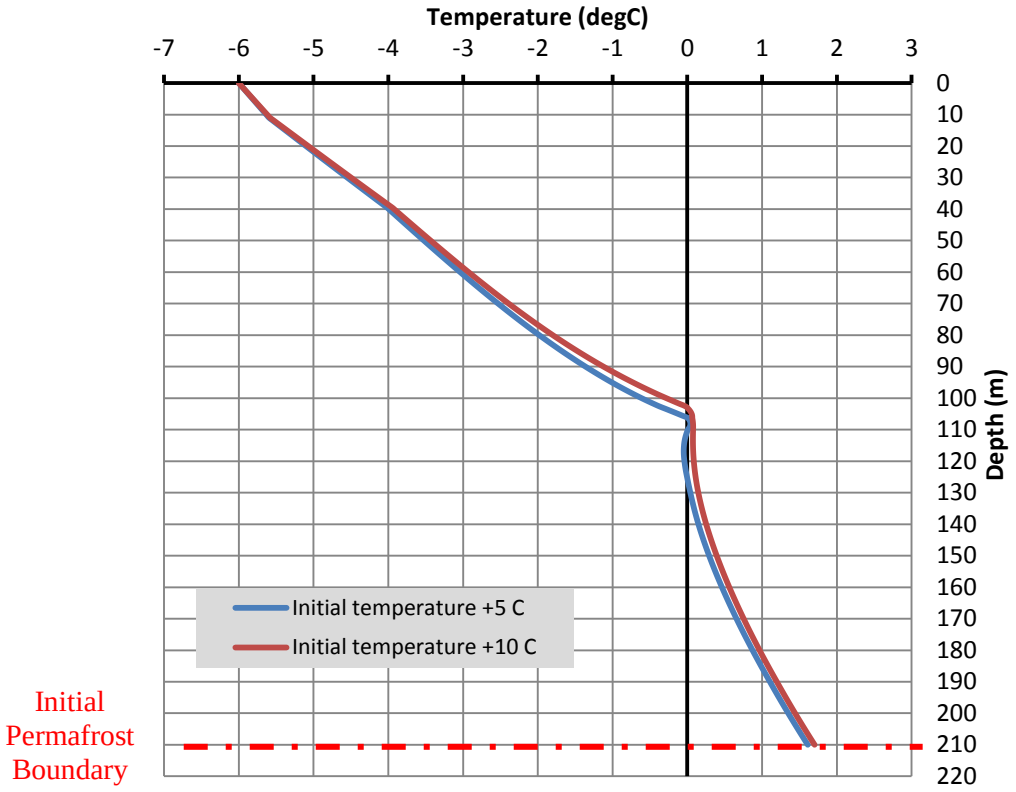

Figure 7-19 Thermal profile along line B-B within the Centre Zone TMF after 2000 years for two different initial tailing temperatures

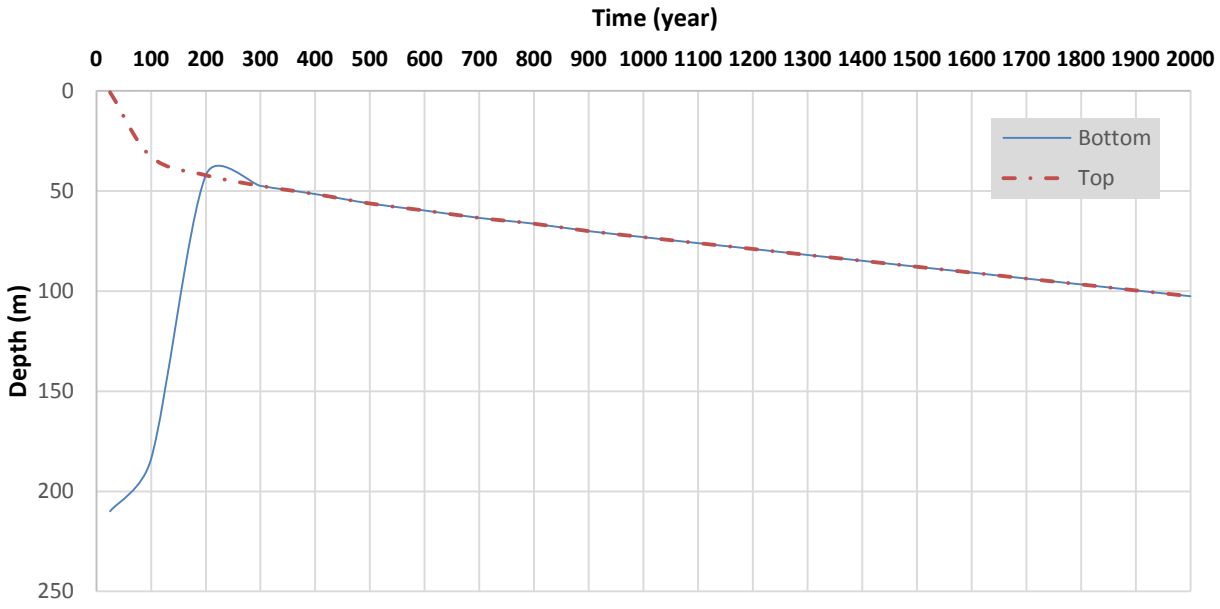

Figure 7-20 Permafrost evolution within the Centre Zone TMF up to 2000 years

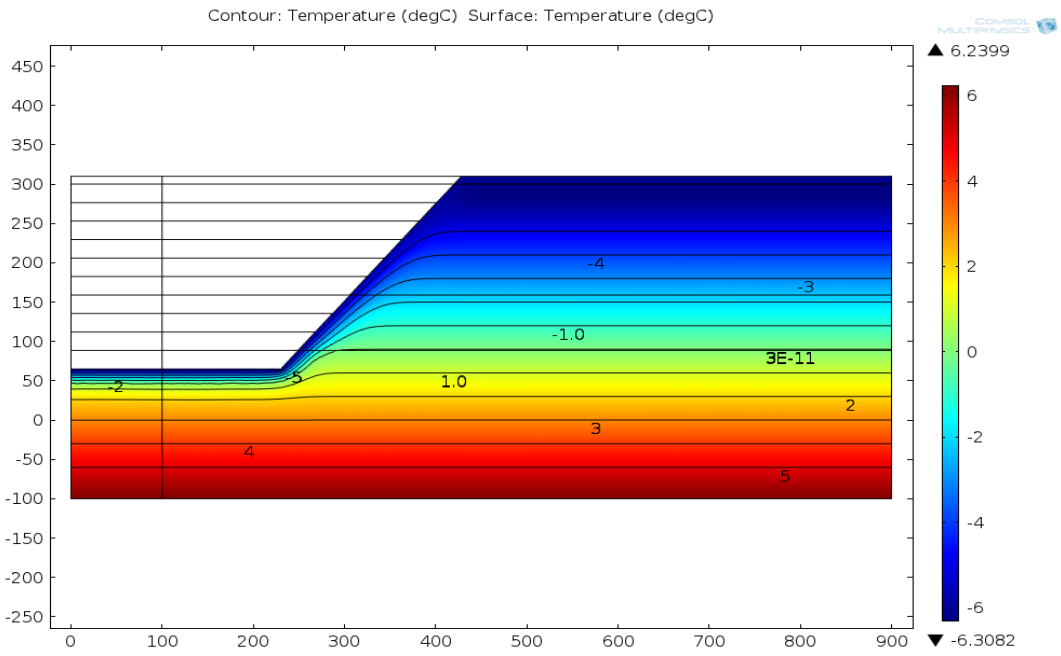

Figure 7-21 Main Zone, End of excavation process, and before filling with tailings

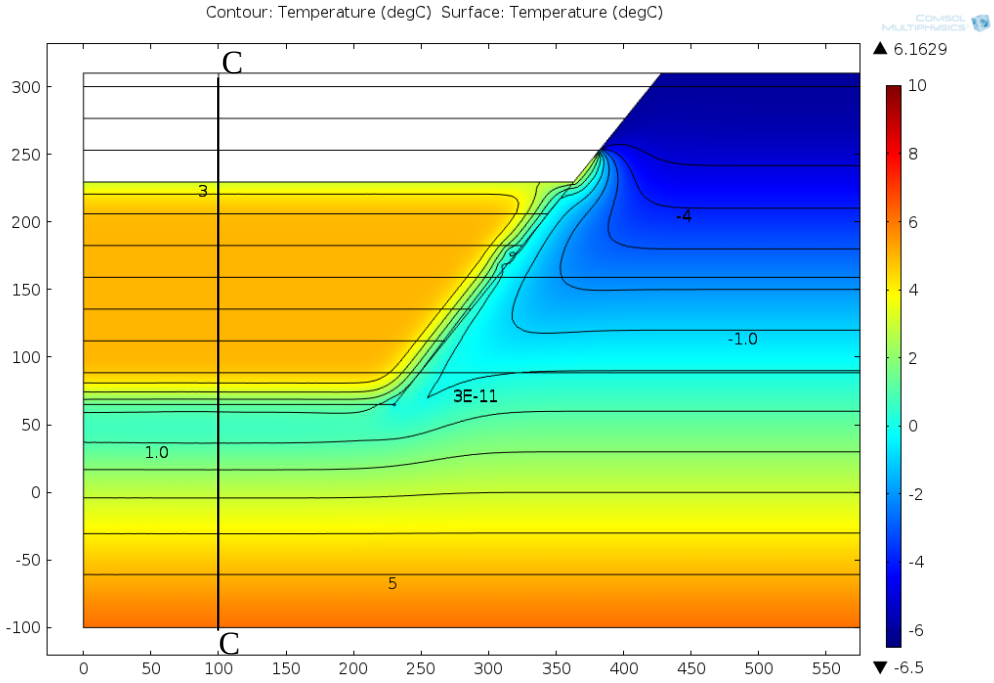

Figure 7-22 Main Zone TMF, Thermal changes at the end of consolidation Process, and initial tailings temperature +5ºC

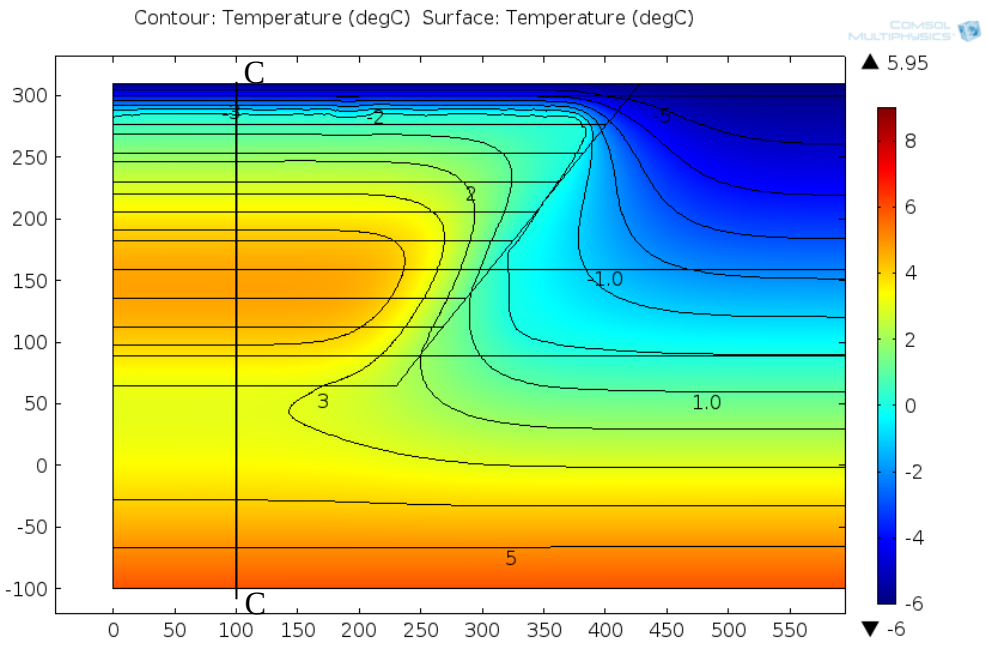

Figure 7-23 Main Zone TMF, Thermal changes after 50 years, mine rocks are placed on top of tailings, and initial tailings temperature +5ºC

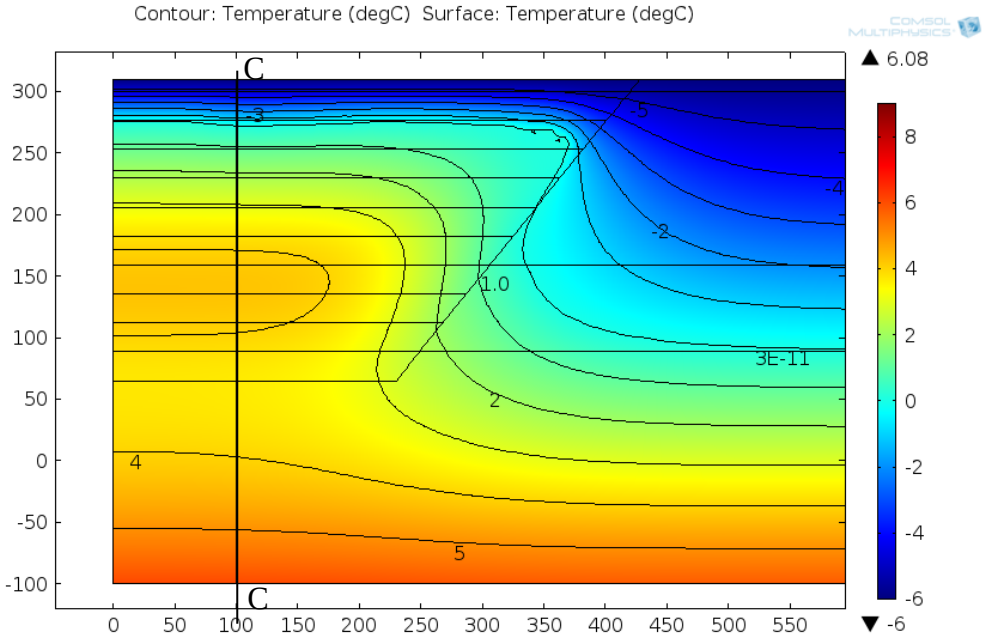

Figure 7-24 Main Zone TMF, Thermal changes after 100 years, mine rocks are placed on top of tailings, and initial tailings temperature +5ºC

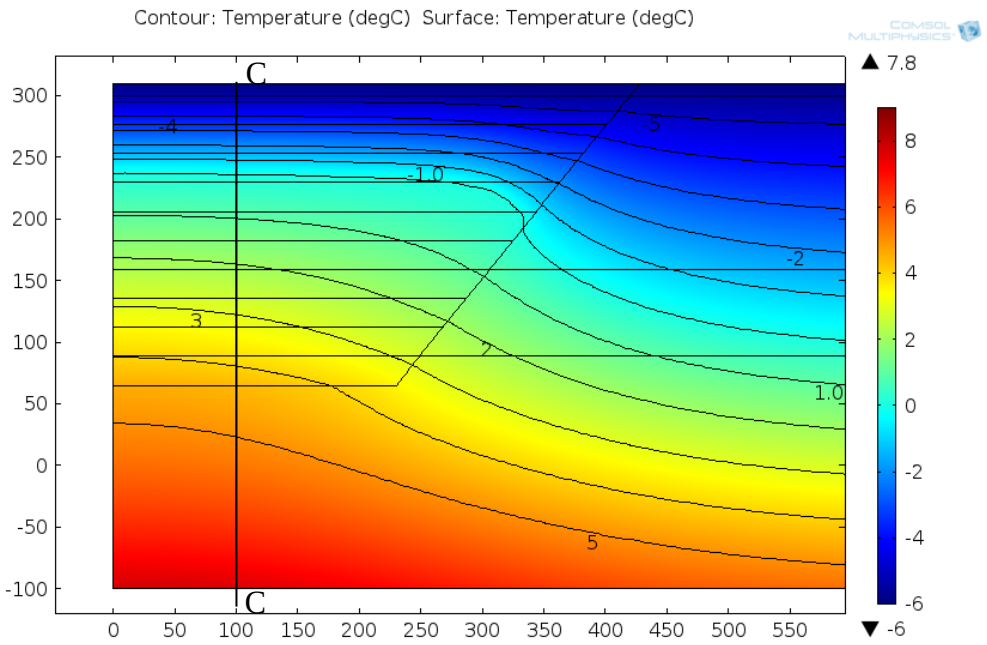

Figure 7-25 Main Zone TMF, Thermal changes after 500 years, mine rocks are places on top of tailings, and initial tailings temperature +5ºC

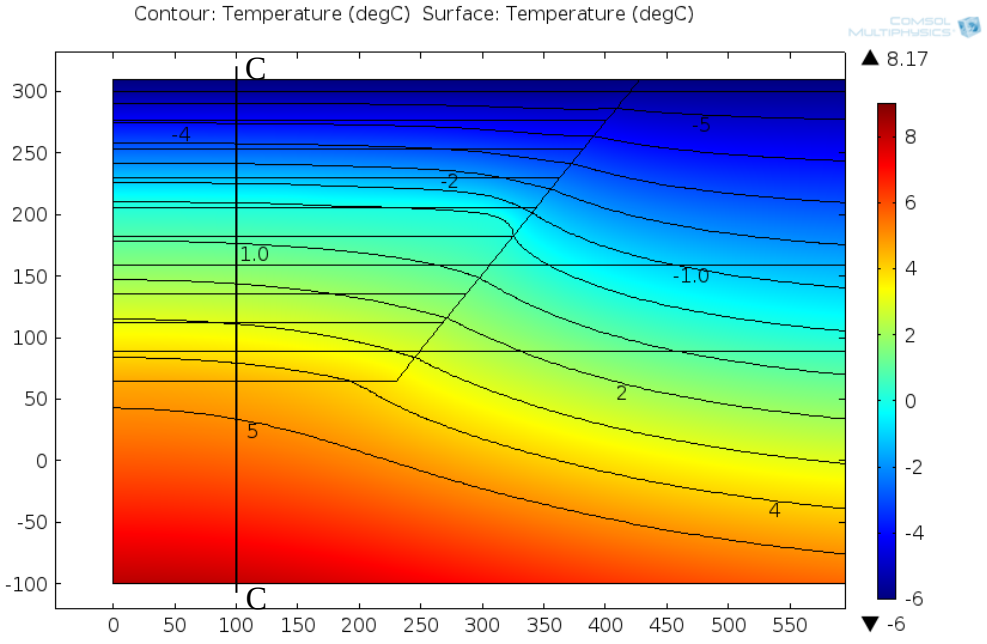

Figure 7-26 Main Zone TMF, Thermal changes after 1000 years, mine rocks are places on top of tailings, and initial tailings temperature +5ºC

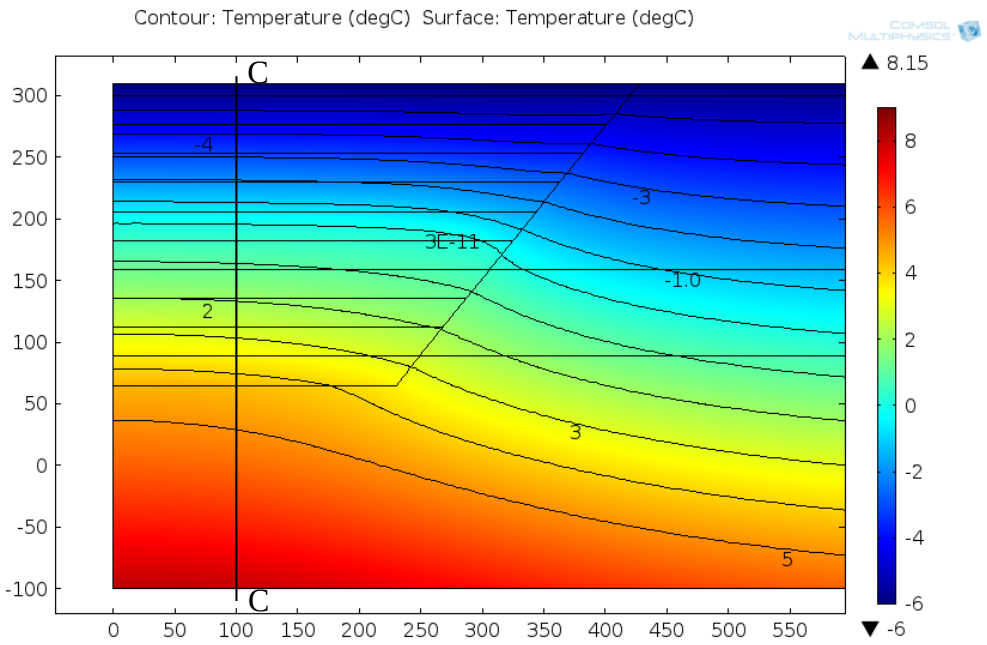

Figure 7-27 Main Zone TMF, Thermal changes after 2000 years, mine rocks are places on top of tailings, and initial tailings temperature +5ºC

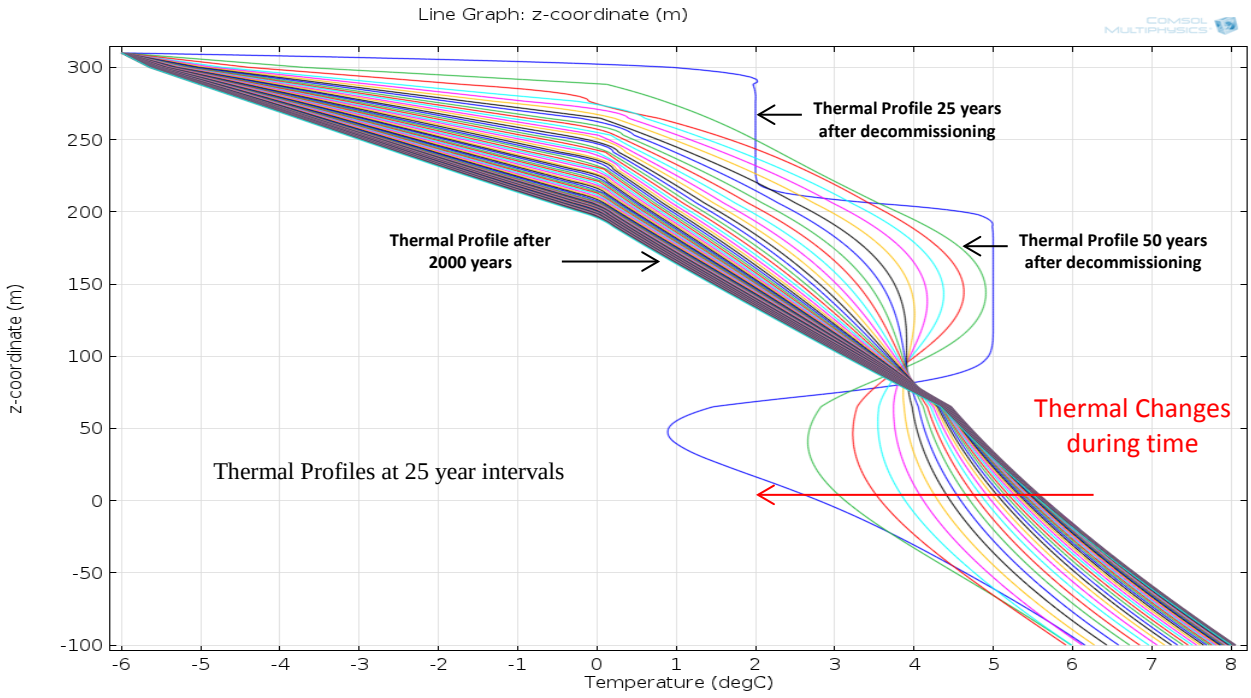

Figure 7-28 Thermal profile changes along line C-C within the Main Zone TMF up to 2000 years after decommissioning at 25 year intervals, and initial tailings temperature +5ºC

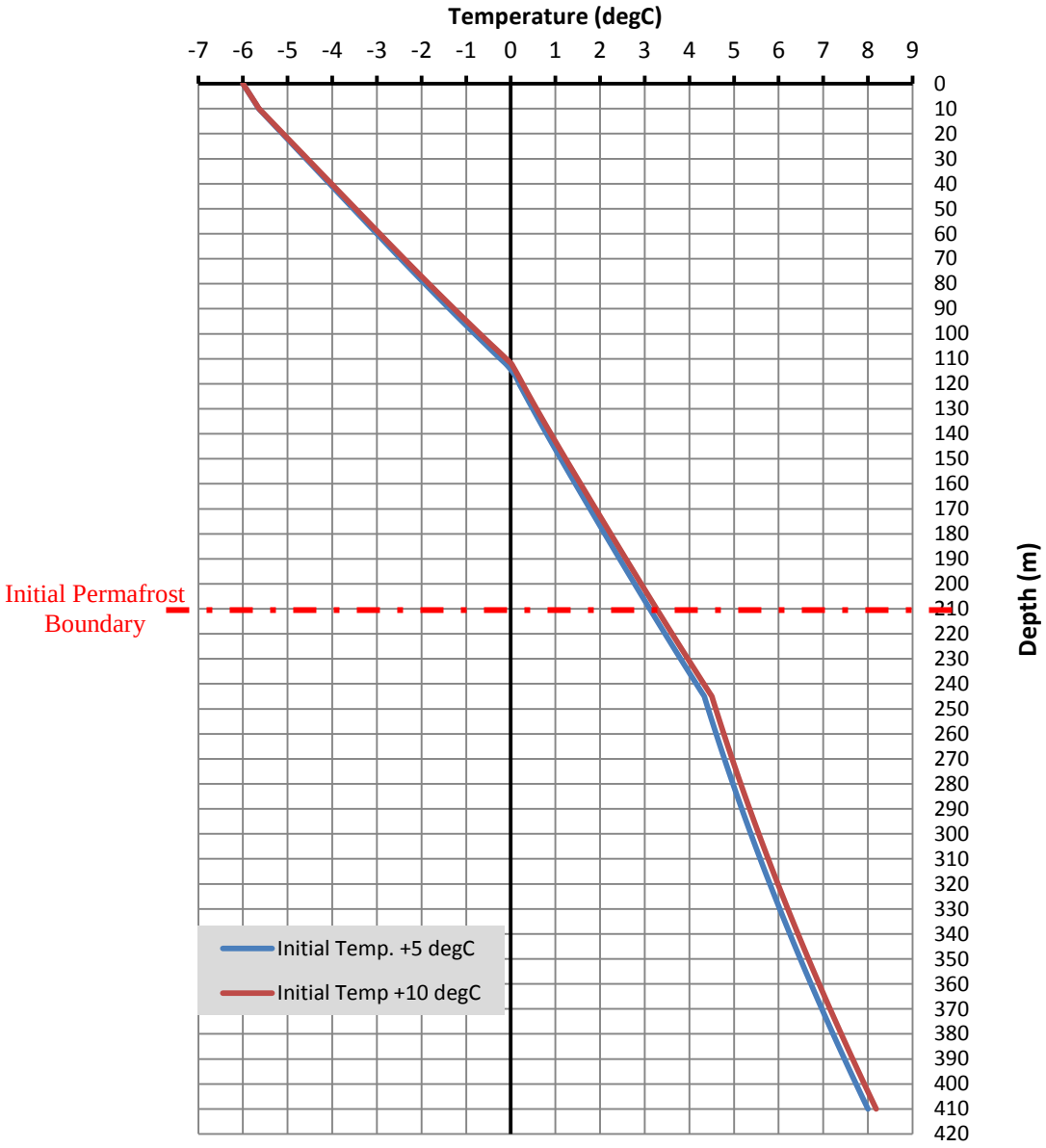

Figure 7-29 Thermal profile along line C-C within the Main Zone TMF after 2000 years for two different initial tailing temperatures

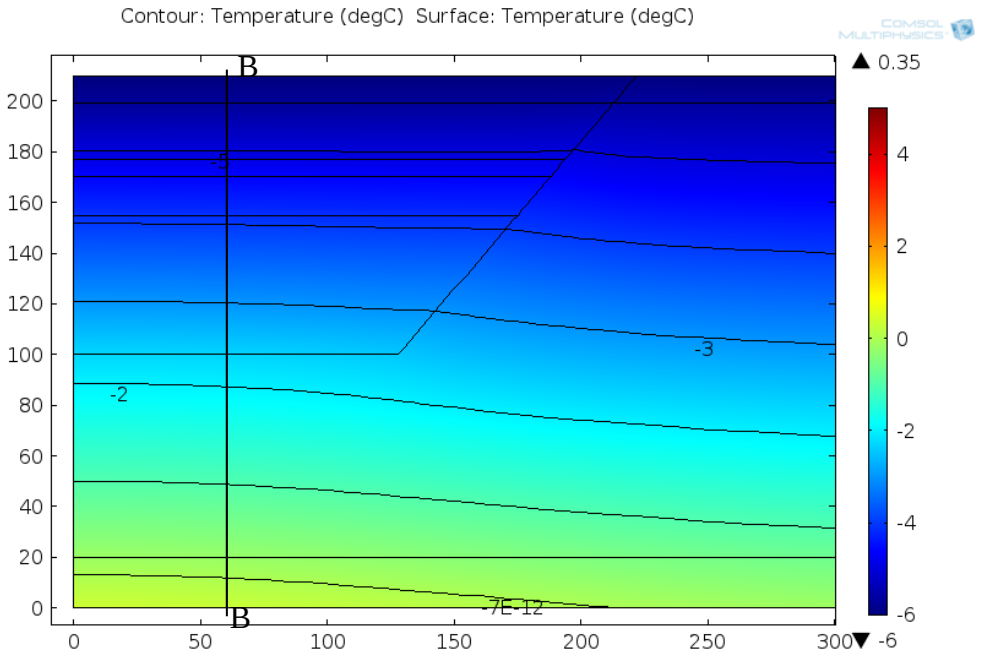

Figure 7-30 Centre Zone TMF, Thermal changes after 3000 years, mine rocks are places on top of tailings, and initial tailings temperature +5°C

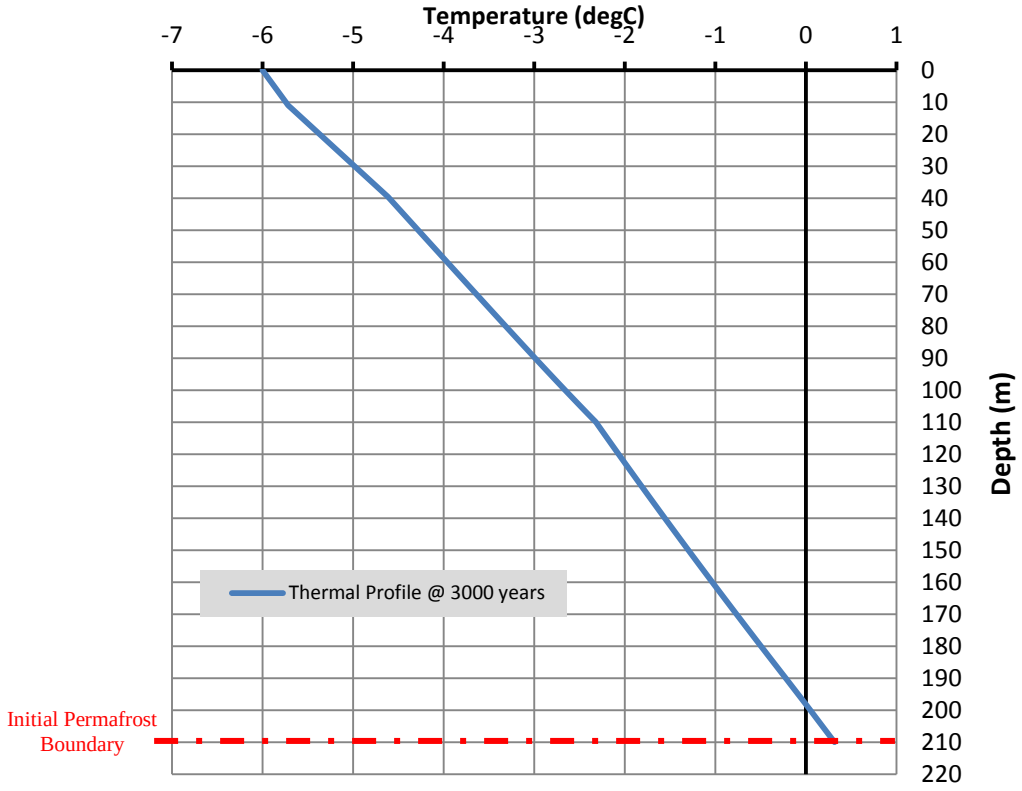

Figure 7-31 Thermal profile along line B-B within the Centre Zone TMF after 3000 years

8 Scenario 2: Temperature Increases from -6ºC to -1ºC

In this second proposed climate change scenario, it is assumed that the mean ground surface temperature in Northern Canada is increasing eventually from -6ºC, the current condition, to -1ºC in a period of 100 years (section 4.2). Impacts of this climate change pattern on the permafrost inside and around the TMFs in the Kiggavik project are hereby assessed.

As results of the first climate change scenario indicate (Figures 7-9, 7-19, and 7-29), the impact of the initial tailings temperature was found to be negligible in the long-term. Therefore, for this scenario, only the case of tailings with an initial temperature of +5ºC is considered. It is also assumed that during the short-term operational time, the climate is almost stable, and climate change becomes operative only after the decommissioning is completed. Since the thermal simulation results during the consolidation stages are the same as in the previous climate change scenario, these are not presented in this section to avoid repetition.

In the following, first the simulation results for all the TMFs are presented followed by the analyses of results in section 9.4.

8.1 Summary of Numerical Result Simulations

Since the mean annual ground surface temperature is increasing in this climate change scenario, it is expected that the permafrost thickness will be reduced in the long-term. However, the tailings material with high water content will change the ground thermal properties and as such impact the thermal changes.

Before investigating the impact of climate change on the pits filled with tailings, as a baseline case, it is better to first examine what will happen to the permafrost in the long-term under a climate change. Figure 8-1 shows the temperature distribution after 2000 years for the permafrost at the Kiggavik project location when temperature increases from -6ºC to -1ºC. Also, the change in the permafrost boundary location as a function of time is shown in Figure 9-2. It is seen that the permafrost boundary reaches a depth of about 45 m to 50 m below ground surface after 2000 years. Based on a review of numerical results presented in Figures 8-3 to 8-25, the following main observations have been identified.

It is found that for all the TMFs, the permafrost boundary reached a depth of about 35 m below the ground surface after about 2000 years; see Figures 8-9, 8-17, and 8-25. However, the ground temperatures around the TMFs are not the same for all the pits. This is in contrast with the case where no pits were considered and where the permafrost thickness reached a depth of 50 m after 2000 years (Figures 8-1 and 8-2). The main reason for this difference is due to the water contents of the tailings and original ground material being dissimilar. It is to be noted that even after consolidation, the tailings contain about 50% water content by volume, while the average original ground material water content is about 5%. Hence, more thermal energy is bound to be exchanged to convert the deposited tailings into frozen materials.

In Figures 8-2, 8-10, and 8-18, permafrost evolution as a result of the climate change is indicated for the original permafrost, East Zone TMF, and Centre Zone TMF, respectively. Considering the original frozen ground far from the mining activity (Figure 8-2), the permafrost thickness is decreasing eventually from about 210m to 50m after 2000 years due to the climate change occurring above the ground surface. Meanwhile, within the East Zone and Centre Zone TMF, the tailings material is freezing from the top since the mean ground surface temperature, $-1^{\circ}C$, is still below the freezing point of water inside the pore spaces. However, the original frozen ground beneath the TMF is thawing due to the changes in the mean ground surface temperature and presence of warm tailings inside the TMF. Eventually, the two freezing fronts merge together after about 500 years for both East Zone and Centre Zone TMF (Figures 8-10 and 8-18).

In summary, within this climate change scenario, although most parts of the TMFs remained unfrozen even after 2000 years, a 35 m thick layer of almost impermeable ground will be formed on top of the tailings. This could act as a protective layer for the facilities at the ground surface from any radioactive or other hazardous material migrating upward to the ground surface. However, these materials could eventually migrate into the underground water regime or large surface water bodies. In the end, the quantity of the migrated contaminants will depend on the hydrogeological properties of the rocks.

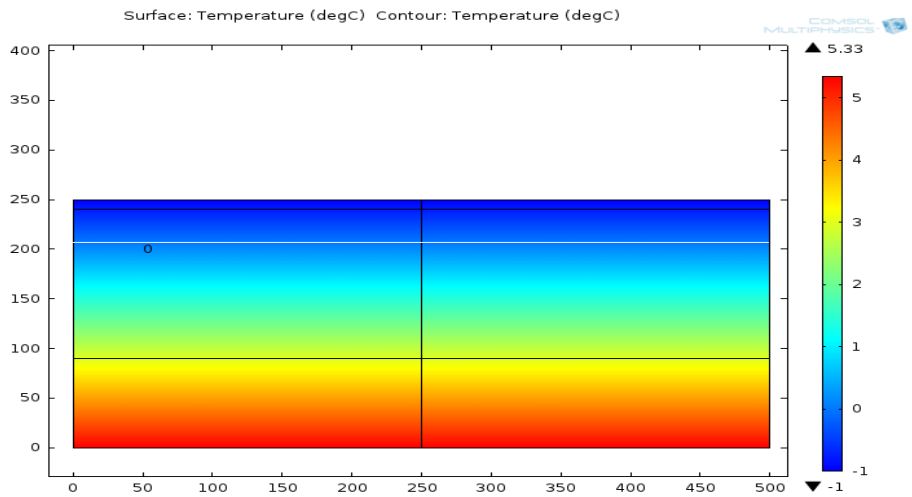

Figure 8-1 Ground temperature after 2000 years, Second climate change scenario

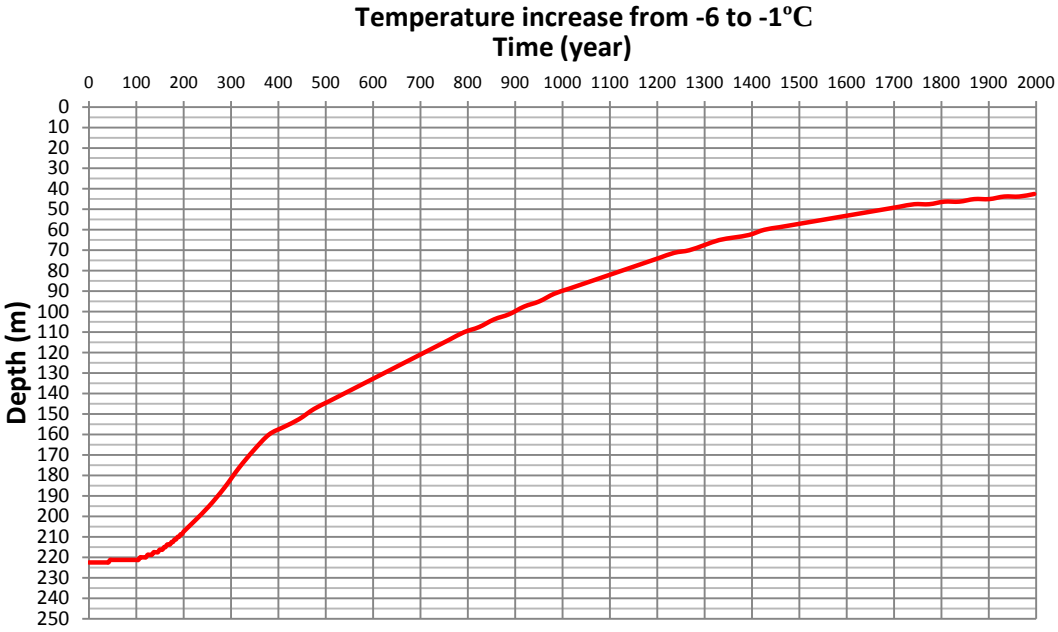

Figure 8-2 Evolution of permafrost boundary, Second climate change scenario

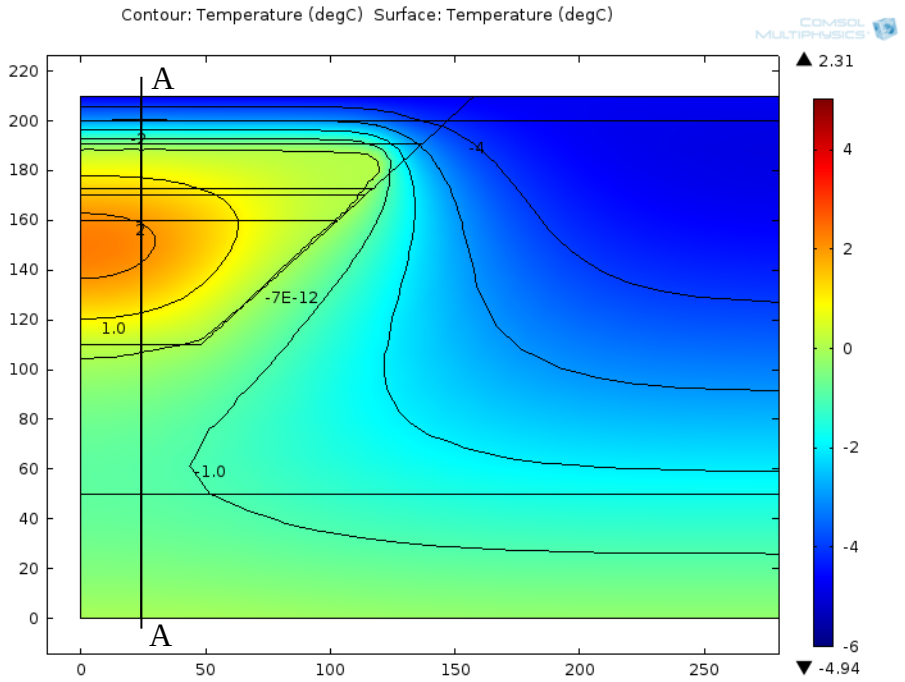

Figure 8-3 East Zone TMF, Thermal changes after 50 years, Second climate change scenario, Initial tailings temperature +5ºC

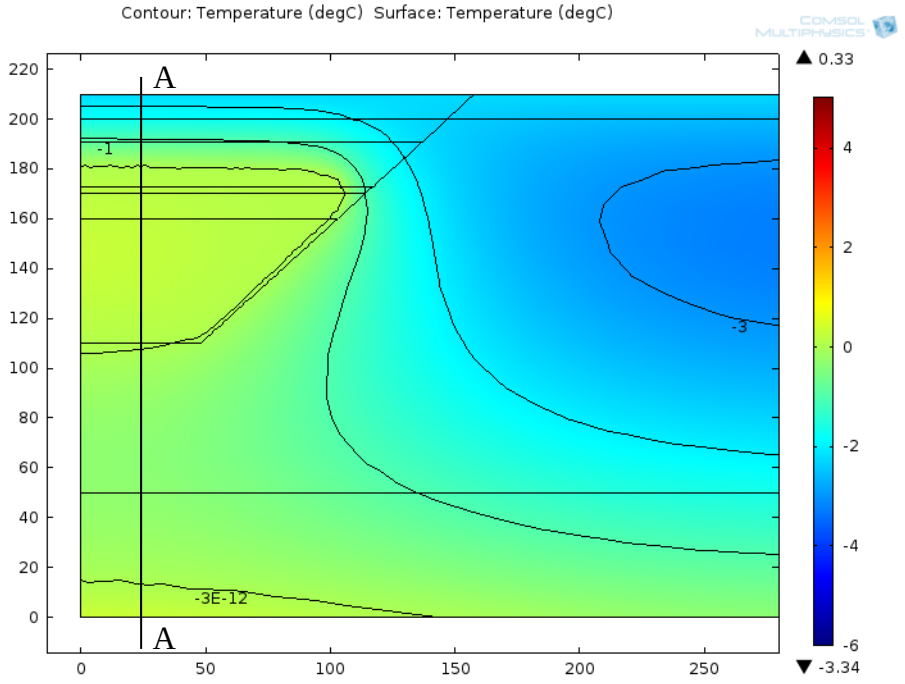

Figure 8-4 East Zone TMF, Thermal changes after 100 years, Second climate change scenario, Initial tailings temperature +5ºC

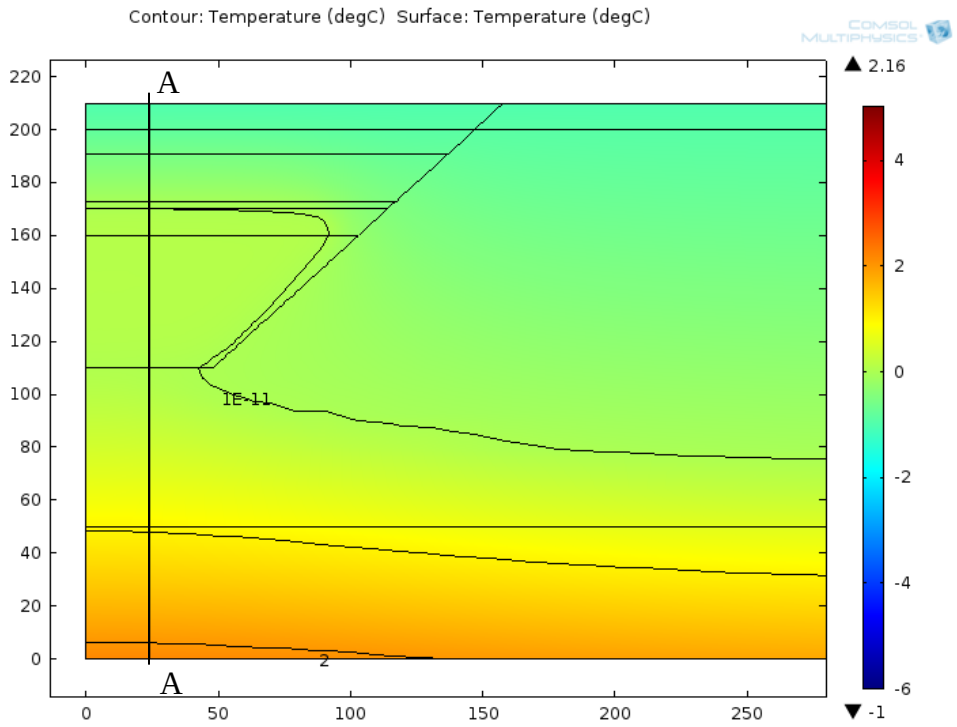

Figure 8-5 East Zone TMF, Thermal changes after 500 years, Second climate change scenario, Initial tailings temperature +5ºC

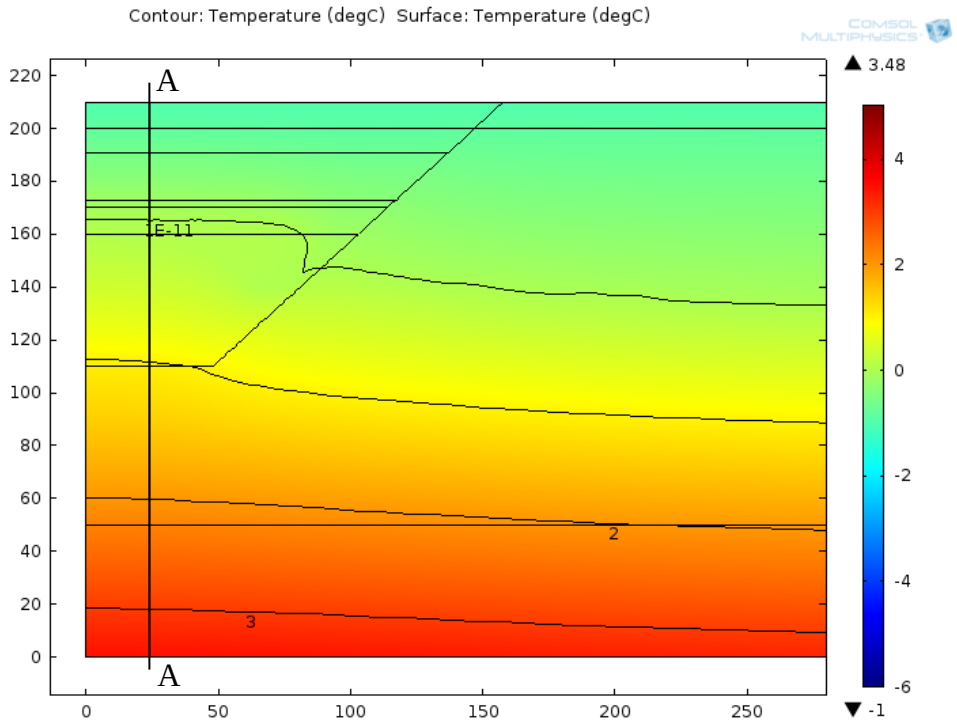

Figure 8-6 East Zone TMF, Thermal changes after 1000 years, Second climate change scenario, Initial tailings temperature +5ºC

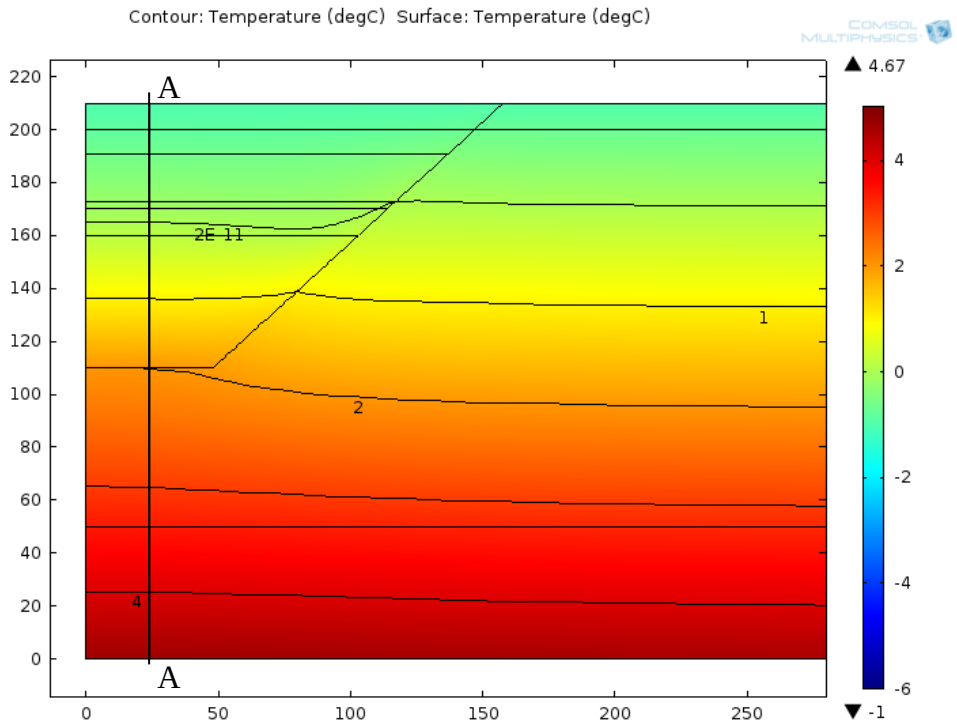

Figure 8-7 East Zone TMF, Thermal changes after 2000 years, Second climate change scenario, Initial tailings temperature +5ºC

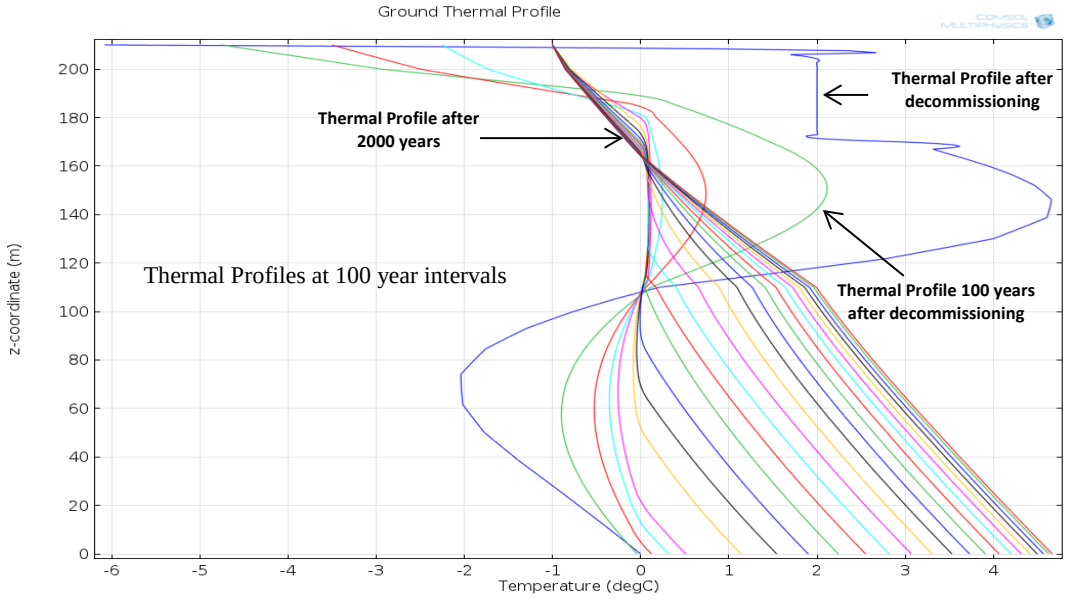

Figure 8-8 Thermal profile changes along line A-A within the East Zone TMF up to 2000 years after decommissioning at 100 year intervals, Initial tailings temperature +5ºC

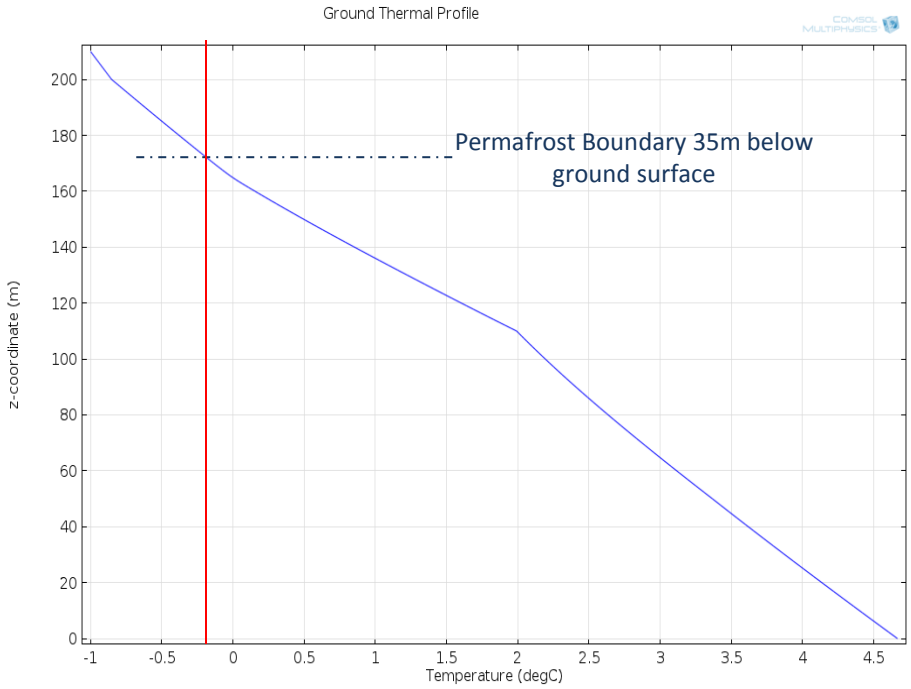

Figure 8-9 Thermal profile along line A-A within the East Zone TMF after 2000 years, Initial tailings temperature +5ºC

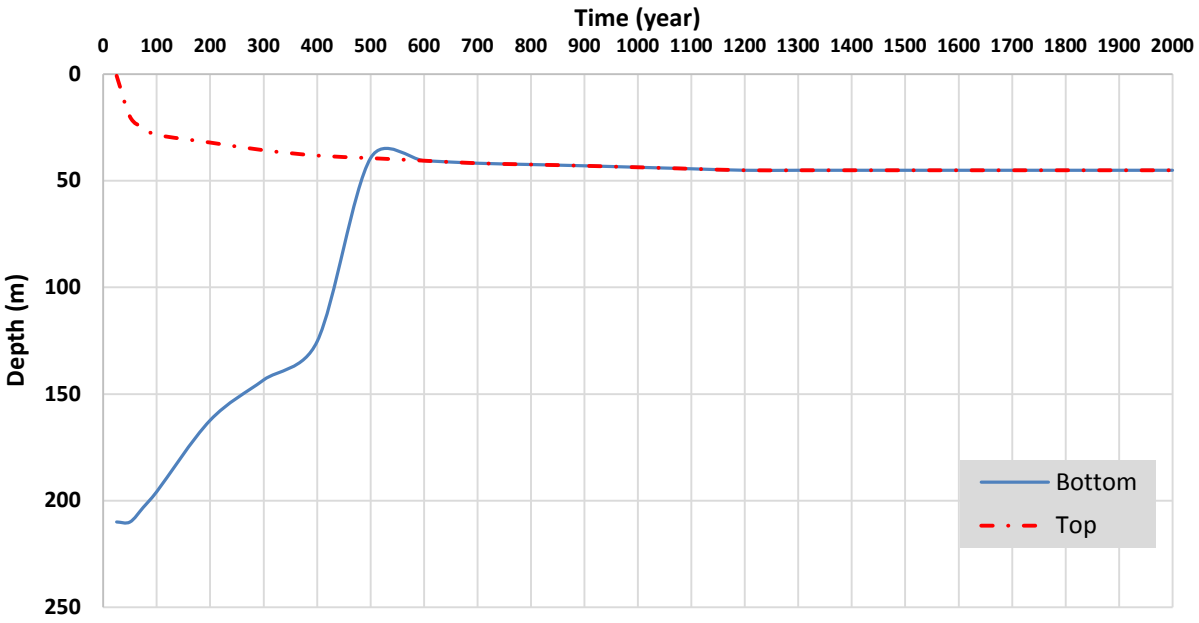

Figure 8-10 Permafrost evolution within the East Zone TMF up to 2000 year

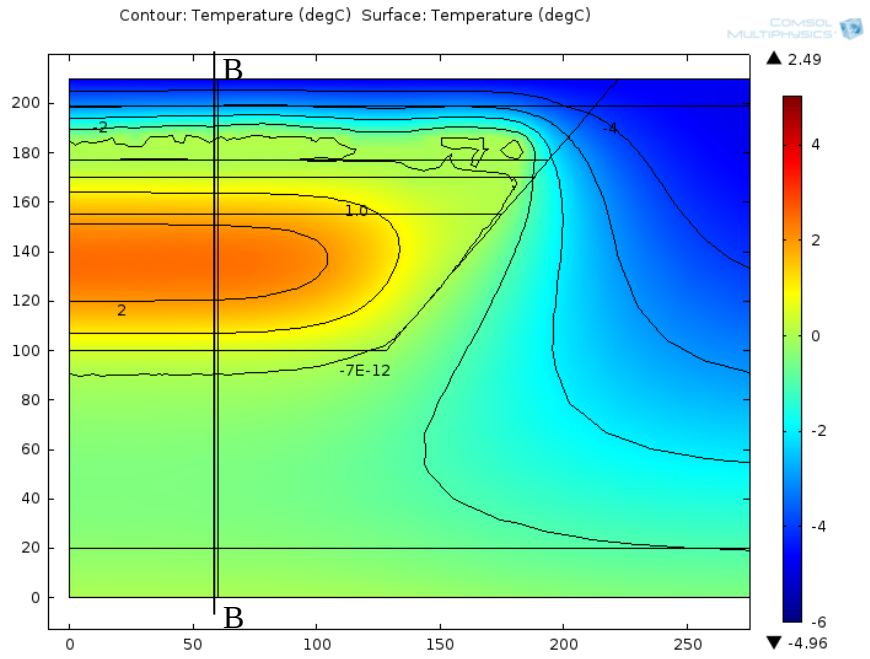

Figure 8-11 Centre Zone TMF, Thermal changes after 50 years, Second climate change scenario, Initial tailings temperature +5ºC

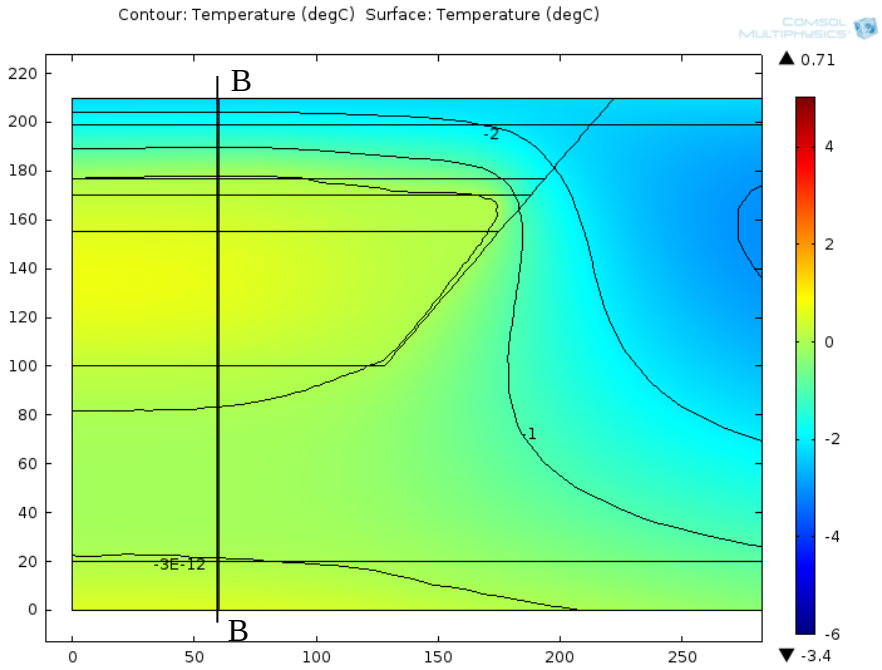

Figure 8-12 Centre Zone TMF, Thermal changes after 100 years, Second climate change scenario, Initial tailings temperature +5ºC

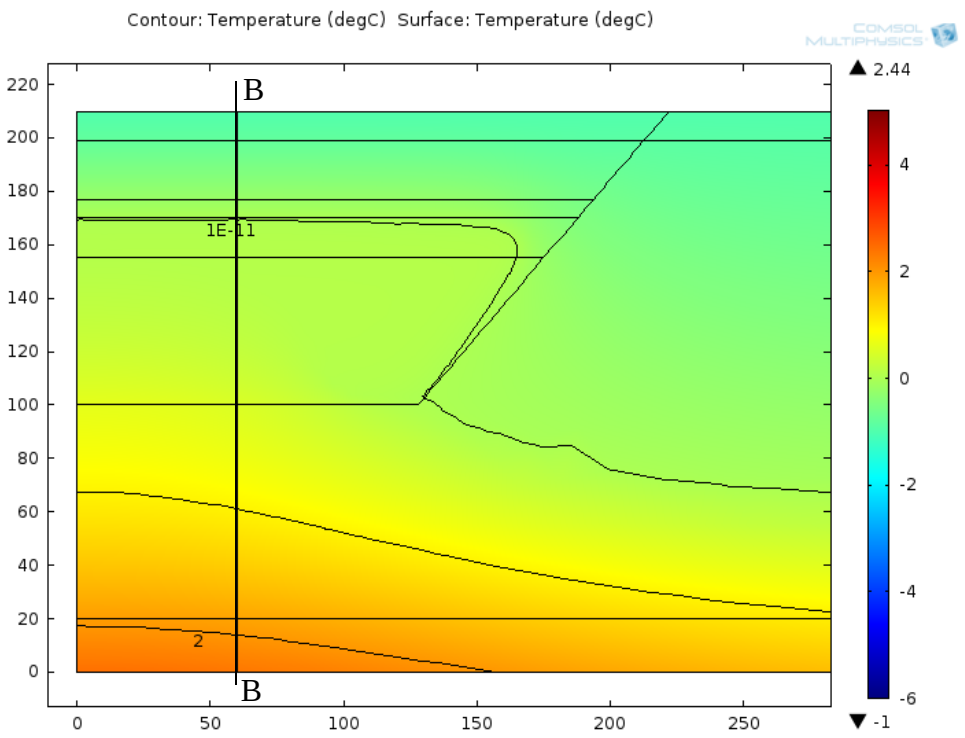

Figure 8-13 Centre Zone TMF, Thermal changes after 500 years, Second climate change scenario, Initial tailings temperature +5ºC

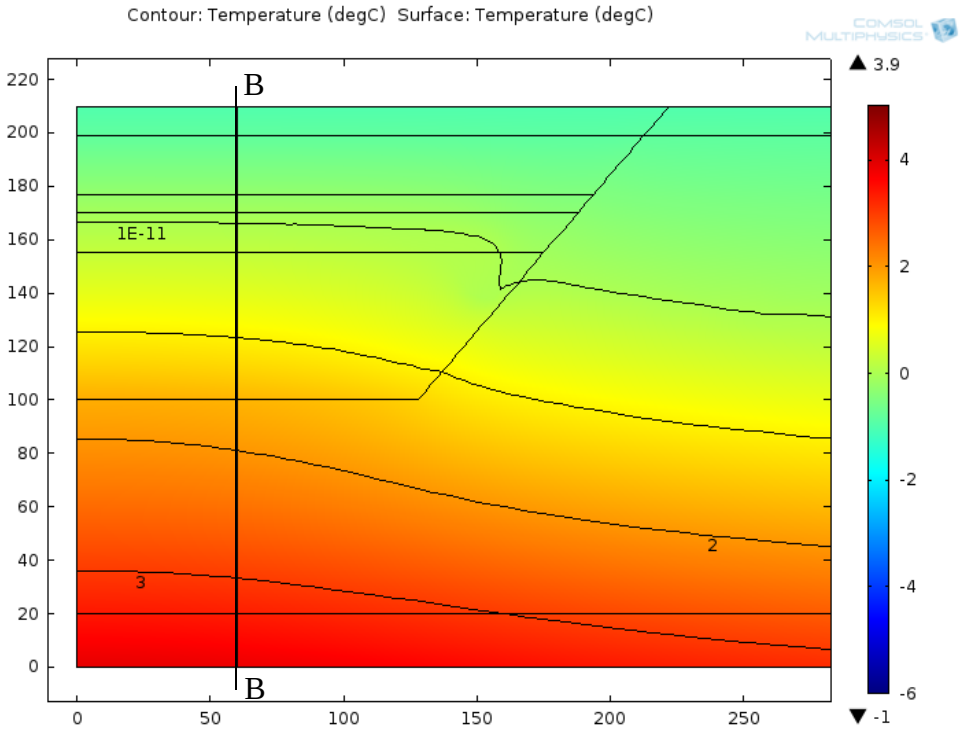

Figure 8-14 Centre Zone TMF, Thermal changes after 1000 years, Second climate change scenario, Initial tailings temperature +5ºC

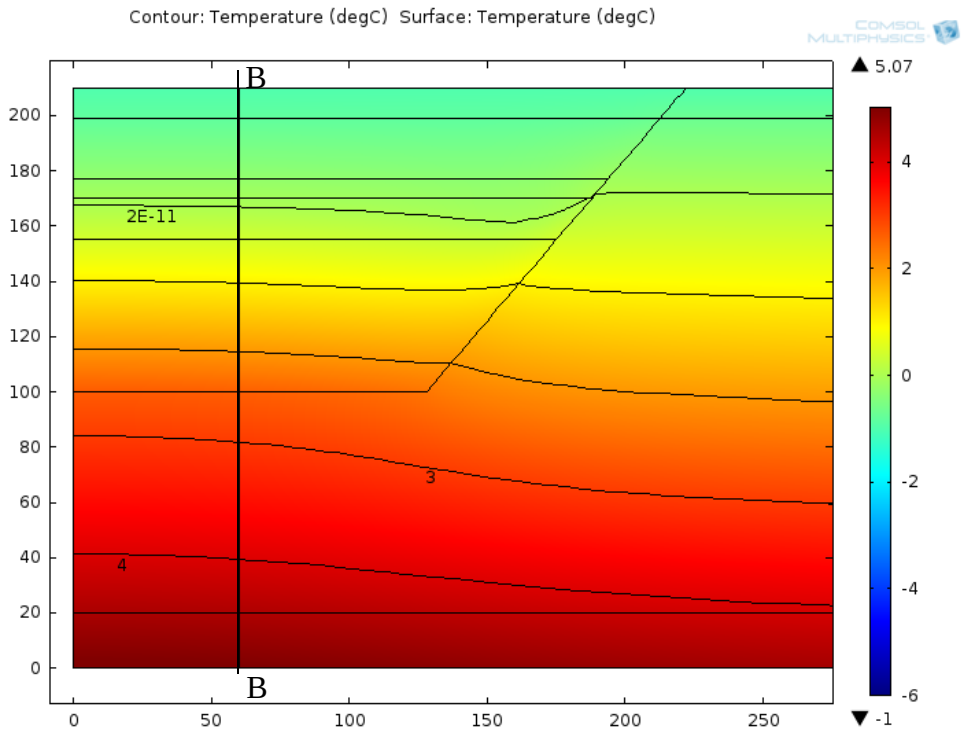

Figure 8-15 Centre Zone TMF, Thermal changes after 2000 years, Second climate change scenario, Initial tailings temperature +5ºC

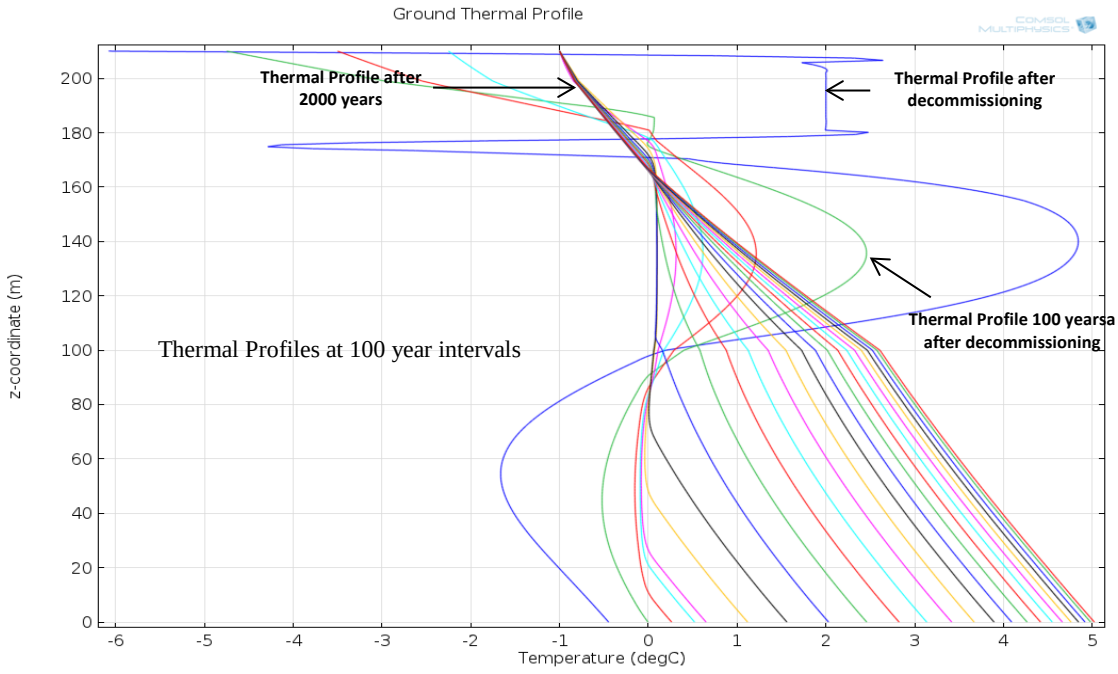

Figure 8-16 Thermal profile changes along line B-B within the Centre Zone TMF up to 2000 years after decommissioning at 100 year intervals, Initial tailings temperature +5ºC

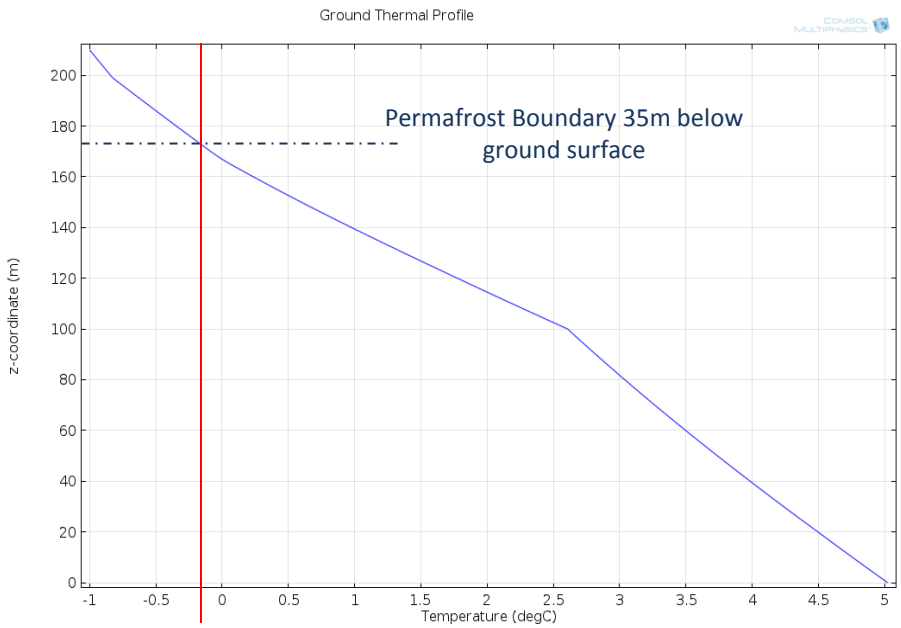

Figure 8-17 Thermal profile along line B-B within the Centre Zone TMF after 2000 years, Initial tailings temperature +5°C

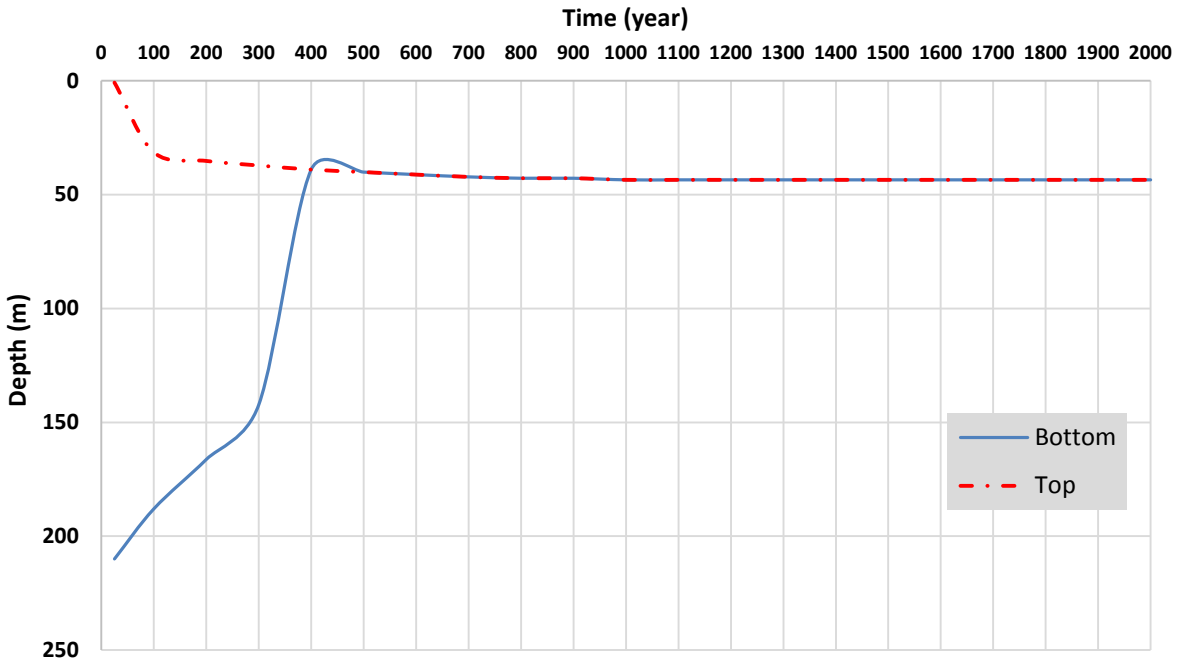

Figure 8-18 Permafrost evolution within the Centre Zone TMF up to 2000 year

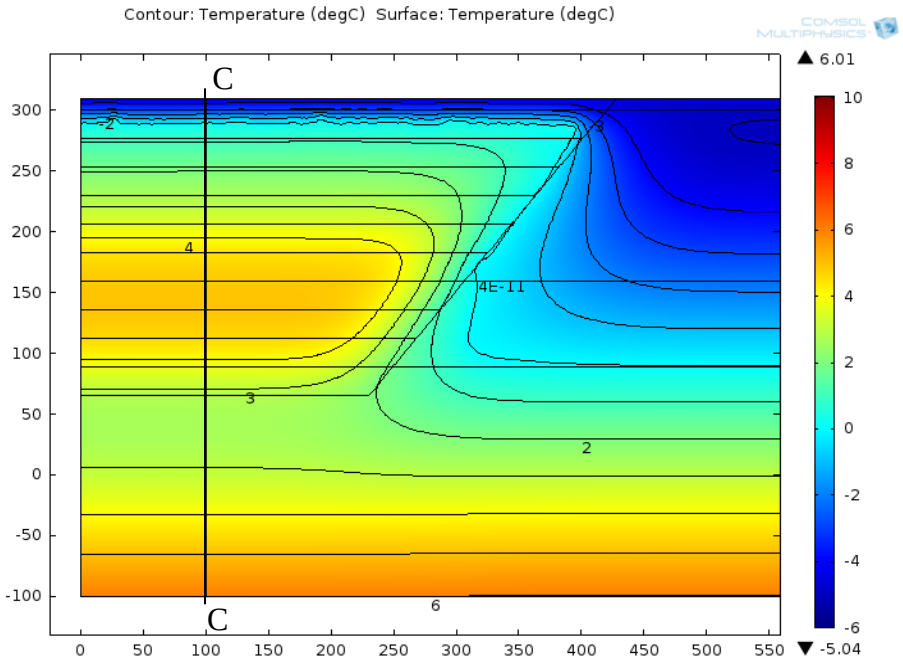

Figure 8-19 Main Zone TMF, Thermal changes after 50 years, Second climate change scenario, Initial tailings temperature +5ºC

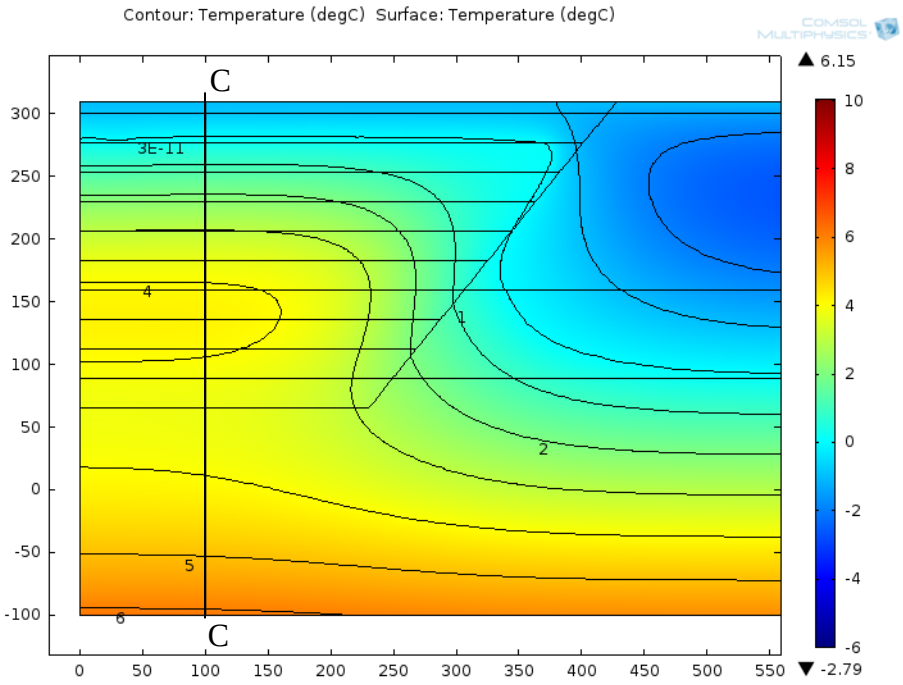

Figure 8-20 Main Zone TMF, Thermal changes after 100 years, Second climate change scenario, Initial tailings temperature +5ºC

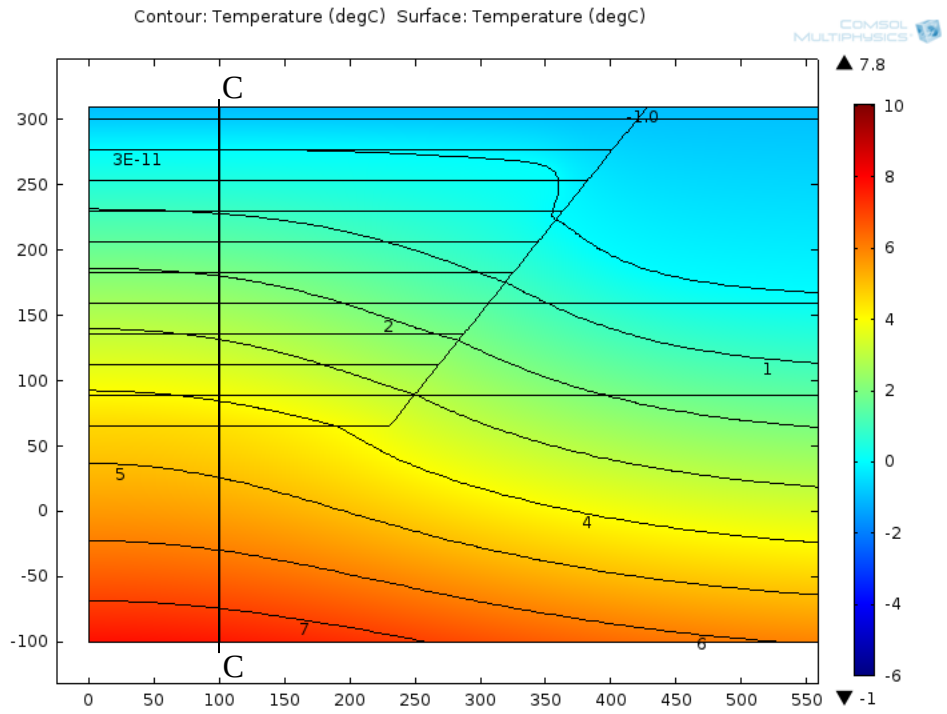

Figure 8-21 Main Zone TMF, Thermal changes after 500 years, Second climate change scenario, Initial tailings temperature +5ºC

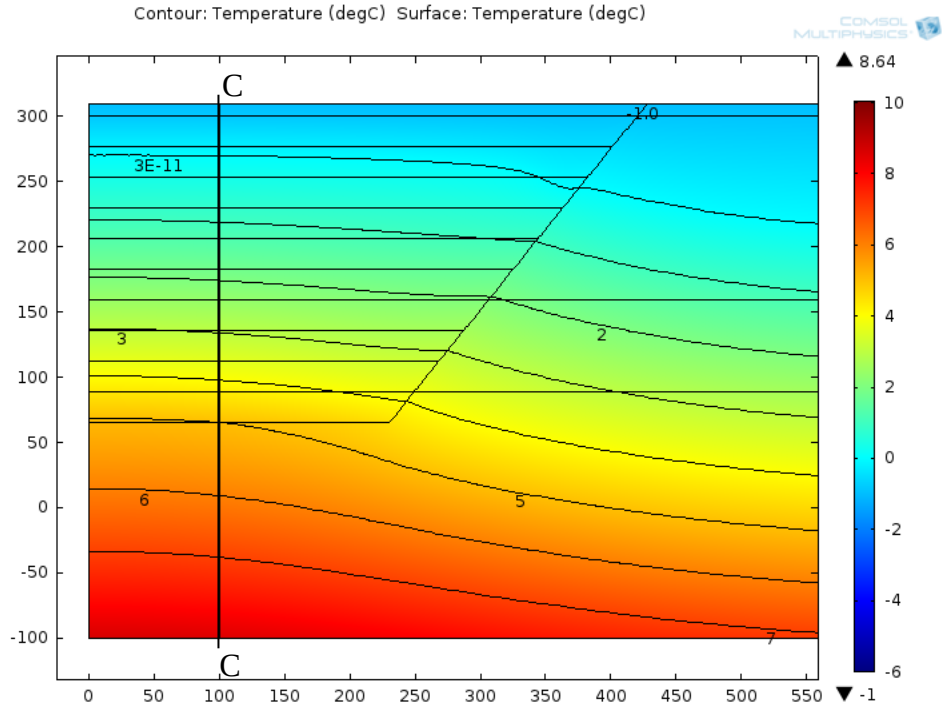

Figure 8-22 Main Zone TMF, Thermal changes after 1000 years, Second climate change scenario, Initial tailings temperature +5ºC

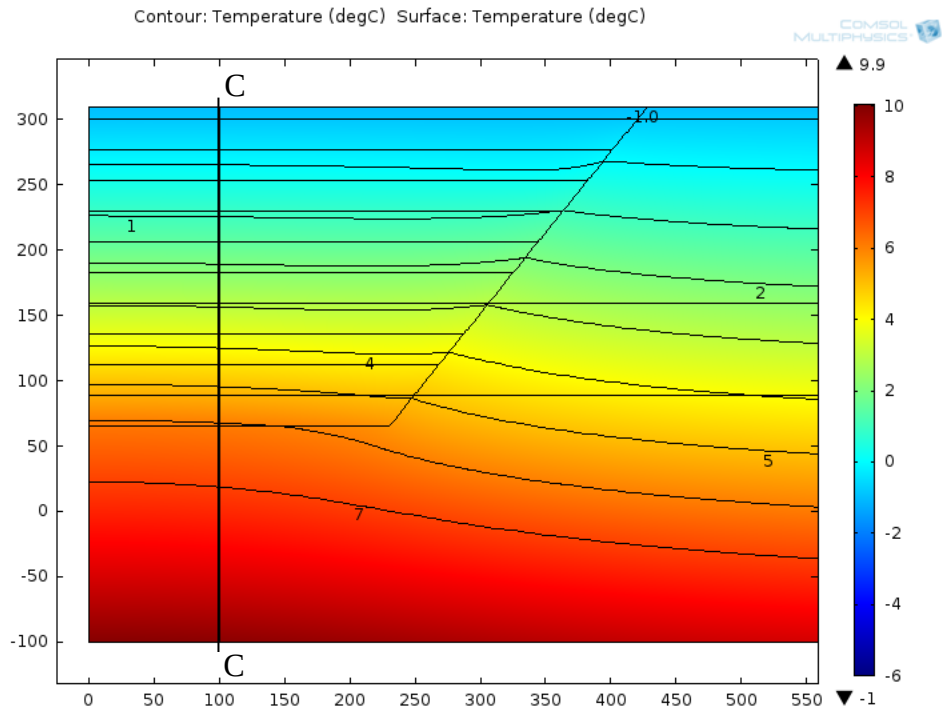

Figure 8-23 Main Zone TMF, Thermal changes after 2000 years, Second climate change scenario, Initial tailings temperature +5ºC

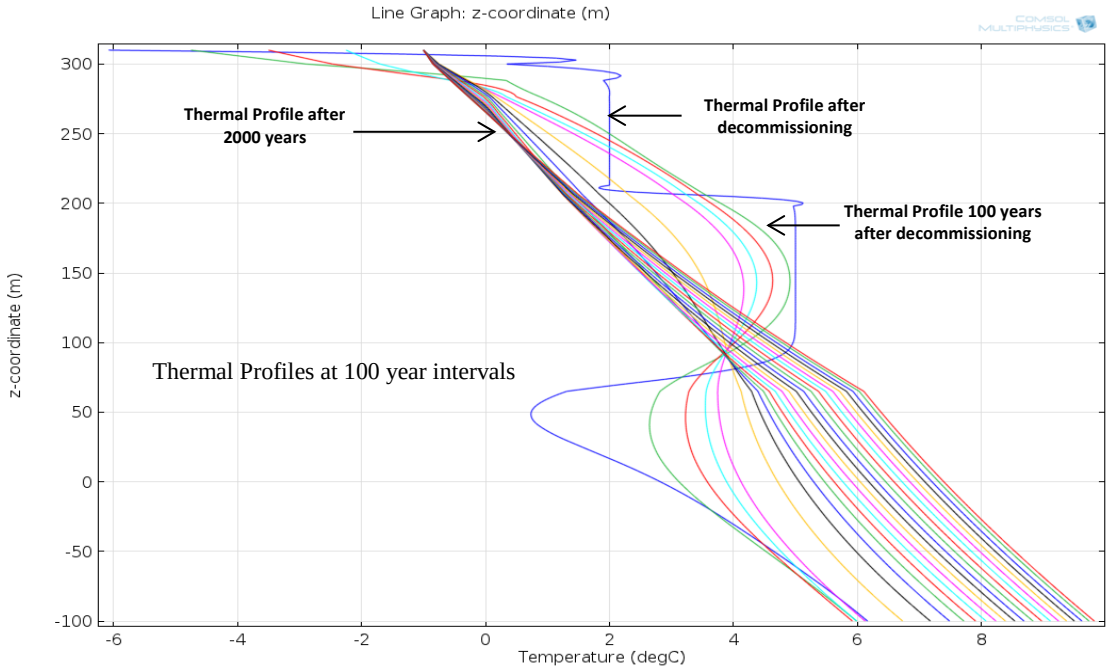

Figure 8-24 Thermal profile changes along line C-C within the Main Zone TMF up to 2000 years after decommissioning at 100 year intervals, Initial tailings temperature +5ºC

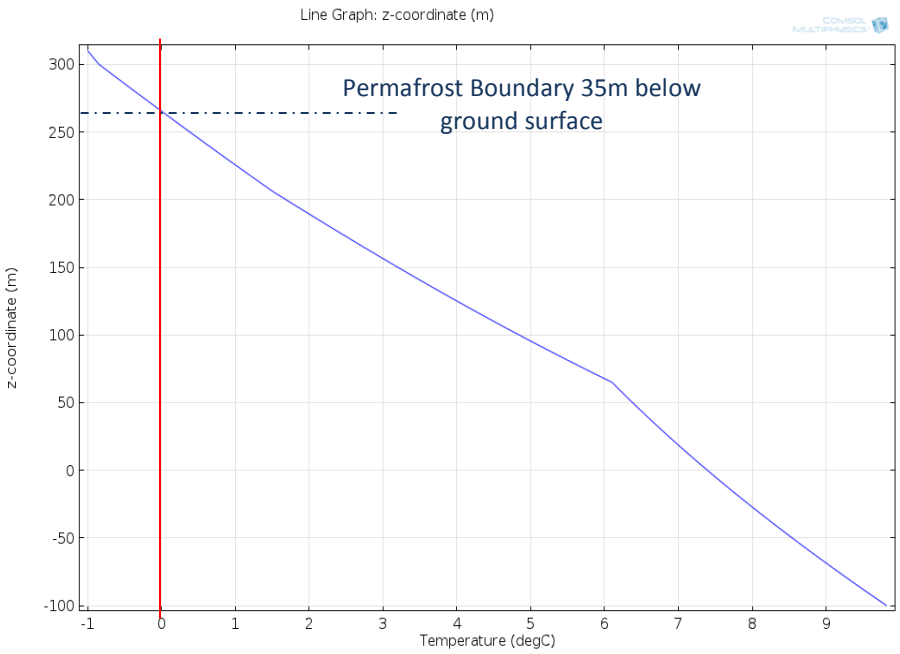

Figure 8-25 Thermal profile along line C-C within the Main Zone TMF after 2000 years, Initial tailings temperature +5ºC

9 Scenario 3: Temperature Increases from -6ºC to +1ºC

When the possible climate change scenarios for Northern Canada were explored in section 2.2, the air temperature could increase by about 7ºC in the worst case according to the climate change studies. This could result in a mean annual ground surface temperature of +1ºC at the site in about 100 years. Such an increase in temperature would result in complete thawing of the permafrost layer in hundreds of years.

Permafrost starts to thaw at the top when the ground surface temperature increases over the freezing point of the water within the pore spaces. Meanwhile, the bottom boundary of permafrost also moves upward as a result of geothermal heat flux from the warmer deeper ground layers. Therefore, the frozen layer shrinks from both top and bottom as indicated schematically in Figure 9-1.

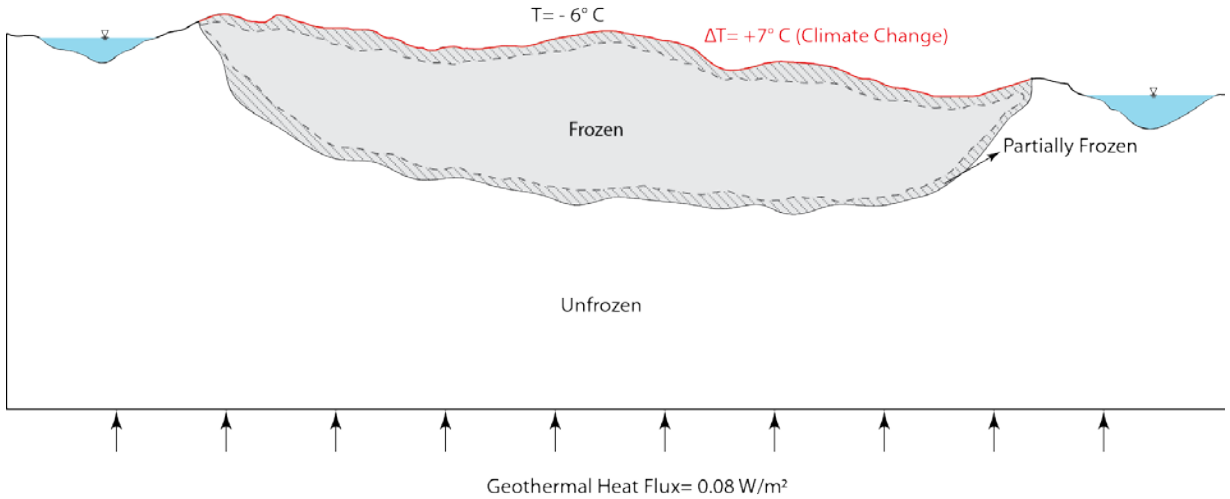

Figure 9-1 Disturbances to the permafrost due to worst climate change scenario

The permafrost layer is usually considered as impermeable due to the fact that the frozen water within the pore spaces blocks the fluid flow paths. However, thermal disturbances result in the formation of new flow paths in the original frozen impermeable ground as shown in Figure 9-2. Therefore, a coupled thermal-fluid flow analysis should be conducted to explore the impact of worst possible climate change scenario on the underground fluid flow system. In addition to modelling heat transfer with phase change phenomena in porous media as explained in section 5, it is also necessary to include fluid flow in partially frozen ground. In the following sections, first the physical basis for simulating fluid flow in partially frozen ground from literature is explained. Then, required material properties and assumptions are explained. Finally, the coupled simulation results are presented and analyzed.

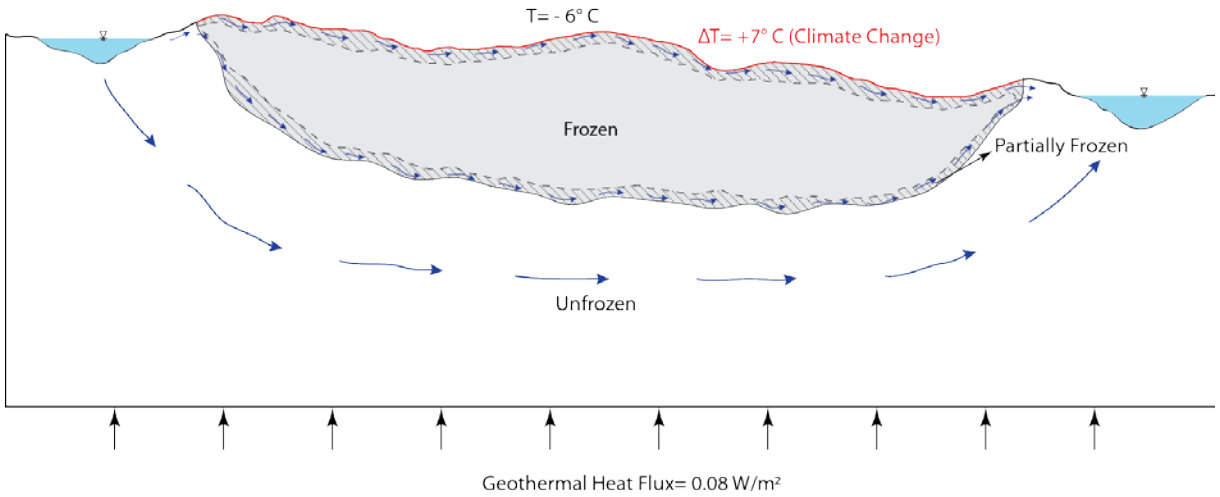

Figure 9-2 New fluid flow paths as a result of thermal disturbances to the permafrost

9.1 Fluid Flow in Partially Frozen Porous Material

Water flow in partially frozen ground materials is one of the most important engineering problems encountered in cold regions. For instance, fluid flow in partially frozen ground is the main mechanism causing floor heave (Konrad and Morgenstern, 1980). In order to model the water flow in partially frozen ground, the most important issue lies in evaluating the hydraulic conductivity of the ground material.

Frozen ground is a mixture of solid particles/rock blocks, unfrozen, and frozen water. Frozen water within the pore spaces impedes the water flow, and as such reduces the hydraulic conductivity of the porous material with respect to the unfrozen condition. At the same time, the unfrozen water content of a soil/rock medium also changes with temperature. Therefore, a major challenge in simulating the fluid flow through partially frozen porous media is how to define the hydraulic conductivity as a function of temperature (Azmatch et. al, 2012).

To formulate the hydraulic conductivity as a function of temperature, two approaches have been suggested in the literature. The first method relates to the direct measurement of hydraulic conductivity via laboratory experiments. Limited number of studies with the direct measurement method is reported in the literature due to the difficulties associated in measuring the hydraulic conductivity (Burt and Williams, 1974, James and Norum, 1976, and Horiguchi and Miller, 1983). The second approach is the indirect method which assumes that there is an analogy between water flow in partially frozen ground and fluid flow in unsaturated soil/rock (Azmatch et. al, 2012; Hansson et. al, 2004).

The idea of the indirect method is based on the similarity between drying and wetting of unsaturated unfrozen soils with the freezing and thawing of saturated frozen soils. While in the drying process of a soil sample, the water within the pore spaces is replaced by air, the pore water converts into ice in a freezing event (Figure 9-3). In other words, the air in the drying/wetting process of unsaturated unfrozen soils is replaced with ice in the freezing/thawing process of saturated frozen soils. Therefore, as a first step, the governing equations for fluid flow in unsaturated unfrozen ground materials should be explored as a study of fundamentals.

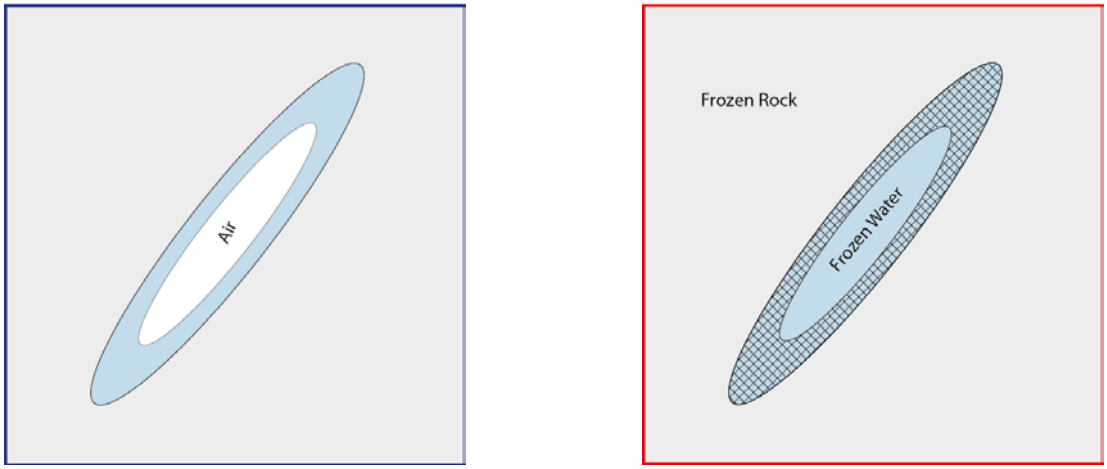

a b

Figure 9-3 a) Drying and wetting of an unsaturated soil/rock, b) Freezing and thawing of a frozen soil/rock

9.1.1 Fluid Flow in Unsaturated Unfrozen Soils

The fluid flow governing equation for saturated porous media is found by considering the mass balance for the fluid phase:

$$\rho_w \frac{\partial \theta_{sw}}{\partial t} + \rho_w \nabla . \left(-K_s \nabla (h_p + z) \right) = Q \qquad 9\text{-}1$$

where ρ_w is water density, θ_{sw} is saturated water content, K_s is saturated hydraulic conductivity, h_p is the water pressure head, z is elevation head, and Q is the source/sink term.

The same relation is valid when a saturated soil sample becomes unsaturated except that the water content and the hydraulic conductivity are now functions of the pressure (suction) head produced due to capillary forces in the pore spaces:

$$\rho_w \frac{\partial \theta_w (h_p)}{\partial t} + \rho_w \nabla . \left(-K(h_p) \nabla (h_p + z) \right) = Q \qquad 9\text{-}2$$

in which $\theta_w (h_p)$ and $K(h_p)$ are the water content and hydraulic head as functions of pressure head, respectively.

The relation between the water content and the suction head in unsaturated soils, i.e. the Soil Water Characteristic Curve (SWCC), can be measured directly in lab experiments. Schematic Soil water characteristic curves for drying and wetting processes are given in Figure 9-4.

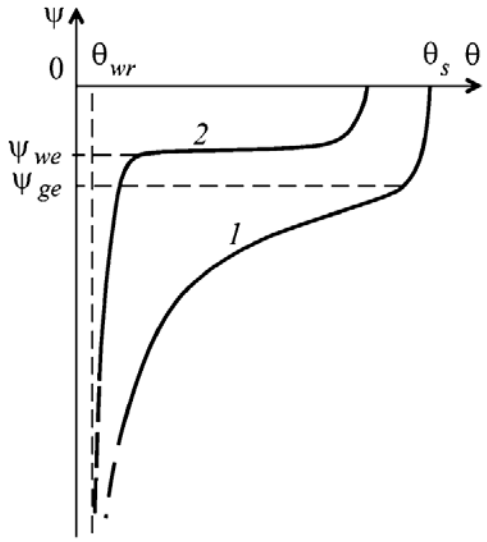

Figure 9-4 Schematic Soil Water Characteristic Curves for 1) drying process and 2) wetting process with gas entry and water entry suction limits

Knowing the relation between water content and the suction term, it is easier to write Eq. 9-2 in the following form which is known as the Richard's Equation:

$$\rho_w C(h_p)\frac{\partial h_p}{\partial t} + \rho_w \nabla \cdot \left(-K(h_p)\nabla(h_p + z)\right) = Q \qquad 9\text{-}3$$

$$C(h_p) = \frac{\partial \theta_w(h_p)}{\partial h_p} \qquad 9\text{-}4$$

As indicated in Eq. 9-4, if the Soil Water Characteristic Curve is known, $C(h_p)$ could be calculated. Therefore, the SWCC should be formulated, so it can easily be used in the mass balance equation.

Various empirical equations such as van Genuchten, Brook and Cory, and Modified van Genuchten have been defined in the literature to formulate the SWCC for its use in numerical simulations. The van Genuchten equation which is widely used for different types of soils and

rocks is adopted in this study (Eq. 9-6 to 9-9). If the storage capacity of the soil/rock is included in the simulation, Richard's Equation is written in the form of Eqs. 9-5-a and 9-5-b.

$$\rho_w \left(C + SeS\right)\frac{\partial h_p}{\partial t} + \rho_w \nabla \cdot \left(-K\nabla(h_p + z)\right) = Q \qquad 9\text{-}5\text{-}a$$

$$Se = \frac{\theta - \theta_r}{\theta_s - \theta_r} \quad \text{and} \quad K = K_s \times k_r \qquad 9\text{-}5\text{-}b$$

$$\theta = \begin{cases} \theta_r + Se(\theta_s - \theta_r) & h_p < 0 \\ \theta_s & h_p \geq 0 \end{cases} \qquad 9\text{-}6$$

$$Se = \begin{cases} \dfrac{1}{\left[1 + \left|\alpha h_p\right|^n\right]^m} & h_p < 0 \\ 1 & h_p \geq 0 \end{cases} \qquad 9\text{-}7$$

$$c = \begin{cases} \dfrac{\alpha m}{1-m}(\theta_s - \theta_r) Se^{\frac{1}{m}}\left(1 - Se^{\frac{1}{m}}\right)^m & h_p < 0 \\ 0 & h_p \geq 0 \end{cases} \qquad 9\text{-}8$$

$$k_r = \begin{cases} Se^l\left[1 - \left(1 - Se^{\frac{1}{m}}\right)^m\right]^2 & h_p < 0 \\ 1 & h_p \geq 0 \end{cases} \qquad 9\text{-}9$$

where h_p is the pressure head, C is the specific moisture capacity, Se is the effective saturation, S is the storage coefficient, K is the hydraulic conductivity, k_r and K_s are the relative and saturated hydraulic conductivities, respectively, θ_s and θ_r denote the saturated and residual water contents, respectively, and $\alpha, m, n,$ and l are model fitting parameters that should be found by using experimental results.

In the van Genuchten equation as indicated in Eqs. 9-6 to 9-9, the soil/rock is considered saturated when the pressure head is equal to or higher than the atmospheric pressure ($h_p \geq 0$).

9.1.2 Analogy between Unsaturated and Partially Frozen

For the partially frozen soils/rocks, a relation between the unfrozen water content and soil temperature or suction must be found—the so-called Soil Freezing Characteristic Curve (SFCC). Some researchers believe that the SWCC could be used instead of the SFCC (Williams, 1964; Koopmans and Miller, 1966; Black and Tice, 1989; Spaans and Baker, 1996). Therefore, when the necessary data for the SFCC is not available, the SWCC can be still be used to give a good estimation of the water flow conditions in the partially frozen ground.

Also to define the relationship between temperature and suction head due to the presence of ice in the pore spaces, the Clausius-Clapeyron equation can be used (Figure 9-5):

$$\psi = \frac{L_f}{g} \mathrm{Ln}\left(\frac{T}{T_f}\right) \qquad 9\text{-}10$$

where ψ denotes the suction head (m), L_f is the latent heat of fusion, g is the acceleration due to gravity, T_f is the freezing temperature of bulk water (K), and T is the soil temperature (K).

In unsaturated soils, two phases of water and air interact through an interfacial surface over which balance of forces must exist. Each water molecule on the air-water interface undergoes unequal hydrostatic pressure due to the pressure deficiency between air and water phases, commonly called matric suction (Khosravani, 2014). In the case of partially frozen soils/rocks, the same phenomenon is occurring between water and ice phases. Therefore, in the pore spaces of partially frozen porous media, the suction term, defined in Eq. 9-10, is the difference between ice and water pressure ($p_i - p_w$). In the end, the linkage between suction and temperature can be established to define a so-called Rock Freezing Characteristic Curve as will be seen in more detail later on when conducting numerical simulations.

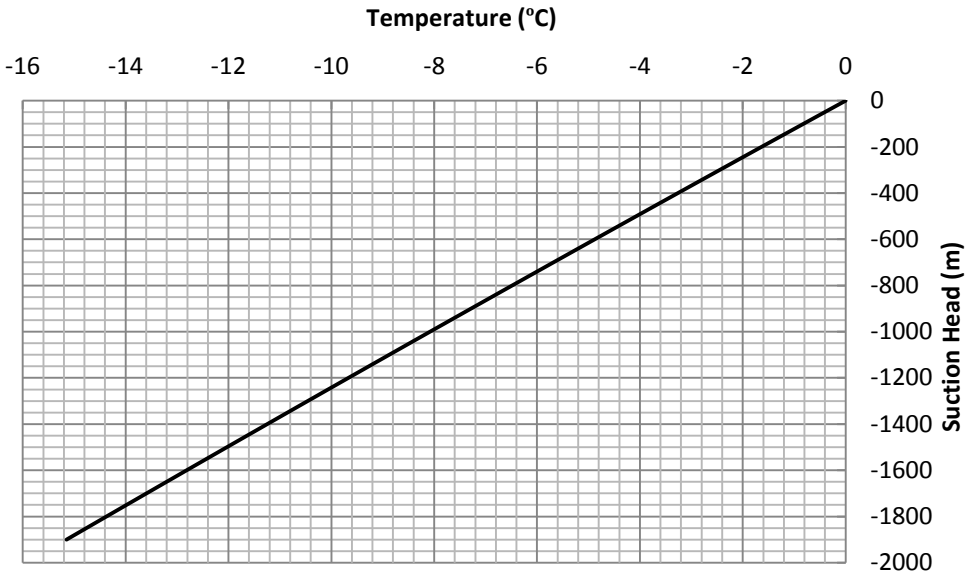

Figure 9-5 Suction head vs temperature in porous media at temperatures below 0°C defined by Clausius-Clapeyron equation

The other important issue in fluid flow in partially frozen ground is how to define the dependency of the hydraulic conductivity on the unfrozen water content at temperatures below the freezing point of pore fluid. Some researchers assumed that the hydraulic conductivity of partially frozen soil/rock is a function of the unfrozen water content, and is equal to the hydraulic conductivity of unfrozen unsaturated soil with the same water content (Harlan, 1973; Tao and Gray, 1994; Newman and Wilson, 1997). On the other hand, other researchers such as James and Norum (1980), Taylor and Luthin (1978), and Lundin (1990) believe that this approach results in over prediction of fluid flow in the partially frozen materials; so they have defined impedance factors to reduce the hydraulic conductivity of partially frozen material relative to the unfrozen unsaturated material with the same water content. However, it is not easy to define a simple relation between impedance factor and the soil/rock type (Azmatch et. al, 2012).

As it was explained, it is assumed that the process of fluid flow in partially frozen materials is the same as the process that occurs in unsaturated soils. In fact, in this approach, the air phase in the unsaturated soil is replaced by ice in the partially frozen soil. However, when the ice within the pore spaces thaws, the resulting unfrozen water acts as a source term to the partially frozen ground (Figure 9-6). Therefore, the source term in the Richard's Equation should be defined in a way so as to account for the amount of water added to the system, i.e.

$$\rho_w \left(C + SeS\right)\frac{\partial h_p}{\partial t} + \rho_w \nabla \cdot \left(-K\nabla(h_p + z)\right) = \rho_i \frac{\partial \theta_i}{\partial t} \qquad 9\text{-}11$$

In Eq. 9-11, ρ_i is ice density and θ_i denotes the ice (frozen water) content which is a function of temperature. Therefore, for analyzing fluid flow in partially frozen materials, a coupled heat-fluid flow simulation approach is necessary.

For the particular case of the Kiggavik project, coupled simulation between heat transfer with phase change in porous media and fluid flow in partially frozen material is conducted. There is unfortunately no information on the impedance factor for the ground material hydraulic conductivity reported in the technical documents. However, the main purpose is to investigate the impact of the worst climate change scenario on the permafrost and underground fluid flow condition. Hence, to simulate the fluid flow in partially frozen ground, the same concept as fluid flow in unsaturated condition is implemented without using any impedance factor, i.e. with enhanced flow and disregarding ice blockage. The material properties and the relations between frozen water content and temperature are summarized in the following section.

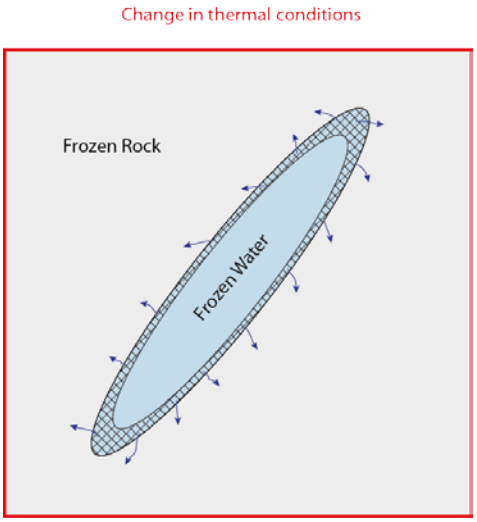

Figure 9-6 Ice converts to water and acts as a source term to the system

9.2 Material Properties

In the coupled heat transfer/water flow model, three distinct domains must be defined. The first one refers to the unfrozen areas beneath the permafrost layer and the open taliks areas below the

major lakes. It is assumed that the domain materials in these areas are initially saturated and will remain saturated during the simulation. Therefore, the hydraulic properties defined in Section 7-1 are used for the material in this area.

The second domain includes the original permafrost layer. While this layer is frozen at the beginning, it will however eventually thaw as a result of warming temperatures. Therefore, the fluid flow in partially frozen ground physics should be considered for this domain.

The third domain is concerned with the pit filled with tailings material. Based on the simulation results in Section 7-2, the consolidated tailings remains saturated. However, the tailings material undergoes freezing and thawing stages due to the change in climate condition at the ground surface. Therefore, this material should be also considered as partially frozen in the simulation to consider the impact of freezing and thawing on the fluid flow system.

In Technical Appendix 5I (AREVA, 2013), van Genuchten parameters for the waste rock matrix was presented. Some data on the unfrozen water content of the tailings were also reported in Technical Appendix 5J. Based on the available data, reasonable values for the necessary parameters are estimated and given in Table 9-1.

Table 9-1 van Genuchten Equation parameters for ground material and tailings

Parameter	Ground Material	Tailings
$\alpha\,(1/\mathrm{kPa})$	0.1	0.15
n	2.0	2.0
l	0.5	0.5
$m = 1 - \frac{1}{n}$	0.5	0.5
θ_s	0.05	0.35
θ_r	0.005	0.005
$K_s\,(m/s)$	10^{-8}	10^{-7}

Hence, considering the parameters in Table 9-1, the Rock Freezing Characteristic Curve for ground material and tailings could be determined as follows. First, by using Eq. 9-10, the suction

head for each temperature could be found. Then, by using Eq. 9-7 and 9-5-b, the relation between frozen water content and the temperature for ground material and tailings is easily determined (see Figure 9-7).

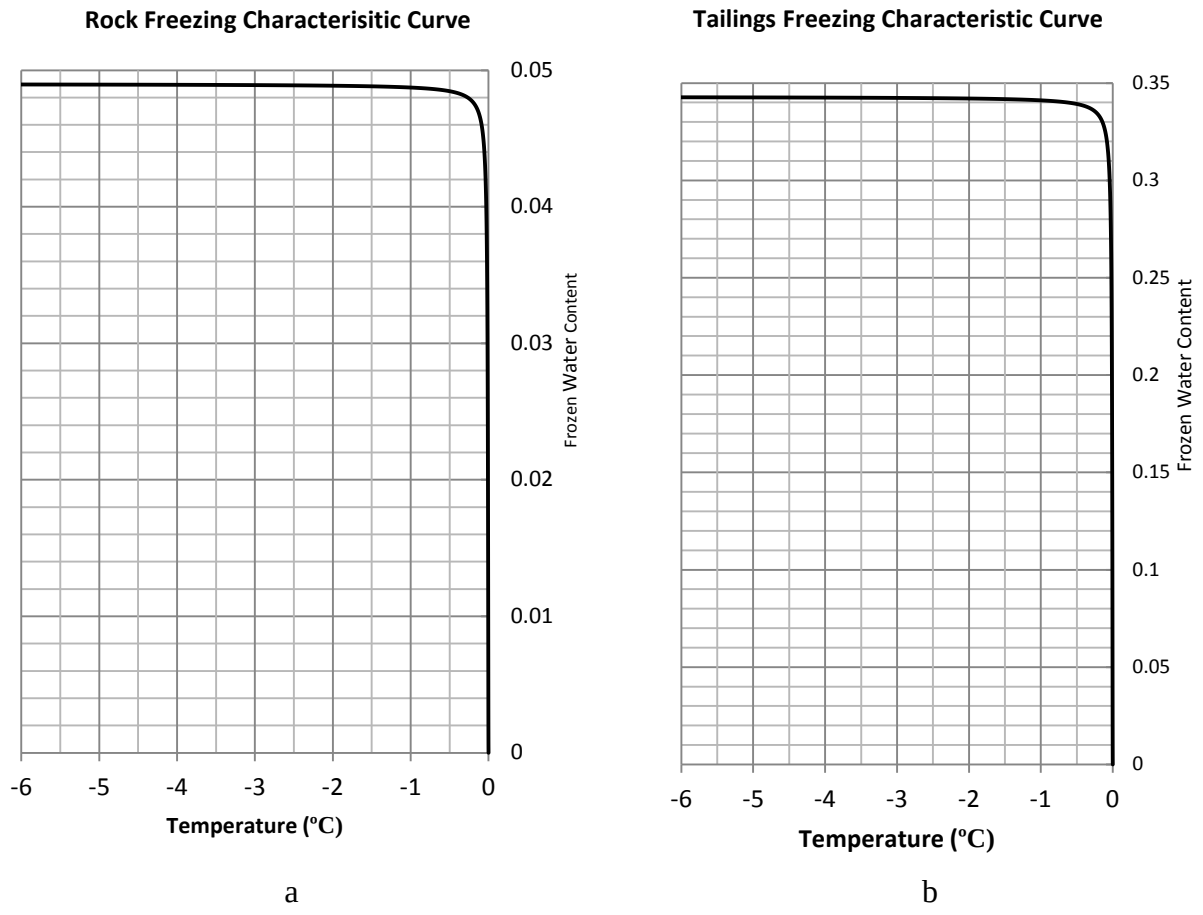

Figure 9-7 Freezing Retention Curves fro a) rock and b) tailings

9.3 Initial and Boundary Conditions

In this scenario, a coupled thermal/water flow simulation is considered. Therefore, both the thermal and hydraulic initial conditions as discussed previously should be defined as follows.

9.3.1 Thermal Initial Condition

For the thermal initial condition, it is assumed that temperature of the permafrost layer is increasing from -6ºC at the ground surface to 0ºC at about 200m below ground surface. The

ground material at deeper parts of the domain is considered unfrozen the temperature of which is increasing according to the geothermal heat flux. Also, it is assumed that beneath the considered lakes open taliks has been formed.

9.3.2 Initial Hydraulic Condition

For the unfrozen areas beneath the permafrost and within the open taliks zones, hydrostatic condition is considered bases on the maximum water elevation inside two surrounding lakes. For the permafrost layer, the initial suction head is calculated based on the Clausius-Clapeyron equation (Eq. 9-10).

9.3.3 Thermal Boundary Condition

For the ground surface, it is assumed that the temperature is increasing from -6ºC to +1ºC in 100 years as explained in Section 4-3 (see Figure 4-1). Since the two major lakes considered for the simulation support open taliks (Technical Appendix 5B & 5J, Areva 2013), the temperature at the bottom of lake is averagely +3ºC during the year.

9.3.4 Hydraulic Boundary Condition

In Technical Appendix 5D (AREVA 2013), some information are presented on lakes potentially supporting talik formation on the vicinity of the project. For this study, the two major lakes, i.e. Squiggly Lake and Judge Sissons Lake, are selected. To consider the worst cases in the underground fluid flow conditions the maximum reported depth of these lakes are considered as the hydraulic boundary conditions at the location of the lakes. Therefore, for the Squiggly Lake, maximum depth of 15m and for the Judge Sissons Lake a maximum depth of 20m is considered in the simulations.

9.4 Discussion of Numerical Results

The coupled TH with unsaturated flow numerical modelling covers an area of about 24 km wide and 750 m deep with one major lake on each side, namely Squiggly Lake and Judge Sissons

Lake. It is intended to investigate the thawing of the permafrost layer in the long term and how the ground water table under the hydraulic heads of the two lakes would be affected. The mesh is comprised of about 20,000 linear triangular elements and a time step of 1 day (86400 seconds) is used for a total time of 750 years.

Numerical simulations results mainly indicate that most of the permafrost layer would disappear in about 600 years after decommissioning if the worst climate change happens. The water level is arising from below the original permafrost layer (200m below ground surface) to about 25m to 30m below the ground surface.

The main issues and findings can be summarized as follows.

The long-term coupled thermal/water flow analysis is initiated at the end of the decommissioning phase with the tailings material inside the pit being still unfrozen as shown in Figure 9-8. However, since the ground surface temperature is below 0ºC during the first 100 years, it is expected that some parts of the in-pit material freeze in the early stages as confirmed by the numerical results. At the same time in accordance with the imposed warming trend, the ground temperature and therefore the water pressure around the pit are increasing (see Figures 9-8 and 9-9).

When the ground surface temperature exceeds the freezing point temperature of the pore fluid, after about 100 years, the permafrost layer starts to thaw from both its upper and lower boundaries. As time proceeds and the permafrost layer ‘shrinks’ or degrades, positive water pressure heads develop in the thawed areas. However, the pressure head within the frozen zones is still below zero, which indicates a suction head due to the concomitant presence of water and ice in the pore spaces.

Changes in the thickness of the permafrost and suction head within the pore spaces of the frozen ground are indicated in Figures 9-16 and 9-18. As shown in these two figures, the frozen layer shrinks during time. Meanwhile, the suction head in the frozen ground is changing. The relation between suction head and temperature is defined with the Clausius-Clapeyron equation defined in section 9.1.2.

As expected, frozen water within the pore spaces converts into water during thawing, and the pressure head in the upper part of the original permafrost layer initially starts to increase as depicted in Figures 9-16 and 9-18. As the unfrozen water content increases in the upper original permafrost layer, the ground material eventually becomes saturated with time. Hydraulic conductivity increases as more pores are freed of ice which in turn induces water transport (seepage) to areas with lower total hydraulic head. As a result, the pressure head decreases in the upper layers as time proceeds, and the ground material becomes unsaturated at this stage (see Figure 9-16 and 9-18).

Within the TMF, the initial water level is considered at the top of consolidated saturated tailings material. As shown in Figure 9-15, initially, the water pressure inside the pit is higher than the surrounding unfrozen material. Therefore, the water level within the pit decreases in the early stages, and subsequently increases due to the thawing of the surrounding permafrost. After 700 years, the water level rises to a depth of about 30m and stays constant thereafter (see Figure 9-19). This final ground water level depth applies to whole region of the study including areas around the TMFs. Therefore, the numerical results suggest that even in the worst conditions (Scenario 3), contaminant transport to the ground surface is not likely to occur as the underground water level does not resurface. This result is, of course, within the limits of the accuracy of the material parameters and assumptions made in the numerical model.

When the permafrost layer thaws, the water pressure increases at both top and bottom of the original permafrost layer. However, the frozen layer impedes the fluid flow paths. Therefore, the unfrozen water at the top and bottom could not merge until the permafrost is completely thawed. In Figure 9-19 shows the evolution of water level as such.

Finally, it should be mentioned that in this study only two major lakes, Squiggly Lake and Judge Sissons Lake, north and south of the proposed location are considered in the 2D simulation. Also, it is assumed that the water level in these two lakes remains constant even after hundreds of years. Therefore, the impact of other surrounding lakes or changes in water level of these two lakes could alter the numerical results in the long-term.

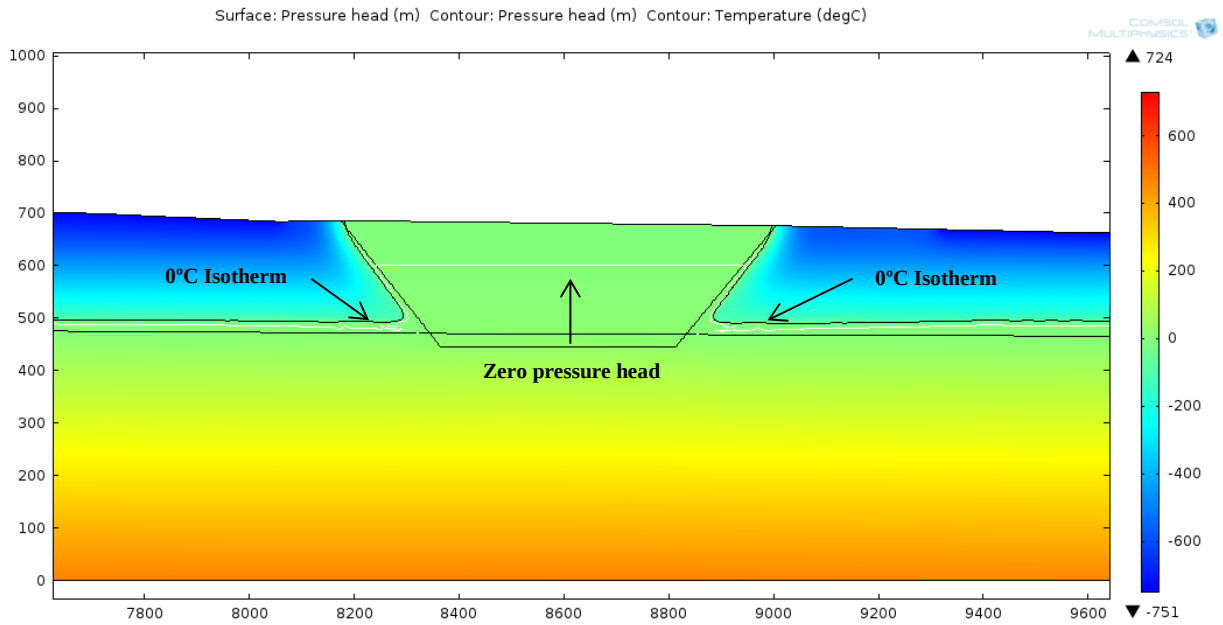

Figure 9-8 Pressure head distribution at the end of operational and decommissioning phase, Black line indicates 0°C temperature, and White line denotes the 0 pressure head

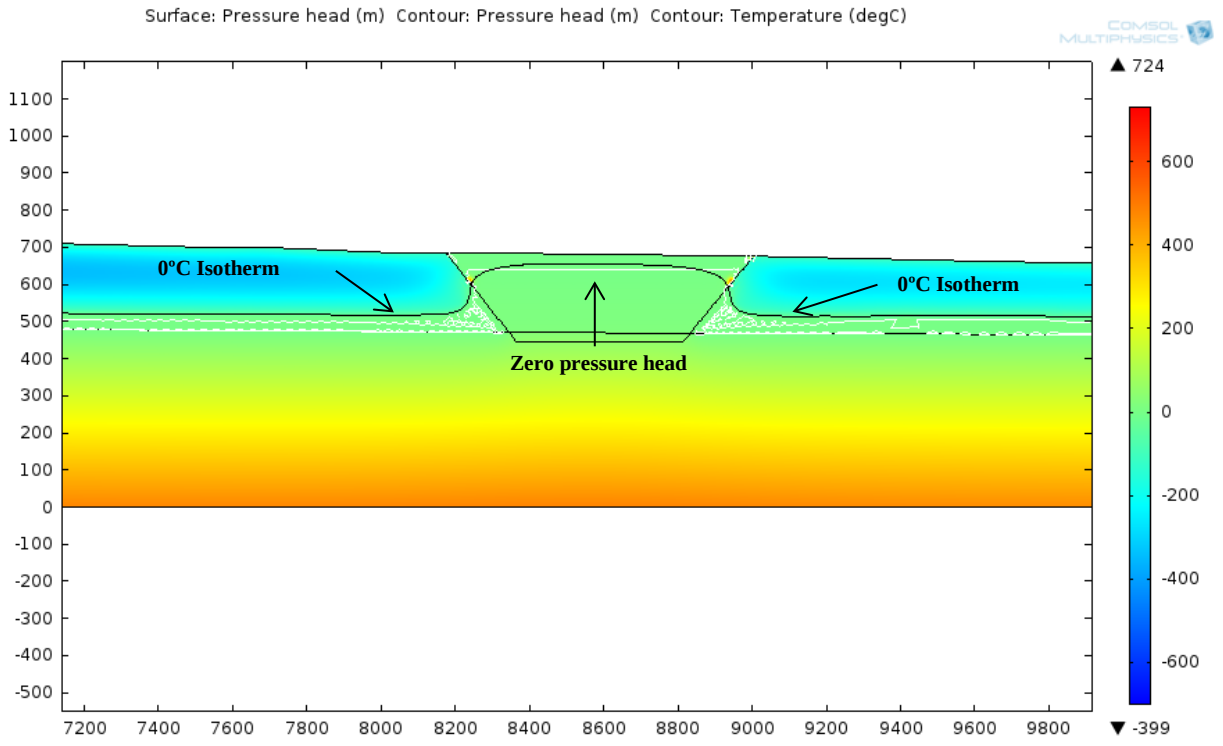

Figure 9-9 50 years after start of climate change, Black line indicates 0°C temperature, and White line denotes the 0 pressure head

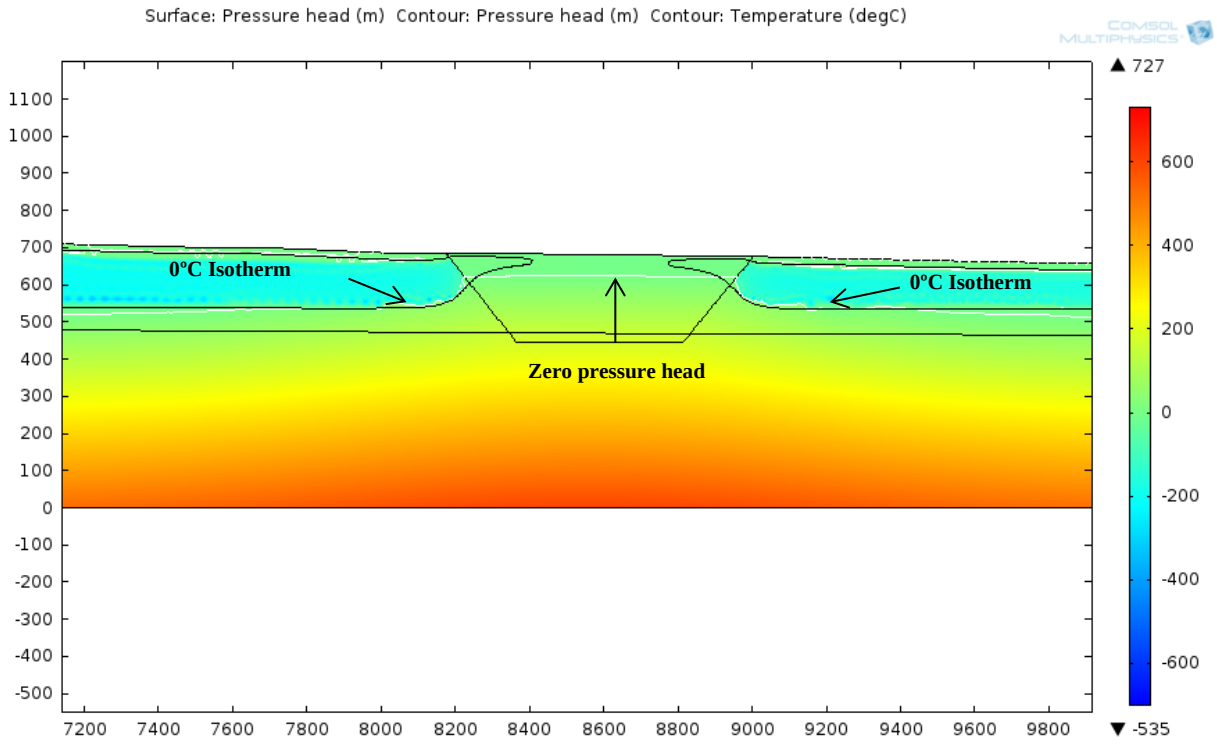

Figure 9-10 Pressure head distribution 150 years after start of climate change, Black line indicates 0°C temperature, and White line denotes the 0 pressure head

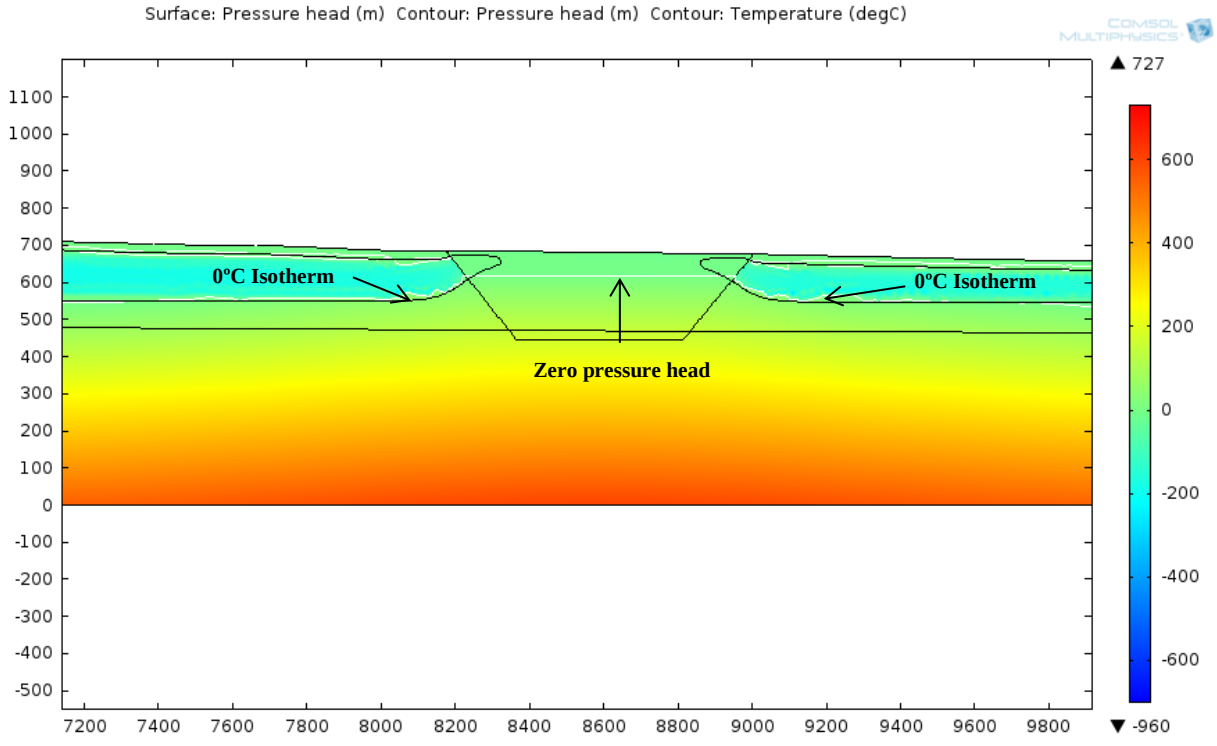

Figure 9-11 Pressure head distribution 200 years after start of climate change, Black line indicates 0°C temperature, and White line denotes the 0 pressure head

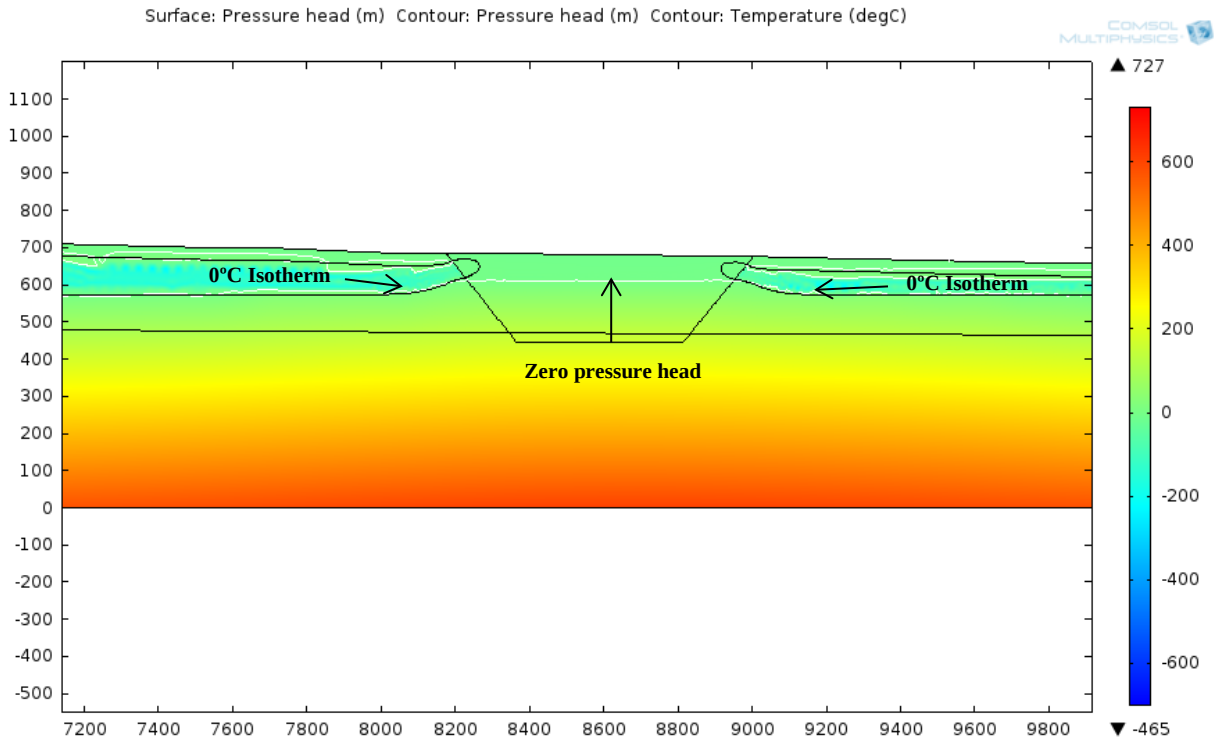

Figure 9-12 Pressure head distribution 300 years after start of climate change, Black line indicates 0°C temperature, and White line denotes the 0 pressure head

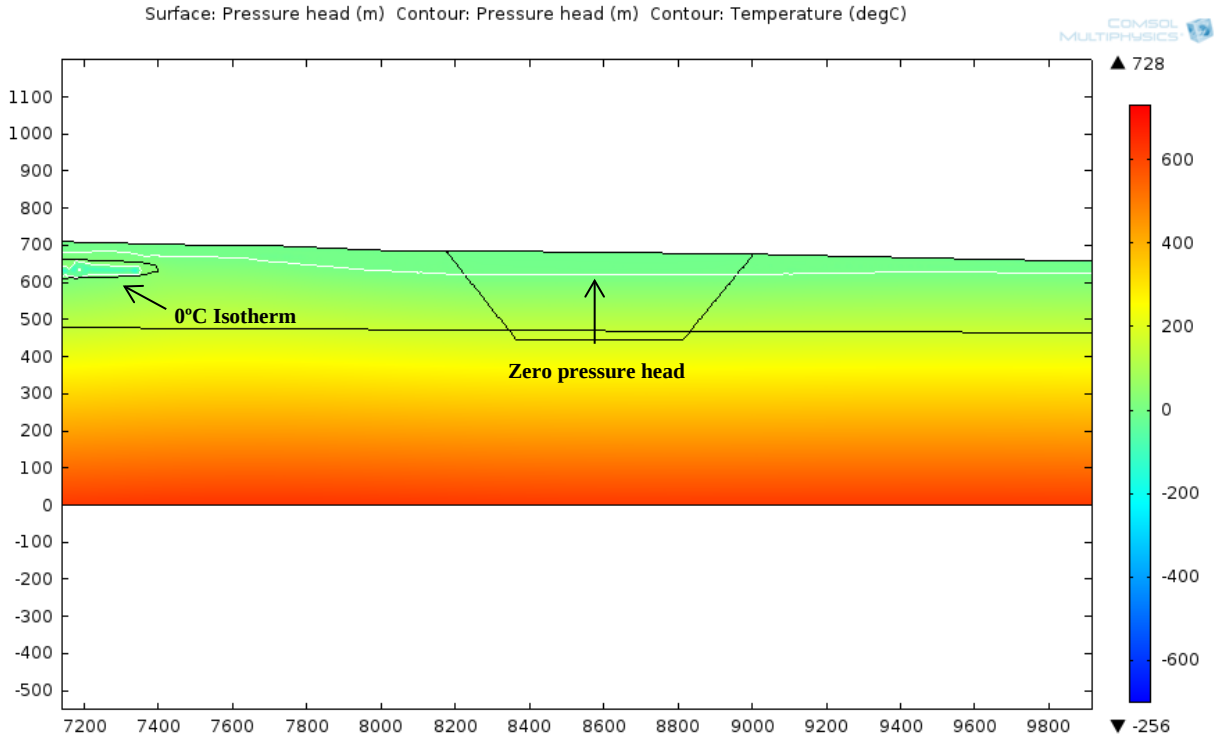

Figure 9-13 Pressure head distribution 450 years after start of climate change, Black line indicates 0°C temperature, and White line denotes the 0 pressure head

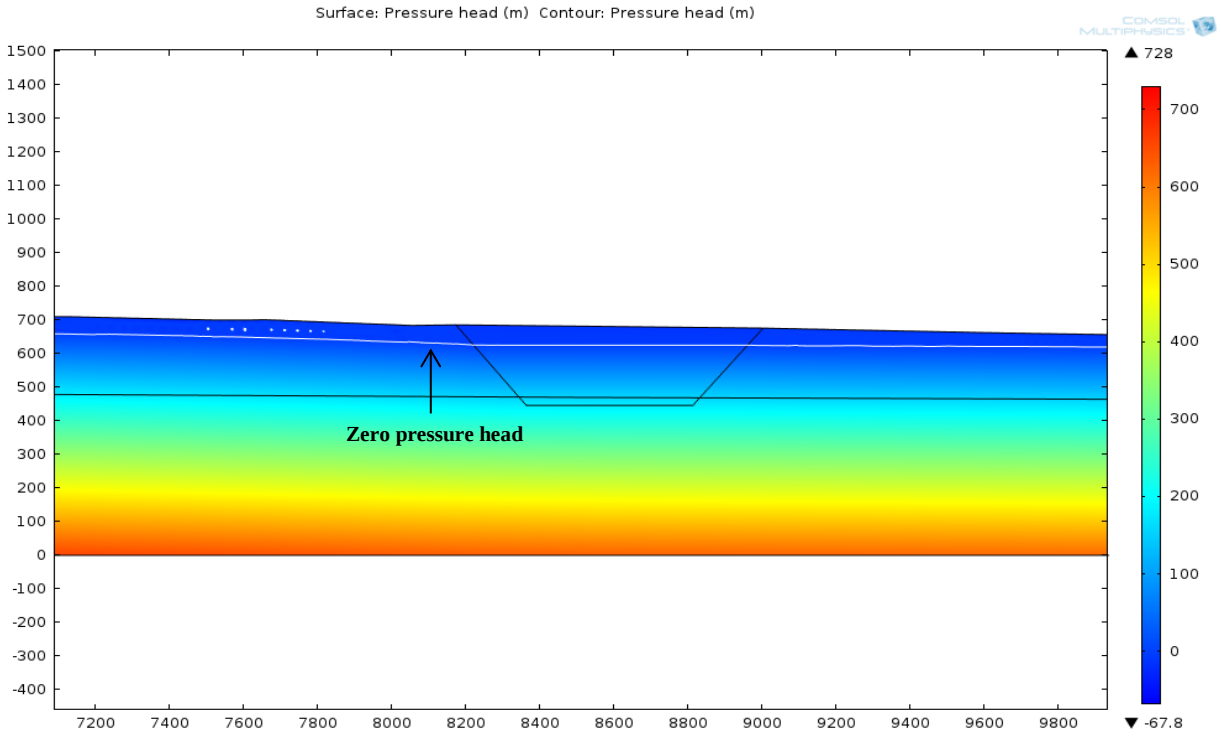

Figure 9-14 Pressure head distribution 600 years after start of climate change, Black line indicates 0°C temperature, and White line denotes the 0 pressure head

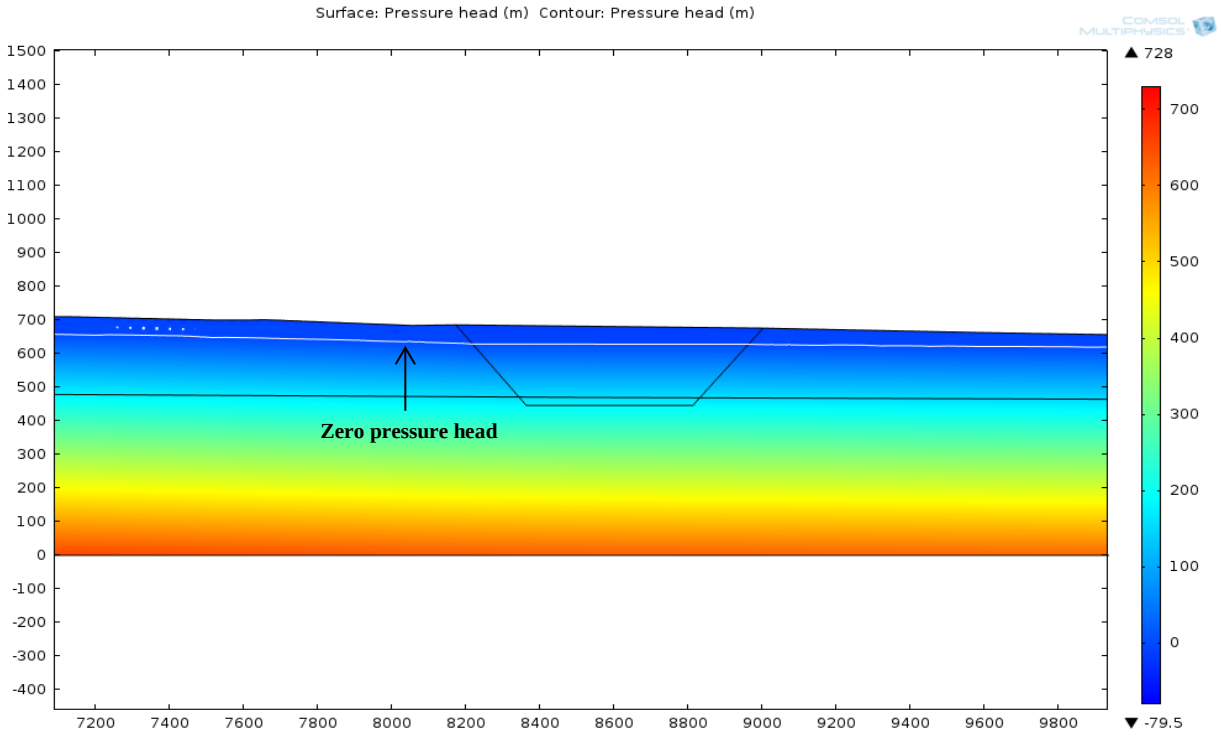

Figure 9-15 Pressure head distribution 750 years after start of climate change, Black line indicates 0°C temperature, and White line denotes the 0 pressure head

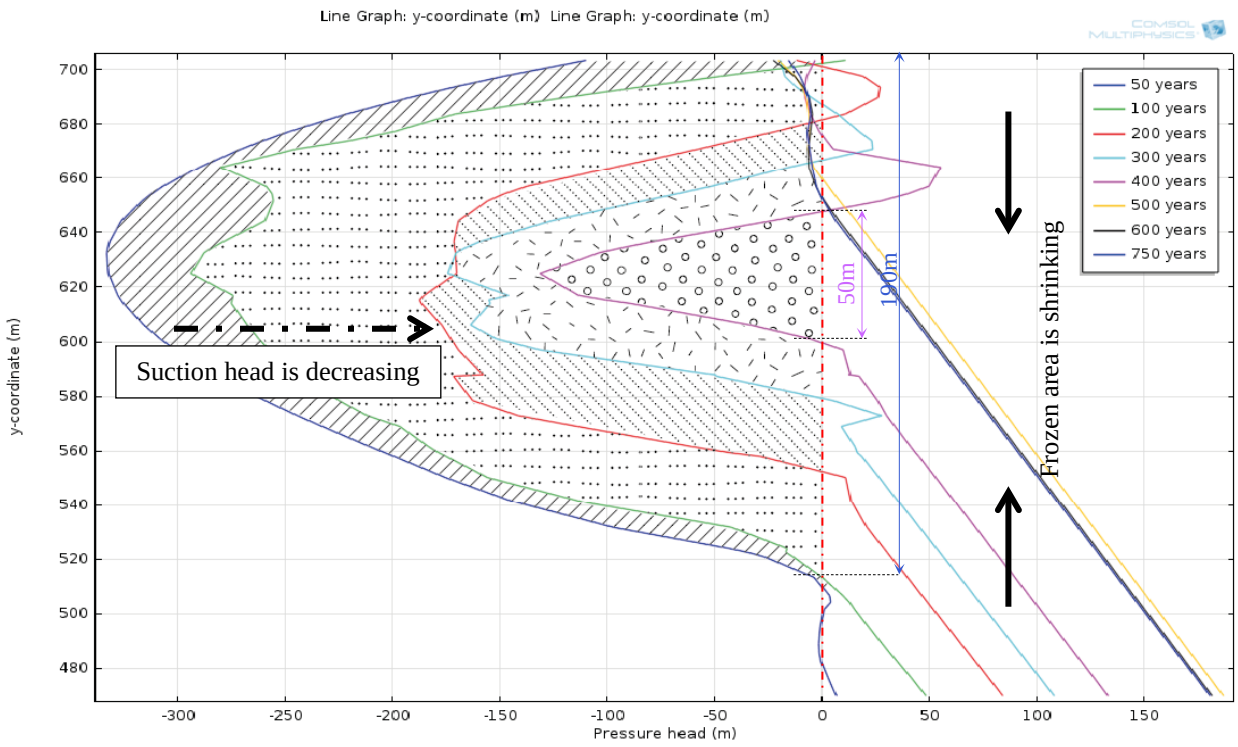

Figure 9-16 Pressure head changes vs depth during time at 800m left side of the TMF

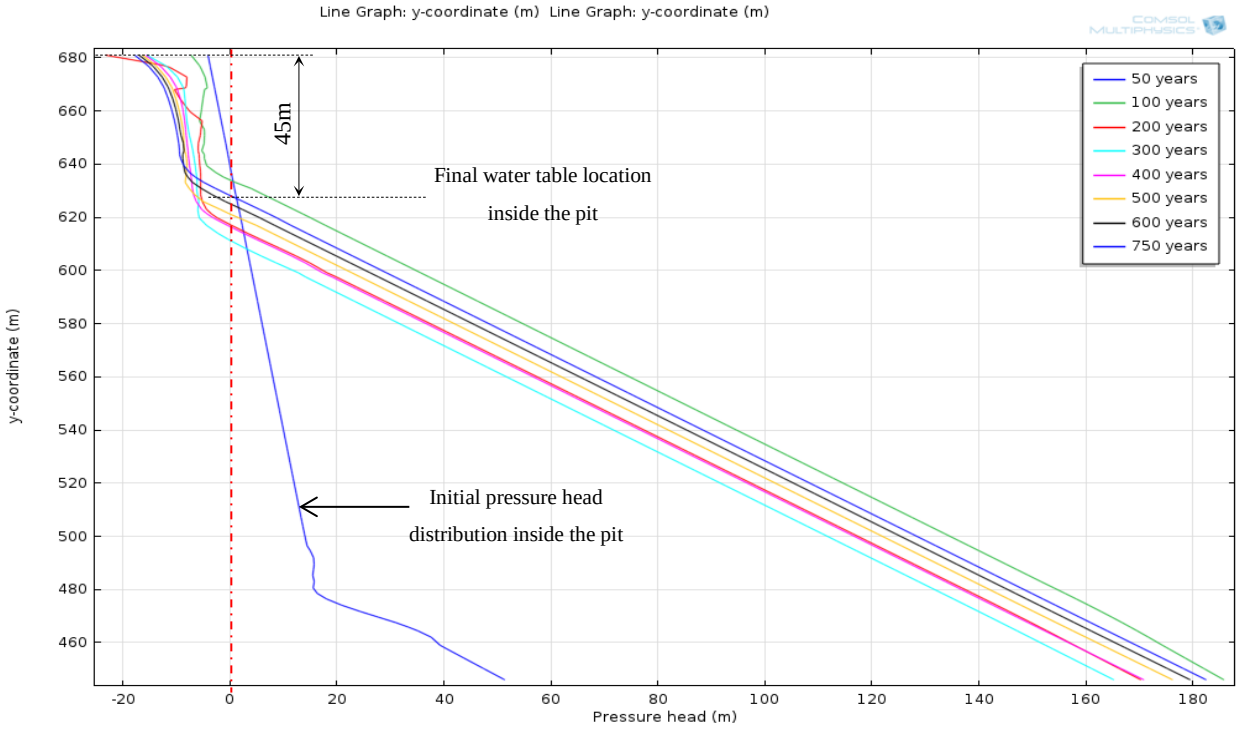

Figure 9-17 Pressure head changes during time within the TMF

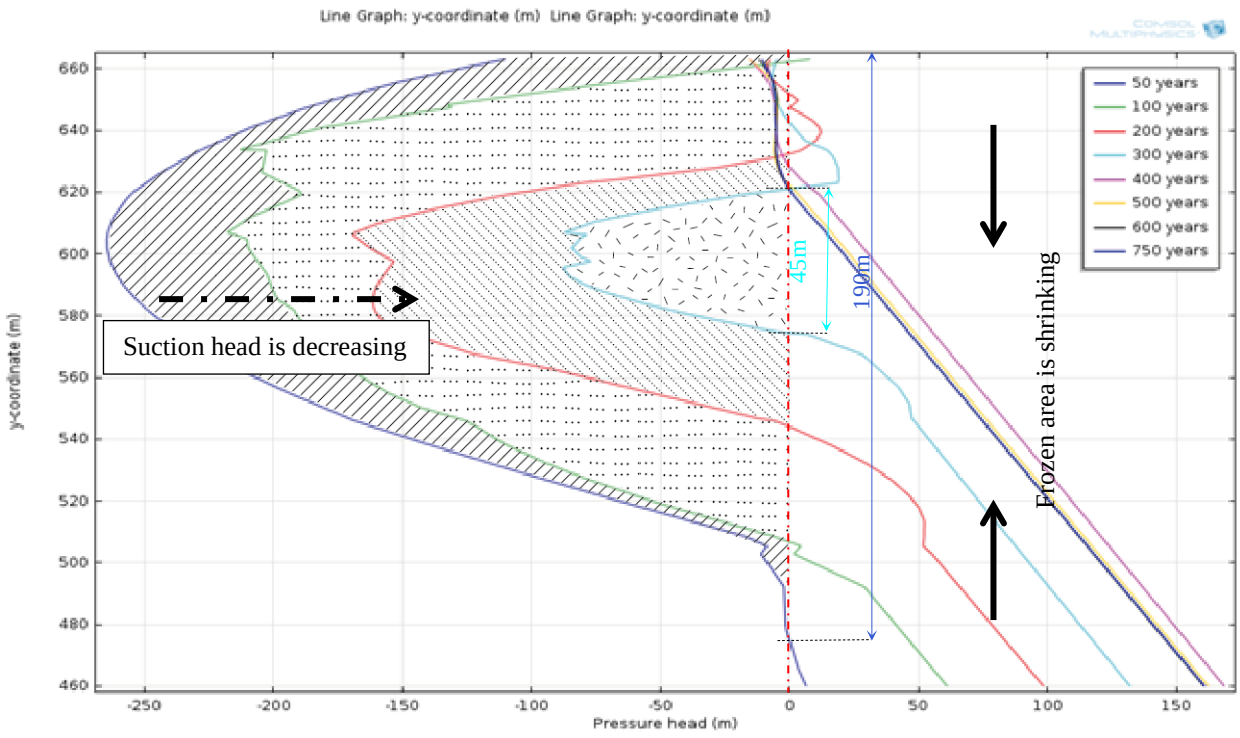

Figure 9-18 Pressure head changes during time at 800m right side of the TMF

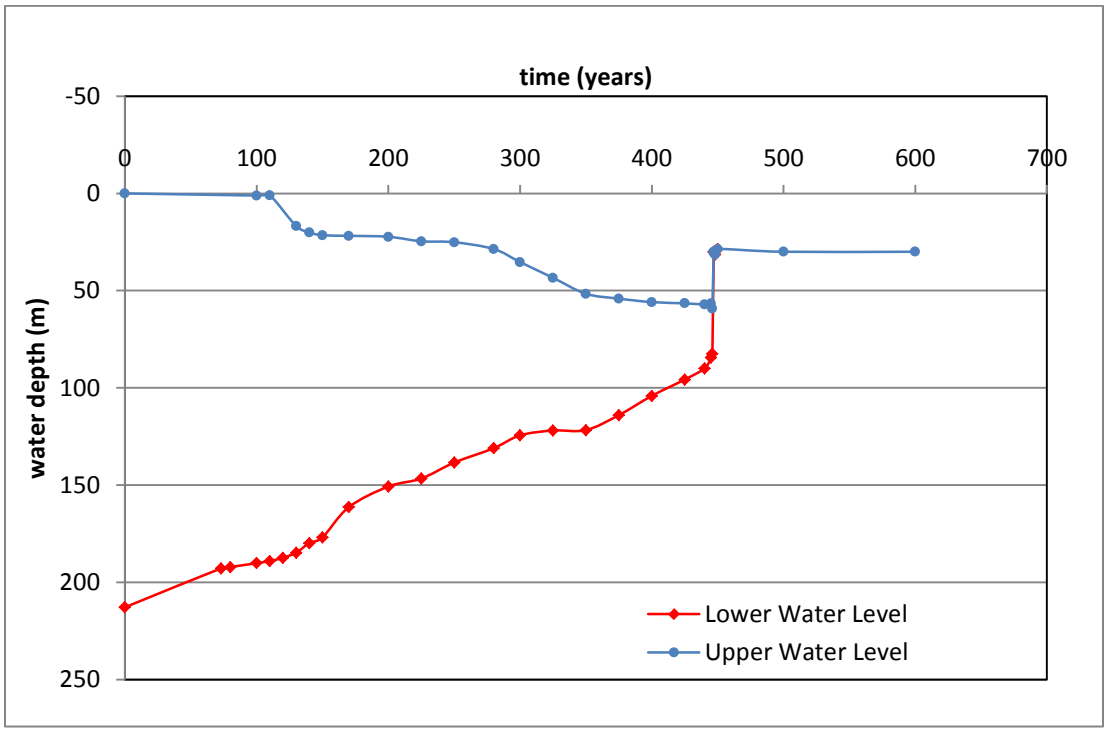

Figure 9-19 Water level evolution as a result of thermal disturbances

10 3D Seepage Modelling

In the previous sections, the main focus was on the thermal impacts on the permafrost as a result of mining activity and climate change. To investigate the consequences on thermal disturbances, 2D numerical models were implemented. When the 2D models are used, only the most important water sources and features are considered. However, there are usually other major lakes surrounding the domain of interest which are not taken into account in the 2D models.

In this section, the main objective is to find out the final water level position within and around the TMFs when the permafrost is completely vanished as a result of climate change in long-term. To achieve this goal, a three dimensional model is constructed that includes the most important geographical features such as ground surface elevations besides the major water sources in the vicinity of the Kiggavik project.

10.1 Study Area

The proposed open pit locations are surrounded by some major lakes which support open taliks (Figure 10-1). For the purpose of 3D numerical simulations, seven lakes are selected as the major lakes; Squiggly Lake, Sleek Lake, Caribou Lake, Pointer Lake, Jaeger Lake, Boulder Lake, and Judge Sissons Lake (Figure 10-1). Three main factors are considered in selecting these lakes including lake size, distance to the TMFs, and the elevation of bottom of the lake. The available information of these major lakes is also summarized in Table 10-1. Although the information for Boulder Lake and Sleek Lake is not available, it could be approximated by considering other close lakes such as Caribou and Pointer Lakes.

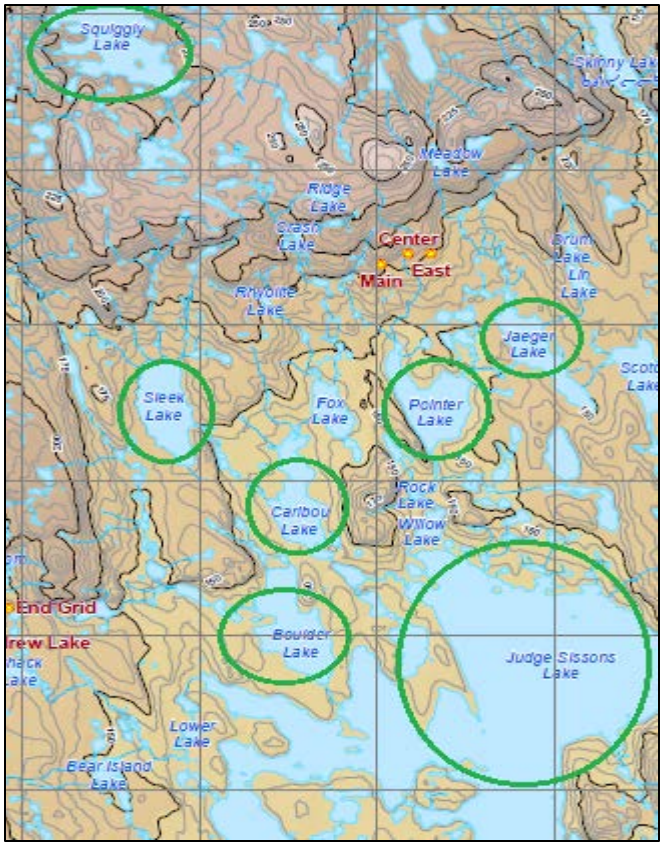

Figure 10-1 Kiggavik project study area including the major lakes (AREVA Resources, Technical Appendix 5B)

Table 10-1 Major lakes available information (AREVA Resources, Technical Appendix 5B)

Lake ID	Surface (km^2)	Mean Depth (m)	Max Depth (m)	Average Lake Elevation (masl)
Boulder	4.78	NA	NA	135
Caribou	3.41	1.4	2.7	136.9
Jaeger	2.81	1.6	4	150.64
Judge Sissons	95.5	4.6	20	132.4
Pointer	3.93	1.39	2.9	141.9
Sleek	3.76	NA	NA	149.7
Squiggly	6.38	6	14	213

10.2 Elevation Data

To construct the 3D model, the most important required data is the ground surface elevation at each point. The Digital Elevation Data (DEM) of Canada is accessible via Geological Survey of Canada (www.geogratis.gc.ca). For our area of interest, the necessary data are gathered and selected with the aid of ArcGIS software. Figure 10-2 shows the Digital Elevation Data (DEM) in the vicinity of the Kiggavik project received from the Geological Survey of Canada.

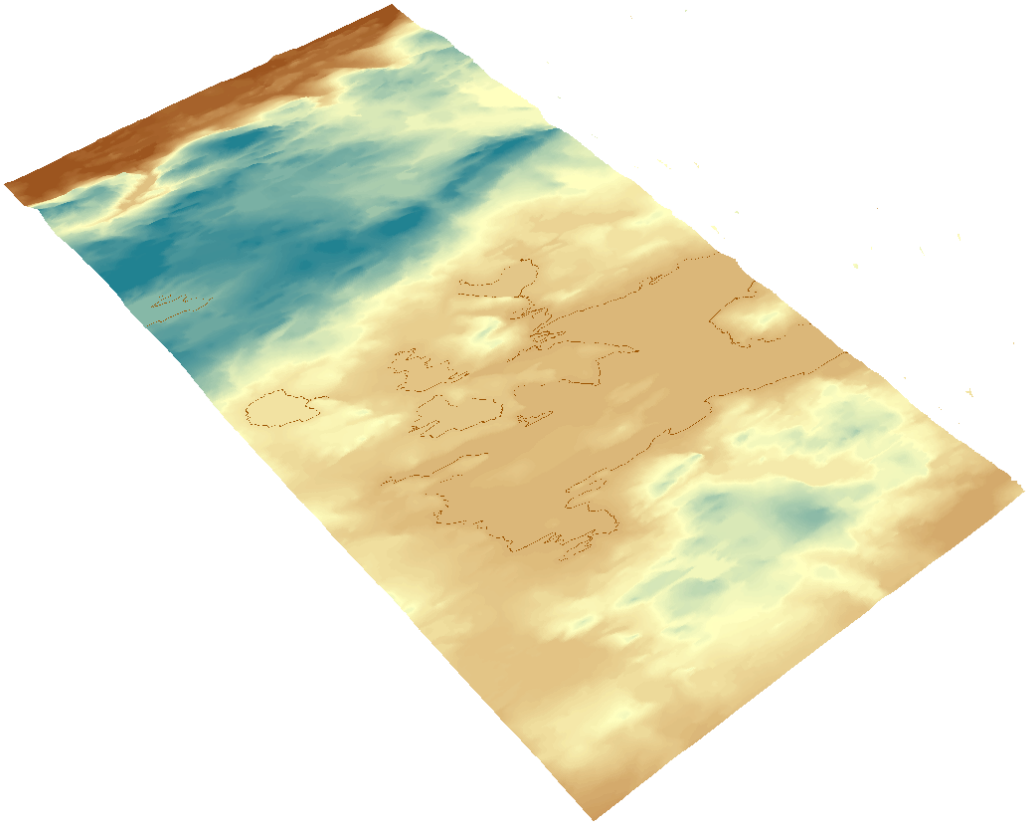

Figure 10-2 Digital elevation data in the vicinity of the Kiggavik Project (geogratis.gc.ca)

Also, in Figure 10-3, the map of the area of interest is presented which indicates the location of major lakes in addition to the proposed location of the Kiggavik mining project. With the aid of the DEM data and the map of the area, the 3D Geometry for the numerical simulation is constructed in the COMSOL Multi-physics software (Figure 10-4).

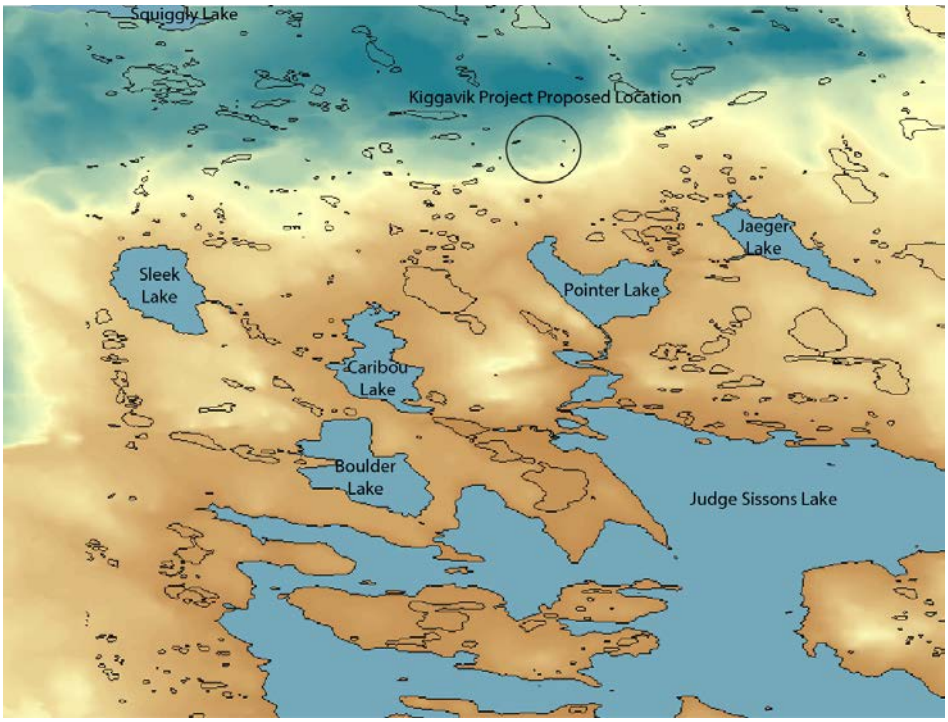

Figure 10-3 Major lakes in the vicinity of the Kiggavik project (The vertical and horizontal scales are different)

All the side boundaries in this 3D model are "no-flow" boundaries

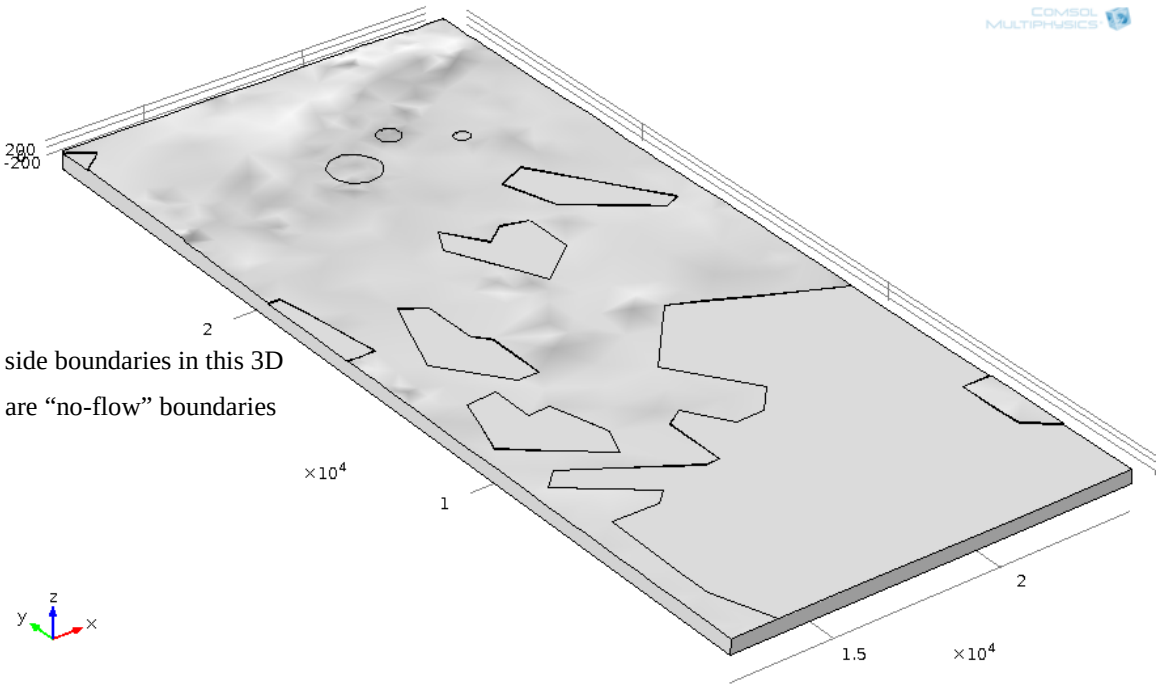

Figure 10-4 3D geometry constructed in COMSOL software

10.3 Material Properties

The material properties for both original ground material and the material inside the TMFs are the same as properties used in Section 9-2.

10.4 Boundary conditions

In the 3D analysis, only underground water flow system is investigated. Therefore, the only important boundary condition is the hydraulic head at the major lakes surrounding the mining project (Figure 10-3). In Table 10-1, information about the mean depth and average elevation of these lakes are presented. In the numerical simulation, the total hydraulic head of each lake is considered as the summation of mean lake depth, pressure head, and the average elevation, the elevation head (Table 10-2). For the case of Boulder Lake and Sleek Lake the mean depth of which are not presented, the mean depth is approximated with the information of Caribou Lake and Pointer Lake, respectively.

Table 10-2 Pressure, Elevation, and Hydraulic Head of major lakes

Lake ID	Average Pressure Head (m)	Elevation Head (m)	Approximate Total Hydraulic Head (m)
Boulder	1.5	135	136.5
Caribou	1.4	136.9	138.5
Jaeger	1.6	150.64	152.3
Judge Sissons	4.6	132.4	137.0
Pointer	1.39	141.9	143.4
Sleek	1.5	149.7	151.2
Squiggly	6.0	213	219.0

Although there are some other lakes in the vicinity of the Kiggavik project, it is assumed that the impact of such lakes could be neglected due to the size of the lake or the large distance between the lake and project location. Therefore, no-flow condition is assumed for the side boundaries of the 3D model as shown in Figure 10-4.

10.5 Simulation Results

The 3D constructed geometry with the appropriate material properties are used in the COMSOL MultiPhysics software to investigate the underground water level in long-term when the permafrost is completely thawed.

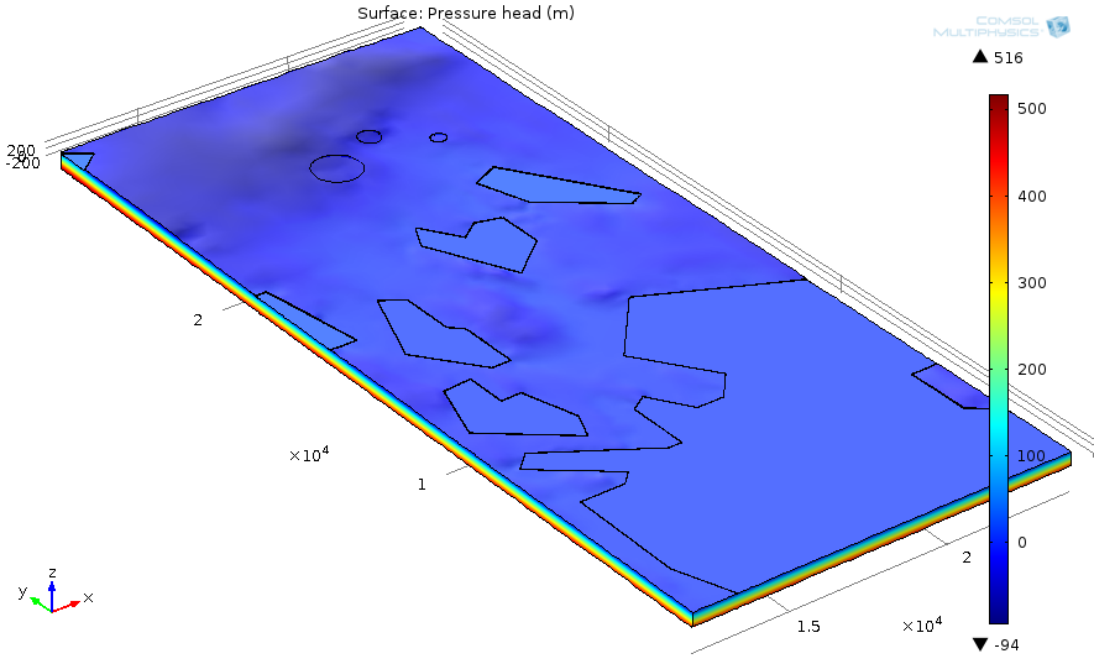

Figure 10-5 Pressure head in the 3D model when the permafrost is completely thawed in long-term

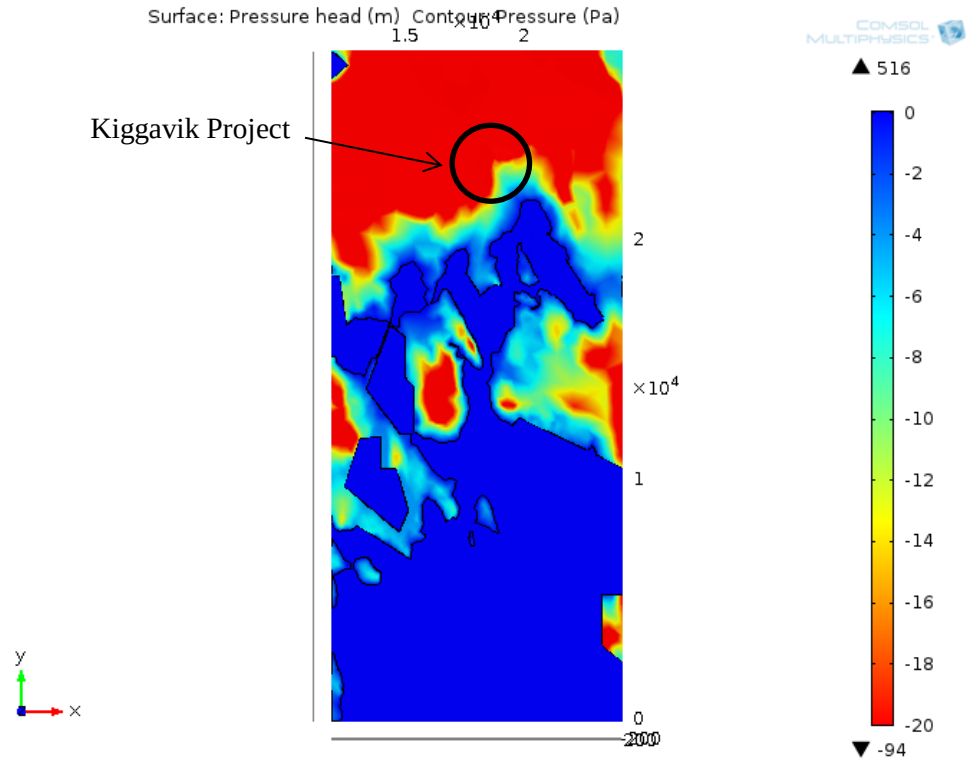

Figure 10-6 Pressure head distribution at ground surface – Plan view

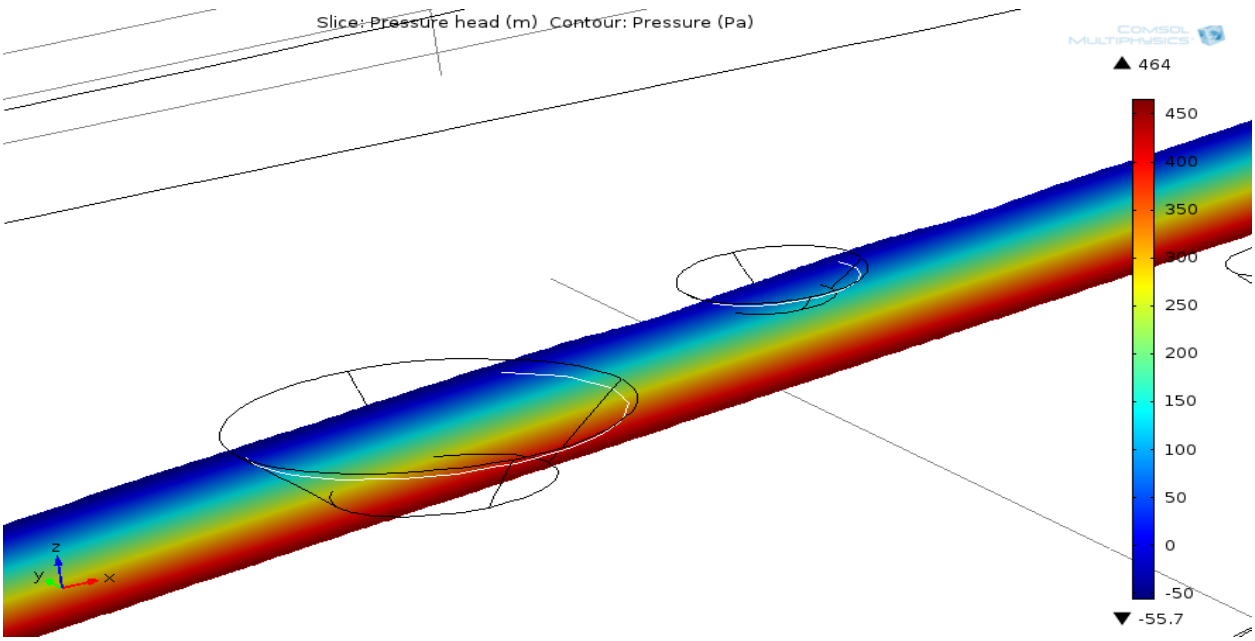

Figure 10-7 Pressure head distribution in the section passing through the Main Zone and Centre Zone TMFs

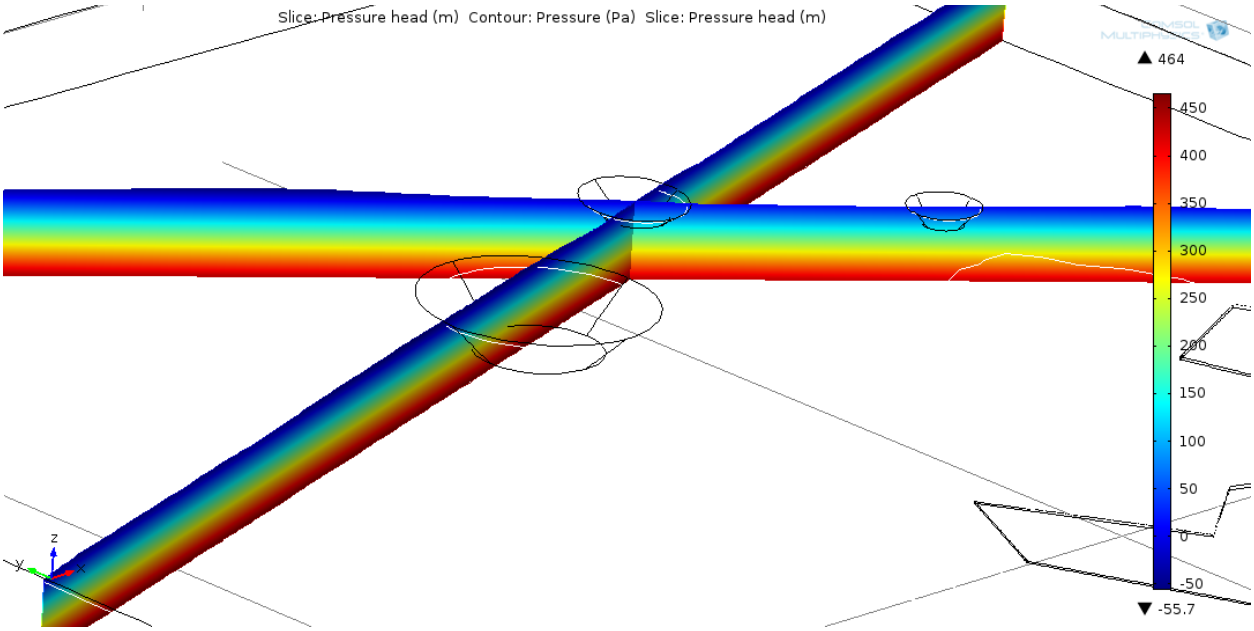

Figure 10-8 Pressure head distribution in the section passing through the Main Zone, Centre Zone, and East Zone TMFs

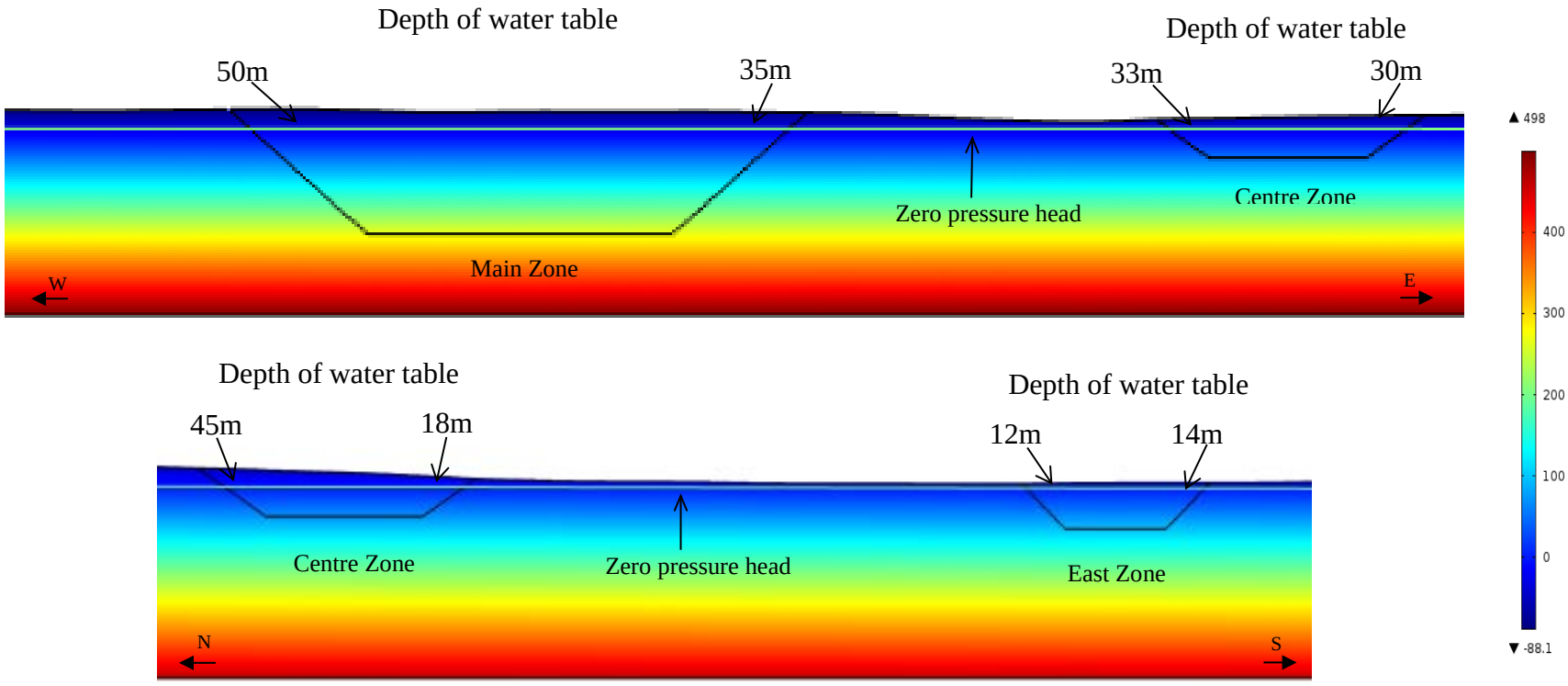

Figure 10-9 Pressure head distribution in 2D cut planes passing through Main Zone and Centre Zone; and through Centre Zone and East Zone

10.6 Analyzing Results

Reviewing the results in Section 10.5, the following main points could be reached:

When the permafrost disappears in the long term, depending on the surface topography, the water table will be either below or above ground surface. The 3D numerical simulation results show that part of the ground surface will be underneath water as shown in Figure 10-6 where the pressure heads are positive or zero. Areas where the water level is below ground surface are shown with negative pressure heads and include the proposed location of the Kiggavik project. Hence, the numerical simulations suggest that water containing contaminants is unlikely to overflow to the ground surface at the location of the TMFs.

To investigate the ground water level in more detail in the vicinity of the pits, two vertical planes cutting on the one hand, the Main zone and Centre zone pit axis, and on the other hand, the Centre Zone and East Zone axis are chosen as illustrated in Figures 10-7 and 10-8. As seen in Figure 10-9, the depth of the ground water table at the Main Zone, Centre Zone, and East Zone pits are on an average of 40, 32, and 13 m, respectively, which are within a safe margin against any potential for water overflow to the ground surface under the considered conditions of climate change and the assumptions used for the simulations. The variations in water table depths for all three pits may seem to vary appreciably over not too long distances, but this is due to the changes in the ground surface elevation in the vicinity of the TMFs.

11 References

1. Anisimov, O. A. 1989. Changing climate and permafrost distribution in the Soviet Arctic. Physical Geography, 10, 285-293.
2. AREVA Resourses Canada Inc., Technical Appendixes 2012.ftp://ftp.nirb.ca/02REVIEWS/ACTIVE REVIEWS/09MN003AREVA KIGGAVIK/2REVIEW/06DRAFT EIS & CONFORMITY REVIEW/0DEIS SUBMISSION/
3. Azmatch, T.F.; Sego, D.C.; Arenson, L.U. and Biggar, K.W., 2012. Using soil characteristic curve to estimate the hydraulic conductivity function of partially frozen soils, Cold Regions Science and Technology, 83-84, 103-109.
4. Black, P.B., Tice, A.R., 1989. Comparison of soil freezing and soil water curve data for Windsor sandy loam. Water Resources Research 25, 2205–2210.
5. Brooks, R.H. and Corey A.T., 1966. Properties of Porous Media Affecting Fluid Flow, J. Irrig. Drainage Div., ASCE Proc, vol. 72 (IR2), pp. 61–88.
6. Burn, C.R., 1992. Recent ground warming inferred from the temperature in permafrost near Mayo, Yukon Territory; in Periglacial Geomorphology, (ed) J.C. Dixon and A.D. Abrahams; John Wiley and Sons Ltd., New York, New York, p. 327-350
7. Burn, C.R. and Smith, M.W. 1993. Issues in Canadian Permafrost Research. Progress in Physical Geography June 1993, 17(2), 156-172.
8. Burn, C.R., 1998a. Field investigation of permafrost and climatic change in northwest North America; in Proceedings of Seventh International Conference on Permafrost, Yellowknife, Canada, June 1998; Collection Nordicana No. 57, Universite Laval, Quebec, p. 107-120.
9. Burt, T.P., Williams, P.J., 1974. Measurement of hydraulic conductivity of frozen soils. Canadian Geotechnical Journal 11, 647–650.
10. COMSOL, 2014, COMSOL Multiphysics 4.4, COMSOL Inc. Los Angeles, CA 90024, USA.
11. French, H.M. and Egorov, I.E., 1998. 20th century variations in the southern limit of permafrost near Thompson, northern Manitoba, Canada; in Proceedings of Seventh International Conference on Permafrost, Yellowknife, Canada, June 1998; Collection Nordicana No. 57, Universite Laval, Quebec, p. 297-304.
12. Halsey, L.A.; Vitt, D.H. and Zoltai, S.C., 1995. Disequilibrium response of permafrost in boreal continental western Canada to climate change, Climate Change, v. 30, p. 57-73
13. Hansson, K.; Simunek, J.; Mizoguchi, M.; Lundin, L. and van Genuchten, M. Th., 2004. Water Flow and Heat Transport in Frozen Soil: Numerical Solution and Freeze-Thaw Application. Vadose Zone Journal, 3, 693-704.

14. Harlan, R.L., 1973. Analysis of coupled heat and mass transfer in partial frozen soil. Water Resources Research 9 (5), 1314–1323.

15. Horiguchi, K., Miller, R.D., 1983. Hydraulic conductivity functions of frozen materials. Proc. 4th Int. Conf. Permafrost, National Academy Press, Washington, D.C, pp. 504–508.

16. IPCC, 2007: Climate Change 2007: The Physical Science Basis. Contribution of Working Group I to the Fourth Assessment Report of the Intergovernmental Panel on Climate Change [Solomon, S., D. Qin, M. Manning, Z. Chen, M. Marquis, K.B. Averyt, M. Tignor and H.L. Miller (eds.)]. Cambridge University Press, Cambridge, United Kingdom and New York, NY, USA, 996 pp.

17. II to the Fifth Assessment Report of the Intergovernmental Panel on Climate Change [Field, C.B., V.R. Barros, D.J. Dokken, K.J. Mach, M.D. Mastrandrea, T.E. Bilir, M. Chatterjee, K.L. Ebi, Y.O. Estrada, R.C. Genova, B. Girma, E.S. Kissel,A.N. Levy, S. MacCracken, P.R. Mastrandrea, and L.L. White (eds.)]. Cambridge University Press, Cambridge, United Kingdom and New York, NY, USA, pp. 1-32.

18. IPCC, 2013: Annex I: Atlas of Global and Regional Climate Projections [van Oldenborgh, G.J., M. Collins, J. Arblaster, J.H. Christensen, J. Marotzke, S.B. Power, M. Rummukainen and T. Zhou (eds.)]. In: Climate Change 2013: The Physical Science Basis. Contribution of Working Group I to the Fifth Assessment Report of the Intergovernmental Panel on Climate Change [Stocker, T.F., D. Qin, G.-K. Plattner, M. Tignor, S.K. Allen, J. Boschung, A. Nauels, Y. Xia, V. Bex and P.M. Midgley (eds.)]. Cambridge University Press, Cambridge, United Kingdom and New York, NY, USA.

19. IPCC, 2013: Annex II: Climate System Scenario Tables [Prather, M., G. Flato, P. Friedlingstein, C. Jones, J.-F. Lamarque, H. Liao and P. Rasch (eds.)]. In: Climate Change 2013: The Physical Science Basis. Contribution of Working Group I to the Fifth Assessment Report of the Intergovernmental Panel on Climate Change [Stocker, T.F., D. Qin, G.-K. Plattner, M. Tignor, S.K. Allen, J. Boschung, A. Nauels, Y. Xia, V. Bex and P.M. Midgley (eds.)]. Cambridge University Press, Cambridge, United Kingdom and New York, NY, USA.

20. IPCC, 2014: Summary for policymakers. In: Climate Change 2014: Impacts, Adaptation, and Vulnerability. Part A: Global and Sectoral Aspects. Contribution of Working Group

21. Jame, Y.W., Norum, D.I., 1980. Heat and mass transfer in freezing unsaturated porous media. Water Resources Research 16, 811–819.

22. Kane, D.L., Hinzman, L.D. and Zarling, J.P. 1991. Thermal response of the active layer to climatic warming in a permafrost environment. Cold Regions Science and Technology 19, 111-22.

23. Khosravani, Sarah, 2014. An Effective Stress Equation for Unsaturated Granular Media in Pendular Regime. University of Calgary, Calgary, Alberta, Canada.

24. Konrad, J.M., Morgenstern, N.R., 1980. A mechanistic theory of ice lens formation in fine-grained soils. Canadian Geotechnical Journal 17, 473–486.

25. Koopmans, R.W.R., Miller, R.D., 1966. Soil freezing and soil water characteristic curves. Soil Science Society of America Proceedings 30, 680–685.

26. Laberge, M.J. and Payette, S., 1995. Long-term monitoring of permafrost change in a palsa peatland in northern Quebec, Canada: 1983-1993; Arctic and Alpine Research, v. 27, p. 167-171.

27. Lachenbruch, A.H. and B.V. Marshall (1986). Changing Climate: Geothermal Evidence from Permafrost in the Alaskan Arctic. Science, 234: 689-696.

28. Lundin, L.Ch., 1990. Hydraulic properties in an operational model of frozen soil. Journal of Hydrology 118, 289–310.

29. Mottaghy, D., Rath, V. 2006. Latent heat effects in subsurface heat transport modelling and their impact on palaeo-temperature reconstructions. International Journal of Geophysics 164, 236–245.

30. Nelson, F.E. and Outcalt, S.I. 1983. A frost index number for spacial prediction of ground-frost zones. Proceedings of the 4th International Permafrost Conference, National Academy Press, Washington DC, 1, 907-911.

31. Newman, G.P., Wilson, G.W., 1997. Heat and mass transfer in unsaturated soils during freezing. Canadian Geotechnical Journal 34, 63–70.

32. Noetzli, J., Gruber, S. 2009. Transient thermal effects in Alpine permafrost. The Cryosphere 3, 85–99.

33. Outcalt, S. I. 1972. The development and application of a simple digital surface climate simulator. Journal of applied meteorology, 11, 629-636.

34. Romero-Lankao, P., J.B. Smith, D.J. Davidson, N.S. Diffenbaugh, P.L. Kinney, P. Kirshen, P. Kovacs, and L. Villers Ruiz, 2014: North America. In: Climate Change 2014: Impacts, Adaptation, and Vulnerability. Part B: Regional Aspects. Contribution of Working Group II to the Fifth Assessment Report of the Intergovernmental Panel on Climate Change [Barros, V.R., C.B. Field, D.J. Dokken, M.D. Mastrandrea, K.J. Mach, T.E. Bilir, M. Chatterjee, K.L. Ebi, Y.O. Estrada, R.C. Genova, B. Girma, E.S. Kissel, A.N. Levy, S. MacCracken, P.R. Mastrandrea, and L.L. White (eds.)]. Cambridge University Press, Cambridge, United Kingdom and New York, NY, USA, pp. 1439-1498.

35. Spaans, E.J.A., Baker, J.M., 1996. The soil freezing characteristic: its measurement and similarity to the soil moisture characteristic. Soil Science Society of America Journal 60, 13–19.

36. Tao, Y.X., Gray, D.M., 1994. Prediction of snowmelt infiltration into frozen soils. Numerical Heat Transfer Part A: Applications 26, 643–665.

37. Taylor, G.S., Luthin, J.N., 1978. A model for coupled heat and moisture transfer during soil freezing. Canadian Geotechnical Journal 15, 548–555.

38. van Genuchten, M.Th., 1980. A Closed-form Equation for Predicting the Hydraulic of Conductivity of Unsaturated Soils, Soil Sci. Soc. Am. J., vol. 44, pp. 892–898.

39. Williams, P., 1964. Unfrozen water content of frozen soil and soil moisture suction. Geotechnique 14, 231–246.

12 Appendix A- Large Strain Consolidation Theory

A 1. Introduction

The mining plan in the Kiggavik project includes the backfilling of excavated pits with tailings. Tailing with high initial water content undergoes large strain consolidations. It is essential to investigate the process of consolidation, especially if the mining plan includes back filling the TMFs free spaces with fresh tailings prior to the consolidation of old tailings during the operational time.

In this Appendix, first, the 1D consolidation of Terzaghi is explained. Then, the Finite Strain theory (Gibson et. al., 1967 & 1981) used for large strain consolidation is explained. The finite strain theory is applied in the COMSOL software to simulate the consolidation of tailings.

A 2. Terzaghi 1D consolidation theory

The first theory enabling the prediction of one-dimensional consolidation in soils was published by Terzaghi (1924). Some simplifying assumptions made for this theory limited its application to the relatively stiff thin layers at large depths. In this theory it is assumed that:

1) The soil is saturated, isotropic, and homogeneous.
2) Darcy's law is valid.
3) Fluid flow only occurs vertically.
4) The strains are small, and relationship between volume change and effective stress is linear.
5) Both solid particles and pore fluid are incompressible.

To find the appropriate governing equation, three physics of vertical equilibrium, pore fluid continuity, and fluid flow should be satisfied.

According to the fluid continuity, the net flow of water out of the soil should be equal to the rate of change of volume.

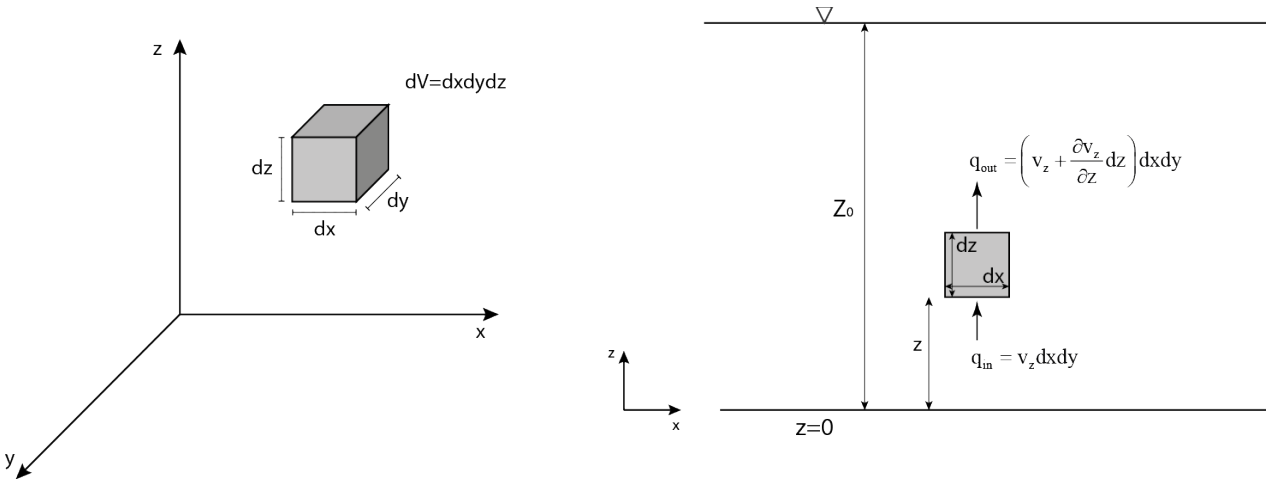

Figure A-1 Small element of soil within the ground profile

$$q = vA \tag{1}$$

$$q_{out} - q_{in} = \frac{\partial(\Delta V)}{\partial t} \tag{2}$$

$$\left[v_z + \frac{\partial v_z}{\partial z} dz \right] dydx - v_z dydx = \frac{\partial(\Delta V)}{\partial t} \tag{3}$$

$$\frac{\partial v_z}{\partial z} = \frac{\partial(\Delta V / dV_0)}{\partial t} = \frac{\partial \varepsilon_z}{\partial t} \tag{4}$$

Where q_{in} and q_{out} are fluid flux into and out of the element, respectively; v_z is the fluid velocity in the vertical direction; dV_0 is the initial volume of the element (see Figure A-1); and ε_z is the vertical strain of the element.

By writing the vertical equilibrium in the soil sample it could be seen that $\Delta\sigma' = -\Delta u_e$, where σ' is the effective stress and u_e is the excess pore pressure. Therefore, we could write:

$$\varepsilon_z = -m_v \Delta\sigma' = m_v \Delta u_e = m_v (u_e - u_{e0}) \tag{5}$$

where m_v is coefficient of compressibility and u_{e0} is the initial excess pore pressure. Replacing ε_z from Eq.(5) into Eq. (4) :

$$\frac{\partial v_z}{\partial z} = \frac{\partial \left(m_v (u_e - u_0) \right)}{\partial t} = m_v \frac{\partial u_e}{\partial t} \qquad 6$$

Now, by using the Darcy's law in vertical direction:

$$v_z = -k \frac{\partial H}{\partial z} \qquad 7$$

$$H = z + \frac{u}{\gamma_w} = z + \frac{u_h + u_e}{\gamma_w} \qquad 8$$

$$v_z = -k \frac{\partial}{\partial z} \left(z + \frac{(Z_0 - z)\gamma_w}{\gamma_w} + \frac{u_e}{\gamma_w} \right) = \frac{-k}{\gamma_w} \frac{\partial u_e}{\partial z} \qquad 9$$

Here, H is the total head; u_h is the hydrostatic pore pressure; k is soil permeability; and Z_0 is the initial depth of ground profile (see Figure 1). Finally, substituting Eq(9) into Eq(6) results in the governing equation for excess pore pressure dissipation in vertical direction.

$$\frac{-k}{m_v \gamma_w} \frac{\partial^2 u_e}{\partial z^2} = \frac{\partial u_e}{\partial t} \qquad 10$$

A 3. Finite strain consolidation theory

While many authors offered alternatives to Terzaghi's 1D equation (e.g. Shiffman and Gibson (1964); Davis and Rymond (1965)), the first general theory of 1D consolidation in soils was published by Gibson, England, and Hussey (1967).

The basic assumptions necessary for the development of the theory of one-dimensional finite strain consolidation are:

1) The soil system is saturated and consists of a compressible soil matrix and incompressible pore fluid. While the soil matrix is considered compressible, individual soil particles are incompressible.
2) Pore fluid flow velocities are small and governed by Darcy's law.
3) There is a unique relationship between soil permeability and void ratio ($k = k(e)$)

4) There is a unique relationship between vertical effective stress and void ratio ($\sigma' = \sigma'(e)$)
5) The material is homogeneous

In this section, in order to explain this general consolidation theory, first, the coordinate system chosen by Gibson et. al. (1967) is explained. Then, the necessary physical relationships and the governing equation are explained.

A 4. Coordinate system

The usual coordinate system used in the geotechnical engineering is the Eulerian coordinate system in which deformation is related to some fixed planes. This system is appropriate for the infinitesimal strain theories of consolidation which assume that the thickness of the compressible layer is almost constant, and the soil layer deformation during consolidation is small compared with its thickness. However, if the deformations are large, the use of the Euilerian system could be very inconvenient.

The other coordinate system that could be used is the Lagrangian system where all the changes are referred to an initial (t=0) configuration ("a" coordinate in Figure 2). Therefore, the Lagrangian system is related to the measurements at t= 0. For time " t " during the consolidation process, measurements should be made in terms of a convective coordinate system that is a function of the Lagrangian coordinate system and time (Figure A-2).

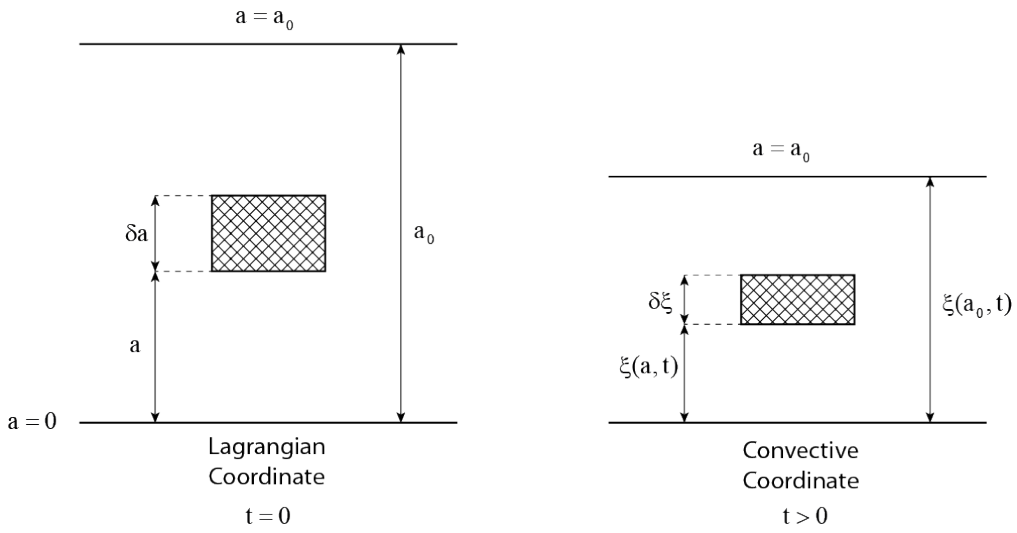

Figure A-2 Lagrangian and Convective coordinate systems

From a physical point of view, it is convenient to express the dependent variables in terms of convective coordinate system (ξ) (see Figure A-2). However, this is mathematically inconvenient since ξ is function of the coordinate " a " and time.

Another set of coordinates defined by Ortenblad (1930) is based upon the volume of soil particles laying between a datum plane (e.g. $a = 0$) and the point being analyzed. This coordinate is named reduced or material coordinate. This coordinate system is suited for the time dependent consolidation problem since it moves with the soil layers, and it is independent of time or amount of settlement. This coordinate is only function of initial coordinate (a).

While, Lagrangian and convective coordinates include both solid soil particles and the pore fluid, the material (reduced) coordinate is only a measure of the volume of solid particles. A comparison of these three systems is made schematically in Figure A-3. In this figure, Lagrangian, convective and material coordinates are indicated by symbols a, ξ , and z, respectively. It is assumed that each grain has a unit volume, the initial soil height was 100 and at the time $t > 0$ the height changes to 80. As shown in this figure, only the Lagrangian and material coordinates are constant for all time for particular points in the soil layer. It is convenient to develop the governing equation in terms of either of these systems. In the equations defined by Gibson et. al. (1967), the material coordinates are used.

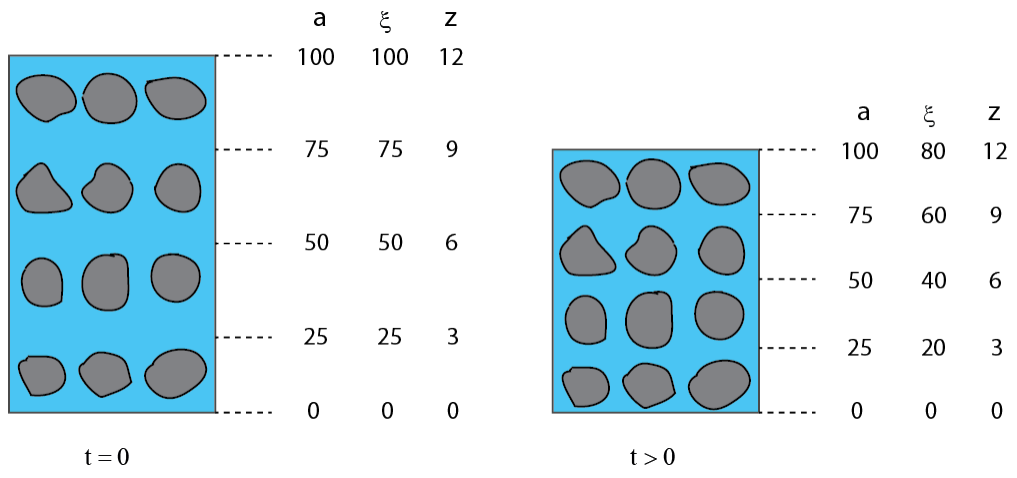

Figure A-3 Comparison of coordinate systems

Since the material coordinates are not measurable in the usual sense, a conversion method should be defined to move from one coordinate to the other. In Figure A-4, differential elements of soils are shown in three coordinate systems. It is assumed that the elements encompass a unit volume of solid particles.

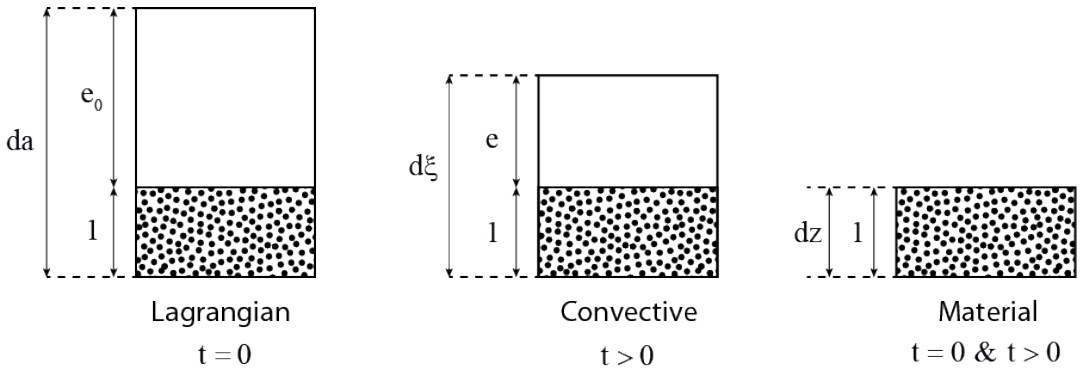

Figure A-4 Differential soil elements in three different coordinates

Regarding the differential soil elements in Figure A-4:

$$da = 1 + e_0 \tag{11}$$

$$d\xi = 1 + e \tag{12}$$

$$dz = 1 \tag{13}$$

Where e_0 is the initial void ration and e is the void ration at time $t > 0$. By simple ration it could be shown that:

$$\frac{dz}{da} = \frac{1}{1 + e_0} \tag{14}$$

$$\frac{\partial \xi}{\partial z} = 1 + e \tag{15}$$

$$\frac{\partial \xi}{\partial a} = \frac{1 + e}{1 + e_0} \tag{16}$$

Therefore, the material coordinate (z) could be easily find by knowing the initial void ration

$$z = \int_0^a \frac{da'}{1+e(a,0)} \qquad 17$$

In the following sections, the physical expressions required to find the governing equation are expressed in the convenient coordinate system, and then they are transformed into material coordinate system.

A 5. Vertical equilibrium

In Figure A-5 an element of soil with unit width and unit volume of solid particles is considered.

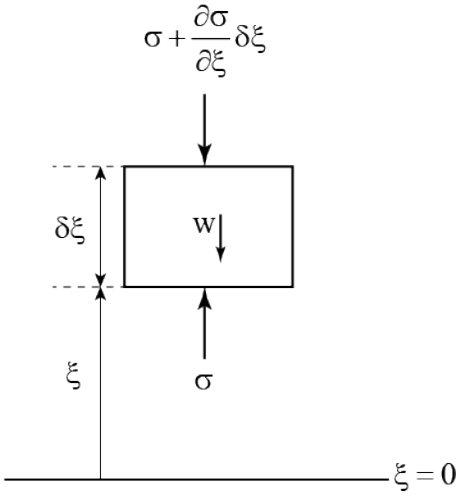

Figure A-5 Vertical forces acting on an element of soil with unit width and unit volume of solids

Weight of sample is the summation of weight of solids and pore fluids:

$$W = e\gamma_w + 1 \times \gamma_s \qquad 18$$

For the vertical equilibrium:

$$\sigma + \frac{\partial \sigma}{\partial \xi}\delta\xi + e\gamma_w + \gamma_s - \sigma = 0 \qquad 19$$

where σ is the total stress. By using Eq(12):

$$\frac{\partial \sigma}{\partial \xi} + \frac{e\gamma_w + \gamma_s}{1+e} = 0 \qquad 20$$

Multiplying Eq(20) by $\frac{\partial \xi}{\partial z}$ gives the equilibrium equation in the material coordinate system:

$$\frac{\partial \sigma}{\partial z} + e\gamma_w + \gamma_s = 0 \qquad 21$$

The relation between total pore pressure (P), hydrostatic pore pressure (u_h), and excess pore pressure (u_e) can be written in the form of:

$$P = u_h + u_e \qquad 22$$

$$\frac{\partial P}{\partial \xi} - \frac{\partial u_e}{\partial \xi} + \gamma_w = 0 \qquad 23$$

$$\frac{\partial P}{\partial z} - \frac{\partial u_e}{\partial z} + \gamma_w (1+e) = 0 \qquad 24$$

A 6. Fluid continuity

To determine the equation of continuity, the net inflow/outflow of fluid must be equal to the time rate of change of weight of fluid inside the element.

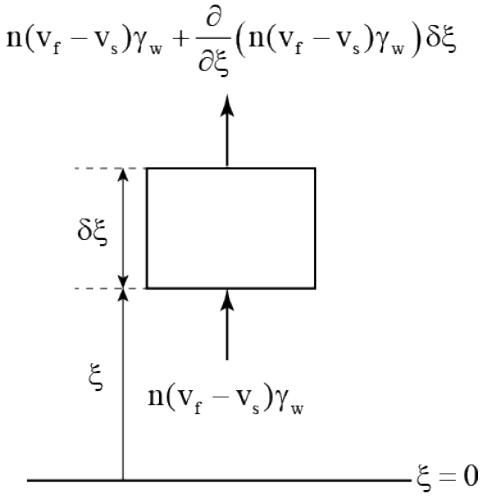

Figure A-6 Fluid flow into and out of an element

$$\frac{\partial}{\partial \xi}\left[n(v_f - v_s)\gamma_w\right]\delta\xi + \frac{\partial}{\partial t}\left(e\gamma_w\right) = 0 \qquad 25$$

Where v_f and v_s are fluid and solid particles velocities, respectively, and n is the soil porosity. Here, it is assumed that the pore fluid is incompressible. Additionally, by considering constant unit weight for the fluid and using Eq(12) and Eq(15) , the continuity equation in the material coordinate system could be written:

$$\frac{\partial}{\partial z}\left[n(v_f - v_s)\right] + \frac{\partial e}{\partial t} = 0 \qquad 26$$

$$\frac{\partial}{\partial z}\left[\frac{e(v_f - v_s)}{1+e}\right] + \frac{\partial e}{\partial t} = 0 \qquad 27$$

A 7. Fluid flow

Gibson et. al. (1967) assumed that the pore fluid flow velocities are small and governed by the Darcy's law.

$$n(v_f - v_s) = -\frac{k}{\gamma_w}\frac{\partial u_e}{\partial \xi} \qquad 28$$

By using Eq(24) the Darcy's law could be written in terms of total pore pressure:

$$\frac{e(v_f - v_s)}{1+e} = -\frac{k}{\gamma_w}\left(\frac{\partial P}{\partial \xi} + \gamma_w\right) \qquad 29$$

$$e(v_f - v_s) = -\frac{k}{\gamma_w}\left[\frac{\partial P}{\partial z} + \gamma_w(1+e)\right] \qquad 30$$

A 8. Governing equation

Now by combining Eqs (21), (27), and (30) with the following definition of effective stress (Eq(31)) could produce the general consolidation governing equation.

$$\sigma = \sigma' + P \qquad 31$$

By combining Eq(27) with Eq(30), the velocity term could be eliminated:

$$\frac{\partial}{\partial z}\left[-\frac{k}{\gamma_w(1+e)}\left(\frac{\partial P}{\partial z}+\gamma_w+e\gamma_w\right)\right]+\frac{\partial e}{\partial t}=0 \qquad 32$$

Then by using Eq(31), total pore pressure (P) will be eliminated:

$$\frac{\partial}{\partial z}\left[-\frac{k}{\gamma_w(1+e)}\left(\frac{\partial \sigma}{\partial z}-\frac{\partial \sigma'}{\partial z}+(1+e)\gamma_w\right)\right]+\frac{\partial e}{\partial t}=0 \qquad 33$$

and finally, using Eq. (21) to eliminate the total stress (σ):

$$\frac{\partial}{\partial z}\left[-\frac{k}{\gamma_w(1+e)}\left(-\gamma_s-\frac{\partial \sigma'}{\partial z}+\gamma_w\right)\right]+\frac{\partial e}{\partial t}=0 \qquad 34$$

Since k and σ' are only functions of void ratio, Eq(34) could be written in the following form:

$$\left(\frac{\gamma_s}{\gamma_w}-1\right)\frac{d}{de}\left[\frac{k(e)}{1+e}\right]\frac{\partial e}{\partial z}+\frac{\partial}{\partial z}\left[\frac{k(e)}{\gamma_w(1+e)}\frac{d\sigma'}{de}\frac{\partial e}{\partial z}\right]+\frac{\partial e}{\partial t}=0 \qquad 35$$

Eq(35) is the general governing equation for one dimensional soil consolidation. In this governing equation, the assumption of small strains is removed, and the relation between stress and strain is not necessarily linear. In fact, the dependence of k and σ' on the void ratio should be find through lab or field testing. Then, by solving this governing equation, the void ration could be find as a function of material coordinate (z) and time ($e(z,t)$). By using appropriate equations, the real depth of soil layer, total and effective stresses, and excess pore pressure at any time could be calculated.

13 Appendix B

The results of numerical simulations for scenario 1, i.e. No Climate Change, are presented in section 8. In that section, only results of numerical models with initial tailing temperature of +5ºC are presented. In this appendix, results of models with initial tailing temperature of +10ºC are indicated.

B 1. East Zone

In this section, the numerical simulation results for Scenario 1, No Climate Change, are presented for the East Zone TMF.

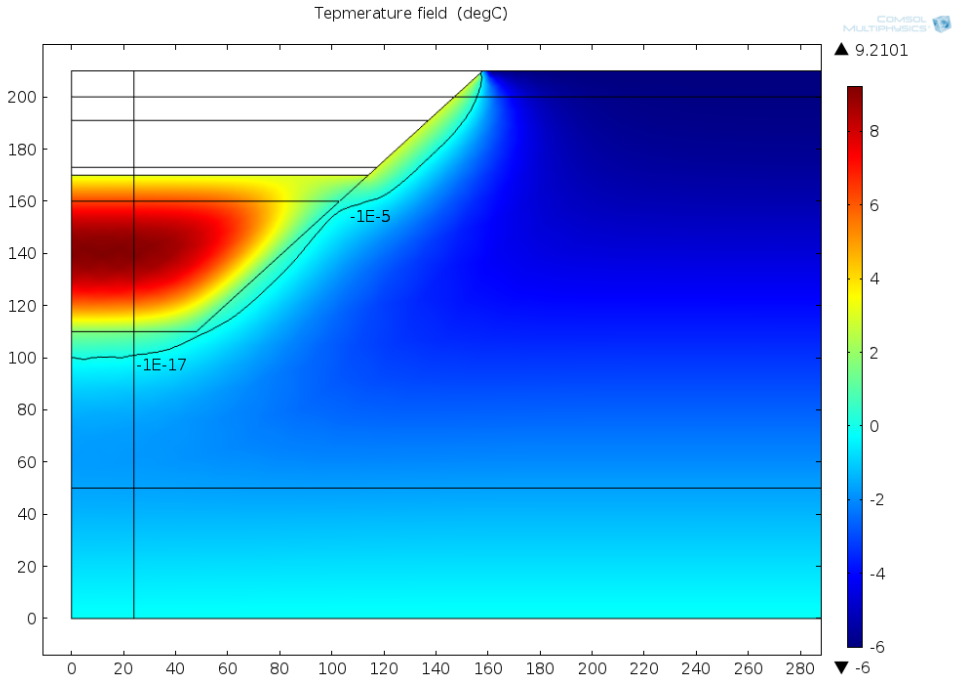

Figure B-1 East Zone TMF, Thermal changes during stage 1 of consolidation, Initial tailings temperature +10ºC

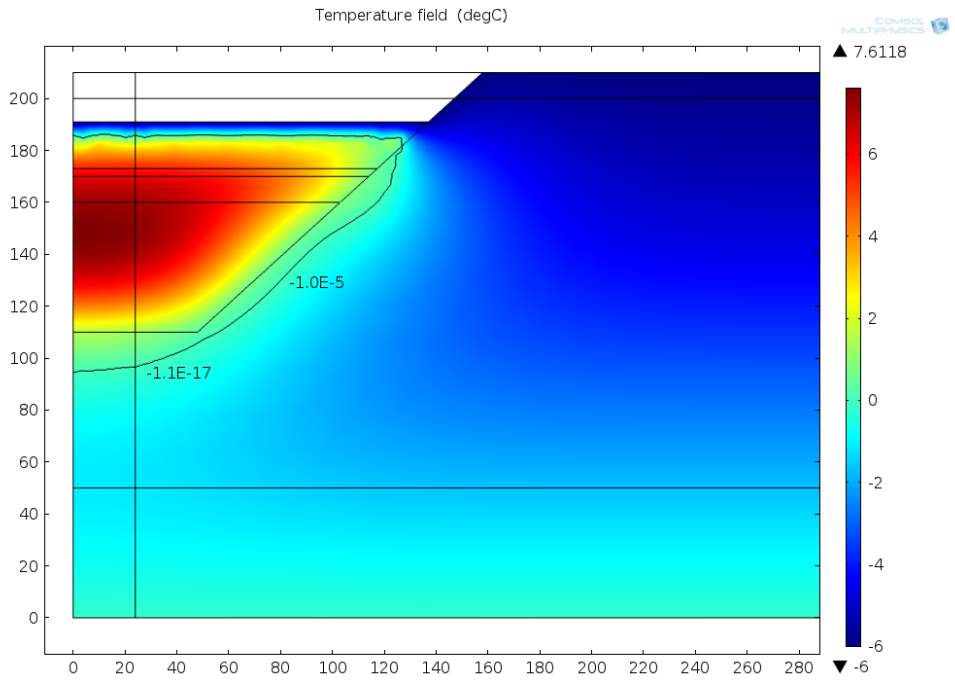

Figure B-2 East Zone TMF, Thermal changes during stage 2 of consolidation, Initial tailings temperature +10ºC

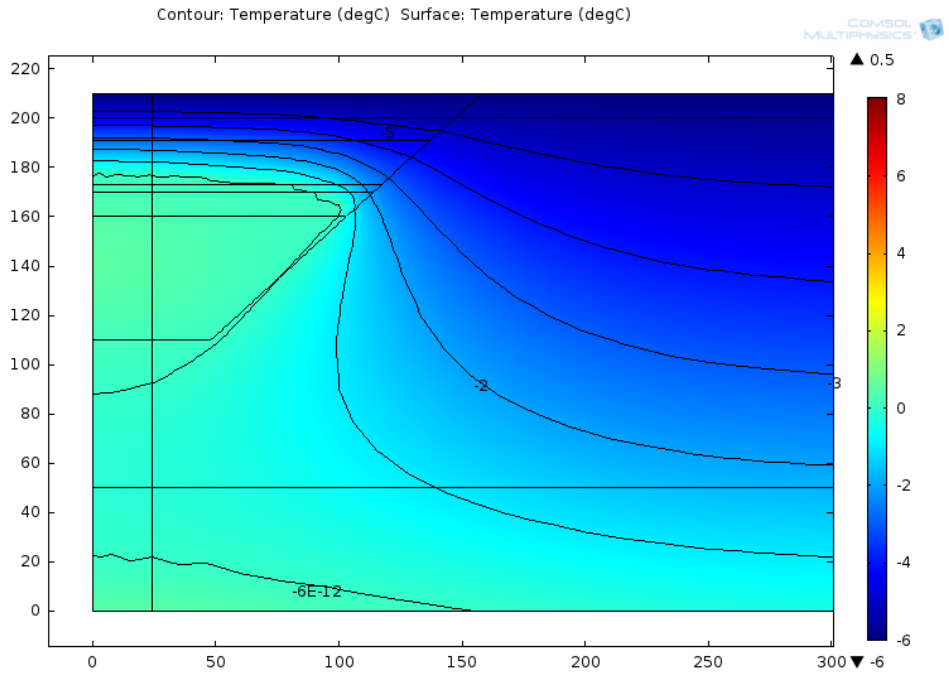

Figure B-3 East Zone TMF, Thermal changes after 100 years, mine rocks are places on top of tailings, Initial tailings temperature +10ºC

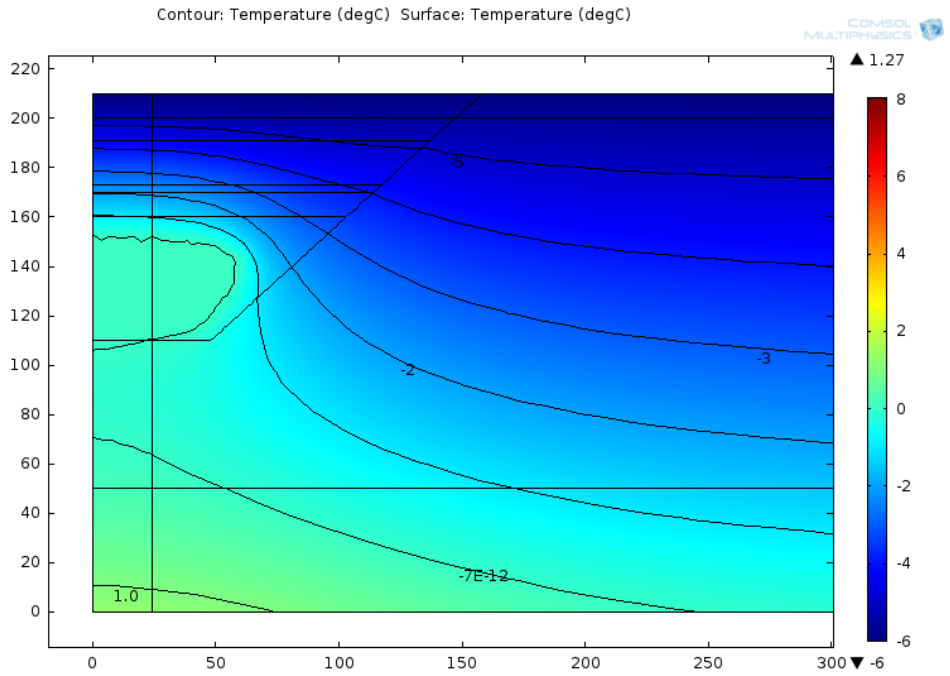

Figure B-4 East Zone TMF, Thermal changes after 500 years, mine rocks are places on top of tailings, Initial tailings temperature +10ºC

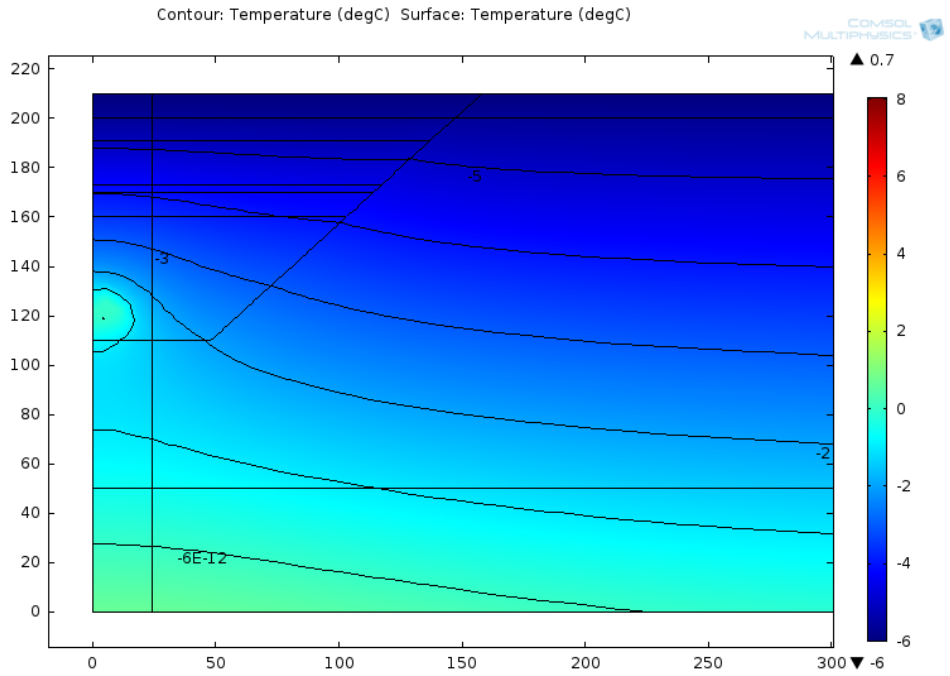

Figure B-5 East Zone TMF, Thermal changes after 1000 years, mine rocks are places on top of tailings, Initial tailings temperature +10ºC

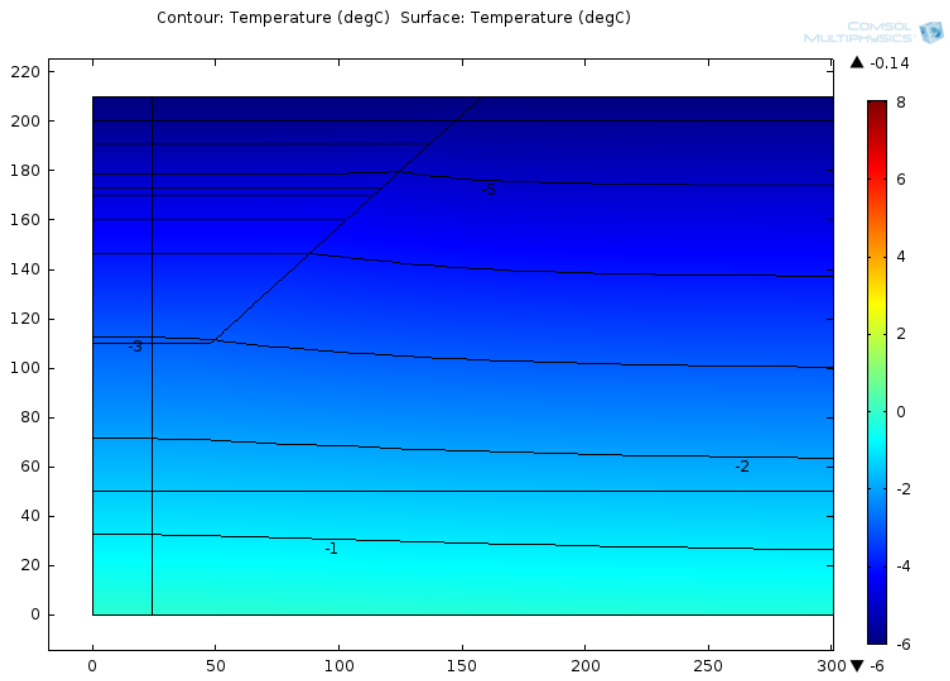

Figure B-6 East Zone TMF, Thermal changes after 2000 years, mine rocks are places on top of tailings, Initial tailings temperature +10ºC

B 2. Centre Zone

In this section, the numerical results of scenario 1, No Climate Change, are presented for Centre Zone TMF. In this section, the results for the initial tailing temperature of +10ºC are presented.

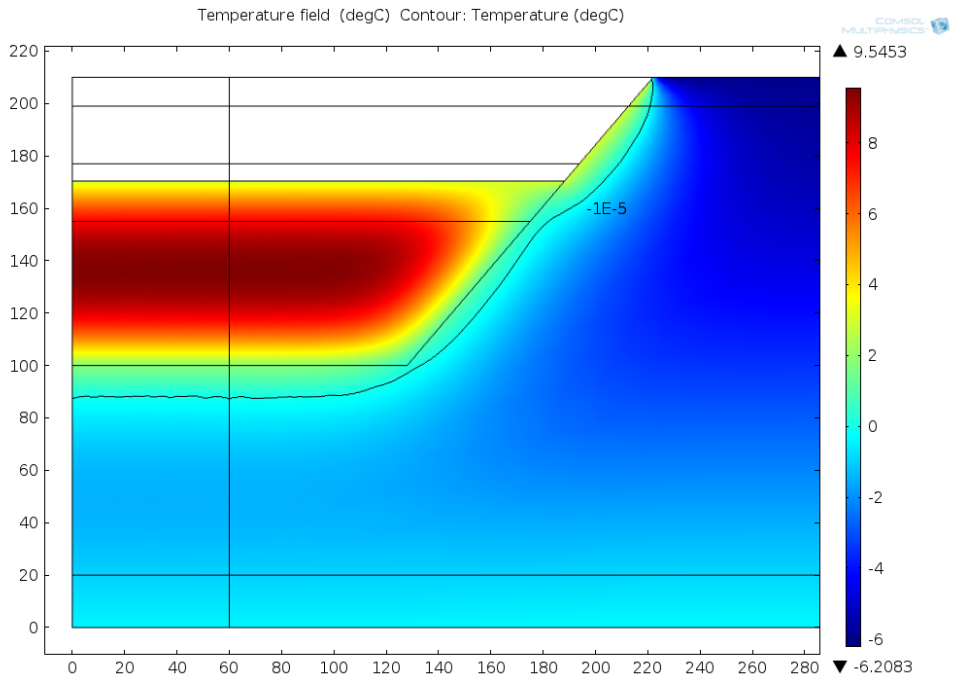

Figure B-7 East Zone TMF, Thermal changes during stage 1 of consolidation, Initial tailings temperature +10ºC

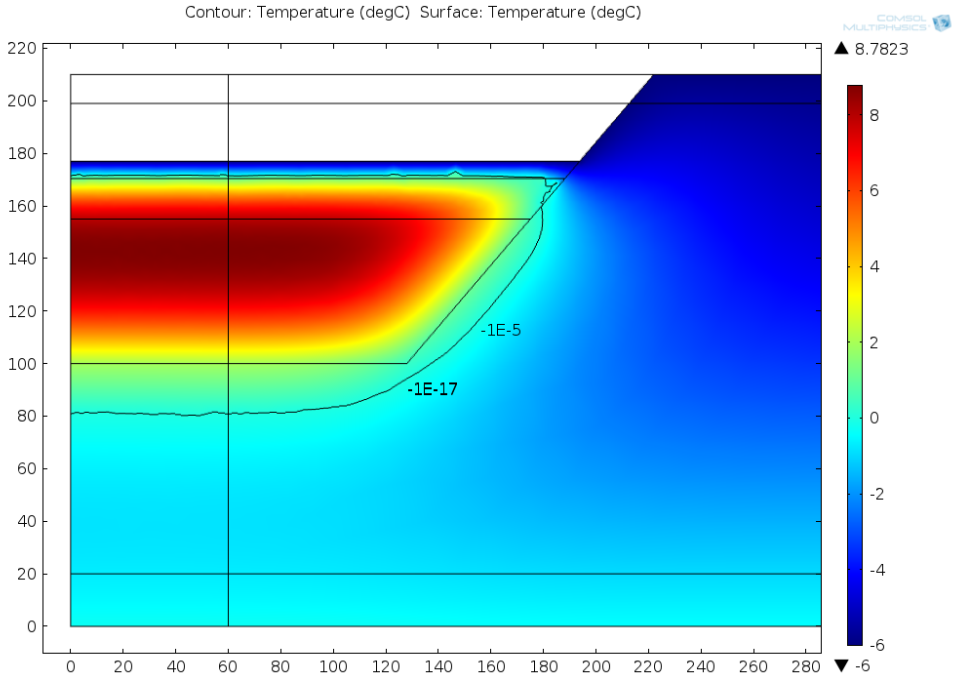

Figure B-8 Centre Zone TMF, Thermal changes at the end of stage 2 of consolidation, Initial tailings temperature +10ºC

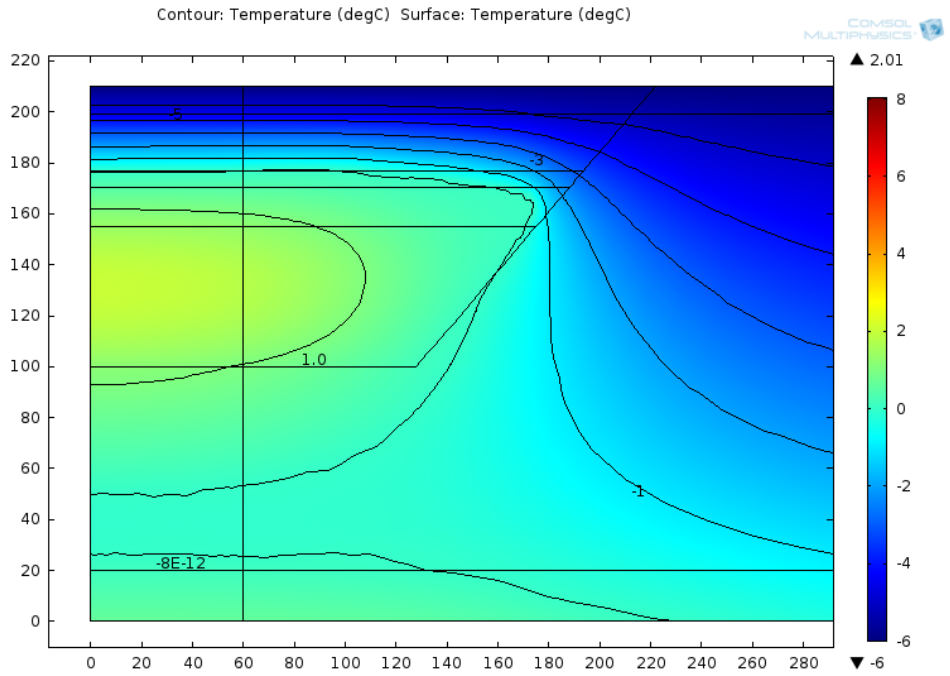

Figure B-9 Centre Zone TMF, Thermal changes after 100 years, mine rocks are places on top of tailings, Initial tailings temperature +10ºC

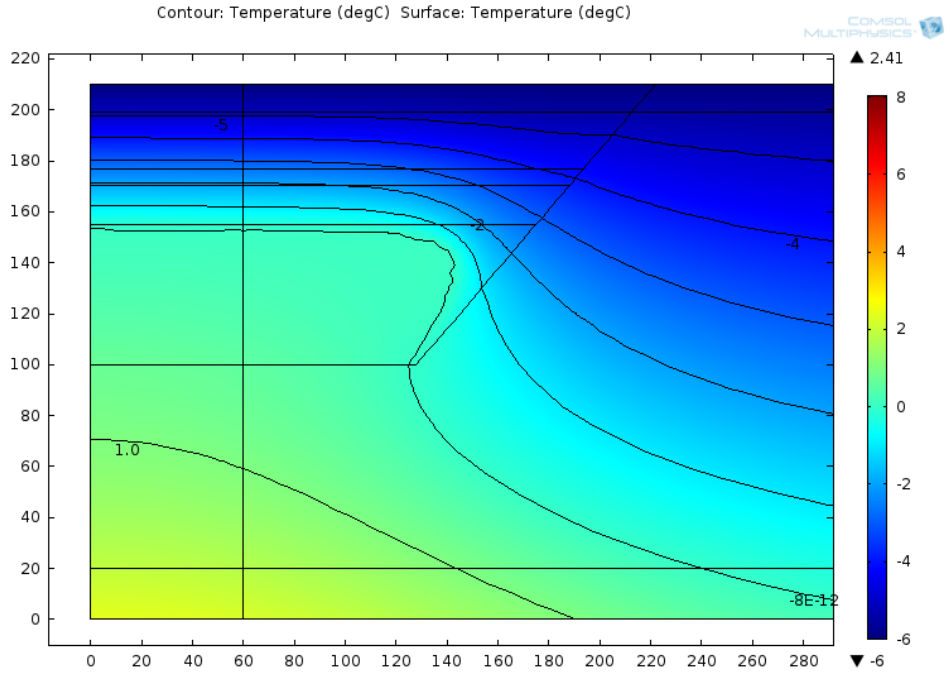

Figure B-10 Centre Zone TMF, Thermal changes after 500 years, mine rocks are places on top of tailings, Initial tailings temperature +10ºC

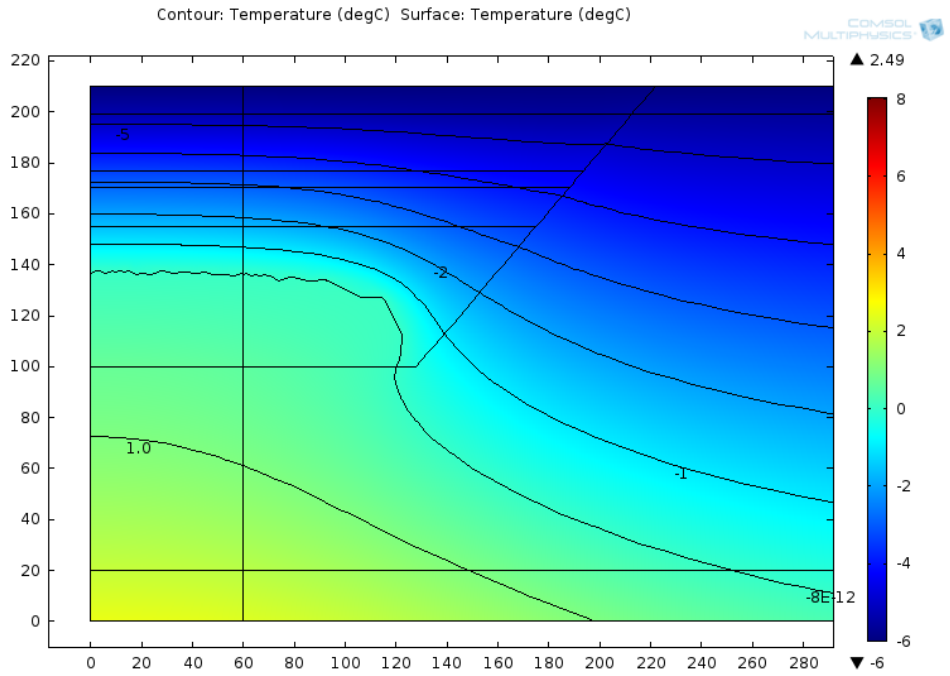

Figure B-11 Centre Zone TMF, Thermal changes after 1000 years, mine rocks are places on top of tailings, Initial tailings temperature +10ºC

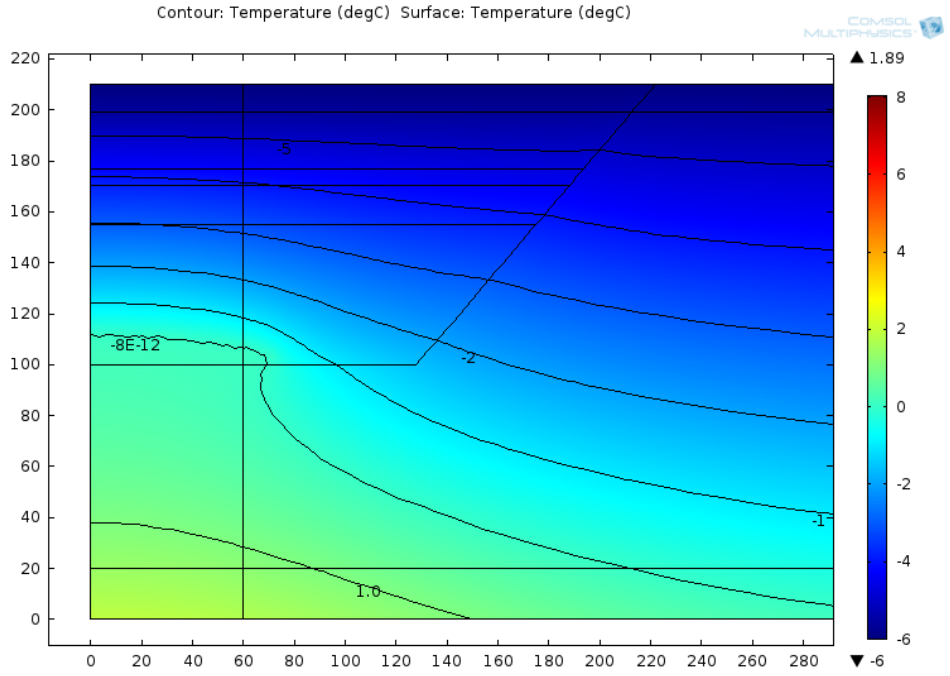

Figure B-12 Centre Zone TMF, Thermal changes after 2000 years, mine rocks are places on top of tailings, Initial tailings temperature +10ºC

B 3. Main Zone

In this section the long-term thermal analyses of the Main Zone TMF are presented. Like the case of East Zone and Centre Zone, two initial temperatures for the tailing material are considered in the simulations. In this section the results for the initial temperature of +10ºC are presented.

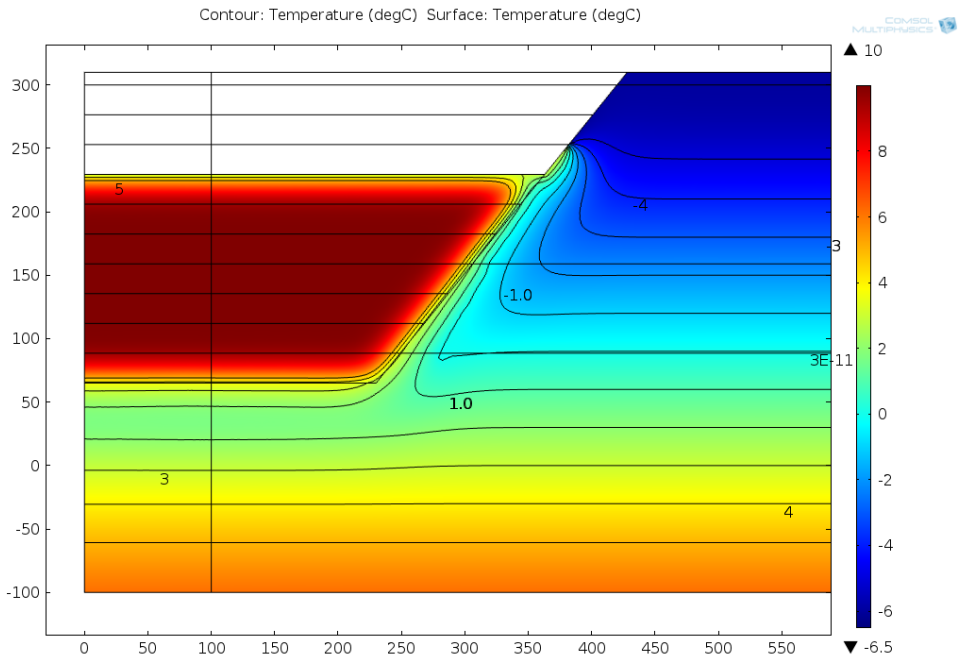

Figure B-13 Main Zone TMF, Thermal changes at the end of consolidation Process, Initial tailings temperature +10ºC

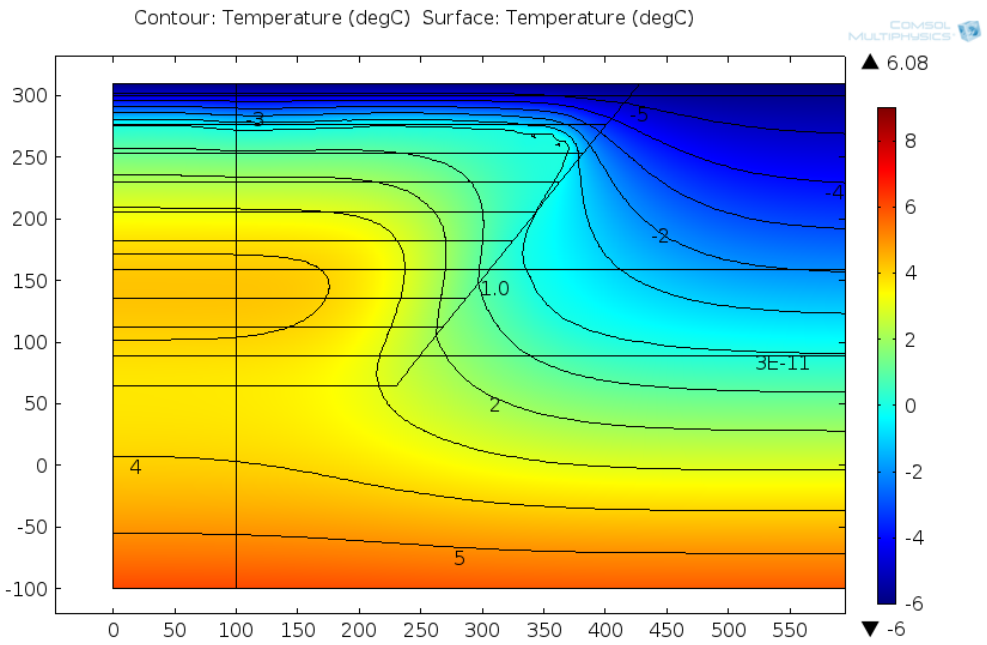

Figure B-14 Main Zone TMF, Thermal changes after 100 years, mine rocks are places on top of tailings, Initial tailings temperature +10ºC

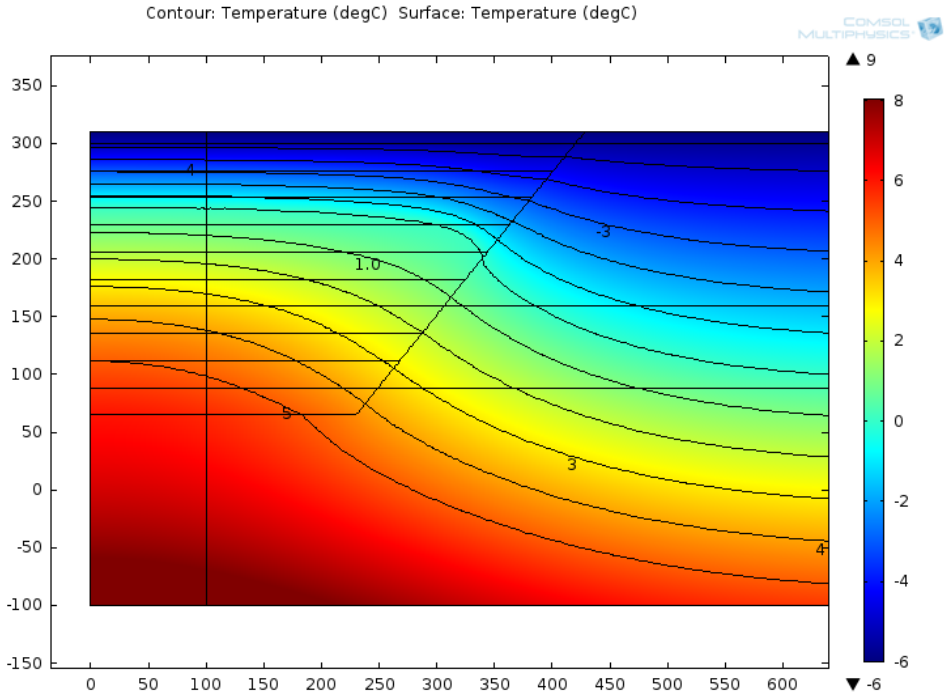

Figure B-15 Main Zone TMF, Thermal changes after 500 years, mine rocks are places on top of tailings, Initial tailings temperature +10ºC

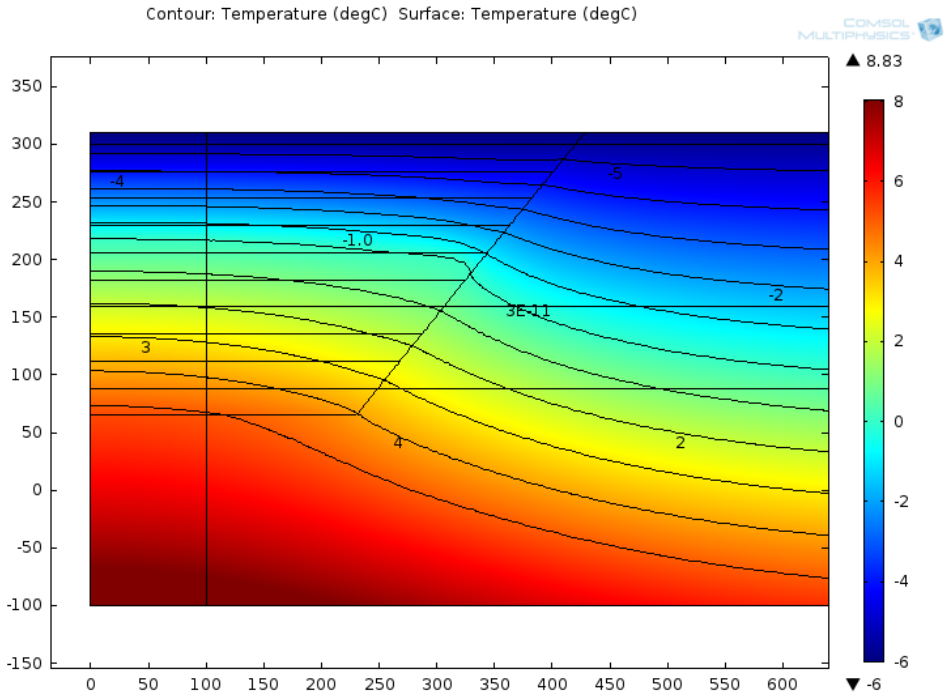

Figure B-16 Main Zone TMF, Thermal changes after 1000 years, mine rocks are places on top of tailings, Initial tailings temperature +10ºC

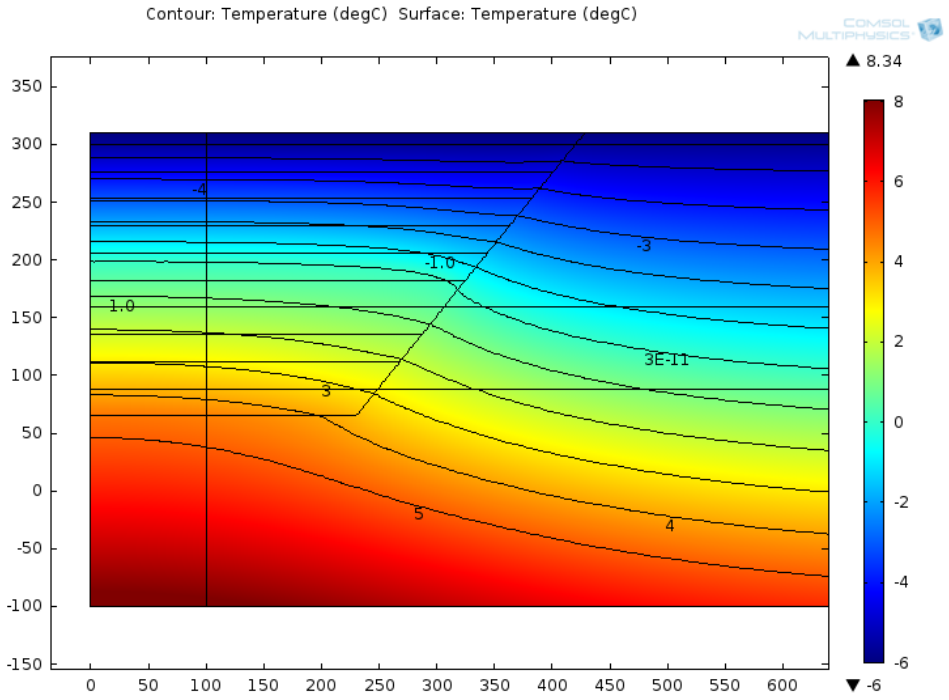

Figure B-17 Main Zone TMF, Thermal changes after 2000 years, mine rocks are places on top of tailings, Initial tailings temperature +10ºC